Title

New insights into single-particle mixing state using aircraft aerosol time-of-flight mass spectrometry

Author

Pratt, Kerri Anne

Publication Date

2009

UNIVERSITY OF CALIFORNIA, SAN DIEGO

New Insights into Single-Particle Mixing State using Aircraft Aerosol Time-of-Flight Mass Spectrometry

A dissertation submitted in partial satisfaction of the requirements for the degree

Doctor of Philosophy

in

Chemistry

by

Kerri Anne Pratt

Committee in charge:

Professor Kimberly A. Prather, Chair
Professor Robert E. Continetti
Professor Katja Lindenberg
Professor Jeffrey P. Severinghaus
Professor Mark H. Thiemens
Professor Wei Wang

2009

This dissertation of Kerri Anne Pratt is approved, and it is acceptable in quality and form for publication on microfilm and electronically:

Chair

University of California, San Diego

2009

Nothing great was ever achieved without enthusiasm.

Ralph Waldo Emerson

Energy and persistence conquer all things.

Benjamin Franklin

Follow your passions, believe in karma,
and you won't have to chase your dreams, they will come to you.

Professor Randy Pausch

Table of Contents

List of Figures

List of Tables

Acknowledgements

First, and foremost, I must thank my thesis advisor Professor Kim Prather for her guidance, encouragement, and support over the past five years. In addition to academic support, Kim was always supportive when life became a little more challenging for me. Thank you for always believing in me. I came to work for Kim because of her enthusiasm. She provided amazing opportunities and helped me to grow and realize my future ambitions. She gave me the opportunity to work on the aircraft project building "Shirley" and then take the ground-based prototype to Riverside several times. Most of all, Kim trusted me to take "SLY" to Colorado, finish building her in her aircraft form, and fly her for the first time. With her encouragement, I have realized that I would like to pursue a career as a university professor and hope to continue in the way of atmospheric chemistry and clouds. Joe Mayer, Kim's husband, taught me much about machining and life, and I enjoyed working with him on the aircraft project. The months proceeding ICE-L were among the most challenging of my life, and Kim and Joe supported me throughout. Thank you.

Several collaborators during ICE-L served as mentors for me in the last years of my graduate studies, widening my breadth of knowledge about cloud and aerosol studies. In particular, Dr. Paul DeMott (Colorado State Univ.) taught me about cloud ice nucleation and sparked my interest in studying ice nucleation, the topic of my future post-doctoral work. Prof. Cindy Twohy (Oregon State Univ.) taught me how to analyze and interpret the cloud probe data; we also had fun together on the plane talking over headset while Harry ate his cookies! Dr. Andy Heymsfield (NCAR) took me under his wing, teaching me about ice nucleation and encouraging me to stay in the field! During ICE-L, Dr. Dave Rogers (NCAR) provided continual encouragement, particularly about the smoke plumes data, and would always check on me to make sure that I wasn't spending all of my time working. Dr. Harry Ochs always provided encouragement with the ever-present question "How's your writing coming along?" and the comic-relief provided by his cookies. While his instrument didn't need that much prep on the C-130, Harry came to work and kept me company while I finishing building the aircraft version of "Shirley". Dr. Shane Murphy (CalTech) was the only other graduate student aboard the C-130; it has been an absolute pleasure to work with Shane. To Shane and Curtis Paxton (DMT), I must ask –"Who's brilliant idea was it to go out to the *Egg & I* before the calibration flight?!" The roller coasters on the C-130 after breakfast were a blast! I hope that I will have the pleasure of working with this cloud ice community for many years to come. The C-130 technicians were always willing to give an extra hand while I was still building Shirley, would meet Shane and myself at the hangar *early* in the morning so that we could pump down our instruments, and tolerated me riding on the C-130 on the tarmac to sample aircraft emissions during tests. I also must thank the fantastic C-130 pilots who guided us through many clouds and who we convinced to fly through the smoke plumes we saw! I've also had the pleasure of working with several other researchers including Dr. Jorgen Jensen (NCAR), Dr. Paul Field (UK Met Office), Dr. Sam Haimov (Univ. of Wyoming), Dr. Jeff French (Univ. of Wyoming), Prof. Zhien Wang (Univ. of Wyoming), Prof. Sonia Kreidenweis (Colorado State Univ.), Dr. R. Subramanian (DMT), and Prof. John Seinfeld (CalTech). There also were countless others during ICE-L who helped make the campaign a success.

In the Prather lab, I have had the pleasure of working with many energetic, helpful people. After TAing for Dr. Gary Poon in my first year, he encouraged me to join the aircraft project, which laid the foundation of my thesis. Gary also sparked my interest in teaching and mentoring, which I hope to continue in my career. For my next two years in the Prather lab, I could usually be found with Dr. Ryan Moffet and John Holecek, who it was a pleasure to learn from and work with. Moffet always challenged me with his teaching method, "play with it and figure it out", but it made me learn and helped me develop troubleshooting skills which proved to be priceless. John, Moffet, and I had a good time building Shirley to the music of Bob Marley. Dr. Matt Spencer was the first to take the time to show me how to do data analysis, and he has proven to be a good friend. Thank you Matt for the Dom Pérignon! Dr. Xueying (Sharon) Qin continually answered my nagging Matlab questions and is a good friend. Together, Sharon, Dr. Laura Shields, Dr. Steve Toner, and I had many enjoyable dinners in Riverside during our field studies. Steve always challenged me and has become a good friend. Dr. Thomas Rebotier was always helpful with Shirley's software, even stopping by lab after he had left the group. It was a pleasure to work with Dr. Hiroshi Furutani, who challenged me in my early years and first introduced me to Swagelok! Hiroshi's mottos "Why not?!" and "You gonna do it!" have guided me through challenges and my experiences in the lab. Andy Ault has always been willing to lend a helping hand for field studies, including driving to and from Colorado, and he is always willing to listen to my newest paper idea. Lindsay Hatch was a great help with Shirley and was a lot of fun to work with on the amine experiments. Cassie Gaston is a great friend who I have had the great pleasure of mentoring during her first years in the group; our trips to the gym have helped keep me 'sane'. Maggie

Yandell has been there for me during my toughest times, and I am ever so grateful. René Sánchez was an amazing undergraduate to work with on the aircraft project. Jessie Creamean has an incorrigible zest for life, whether we are going to ice hockey lessons together or she is chanting “Come back Kerri!” after I left the field site outside Colfax. Before even officially joining the Prather Lab, Dr. Bob Moision helped with machining parts for Shirley when Joe and I were low on time, and I am very much appreciate him taking the time to help us and even teach me a little about design. For discussions and help with field study prep, many thanks also go to Prather lab members past and present: Dr. Yongxuan Su, Dr. Sergio Guazzotti, Michelle Sipin, Dr. Ying Wang, Dr. Ryan Sullivan, Jessie Charrier, Meagan Moore, Melanie Zauscher, Liz Fitzgerald, Kaitlyn Suski, Brandon Heilman, and Daniel Phung. While not officially in the Prather lab, Dr. Manuel Dall’Osto (National Univ. of Ireland) has visited every year that I have been in graduate school, and I look forward to continuing to collaborate with him. I must also thank another honorary Prather lab group member Myra Kosak for processing my numerous field study travel receipts and always caring about me.

I also thank many SOAR collaborators who it has been a pleasure to work with: Prof. Paul Ziemann (UC-Riverside), Dr. Ken Docherty (CU-Boulder), Dr. Mike Cubison (CU-Boulder), Dr. Susanne Hering (Aerosol Dynamics), Dr. Greg Lewis (Aerosol Dynamics), and Dr. Brent Williams (UC-Berkeley). Most of all Prof. Jose Jimenez and Dr. Alex Huffmann (CU-Boulder) provided the thermodenuder for the 2005 and 2006 Riverside studies. In addition, Dr. Marc Gonin and Dr. Katrin Fuhrer (Tofwerk) were always available for questions about Shirley’s mass spectrometer.

I am also very thankful to my thesis committee: Prof. Bob Continetti, Prof. Wei Wang, Prof. Katja Lindenberg, Prof. Mark Thiemens, and Prof. Jeff Severinghaus. I am particularly thankful for Prof. Lindenberg for keeping her door open over the past years; she always welcomed me in to office to discuss whatever was on my mind, whether it was my thesis or my future. I also thoroughly enjoyed Prof. Severinghaus' ice cores class, and I hope that I can someday do research in the Arctic!

I would not be where I am today without Prof. Dan Jones and Prof. Karl Mueller who guided me as a young undergraduate at Penn State. I remember one of my first days in lab when Dan patiently taught me how to use a rotovap. Dan led me to my research advisors, Karl, Prof. Scott Mabury, and Kim, and for that, I am incredibly thankful. When other professors weren't interested in a freshman who "didn't know anything yet", Karl took me on saying that I didn't know anything, which meant he could teach me! I will never forget my first day in the solid-state NMR lab as a freshman when he told me not to touch anything because it was either very expensive or would electrocute me! On several occasions Karl and his family welcomed me into his home so that I could continue research over my school breaks. I am ever so grateful for the support and encouragement of Dan and Karl over the years. During the summer of 2002, I ventured to the University of Toronto and worked for Dr. David Ellis and Prof. Scott Mabury who challenged me to "get a paper out of a 10-week research project", and we did! For that summer, I was the resident NMR 'expert' in the Mabury lab who wanted to keep her samples running around the clock!

In my personal life, many individuals have impacted my life and for that I am grateful. My parents Kelly and Markie Pratt and family have encouraged and supported me, for which I am very thankful. In particular, I wish that my Grandma Manzer were here to attempt to read this thesis; I think would have been proud. Through the past couple years, my aunt Linda Hay has always been there for me to share my good times and sad times; I am ever so grateful for her unyielding support no matter the circumstance. Tom, Dave, Martha, and Charlie Denkenberger encouraged me to try in high school; as a result of their encouragement, I attended the Pennsylvania Governor's School of Agriculture, where my excitement for learning was cultivated. When I became bored as an environmental resource management major, Tom helped support and challenge me as a chemistry major. Through undergrad and grad school, we shared many great backpacking and fishing trips. At Penn State, Dave was a great "big brother", helping to tutor me in calculus so that I could get the highest grade in the class! During ICE-L, Dave and Jill took me out hiking several times and invited me over to their home, welcoming me to Boulder. My high school friend Jennifer Reed has always been supportive no matter the situation, and I am so thankful for the phone conversations when I needed a friend. Jon Oakman helped me realized that I no longer fit into the mold of where I am from, but that that is okay. I know that I can always count on Andy, Jon, Chris, and Diana for a relaxing Sunday afternoon of football with our laptops! And, thank you for Markley and Arthi for always being around to chat. Lastly, I also must thank Andy Ault, who has provided incredible support and encouragement recently and who has helped me see my dreams. You have helped me realize that life is amazing and has much potential; I have never been happier. Thank you also for introducing me to bluegrass music which has helped me push through my last bit of thesis writing! Thank you also to Bruce and Helene Ault for your steadfast support and encouragement.

It is because of all the people above, from Kim to the many people that I could not list here, that I am who I am. They have helped me develop the dreams that I originally didn't even know existed. It is because of these individuals that I will continue to strive to do good scientific research and mentor young scientists. It is because of them that I will seek out the full potential of life. Thank you.

I also cannot forget to thank "Shirley" for sticking with me through my thesis. We did it! We flew! Thank you so much for being there with me through the field campaigns even when you had to work really hard!

The work in this dissertation was supported by the National Science Foundation (NSF), California Air Resources Board (CARB), Environmental Protection Agency (EPA), and the National Center for Atmospheric Research (NCAR). I am also incredibly grateful for an NSF Graduate Research Fellowship and an EPA STAR Graduate Fellowship, which have provided me with flexibility during my thesis study.

Chapter 1 is in preparation for submission to *Mass Spectrometry Reviews*: Pratt, K.A., Prather, K.A. Mass spectrometry of atmospheric aerosols – Recent developments & applications. Part II: Real-time mass spectrometry techniques.

Chapter 2 is reproduced with permission from the American Chemical Society: Pratt, K.A., Mayer, J.E., Holecek, J.C., Moffet, R.C., Sanchez, R.O., Rebotier, T., Furutani, H., Gonin, M., Fuhrer, K., Su, Y., Guazzotti, S., Prather, K.A. Development and characterization of an aircraft aerosol time-of-flight mass spectrometer. *Analytical Chemistry*. 2009, 81, 1792-1800.

Chapter 3 is reproduced with permission from the American Chemical Society: Denkenberger, K.A., Moffet, R.C., Holecek, J.C., Rebotier, T.P., Prather, K.A. Real-time, single-particle measurements of oligomers in aged ambient aerosol particles. *Environmental Science & Technology*. 2007, 41, 5439-5446.

Chapter 4 has been submitted to *Environmental Science & Technology*: Pratt, K.A., Prather, K.A. Real-time, single-particle volatility, size, and chemical composition measurements of aged urban aerosols.

Chapter 5 is reproduced with permission from the American Chemical Society: Pratt, K.A., Hatch, L.E., Prather, K.A. Seasonal volatility dependence of ambient particle phase amines. *Environmental Science & Technol*ogy, 2009, 43, 5276-5281.

Chapter 6 is in preparation for submission to the *Journal of Geophysical Research*: Pratt, K.A., Prather, K.A. Real-time, flight-based measurements of vertical profiles of single-particle mixing states.

Chapter 7 is reproduced with permission from the Nature Publishing Group: Pratt, K.A., DeMott, P.J., French, J.R., Wang, Z., Westphal, D.L., Heymsfield, A.J., Twohy, C.H., Prenni, A.J., Prather, K.A. In-situ detection of biological particles in cloud ice crystals. *Nature Geoscience*, 2009, 2, 398-401.

Chapter 8 is in preparation for submission to the *Journal of Geophysical Research*: Pratt, K.A., Twohy, C.H., Murphy, S.M., Moffet, R.M., Heymsfield, A.J., Gaston, C.J., DeMott, P.J., Field, P.R., Rogers, D.C., Henn, T.R., Gilles, M.K., Seinfeld, J.H., Prather, K.A. Playa salts serve as natural cloud nuclei.

Vita

2004	B.S. with honors in Chemistry with a minor in Watersheds & Water Resources, Pennsylvania State University
2004 – 2005	Teaching Assistant, Department of Chemistry & Biochemistry, University of California, San Diego
2004 – 2009	Graduate Research Assistant, Department of Chemistry & Biochemistry, University of California, San Diego
2006	M.S. in Chemistry, University of California, San Diego
2009	Ph.D. in Chemistry, University of California, San Diego

Publications

Pratt, K.A. *Nuclear magnetic resonance studies of perfluorinated compounds with environmental relevance.* B.S. Thesis. (Pennsylvania State University, University Park, PA, 2004).

Ellis, D.A., Denkenberger, K.A., Burrow, T.E., Mabury, S.A. The use of ^{19}F NMR to interpret the structural properties of perfluorocarboxylate acids: A possible correlation with their environmental disposition. *Journal of Physical Chemistry A.* 2004, 108, 10099-10106.

Denkenberger, K.A., Bowers, R.A., Jones, A.D., Mueller, K.T. NMR studies of the thermal degradation of a perfluoropolyether on the surfaces of γ-alumina and kaolinite. *Langmuir*. 2007, 23, 8855-8860.

Denkenberger, K.A., Moffet, R.C., Holecek, J.C., Rebotier, T.P., Prather, K.A. Real-time, single-particle measurements of oligomers in aged ambient aerosol particles. *Environmental Science & Technology.* 2007, 41, 5439-5446.

Pratt, K.A., Mayer, J.E., Holecek, J.C., Moffet, R.C., Sanchez, R.O., Rebotier, T., Furutani, H., Gonin, M., Fuhrer, K., Su, Y., Guazzotti, S., Prather, K.A. Development and characterization of an aircraft aerosol time-of-flight mass spectrometer. *Analytical Chemistry*. 2009, 81, 1792-1800.

Pratt, K.A., DeMott, P.J., French, J.R., Wang, Z., Westphal, D.L., Heymsfield, A.J., Twohy, C.H., Prenni, A.J., Prather, K.A. In-situ detection of biological particles in cloud ice crystals. *Nature Geoscience*, 2009, 2, 398-401.

Pratt, K.A., Hatch, L.E., Prather, K.A. Seasonal volatility dependence of ambient particle phase amines. *Environmental Science & Technology*, 2009, 43, 5276-5281.

Pratt, K.A., Prather, K.A. Real-time, single-particle volatility, size, and chemical composition measurements of aged urban aerosols. *Environmental Science & Technology*, 2009, Submitted.

Field, P.R., Heymsfield, A.J., Rogers, D.C., Stith, J., DeMott, P.J., Haimov, S., Murphy, S.M., Pratt, K.A., Twohy, C., Prather, K.A., Seinfeld, J.H., Shipway, B.J., Eidhammer, T., Prenni, A.J. Contrasting the ice nucleation in two lee wave clouds observed during the ICE-L campaign. *Journal of Atmospheric Science*, 2009, Submitted.

Eidhammer, T., DeMott, P.J., Prenni, A.J., Petters, M.D., Twohy, C. H., Rogers, D.C., Stith, J., Heymsfield, A., Wang, Z., Pratt, K.A., Prather, K.A., Murphy, S.M., Seinfeld, J.H., Subramanian, R., Kreidenweis, S.M. Ice initiation by aerosol particles: Measured and predicted ice nuclei concentrations versus measured ice crystal concentrations in an orographic wave cloud. *Journal of Atmospheric Science*, 2009, Submitted.

Gaston, C.J., Pratt, K.A., Qin, X., Prather, K.A. Real-time detection of the mixing state of methanesulfonate in single aerosol particles at an inland urban location during a major phytoplankton bloom. *Environmental Science & Technology*, 2009, Submitted.

Pratt, K.A., Prather, K.A. Real-time, flight-based measurements of vertical profiles of single-particle mixing states. *Journal of Geophysical Research*, 2009, In Preparation.

Pratt, K.A., Twohy, C.H., Murphy, S.M., Moffet, R.M., Heymsfield, A.J., Gaston, C.J., DeMott, P.J., Field, P.R., Rogers, D.C., Henn, T.R., Gilles, M.K., Seinfeld, J.H., Prather, K.A. Playa salts serve as natural cloud nuclei. *Journal of Geophysical Research*, 2009, In Preparation.

Pratt, K.A., Prather, K.A. Mass spectrometry of atmospheric aerosols – Recent developments & applications. Part I: Off-line mass spectrometry techniques. *Mass Spectrometry Reviews*, 2009, In Preparation.

Pratt, K.A., Prather, K.A. Mass spectrometry of atmospheric aerosols – Recent developments & applications. Part II: Real-time mass spectrometry techniques. *Mass Spectrometry Reviews*, 2009, In Preparation.

Qin, X., Shields, L.G., Toner, S.M., Pratt, K.A., Prather, K.A. Seasonal comparisons of the single particle mixing state in Riverside, CA during the SOAR 2005 Campaign. *Aerosol Science & Technology*, 2009, In Preparation.

Yandell, M., Ault, A.P., Pratt, K.A., Wang, Y., Zauscher, M., Gaston, C.J., Prather, K.A. Air pollution transport from the Ports of Long Beach and Los Angeles and its impact on the local community. *Aerosol Science & Technology*, 2009, In Preparation.

Creamean, J.M., Pratt, K.A., Ault, A.P., Qin, X., Gaston, C.J., Prather, K.A. Inter-annual comparison of real-time, single-particle ambient aerosol measurements using ATOFMS in Riverside, CA. *Aerosol Science & Technology*, 2009, In Preparation.

Pratt, K.A., Twohy, C.H., Murphy, S.M., Subramanian, R., Heymsfield, A.J., Hudson, J.G., Seinfeld, J.H., Prather, K.A. In-situ chemical characterization of aged biomass burning aerosols impacting cold wave clouds. *Journal of Atmospheric Science*, 2009, In Preparation.

Pratt, K.A., Murphy, S.M., Subramanian, R., DeMott, P.J., Kok, G.L., Rogers, D.C., Heymsfield, A.J., Seinfeld, J.H., Prather, K.A. Flight-based chemical characterization of biomass burning aerosols within two prescribed burn smoke plumes. *Journal of Geophysical Research*, 2009, In Preparation.

Fields of Study

Major Field: Chemistry

Studies in Mass Spectrometry:
Professor Kimberly A. Prather

Studies in Atmospheric Chemistry:
Professor Kimberly A. Prather

ABSTRACT OF THE DISSERTATION

New Insights into Single-Particle Mixing State using Aircraft Aerosol Time-of-Flight Mass Spectrometry

by

Kerri Anne Pratt

Doctor of Philosophy in Chemistry

University of California, San Diego, 2009

Professor Kimberly A. Prather, Chair

Atmospheric aerosols strongly influence the energy balance of the Earth and the hydrological cycle by scattering and absorbing radiation and acting as cloud condensation and ice nuclei. The climate and human health impacts of aerosols are strongly dependent on particle size, chemical composition, and mixing state. During transport in the atmosphere, aerosol particles undergo physical and chemical transformations (atmospheric aging) through heterogeneous reactions with trace gases and gas-particle partitioning of semivolatile species. The size-resolved chemical composition of individual particles may be examined in real-time using aerosol time-of-flight mass spectrometry (ATOFMS). A smaller ATOFMS with increased data acquisition capabilities was developed for aircraft-based studies. Particle volatility was examined through ground-based measurements during the Study of Organic Aerosols in Riverside, CA (SOAR), and vertical mixing state profiles and cloud residues were examined through flight-based measurements during the Ice in Clouds Experiment – Layer Clouds (ICE-L).

An automated thermodenuder (TD) was coupled to the aircraft (A)-ATOFMS to provide the first real-time, individual-particle size and volatility-resolved chemical composition measurements. This work provided insight into the volatility of secondary species, as well as the sources and chemistry of ambient particle cores. Seasonal differences in the volatility of amine species were attributed to the formation of aminium sulfate and nitrate salts in the summer. Oligomeric species were detected in real-time for the first time in individual ambient aerosol particles; increased oligomer ion intensities were associated with increased particle acidity and heating.

During ICE-L, vertical profiles of particle types, such as soot, mixed with secondary species, such as sulfuric acid, were examined. For cloud sampling, a counterflow virtual impactor was utilized in series with the A-ATOFMS to examine the residues of cloud droplets and ice crystals. This resulted in the first in-situ detection of biological particles in high altitude ice clouds influenced by long-range transported dust. Playa salts were observed to serve as cloud condensation nuclei and were preferentially observed as residues of large droplets.

Chapter 1

1 Introduction

1.1 Synopsis

Many of the significant advances in our understanding of atmospheric particles can be attributed to the application of mass spectrometry. Mass spectrometry provides high sensitivity with a fast response time to probe chemically complex particles. This review focuses on recent developments and applications in the field of mass spectrometry of atmospheric aerosols. In Part II of this two-part review, we concentrate on real-time mass spectrometry techniques, which provide high time resolution for insight into brief events and diurnal changes while eliminating the potential artifacts acquired during long-term filter sampling. In particular, real-time mass spectrometry has been shown recently to provide the ability to probe the chemical composition of ambient individual particles <30 nm in diameter to further our understanding of how particles are formed through nucleation in the atmosphere. Further, transportable real-time mass spectrometry techniques are now used frequently on ground-, ship-, and aircraft-based studies around the globe to further our understanding of the spatial distribution of atmospheric aerosols. Lastly, coupling aerosol mass spectrometry techniques with other measurements in series has allowed the in-situ determination of chemically-resolved particle effective density, refractive index, volatility, and cloud activation properties.

1.2 Mass spectrometry and atmospheric aerosols

Atmospheric aerosol particles are of considerable importance due to their impacts on global climate, regional air pollution, and human health [*Poschl*, 2005]. Defined as a solid or liquid suspended in a gas, aerosol particle range in size from approximately 3 nm to 10 μm in diameter [*Finlayson-Pitts and Pitts*, 2000]. Atmospheric aerosols strongly influence visibility, the energy balance of the Earth, and the hydrological cycle by scattering and absorbing solar (UV/visible) and terrestrial (IR) radiation and acting as cloud condensation and ice nuclei [*Poschl*, 2005]. Further, exposure to particulate matter, particularly those with diameters less than 2.5 μm in diameter ($PM_{2.5}$), is linked to negative health effects, including cardiopulmonary morbidity and mortality [*Pope and Dockery*, 2006]. Primary aerosol particles originate from a variety of both natural and anthropogenic sources, such as biomass burning, incomplete fossil fuel combustion, and the wind-driven suspension of soil, sea spray, and biological materials (plant fragments, microorganisms, etc.) [*Poschl*, 2005]. Secondary particulate matter is formed in the atmosphere due to gas-to-particle partitioning and nucleation [*Poschl*, 2005]. Depending on particle size, chemical composition, and local meteorology, lifetimes of atmospheric particles range from seconds to approximately 1 month, allowing them to be transported on a hemispheric scale [*Raes et al.*, 2000; *Williams et al.*, 2002]. During transport, atmospheric particles undergo physical and chemical transformations, due to coagulation, heterogeneous reactions of particles with trace gases, gas-particle partitioning of semivolatile species, and cloud processing, leading to changes in particle size, structure, and chemistry [*Poschl*, 2005].

Due to the complex and ever-changing physical and chemical properties of aerosols, the quantification of aerosols and their impacts on radiative forcing, clouds, visibility, and human health represents a challenging task. Single aerosol particles are complex mixtures containing on the order of ~10^2 to 10^{15} molecules per particles with masses on the order of ~10^{-20} to 10^{-6} grams per particle. Mass spectrometry is one of the few analytical techniques capable of spanning such a broad mass range. Typical particulate number concentrations range from ~15 cm^{-3} in the remote free troposphere to greater than 10^5 cm^{-3} in urban atmospheres [*Finlayson-Pitts and Pitts*, 2000]. Thus, the measurement of atmospheric particles represents a significant analytical challenge. McMurry [2000] defined the perfect aerosol measurement as continuously measuring the complete chemistry of single particles with continuous size and time resolution. Further, McMurry [2000] emphasized the importance of simultaneously measuring particle concentrations, size distributions, morphologies, chemical compositions, densities, refractive indices, volatilities, and hygroscopicities, among other properties. With high sensitivity and the ability to be coupled to various other techniques, as discussed below, mass spectrometry is well-suited for the analysis of atmospheric aerosols.

Over the past decade, the field of real-time aerosol mass spectrometry has developed considerably with most recent advances in the measurement of chemistry coupled with other measured properties, such as size, effective density, refractive index, volatility, and hygroscopicity, for example. In particular, real-time aerosol mass spectrometry provides high time resolution to probe rapid events and diurnal changes; further, portable instruments allow aerosol spatial variability to be examined. The specific aerosol mass spectrometry method of choice is dependent on the particular questions to be answered and whether single-particle or bulk (multi-particle) information is important. Further, real-time techniques avoid partitioning artifacts associated with off-line analysis methods, such as evaporation and chemical reactions of particles during sample collection and analysis [*Sullivan and Prather*, 2005]. The field of aerosol mass spectrometry has been reviewed most recently by Suess and Prather [1999], Sipin et al. [2003], Murphy [2005], Nash et al. [2006], and Prather et al. [2008] with particular emphasis on real-time mass spectrometry by Sullivan and Prather [2005] and Hinz and Spengler [2007] and single-particle mass spectrometry by Noble and Prather [2000], Hunt and Petrucci [2002], and Murphy [2007]. In particular, the general design of real-time aerosol mass spectrometers has been discussed in detail recently by Nash et al. [2006] and Murphy [2007]. Herein, we present an overview of real-time atmospheric aerosol mass spectrometry techniques with particular emphasis on recent developments and applications since 2006, as well as the coupling of real-time aerosol mass spectrometry with other instrumentation to yield chemically-resolved properties. For ease of use, this review is organized by bulk and single-particle techniques and broken down by sub-categories of ionization methods.

1.3 Real-time mass spectrometry

1.3.1 Bulk measurements – Electron impact ionization

Electron ionization (EI) is a universal ionization method which benefits from comparisons of analyte mass spectra with a large database of standard mass spectra collected at 70 eV, as well as the ability to quantitatively relate ion peak intensities to molecular concentrations.

Aerodyne aerosol mass spectrometer (AMS)

Recently reviewed by Canagaratna et al. [2007], the Aerodyne aerosol mass spectrometer (AMS) is the most common real-time aerosol mass spectrometry technique employing electron ionization (EI). Generally, particles with aerodynamic diameters of ~50-1000 nm are collimated in an aerodynamic lens systems, after which they are sized using a chopper [*Canagaratna et al.*, 2007]. Following flash vaporization upon impaction on a heated porous tungsten surface (~600 °C), non-refractory components are analyzed via EI and either a quadrupole (Q), time-of-flight (TOF), or high-resolution TOF mass analyzer [*Canagaratna et al.*, 2007]. This method allows for the real-time analysis of size-resolved mass concentrations of non-refractory aerosol components, including most organics, ammonium, sulfate, and nitrate, contributing to PM_1, hereon referred to as non-refractory (NR)-PM_1 [*Canagaratna et al.*, 2007]. A full listing of manuscripts utilizing the AMS can be found at http://cires.colorado.edu/~jjose/ams-papers.html. As numerous manuscripts utilizing the AMS have been published since the Canagaratna et al. [2007] review, herein we focus on highlights of more recent work.

An overview of AMS ambient NR-PM_1 measurements of organics, sulfate, nitrate, ammonium, and chloride was recently published by Zhang et al. [2007]; for most of the mid-latitude northern hemisphere locations, organics and sulfate were found to be the main contributors to NR-PM_1. Oxygenated organic aerosol (OOA) was found to contribute the majority of the organic aerosol in all locations, including urban and remote sites, compared to hydrocarbon-like organic aerosol (HOA), suggesting that most particle-phase organics are highly aged and influenced by secondary organic aerosol [*Zhang et al.*, 2007]. Recently, AMS instrumentation has been integrated into mobile laboratories to study traffic emissions while driving [*Schneider et al.*, 2008; *Zavala et al.*, 2009]. AMS measurements have also been made aboard aircraft during several recent campaigns: the 2002 New England Air Quality Study [*Kleinman et al.*, 2007], 2004 International Consortium for Atmospheric Research on Transport and Transformation (ICARTT) program [*Hayden et al.*, 2008], 2005 Marine Stratus/Stratocumulus Experiment (MASE) [*Wang et al.*, 2008], 2006 Aerosol and Chemical Transport in tropical conVEction (ACTIVE) campaign [*Allen et al.*, 2008], 2006 Dust and Biomass-burning Experiment (DABEX) and Dust Outflow and Deposition to the Ocean (DODO) studies over West Africa [*Capes et al.*, 2008], and 2006 Megacity Initiative: Local and Global Research Observations (MILAGRO) over Mexico City [*DeCarlo et al.*, 2008; *Kleinman et al.*, 2008]. Further, Cho et al. [2009] used aircraft-based AMS measurements of sulfate over Edmonton, Canada to evaluate the predictions of a regional air-quality model with integrated major-point source emissions data.

To understand and predict the impact of atmospheric aerosols on clouds, several AMS studies have focused on the use of ambient measurements for cloud condensation nuclei (CCN) closure studies in which CCN measurements are compared to predicted CCN values based on measured aerosol chemistry. Recently, AMS CCN closure studies have been carried out in rural North Carolina [*Stroud et al.*, 2007], rural New Hampshire [*Medina et al.*, 2007], rural Ontario [*Chang et al.*, 2007], Houston, TX/Gulf of Mexico [*Quinn et al.*, 2008], eastern Los Angeles basin [*Cubison et al.*, 2008], and the marine troposphere [*Wang et al.*, 2008]. Wang et al. [2008] found that an accurate representation of the hygroscopicity of the organic aerosol fraction is needed to predict CCN concentrations in locations dominated by organics. Thus, aerosol hygroscopcity measurements using a hygroscopity tandem differential mobility analyzer (HTDMA) have been compared to AMS measurements to provide more accurate inputs for CCN closure studies [*Ervens et al.*, 2007] and growth factor studies [*Gysel et al.*, 2007; *Hersey et al.*, 2009; *Sjogren et al.*, 2008]. In addition, Shantz et al. [2008] examined water uptake rates of aerosols within a CCN counter in parallel to AMS measurements, which were then used to constrain simulations of particle growth rates; organics were found to become increasingly important as the organic mass increased relative to the sulfate mass present. The inclusion of AMS data into CCN predictions has decreased the necessary assumptions and reduced model overprediction by providing insight into size-resolved aerosol chemistry; however, uncertainties still exist due to assumed organic speciation, organic solubility, and aerosol mixing state [*Medina et al.*, 2007; *Stroud et al.*, 2007].

Primary source emissions and subsequent aging have been the focus of several recent AMS laboratory studies. For example, Alfarra et al. [2007] and Weimer et al. [2008] examined the organic mass spectral signatures of fresh particulate wood-burning emissions. Grieshop et al. [2009a; 2009b] examined the evolution of the photooxidation of organic aerosols from wood-burning and observed similarities between the oxidized wood burning organics and the OOA signature commonly observed in AMS datasets, as well as photooxidized diesel exhaust [*Sage et al.*, 2008; *Weitkamp et al.*, 2007]. Other recent studies have focused on AMS emissions studies of meat cooking, trash burning, vehicles [*Mohr et al.*, 2009], and animal husbandry [*Martin et al.*, 2008; *Sorooshian et al.*, 2008].

Numerous AMS laboratory studies have also focused on heterogeneous reactions and the production and evolution of secondary organic aerosol (SOA). Due to recent

AMS field work showing the importance of amines in ambient aerosol [*Silva et al.*, 2008], several chamber studies have investigated SOA formation from the photooxidation and dark (nighttime) oxidation of a variety of gas-phase aliphatic amines with several reactive oxidants: OH, O_3, NO_3, NO_2, and HNO_3 [*Malloy et al.*, 2009; *Murphy et al.*, 2007c; *Silva et al.*, 2008]. Using a Q-AMS, polymerization of several biogenic olefins has been observed on acidic sulfate aerosols; reactive uptake was observed to depend on relative humidity and particle acidity [*Liggio and Li*, 2008; *Liggio et al.*, 2007]. George et al. [2007] examined the heterogeneous oxidation of bis(2-ethylhexyl) sebacate (BES) particles by OH radicals and monitored uptake kinetics through examination of the particle phase using a TOF-AMS. In the dark ozonolysis of α-pinene, Shilling et al. [2009] found that the SOA elemental composition, monitored by a HR-TOF-AMS was dependent on the concentration of reacted α-pinene. To gain insight into cloud activation and properties, several laboratory studies have simultaneously measured particle chemical composition and CCN activity. For example, Shilling et al. [2007] reacted oleic acid aerosol particles with ozone and monitored the CCN activated fraction over different levels of exposure. King et al. [2007] examined the CCN activities of SOA particles with variable organic-sulfate volume ratios.

Many recent AMS advances have involved new data analysis techniques, as well as instrument characterization studies. To separate different source contributions to the bulk organic aerosol mass spectra, Positive Matrix Factorization (PMF) methods have been applied using temporally-resolved patterns, leading to the identification of hydrocarbon-like organic aerosol (HOA), highly-oxygenated OA (OOA-1), and a less-oxygenated, semi-volatile OA (OOA-2), which classify the particle-phase organics by their level of oxidation [*Lanz et al.*, 2007; *Ulbrich et al.*, 2009]. Using the HR-TOF-AMS, O/C, H/C, N/C, and OM/OC ratios may be calculated for standards and applied to ambient measurements of organic aerosols to further characterize the oxidation state of organic aerosol [*Aiken et al.*, 2007; *Aiken et al.*, 2008]. AMS studies have also investigated the contribution of PAHs [*Dzepina et al.*, 2007] and dicarboxylic and ω-oxocarboxylic acids [*Takegawa et al.*, 2007] to ambient aerosols. To improve the detection limits and time resolution of the Q-AMS, Crosier et al. [2007] developed a jump mass spectrum mode in which certain *m/z*'s may be targeted by the user. To characterize the transmission efficiency of the aerodynamic lens system used within the AMS, Liu et al. [2007] compared laboratory results taken under different conditions with computational fluid dynamics calculations. To monitor particle collection efficiency, Salcedo et al. [2007] used a beam width probe during ambient measurements to evaluate losses of particles within the AMS due to beam broadening caused by particle size and particle shape (i.e. deviations from sphericity due to relative humidity). Using laboratory generated aerosols, Matthew et al. [2008] reported higher collection efficiencies for liquid particles compared to solid particles and attributed this to solid particles bouncing off the vaporizer, whereas the wet or coated particles were hypothesized to stick upon impaction. Recently, Drewnick et al. [2009] performed systematic laboratory experiments on the Q-AMS and compact TOF-AMS to examine detection limits. The compact TOF-AMS was found to have ~10 times lower detection limits compared to the Q-AMS, with detection limits between 0.003 $\mu g\ m^{-3}$ (nitrate, sulfate) and 0.03 $\mu g\ m^{-3}$ (ammonium, organics) [*Drewnick et al.*, 2009]. In addition to increased sensitivity due to higher ion throughput, the compact TOF-AMS can provide complete size-resolved mass spectra unlike the Q-AMS [*Canagaratna et al.*, 2007].

Recently, Kürten et al. [2007] modified an Aerodyne AMS and replaced the mass analyzer with a three-dimensional quadrupole ion trap to perform MS^n experiments, as well as ion/molecule reactions. In urban air, good agreement was observed for this ion trap (IT)-AMS and a Q-AMS for the quantification of nitrate [*Kürten et al.*, 2007]. MS/MS experiments showed collision-induced dissociation efficiencies of greater than 60% for ions formed from polystyrene latex spheres [*Kürten et al.*, 2007]. With high mass resolving power (>1500) and the ability to perform MS/MS experiments, it is expected that the IT-AMS will assist in the speciation of unknown organic aerosols [*Kürten et al.*, 2007].

Thermal desorption particle beam mass spectrometer (TDPBMS)

The thermal desorption particle beam mass spectrometer (TDPBMS), developed by Tobias et al. [2000], also employs an aerodynamic lens system for particle collimation, followed by thermal vaporization, EI, and a quadrupole mass spectrometer. Significantly, the TDPBMS employs temperature-programmed thermal desorption, allowing the measurement of vapor pressures of low-volatility organic aerosols during real-time chemical composition analysis [*Chattopadhyay et al.*, 2001]. In recent years, the TDPBMS has been utilized in several chamber studies of heterogeneous reactions and SOA formation to elucidate reaction mechanisms and products [*Docherty and Ziemann*, 2006; *Lim and Ziemann*, 2009a; *Lim and Ziemann*, 2009b; *Matsunaga et al.*, 2009; *Matsunaga and Ziemann*, 2009]. For the first measurements of yields of β-hydroxynitrates and dihydroxynitrates in SOA, Matsunaga and Ziemann [2009] monitored SOA formation in real-time using the TDPBMS, utilized temperature-programmed thermal desorption to examine product volatility, and coupled a high performance liquid chromatography (HPLC) to the TDPBMS for off-line analysis of filter extracts.

Thermal desorption aerosol gas chromatography/mass spectrometry (TAG)

The thermal desorption aerosol gas chromatography/mass spectrometry-flame ionization detector (TD-GC/MS-FID), or TAG, was recently developed by Williams et al. [2006] for hourly measurements of speciated organic compounds in atmospheric aerosols (0.06-2.5 μm). During in-situ automated sampling, aerosols are collected in a thermal desorption cell for 30 minutes by humidification and inertial impaction [*Williams et al.*, 2006]. Following purging at 50°C, organics are thermally desorbed by heating to 300°C with He used as the carrier gas to transfer the desorbed species to the GC column [*Williams et al.*, 2006]. Following GC separation, a quadrupole mass spectrometer is used for mass spectral identification with simultaneous analysis by a flame ionization detector for quantification [*Williams et al.*, 2006]. The first hourly in situ measurements of speciated organics were made using the TAG during ICARTT in Nova Scotia [*Williams et al.*, 2007]. The high time resolution of the TAG allowed specific organic compounds to be used to identify relative contributions of different sources of organic aerosol – anthropogenic, isoprene oxidation products, local terpene oxidation products, locally produced alkane-containing aerosols, and a marine or dairy source over the course of the study [*Williams et al.*, 2007]. Kreisberg et al. [2009] developed a new collection and thermal desorption cell to incorporate an injection port for in-situ calibrations with standard liquid mixtures; the method was demonstrated using field data from Riverside, CA. For aerosol particles in a ponderosa pine forest, Bouvier-Brown et al. [2009] used the TAG to measure methyl chavicol, a biogenic oxygenated aromatic compound, and its oxidation products.

Two-dimensional gas chromatography (GC x GC) has recently been applied to the TAG technique to provide increased resolution, structured chromatograms, and enhanced sensitivity compared to the 1D-TAG, described above [*Goldstein et al.*, 2008]. For ambient aerosols, the 1D-TAG often suffers from unresolved mixtures leading to an elevated baseline; however, the 2D-TAG separates compounds based on polarity, allowing separation of an order of magnitude more compounds with a near zero baseline [*Goldstein et al.*, 2008]. The 2D-TAG requires longer analysis times, giving 2 hour time resolution, as shown for ambient aerosols in Berkeley, CA. However, since a fast scanning detector was required to sample all chromatographic peaks, detection was accomplished via FID alone in this version of the instrument [*Goldstein et al.*, 2008]. While compound quantification was not possible using the quadrupole mass spectrometer, it was utilized for compound identification; a future version of the 2D-TAG will utilize a TOF-MS as the detector [*Goldstein et al.*, 2008].

Other aerosol EI-based mass spectrometers

An aerosol composition mass spectrometer was developed by Schreiner et al. [1999; 2002] for the balloon-borne analysis of polar stratospheric aerosols. The instrument utilizes an isobaric aerodynamic inlet, followed by thermal desorption, EI, and mass analysis using a magnetic mass spectrometer [*Schreiner et al.*, 2002]. Using this instrument, Weisser et al. [2006] observed HCl in liquid particles for the first time, in addition to solid nitric acid trihydrate particles within polar stratospheric clouds.

1.3.2 Bulk measurements – Chemical ionization

There is a major need for methods that provide speciation of the organic species in aerosols. Chemical ionization (CI) produces ions through collisions of reagent molecules with primary source ions; this process results in significantly less fragmentation than EI (70 eV), allowing molecular species to be identified. As discussed in a review by Mazurek [2002], while molecular identification can often be achieved using EI-based GC-MS, the fraction of resolvable organics is often low; for example, Rogge et al. [1993] resolved ~13-17% of the organics present in urban aerosol samples. As briefly mentioned in a review of chemical ionization mass spectrometry (CI-MS) applied to atmospheric trace species by Huey [2007], several online aerosol mass spectrometry techniques utilizing CI have been developed in recent years, particularly for the speciation of organics.

Thermal desorption chemical ionization mass spectrometer (TD-CI-MS)

The thermal desorption chemical ionization mass spectrometer (TD-CI-MS) for chemical composition analysis of ultrafine aerosol particles was developed by Voisin et al. [2003]. Ultrafine particles down to a minimum diameter of 4 nm are first charged and size-selected with a nanometer aerosol differential mobility analyzer (nano-DMA) prior to collection by electrostatic deposition on a metal filament [*Smith et al.*, 2004; *Voisin et al.*, 2003]. Following deposition, particles are thermally vaporized at 100°C, chemically ionized by reactions with NH_4^+, H_3O^+, or O_2^-, declustered in a drift cell, and mass analyzed using a triple quadrupole mass spectrometer [*Smith et al.*, 2005; *Smith et al.*, 2004; *Voisin et al.*, 2003]. Using this TD-CI-MS, Smith et al. [2004] reported the first online chemical composition measurements of 6-20 nm ambient particles, sampled in Boulder, CO. With a time resolution of 10 min, Smith et al. [2005] also reported the first direct, in situ chemical composition measurements of size-segregated 6-15 nm ambient particles during nucleation events in Atlanta, GA. Recently, Smith et al. [2008] showed contributions of nitrogen-containing organics, organic acids, and hydroxyl organic acids, in addition to nitrate and sulfur species, to 10-33 nm particles formed through nucleation in Tecamac, Mexico. In addition, Smith and Rathbone [2008] examined pictogram quantities of pure and multicomponent 8-40 nm aerosols of monocarboxylic and dicarboxylic acids to characterize the sensitivity and uncertainties associated with the TD-CI-MS. Based on the design of the TD-CI-MS, Held et al. [2009] recently incorporated an ion trap mass spectrometer into a modified version of the instrument. In contrast, this TD-CI-IT-MS uses a radial DMA for size-selection to reduce aerosol residence time and diffusive losses and incorporates temperature programmed thermal desorption [*Held et al.*, 2009]; measurements of ~30 nm particles in Colorado showed them to be 2-20% ammonium by mass.

Aerosol chemical ionization mass spectrometer (Aerosol CI-MS)

Another CI-based aerosol technique, termed the aerosol CI-MS, was developed by Hearn and Smith [2004] and has primarily been used for detailed analysis of organic aerosols in laboratory-based heterogeneous reactions. The aerosol CI-MS utilizes thermal desorption at temperatures up to 480°C followed by CI and a quadrupole mass spectrometer [*Hearn and Smith*, 2004]. The aerosol CI-MS can utilize a range of positive ($H^+(H_2O)_2$, $H^+(CH_3OH)_2$, NO^+, O_2^+) and negative (O_2^-, F^-, SF_6^-) reagent ions for flexibility in detection sensitivity and specificity [*Hearn and Smith*, 2004]; on-line detection limits were found to be 100-200 ng/m^3. Hearn and Smith [2006b] monitored in real-time the ozonolysis of mixed oleic acid/palmitic acid particles, which were used as proxies of meat-cooking aerosols, and found that the reaction of oleic acid with ozone was inhibited in the complex particles compared to pure oleic acid particles. To determine heterogeneous rates of reaction, Hearn and Smith [2006a] used the aerosol CI-MS to monitor gas-phase (reference) and particle species in reactions between methyl oleate particles and ozone, bis(2-ethylhexyl) sebacate and Cl radicals, and bis(2-ethylhexyl) sebacate and OH radicals. Similarly, Hearn and Smith [2007] studied the reaction kinetics of ozone with mixed oleic acid/*n*-docosane particles to examine the roles of particle phase, morphology, and metastable states. To gain a better understanding of heterogeneous reaction mechanisms, Hearn et al. [2007] monitored the aerosol products of the reaction of Cl radicals with bis(2-ethylhexyl) sebacate and observed two primary products: ketone and alcohol. Recently, Renbaum and Smith [2009] examined the Cl-initiated reaction of solid and supercooled liquid brassidic acid particles, allowing the products and reaction rates to be examined for the first time for particles with identical chemical composition with different phases. Aerosol CI-MS has also been used to monitor sulfate concentrations in ambient particles in real-time [*Hearn and Smith*, 2006b]. To concentrate the aerosol and differentiate between semi-volatile and non-volatile organics, the aerosol CI-MS has been run in an off-line mode with thermal desorption following off-line sample collection to examine smoke particles from cigarette, white oak, and pine combustion, particle-phase products of the ozonolysis of R-limonene and volatile compounds from orange peel, meat-cooking aerosol, and ambient aerosols [*Hearn and Smith*, 2006b].

Other aerosol CI-based mass spectrometers

To monitor organics in the gas and particle phases simultaneously, McNeill et al. [2007] added a heated inlet for aerosol volatilization to a chemical ionization mass spectrometer. Using I^- as the reagent ion, the oxidation of particles consisting of internal mixtures of sodium oleate, sodium dodecyl sulfate, and inorganic salts by O_3, NO_3/N_2O_5, and OH was monitored [*McNeill et al.*, 2007]. In another study, the OH oxidation of pure palmitic acid particles and inorganic salt particles with thin palmitic acid coatings was examined using this CI-MS [*McNeill et al.*, 2008]. To distinguish between the gas and particle phases using proton transfer reaction mass spectrometry (PTR-MS), which utilizes H_3O^+ as the reagent ion, Hellén et al. [2008] modified the inlet of a commercial PTR-MS instrument to create separate particle and gas + particle phase inlets, which allow partitioning coefficients to be calculated. In the particle line, a charcoal denuder was used to remove gas-phase organics; particle vaporization is accomplished at 120°C or 150°C [*Hellén et al.*, 2008]. Using this method, the photooxidation of 1,3,5-trimethylbenzene and α-pinene with NO_x was monitored [*Hellén et al.*, 2008]. Lastly, Thornberry et al. [2009] recently developed a PTR ion trap mass spectrometer for the real-time measurement of speciated organic aerosols. Using novel aerosol collection/desorption chamber, particles greater than 0.45 μm are collected on an impactor and flash vaporized at 150°C [*Thornberry et al.*, 2009]. Laboratory tests of particle-phase glutaric acid show a 12 ng m^{-3} detection limit, or ~1% of typical organic aerosol mass loadings, for a sampling time of 10 minutes [*Thornberry et al.*, 2009]. The first field deployment was completed aboard the NOAA R/V *Ronald H. Brown* near

Houston, TX and showed the possible presence of primary emissions of pyridine in the aerosol phase [*Thornberry et al.*, 2009].

1.3.3 Bulk measurements – Laser ionization

By coupling thermal vaporization with "soft" vacuum ultraviolet (VUV) photoionization, reduced fragmentation of organic ions in aerosols may be achieved compared to EI [*Sykes et al.*, 2002]. Recently, Northway et al. [2007] modified an Aerodyne AMS, described above, incorporating VUV ionization at 123.6 nm (10 eV) and 118 nm (10.6 eV) and replacing the quadrupole mass spectrometer with a compact orthogonal extraction TOF-MS. For pristane, oleic acid, and cigarette smoke particles, VUV spectra were found to be less fragmented than EI spectra collected within the same instrument; fragmentation as a function of vaporizer temperature was also investigated for the oleic acid particles [*Northway et al.*, 2007]. Similarly, Shu et al. [2008] designed an aerosol mass spectrometer featuring an aerodynamic lens inlet, thermal vaporization at temperatures up to ~330°C, VUV ionization at 123.6 nm, and mass analysis using a reflection TOF-MS. Oleic acid and cholesterol in aerosol particles were able to be quantified and showed little fragmentation [*Shu et al.*, 2008]. Gao et al. [2008] compared this technique to off-line GC/MS for coal soot and multi-component PAH particles and found that while both methods were consistent in the identification of the PAHs, quantification was a challenge for the VUV aerosol mass spectrometer due to differences in the photoionization efficiencies of the compounds present. Gao et al. [2009b] used the VUV aerosol mass spectrometer recently to examine the organics present in soot particles generated from coal combustion and pyrolysis, as well as the reaction products of ozone with pyrene and benz[*a*]anthracene adsorbed on azelaic acid particles [*Gao et al.*, 2009a].

A synchrotron radiation source can be coupled to an aerosol mass spectrometer and provides a tunable, quasicontinuous (500 MHz) source of VUV radiation (7-25 eV), which can be tuned to an energy close to the ionization energy of the sample molecules, reducing fragmentation through single photon ionization and allowing the acquisition of photoionization efficiency curves [*Mysak et al.*, 2005]. Shu et al. [2006] applied this technique to the examination of steric acid, a common constituent in meat-cooking aerosols. Gloaguen et al. [2006] examined the reaction of anthracene coated sodium chloride particles using a synchrotron radiation-based aerosol mass spectrometer. The added sensitivity allowed for the detection of a monolayer of organic material deposited on the inorganic particles, and the measured photoionization efficiency curves assisted in the identification of reaction products [*Gloaguen et al.*, 2006].

In the photoionization aerosol mass spectrometer (PIAMS) developed by Öktem et al. [2004], ~30-500 nm particles enter through an aerodynamic lens system and are deposited on a cooled probe, following which 10.6 μm radiation is utilized for vaporization. Ionization is achieved using VUV radiation at 118 nm, and organic species are analyzed using a reflection TOF-MS [*Öktem et al.*, 2004]. Tolocka et al. [2006a] used PIAMS to examine the chemical composition of 30-50 nm particles produced from the ozonolysis of α-pinene, showing that the stabilized Criegee intermediate and hydroperoxide pathways are both involved in SOA formation. Similarly, using the PIAMS, Heaton et al. [2007] found that dimers and higher order oligomers form within seconds of the reaction of ozone with monoterpenes. Ambient aerosol sampling in

Wilmington, Delaware has been shown to provide 3.5 min time resolution for organic molecular composition measurements using the PIAMS [*Dreyfus et al.*, 2009; *Dreyfus and Johnston*, 2008].

Recently, Lloyd and Johnston [2009] developed an ion trap time-of-flight mass spectrometer for increased sensitivity and resolution in the online analysis of organic aerosols, as shown through the online analysis of perylene and C_{60} aerosols. Particles pass through an aerodynamic lens inlet and are deposited on a collection probe within an ion trap [*Lloyd and Johnston*, 2009]. Within the ion trap cavity, 355 nm radiation is used for laser desorption ionization (LDI); following collisional cooling, ions are extracted into a reflection TOF-MS [*Lloyd and Johnston*, 2009]. This IT-TOF-MS has also be operated using thermal desorption at 355 nm or 1064 nm, followed by EI; using this method, the ozonolysis of α-pinene [*Lloyd and Johnston*, 2009] and the reactive uptake of trimethylamine into ammonium nitrate particles [*Lloyd et al.*, 2009] have been investigated.

1.3.4 Bulk measurements – Other ionization techniques

Resulting in minimal fragmentation of ions due to the use of low energy (<1 eV) electrons, photoelectron resonance capture ionization (PERCI) has been shown to be a sensitive ionization technique for the analysis of organic aerosols [*LaFranchi and Petrucci*, 2004; *LaFranchi and Petrucci*, 2006]. PERCI is accomplished by focusing a low energy (sub-mJ) pulsed (10 Hz), tunable (235-300 nm) ultraviolet laser onto the surface of a pure aluminum photoelectrode, which generates short (5 ns) burst of photoelectrons [*LaFranchi and Petrucci*, 2006]. In this aerosol mass spectrometer, aerosols are thermally vaporized following collection of a probe, and ionized species are analyzed using a reflectron TOF-MS with delayed pulse ion extraction [*LaFranchi and Petrucci*, 2006]. The influence of vaporization temperature on ion intensity of different organics was examined by LaFranchi and Petrucci [2006], and the technique was demonstrated on standard organic aerosols, as well as aerosolized biodiesel fuel, which was found to be primarily fatty acid methyl esters. Recent work using PERCI has included: the observation of polymerization in the ozonolysis of oleic acid [*Zahardis et al.*, 2006a], detection of acid, aldehyde, and ketone products from the ozonolysis of multicomponent aerosols composed of fatty acids and methyl esters [*Zahardis et al.*, 2006b], examination of the ozonolysis of mixed oleic acid-amino acid particles serving as proxies for organic marine aerosols [*Zahardis et al.*, 2008a], and the investigation of the ozonolysis of primary aliphatic amines [*Zahardis et al.*, 2008b].

Recently, Eyglunet et al. [2008] modified the inlet of a commercial atmospheric pressure chemical ionization (APCI) mass spectrometer to allow for the online analysis of atmospheric aerosols. A charcoal denuder is used to trap gas phase organics; the temperature of particle thermal desorption is variable and can be optimized for the organics of interest to avoid degradation by pyrolytic processes [*Eyglunent et al.*, 2008]. In positive ion mode, ionized methanol is used for PTR; whereas, in negative ion mode, primary O_2^- ions are utilized, particularly in the detection of carboxylic and dicarboxylic acids [*Eyglunent et al.*, 2008]. This method has been used to characterize SOA resulting from the ozonolysis of α-pinene and 2-buten-1-ol [*Eyglunent et al.*, 2008].

1.3.5 Single-particle measurements – Laser ionization

Knowledge of the mixing state, or distribution of chemical species within individual particles, is vital for the evaluation of the climate and health impacts of aerosols. For example, particle physical, optical, hygroscopic, and toxicological properties strongly depend on how chemical species are mixed within individual particles and whether they are mixed within a single particle (internal mixing) or in different particles (external mixing) [*Fuzzi et al.*, 2006; *Schlesinger et al.*, 2006]. A recent review by Prather et al. [2008] details the advantages of single-particle mass spectrometry (SPMS), including improved insight into gas-particle partitioning, heterogeneous reactions, and particle sources, for example.

Laser desorption/ionization (LDI) is the primary ionization method used for the real-time mass spectrometry analysis of single particles, as reviewed by Noble and Prather [2000] and Hunt and Petrucci [2002]; in contrast to methods utilizing thermal desorption, LDI provides the ability to analyze both non-refractory (eg. organics, ammonium nitrate) and refractory (eg. mineral dust, soot) components of atmospheric aerosols. The design considerations for the development of single particle laser mass spectrometers was recently reviewed by Murphy [2007]. Overall, SPMS instruments have the same general components: vacuum inlet, laser-based particle trigger and sizing, laser desorption/ionization, and a mass spectrometer [*Murphy*, 2007]. Herein, we focus on the laser-based SPMS techniques currently being utilized in the characterization of atmospheric particles.

Rapid single-particle mass spectrometer (RSMS)

The rapid single-particle mass spectrometer (RSMS) initially developed by McKeown et al. [1991] has since been utilized in several field campaigns and further developed. For the analysis of ~30-1200 nm particles, the RSMS-2, described by Mallina et al. [2000], uses a size-selective inlet to transmit only particles of a particular diameter followed by LDI using a free-firing, pulsed 193 nm laser beam and analysis with a single-polarity, linear TOF-MS. The presence of lead in single atmospheric particles from RSMS measurement campaigns in Atlanta, GA, Houston, TX, Pittsburg, PA, Baltimore, MD, and Wilmington, DE was recently overviewed by Murphy et al. [2007b]. The RSMS-3, described by Bein et al. [2005], incorporated another linear TOF-MS to obtain dual-polarity mass spectra, increased dynamic range, and automation and remote control of the instrument. Recent field campaigns have used the RSMS-3 to examine the sources influencing particulate pollution in several cities: Pittsburgh, PA [*Bein et al.*, 2007; *Bein et al.*, 2008; *Bein et al.*, 2006; *Pekney et al.*, 2006], Baltimore, MD [*Tolocka et al.*, 2006b], and Wilmington, DE [*Reinard et al.*, 2007].

Particle analysis by laser mass spectrometry (PALMS)

Developed by Murphy and Thomson [1995], the particle analysis by laser mass spectrometry (PALMS) instrument has been used for numerous upper tropospheric and stratospheric aerosol measurements. The aircraft-based PALMS, described by Thomson et al. [2000], utilized a capillary inlet and reflectron TOF-MS to examine particles larger than ~200 nm. Particles scatter the light of a 532 nm laser beam, which is used to provide an approximate particle size and timing to trigger the excimer laser operating at 193 nm for LDI [*Thomson et al.*, 2000]. This PALMS instrument was used by Murphy et al. [2006b] to examine mercury-containing stratospheric aerosols during on-line analysis aboard the NASA WB-57F aircraft. To increase particle transmission and accuracy of particle sizing, Cziczo et al. [2006] replaced the capillary inlet with an isobaric aerodynamic inlet based on the design by Schreiner et al. [2002]. In addition, a higher energy 532 nm laser beam was split in two to provide particle velocity, and therefore, particle diameter [*Cziczo et al.*, 2006]. This improved PALMS instrument has been used in the study of the chemical composition of tropospheric particles during both airborne and ground-based campaigns [*Murphy et al.*, 2006a], carbonaceous material in particles in the lower stratosphere and tropopause [*Murphy et al.*, 2007a], lead in atmospheric particles [*Murphy et al.*, 2007b], and the chemical composition of mineral dust [*Gallavardin et al.*, 2008a].

Aerosol time-of-flight mass spectrometer (ATOFMS)

For the analysis of ~0.2-3.0 μm particles, the aerosol time-of-flight mass spectrometer (ATOFMS), initially developed by Prather et al. [1994], uses a converging nozzle inlet, two 532 nm lasers for particle triggering and sizing, 266 nm radiation for LDI, and a dual-polarity reflectron TOF-MS for mass analysis [*Gard et al.*, 1997]. For the study of single-particle mixing state, this ATOFMS has been used in numerous ground- and ship-based field campaigns, such as the 2000-2001 California Regional Particulate Air Quality Study [*Qin and Prather*, 2006], 2001 Asian Pacific Regional Aerosol Characterization Experiment (ACE-Asia) [*Sullivan et al.*, 2007], 2004 California Cooperative Oceanic Fisheries Investigations (CalCOFI) [*Furutani et al.*, 2008], 2004 Atmospheric Brown Cloud Post Monsoonal Experiment (APMEX) [*Spencer et al.*, 2008], and 2006 Mexico City Metropolitan Area-2006 campaign (MCMA-2006) [*Moffet et al.*, 2008a]. For aerosol source apportionment, Shields et al. [2007] examined the mass spectral signatures of heavy-duty diesel vehicle emissions, and Spencer et al. [2006] compared the chemical signatures of oil and fuel particles to those of heavy and light duty vehicle emissions. A similar version of this ATOFMS, commercialized by TSI, Inc., has been used to study ambient particles in several locations, including: New York City [*Zhou et al.*, 2006a], Athens, Greece [*Dall'Osto and Harrison*, 2006], and Mace Head, Ireland [*Dall'Osto et al.*, 2006]. It has also been utilized in studies of human exposure to fine concentrated ambient particles [*Freney et al.*, 2006], oligomer formation from the photooxidation of 1,3,5-trimethylbenzene with NO_x [*Gross et al.*, 2006], and the sources of indoor particles [*Dall'Osto et al.*, 2007].

To increase particle transmission and reduce the smallest sampled particle size, an aerodynamic lens inlet was incorporated into the ATOFMS [*Su et al.*, 2004]. The TSI ATOFMS with an aerodynamic lens inlet has been used in several field studies of lead in atmospheric particles [*Murphy et al.*, 2007b], particulate emissions from an iron and steelmaking site [*Dall'Osto et al.*, 2008], grass mowing particles [*Drewnick et al.*, 2008], a fog event in London [*Dall'Osto et al.*, 2009], and nitrate formation in Shanghai [*Wang et al.*, 2009]. To provide increased detection of 50-300 nm particles, the ultrafine (UF)-ATOFMS incorporates a microorifice uniform deposit impactor (MOUDI) prior to the aerodynamic lens inlet to remove particles larger than 250 nm [*Su et al.*, 2004]. The UF-ATOFMS has been utilized in the study of ultrafine particles emitted from particle concentrators for human exposure studies [*Su et al.*, 2006], heavy duty diesel vehicle emissions [*Toner et al.*, 2006], and wildfires [*Muhle*, 2006]. Most recently, UF-ATOFMS has been used to apportion gasoline and diesel-powered vehicles in a freeway study [*Toner et al.*, 2008] and to examine the size-resolved chemistry of particles in an aged urban environment [*Shields et al.*, 2008]. For the aircraft-based study of ~70-1000 nm particles, an aircraft (A)-ATOFMS utilizing an aerodynamic lens inlet has been developed and has shown a faster data acquisition rate with improved ion transmission and mass resolution, as well as reduced physical size and power consumption (Chapter 2). Ground-based A-ATOFMS measurements during the 2005 Study of Organic Aerosols in Riverside, CA (SOAR) resulted in the first detection of oligomers in individual ambient particles (Chapter 3).

Other SPMS

Mahadevan et al. [2002] developed an SPMS which incorporates an aerodynamic lens inlet, free-firing LDI at 532 nm, and a linear TOF-MS; total peak area is used to estimate particle size [*Lee et al.*, 2005]. Lee et al. [2006] used this technique to examine metal-containing diesel exhaust particles. Recent development work has involved newly design ion optics to increase ion detection [*Cho and Lee*, 2007] and characterization of the aerodynamic lens inlet [*Lee et al.*, 2008].

SPMS of biological aerosols

The use of SPMS for the real-time characterization of biological aerosol particles was recently reviewed by Demirev and Fenselau [2008] and Russell [2009]. Based on the design of the ATOFMS, the bioaerosol mass spectrometer (BAMS) has been modified to increase sensitivity by incorporating a “flattop” desorption/ionization laser profile to decrease inhomogeneities leading to shot-to-shot variability [*Steele et al.*, 2005], as well as a linear TOF-MS with delayed extraction and an electrostatic ion guide for increased mass range and sensitivity [*Russell et al.*, 2005]. In recent work, the BAMS has been used to observe the sporulation process of *Bacillus atrophaeus* cells [*Tobias et* *al.*, 2006]. For defense purposes, this SPMS, using 660 nm tracking lasers and dual-polarity reflectron TOF-MS, has been used to identify single particles of explosives [*Martin et al.*, 2007b] and liquid nerve agent simulants [*Martin et al.*, 2007a]; it has been lab- and field-tested at the San Francisco International Airport for rapid detection of hazardous aerosols [*Steele et al.*, 2008]. Further development of the BAMS has included characterization using polyethylene glycol particles [*Bogan et al.*, 2007], incorporation of a fluorescence detection stage [*Steele et al.*, 2008], and incorporation of matrix molecules into single particles for MALDI [*McJimpsey et al.*, 2008].

The SPMS developed by Weiss et al. [1997] incorporates a split 632.8 nm laser beam for particle triggering, 308 nm radiation for LDI, followed by a mass analysis using a single-polarity linear TOF-MS [*Stowers et al.*, 2000]. Recent work has involved optimization of this SPMS for bioaerosol detection and analysis. Replacing one continuous wave laser beam, fluorescence emitted under 266 nm excitation is used to detect and preselect 0.5-10 μm bioaerosol particles for further MS analysis [*Stowers et al.*, 2006]. This method has been shown to differentiate bacteria from nearly all other atmospheric particles with a minor potential influence from diesel soot particles [*Kleefsman et al.*, 2007]. Recent development has incorporated delayed ion extraction and a 532 nm scattering laser with on-line aerosol matrix-assisted laser desorption/ionization (MALDI), showing 1 zmol sensitivity with a mass range up to 15 kDa [*Kleefsman et al.*, 2008].

Nanoaerosol mass spectrometer (NAMS)

Reviewed by Johnston et al. [2006], recent work has pushed the limits of SPMS analysis to the detection and chemical characterization of <100 nm particles, which are suggested to have negative health impacts. The nanoaerosol mass spectrometer (NAMS), developed by Wang et al. [2006], has been demonstrated to chemically characterize individual sub-10 nm particles. In the NAMS, particles charged using a radioactive neutralizer are drawn through an aerodynamic lens inlet, focused through a quadrupole ion guide and captured in a quadrupole ion trap [*Wang et al.*, 2006]. Using 532 nm radiation, trapped particles undergo LDI and are mass analyzed within a single-polarity reflectron TOF-MS [*Wang et al.*, 2006]. In a modified version of the NAMS, the conventional sinusoidal quadrupole ion trap was replaced with a digital ion trap, which allows the selective trapping of 7-25 nm particles [*Wang and Johnston*, 2006]. The NAMS has been utilized to examine early SOA formation from the ozonolysis of α-pinene [*Tolocka et al.*, 2006a] and various monoterpenes [*Heaton et al.*, 2007]. Recently, Zordon et al. [2008] used NAMS to examine the chemical composition of 25 nm (mass-normalized diameter) ambient particles in Wilmington, DE; most particles were found to contain carbon, nitrogen, oxygen, and sulfur.

SPMS using two-step LDI

For soft ionization of single particles, the laser desorption and ionization steps may be decoupled; in the design by Morrical et al. [1998], two-step LDI was accomplished using a CO_2 (10.6 μm) laser for desorption and a Nd:YAG (266 nm) laser for ionization and was shown to produce low fragmentation mass spectra of organic molecules. Compared to single-step ultraviolet LDI, two-step LDI allows molecular identification and reduces particle-to-particle fluctuations with mass spectral intensities linearly correlated with organic mass [*Zelenyuk et al.*, 2009b]. The single particle laser ablation time-of-flight mass spectrometer (SPLAT), described by Zelenyuk and Imre

[2005], utilizes an aerodynamic lens inlet, two 532 nm lasers for particle sizing and triggering, two-step LDI at 10.6 µm and 193 nm, and a reflectron TOF-MS. The SPLAT II is an aircraft-compatible version of the original SPLAT that also features higher sampling rates for improved temporal resolution [*Zelenyuk et al.*, 2009a]. Zelenyuk et al. [2009c] compensated for a size-dependent hit-rate using a laser trigger delay coefficient dependent on particle size. Using the SPLAT-II, Yu et al. [2008] examined the chemical composition of SOA particles formed from the photooxidation of α-pinene in the presence of increasing concentrations of NO_2. Using an SPMS similar to the SPLAT, Rosen et al. [2008] used two-step LDI at 9.3-10 µm and 118 nm to examine the ozonolysis of oleic acid on polystyrene latex and silica particles. Similarly, Hanna et al. [2009] developed a two-step LDI SPMS with a tunable (7.4-10.2 eV) laser based VUV light source for single photon ionization, followed by ion trap mass spectrometry.

An on-line mass spectrometer featuring a dual-polarity reflectron TOF-MS with three different laser based ionization methods was developed recently by Bente et al. [2006]. In the first mode, single-particle LDI is accomplished in one step using 248 nm radiation for the detection of inorganic components, elemental carbon, and organic carbon, particularly PAHs [*Bente et al.*, 2006]. In the second mode, desorption of single particles is accomplished using a CO_2 laser (10.6 µm) with ionization at 248 nm for resonance enhanced multiphoton ionization (REMPI) to target aromatic compounds [*Bente et al.*, 2006]. In the third mode, thermal desorption at 300°C is followed by REMPI at 248 nm for the analysis of an ensemble of particles, providing detection of trace aromatic species [*Bente et al.*, 2006]. Using laser desorption, followed by REMPI, Bente et al. [2008] examined molecular source indicators for particles emitted from wood combustion and car exhaust. In the most recent work of this SPMS, Bente et al. [2009] implemented thermal desorption with REMPI of single particles; the method was tested on ambient and vehicle exhaust particles, showing organic molecular tracers of different sources.

SPMS data analysis

The mass spectra resulting from SMPS analysis can be considered "chemical fingerprints" of the individual particles. Due to the large volume of data acquired during sampling, clustering techniques are typically employed to classify the millions of single-particle mass spectra produced from single field campaigns [*Hinz and Spengler*, 2007]. Several recent efforts have involved the development and testing of new and existing clustering methods [*Rebotier and Prather*, 2007; *Zelenyuk et al.*, 2006b; *Zelenyuk et al.*, 2008b; *Zhao et al.*, 2008]. In addition, while SPMS techniques generally produce qualitative data, recent work has involved using external calibration data to provide chemically-resolved scaled number and mass concentrations [*Allen et al.*, 2006; *Bein et al.*, 2006; *Cai et al.*, 2006; *Ferge et al.*, 2006; *Hopke*, 2008; *Qin et al.*, 2006; *Reinard et al.*, 2007; *Spencer and Prather*, 2006; *Zhou et al.*, 2007; *Zhou et al.*, 2006b]. Further, to advance quantification, Zhou et al. [2007] and Reinard and Johnston [2008] have examined ion formation mechanisms in LDI mass spectrometry of single particles.

1.3.6 Single-particle measurements – Other ionization techniques

To examine the alkali metal content of individual aerosol particles, Svane et al. [2004] used an aerodynamic lens inlet for particle focusing onto a hot platinum surface where particles decompose and are surface ionized, following by mass analysis using a quadrupole mass spectrometer; the use of a platinum surface with a work function of 5.65 eV allows the selective detection of alkali atoms with low ionization potentials (eg. Na, K, Rb, Cs). In a modified version of this surface ionization particle beam mass spectrometer, Svane et al. [2009] coupled a Pt surface heated to 1500 K to an orthogonal TOF-MS for increased sensitivity. Using a differential mobility analyzer for particle size-selection, the quantification of alkali metal content in 50-500 nm single particles was demonstrated for ambient urban aerosols with sea spray and biomass burning particles identified by sodium and potassium contents [*Svane et al.*, 2009].

To avoid the matrix effects presented by LDI, Simpson et al. [2009] developed an aerosol mass spectrometer incorporating CO_2 laser for particle desorption, followed by EI, and an ion trap mass spectrometer for MS^n experiments. This technique was tested on a variety of standard aromatic and aliphatic aerosols, and tandem mass spectrometry studies (up to MS^3) were performed for single caffeine particles [*Simpson et al.*, 2009].

1.4 Coupling of aerosol mass spectrometry with other techniques

The chemistry of a particle imparts its physical, optical, and hygroscopic properties [*Fuzzi et al.*, 2006]. Since aerosol chemistry changes during transport due to coagulation, heterogeneous reactions, gas-particle partitioning, and cloud processing [*Poschl*, 2005], it is important to understand and track the corresponding changes in physical, optical, and hygroscopic properties to better understand the impacts of aerosols on global climate, regional air pollution, and human health. By measuring chemical composition concurrently with aerosol properties, a greater understanding of the connections between these characteristics may be gained. With high time resolution, real-time aerosol mass spectrometry is ideal for the study of chemically-resolved aerosol properties, particularly for ambient particles where a changing aerosol population can be monitored. Here, we discuss chemically-resolved particle effective density, refractive index, volatility, and cloud activation properties.

1.4.1 Particle effective density

An understanding of particle density and morphology is important to properly predict heterogeneous chemistry processes and cloud activation properties and model aerosol transport and human health effects. By coupling a differential mobility analyzer (DMA) measuring mobility diameter (d_m) with a real-time aerosol mass spectrometer measuring vacuum aerodynamic diameter (d_{va}), the chemically-resolved particle effective density (ρ_{eff}) may be derived, as discussed by DeCarlo et al. [2004]. d_m and d_{va} are related in the following equation:

$$\rho_{eff} = \frac{d_{va}}{d_m}\rho_0 \qquad (1)$$

where ρ_{eff} is the particle effective density and ρ_0 is the standard density (1 g cm^{-3}) [*Jimenez et al.*, 2003]. For a spherical particle with no voids, ρ_{eff} is equal to ρ_p, the average particle density for a multiple component particle [*DeCarlo et al.*, 2004]. For non-spherical particles, $\rho_{eff} < \rho_p$; the effective density is proportional to the material density, but it also depends on particle shape, wherein the more irregular the particle, the lower effective density [*DeCarlo et al.*, 2004].

Several studies have coupled a DMA with an AMS for real-time, chemically-resolved aerosol measurements of effective density. Using a DMA-ATOFMS system, Slowik et al. [2004] examined soot particles generated from a propane/O_2 flame as a function of fuel equivalence ratio. Type 1 soot, produced from a lower fuel equivalence ratio (lower propane/O_2), was found to contain a lower non-refractory mass fraction (mostly PAHs) and have a lower ρ_{eff} (0.25-1.00 g/cm^3) compared to type 2 soot, which was produced from a higher fuel equivalence ratio and was found to contain a higher non-refractory mass fraction and have a higher ρ_{eff} (1.3 g/cm^3) [*Slowik et al.*, 2004]. By examining the relationship between particle mass and d_m, the soot fractal dimensions were also examined [*Slowik et al.*, 2004]. For the ozonolysis of oleic acid layers on polystyrene latex cores, Katrib et al. [2005] found that the reacted layer ρ_{eff}, equivalent to ρ_p for these spherical particles, increased from 0.89 to 1.12 g/cm^3 for increasing ozone exposure; AMS results showed that oxygen content of the outer layer increased concurrently. For the irradiation of 1,3,5-trimethylbenzene (1,3,5-TMB) and α-pinene in the presence of NO, NO_2, and propene, Alfarra et al. [2006] found effective densities of 1.35-1.40 g/cm^3 for the 1,3,5-TMB SOA and 1.29-1.32 g/cm^3 for the α-pinene SOA, where ρ_{eff} was not dependent on particle diameter; the SOA particles were found to be spherical, as shown by a narrow particle beam measured by a beam width probe. For non-spherical combustion particles from biomass burning using different fuels, Schneider et al. [2006] examined the relationship between d_{va} and d_m; by varying the dynamic shape factor, particle density was fit. Dinar et al. [2006] examined the ρ_{eff} of humic acid and humic like substance (HULIS) extracts from wood burning and pollution aerosol particles; through comparison of daytime and nighttime samples, atmospheric aging is suggested to increase the ρ_{eff} due to oxidation. Slowik et al. [2007] coated soot particles produced from an ethylene/O_2 flame with oleic acid and anthracene and examined the corresponding impacts on morphology (dynamic shape factor) and effective density.

Comparison of scanning mobility particle sizer (SMPS) mobility volume distributions with Aerodyne AMS mass distributions measured in parallel may be used to obtain average effective density for an entire ensemble of particles [*Jimenez et al.*, 2003]. For new particle formation resulting from the photooxidation of CH_2I_2, Jimenez et al. [2003] found that ρ_{eff} decreased with increasing photolysis time; particle composition was not found to be changing, suggesting that the particles were becoming less compact with time. For SOA resulting from the ozonolysis of cycloalkenes and biogenic hydrocarbons, Bahreini et al. [2005] found effective densities of 0.64-1.45 g/cm^3 depending on the particular system. For photooxidation of a range of monoterpenes and oxygenated terpenes under ~50% relative humidity, Varutbangkul et al. [2006] derived effective densities of 1.20-1.40 g/cm^3, which were then weighted by the mass of organic present, as measured by the AMS, to give the SOA density. Kostenidou et al. [2007] developed an algorithm to calculate organic aerosol density for multicomponent systems in which particle composition varied with size. For all but two cases, the ρ_{eff} of SOA resulting from the ozonolysis of α-pinene, β-pinene, and d-limonene with and without ammonium sulfate seeds was found to be within the range of 1.4-1.65 g/cm^3, suggesting that the SOA particles may be solid or waxy [*Kostenidou et al.*, 2007].

Using a DMA coupled to the SPLAT, individual particle ρ_{eff} has been measured for several spherical aerosol standards and compared to known literatures densities [*Zelenyuk et al.*, 2005]. In addition, through the measurement of ρ_{eff} for standard hygroscopic particles ($Ca(NO_3)_2$, $NaHSO_4$, $NaNO_3$, NH_4HSO_4, and NH_4NO_3), it is shown that once deliquesced, droplets persist in metastable phases near zero relative humidity with densities 7-10% lower than crystal densities, with the exception of ammonium bisulfate [*Zelenyuk et al.*, 2005]. Based on the examination of effective densities of hygroscopic droplets, Zelenyuk et al. [2006c] found that evaporation of water occurs in the aerodynamic lens inlet of real-time aerosol mass spectrometers. For agglomerates and irregularly shaped standard particles of known density, the dynamic shape factor was derived based on d_{va} and d_m for multiply charged particles; the dynamic shape factor was found to increase with increasing d_m for ammonium sulfate particles, for example [*Zelenyuk et al.*, 2006a]. For spherical dioctyl phthalate coated NaCl particles, the measured density (1.16 ± 0.01 g/cm^3) was in agreement with that calculated from volume fractions of NaCl and dioctyl phthalate with known densities: 2.165 and 0.986 g/cm^3, respectively [*Zelenyuk et al.*, 2008d]. In contrast, NaCl particles partially coated with pyrene, a solid PAH, are aspherical with an exposed NaCl core and pyrene nodules, as shown by an ρ_{eff} of 1.13 g/cm^3 compared to standard densities of 2.165 and 1.271 g/cm^3, respectively [*Zelenyuk et al.*, 2008c]. The asphericity of these particles is confirmed by examining the mass spectra at different laser intensities, allowing "depth-profiling" of the particles, where the pyrene-NaCl particles have higher Na^+ intensities at lower laser fluences compared to the dioctyl phthalate coated NaCl particles, which were spherical and fully coated [*Zelenyuk et al.*, 2008c]. For ozonolysis of α-pinene in the presence and absence of an OH scavenger, Zelenyuk et al. [2008d] derived effective densities of 1.198 ± 0.004 and 1.213 ± 0.003 g/cm^3, respectively. Similarly, Yu et al. [2008] measured a density of 1.21 ± 0.02 g/cm^3 for spherical SOA particles consisting of organic nitrates and oxygenates resulting from the photoxidation of α-pinene in the presence of NO_2.

Lastly, Zelenyuk et al. [2008a] recently measured ρ_{eff} for individual ambient particles of different chemical compositions: processed sea salt, biomass burning, sodium vanadium, and organic amines, for example.

A DMA has also been coupled to an ATOFMS for individual particle ρ_{eff} measurements. Concurrent with UF-ATOFMS chemical composition measurements for organic carbon/ elemental carbon (OC/EC) ratios, Spencer and Prather [2006] examined the ρ_{eff} of uncoated EC particles and EC particles coated with known amounts of organic liquid (gasoline). In the summer in Riverside, CA, particle effective densities were found to be ~1.0-1.5 g/cm^3 for all distinct single particle types (i.e., OC-sulfate-nitrate, vanadium-sulfate-nitrate, biomass burning) due to the dominance of secondary species and high water content [*Spencer et al.*, 2007]. In constrast, in the fall, individual particles composed primarily of EC, lubricating oil, and aged organic carbon were found to have ρ_{eff} of ~0.27 g/cm^3, 0.87 g/cm^3, and 0.93 g/cm^3, respectively due to the influence of clean and dry Santa Ana conditions [*Spencer et al.*, 2007]. DMA-ATOFMS studies of chemically-resolved individual particle ρ_{eff} have also been completed for agglomerate soot particles and diesel exhaust [*Park et al.*, 2008].

1.4.2 Particle refractive index

Knowledge of size- and chemically-resolved particle optical properties is critical for modeling the impact of different particle sources on direct radiative forcing [*Ghan and Schwartz*, 2007]. The ATOFMS and PALMS have been used to measure light scattering intensity concurrent with individual particle chemical composition [*Murphy et al.*, 2004a; *Salt et al.*, 1996]. Thus, to determine particle refractive index using the

ATOFMS, Moffet and Prather [2005] developed a method to calibrate the light scattering signal collected from individual particles using Mie theory to calculate the partial scattering cross section as a function of d_{va}. Using this method, particle density is used to fit the partial scattering cross section to Mie theory [*Moffet and Prather*, 2005]. For standard polystyrene latex (PSL) and dioctyl sebacate (DOS) spherical particles, retrieved refractive indices and densities were within literature values [*Moffet and Prather*, 2005]. For laboratory generated NaCl, refractive index (n) and ρ_{eff} were found to decrease for increasing relative humidity (RH) from 15-70% as these particles took up water [*Moffet et al.*, 2008b]. Similarly, for aged urban particles (Riverside, CA) containing elemental carbon, organic carbon, and ammonium nitrate, n and ρ_{eff} decreased with increasing RH for three different regimes: <40%, 40-70%, and >70% [*Moffet et al.*, 2008b]. For Mexico City particles containing fewer secondary species and water, higher n and ρ_{eff} were observed for a range of different particle types [*Moffet et al.*, 2008b]. By assuming refractive indices, the highest effective densities were calculated for nonspherical ambient lead- and zinc-rich particles: 2.4-3.4 g/cm^3 [*Moffet et al.*, 2008b]. Recently, Moffet and Prather [2009] reported the first coupled in-situ measurements of the size-resolved mixing state, optical properties, and aging timescales for soot particles. For modeling the direct radiative forcing of soot particles, Moffet and Prather [2009] suggest the use of a 100-200 nm core with age dependent coatings of sulfate, nitrate, water, and organic carbon having refractive indices of 1.44-1.49.

Similarly, Cross et al. [2007] incorporated a light scattering module, consisting of a 405 nm continuous wave laser, ellipsoidal mirror for scattered light collection, and photomultiplier tube (PMT) for light detection, into an Aerodyne AMS. In contrast to the light scattering modules within the ATOFMS and PALMS, this light scattering (LS)-AMS uses a broad laser beam, allowing particle optical diameter to be acquired from the scattered light intensity; particle density is calculated based on comparison of the optical and vacuum aerodynamic diameters [*Cross et al.*, 2007]. Refractive indices for standard spherical particles were calculated through comparison of the scattered light intensity with Mie theory [*Cross et al.*, 2007].

1.4.3 Particle volatility

To understand gas-particle partitioning of semivolatile species in the atmosphere, a thermodenuder (TD) may be coupled to a real-time aerosol mass spectrometer for size- and chemically-resolved volatility measurements. Huffman et al. [2008] developed an automated valve-controlled TD system in which particles are heated; volatilized species are removed using an activated charcoal diffusion denuder. Thus, in contrast to temperature programmed thermal desorption, the less volatile species remaining in the particle phase are sampled, rather than the desorbed species [*Huffman et al.*, 2008]. The TD temperature is varied, and the resulting heated particles are chemically analyzed by a real-time aerosol mass spectrometer with comparison to an ambient temperature sampling line every 10 minutes [*Huffman et al.*, 2008]. Using an AMS, Huffman et al. [2008] examined the mass fraction remaining at different TD temperatures for several aerosol standards. Using the TD-AMS system, volatility profiles of several non-refractory aerosol species (i.e. sulfate, ammonium, organics, chloride, nitrate) were examined for the first time for 54-230°C with 1-3 h time resolution for ambient particles in Mexico City, as well as laboratory biomass burning particles [*Huffman et al.*, 2008]. Huffman et al. [2009] also used the TD-AMS system to characterize the volatility of organic aerosol emitted from various sources, including biomass burning, trash burning, meat cooking, and chamber-generated secondary organic aerosol. Denkenberger et al. [2007], Chapter 3, coupled the TD to an ATOFMS during characterization of ambient particles in Riverside, CA; oligomeric mass spectral patterns were found to increase with heating, suggesting that increasing particle acidity and heating accelerate non-volatile oligomer formation. Similarly, Park et al. [2008] coupled a volatility tandem DMA (VTDMA) to an ATOFMS for chemical characterization of "more volatile" and "less volatile" particles in Atlanta, GA. Recently, using the TD-ATOFMS system, Pratt et al. [2009a], Chapter 5) observed a seasonal volatility dependence in ambient particle phase amines, which was attributed to the formation of non-volatile aminium nitrate and sulfate salts, compared to semi-volatile neutral amines.

Several laboratory studies have used the TD to examine the impacts of atmospheric aging on volatility and to further understand the partitioning of SOA. Using the TD-AMS system to examine the photooxidation of organic aerosol emissions from wood burning, Grieshop et al. [2009b] observed reduced volatility of aged organic aerosol compared to the primary organic aerosol. The aged wood burning organic aerosol was found to be highly oxygenated with similar mass spectral features compared to photooxidized diesel exhaust [*Grieshop et al.*, 2009a]. For SOA produced from the ozonolysis of α-pinene, β-pinene, limonene, and β-caryophyllene, Kostenidou et al. [2009] observed more volatile SOA species for higher precursor concentrations, whereas less volatile, more oxygenated SOA resulted from lower precursor concentrations. Lastly, Faulhaber et al. [2009] coupled the TD developed by Huffman et al. [2008] to the

TDPBMS to examine the volatility of SOA produced from the reaction of pentadecane with OH radicals in the presence of NO_x.

1.4.4 Cloud activation properties

As cloud activation properties are dependent on particle size and chemical composition, several techniques have been coupled to real-time aerosol mass spectrometers to further our understanding of cloud formation processes. In several studies, a hygroscopicity tandem DMA (HTDMA) system has been coupled to a SPMS to examine the chemical composition of particles as a function of hygroscopicity. Using a HTDMA coupled to the SPLAT for single particle analysis, Buzorius et al. [2002] demonstrated this technique using pure ammonium nitrate particles externally mixed from polystyrene latex spheres coated with ammonium nitrate. In addition, analysis of ambient particles revealed that the majority of the more hygroscopic particles were internally mixed sulfate and organics; whereas, the less hygroscopic mode was primarily composed of crustal material [*Buzorius et al.*, 2002]. Recently, Zelenyuk et al. [2008a] measured individual ambient particle hygroscopic growth factors using the HTDMA-SPLAT system for several particle types, including organics/sulfate, processed sea salt, biomass burning, sodium/vanadium, and organic amines. Using a HTDMA coupled to an ATOFMS, Herich et al. [2008] examined hygroscopic growth factors for individual particles sampled in urban Zurich, Switzerland and at the remote high alpine research station Jungfraujoch. Organics and combustion species were found in the less hygroscopic growth mode with noncombustion refractory material (e.g., metals, mineral dust, fly ash) in the non-hygroscopic mode [*Herich et al.*, 2008]. Sulfate was internally mixed with nearly all particles independent of their hygroscopic growth factor [*Herich et al.*, 2008].

To characterize particles with the ability to act as heterogeneous ice nuclei (IN) in clouds, PALMS has been utilized in series with a continuous flow diffusion chamber (CFDC), which detects and separates these IN-active particles. Using the method developed by Cziczo et al. [2003; 2006], aerosol particles with the ability to serve as IN are grown as ice crystals in simulated ice cloud conditions within the CFDC, after which these ice crystals are separated for unactivated particles and sampled by the PALMS. During CFDC-PALMS sampling in western Colorado, DeMott et al. [2003] observed mineral dust/fly ash and metallic particles to be enriched in the heterogeneous IN compared to the background aerosol which was primarily composed of sulfate/organic particles. In the examination of homogeneous freezing of ice, particles with high organic signals preferentially remained unfrozen [*Cziczo et al.*, 2004a]. In particular, lead-containing particles have been identified an efficient IN [*Cziczo et al.*, 2009]. Using a similar method, Gallavardin et al. [2008b] examined IN particles with PALMS following ice crystal growth within an ice nucleation chamber; bare mineral dust particles were found to be the most efficient IN with contamination from trace gas-phase species adding nitrate, sulfate, and organics to mineral dust and reducing IN efficiencies.

To study the particles found within actual cloud droplets and ice crystals, a counterflow virtual impactor (CVI) has been employed to separate these cloud particles from atmospheric trace gases and unactivated particles [*Ogren et al.*, 1985]. Following separation, water is evaporated from the cloud particles, and the cloud particles are either collected on filters or sampled directly by real-time aerosol techniques. Using laser microprobe mass spectrometry, an off-line LDI technique, Gieray et al. [1993] examined residual cloud droplet particles collected using a CVI; in particular, mineral dust particles were found to be incorporated into large droplets. For CVI sampling in clouds in the U.K. with laser microprobe mass spectrometry analysis, large droplet residues were observed to be sea-salt particles; whereas, smaller droplets contained sulfate and methansulfonate [*Gieray et al.*, 1997]. Recently, Hopkins et al. [2008] used off-line time-of-flight secondary ionization mass spectrometry (TOF-SIMS) to examine marine stratus cloud droplets collected via CVI sampling; sea salt methanesulfonate particles and ammonium sulfate particles were observed.

Counterflow virtual impactors have also been utilized in series with single particle mass spectrometers for the analysis of individual cloud particle residuals. During CVI-PALMS sampling during the 2002 Cirrus Regional Study of Tropical Anvils and Cirrus Layers – Florida Area Cirrus Experiment (CRYSTAL-FACE), Cziczo et al. [2004b] observed contributions from sea salt and mineral dust to ice crystals formed through homogeneous and heterogeneous processes, respectively. Further, the organic content of residues of homogeneously frozen ice particles was less than that of unfrozen interstitial particles [*Cziczo et al.*, 2004a]. In addition, lead was found to be the most common component of mineral dust ice residues impacted by heterogeneous freezing [*Cziczo et al.*, 2009]. ATOFMS sampling using the Ice-CVI at the high alpine research station Jungfraujoch showed black carbon particles internally mixed with organic carbon and often potassium to be enriched in ice residues [*Cozic et al.*, 2008]. Lastly, recent aircraft-based CVI sampling over Wyoming using the A-ATOFMS showed significant contributions of mineral dust and biological residues to cloud ice impacted by heterogeneous freezing (Chapter 7). While CVI studies have provided valuable information about cloud formation, it should be noted that Murphy et al. [2004b] found that generation and resuspension of particles, particularly metal particles, can occur during sampling of ice crystals and to a lesser extent cloud droplets.

Via CVI sampling, the AMS has also been utilized to study the chemical composition of non-refractory aerosol species within cloud droplets and ice crystals. During a study of warm clouds over central Sweden, Drewnick et al. [2007] and Targino et al. [2007] observed nitrate to be enriched in the cloud droplet residuals with additional contributions from organics, sulfate, and ammonium. For aircraft-based CVI-AMS measurements over the U.K., Choularton et al. [2008] observed residual particles of sulfate mixed with highly oxidized organics within stratocumulus cloud droplets. For aircraft measurements during the 2004 ICARTT program, higher nitrate/sulfate ratios were detected within cloud droplet residuals compared to the below cloud aerosol despite nitrate being observed in small residues than sulfate [*Hayden et al.*, 2008]. CVI-AMS measurements of warm clouds over Puerto Rico showed cloud droplet residuals primarily composed of sulfate with small contributions from nitrate and chloride [*Allan et al.*, 2008]. For the examination of 5-20 μm ice particles within mixed phase clouds, Mertes et al. [2007] developed an Ice-CVI which removes interstitial aerosol, supercooled droplets, and large ice crystals prior to filter-based and real-time chemical composition analysis. By coupling the Ice-CVI to an AMS, Mertes et al. [2007] and Cozic et al. [2008] found that the majority of the residual mass was refractory and unable to be detected by the AMS.

1.5 Summary and future outlook

In reviews of atmospheric aerosols, Poschl [2005] and Fuzzi et al. [2006] emphasized the need for future research to quantify and elucidate the mechanisms and kinetics of the nucleation, growth, and aging of atmospheric aerosols, in addition to further identifying primary aerosol emissions. Further, Poschl [2005] and Fuzzi et al. [2006] recommended that detailed aerosol chemical composition measurements be coupled with meteorology data and aerosol measurements of cloud condensation nuclei activity, ice nuclei activity, surface tension, density, and volatility. Herein, we have shown that real-time aerosol mass spectrometry has made significant advances toward these goals. Numerous chamber experiments have investigated the kinetics and mechanisms of SOA formation and heterogeneous reactions, giving insight into atmospheric reactions. Currently, transportable real-time mass spectrometers are used frequently on ground-, ship-, and aircraft-based studies across the globe to further our understanding of the spatial distribution of atmospheric aerosols. The development and field applications of the TD-CI-MS [*Held et al.*, 2009; *Voisin et al.*, 2003] and NAMS [*Wang et al.*, 2006] have provided highly time resolved chemical composition information for <30 nm ambient particles, significantly advancing our understanding of particle nucleation and growth. The TAG [*Williams et al.*, 2006] and 2D-TAG [*Goldstein et al.*, 2008] show the ability to provide organic molecular speciation on 1-2 hour timescales and with the incorporation of a TOF-MS, the 2D-TAG is expected to hold particular promise.

Further applications of the recently developed HR-TOF-AMS [*DeCarlo et al.*, 2006], A-ATOFMS [*Pratt et al.*, 2009b], and SPLAT-II [*Zelenyuk et al.*, 2009a] will provide additional information about the spatial distribution of atmospheric aerosols, as well as chemically-resolved particle effective density, refractive index, volatility, and cloud properties, as discussed above. Characterization of atmospheric aerosols using real-time mass spectrometers containing multiple vaporization/ionization techniques, such as those developed by Northway et al. [2007] and Bente et al. [*Bente et al.*, 2006], are expected to provide increased insight into ion fragmentation pathways and, therefore, aerosol chemical composition. Aerosol measurements using the surface ionization-based aerosol mass spectrometer developed by Svane et al. [2004] alongside the Aerodyne AMS and black carbon instrumentation should provide a more complete chemically-resolved quantification of aerosol mass. Future real-time aerosol mass spectrometry development work should focus on further understanding particle collection efficiencies for instruments with collection probes, such as the Aerodyne AMS, and quantification in SPMS using LDI. In the long term, miniature mass spectrometers, such as those overviewed by Ouyang et al. [2009] and used for atmospheric gas-phase analysis [*Keil et al.*, 2008], should be developed for the analysis of atmospheric aerosols for automated use on platforms such as unmanned aircraft vehicles (UAVs) [*Corrigan et al.*, 2008].

Future laboratory and field-based measurements should involve multiple aerosol mass spectrometry instruments side-by-side for quantitative, comprehensive, mixing state, and molecular speciation measurements of atmospheric aerosols, as well as real-time gas-phase mass spectrometry measurements to fully characterize gas-particle partitioning and heterogeneous chemistry. Further, additional measurements of chemically-resolved particle effective density, refractive index, volatility, cloud activation, and other microphysical properties are necessary to understand the atmospheric cycling and climate and human health impacts of aerosol particles. In addition, integration of in-situ aerosol chemical composition measurements into models, such as that accomplished by Cho et al. [2009], is necessary to validate and predict future air pollution and climate change [*Ghan and Schwartz*, 2007]. In particular, future applications of and developments in real-time aerosol mass spectrometry should focus on the following high priority tasks (in no particular order) recently identified by the U.S. Climate Change Program [*Chin et al.*, 2009]: a) measurement of the "formation, evolution, and properties of aerosols under controlled laboratory conditions to develop mechanistic and quantitative understanding of aerosol formation, chemistry, and dynamics", b) "coordinated field campaigns…to validate remote-sensing retrieval products, to evaluate chemistry transport models," and to distinguish between anthropogenic and natural aerosols, c) "simultaneous measurement[s] of aerosol composition and size distribution, cloud microphysical properties, and precipitation variables", d) "develop and evaluate emission inventories of aerosol particles and precursor gases", and e) profile "the vertical distributions of aerosols".

1.6 Acknowledgments

We thank Andrew Ault for helping edit this review.

Chapter 1 is in preparation for submission to *Mass Spectrometry Reviews*: Pratt, K.A., Prather, K.A. Mass spectrometry of atmospheric aerosols – Recent developments & applications. Part II: Real-time mass spectrometry techniques.

1.7 References

Aiken, A.C., P.F. DeCarlo, and J.L. Jimenez (2007), Elemental analysis of organic species with electron ionization high-resolution mass spectrometry, *Anal. Chem.*, *79*(21), 8350-8358.

Aiken, A.C., P.F. DeCarlo, J.H. Kroll, D.R. Worsnop, J.A. Huffman, K.S. Docherty, I.M. Ulbrich, C. Mohr, J.R. Kimmel, D. Sueper, Y. Sun, Q. Zhang, A. Trimborn, M. Northway, P.J. Ziemann, M.R. Canagaratna, T.B. Onasch, M.R. Alfarra, A.S.H. Prevot, J. Dommen, J. Duplissy, A. Metzger, U. Baltensperger, and J.L. Jimenez (2008), O/C and OM/OC ratios of primary, secondary, and ambient organic aerosols with high-resolution time-of-flight aerosol mass spectrometry, *Environ. Sci. Technol.*, *42*(4478-4485.

Alfarra, M.R., D. Paulsen, M. Gysel, A.A. Garforth, J. Dommen, A.S.H. Prévôt, D.R. Worsnop, U. Baltensperger, and H. Coe (2006), A mass spectrometric study of secondary organic aerosols formed from the photooxidation of anthropogenic and biogenic precursors in a reaction chamber, *Atmos. Chem. Phys.*, *6*(5279-5293.

Alfarra, M.R., A.S.H. Prevot, S. Szidat, J. Sandradewi, S. Weimer, V.A. Lanz, D. Schreiber, M. Mohr, and U. Baltensperger (2007), Identification of the mass spectral signature of organic aerosols from wood burning emissions, *Environ. Sci. Technol.*, *41*(5770-5777.

Allan, J.D., D. Baumgardner, G.B. Raga, O.L. Mayol-Bracero, F. Morales-García, F. García-García, G. Montero-Martínez, S. Borrmann, J. Schneider, S. Mertes, S. Walter, M. Gysel, U. Dusek, G.P. Frank, and M. Krämer (2008), Clouds and aerosols in Puerto Rico - a new evaluation, *Atmos. Chem. Phys.*, *8*(1293-1309.

Allen, G., G. Vaughan, K.N. Bower, P.I. Williams, J. Crosier, M. Flynn, P. Connolly, J.F. Hamilton, J.D. Lee, J.E. Saxton, N.M. Watson, M. Gallagher, H. Coe, J. Allan, T.W. Choularton, and A.C. Lewis (2008), Aerosol and trace-gas measurements in the Darwin area during the wet season, *J. Geophys. Res.*, *113*(D06306), doi:10.1029/2007JD008706.

Allen, J.O., P.V. Bhave, J.R. Whiteaker, and K.A. Prather (2006), Instrument busy time and mass measurement using aerosol time-of-flight mass spectrometry, *Aerosol Sci. Technol.*, *40*(8), 615-626.

Bahreini, R., M.D. Keywood, N.L. Ng, V. Varutbangkul, S. Gao, R.C. Flagan, J.H. Seinfeld, D.R. Worsnop, and J.L. Jimenez (2005), Measurements of secondary organic aerosol from oxidation of cycloalkenes, terpenes, and m-xylene using an Aerodyne aerosol mass spectrometer, *Environ. Sci. Technol.*, *39*(15), 5674-5688.

Bein, K.J., Y. Zhao, M.V. Johnston, and A.S. Wexler (2007), Identification of sources of atmospheric PM at the Pittsburgh Supersite - Part III: Source characterization, *Atmos. Environ.*, *41*(3974-3992.

Bein, K.J., Y. Zhao, M.V. Johnston, and A.S. Wexler (2008), Interactions between boreal wildfire and urban emissions, *J. Geophys. Res.*, *113*(D07304), doi:10.1029/2007JD008910.

Bein, K.J., Y. Zhao, N.J. Pekney, C.I. Davidson, M.V. Johnston, and A.S. Wexler (2006), Identification of sources of atmospheric PM at the Pittsburgh Supersite - Part II: Quantitative comparisons of single particle, particle number, and particle mass measurements, *Atmos. Environ.*, *40*(S424-S444.

Bein, K.J., Y. Zhao, A.S. Wexler, and M.V. Johnston (2005), Speciation of size-resolved individual ultrafine particles in Pittsburgh, Pennsylvania, *J. Geophys. Res.*, *110*(D07S05), doi:10.1029/2004JD004708.

Bente, M., T. Adam, T. Ferge, S. Gallavardin, M. Sklorz, T. Streibel, and R. Zimmermann (2006), An on-line aerosol laser mass spectrometer with three, easily interchangeable laser based ionisation methods for characterisation of inorganic and aromatic compounds on particles, *Int. J. Mass Spectrom.*, *258*(86-94.

Bente, M., M. Sklorz, T. Streibel, and R. Zimmermann (2008), Online laser desorption-multiphoton postionization mass spectrometry of individual aerosol particles: Molecular source indicators for particles emitted from different traffic-related and wood combustion sources, *Anal. Chem.*, *80*(8991-9004.

Bente, M., M. Sklorz, T. Streibel, and R. Zimmermann (2009), Thermal desorption-multiphoton ionization time-of-flight mass spectrometry of individual aerosol particles: A simplified approach for online single-particle analysis of polycyclic aromatic hydrocarbons and their derivatives, *Anal. Chem.*, *81*(2525-2536.

Bogan, M.J., E. Patton, A. Srivastava, S. Martin, D.P. Fergenson, P.T. Steele, H.J. Tobias, E.E. Gard, and M. Frank (2007), Online aerosol mass spectrometry of single micrometer-sized particles containing poly(ethylene glycol), *Rapid Commun. Mass Spectrom.*, *21*(1214-1220.

Bouvier-Brown, N.C., A.H. Goldstein, D.R. Worton, D.M. Matross, J.B. Gilman, W.C. Kuster, D. Welsh-Bon, C. Warneke, J.A. de Gouw, T.M. Cahill, and R. Holzinger (2009), Methyl chavicol: characterization of its biogenic emission rate, abundance, and oxidation products in the atmosphere, *Atmos. Chem. Phys.*, *9*(2061-2074.

Buzorius, G., A. Zelenyuk, F. Brechtel, and D. Imre (2002), Simultaneous determination of individual particle size, hygroscopicity and composition, *Geophys. Res. Lett.*, *29*(20), doi:10.1029/2001GL014221.

Cai, Y., A. Zelenyuk, and D. Imre (2006), A high resolution study of the effect of morphology on the mass spectra of single PSL particles with Na-containing layers and nodules, *Aerosol Sci. Technol.*, *40*(12), 1111-1122.

Canagaratna, M.R., J.T. Jayne, J.L. Jimenez, J.D. Allan, M.R. Alfarra, Q. Zhang, T.B. Onasch, F. Drewnick, H. Coe, A. Middlebrook, A. Delia, L.R. Williams, A.M. Trimborn, M.J. Northway, P.F. DeCarlo, C.E. Kolb, P. Davidovits, and D.R. Worsnop (2007), Chemical and microphysical characterization of ambient aerosols with the aerodyne aerosol mass spectrometer, *Mass Spectrom. Rev.*, *26*(2), 185-222.

Capes, G., B. Johnson, G. McFiggans, P.I. Williams, J. Haywood, and H. Coe (2008), Aging of biomass burning aerosols over West Africa: Aircraft measurements of chemical composition, microphysical properties, and emission ratios, *J. Geophys. Res.*, *113*(D00C15), doi:10.1029/2008JD009845.

Chang, R.Y.-W., P.S.K. Liu, W.R. Leaitch, and J.P.D. Abbatt (2007), Comparison between measured and predicted CCN concentrations at Egbert, Ontario: Focus on the organic aerosol fraction at a semi-rural site, *Atmos. Environ.*, *42*(8172-8182.

Chattopadhyay, S., H.J. Tobias, and P.J. Ziemann (2001), A method for measuring vapor pressures of low-volatility organic aerosol compounds using a thermal desorption particle beam mass spectrometer, *Anal. Chem.*, *73*(16), 3797-3803.

Chin, M., R.A. Kahn, and S.E. Schwartz, Atmospheric aerosol properties and climate impacts, U.S. Climate Change Science Program Synthesis and Assessment Product 2.3, National Aeronautics and Space Administration, Washington, D.C., 2009.

Cho, S.-W., and D. Lee (2007), An ion optics for effective ion detection in single particle mass spectrometry, *Rapid Commun. Mass Spectrom.*, *21*(3286-3294.

Cho, S., P.A. Makar, W.S. Lee, T. Herage, J. Liggio, S.M. Li, B. Wiens, and L. Graham (2009), Evaluation of a unified regional air-quality modeling system (AURAMS) using PrAIRie2005 field study data: The effects of emissions data accuracy on particle sulphate predictions, *Atmos. Environ.*, *43*(1864-1877.

Choularton, T.W., K.N. Bower, E. Weingartner, I. Crawford, H. Coe, M.W. Gallagher, M. Flynn, J. Crosier, P. Connolly, A. Targino, M.R. Alfarra, U. Baltensperger, S. Sjogren, B. Verheggen, J. Cozic, and M. Gysel (2008), The influence of small aerosol particles on the properties of water and ice clouds, *Faraday Discuss.*, *137*(205-222.

Corrigan, C.E., G.C. Roberts, M.V. Ramana, D. Kim, and V. Ramanathan (2008), Capturing vertical profiles of aerosols and black carbon over the Indian Ocean using autonomous unmanned aerial vehicles, *Atmos. Chem. Phys.*, *8*(737-747.

Cozic, J., S. Mertes, B. Verheggen, D.J. Cziczo, S.J. Gallavardin, S. Walter, U. Baltensperger, and E. Weingartner (2008), Black carbon enrichment in atmospheric ice particle residuals observed in lower tropospheric mixed-phase clouds, *J. Geophys. Res.*, *113*(D15209), doi:10.1029/2007JD009266.

Crosier, J., J.L. Jimenez, J.D. Allan, K.N. Bower, P.I. Williams, M.R. Alfarra, M.R. Canagaratna, J.T. Jayne, D.R. Worsnop, and H. Coe (2007), Technical Note: Description and use of the new jump mass spectrum mode of operation for the Aerodyne quadrupole mass spectrometers (Q-AMS), *Aerosol Sci. Technol.*, *41*(865-872.

Cross, E.S., J.G. Slowik, P. Davidovits, J.D. Allan, D.R. Worsnop, J.T. Jayne, D.K. Lewis, M. Canagaratna, and T.B. Onasch (2007), Laboratory and ambient particle density determinations using light scattering in conjunction with aerosol mass spectrometry, *Aerosol Sci. Technol.*, *41*(343-359.

Cubison, M.J., B. Ervens, G. Feingold, K.S. Docherty, I.M. Ulbrich, L. Shields, K. Prather, S. Hering, and J.L. Jimenez (2008), The influence of chemical composition and mixing state of Los Angeles urban aerosol on CCN number and cloud properties, *Atmos. Chem. Phys.*, *8*(5649-5667.

Cziczo, D.J., P.J. DeMott, C. Brock, P.K. Hudson, B. Jesse, S.M. Kreidenweis, A.J. Prenni, J. Schreiner, D.S. Thomson, and D.M. Murphy (2003), A method for single particle mass spectrometry of ice nuclei, *Aerosol Sci. Technol.*, *37*(5), 460-470.

Cziczo, D.J., P.J. DeMott, S.D. Brooks, A.J. Prenni, D.S. Thomson, D. Baumgardner, J.C. Wilson, S.M. Kreidenweis, and D.M. Murphy (2004a), Observations of organic species and atmospheric ice formation, *Geophys. Res. Lett.*, *31*(12).

Cziczo, D.J., D.M. Murphy, P.K. Hudson, and D.S. Thomson (2004b), Single particle measurements of the chemical composition of cirrus ice residue during CRYSTAL-FACE, *J. Geophys. Res.*, *109*(D04201), doi:10.1029/2003JD004032.

Cziczo, D.J., O. Stetzer, A. Worringen, M. Ebert, S. Weinbruch, M. Kamphus, S.J. Gallavardin, J. Curtius, S. Borrmann, K.D. Froyd, S. Mertes, O. Möhler, and U. Lohmann (2009), Inadvertent climate modification due to anthropogenic lead, *Nature Geoscience*, *2*(333-336.

Cziczo, D.J., D.S. Thomson, T.L. Thompson, P.J. DeMott, and D.M. Murphy (2006), Particle analysis by laser mass spectrometry (PALMS) studies of ice nuclei and other low number density particles, *Int. J. Mass Spectrom.*, *258*(1-3), 21-29.

Dall'Osto, M., M.J. Booth, W. Smith, R. Fisher, and R.M. Harrison (2008), A study of the size distributions and the chemical characterization of airborne particles in the vicinity of a large integrated steelworks, *Aerosol Sci. Technol.*, *42*(981-991.

Dall'Osto, M., and R.M. Harrison (2006), Chemical characterisation of single airborne particles in Athens (Greece) by ATOFMS, *Atmos. Environ.*, *40*(7614-7631.

Dall'Osto, M., R.M. Harrison, D.C.S. Beddows, E.J. Freney, M.R. Heal, and R.J. Donovan (2006), Single-particle detection efficiencies of aerosol time-of-flight mass spectrometry during the North Atlantic marine boundary layer experiment, *Environ. Sci. Technol.*, *40*(16), 5029-5035.

Dall'Osto, M., R.M. Harrison, E. Charpantidou, G. Loupa, and S. Rapsomanikis (2007), Characterisation of indoor airborne particles by using real-time aerosol mass spectrometry, *Sci. Total Environ.*, *384*(120-133.

Dall'Osto, M., R.M. Harrison, H. Coe, and P. Williams (2009), Real-time secondary aerosol formation during a fog event in London, *Atmos. Chem. Phys.*, *9*(2459-2469.

DeCarlo, P.F., E.J. Dunlea, J.R. Kimmel, A.C. Aiken, D. Sueper, J. Crounse, P.O. Wennberg, L. Emmons, Y. Shinozuka, A. Clarke, J. Zhou, J. Tomlinson, D.R. Collins, D. Knapp, A.J. Weinheimer, D.D. Montzka, T. Campos, and J.L. Jimenez (2008), Fast airborne aerosol size and chemistry measurements above Mexico City and Central Mexico during the MILAGRO campaign, *Atmos. Chem. Phys.*, *8*(4027-4048.

DeCarlo, P.F., J.R. Kimmel, A. Trimborn, M.J. Northway, J.T. Jayne, A.C. Aiken, M. Gonin, K. Fuhrer, T. Horvath, K.S. Docherty, D.R. Worsnop, and J.L. Jimenez (2006), Field-deployable, high-resolution, time-of-flight aerosol mass spectrometer, *Anal. Chem.*, *78*(24), 8281-8289.

DeCarlo, P.F., J.G. Slowik, D.R. Worsnop, P. Davidovits, and J.L. Jimenez (2004), Particle morphology and density characterization by combined mobility and aerodynamic diameter measurements. Part 1: Theory, *Aerosol Sci. Technol.*, *38*(12), 1185-1205.

Demirev, P.A., and C. Fenselau (2008), Mass spectrometry in biodefense, *J. Mass Spectrom.*, *43*(1441-1457.

DeMott, P.J., D.J. Cziczo, A.J. Prenni, D.M. Murphy, S.M. Kreidenweis, D.S. Thomson, R. Borys, and D.C. Rogers (2003), Measurements of the concentration and composition of nuclei for cirrus formation, *Proc. Natl. Acad. Sci. U. S. A.*, *100*(25), 14655-14660.

Denkenberger, K.A., R.C. Moffet, J.C. Holecek, T.P. Rebotier, and K.A. Prather (2007), Real-time, single-particle measurements of oligomers in aged ambient aerosol particles, *Environ. Sci. Technol.*, *41*(5439-5446.

Dinar, E., T.F. Mentel, and Y. Rudich (2006), The density of humic acids and humic like substances (HULIS) from fresh and aged wood burning and pollution aerosol particles, *Atmos. Chem. Phys.*, *6*(5213-5224.

Docherty, K.S., and P.J. Ziemann (2006), Reaction of oleic acid particles with NO radicals: Products, mechanism, and implications for radical-initated organic aerosol oxidation, *J. Phys. Chem. A*, *110*(10), 3567-2577.

Drewnick, F., M. Dall'Osto, and R. Harrison (2008), Characterization of aerosol particles from grass mowing by joint deployment of ToF-AMS and ATOFMS instruments, *Atmos. Environ.*, *42*(3006-3017.

Drewnick, F., S.S. Hings, M.R. Alfarra, A.S.H. Prevot, and S. Borrmann (2009), Aerosol quantification with the Aerodyne Aerosol Mass Spectrometer: detection limits and ionizer background effects, *Atmos. Meas. Tech.*, *2*(33-46.

Drewnick, F., J. Schneider, S.S. Hings, N. Hock, K. Noone, A. Targino, S. Weimer, and S. Borrmann (2007), Measurement of ambient, interstitial, and residual aerosol particles on a mountaintop site in central Sweden using an aerosol mass spectrometer and a CVI, *J. Atmos. Chem.*, *56*(1-20.

Dreyfus, M.A., K. Adou, S.M. Zucker, and M.V. Johnston (2009), Organic aerosol source apportionment from highly time-resolved molecular composition measurements, *Atmos. Environ.*, *43*(2901-2910.

Dreyfus, M.A., and M.V. Johnston (2008), Rapid sampling of individual organic aerosol species in ambient air with the photoionization aerosol mass spectrometer, *Aerosol Sci. Technol.*, *42*(1), 18-27.

Dzepina, K., J. Arey, L.C. Marr, D.R. Worsnop, D. Salcedo, Q. Zhang, T.B. Onasch, L.T. Molina, M.J. Molina, and J.L. Jimenez (2007), Detection of particle-phase polycyclic aromatic hydrocarbons in Mexico City using an aerosol mass spectrometer, *Int. J. Mass Spectrom.*, *263*(152-170.

Ervens, B., M. Cubison, E. Andrews, G. Feingold, J.A. Ogren, J.L. Jimenez, P. DeCarlo, and A. Nenes (2007), Prediction of cloud condensation nucleus number concentration using measurements of aerosol size distributions and composition and light scattering enhancement due to humidity, *J Geophys. Res.*, *112*(D10S32), doi:10.1029/2006JD007426.

Eyglunent, G., A. Le Person, J. Dron, A. Monod, D. Voisin, A. Mellouki, N. Marchand, and H. Wortham (2008), Simple and reversible transformation of an APCI/MS/MS into an aerosol mass spectrometer: Development and characterization of a new inlet, *Aerosol Sci. Technol.*, *42*(182-193.

Faulhaber, A.E., B.M. Thomas, J.L. Jimenez, J.T. Jayne, D.R. Worsnop, and P.J. Ziemann (2009), Characterization of a thermodenuder-particle beam mass spectrometer system for the study of organic aerosol volatility and composition, *Atmos. Meas. Tech.*, *2*(15-31.

Ferge, T., E. Karg, A. Schröppel, K.R. Coffee, H.J. Tobias, M. Frank, E.E. Gard, and R. Zimmermann (2006), Fast determination of the relative elemental and organic carbon content of aerosol samples by on-line single-particle aerosol time-of-flight mass spectrometry, *Environ. Sci. Technol.*, *40*(3327-3335.

Finlayson-Pitts, B.J., and J.N. Pitts, *Chemistry of the upper and lower atmosphere: Theory, experiments, and applications*, 969 pp., Academic Press, San Diego, 2000.

Freney, E.J., M.R. Heal, R.J. Donovan, N.L. Mills, K. Donaldson, D.E. Newby, P.H.B. Fokkens, and F.R. Cassee (2006), A single-particle characterization of a mobile Versatile Aerosol Concentration Enrichment System for exposure studies, *Part. Fibre Toxicol.*, *3*(8), doi:10.1186/1743-9877-3-8.

Furutani, H., M. Dall'Osto, G. Roberts, and K.A. Prather (2008), Assessment of the relative importance of atmospheric aging on CCN activity derived from field observations, *Atmos. Environ.*, *42*(3130-3142.

Fuzzi, S., M.O. Andreae, B.J. Huebert, M. Kulmala, T.C. Bond, M. Boy, S.J. Doherty, A. Guenther, M. Kanakidou, K. Kawamura, V.M. Kerminen, U. Lohmann, L.M. Russell, and U. Poschl (2006), Critical assessment of the current state of scientific knowledge, terminology, and research needs concerning the role of organic aerosols in the atmosphere, climate, and global change, *Atmos. Chem. Phys.*, *6*(2017-2038.

Gallavardin, S., U. Lohmann, and D. Cziczo (2008a), Analysis and differentiation of mineral dust by single particle laser mass spectrometry, *Int. J. Mass Spectrom.*, *274*(56-63.

Gallavardin, S.J., K.D. Froyd, U. Lohmann, O. Moehler, D.M. Murphy, and D.J. Cziczo (2008b), Single particle laser mass spectrometry applied to differential ice nucleation experiments at the AIDA chamber, *Aerosol Sci. Technol.*, *42*(773-791.

Gao, S., Y. Zhang, Y. Li, J. Meng, H. He, and J. Shu (2008), A comparison between the vacuum ultraviolet photoionization time-of-flight mass spectra and the GC/MS total ion chromatograms of polycyclic aromatic hydrocarbons contained in coal soot and multi-component PAH particles, *Int. J. Mass Spectrom.*, *274*(64-69.

Gao, S., Y. Zhang, J. Meng, and J. Shu (2009a), Online investigations on ozonation products of pyrene and benz[*a*]anthracene particles with a vacuum ultraviolet photoionization aerosol time-of-flight mass spectrometer, *Atmos. Environ.*, *43*(3319-3325.

Gao, S., Y. Zhang, J. Meng, and J. Shu (2009b), Real-time analysis of soot emissions from bituminous coal pyrolysis and combustion with a vacuum ultraviolet photoionization aerosol time-of-flight mass spectrometer, *Sci. Total Environ.*, *407*(1193-1199.

Gard, E., J.E. Mayer, B.D. Morrical, T. Dienes, D.P. Fergenson, and K.A. Prather (1997), Real-time analysis of individual atmospheric aerosol particles: Design and performance of a portable ATOFMS, *Anal. Chem.*, *69*(20), 4083-4091.

George, I.J., S. Vlasenko, J.G. Slowik, K. Broekhuizen, and J.P.D. Abbatt (2007), Heterogeneous oxidation of saturated organic aerosols by hydroxyl radicals: uptake kinetics, condensed-phase products, and particle size change, *Atmos. Chem. Phys.*, *7*(4187-4201.

Ghan, S.J., and S.E. Schwartz (2007), Aerosol properties and processes - A path from field and laboratory measurements to global climate models, *Bulletin Of The American Meteorological Society*, *88*(7), 1059-1083.

Gieray, R., G. Lammel, G. Metzig, and P. Wieser (1993), Size dependent single particle and chemical bulk analysis of droplets and interstitial particles in an orographic cloud, *Atmospheric Research*, *30*(263-293.

Gieray, R., P. Wieser, T. Engelhart, E. Swietlicki, H.-C. Hansson, B. Mentes, D. Orsini, B. Martinsson, B. Svenningsson, K.J. Noone, and J. Heintzenberg (1997), Phase partitioning of aerosol constituents in cloud based on single-particle and bulk analysis, *Atmos. Environ.*, *31*(16), 2491-2502.

Gloaguen, E., E.R. Mysak, S.R. Leone, M. Ahmed, and K.R. Wilson (2006), Investigating the chemical composition of mixed organic-inorganic particles by "soft" vacuum ultraviolet photoionization: The reaction of ozone with anthracene on sodium chloride particles, *Int. J. Mass Spectrom.*, *258*(74-85.

Goldstein, A.H., D.R. Worton, B.J. Williams, S.V. Hering, N.M. Kreisberg, O. Panić, and T. Górecki (2008), Thermal desorption comprehensive two-dimensional gas chromatography for in-situ measurements of organic aerosols, *J. Chromatogr. A*, *1186*(340-347.

Grieshop, A.P., N.M. Donahue, and A.L. Robinson (2009a), Laboratory investigation of photochemical oxidation of organic aerosol from wood fires 2: analysis of aerosol mass spectrometer data, *Atmos. Chem. Phys.*, *9*(2227-2240.

Grieshop, A.P., J.M. Logue, N.M. Donahue, and A.L. Robinson (2009b), Laboratory investigation of photochemical oxidation of organic aerosol from wood fires 1: measurement and simulation of organic aerosol evolution, *Atmos. Chem. Phys.*, *9*(1263-1277.

Gross, D.S., M.E. Gälli, M. Kalberer, A.S.H. Prevot, J. Dommen, M.R. Alfarra, J. Duplissy, K. Gaeggeler, A. Gascho, A. Metzger, and U. Baltensperger (2006), Real time measurement of oligomeric species in secondary organic aerosol with the aerosol time-of-flight mass spectrometer, *Anal. Chem.*, *78*(7), 2130-2137.

Gysel, M., J. Crosier, D.O. Topping, J.D. Whitehead, K.N. Bower, M.J. Cubison, P.I. Williams, M.J. Flynn, G.B. McFiggans, and H. Coe (2007), Closure study between chemical composition and hygroscopic growth of aerosol particles during TORCH2, *Atmos. Chem. Phys.*, *7*(6131-6144.

Hanna, S.J., P. Campuzano-Jost, E.A. Simpson, D.B. Robb, I. Burak, M.W. Blades, J.W. Hepburn, and A.K. Bertram (2009), A new broadly tunable (7.4-10.2 eV) laser based VUV light source and its first application to aerosol mass spectrometry, *Int. J. Mass Spectrom.*, *279*(134-146.

Hayden, K.L., A.M. Macdonald, W. Gong, D. Toom-Sauntry, K.G. Anlauf, A. Leithead, S.-M. Li, W.R. Leaitch, and K. Noone (2008), Cloud processing of nitrate, *J. Geophys. Res.*, *113*(D18201), doi:10.1029/2007JD009732.

Hearn, J.D., L.H. Renbaum, X. Wang, and G.D. Smith (2007), Kinetics and products from reaction of Cl radicals with dioctyl sebacate (DOS) particles in O_2: a model for radical-initiated oxidation of organic aerosols, *Phys. Chem. Chem. Phys.*, *9*(4803-4813.

Hearn, J.D., and G.D. Smith (2004), A chemical ionization mass spectrometry method for the online analysis of organic aerosols, *Anal. Chem.*, *76*(2820-2826.

Hearn, J.D., and G.D. Smith (2006a), A mixed-phase relative rates technique for measuring aerosol reaction kinetics, *Geophys. Res. Lett.*, *33*(L17805), doi:10.1029/2006GL026963.

Hearn, J.D., and G.D. Smith (2006b), Reactions and mass spectra of complex particles using Aerosol CIMS, *Int. J. Mass Spectrom.*, *258*(95-103.

Hearn, J.D., and G.D. Smith (2007), Ozonolysis of mixed oleic acid/*n*-docosane particles: The roles of phase, morphology, and metastable states, *J. Phys. Chem. A*, *111*(11059-11065.

Heaton, K.J., M.A. Dreyfus, S. Wang, and M.V. Johnston (2007), Oligomers in the early stage of biogenic secondary organic aerosol formation and growth, *Environ. Sci. Technol.*, *41*(6129-6136.

Held, A., G.J. Rathbone, and J.N. Smith (2009), A thermal desorption chemical ionization ion trap mass spectrometer for the chemical characterization of ultrafine aerosol particles, *Aerosol Sci. Technol.*, *43*(3), 264-272.

Hellén, H., J. Dommen, A. Metzger, A. Gascho, J. Duplissy, T. Tritscher, A.S.H. Prevot, and U. Baltensperger (2008), Using proton transfer reaction mass spectrometry for online analysis of secondary organic aerosols, *Environ. Sci. Technol.*, *42*(7347-7353.

Herich, H., L. Kammermann, M. Gysel, E. Weingartner, U. Baltensperger, U. Lohmann, and D.J. Cziczo (2008), In situ determation of atmospheric aerosol composition as a function of hygroscopic growth, *J. Geophys. Res.*, *113*(D16213), doi:10.1029/2008JD009954.

Hersey, S.P., A. Sorooshian, S.M. Murphy, R.C. Flagan, and J.H. Seinfeld (2009), Aerosol hygroscopicity in the marine atmosphere: a closure study using high-time-resolution, multiple-RH DASH-SP and size-resolved C-ToF-AMS data, *Atmos. Chem. Phys.*, *9*(2543-2554.

Hinz, K.P., and B. Spengler (2007), Instrumentation, data evaluation and quantification in on-line aerosol mass spectrometry, *J. Mass Spectrom.*, *42*(7), 843-860.

Hopke, P.K. (2008), Quantitative results from single-particle characterization data, *J. Chemom.*, *22*(528-532.

Hopkins, R.J., Y. Desyaterik, A.V. Tivanski, R.A. Zaveri, C.M. Berkowitz, T. Tyliszczak, M.K. Gilles, and A. Laskin (2008), Chemical speciation of sulfur in marine cloud droplets and particles: Analysis of individual particles from the marine boundary layer over the California current, *J. Geophys. Res.*, *113*(D04209), doi:10.1029/2007JD008954.

Huey, L.G. (2007), Measurement of trace atmospheric species by chemical ionization mass spectrometry: Speciation of reactive nitrogen and future directions, *Mass Spectrom. Rev.*, *26*(166-184.

Huffman, J.A., K.S. Docherty, C. Mohr, M.J. Cubison, I.M. Ulbrich, P.J. Ziemann, T.B. Onasch, and J.L. Jimenez (2009), Chemically-resolved volatility measurements of organic aerosol from different sources, *Environ. Sci. Technol.*, *In Press*(

Huffman, J.A., P.J. Ziemann, J.T. Jayne, D.R. Worsnop, and J.L. Jimenez (2008), Development and characterization of a fast-stepping/scanning thermodenuder for chemically-resolved aerosol volatility measurements, *Aerosol Sci. Technol.*, *42*(5), 395-407.

Hunt, A.L., and G.A. Petrucci (2002), Analysis of ultrafine and organic particles by aerosol mass spectrometry, *Trends Anal. Chem.*, *21*(2), 74-81.

Jimenez, J.L., R. Bahreini, D.R. Cocker, H. Zhuang, V. Varutbangkul, R.C. Flagan, J.H. Seinfeld, C.D. O'Dowd, and T. Hoffmann (2003), New particle formation from photooxidation of diiodomethane (CH_2I_2), *J. Geophys. Res.*, *108*(D10), doi:10.1029/2002JD002452.

Johnston, M.V., S. Wang, and M.S. Reinard (2006), Nanoparticle mass spectrometry: Pushing the limit of single particle analysis, *Appl. Spectrosc.*, *60*(10), 264A-272A.

Katrib, Y., S.T. Martin, Y. Rudich, P. Davidovits, J.T. Jayne, and D.R. Worsnop (2005), Density changes of aerosol particles as a result of chemical reaction, *Atmos. Chem. Phys.*, *5*(275-291.

Keil, A., H. Hernandez-Soto, R.J. Noll, M. Fico, L. Gao, Z. Ouyang, and R.G. Cooks (2008), Monitoring of toxic compounds in air using a handheld rectilinear ion trap mass spectrometer, *Anal. Chem.*, *80*(734-741.

King, S.M., T. Rosenoern, J.E. Shilling, Q. Chen, and S.T. Martin (2007), Cloud condensation nucleus activity of secondary organic aerosol particles mixed with sulfate, *Geophys. Res. Lett.*, *34*(L24806), doi:10.1029/2007GL030390.

Kleefsman, I., M.A. Stowers, P.J.T. Verheijen, A.L. van Wuijckhuijse, C.E. Kientz, and J.C.M. Marijnissen (2007), Bioaerosol analysis by single particle mass spectrometry, *Part. Part. Syst. Charact.*, *24*(85-90.

Kleefsman, W.A., M.A. Stowers, P.J.T. Verheijen, and J.C.M. Marijnissen (2008), Single particle mass spectrometry - Bioaerosol analysis by MALDI MS, *KONA Power and Particle Journal*, *26*(205-214.

Kleinman, L.I., P.H. Daum, Y.-N. Lee, G.I. Senum, S.R. Springston, J. Wang, C. Berkowitz, J. Hubbe, R.A. Zaveri, F.J. Brechtel, J. Jayne, T.B. Onasch, and D. Worsnop (2007), Aircraft observations of aerosol composition and ageing in New England and Mid-Atlantic States during the summer 2002 New England Air Quality Study field campaign, *J. Geophys. Res.*, *112*(D09310), doi:10.1029/2006JD007786.

Kleinman, L.I., S.R. Springston, P.H. Daum, Y.-N. Lee, L.J. Nunnermacker, G.I. Senum, J. Wang, J. Weinstein-Lloyd, M.L. Alexander, J. Hubbe, J. Ortega, M.R. Canagaratna, and J. Jayne (2008), The time evolution of aerosol composition over the Mexico City plateau, *Atmos. Chem. Phys.*, *8*(1559-1575.

Kostenidou, E., B.-H. Lee, G.J. Engelhart, J.R. Pierce, and S.N. Pandis (2009), Mass spectra deconvolution of low, medium, and high volatility biogenic secondary organic aerosol, *Environ. Sci. Technol.*, *In Press*(

Kostenidou, E., R.K. Pathak, and S.N. Pandis (2007), An algorithm for the calculation of secondary organic aerosol density combining AMS and SMPS data, *Aerosol Sci. Technol.*, *41*(1002-1010.

Kreisberg, N.M., S.V. Hering, B.J. Williams, D.R. Worton, and A.H. Goldstein (2009), Quantification of hourly speciated organic compounds in atmospheric aerosols, measured by an in-situ thermal desorption aerosol gas chromatograph (TAG), *Aerosol Sci. Technol.*, *43*(38-52.

Kürten, A., J. Curtius, F. Helleis, E.R. Lovejoy, and S. Borrmann (2007), Development and characterization of an ion trap mass spectrometer for the on-line chemical analysis of atmospheric aerosol particles, *Int. J. Mass Spectrom.*, *265*(30-39.

LaFranchi, B.W., and G.A. Petrucci (2004), Photoelectron resonance capture ionization (PERCI): A novel technique for the soft-ionization of organic compounds, *J. Am. Soc. Mass Spectrom.*, *15*(424-430.

LaFranchi, B.W., and G.A. Petrucci (2006), A comprehensive characterization of photoelectron resonance capture ionization aerosol mass spectrometry for the quantitative and qualitative analysis of organic particulate matter, *Int. J. Mass Spectrom.*, *258*(120-133.

Lanz, V.A., M.R. Alfarra, U. Baltensperger, B. Buchmann, C. Hueglin, and A.S.H. Prévôt (2007), Source apportionment of submicron organic aerosols at an urban site by factor analytical modelling of aerosol mass spectra, *Atmos. Chem. Phys.*, *7*(1503-1522.

Lee, D., A. Miller, D. Kittelson, and M.R. Zachariah (2006), Characterization of metal-bearing diesel nanoparticles using single-particle mass spectrometry, *J. Aerosol Sci.*, *37*(88-110.

Lee, D., K. Park, and M.R. Zachariah (2005), Determination of the size distribution of polydisperse nanoparticles with single-particle mass spectrometry: The role of ion kinetic energy, *Aerosol Sci. Technol.*, *39*(2), 162-169.

Lee, K.-S., S.-W. Cho, and D. Lee (2008), Development and experimental evaluation of aerodynamic lens as an aerosol inlet of single particle mass spectrometry, *J. Aerosol Sci.*, *39*(287-304.

Liggio, J., and S.-M. Li (2008), Reversible and irreversible processing of biogenic olefins on acidic aerosols, *Atmos. Chem. Phys.*, *8*(2039-2055.

Liggio, J., S.-M. Li, J.R. Brook, and C. Mihele (2007), Direct polymerization of isoprene and α-pinene on acidic aerosols, *Geophys. Res. Lett.*, *34*(L05814), doi:10.1029/2006GL028468.

Lim, Y.B., and P.J. Ziemann (2009a), Chemistry of secondary organic aerosol formation from OH radical-initiated reactions of linear, branched, and cyclic alkanes in the presence of NO_x, *Aerosol Sci. Technol.*, *43*(604-619.

Lim, Y.B., and P.J. Ziemann (2009b), Effects of molecular structure on aerosol yields from OH radical-initiated reactions of linear, branched, and cyclic alkanes in the presence of NO_x, *Environ. Sci. Technol.*, *43*(2328-2334.

Liu, P.S.K., R. Deng, K.A. Smith, L.R. Williams, J.T. Jayne, M.R. Canagaratna, K. Moore, T.B. Onasch, D.R. Worsnop, and T. Deshler (2007), Transmission efficiency of an aerodynamic focusing lens system: Comparison of model calculations and laboratory measurements for the Aerodyne aerosol mass spectrometer, *Aerosol Sci. Technol.*, *41*(8), 721-733.

Lloyd, J.A., K.J. Heaton, and M.V. Johnston (2009), Reactive uptake of trimethylamine into ammonium nitrate particles, *J. Phys. Chem. A*, *113*(4840-4843.

Lloyd, J.A., and M.V. Johnston (2009), An IT-TOF mass spectrometer for the analysis of organic aerosol, *Int. J. Mass Spectrom.*, *281*(8-14.

Mahadevan, R., D. Lee, H. Sakurai, and M.R. Zachariah (2002), Measurement of condensed-phase reaction kinetics in the aerosol phase using single particle mass spectrometry, *J. Phys. Chem. A*, *106*(11083-11092.

Mallina, R.V., A.S. Wexler, K.P. Rhoads, and M.V. Johnston (2000), High speed particle beam generation: A dynamic focusing mechanisms for selecting ultrafine particles, *Aerosol Sci. Technol.*, *33*(87-104.

Malloy, Q.G.J., L. Qi, B. Warren, D.R. Cocker, M.E. Erupe, and P.J. Silva (2009), Secondary organic aerosol formation from primary aliphatic amines with NO_3 radical, *Atmos. Chem. Phys.*, *9*(2051-2060.

Martin, A.N., G.R. Farquar, M. Frank, E.E. Gard, and D.P. Fergenson (2007a), Single-particle aerosol mass spectrometry for the detection and identification of chemical warfare agent simulants, *Anal. Chem.*, *79*(6368-6375.

Martin, A.N., G.R. Farquar, E.E. Gard, M. Frank, and D.P. Fergenson (2007b), Identification of high explosives using single-particle aerosol mass spectrometry, *Anal. Chem.*, *79*(5), 1918-1925.

Martin, R.S., P.J. Silva, K. Moore, M. Erupe, and V.S. Doshi (2008), Particle composition and size distributions in and around a deep-pit swine operation, Ames, IA, *J. Atmos. Chem.*, *59*(135-150.

Matsunaga, A., K.S. Docherty, Y.B. Lim, and P.J. Ziemann (2009), Composition and yields of secondary organic aerosol formed from OH radical-initiated reactions of linear alkenes in the presence of NO_x: Modeling and measurements, *Atmos. Environ.*, *43*(1349-1357.

Matsunaga, A., and P.J. Ziemann (2009), Yield of β-hydroxynitrates and dihydroxynitrates in aerosol formed from OH radical-initiated reactions of linear alkenes in the presence of NO_x, *J. Phys. Chem. A*, *113*(599-606.

Matthew, B.M., A.M. Middlebrook, and T.B. Onasch (2008), Collection efficiencies in an Aerodyne aerosol mass spectrometer as a function of particle phase for laboratory generated aerosols, *Aerosol Sci. Technol.*, *42*(884-898.

Mazurek, M.A. (2002), Molecular identification of organic compounds in atmospheric complex mixtures and relationship to atmospheric chemistry and sources, *Environ. Health Perspect.*, *110*(Supplement 6), 995-1003.

McJimpsey, E.L., W.M. Jackson, C.B. Lebrilla, H. Tobias, M.J. Bogan, E.E. Gard, M. Frank, and P.T. Steele (2008), Parameters contributing to efficient ion generation in aerosol MALDI mass spectrometry, *J. Am. Soc. Mass Spectrom.*, *19*(315-324.

McKeown, P.J., M.V. Johnston, and D.M. Murphy (1991), On-line single-particle analysis by laser desorptioni mass spectrometry, *Anal. Chem.*, *63*(2069-2073.

McMurry, P.H. (2000), A review of atmospheric aerosol measurements, *Atmos. Environ.*, *34*(1959-1999.

McNeill, V.F., G.M. Wolfe, and J.A. Thornton (2007), The oxidation of oleate in submicron aqueous salt aerosols: Evidence of a surface process, *J. Phys. Chem. A*, *111*(1073-1083.

McNeill, V.F., R.L.N. Yatavelli, J.A. Thornton, C.B. Stipe, and O. Landgrebe (2008), Heterogeneous OH oxidation of palmitic acid in single component and internally mixed aerosol particles: vaporization and the role of particle phase, *Atmos. Chem. Phys.*, *8*(5465-5476.

Medina, J., A. Nenes, R.-E.P. Sotiropoulou, L.D. Cottrell, L.D. Ziemba, P.J. Beckman, and R.J. Griffin (2007), Cloud condensation nuclei closure during the International Consortium for Atmospheric Research on Transport and Transformation 2004 campaign: Effects of size-resolved composition, *J. Geophys. Res.*, *112*(D10S31), doi:10.1029/2006JD007588.

Mertes, S., B. Verheggen, S. Walter, P. Connolly, M. Ebert, J. Schneider, K.N. Bower, J. Cozic, S. Weinbruch, U. Baltensperger, and E. Weingartner (2007), Counterflow virtual impactor based collection of small ice particles in mixed-phase clouds for the physico-chemical characterization of tropospheric ice nuclei: Sampler description and first case study, *Aerosol Sci. Technol.*, *41*(9), 848-864.

Moffet, R.C., B. de Foy, L.T. Molina, M.J. Molina, and K.A. Prather (2008a), Measurement of ambient aerosols in northern Mexico City by single particle mass spectrometry, *Atmos. Chem. Phys.*, *8*(4499-4516.

Moffet, R.C., and K.A. Prather (2005), Extending ATOFMS measurements to include refractive index and density, *Anal. Chem.*, *77*(20), 6535-6541.

Moffet, R.C., and K.A. Prather (2009), In-situ measurements of the mixing state and optical properties of soot: Implications for radiative forcing estimates, *Proc. Natl. Acad. Sci. U. S. A.*, *Accepted*(

Moffet, R.C., X. Qin, T. Rebotier, H. Furutani, and K.A. Prather (2008b), Chemically segregated optical and microphysical properties of ambient aerosols measured in a single-particle mass spectrometer, *J. Geophys. Res.*, *113*(doi:10.1029/2007JD009393.

Mohr, C., J.A. Huffman, M.J. Cubison, A.C. Aiken, K.S. Docherty, J.R. Kimmel, I.M. Ulbrich, M. Hannigan, and J.L. Jimenez (2009), Characterization of primary organic aerosol emissions from meat cooking, trash burning, and motor vehicles with high-resolution aerosol mass spectrometry and comparison with ambient and chamber observations, *Environ. Sci. Technol.*, *43*(2443-2449.

Morrical, B.D., D.P. Fergenson, and K.A. Prather (1998), Coupling two-step laser desorption/ionization with aerosol time-of-flight mass spectrometry for the analysis of individual organic particles, *J. Am. Soc. Mass Spectrom.*, *9*(10), 1068-1073.

Muhle, J., Lueker, T.J., Su, Y., Miller, B.R., Prather, K.A., Weiss, R.F. (2006), Trace gas and particulate emissions from the 2003 southern California wildfires, *J. Geophys. Res.*, *Accepted.*(

Murphy, D.M. (2005), Something in the air, *Science*, *307*(5717), 1888-1890.

Murphy, D.M. (2007), The design of single particle laser mass spectrometers, *Mass Spectrom. Rev.*, *26*(2), 150-165.

Murphy, D.M., D.J. Cziczo, K.D. Froyd, P.K. Hudson, B.M. Matthew, A.M. Middlebrook, R.E. Peltier, A. Sullivan, D.S. Thomson, and R.J. Weber (2006a), Single-particle mass spectrometry of tropospheric aerosol particles, *J. Geophys. Res.*, *111*(D23S32), doi:10.1029/2006JD007340.

Murphy, D.M., D.J. Cziczo, P.K. Hudson, M.E. Schein, and D.S. Thomson (2004a), Particle density inferred from simultaneous optical and aerodynamic diameters sorted by composition, *J. Aerosol Sci.*, *35*(135-139.

Murphy, D.M., D.J. Cziczo, P.K. Hudson, and D.S. Thomson (2007a), Carbonaceous material in aerosol particles in the lower stratosphere and tropopause region, *J. Geophys. Res.*, *112*(D4).

Murphy, D.M., D.J. Cziczo, P.K. Hudson, D.S. Thomson, J.C. Wilson, T. Kojima, and P.R. Buseck (2004b), Particle generation and resuspension in aircraft inlets when flying in clouds, *Aerosol Sci. Technol.*, *38*(4), 400-408.

Murphy, D.M., P.K. Hudson, D.J. Cziczo, S. Gallavardin, K.D. Froyd, M.V. Johnston, A.M. Middlebrook, M.S. Reinard, D.S. Thomson, T. Thornberry, and A.S. Wexler (2007b), Distribution of lead in single atmospheric particles, *Atmos. Chem. Phys.*, *7*(3195-3210.

Murphy, D.M., P.K. Hudson, D.S. Thomson, P.J. Sheridan, and J.C. Wilson (2006b), Observations of mercury-containing aerosols, *Environ. Sci. Technol.*, *40*(10), 3163-3167.

Murphy, D.M., and D.S. Thomson (1995), Laser ionization mass spectroscopy of single aerosol particles, *Aerosol Sci. Technol.*, *22*(3), 237-249.

Murphy, S.M., A. Sorooshian, J.H. Kroll, N.L. Ng, P. Chhabra, C. Tong, J.D. Surratt, E. Knipping, R.C. Flagan, and J.H. Seinfeld (2007c), Secondary aerosol formation from atmospheric reactions of aliphatic amines, *Atmos. Chem. Phys.*, *7*(9), 2313-2337.

Mysak, E.R., K.R. Wilson, M. Jimenez-Cruz, M. Ahmed, and T. Baer (2005), Synchrotron radiation based aerosol time-of-flight mass spectrometry for organic constituents, *Anal. Chem.*, *77*(18), 5953-5960.

Nash, D.G., T. Baer, and M.V. Johnston (2006), Aerosol mass spectrometry: An introductory review, *Int. J. Mass Spectrom.*, *258*(1-3), 2-12.

Noble, C.A., and K.A. Prather (2000), Real-time single particle mass spectrometry: A historical review of a quarter century of the chemical analysis of aerosols, *Mass Spectrom. Rev.*, *19*(4), 248-274.

Northway, M.J., J.T. Jayne, D.W. Toohey, M.R. Canagaratna, A. Trimborn, K.-I. Akiyama, A. Shimono, J.L. Jimenez, P.F. DeCarlo, K.R. Wilson, and D.R. Worsnop (2007), Demonstration of a VUV lamp photoionization source for improved organic speciation in an aerosol mass spectrometer, *Aerosol Sci. Technol.*, *41*(828-839.

Ogren, J.A., J. Heintzenberg, and R.J. Charlson (1985), In-situ sampling of clouds with a droplet to aerosol converter, *Geophys. Res. Lett.*, *12*(3), 121-124.

Öktem, B., M.P. Tolocka, and M.V. Johnston (2004), On-line analysis of organic components in fine and ultrafine particles by photoionization aerosol mass spectrometry, *Anal. Chem.*, *76*(2), 253-261.

Ouyang, Z., R.J. Noll, and R.G. Cooks (2009), Handheld miniature ion trap mass spectrometers, *Anal. Chem.*, *81*(2421-2425.

Park, K., D. Dutcher, M. Emery, J. Pagels, H. Sakurai, J. Scheckman, S. Qian, M.R. Stolzenburg, Z. Wang, J. Yang, and P.H. McMurry (2008), Tandem measurements of aerosol properties - A review of mobility techniques with extensions, *Aerosol Sci. Technol.*, *42*(801-816.

Pekney, N.J., C.I. Davidson, K.J. Bein, A.S. Wexler, and M.V. Johnston (2006), Identification of sources of atmospheric PM at the Pittsburgh Supersite, Part I: Single particle analysis and filter-based positive matrix factorization, *Atmos. Environ.*, *40*(S411-S423.

Pope, C.A., and D.W. Dockery (2006), Health effects of fine particulate air pollution: Lines that connect, *J. Air Waste Manage. Assoc.*, *56*(709-742.

Poschl, U. (2005), Atmospheric aerosols: Composition, transformation, climate and health effects, *Angewandte Chemie-International Edition*, *44*(46), 7520-7540.

Prather, K.A., C.D. Hatch, and V.H. Grassian (2008), Analysis of atmospheric aerosols, *Annu. Rev. Anal. Chem.*, *1*(16.1-16.30.

Prather, K.A., T. Nordmeyer, and K. Salt (1994), Real-time characterization of individual aerosol-particles using time-of-flight mass-spectrometry, *Anal. Chem.*, *66*(9), 1403-1407.

Pratt, K.A., L.E. Hatch, and K.A. Prather (2009a), Seasonal volatility dependence of ambient particle phase amines, *Environ. Sci. Technol.*, *In Press*(

Pratt, K.A., J.E. Mayer, J.C. Holecek, R.C. Moffet, R.O. Sanchez, T.P. Rebotier, H. Furutani, M. Gonin, K. Fuhrer, Y. Su, S. Guazzotti, and K.A. Prather (2009b), Development and characterization of an aircraft aerosol time-of-flight mass spectrometer, *Anal. Chem.*, *81*(5), 1792-1800.

Qin, X., and K.A. Prather (2006), Impact of biomass emissions on particle chemistry during the California Regional Particulate Air Quality Study, *Int. J. Mass Spectrom.*, *258*(142-150.

Qin, X.Y., P.V. Bhave, and K.A. Prather (2006), Comparison of two methods for obtaining quantitative mass concentrations from aerosol time-of-flight mass spectrometry measurements, *Anal. Chem.*, *78*(17), 6169-6178.

Quinn, P.K., T.S. Bates, D.J. Coffman, and D.S. Covert (2008), Influence of particle size and chemistry on the cloud nucleating properties of aerosols, *Atmos. Chem. Phys.*, *8*(1029-1042.

Raes, F., R. Van Dingenen, E. Vignati, J. Wilson, J.P. Putaud, J.H. Seinfeld, and P. Adams (2000), Formation and cycling of aerosols in the global troposphere, *Atmos. Environ.*, *34*(4215-4240.

Rebotier, T.P., and K.A. Prather (2007), Aerosol time-of-flight mass spectrometry data analysis: A benchmark of clustering algorithms, *Anal. Chim. Acta*, *585*(38-54.

Reinard, M.S., K. Adou, J.M. Martini, and M.V. Johnston (2007), Source characterization and identification by real-time single particle mass spectrometry, *Atmos. Environ.*, *41*(9397-9409.

Reinard, M.S., and M.V. Johnston (2008), Ion formation mechanism in laser desorption ionization of individual nanoparticles, *J. Am. Soc. Mass Spectrom.*, *19*(389-399.

Renbaum, L.H., and G.D. Smith (2009), The importance of phase in the radical-initiated oxidation of model organic aerosols: reactions of solid and liquid brassidic acid particles, *Phys. Chem. Chem. Phys.*, *11*(2441-2451.

Rogge, W.F., M.A. Mazurek, L.M. Hildemann, G.R. Cass, and B.R.T. Simoneit (1993), Quantification of urban organic aerosols at a molecular-level - Identification, abundance and seasonal-variation, *Atmos. Environ.*, *27*(8), 1309-1330.

Rosen, E.P., E.R. Garland, and T. Baer (2008), Ozonolysis of oleic acid adsorbed to polar and nonpolar aerosol particles, *J. Phys. Chem. A*, *112*(10315-10324.

Russell, S.C. (2009), Microorganism characterization by single particle mass spectrometry, *Mass Spectrom. Rev.*, *28*(376-387.

Russell, S.C., G. Czerwieniec, C. Lebrilla, P. Steele, V. Riot, K. Coffee, M. Frank, and E.E. Gard (2005), Achieving high detection sensitivity (14 zmol) of biomolecular ions in bioaerosol mass spectrometry, *Anal. Chem.*, *77*(4734-4741.

Sage, A.M., E.A. Weitkamp, A.L. Robinson, and N.M. Donahue (2008), Evolving mass spectra of the oxidized component of organic aerosol: results from aerosol mass spectrometer analyses of aged diesel emissions, *Atmos. Chem. Phys.*, *8*(1139-1152.

Salcedo, D., T.B. Onasch, M.R. Canagaratna, K. Dzepina, J.A. Huffman, J.T. Jayne, D.R. Worsnop, C.E. Kolb, S. Weimer, F. Drewnick, J.D. Allan, A.E. Delia, and J.L. Jimenez (2007), Technical Note: Use of a beam width probe in an Aerosol Mass Spectrometer to monitor particle collection efficiency in the field, *Atmos. Chem. Phys.*, *7*(549-556.

Salt, K., C.A. Noble, and K.A. Prather (1996), Aerodynamic particle sizing versus light scattering intensity measurement as methods for real time particle sizing coupled with time-of-flight mass spectrometry, *Anal. Chem.*, *68*(1), 230-234.

Schlesinger, R.B., N. Kunzli, G.M. Hidy, T. Gotschi, and M. Jerrett (2006), The health relevance of ambient particulate matter characteristics: Coherence of toxicological and epidemiological inferences, *Inhalation Toxicol.*, *18*(2), 95-125.

Schneider, J., U. Kirchner, S. Borrmann, R. Vogt, and V. Scheer (2008), In situ measurements of particle number concentration, chemically resolved size distributions and black carbon content of traffic-related emissions on German motorways, rural roads and in city traffic, *Atmos. Environ.*, *42*(4257-4268.

Schneider, J., S. Weimer, F. Drewnick, S. Borrmann, G. Helas, P. Gwaze, O. Schmid, M.O. Andreae, and U. Kirchner (2006), Mass spectrometric analysis and aerodynamic properties of various types of combustion-related aerosol particles, *Int. J. Mass Spectrom.*, *258*(37-49.

Schreiner, J., C. Voigt, A. Kohlmann, F. Arnold, K. Mauersberger, and N. Larsen (1999), Chemical analysis of polar stratospheric cloud particles, *Science*, *283*(968-970.

Schreiner, J., C. Voigt, P. Zink, A. Kohlmann, D. Knopf, C. Weisser, P. Budz, and K. Mauersberger (2002), A mass spectrometer system for analysis of polar stratospheric aerosols, *Rev. Sci. Instrum.*, *73*(2), 446-452.

Shantz, N.C., W.R. Leaitch, L. Phinney, M. Mozurkewich, and D. Toom-Sauntry (2008), The effect of organic compounds on the growth rate of cloud droplets in marine and forest settings, *Atmos. Chem. Phys.*, *8*(5869-5887.

Shields, L.G., X. Qin, S.M. Toner, and K.A. Prather (2008), Detection of ambient ultrafine aerosols by single particle techniques during the SOAR 2005 campaign, *Aerosol Sci. Technol.*, *42*(674-684.

Shields, L.G., D.T. Suess, and K.A. Prather (2007), Determination of single particle mass spectral signatures from heavy-duty diesel vehicle emissions for PM2.5 source apportionment, *Atmos. Environ.*, *41*(18), 3841-3852.

Shilling, J.E., Q. Chen, S.M. King, T. Rosenoern, J.H. Kroll, D.R. Worsnop, P.F. DeCarlo, A.C. Aiken, D. Sueper, J.L. Jimenez, and S.T. Martin (2009), Loading-dependent elemental composition of α-pinene SOA particles, *Atmos. Chem. Phys.*, *9*(771-782.

Shilling, J.E., S.M. King, M. Mochida, D. Worsnop, and S.T. Martin (2007), Mass spectral evidence that small changes in composition caused by oxidative aging process alter aerosol CCN properties, *J. Phys. Chem. A*, *111*(17), 3358-3368.

Shu, J., S. Gao, and Y. Li (2008), A VUV photoionization aerosol time-of-flight mass spectrometer with a RF-powered VUV lamp for laboratory-based organic aerosol measurements, *Aerosol Sci. Technol.*, *42*(110-113.

Shu, J., K.R. Wilson, M. Ahmed, and S.R. Leone (2006), Coupling a versatile aerosol apparatus to a synchrotron: Vacuum ultraviolet light scattering, photoelectron imaging, and fragment free mass spectrometry, *Rev. Sci. Instrum.*, *77*(043106.

Silva, P.J., M.E. Erupe, D. Price, J. Elias, Q.G.J. Malloy, Q. Li, B. Warren, and D.R. Cocker (2008), Trimethylamine as precursor to secondary organic aerosol formation via nitrate radical reaction in the atmosphere, *Environ. Sci. Technol.*, *42*(13), 4689-4696.

Simpson, E.A., P. Campuzano-Jost, S.J. Hanna, D.B. Robb, J.H. Hepburn, M.W. Blades, and A.K. Bertram (2009), A laser desorption-electron impact ionization ion trap mass spectrometer for real-time analysis of single atmospheric particles, *Int. J. Mass Spectrom.*, *281*(1401-49.

Sipin, M.F., S.A. Guazzotti, and K.A. Prather (2003), Recent advances and some remaining challenges in analytical chemistry of the atmosphere, *Anal. Chem.*, *75*(12), 2929-2940.

Sjogren, S., M. Gysel, E. Weingartner, M.R. Alfarra, J. Duplissy, J. Cozic, J. Crosier, H. Coe, and U. Baltensperger (2008), Hygroscopicity of the submicrometer aerosol at the high-alpine site Jungfraujoch, 3580 a.s.l., Switzerland, *Atmos. Chem. Phys.*, *8*(5715-5729.

Slowik, J.G., E.S. Cross, J.-H. Han, J. Kolucki, P. Davidovits, L.R. Williams, T.B. Onasch, J.T. Jayne, C.E. Kolb, and D.R. Worsnop (2007), Measurements of morphology changes of fractal soot particles using coating and denuding experiments: Implications for optical absorption and atmospheric lifetime, *Aerosol Sci. Technol.*, *41*(734-750.

Slowik, J.G., K. Stainken, P. Davidovits, L.R. Williams, J.T. Jayne, C.E. Kolb, D.R. Worsnop, Y. Rudich, P.F. DeCarlo, and J.L. Jimenez (2004), Particle morphology and density characterization by combined mobility and aerodynamic diameter measurements. Part 2: Application to combustion-generated soot aerosols as a function of fuel equivalence ratio, *Aerosol Sci. Technol.*, *38*(1206-1222.

Smith, J.N., M.J. Dunn, T.M. VanReken, K. Iida, M.R. Stolzenburg, P.H. McMurry, and L.G. Huey (2008), Chemical composition of atmospheric nanoparticles formed from nucleation in Tecamac, Mexico: Evidence for an important role for organic species in nanoparticle growth, *Geophys. Res. Lett.*, *35*(L04808), doi:10.1029/2007GL032523.

Smith, J.N., K.F. Moore, F.L. Eisele, D. Voisin, A.K. Ghimire, H. Sakurai, and P.H. McMurry (2005), Chemical composition of atmospheric nanoparticles during nucleation events in Atlanta, *J. Geophys. Res.*, *110*(D22S03), doi:10.1029/2005JD005912.

Smith, J.N., K.F. Moore, P.H. McMurry, and F.L. Eisele (2004), Atmospheric measurements of sub-20 nm diameter particle chemical composition by thermal desorption chemical ionization mass spectrometry, *Aerosol Sci. Technol.*, *38*(2), 100-110.

Smith, J.N., and G.J. Rathbone (2008), Carboxylic acid characterization in nanoparticles by thermal desorption chemical ionization mass spectrometry, *Int. J. Mass Spectrom.*, *274*(8-13.

Sorooshian, A., S.M. Murphy, S. Hersey, H. Gates, L.T. Padro, A. Nenes, F.J. Brechtel, H. Jonsson, R.C. Flagan, and J.H. Seinfeld (2008), Comprehensive airborne characterization of aerosol from a major bovine source, *Atmos. Chem. Phys.*, *8*(5489-5520.

Spencer, M.T., J.C. Holecek, C.E. Corrigan, V. Ramanathan, and K.A. Prather (2008), Size-resolved chemical composition of aerosol particles during a monsoonal transition period over the Indian Ocean, *J. Geophys. Res.*, *113*(D16305), doi:10.1029/2007JD008657.

Spencer, M.T., and K.A. Prather (2006), Using ATOFMS to determine OC/EC mass fractions in particles, *Aerosol Sci. Technol.*, *40*(8), 585-594.

Spencer, M.T., L.G. Shields, and K.A. Prather (2007), Simultaneous measurement of the effective density and chemical composition of ambient aerosol particles, *Environ. Sci. Technol.*, *41*(4), 1303-1309.

Spencer, M.T., L.G. Shields, D.A. Sodeman, S.M. Toner, and K.A. Prather (2006), Comparison of oil and fuel particle chemical signatures with particle emissions from heavy and light duty vehicles, *Atmos. Environ.*, *40*(27), 5224-5235.

Steele, P.T., G.R. Farquar, A.N. Martin, K.R. Coffee, V.J. Riot, S.I. Martin, D.P. Fergenson, E.E. Gard, and M. Frank (2008), Autonous, broad-spectrum detection of hazardous aerosols in seconds, *Anal. Chem.*, *80*(4583-4589.

Steele, P.T., A. Srivastava, M.E. Pitesky, D.P. Fergenson, H.J. Tobias, E.E. Gard, and M. Frank (2005), Desorption/ionization fluence thresholds and improved mass spectral consistency measured using a flattop laser profile in the bioaerosol mass spectrometry of single Bacillus endospores, *Anal. Chem.*, *77*(22), 7448-7454.

Stowers, M.A., A.L. van Wuijckhuijse, J.C.M. Marijnissen, C.E. Kientz, and T. Ciach (2006), Fluorescence preselection of bioaerosol for single-particle mass spectrometry, *Appl. Opt.*, *45*(33), 8531-8536.

Stowers, M.A., A.L. van Wuijckhuijse, J.C.M. Marijnissen, B. Scarlett, B.L.M. van Baar, and C.E. Kientz (2000), Application of matrix-assisted laser desorption/ionization to on-line aerosol time-of-flight mass spectrometry, *Rapid Commun. Mass Spectrom.*, *14*(829-833.

Stroud, C.A., A. Nenes, J.L. Jimenez, P.F. DeCarlo, J.A. Huffman, R. Bruintjes, E. Nemitz, A.E. Delia, D.W. Toohey, A.B. Guenther, and S. Nandi (2007), Cloud activating properties of aerosol observed during CELTIC, *Journal Of The Atmospheric Sciences*, *64*(441-459.

Su, Y.X., M.F. Sipin, H. Furutani, and K.A. Prather (2004), Development and characterization of an aerosol time-of-flight mass spectrometer with increased detection efficiency, *Anal. Chem.*, *76*(3), 712-719.

Su, Y.X., M.F. Sipin, M.T. Spencer, X.Y. Qin, R.C. Moffet, L.G. Shields, K.A. Prather, P. Venkatachari, C.H. Jeong, E. Kim, P.K. Hopke, R.M. Gelein, M.J. Utell, G. Oberdorster, J. Berntsen, R.B. Devlin, and L.C. Chen (2006), Real-time characterization of the composition of individual particles emitted from ultrafine particle concentrators, *Aerosol Sci. Technol.*, *40*(6), 437-455.

Suess, D.T., and K.A. Prather (1999), Mass spectrometry of aerosols, *Chemical Reviews*, *99*(10), 3007-3035.

Sullivan, R.C., S.A. Guazzotti, D.A. Sodeman, and K.A. Prather (2007), Direct observations of the atmospheric processing of Asian mineral dust, *Atmos. Chem. Phys.*, *7*(1213-1236.

Sullivan, R.C., and K.A. Prather (2005), Recent advances in our understanding of atmospheric chemistry and climate made possible by on-line aerosol analysis instrumentation, *Anal. Chem.*, *77*(12), 3861-3885.

Svane, M., T.L. Gustafsson, B. Kovacevik, J. Noda, P.U. Andersson, E.D. Nilsson, and J.B.C. Pettersson (2009), On-line chemical analysis of individual alkali-containing aerosol particles by surface ionization combined with time-of-flight mass spectrometry, *Aerosol Sci. Technol.*, *43*(653-661.

Svane, M., M. Hagström, and J.B.C. Pettersson (2004), Chemical analysis of individual alkali-containing aerosol particles: Design and performance of a surface ionization particle beam mass spectrometer, *Aerosol Sci. Technol.*, *38*(655-663.

Sykes, D.C., E. Woods, G.D. Smith, T. Baer, and R.E. Miller (2002), Thermal vaporization-vacuum ultraviolet laser ionization time-of-flight mass spectrometry of single aerosol particles, *Anal. Chem.*, *74*(2048-2052.

Takegawa, N., T. Miyakawa, K. Kawamura, and Y. Kondo (2007), Contribution of selected dicarboxylic and ω-oxocarboxylic acids in ambient aerosol to the m/z 44 signal of an Aerodyne aerosol mass spectrometer, *Aerosol Sci. Technol.*, *41*(418-437.

Targino, A.C., K.J. Noone, F. Drewnick, J. Schneider, R. Krejci, G. Olivares, S. Hings, and S. Borrmann (2007), Microphysical and chemical chracteristics of cloud droplet residuals and interstitial particles in continental stratocumulus clouds, *Atmospheric Research*, *86*(225-240.

Thomson, D.S., M.E. Schein, and D.M. Murphy (2000), Particle analysis by laser mass spectrometry WB-57F instrument overview, *Aerosol Sci. Technol.*, *33*(153-169.

Thornberry, T., D.M. Murphy, D.S. Thomson, J. de Gouw, C. Warneke, T.S. Bates, P.K. Quinn, and D. Coffman (2009), Measurement of aerosol organic compounds using a novel collection/thermal-desorption PTR-ITMS instrument, *Aerosol Sci. Technol.*, *43*(486-501.

Tobias, H.J., P.M. Kooiman, K.S. Docherty, and P.J. Ziemann (2000), Real-time chemical analysis of organic aerosols using a thermal desorption particle beam mass spectrometer, *Aerosol Sci. Technol.*, *33*(170-190.

Tobias, H.J., M.E. Pitesky, D.P. Fergenson, P.T. Steele, J. Horn, M. Frank, and E.E. Gard (2006), Following the biochemical and morphological changes of Bacillus atrophaeus cells during the sporulation process using Bioaerosol Mass Spectrometry, *J. Microbio. Methods*, *67*(56-63.

Tolocka, M.P., K.J. Heaton, M.A. Dreyfus, S. Wang, C.A. Zordon, T.D. Saul, and M.V. Johnston (2006a), Chemistry of particle inception and growth during α-pinene ozonolysis, *Environ. Sci. Technol.*, *40*(1843-1848.

Tolocka, M.P., M.S. Reinard, D.A. Lake, J.M. Ondov, A.S. Wexler, and M.V. Johnston (2006b), Characterization of short-term particulate matter events by real-time single particle mass spectrometry, *Aerosol Sci. Technol.*, *40*(10), 873-882.

Toner, S.M., L.G. Shields, D.A. Sodeman, and K.A. Prather (2008), Using mass spectral source signatures to apportion exhaust particles from gasoline and diesel powered vehicles in a freeway study using UF-ATOFMS, *Atmos. Environ.*, *42*(568-581.

Toner, S.M., D.A. Sodeman, and K.A. Prather (2006), Single particle characterization of ultrafine and accumulation mode particles from heavy duty diesel vehicles using aerosol time-of-flight mass spectrometry, *Environ. Sci. Technol.*, *40*(12), 3912-3921.

Ulbrich, I.M., M.R. Canagaratna, Q. Zhang, D. Worsnop, and J.L. Jimenez (2009), Interpretation of organic components from Positive Matrix Factorization of aerosol mass spectrometric data, *Atmos. Chem. Phys.*, *9*(2891-2918.

Varutbangkul, V., F.J. Brechtel, R. Bahreini, N.L. Ng, M.D. Keywood, J.H. Kroll, R.C. Flagan, J.H. Seinfeld, A. Lee, and A.H. Goldstein (2006), Hygroscopicity of secondary organic aerosols formed by oxidation of cycloalkenes, monoterpenes, sesquiterpenes, and related compounds, *Atmos. Chem. Phys.*, *6*(2367-2388.

Voisin, D., J.N. Smith, H. Sakurai, P.H. McMurry, and F.L. Eisele (2003), Thermal desorption chemical ionization mass spectrometer for ultrafine particle chemical composition, *Aerosol Sci. Technol.*, *37*(6), 471-475.

Wang, J., Y.-N. Lee, P.H. Daum, J. Jayne, and M.L. Alexander (2008), Effects of aerosol organics on cloud condensation nucleus (CCN) concentration and first indirect aerosol effect, *Atmos. Chem. Phys.*, *8*(6325-6339.

Wang, S., and M.V. Johnston (2006), Airborne nanoparticle characterization with a digital ion trap-reflectron time of flight mass spectrometer, *Int. J. Mass Spectrom.*, *258*(50-57.

Wang, S., C.A. Zordon, and M.V. Johnston (2006), Chemical characterization of individual, airborne sub-10-nm particles and molecules, *Anal. Chem.*, *78*(1750-1754.

Wang, X., Y. Zhang, H. Chen, X. Yang, J. Chen, and F. Geng (2009), Particulate nitrate formation in a highly polluted urban area: A case study by single-particle mass spectrometry in Shanghai, *Environ. Sci. Technol.*, *43*(9), 3061-3066.

Weimer, S., M.R. Alfarra, D. Schreiber, M. Mohr, A.S.H. Prévôt, and U. Baltensperger (2008), Organic aerosol mass spectral signatures from wood-burning emissions: Influence of burning conditions and wood type, *J. Geophys. Res.*, *113*(D10304), doi:10.1029/2007JD009309.

Weiss, M., P.J.T. Verheijen, J.C.M. Marijnissen, and B. Scarlett (1997), On the performance of an on-line time-of-flight mass spectrometer for aerosols, *J. Aerosol Sci.*, *28*(1), 159-171.

Weisser, C., K. Mauersberger, J. Schreiner, N. Larsen, F. Cairo, A. Adriani, J. Ovarlez, and T. Deshler (2006), Composition analysis of liquid particles in the Arctic stratosphere under synoptic conditions, *Atmos. Chem. Phys.*, *6*(689-696.

Weitkamp, E.A., A.M. Sage, J.R. Pierce, N.M. Donahue, and A.L. Robinson (2007), Organic aerosol formationi from photochemical oxidation of diesel exhaust in a smog chamber, *Environ. Sci. Technol.*, *41*(6969-6975.

Williams, B.J., A.H. Goldstein, N.M. Kreisberg, and S.V. Hering (2006), An in-situ instrument for speciated organic composition of atmospheric aerosols: Thermal desorption aerosol GC/MS-FID, *Aerosol Sci. Technol.*, *40*(627-638.

Williams, B.J., A.H. Goldstein, D.B. Millet, R. Holzinger, N.M. Kreisberg, S.V. Hering, A.B. White, D.R. Worsnop, J.D. Allan, and J.L. Jimenez (2007), Chemical speciation of organic aerosol during the International Consortium for Atmospheric Research on Transport and Transformation 2004: Results from in situ measurements, *J. Geophys. Res.*, *112*(D10S26), doi:10.1029/2006JD007601.

Williams, J., M. de Reus, R. Krejci, H. Fischer, and J. Ström (2002), Application of the variability-size relationship to atmospheric aerosol studies: estimating aerosol lifetimes and ages, *Atmos. Chem. Phys.*, *2*(133-145.

Yu, Y., M.J. Ezell, A. Zelenyuk, D. Imre, L. Alexander, J. Ortega, B. D'Anna, C.W. Harmon, S.N. Johnson, and B.J. Finlayson-Pitts (2008), Photooxidation of α-pinene at high relative humidity in the presence of increasing concentrations of NO_x, *Atmos. Environ.*, *42*(5044-5060.

Zahardis, J., S. Geddes, and G.A. Petrucci (2008a), Detection of free amino acids in proxies of marine aerosol by photoelectron resonance capture ionization aerosol mass spectrometry, *Int. J. Environ. Anal. Chem.*, *88*(3), 177-184.

Zahardis, J., S. Geddes, and G.A. Petrucci (2008b), The ozonolysis of primary aliphatic amines in fine particles, *Atmos. Chem. Phys.*, *8*(1181-1194.

Zahardis, J., B.W. LaFranchi, and G.A. Petrucci (2006a), Direct observation of polymerization in the oleic acid-ozone heterogeneous reaction system by photoelectron resonance capture ionization aerosol mass spectrometry, *Atmos. Environ.*, *40*(9), 1661.

Zahardis, J., B.W. LaFranchi, and G.A. Petrucci (2006b), The heterogeneous reaction of particle-phase methyl esters and ozone elucidated by photoelectron resonance capture ionization: Direct products of ozonolysis and secondary reactions leading to the formation of ketones, *Int. J. Mass Spectrom.*, *253*(38-47.

Zavala, M., S.C. Herndon, E.C. Wood, J.T. Jayne, D.D. Nelson, A.M. Trimborn, E. Dunlea, W.B. Knighton, A. Mendoza, D.T. Allen, C.E. Kolb, M.J. Molina, and L.T. Molina (2009), Comparison of emissions from on-road sources using a mobile laboratory under various driving and operational sampling modes, *Atmos. Chem. Phys.*, *9*(1-14.

Zelenyuk, A., Y. Cai, L. Chieffo, and D. Imre (2005), High precision density measurements of single particles: The density of metastable phases, *Aerosol Sci. Technol.*, *39*(972-986.

Zelenyuk, A., Y. Cai, and D. Imre (2006a), From agglomerates of spheres to irregularly shaped particles: Determination of dynamic shape factors from measurements of mobility and vacuum aerodynamic diameters, *Aerosol Sci. Technol.*, *40*(197-217.

Zelenyuk, A., and D. Imre (2005), Single particle laser ablation time-of-flight mass spectrometer: An introduction to SPLAT, *Aerosol Sci. Technol.*, *39*(554-568.

Zelenyuk, A., D. Imre, Y. Cai, K. Mueller, Y. Han, and P. Imrich (2006b), SpectraMiner, an interactive data mining and visualization software for single particle mass spectroscopy: A laboratory test case, *Int. J. Mass Spectrom.*, *258*(58-73.

Zelenyuk, A., D. Imre, and L.A. Cuadra-Rodriguez (2006c), Evaporation of water from particles in the aerodynamic lens inlet: An experimental study, *Anal. Chem.*, *78*(19), 6942-6947.

Zelenyuk, A., D. Imre, J.-H. Han, and S. Oatis (2008a), Simultaneous measurements of individual ambient particle size, composition, effective density, and hygroscopicity, *Anal. Chem.*, *80*(1401-1407.

Zelenyuk, A., D. Imre, E.J. Nam, Y. Han, and K. Mueller (2008b), ClusterSculptor: Software for expert-steered classification of single particle mass spectra, *Int. J. Mass Spectrom.*, *275*(1-10.

Zelenyuk, A., J. Yang, E. Choi, and D. Imre (2009a), SPLAT II: An aircraft compatible, ultra-sensitive, high precision instrument for in-situ characterization of the size and composition of fine and ultrafine particles, *Aerosol Sci. Technol.*, *43*(411-424.

Zelenyuk, A., J. Yang, and D. Imre (2009b), Comparison between mass spectra of individual organic particles generated by UV laser ablation and in the IR/UV two-step mode, *Int. J. Mass Spectrom.*, *282*(6-12.

Zelenyuk, A., J. Yang, D. Imre, and E. Choi (2009c), Achieving size independent hit-rate in single particle mass spectrometry, *Aerosol Sci. Technol.*, *43*(305-310.

Zelenyuk, A., J. Yang, C. Song, R.A. Zaveri, and D. Imre (2008c), "Depth-profiling" and quantitative characterization of the size, composition, shape, density, and morphology of fine particles with SPLAT, a single-particle mass spectrometer, *J. Phys. Chem. A*, *112*(669-677.

Zelenyuk, A., J. Yang, C. Song, R.A. Zaveri, and D. Imre (2008d), A new real-time method for determining particles' sphericity and density: Application to secondary organic aerosol formed by ozonolysis of α-pinene, *Environ. Sci. Technol.*, *42*(8033-8038.

Zhang, Q., J.L. Jimenez, M.R. Canagaratna, J.D. Allan, H. Coe, I. Ulbrich, M.R. Alfarra, A. Takami, A.M. Middlebrook, Y.L. Sun, K. Dzepina, E. Dunlea, K. Docherty, P.F. DeCarlo, D. Salcedo, T. Onasch, J.T. Jayne, T. Miyoshi, A. Shimono, S. Hatakeyama, N. Takegawa, Y. Kondo, J. Schneider, F. Drewnick, S. Borrmann, S. Weimer, K. Demerjian, P. Williams, K. Bower, R. Bahreini, L. Cottrell, R.J. Griffin, J. Rautiainen, J.Y. Sun, Y.M. Zhang, and D.R. Worsnop (2007), Ubiquity and dominance of oxygenated species in organic aerosols in anthropogenically-influenced Northern Hemisphere midlatitudes, *Geophys. Res. Lett.*, *34*(L13801), doi:10.1029/2007GL029979.

Zhao, W., P.K. Hopke, and K.A. Prather (2008), Comparison of two cluster analysis methods using single particle mass spectra, *Atmos. Environ.*, *42*(881-892.

Zhou, L., P.K. Hopke, and P. Venkatachari (2006a), Cluster analysis of single particle mass spectra measured at Flushing, NY, *Anal. Chim. Acta*, *555*(47-56.

Zhou, L., K. Park, H.M. Milchberg, and M.R. Zachariah (2007), Understanding the interaction of an intense laser pulse with nanoparticles: Application to the quantification of single particle mass spectrometry, *Aerosol Sci. Technol.*, *41*(818-827.

Zhou, L., A. Rai, and M.R. Zachariah (2006b), Component and morphology biases on quantifying the composition of nanoparticles using single-particle mass spectrometry, *Int. J. Mass Spectrom.*, *258*(104-112.

Zordan, C.A., S. Wang, and M.V. Johnston (2008), Time-resolved chemical composition of individual nanoparticles in urban air, *Environ. Sci. Technol.*, *42*(6631-6636.

Chapter 2

2 Development and Characterization of an Aircraft Aerosol Time-of-Flight Mass Spectrometer

2.1 Synopsis

Vertical and horizontal profiles of atmospheric aerosols are necessary for understanding the impact of air pollution on regional and global climate. To gain further insight into the size-resolved chemistry of individual atmospheric particles, a smaller aerosol time-of-flight mass spectrometer (ATOFMS) with increased data acquisition capabilities was developed for aircraft-based studies. Compared to previous ATOFMS systems, the new instrument has a faster data acquisition rate with improved ion transmission and mass resolution, as well as reduced physical size and power consumption, all required advances for use in aircraft studies. In addition, real-time source apportionment software allows the immediate identification and classification of individual particles to guide sampling decisions while in the field. The aircraft (A)-ATOFMS was field-tested on the ground during the Study of Organic Aerosols in Riverside, CA (SOAR) and aboard an aircraft during the Ice in Clouds Experiment – Layer Clouds (ICE-L). Results from ICE-L represent the first reported aircraft-based single-particle dual-polarity mass spectrometry measurements and provide an increased understanding of particle mixing state as a function of altitude. Improved ion transmission allows for the first single-particle detection of species out to ~*m/z* 2000, an important mass range for the detection of biological aerosols and oligomeric species. In addition, high time resolution measurements of single-particle mixing state are demonstrated and shown to be important for airborne studies where particle concentrations and chemistry vary rapidly.

2.2 Introduction

During transport in the atmosphere, aerosol particles undergo physical and chemical transformations through cloud processing and reactions with atmospheric gases; these particles can also be removed from the atmosphere through wet and dry deposition [*Poschl*, 2005]. Due to the ever-changing physical and chemical properties and the spatial and temporal variability of the distribution of aerosols, the quantification of the aerosol impacts on radiative forcing represents a challenging task [*Forster et al.*, 2007]. The majority of in situ aerosol measurements, essential for validation of global climate models, have been made at the surface; however, the direct and indirect radiative forcings depend on aerosol vertical and horizontal profiles [*Forster et al.*, 2007].

Real-time aerosol analysis methods avoid sampling artifacts and allow direct measurements of changing aerosol populations with high temporal resolution [*Sullivan and Prather*, 2005]. Recently, real-time aerosol mass spectrometry techniques, including particle analysis by laser mass spectrometry (PALMS) [*Murphy et al.*, 1998] and aerosol mass spectrometry (AMS) [*Bahreini et al.*, 2003], have been used for aircraft-based measurements of aerosol vertical profiles and interactions with clouds. In particular, real-time single particle mass spectrometry allows the online analysis of single particle size, chemical composition, density, and optical properties [*Moffet and Prather*, 2005; *Sullivan* *and Prather*, 2005]. This technique provides greatly enhanced spatial and temporal resolution and can yield new insights into heterogeneous chemical reactions [*Gard et al.*, 1998], source apportionment and chemical aging [*Brock et al.*, 2004; *Sodeman et al.*, 2005; *Toner et al.*, 2006], and the role of particles in cloud nucleation [*Cziczo et al.*, 2003; *Cziczo et al.*, 2004].

The aerosol time-of-flight mass spectrometer (ATOFMS) detects both positive and negative ions simultaneously from individual particles, providing an increased understanding of particle mixing state [*Gard et al.*, 1997]. A smaller ATOFMS with increased data acquisition capabilities has been developed for aircraft-based studies. This aircraft (A)-ATOFMS has been used to obtain the first aircraft-based dual-polarity single-particle mass spectrometry results, which will improve our understanding of vertical profiles of particle mixing state, particularly through comparison with previous ATOFMS surface-based measurements conducted around the world during several major field campaigns, including INDOEX (Indian Ocean, 1999) [*Guazzotti et al.*, 2001], ACE-Asia (Sea of Japan, 2001) [*Sullivan et al.*, 2007], and MILAGRO (Mexico City, 2006) [*Moffet et al.*, 2008]. Herein, the development of the A-ATOFMS is described with particular focus placed on the improvements in the ATOFMS design and characterization of instrument performance through both laboratory and field measurements.

2.3 Experimental

The A-ATOFMS, shown in Figures 2.1 and 2.2, represents an improved, flight-capable version of the transportable ATOFMS described previously [*Gard et al.*, 1997; *Su et al.*, 2004]. Aerosols enter the system by first passing through a ^{210}Po neutralizer

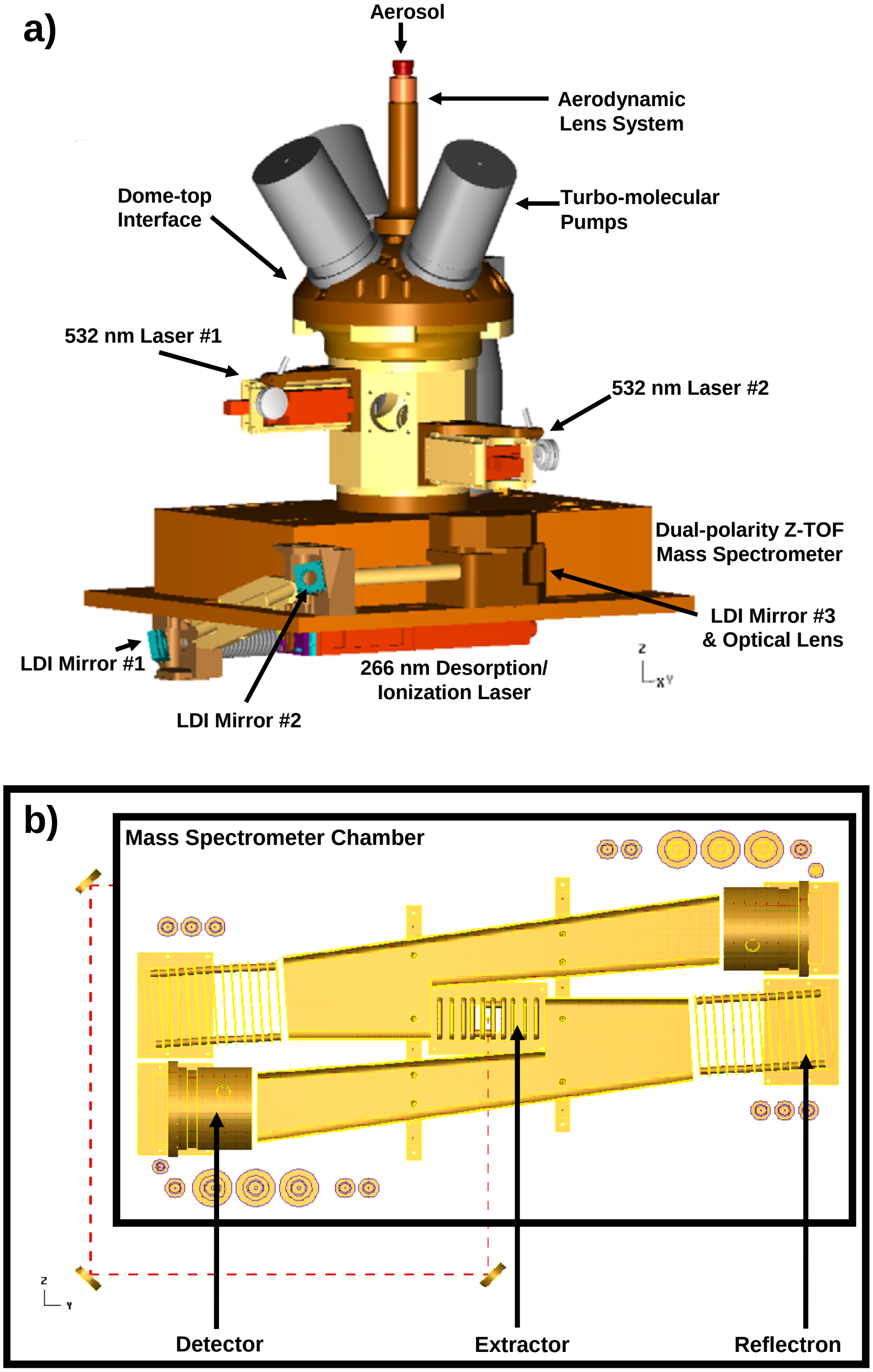

Figure 2.1. (a) Schematic of the A-ATOFMS illustrating the dome-top alignment interface, aerodynamic sizing region, desorption/ionization laser alignment, and dual-polarity Z-TOF mass spectrometer. (b) Schematic of the dual polarity Z-TOF mass spectrometer illustrating ion extraction region and ion trajectory.

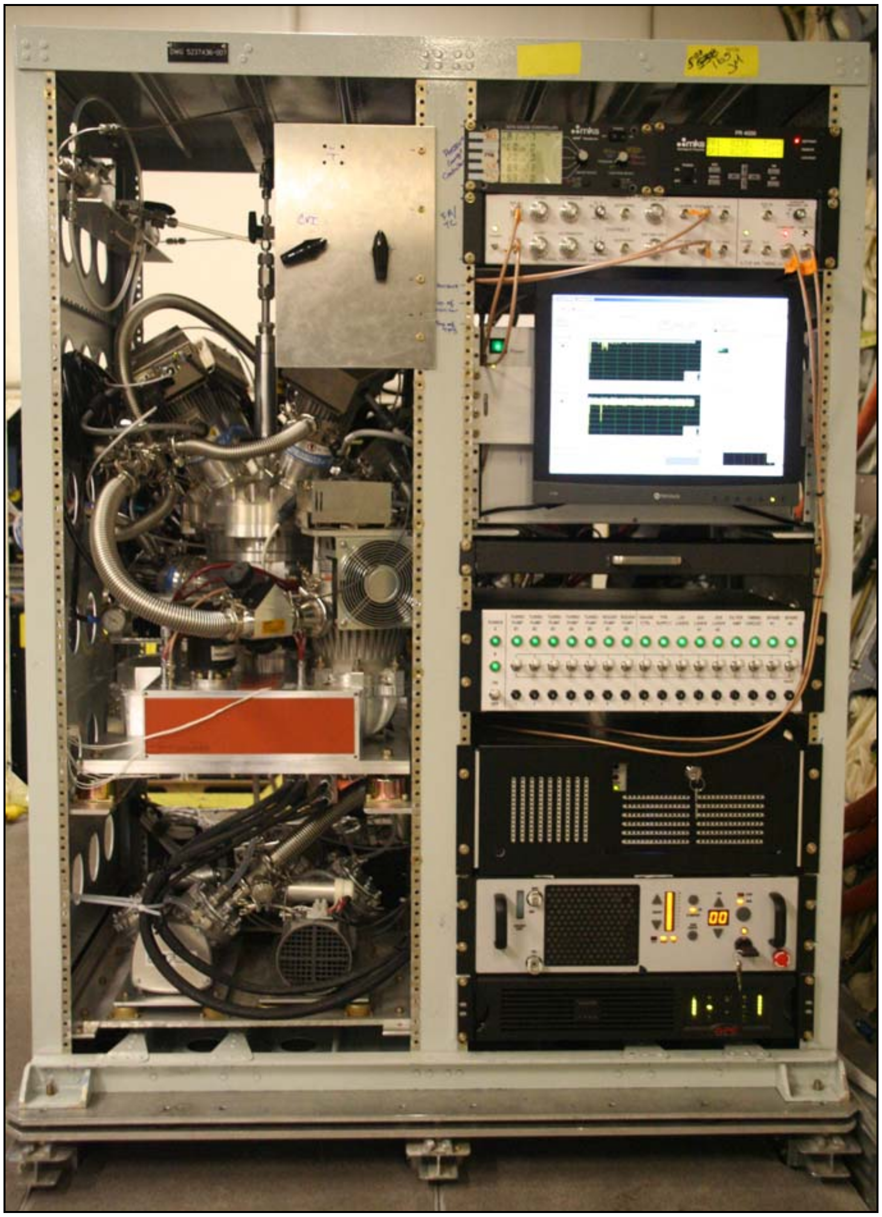

Figure 2.2. Photograph of the A-ATOFMS aboard the National Center for Atmospheric Research (NCAR) C-130 aircraft.

(1U400, Amstat Industries, Inc., Glenview, IL; custom holder design: 1.5 mCi/0.08 cm^3) which imparts a Boltzmann equilibrium charge distribution [*Hinds*, 1999]. For aircraft-based studies, a pressure-controlled inlet (not shown) based on the design by Bahreini et al. [2008] was utilized prior to the aerodynamic lens system for constant inlet pressure with changing altitude; for the aircraft results shown herein, the inlet was set to 270 Torr using a 180 µm critical orifice prior to the aerodynamic lens system to obtain an upstream pressure of 2.0 Torr. Particles are subsequently focused into a tightly collimated particle beam with an aerodynamic lens system originally designed by Liu et al. [1995a; 1995b] and further developed by Zhang et al. [2002; 2004]. The exact dimensions are described by Su et al. [2004], with two differences being that the critical orifice used by the Ultrafine (UF)-ATOFMS is ~100 µm in diameter, whereas the one employed in the A-ATOFMS is ~110 µm, and the exit nozzle is 17 mm (L) x 5.8 mm (ID) stepping down to 3.0 mm compared to the 5.1 mm ID nozzle terminated by a 3 mm diameter orifice used in the UF-ATOFMS [*Su et al.*, 2004]. The particle beam passes through a 1.0 mm diameter skimmer followed by an aerodynamic sizing region where particles are optically detected by the light scattered by the particles from two mutually orthogonal continuous wave frequency-doubled diode-pumped 532 nm solid-state lasers (CDPS532M, JDS Uniphase GmbH, Eching, Germany) spaced 6.0 cm apart. The scattered light is focused with 45 mm diameter electroformed elliptical mirrors onto photomultiplier tubes (PMTs) with a mirror collection angle of 7.2º – 172.8º [*Moffet and Prather*, 2005]. The signals from the PMTs are filtered, amplified, and turned into +5V square waves for a timing circuit [*Su et al.*, 2004] which controls the precise firing time for laser desorption-ionization when particles reach the center of the ion source in the mass spectrometer. In addition, as described by Moffet and Prather [2005], the light scattering signals produced during particle sizing are collected and coupled with size-resolved chemical composition information to establish a direct link between optical properties and particle mixing state.

At the calculated time a sized particle reaches the desorption/ionization (DI) region of the mass spectrometer (Figure 2.1), the 266 nm Nd:YAG DI laser (ULTRA CFR, Quantel USA, Bozeman, MT) is fired, simultaneously generating positive and negative ions which are extracted and accelerated to several kV, after which the ion beam is steered and temporally refocused in a TOF reflectron onto an ion detector (25 mm bipolar time-of-flight detector, BURLE Industries Inc., Lancaster, PA). The single-particle positive and negative ion mass spectra are collected by two data acquisition boards (DP 240, Agilent Technologies, Inc., Monroe, NY) and processed using custom software, discussed herein.

Polystyrene latex spheres (PSLs, Interfacial Dynamics Corp., Portland, OR) of known size (95 – 2920 nm) were generated by atomizing a water solution of PSLs using a Collison atomizer. Particles generated were then passed through a dilution chamber before entering a silica gel diffusion drier and a Nafion drier to remove water. For PSLs $\leq$ 1 μm, the PSL flow was further size-selected with a differential mobility analyzer (DMA, model 3080, TSI Inc., St. Paul, MN) before introduction into the sampling inlet of the A-ATOFMS. Particle number concentration was measured using a condensation particle counter (CPC, model 3010, TSI Inc., St. Paul, MN) for particles < 1.4 μm and an aerodynamic particle sizer (APS, model 3321, TSI Inc., St. Paul, MN) for particles > 1.4 μm. PSL particles are spherical with a density of ~1.0 g/m^3; thus, their vacuum aerodynamic diameters (d_{va}) and geometric diameters are identical.

Ground-based measurements of single ambient aerosol particles by A-ATOFMS, UF-ATOFMS, and nozzle-inlet ATOFMS were conducted during the Study of Organic Aerosols field campaign in Riverside, CA (SOAR, August and November 2005, http://cires.colorado.edu/jimenez-group/Field/Riverside05/). The sampling site was on the University of California, Riverside campus, located ~60 miles east of Los Angeles, CA. A co-located scanning mobility particle sizer (SMPS, model 3936L10, TSI Inc., St. Paul, MN) was operated during SOAR to obtain size-resolved particle number concentrations from 15-866 nm. Aircraft-based measurements of single ambient aerosol particles by A-ATOFMS were conducted aboard the National Center for Atmospheric Research (NCAR) C-130 aircraft during the Ice in Clouds Experiment – Layer Clouds (ICE-L) based in Broomfield, CO from November to December 2007 (www.eol.ucar.edu/projects/ice-l/).

2.4 Results and Discussion

2.4.1 Design Modifications for Aircraft-based Measurements

For aircraft-based measurements, the ATOFMS was reduced in size by a factor of 1.8 to fit in a double-wide 19-inch aircraft-approved rack (~0.95 m^3) (see Figure 2.2). The design process took into consideration the stringent structural and electrical requirements for flying on the NCAR C-130Q and Gulfstream V. Total instrument power consumption was reduced to 1.2 kW of 110 V 60 Hz AC power during ground sampling; in comparison, the UF-ATOFMS draws 1.75 kW of a combination of 110 V and 220 V 60 Hz AC power. Using a pressure-controlled inlet during flight increases the A-ATOFMS power consumption to 1.4 kW of 110 V 60 Hz AC power. The following sections detail the major ATOFMS revisions, including an improved inlet design, reduced pumping configuration, increased particle size range, innovative mass spectrometer and desorption/ionization laser alignment design, and real-time source apportionment. Summaries of the structural components and power draw requirements of the A-ATOFMS within the NCAR C-130 rack are given in Tables 2.1 and 2.2. Note that dimensions are given for each of the three diaphragm pumps.

Improved Inlet Design. To fit in the aircraft rack, the inlet system was reduced in volume by 3/4 compared to the previous UF-ATOFMS [*Su et al.*, 2004]. The system features a dome-top interface to allow for symmetric pumping by a variable number (1-4) of 70 L/s turbomolecular pumps (V70LP, Varian Vacuum Technologies, Torino, Italy) at the exit of the aerodynamic lens system. An adjustable dome-top, consisting of two concentric hemispheres mating with hardened aluminum surfaces, was first constructed to allow for angled adjustment of the particle beam alignment. Threaded adjusters varied the dome position, which was monitored with four analog dial gauges, allowing for accurate alignment and quick verification that alignment had not changed with instrument transport or maintenance. Small dome alignment adjustments (± 0.127 mm from the spherical mount center) resulted in no measurable effect on the scattering rate; thus, a fixed dome interface was constructed to minimize weight and complexity while rigidly maintaining alignment in the harsh vibrating operating environment during flight.

Reduced Pumping Configuration. The instrument consists of three differentially pumped sections: the aerodynamic lens system, sizing region, and mass spectrometer. Compared to the UF-ATOFMS [*Su et al.*, 2004], the A-ATOFMS

Table 2.1. Primary structural components of the A-ATOFMS within the NCAR C-130 rack. The center of gravity height is abbreviated CG Ht.

Location	**Component**	**Weight (lbs)**	**Depth (in)**	**Width (in)**	**Height (in)**	**CG Ht (in)**	**Moment (in-lbs)**
Front	LDI ICE	33.3	18	19	5.25	9	300
	Computer	25.75	21	19	7	15	386
	PDU	19.9	14	19	5.25	23	458
	Keyboard	9.75	14.5	19	1.75	28	273
	Vacuum gauge controller	8	12.25	9.5	3.5	48.5	388
	Inlet pressure readout	3.3	9.4	9.5	3.5	48.5	160
	Timing Circuit/Filter Amp	7.3	14	19	3.5	44.5	325
	UPS	61.2	18	19	3.5	4.5	275.4
	Valves	2	0.13	8	12	44	88
Rear	NCAR Power Box	15	3.25	19	3.5	4.5	67.5
	NCAR Power Strip	2.2	2.25	19	1.75	7.5	16.5
	Shelf with RS232 breakout box & inlet pressure controller	10	8	19	5	44	440
Side	Vacuum rough pumps	39	10.5	7.5	5.5	6	153
	A-ATOFMS Vacuum Chamber	155	24	19	30	24	3720
	Neutralizer/ Expansion chamber	5.6	24	3	3	47.5	266
	Monitor	8	1.75	13.75	11.5	37	296
	LFE	3.8	12	7	4	47.5	180.5
	TPS	33	14.25	19	10.5	35	1155
	SUM	442.1					8947.9

Table 2.2. Power draw requirements of the A-ATOFMS within the NCAR C-130 rack. Average power refers to when the ATOFMS is running. AC power circuit #1 is configured to go through the UPS (APC SUA1500RM2U).

AC power circuit #1, 110VAC @ 60 Hz, for all units				
Item	**Description**	**Average power**	**Peak power**	**Circuit breaker**
		(Amps)	**(Amps)**	**(Amps)**
1	Rough pump #1	1.33	1.36	5
2	Rough pump #2	1.36	1.36	5
3	Turbo pump #1	0.63	0.63	5
4	Turbo pump #2	0.64	0.64	5
5	Turbo pump #3	0.61	0.61	5
6	Turbo pump #4	0.33	0.33	5
7	Turbo pump #5	0.71	0.71	5
8	Pressure gauge	0.05	0.05	3
9	Computer	2.54	2.63	10
10	PDU	0.09	0.09	20
Total:		8.29	8.41	
AC power circuit #2, 110VAC @ 60 Hz, for all units				
Item	**Description**	**Average power**	**Peak power**	**Circuit breaker**
		(Amps)	**(Amps)**	**(Amps)**
1	Tofwerk Power Supply (TPS)	0.51	0.51	3.15
2	Desorption/Ionization Laser (LDI)	2.35	3.00	5.0
3	JDS Scattering Laser #1	0.12	0.28	3
4	JDS Scattering Laser #2	0.14	0.33	3
5	Timing circuit	0.18	0.18	1
6	Filter amp	0.22	0.22	1
7	PR 4000 (pressure readout)	0.17	0.17	10
8	Inlet pump	1.80	1.81	10
9	Power distribution unit	0.09	0.09	20
10	Monitor	0.14	0.14	None
11	Laminar flow element	0.01	0.01	None
Total:		5.73	6.74	

pumping scheme uses smaller pumps to reduce space and weight requirements. For the pumping on the dome-top interface at the exit of the aerodynamic lens system, the use of three 70 L/s turbo-molecular pumps was found to be optimal based on a balance between transmission, power draw, and strain on the pumps. In addition, one 70 L/s turbomolecular pump is located on the sizing region (V70, Varian Vacuum Technologies, Torino, Italy) and one 250 L/s split-flow turbomolecular pump (V301SF, Varian Vacuum Technologies, Torino, Italy) on the mass spectrometer. The secondary inlet (11 L/s) on the V301SF backs the 70 L/s pumps. The V301SF is backed by two diaphragm roughing pumps: UN726.1.2 ANI parallel (38 L/min) and UN726.3 ANI two stage (20 L/min) (KNF NEUBERGER, INC., Trenton, NJ). For ground-based measurements, typical operating pressures are ~1.7 Torr upstream of aerodynamic lens inlet, ~6 x 10^{-3} Torr following the lens, ~3 x 10^{-4} Torr in the sizing region, ~7 x 10^{-7} Torr in the mass spectrometer, and ~5 Torr between the V-301SF and first roughing pump. The sizing region is separated from the mass spectrometer by a ball valve which can be closed to isolate the mass spectrometer and keep the ion detectors under vacuum while the remainder of the instrument is serviced.

Increased Submicron Particle Size Range. The A-ATOFMS utilizes an aerodynamic lens inlet, resulting in an approximate ambient particle size range of 70 – 1000 nm. In comparison, the nozzle-inlet ATOFMS [*Gard et al.*, 1997] and UF-ATOFMS [*Su et al.*, 2004] have particle size ranges of ~200 – 3000 nm and ~50 – 300 nm, respectively. While the A-ATOFMS and UF-ATOFMS have nearly identical aerodynamic lens inlets, the UF-ATOFMS operates with a microorifice uniform deposit impactor (MOUDI) upstream of the inlet to select only particles less than 300 nm to increase data acquisition of ultrafine particles [*Su et al.*, 2004]. With new developments to the data acquisition system discussed below, the A-ATOFMS is no longer overwhelmed by high particle counts and can target a larger size range of particles simultaneously. A neutralizer was added to the A-ATOFMS inlet to reduce the deflection of charged ultrafine particles in the ionization region of the A-ATOFMS, which has an electric field strength of approximately 4 times greater than previous ATOFMS instruments as a result of a higher voltage (~2x) applied with only half the extractor plate separation distance. Large deflections of 0.80 mm in the ionization region of the mass spectrometer were observed for 170 nm PSL particles due to high electrostatic gradients. In comparison, 170 nm PSL particles are only deflected by ~0.3 mm in the ionization region of the UF-ATOFMS [*Su et al.*, 2004]. Thus, the lowest detectable particle size in the A-ATOFMS was extended by ~120 nm to ~70 nm through the addition of the ^{210}Po neutralizer; the neutralizer has since been applied to the UF-ATOFMS as well.

Standard PSL particles were used to characterize the transmission and scattering efficiency of the aerodynamic lens system and aerodynamic sizing region; these observations were compared to modeled lens transmission efficiency using aerodynamic lens system design and testing software developed by Wang and McMurry [2006]. The scattering efficiency E_s is defined as the ratio of the number of particles detected in the sizing region per unit time N_s (particles/minute) to the total number of particles entering the aerodynamic lens during the same time period, where

$$E_s = N_s/CQ_I \tag{1}$$

C is the number concentration as measured by the condensation particle counter (CPC, model 3010, TSI Inc., MN) or aerodynamic particle sizer (APS, model 3321, TSI Inc., MN) (particles/cm^3) and Q_I is the volumetric flow rate (cm^3/minute) of the inlet system. A comparison of the scattering efficiency of the A-ATOFMS with the UF-ATOFMS and modeled particle transmission results are shown in Figure 2.3. The A-ATOFMS aerodynamic lens system was shown to have a maximum sizing efficiency of 49% for 600 nm PSL particles with minimums of 0.4% at 120 nm and 16% at 2920 nm. The sizing efficiency is greater than 29% over the 220 – 2000 nm size range. The scattering efficiency of UF-ATOFMS over the size range of 95 – 700 nm was 0.5 – 62%.

Differences in scattering efficiency between the A-ATOFMS and UF-ATOFMS may result from differences in tuning of the aerodynamic lens alignment and scattering lasers. The A-ATOFMS curve was generated from a fixed tuning position, i.e. the system was set to a good overall position, and not optimized for each particle size, as was completed for the UF-ATOFMS. The modeled transmission performance based on the simulation program by Wang and McMurry [2006] is shown for comparison. The modeled total transmission is above 97% for particles 50 – 500 nm and falls off sharply to ~10% for particles larger than 500 nm. As the E_s is a convolution of total transmission and scattering detection, we expect the A-ATOFMS scattering efficiency to be lower than modeled, particularly for the smaller sizes (< 100 nm) near the limit of detection by the scattering lasers. Interestingly, the observed transmission is greater than simulations for sizes larger than 700 nm, likely due to inaccuracy in the model. Previously, Liu et al. [2007] found measured transmission efficiencies to be greater than predicted for particles >350 nm (d_{va}) at an ambient pressure of 585 torr. As a result, Liu et al. [2007] suggest

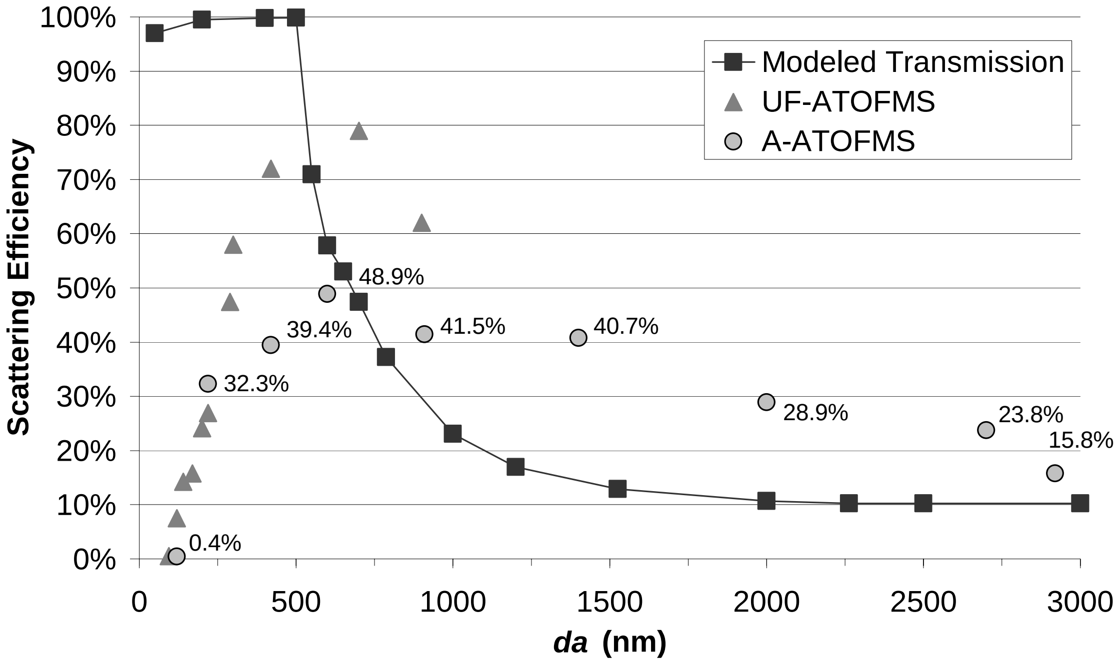

Figure 2.3. A-ATOFMS transmission/sizing efficiency compared to modeled results and observed UF-ATOFMS results.

that the transmission efficiency of particles >400 nm is controlled by the orifice assembly in the aerodynamic lens system. Further, Jayne et al. [2000] observed high transmission efficiencies for particles >350 nm, which Liu et al. [2007] attribute to the skimmer cone just after the aerodynamic lens exit in the ATOFMS. Thus, it is suggested that the higher measured transmission efficiency for particles greater than ~700 nm is controlled by the orifice assembly at the entrance to the aerodynamic lens system and the skimmer cone following the lens exit.

As shown in Figure 2.4, a fifth order polynomial (R^2 0.9983) fits the PSL size calibration data to provide high resolution size data for ambient particles with d_{va} of 100 – 3000 nm. For particles below 100 nm, a power curve (R^2 0.9561) fits PSLs in the 95 to 300 nm range and can be extrapolated down to 70 nm for ambient particles. Ambient particles as small as 70 nm and as large as 3000 nm were detected in Riverside, CA during SOAR, allowing both ultrafine vehicle emissions and supermicron dust to be detected by the A-ATOFMS.

Mass Spectrometer and Desorption/Ionization Laser Optical Configuration. The overall dimensions of the high performance dual-polarity Z-configuration time-of-flight (Z-TOF) mass spectrometer (Figure 2.1b) are substantially smaller (length decreased by 69%, volume decreased by 57%, weight decreased by 33%) than the previous ATOFMS coaxial mass spectrometer design [*Gard et al.*, 1997]. The A-ATOFMS mass spectrometer dimensions are 49 cm x 29 cm x 11.3 cm *(L x W x H)* compared to 159 cm x 15 cm x 15.5 cm for the transportable ATOFMS. The shorter length allows for a much smaller package, which is necessary for incorporation into aircraft racks.

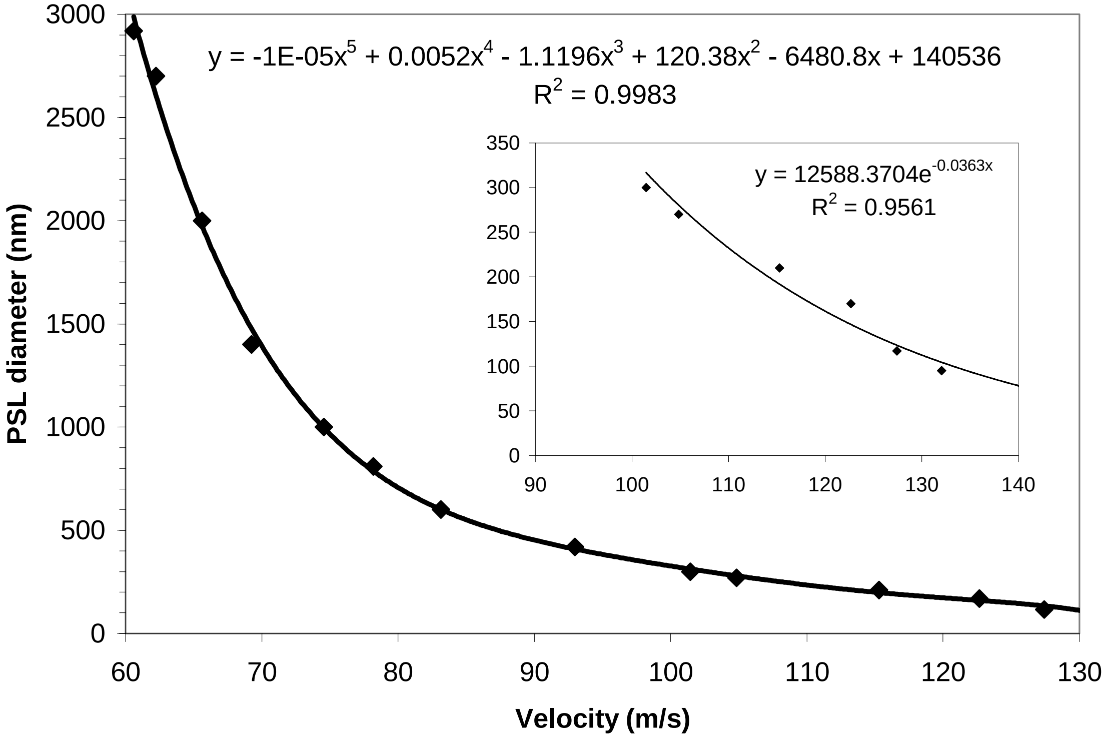

Figure 2.4. A-ATOFMS size calibration curve generated from standard PSL particles. A 5th order polynomial is fit to 95 – 2920 nm. To size ambient particles below 100 nm, a power curve (inset) is used from 95 - 300 nm PSL data.

To decrease particle-to-particle variability in the mass spectral ion intensities, the desorption/ionization laser alignment was designed to incorporate an aperture to produce a homogeneous flat-top laser profile similar to the method described by Wenzel and Prather [2004] which incorporated a fiber-optic. Shot-to-shot variability of the ion signal results from differences in the laser energy received by different particles due to the laser's Gaussian profile and the presence of hot spots. However, a fiber-optic is fragile and cannot withstand repeated 266 nm laser pulses. Thus, a new laser homogenization method incorporating a gold-plated 2.0 mm aperture was developed in collaboration with researchers at the National Research Council of Canada's flame combustion group. The aperture removes the low energy wings of the Gaussian laser profile to produce a homogeneous flat-top laser beam, which substantially reduces particle-to-particle ion signal variability.

The aperture used for LDI homogenization must be positioned 625 mm from the center of the mass spectrometer source region. Thus, to accommodate this longer path length within the small amount of space available within the aircraft rack, the laser was mounted below the mass spectrometer (see Figure 2.1a). Following three mirrors and an optical lens mounted on the sides of the mass spectrometer chamber, the laser light surrounded by protective shielding reaches the mass spectrometer. To further vibration isolate the DI laser, as well as the sizing lasers, the entire mass spectrometer is situated on vibration isolators which mount to the mass spectrometer lid (see Figure 2.2).

Source Apportionment. To identify source plumes and guide sampling routes during aircraft-based measurements, real-time particle source apportionment is used to immediately identify and classify particles sampled based upon comparison of the mass spectra to a library of source signatures, similar to the off-line ATOFMS source apportionment technique developed by Toner et al. [2008] The custom software calibrates the spectra from each particle and computes lists of ion (*m*/*z)* peaks, which are then compared to spectra from different sources. The source library contains spectra from over 10 years of ambient studies, as well as studies focused on emissions from specific sources, including biomass burning [*Silva et al.*, 1999], cars [*Sodeman et al.*, 2005], aged organic carbon, diesel trucks [*Sodeman et al.*, 2005; *Toner et al.*, 2006], dust [*Silva et al.*, 2000], and sea salt [*Gard et al.*, 1998].

2.4.2 Faster Data Acquisition

Aircraft-based measurements require fast data acquisition speeds to provide high spatial resolution during flights. The 20 Hz 266 nm Nd:YAG DI laser (ULTRA CFR, Quantel USA, Bozeman, MT) was modified by Quantel USA with a smaller 2.5 mm laser rod and optimized for a 50 Hz repetition rate. Since the DI laser is externally triggered by particles detected in the aerodynamic sizing region, the timing circuit was altered to accommodate this new laser. In addition, the data acquisition and control software were redesigned for a faster data acquisition rate. With these new developments, the data acquisition system is not as overwhelmed and can target a larger size range of particles, unlike the previous UF-ATOFMS. The new timing circuit and software are described in detail below.

Improved Timing Circuit. The A-ATOFMS timing circuit, which uses a programmable logic device, was created based on the designs of Prather et al. [1994] and Mysak et al. [2006] to provide the logic for the operation of the DI laser based on the individual particle scattering pulses measured by the PMTs in the aerodynamic sizing region of the A-ATOFMS. The timing circuit triggers the DI laser flashlamp 185 μs prior to the desired laser output pulse, or the time at which the particle is expected in the source region of the mass spectrometer. Following the flashlamp trigger pulse, a Q-switch trigger pulse is sent to fire the DI laser. However, to maintain proper heat load, the flashlamp must be discharged 50 times per second, or every 20 ms. Therefore, during periods of low particle concentrations when the laser is externally triggered by the aerodynamic sizing region at a rate of less than 50 Hz, substitute flashlamp trigger pulses are sent to the laser at a variable rate of 0 (no substitute pulses), 10, 20, 30, 40, or 50 Hz, which can be chosen by the user. Preliminary results show maximum laser output power for the 30 Hz substitute pulse condition during ambient sampling, keeping the power at ~1.2 mJ during low particle concentration sampling periods when the power would previously drop to ~0.6 mJ without substitute flashlamp trigger pulses.

Faster Data Acquisition Software. Previously, for the nozzle-inlet ATOFMS, instrument busy time, that is the time during which the instrument is processing the size and/or chemical composition information for a particular particle and therefore cannot continue to detect particles during this time, was found to be 5-95% of the nominal sampling time [*Allen et al.*, 2006]. Thus, to decrease instrument busy time and increase data acquisition speed, custom software was developed using a combination of LabVIEW and C to monitor the status of instrument components, process mass spectra, display particle size histograms, and provide real-time source apportionment. To maximize data processing speed, displays of instrument and data status, as well as real-time source apportionment, can be selectively turned off to increase the data acquisition rate.

Configured for maximum data acquisition rate, tests show 33.5 ms are required to detect, read, and save the mass spectrum of a hit particle, resulting in a maximum data acquisition rate of 30 Hz. With all displays on with real-time source apportionment, 120 ms are required per hit particle, giving a maximum rate of 8.3 Hz. However, observed data acquisition rates fall below the maximum theoretical rate in part due to the non-ideal spacing of particles passing through the aerodynamic sizing region; thus, there is often a period of waiting time between acquisition of a particle's mass spectra and the identification of the next particle in the sizing region.

Ambient Particle Comparison. Total ATOFMS ambient particle counts and size distributions primarily depend on three factors: instrument inlet transmission, data acquisition rate, and ambient particle concentrations. Representative particle size distributions (50-1000 nm, 50 nm bins) detected during SOAR-1 (August 2005) by the nozzle-inlet ATOFMS, UF-ATOFMS, and ground-based prototype of the A-ATOFMS are shown in Figure 2.5 for night, morning, and afternoon periods. Sized particles are those particles for which velocity, and thus size, information was acquired; hit particles refer to those for which both size and chemical composition information was obtained. The overall shapes of the ambient hit particle distributions compare well with those of the sized particles, demonstrating an overall lack of size biasing in the hit particles from 50-1000 nm. For the A-ATOFMS, small divergences in the shapes of the sized and hit particle distributions below 100 nm and above ~300 nm are likely due to increased deflection of ultrafine particles in the ionization region and divergence of particles from the focused particle beam due to the size and shape-dependent transmission of particles through the aerodynamic lens system [*Huffman et al.*, 2005].

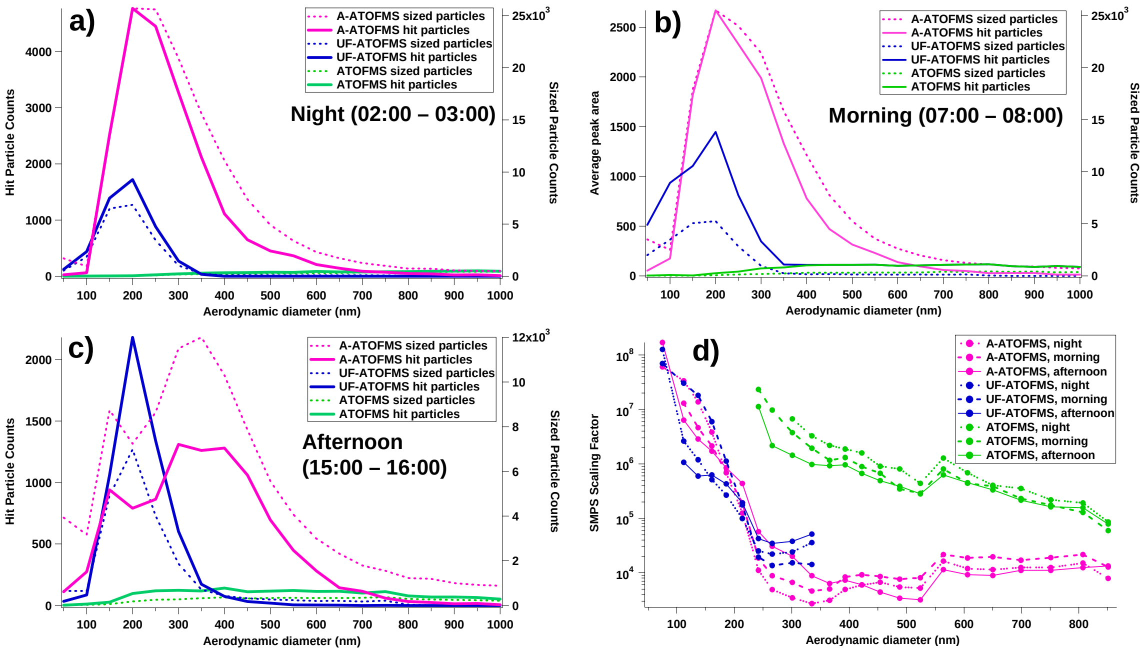

Figure 2.5. A-ATOFMS, UF-ATOFMS, and ATOFMS hit and sized particle distributions (50-1000 nm with 50 nm bins) for representative one hour time periods during SOAR-1 (August 2005): (a) night, (b) morning, and (c) afternoon. SMPS scaling factors (d) are given for these three time periods.

During the peak time period for the A-ATOFMS (night), size information was collected for 148,266 particles, and chemical composition information for 20,566 particles by the A-ATOFMS. In comparison, during the peak time period for the UF-ATOFMS (afternoon), size information was collected for 21,875 particles and chemical composition information for 5,611 particles by the UF-ATOFMS. During the peak time period for the ATOFMS (morning), size information was collected for 14,842 particles, with chemical composition information for 4,100 particles by the ATOFMS. During these time periods of interest, 47-72% of the particles observed by the nozzle-inlet ATOFMS were in the size range of 1.0-2.5 µm, showing the utility of the ATOFMS for the study of supermicron particles, such as dust and sea salt.

Overall, the A-ATOFMS sized and hit particles (70 nm – 2.5 µm) with average rates of 31-45 Hz and 3-6 Hz, respectively. In comparison, the UF-ATOFMS sized and hit particles (50-1000 nm) with average rates of 5.8-6.1 Hz and 1.4-1.6 Hz, respectively. Lastly, for 0.1 – 2.5 µm particles, the ATOFMS results showed average sized particle rates of 2.9-4.6 Hz and average hit particle rates of 0.9-1.1 Hz. Despite the transmission size biases of the three instruments, shifts in the instrument size distributions (Figure 2.5) reflect changes in ambient size distributions. For example, the shift toward more ultrafine particles in the morning results from increased traffic emissions [*Shields et al.*, 2008]. Similarly, the significant shift toward larger particles in the afternoon indicates particle aging and SOA formation.

To further compare the size ranges of the A-ATOFMS, UF-ATOFMS, and nozzle-inlet ATOFMS, ultrafine and submicron hit particle counts were scaled to 1 h average SMPS data using the following size bins: 50.5-100.1, 100.1-124, 124-149, 149-

172, 172-199, 199-229, 229-255, 255-284, 284-317, 317-353, 353-379, 379-407, 407-437, 437-470, 470-505, 505-543, 543-584, 584-627, 627-673, 673-724, 724-778, 778-836, and 836-866 nm. Scaling conversions between aerodynamic and mobility diameter have been completed previously by making assumptions regarding particle density and shape [*Reinard et al.*, 2007]. However, while significant size differences can exist between aerodynamic diameter (ATOFMS) and mobility diameter (SMPS) for certain chemical particle types, Spencer et al. [2007] found that chemically diverse particle types observed by ATOFMS during SOAR had similar effective densities due to the abundance of secondary species, such as organic carbon, sulfate, and nitrate. It is assumed herein that scaling ultrafine and submicron ATOFMS data directly to SMPS data yields negligible sizing errors for comparison of total particle counts between ATOFMS instruments. As shown in Figure 2.5d, the SMPS scaling factor is defined as the SMPS particle number concentration for a particular size bin divided by the ATOFMS hit particle number concentration for that size bin. The A-ATOFMS had similar or lower scaling factors over the given size range compared to the UF-ATOFMS and ATOFMS. Below ~200 nm, the utility of the UF-ATOFMS is shown through lower scaling factors, and thus, higher particle data acquisition rates. Similarly, the A-ATOFMS had lower scaling factors over the entire given size range compared to the ATOFMS; however, the utility of ATOFMS lies in its ability to detect supermicron particles at higher frequencies (not shown).

Thus, the faster data acquisition system and Nd:YAG laser of the A-ATOFMS resulted in an average 2-6 fold improvement in data acquisition speed over previous ATOFMS. However, it should be noted that the UF-ATOFMS and ATOFMS usually experienced higher hit particle rates than the A-ATOFMS for the ultrafine (50-100 nm) and supermicron (1.0-2.5 μm) size ranges, respectively. Following SOAR-1, the new software developed for the A-ATOFMS was applied to the UF-ATOFMS and ATOFMS, providing higher ambient hit particle rates of >10 Hz for the UF-ATOFMS and >4 Hz for the ATOFMS. Further optimization of the A-ATOFMS also shows ambient hit particle rates of >10 Hz.

2.4.3 Improved Ion Transmission and Mass Resolution

The Z-TOF mass spectrometer, shown in Figure 2.1b and utilized in the A-ATOFMS, has a compact dual-polarity grid-less reflectron design and was developed through collaboration between the University of California, San Diego and Tofwerk AG. It was designed to increase ion transmission and mass range while minimizing the footprint of the dual-polarity mass spectrometer for use in an aircraft rack. Improved performance was made possible through detailed geometry optimization (custom software, Tofwerk AG, Thun, Switzerland) and ion simulations (SIMION 3D 7.0, developed by David Dahl, Idaho National Laboratory, Scoville, ID). The Z-TOF design consists of a single source region, two flight tubes, two reflectrons, and two detectors. The Z-shaped flight path corresponds to a V-shaped flight path in a single polarity TOF analyzer. For dual polarity measurements, the Z configuration allows for the use of a full detector without a center hole, as used in the coaxial TOF design; this results in higher ion transmission. The use of a gridless ion extractor [*Bechtold et al.*, 1991; *Koster*, 1998], providing higher ion transmission, is possible due to the well-defined starting position of the ions, defined by the laser beam position and diameter. The gridless reflectron also results in higher resolution and ion transmission [*Bergmann et al.*, 1989; *Frey and Schlag*, 1988; *Wollnik and Przewloka*, 1990]. The negative/positive ions are extracted with electrodes separated by 6.0 mm at +/- 2.4 kV, spatially focused with a lens at +/- 1.6 kV before entering a field free region at +/- 8 kV, refocused in a reflectron set at +/- 4/1.8/0.5 kV, and detected by an ion detector set at +/- 0.8/2.8/0.6 kV. The nominal ion flight path is 87 cm long, and typical flight times are ~7 µs for m/z 100; the decreased flight path of the Z-TOF compared to the coaxial TOF (172 cm) provides higher ion transmission for higher mass ions. The bipolar detectors (25 mm bipolar, BURLE Industries Inc., Lancaster, PA) each employ a microchannel plate (MCP) for ion-to-electron conversion and amplification, a scintillator electron-to-photon conversion surface, and PMT detector; hence, the signal is optically decoupled from high voltage, thereby additionally providing protection from damage to the data acquisition boards and preventing cross-talk between the two detectors.

Ion simulations, using identical ion parameters, were performed to compare the Z-TOF design used in the A-ATOFMS with the previous coaxial design used in the nozzle-inlet ATOFMS and UF-ATOFMS (Table 2.3). Using SIMION 3D 7.0, developed by David Dahl (Idaho National Lab, Scoville, ID), the following ion parameters were modeled. 5000 ions starting in random directions had random initial positions within a spherical volume (radius = 0.3 mm); random initial velocities were assigned from 1100-1400 m/s. The reported resolving power is calculated from all ions arriving at the detector at half height of the *m/z* peak. For the Z-TOF, ion simulations indicate a mass resolving power of 1072 at *m/*z 100 with 100% ion transmission up to *m/z* 2000, providing a mass range of approximately *m/z* 5000. In comparison, simulations for

Table 2.3. Comparison of simulated resolving powers and ion transmissions at different *m/z* for the A-ATOFMS and coaxial ATOFMS.

	A-ATOFMS		coaxial ATOFMS	
m/z	**Resolving power**	**Ion transmission**	**Resolving power**	**Ion transmission**
100	1072	100%	247	79%
500	678	100%	243	10%
2000	394	100%	217	7%

the previous coaxial ATOFMS yield a mass resolving power of 247 and ion transmission of 79% for *m/z* 100 with ion transmission decreasing to 7% by *m/z* 2000. To compare the observed performance of the A-ATOFMS with the previous coaxial mass spectrometer, standard 270 nm PSL particles were analyzed. For the Z-TOF mass spectrometer, typical mass resolving powers at *m/z* 100 were 500 for positive ions and 800 for negative ions, although mass resolving power was found at times to be as high as 1500 for negative ions. The observed lower mass resolving power for the positive ions is likely due to space charge effects since positive ions are often more abundant by a factor of up to 10 [*Murphy*, 2007]. The previous coaxial mass spectrometer design yielded a mass resolving power of 500 for both positive and negative ions produced from the 270 nm PSL particles. Thus, the Z-TOF design has higher mass resolving power than the coaxial design despite having half the nominal ion flight path (87 cm vs. 172 cm).

The increased ion transmission of the A-ATOFMS has opened up new possibilities for detecting high molecular weight molecules, such as oligomeric and biological species, in single aerosol particles. The A-ATOFMS has already yielded new insights into ambient particle chemistry, by allowing the detection of oligomeric species from *m/z* -200 to -400 in ambient particles during SOAR [*Denkenberger et al.*, 2007]. Furthermore, during ICE-L flights, high mass positive ions were detected out to ~*m/z* 2000 in single organic carbon particles. As an example, Figure 2.6 shows a 480 nm particle detected by A-ATOFMS at an altitude of 4720 m (3300 m above ground level) over southeastern Wyoming. These ICE-L A-ATOFMS results represent the first real-time, single-particle detection of species heavier than 400 Da in ambient particles. These observations would not have been possible with the previous coaxial ATOFMS

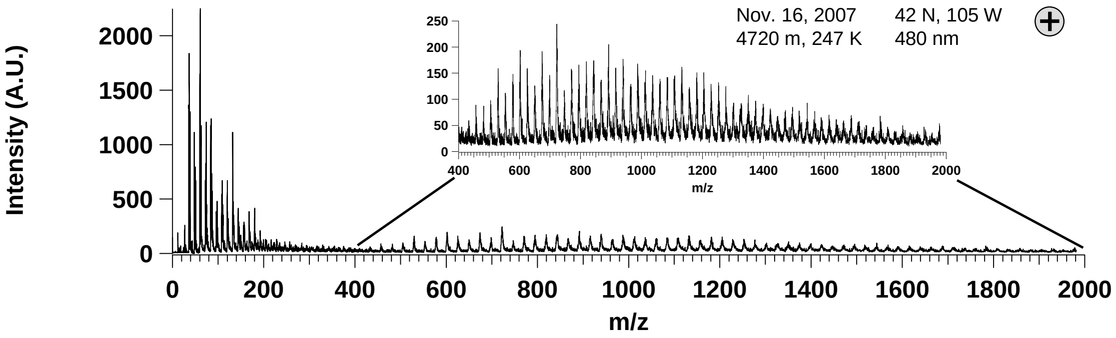

Figure 2.6. Single-particle positive ion mass spectrum showing high mass species from a 480 nm organic carbon particle detected at 4720 m in southeastern Wyoming during ICE-L.

instruments, which are normally operated out to only *m/z* 350 with rapidly decreasing ion transmission efficiencies at higher m/z values compared to the A-ATOFMS.

2.4.4. First Dual-Polarity Single-Particle Mass Spectrometry Aircraft-based Measurements

The ATOFMS detects both positive and negative ions simultaneously, providing an increased understanding of particle mixing state [*Gard et al.*, 1997]. Specifically, secondary species, such as nitrate and sulfate, are primarily detected as negative ions; whereas, the primary particle source signature occurs principally in the positive ions [*Gard et al.*, 1997; *Hinz et al.*, 1996]. Figure 2.7 shows example single-particle mass spectra of several common particle types observed during A-ATOFMS ICE-L measurements in Wyoming, Colorado, and Nebraska. An example organic carbon (OC)-sulfate-nitrate particle detected at 6740 m over northern Colorado (Figure 2.7a) is characterized by positive ions peaks corresponding to organic carbon (*m/z* 27($C_2H_3^+$/CHN^+), 37(C_3H^+), 39($C_3H_3^+$), 50($C_4H_2^+$/C_3N^+)) and amines (*m/z* 59($(CH_3)_3N^+$), 118 ($(C_2H_5)_3NOH^+$)), in particular. The negative ions are dominated by nitrate and sulfate at *m/z* -46(NO_2^-), -62(NO_3^-), and -97(HSO_4^-) with organic nitrogen ion peaks at *m/z* -26(CN^-), -42(CNO^-), and -43(CH_3COO^-). The mass spectra of a biomass/biofuel burning particle, shown in Figure 2.7b (2860 m over northern Colorado), are characterized by a large potassium ion peak at *m/z* 39(K^+) coupled with smaller carbonaceous ion peaks at *m/z* 36(C_3^+) and 37(C_3H^+), potassium-sulfate clusters at *m/z* 175($K_2HSO_4^+$) and 213($K_3HSO_4^+$), and a negative ion sulfate peak at *m/z* -97(HSO_4^-). Figure 2.7c shows a pure elemental carbon (EC) particle detected at 3660 m over northern Colorado and is

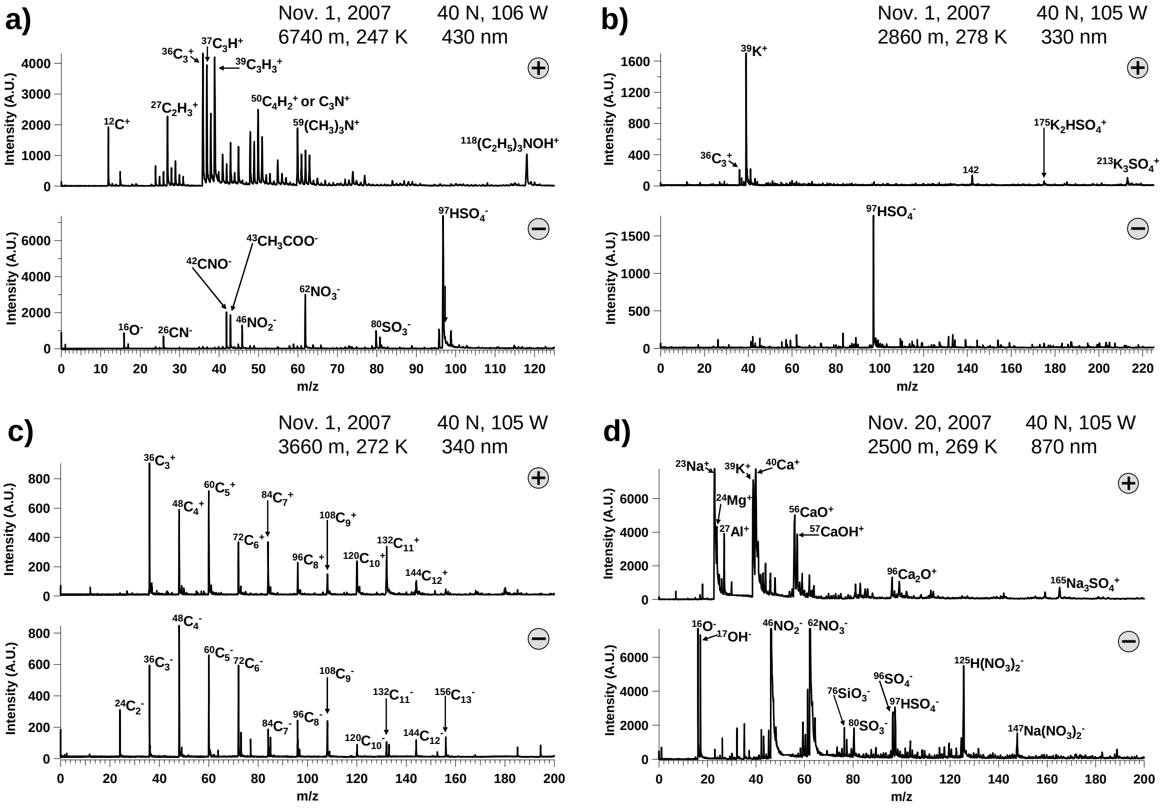

Figure 2.7. Example single-particle mass spectra during flight during ICE-L: (a) organic carbon-sulfate-nitrate, (b) biomass/biofuel burning, (c) elemental carbon, (d) dust-nitrate-sulfate. Acquisition parameters shown for each particle include date, latitude, longitude, altitude, ambient temperature, and particle size.

characterized by carbon cluster ion peaks ($C_n^{+/-}$). Detected at 2500 m over northern Colorado, the mass spectra of an example dust-nitrate-sulfate particle are shown in Figure 2.7d. It is characterized by intense inorganic positive ion peaks at *m/z* 23(Na^+), 24(Mg^+), 27(Al^+), 39(K^+), 40(Ca^+), 56(CaO^+), 57($CaOH^+$), 96(Ca_2O^+), and 165($Na_3SO_4^+$), in particular. Silicate (*m/z* -76(SiO_3^-)), nitrate (*m/z* -46(NO_2^-), -62(NO_3^-), -125($H(NO_3)_2^-$), and -147($Na(NO_3)_2^-$), and sulfate (*m/z* -80(SO_3^-), -96(SO_4^-), and -97(HSO_4^-)) are found in the negative ions of this reacted dust particle. These results show the ability of the A-ATOFMS to provide distinct single-particle mixing state and to distinguish between elemental carbon and organic carbon, which is important for predictions of direct and indirect radiative forcing.

The high time resolution of the A-ATOFMS is essential for airborne studies and ground-based studies near particle sources where particle concentrations and chemistry vary rapidly. For the first time, 2 min ambient single-particle mixing state is presented in Figure 2.8a; 4 min resolution is shown beginning after take-off. For comparison, the data shown in Figure 2.8a are also shown in Figure 2.8b in 1 h bins. Briefly, the OC-nitrate-sulfate type is characterized by organic carbon, nitrate, and sulfate. The amine-sulfate-nitrate particle type is dominated by amine marker ions, discussed above, as well as organic carbon, sulfate, and nitrate. The aromatic particle type is dominated by organic carbon marker ions indicative of aromatic species; the negative ions of this particle type often include chloride and nitrate. The biogenic particle type is dominated by inorganic positive ions, including sodium, potassium, and/or calcium, with nitrate or phosphate in the negative ion spectra. The elemental carbon-organic carbon (ECOC)-nitrate-sulfate type is characterized by both elemental and organic carbon mixed with nitrate and sulfate.

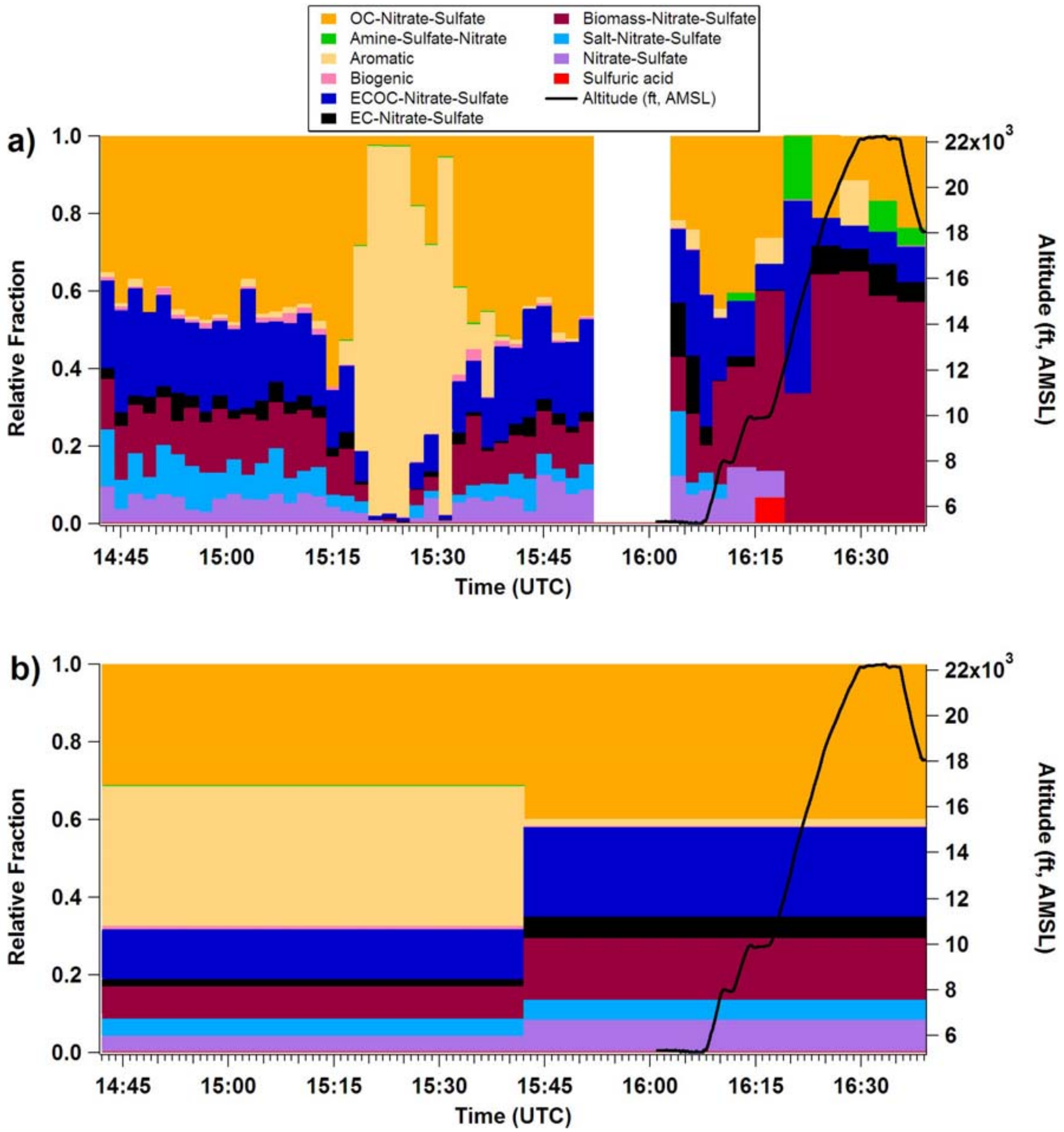

Figure 2.8. Relative fractions of particle types detected via A-ATOFMS (ICE-L, December 13, 2007). (a) Two-minute resolution is shown during ground sampling. Four-minute resolution is shown just after flight take-off. (b) One-hour resolution is shown for comparison.

The EC-nitrate-sulfate type is dominated by carbon cluster ions, described above, and indicative of elemental carbon mixed with nitrate and sulfate. The biomass-nitrate-sulfate particles are described above and include secondary nitrate and sulfate. The salt-nitrate-sulfate particle type is characterized by sodium and potassium chloride salts with nitrate and sulfate. The nitrate-sulfate type includes particles which only produced negative ion spectra characterized by nitrate and sulfate. The sulfuric acid type includes particles producing only negative ions and characterized by sulfate (m/z -97 (HSO_4^-)) and sulfuric acid (m/z -195 ($H_2SO_4HSO_4^-$)).

During ground-based sampling prior to flight, an increase in particle concentration from a short-term local source at the airport, likely another airplane or helicopter, results in the aromatic particle type dominating the particle phase from 15:18-15:32 (Figure 2.8a and 2.9). Also, during take-off and ascent, the contribution of organic carbon particles diminishes with biomass burning particles becoming more dominant. As can be seen, the high time-resolved mixing state information provides critical insight into transient events that could not be observed previously by the UF-ATOFMS and ATOFMS due to slower data acquisition rates (as illustrated in the 1 h time resolution plot).

2.5 Conclusions

A smaller ATOFMS with increased data acquisition capabilities and lower power consumption has been developed for aircraft-based studies. This A-ATOFMS is the first reported dual-polarity laser mass spectrometer for aircraft-based studies, allowing the complete mixing state, including both refractory and non-refractory species, of single

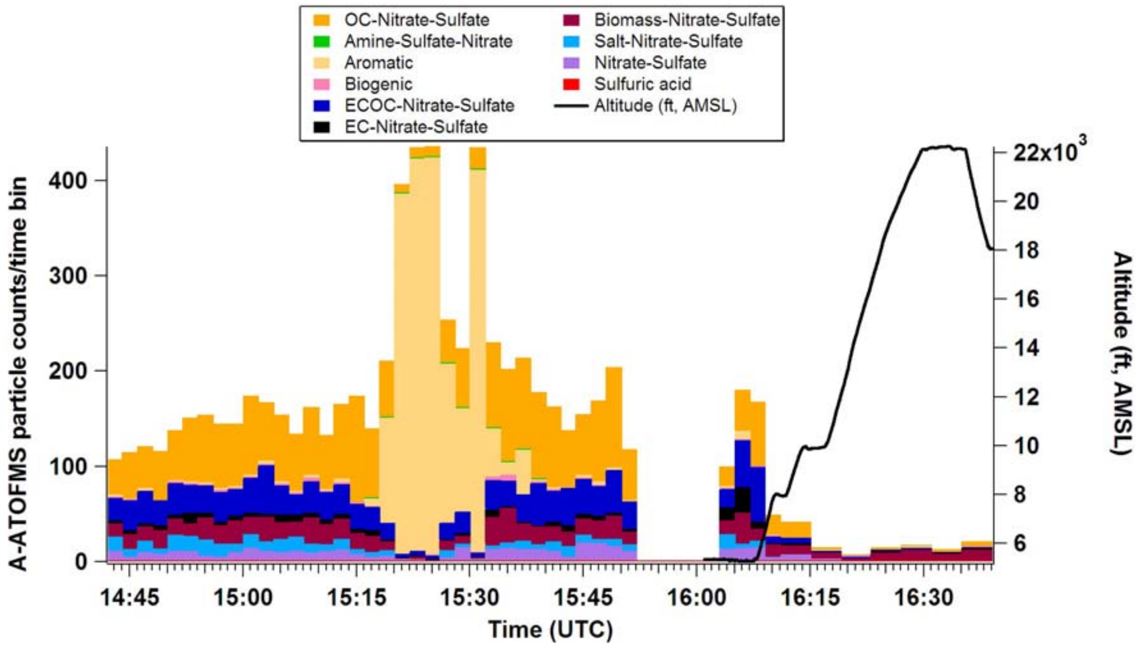

Figure 2.9. A-ATOFMS particle counts with 2-4 minute resolution for A-ATOFMS measurements during ICE-L on December 13, 2007.

particles to be investigated with respect to altitude. The A-ATOFMS features an improved inlet design, reduced pumping configuration, increased particle size range (~70-1000 nm), innovative mass spectrometer and desorption/ionization laser alignment design, and real-time source apportionment, which will be useful for targeting and studying source plumes of interest during flights. Ground-based field testing during SOAR shows increased data acquisition rates (>3x), mass resolution, and ion transmission compared to previous ATOFMS. ICE-L A-ATOFMS results represent the first real-time, single-particle detection of high mass positive ions out to ~*m/z* 2000. For the first time, dual-polarity single-particle mass spectra collected in real-time during flight are shown from ICE-L; these results will provide insight into the direct and indirect radiative forcing of specific particle mixing states. In addition, high time resolution of single-particle mixing state is shown to be important for airborne studies as well as ground-based studies near particle sources where particle concentrations and chemistry vary rapidly.

2.6 Acknowledgements

A-ATOFMS development funding was provided through the National Science Foundation (ATM-0321262); participation in SOAR and ICE-L was funded in part by the California Air Resources Board and the National Science Foundation (ATM-0650659), respectively. Kerri Pratt, Joseph Mayer, John Holecek, and Ryan Moffet together designed and built the A-ATOFMS. Kerri Pratt ran the A-ATOFMS during the SOAR and ICE-L field campaigns and analyzed the data. Rene Sanchez and Thomas Rebotier designed the A-ATOFMS software and real-time source apportionment. Mark Gonin and

Katrin Fuhrer (Tofwerk AG) worked in collaboration with the Prather Lab in the design and development of the Z-TOF mass spectrometer. Hiroshi Furutani, Yongxuan Su, and Sergio Guazzotti served advisory roles in the development of the A-ATOFMS. Gary Poon contributed to the design and construction of the ground-based prototype of the A-ATOFMS. The authors acknowledge Dan Murphy (National Oceanic and Atmospheric Admistration) and Prof. Jose Jimenez (University of Colorado, Boulder) for their discussions and advice on aerosol instrument designs for aircraft. Ryan Sullivan is acknowledged for work on the LDI aperture implementation. Laura Shields and Xueying Qin are thanked for providing SOAR-1 UF-ATOFMS and ATOFMS data, respectively. Xueying Qin provided PSL particle data for the previous coaxial design ATOFMS. Urs Rohner (Tofwerk AG) ran ion simulations for the A-ATOFMS and ground-based coaxial design ATOFMS.

Publication Acknowledgment

Chapter 2 has been reproduced with permission from: Pratt, K.A., Mayer, J.E., Holecek, J.C., Moffet, R.C., Sanchez, R.O., Rebotier, T., Furutani, H., Gonin, M., Fuhrer, K., Su, Y., Guazzotti, S., Prather, K.A. Development and characterization of an aircraft aerosol time-of-flight mass spectrometer. *Analytical Chemistry*. 2009, 81, 1792-1800. Copyright 2009, American Chemical Society.

2.7 References

Allen, J.O., P.V. Bhave, J.R. Whiteaker, and K.A. Prather (2006), Instrument busy time and mass measurement using aerosol time-of-flight mass spectrometry, *Aerosol Sci. Technol.*, *40*(8), 615-626.

Bahreini, R., E.J. Dunlea, B.M. Matthew, C. Simons, K.S. Docherty, P.F. DeCarlo, J.L. Jimenez, C.A. Brock, and A.M. Middlebrook (2008), Design and operation of a pressure-controlled inlet for airborne sampling with an aerodynamic aerosol lens, *Aerosol Sci. Technol.*, *42*(6), 465-471.

Bahreini, R., J.L. Jimenez, J. Wang, R.C. Flagan, J.H. Seinfeld, J.T. Jayne, and D.R. Worsnop (2003), Aircraft-based aerosol size and composition measurements during ACE-Asia using an Aerodyne aerosol mass spectrometer, *J. Geophys. Res.*, *108*(D23).

Bechtold, P.S., M. Mihelcic, and K. Wingerath, Time-of-flight spectrometer with gridless ion source, U.S. Patent 5,065,018, 1991.

Bergmann, T., T.P. Martin, and H. Schaber (1989), High-resolution time-of-flight mass spectrometers: Part 1. Effects of field distortions in the vicinity of wire meshes, *Rev. Sci. Instrum.*, *60*(3), 347-349.

Brock, C.A., P.K. Hudson, E.R. Lovejoy, A. Sullivan, J.B. Nowak, L.G. Huey, O.R. Cooper, D.J. Cziczo, J. de Gouw, F.C. Fehsenfeld, J.S. Holloway, G. Hubler, B.G. Lafleur, D.M. Murphy, J.A. Neuman, D.K. Nicks, D.A. Orsini, D.D. Parrish, T.B. Ryerson, D.J. Tanner, C. Warneke, R.J. Weber, and J.C. Wilson (2004), Particle characteristics following cloud-modified transport from Asia to North America, *J. Geophys. Res.*, *109*(D23).

Cziczo, D.J., P.J. DeMott, C. Brock, P.K. Hudson, B. Jesse, S.M. Kreidenweis, A.J. Prenni, J. Schreiner, D.S. Thomson, and D.M. Murphy (2003), A method for single particle mass spectrometry of ice nuclei, *Aerosol Sci. Technol.*, *37*(5), 460-470.

Cziczo, D.J., D.M. Murphy, P.K. Hudson, and D.S. Thomson (2004), Single particle measurements of the chemical composition of cirrus ice residue during CRYSTAL-FACE, *J. Geophys. Res.*, *109*(D4), -.

Denkenberger, K.A., R.C. Moffet, J.C. Holecek, T.P. Rebotier, and K.A. Prather (2007), Real-Time, Single-Particle Measurement of Ambient Aerosol Particles Containing Oligomeric Species, *Environ. Sci. Technol.*, *41*(5439-5446.

Forster, P., V. Ramaswamy, P. Artaxo, T. Berntsen, R. Betts, D.W. Fahey, J. Haywood, J. Lean, D.C. Lowe, G. Myhre, J. Nganga, R. Prinn, G. Raga, M. Schulz, and R. Van Dorland, *Climate Change 2007: The Physical Science Basis. Contribution of*

Working Group I to the Fourth Assessment Report of the Intergovernmental Panel on Climate Change, Cambridge University Press, Cambridge, UK, 2007.

Frey, R., and E.W. Schlag, Time of flight mass spectrometer using an ion reflector, U.S. Patent 4,731,532, 1988.

Gard, E., J.E. Mayer, B.D. Morrical, T. Dienes, D.P. Fergenson, and K.A. Prather (1997), Real-time analysis of individual atmospheric aerosol particles: Design and performance of a portable ATOFMS, *Anal. Chem.*, *69*(20), 4083-4091.

Gard, E.E., M.J. Kleeman, D.S. Gross, L.S. Hughes, J.O. Allen, B.D. Morrical, D.P. Fergenson, T. Dienes, M.E. Galli, R.J. Johnson, G.R. Cass, and K.A. Prather (1998), Direct observation of heterogeneous chemistry in the atmosphere, *Science, 279*(5354), 1184-1187.

Guazzotti, S.A., K.R. Coffee, and K.A. Prather (2001), Continuous measurements of size-resolved particle chemistry during INDOEX-Intensive Field Phase 99, *J. Geophys. Res.*, *106*(D22), 28607-28627.

Hinds, W.C., Aerosol technology: properties, behavior, and measurement of airborne particles, pp. 335-338, Wiley, New York, 1999.

Hinz, K.P., R. Kaufmann, and B. Spengler (1996), Simultaneous detection of positive and negative ions from single airborne particles by real-time laser mass spectrometry, *Aerosol Sci. Technol.*, *24*(4), 233-242.

Huffman, J.A., J.T. Jayne, F. Drewnick, A.C. Aiken, T. Onasch, D.R. Worsnop, and J.L. Jimenez (2005), Design, modeling, optimization, and experimental tests of a particle beam width probe for the aerodyne aerosol mass spectrometer, *Aerosol Sci. Technol., 39*(12), 1143-1163.

Jayne, J.T., D.C. Leard, X.F. Zhang, P. Davidovits, K.A. Smith, C.E. Kolb, and D.R. Worsnop (2000), Development of an aerosol mass spectrometer for size and composition analysis of submicron particles, *Aerosol Sci. Technol., 33*(1-2), 49-70.

Koster, C., Method for time-of-flight mass spectrometry of daughter ions, U.S. Patent 5,734,161, 1998.

Liu, P., P.J. Ziemann, D.B. Kittelson, and P.H. Mcmurry (1995a), Generating Particle Beams of Controlled Dimensions and Divergence.1. Theory of Particle Motion in Aerodynamic Lenses and Nozzle Expansions, *Aerosol Sci. Technol.*, *22*(3), 293-313.

Liu, P., P.J. Ziemann, D.B. Kittelson, and P.H. Mcmurry (1995b), Generating Particle Beams of Controlled Dimensions and Divergence.2. Experimental Evaluation of

Particle Motion in Aerodynamic Lenses and Nozzle Expansions, *Aerosol Sci. Technol.*, *22*(3), 314-324.

Liu, P.S.K., R. Deng, K.A. Smith, L.R. Williams, J.T. Jayne, M.R. Canagaratna, K. Moore, T.B. Onasch, D.R. Worsnop, and T. Deshler (2007), Transmission efficiency of an aerodynamic focusing lens system: Comparison of model calculations and laboratory measurements for the Aerodyne aerosol mass spectrometer, *Aerosol Sci. Technol.*, *41*(8), 721-733.

Moffet, R.C., B. de Foy, L.T. Molina, M.J. Molina, and K.A. Prather (2008), Measurement of ambient aerosols in northern Mexico City by single particle mass spectrometry, *Atmos. Chem. Phys.*, *8*(4499-4516.

Moffet, R.C., and K.A. Prather (2005), Extending ATOFMS measurements to include refractive index and density, *Anal. Chem.*, *77*(20), 6535-6541.

Murphy, D.M. (2007), The design of single particle laser mass spectrometers, *Mass Spec. Rev.*, *26*(2), 150-165.

Murphy, D.M., D.S. Thomson, and T.M.J. Mahoney (1998), In situ measurements of organics, meteoritic material, mercury, and other elements in aerosols at 5 to 19 kilometers, *Science*, *282*(5394), 1664-1669.

Mysak, E.R., Y.N. Dessiaterik, C.J. McKinney, R.E. Miller, and T. Baer (2006), Design of a timing circuit for random laser triggering on aerosol particles, *Rev. Sci. Instrum.*, *77*(1).

Poschl, U. (2005), Atmospheric aerosols: Composition, transformation, climate and health effects, *Angewandte Chemie-International Edition*, *44*(46), 7520-7540.

Prather, K.A., T. Nordmeyer, and K. Salt (1994), Real-Time Characterization Of Individual Aerosol-Particles Using Time-Of-Flight Mass-Spectrometry, *Anal. Chem.*, *66*(9), 1403-1407.

Reinard, M.S., K. Adou, J.M. Martini, and M.V. Johnston (2007), Source characterization and identification by real-time single particle mass spectrometry, *Atmos. Environ.*, *41*(9397-9409.

Shields, L.G., X. Qin, S.M. Toner, and K.A. Prather (2008), Detection of ambient ultrafine aerosols by single particle techniques during the SOAR 2005 campaign, *Aerosol Sci. Technol.*, *42*(674-684.

Silva, P.J., R.A. Carlin, and K.A. Prather (2000), Single particle analysis of suspended soil dust from Southern California, *Atmos. Environ.*, *34*(11), 1811-1820.

Silva, P.J., D.Y. Liu, C.A. Noble, and K.A. Prather (1999), Size and chemical characterization of individual particles resulting from biomass burning of local

Southern California species, *Environmental Science & Technology*, *33*(18), 3068-3076.

Sodeman, D.A., S.M. Toner, and K.A. Prather (2005), Determination of single particle mass spectral signatures from light-duty vehicle emissions, *Environ. Sci. Technol.*, *39*(12), 4569-4580.

Spencer, M.T., L.G. Shields, and K.A. Prather (2007), Simultaneous measurement of the effective density and chemical composition of ambient aerosol particles, *Environ. Sci. Technol.*, *41*(4), 1303-1309.

Su, Y.X., M.F. Sipin, H. Furutani, and K.A. Prather (2004), Development and characterization of an aerosol time-of-flight mass spectrometer with increased detection efficiency, *Anal. Chem.*, *76*(3), 712-719.

Sullivan, R.C., S.A. Guazzotti, D.A. Sodeman, and K.A. Prather (2007), Direct observations of the atmospheric processing of Asian mineral dust, *Atmos. Chem. Phys.*, *7*(1213-1236.

Sullivan, R.C., and K.A. Prather (2005), Recent advances in our understanding of atmospheric chemistry and climate made possible by on-line aerosol analysis instrumentation, *Anal. Chem.*, *77*(12), 3861-3885.

Toner, S.M., L.G. Shields, and K.A. Prather (2008), Source apportionment of freeway-side PM2.5 using ATOFMS, *Atmos. Environ.*, *In Preparation*(

Toner, S.M., D.A. Sodeman, and K.A. Prather (2006), Single particle characterization of ultrafine and accumulation mode particles from heavy duty diesel vehicles using aerosol time-of-flight mass spectrometry, *Environ. Sci. Technol.*, *40*(12), 3912-3921.

Wang, X.L., and P.H. McMurry (2006), A design tool for aerodynamic lens systems, *Aerosol Sci. Technol.*, *40*(5), 320-334.

Wenzel, R.J., and K.A. Prather (2004), Improvements in ion signal reproducibility obtained using a homogeneous laser beam for on-line laser desorption/ionization of single particles, *Rapid Commun. Mass Spectrom.*, *18*(1525-1533.

Wollnik, H., and M. Przewloka (1990), Time-of-flight mass spectrometers with multiply reflected ion trajectories, *Int. J. Mass Spectrom. Ion Processes*, *96*(3), 267-274.

Zhang, X.F., K.A. Smith, D.R. Worsnop, J. Jimenez, J.T. Jayne, and C.E. Kolb (2002), A numerical characterization of particle beam collimation by an aerodynamic lens-nozzle system: Part I. An individual lens or nozzle, *Aerosol Sci. Technol., 36*(5), 617-631.

Zhang, X.F., K.A. Smith, D.R. Worsnop, J.L. Jimenez, J.T. Jayne, C.E. Kolb, J. Morris, and P. Davidovits (2004), Numerical characterization of particle beam collimation: Part II - Integrated aerodynamic-lens-nozzle system, *Aerosol Sci. Technol.*, *38*(6), 619-638.

Chapter 3

3 Real-Time, Single-Particle Measurements of Oligomers in Aged Ambient Aerosol Particles

3.1 Synopsis

Unique high mass negative ions in the -200 to -400 mass/charge range with repetitive spacings of 12, 14, and 16 units, representative of oligomeric species, have been detected in single ambient submicrometer aerosol particles using real-time, single-particle mass spectrometry during the Study of Organic Aerosols field campaign conducted in Riverside, CA (SOAR) in August and November 2005. These oligomer-containing particles represented 33-40% of the total detected particles and contained other indicators of aging including oxidized organic carbon, amine, nitrate, and sulfate ion markers. Overall, the highest mass oligomeric patterns were observed in small acidic 140-200 nm particles in the summer. Also during the summer, increased oligomer intensities were observed when the particles were heated with a thermodenuder. We hypothesize that heat removed semivolatile species, thereby increasing particle acidity, while concentrating the oligomeric precursors and accelerating oligomer formation. Differences in oligomer behavior with respect to particle size and heating can be attributed to seasonal differences in photochemical oxidation, the relative amount of ammonium, and particle acidity.

3.2 Introduction

While the formation and presence of polymers in aerosols during Los Angeles (LA) smog events was initially predicted by Haagen-Smit [1952], oligomeric species have only recently been identified as an important component of the secondary organic aerosol (SOA) mass through laboratory studies [*Jang and Kamens*, 2001; *Jang et al.*, 2002; *Kalberer et al.*, 2004]. In the eastern LA basin, SOA has been found to comprise up to 80% of the total organic aerosol mass [*Turpin and Huntzicker*, 1995], and laboratory studies have suggested that possibly up to 50% of the SOA mass may be composed of oligomers, suggesting the potential importance of these species in ambient aerosols [*Kalberer et al.*, 2004]. The presence of oligomeric species in SOA particles is expected to significantly affect gas-particle partitioning, hygroscopic growth, particle reactivity, and health effects [*Kanakidou et al.*, 2005].

Several laboratory-based mass spectrometry studies have reported the formation of SOA oligomers, characterized by a high mass envelope of peaks with a mass difference pattern of 12, 14, or 16 Da [*Baltensperger et al.*, 2005; *Gao et al.*, 2004a; *Gao et al.*, 2004b; *Gross et al.*, 2006; *Kalberer et al.*, 2004; *Tolocka et al.*, 2004]. For example, Kalberer et al. [2004] used off-line laser desorption/ionization mass spectrometry (LDI-MS) to detect oligomers in aerosol particles formed through the photooxidation of 1,3,5-trimethylbenzene. In addition to chamber studies, high mass species (oligomers and/or macromolecules) have been detected in ambient particles through off-line mass spectrometry [*Baltensperger et al.*, 2005; *Kalberer et al.*, 2006; *Kiss et al.*, 2003; *Reemtsma et al.*, 2006; *Samburova et al.*, 2005; *Streibel et al.*, 2006; *Tolocka et al.*, 2004]. For example, using LDI-MS, a repetitive mass difference pattern of *m/z* 14 and 16 from *m/z* 200-450 was observed in water-soluble organic matter extracted from a filter sample collected in Zurich, Switzerland [*Samburova et al.*, 2005]. Recently, off-line high-resolution mass spectrometry techniques have been applied to the molecular identification of ambient and laboratory oligomers [*Reemtsma et al.*, 2006; *Reinhardt et al.*, 2007].

Herein, we report the first real-time detection of oligomeric species in individual ambient aerosol particles by aerosol time-of-flight mass spectrometry (ATOFMS) during the Study of Organic Aerosols field campaign conducted in Riverside, California (SOAR) in August and November 2005. An inland site in the LA basin, Riverside serves as a receptor of LA air pollutants, which undergo significant evolution during transport eastward [*Appel et al.*, 1978; *Hughes et al.*, 2000]. A significant fraction (33-40%) of submicrometer particles detected by ATOFMS during SOAR show evidence of aging and are characterized by high mass negative ions in the -200 to -400 mass/charge range with spacings of 12, 14, and 16 units, characteristic of oligomeric species. The effects of particle acidity on the degree of oligomerization are discussed.

3.3 Experimental

Measurements of single submicrometer ambient aerosol particles by ATOFMS were conducted during the SOAR-1 and 2 field campaigns (August and November 2005; http://cires.colorado.edu/jimenez-group/Field/Riverside05/). The sampling site was on the University of California, Riverside campus, located ~60 miles east of Los Angeles, CA. ATOFMS sampling in series with an automated thermodenuder was completed on August 12, 2005 and November 2-13, 2005. All times are given in Pacific Standard Time

(PST), 1 h behind PDT (local time during the summer study). From July 30 to August 15, 2005, a strong diurnal pattern with a similar range of average values was observed for ozone, $PM_{2.5}$ mass concentrations, and ambient meteorological conditions, including wind direction, wind speed, ambient temperature, and relative humidity; therefore, August 12, 2005 was found to be a representative day during SOAR-1 [*Qin et al.*, 2009]. Ambient temperature and relative humidity measurements were made using a shielded Vaisala HMP 45AC temperature and relative humidity probe. Ozone data were collecting using a UV photometric O_3 analyzer (TEI 49C).

The ground-based prototype of the aircraft (A)-ATOFMS, recently developed by the University of California, San Diego and Tofwerk AG (Thun, Switzerland), was utilized to measure the vacuum aerodynamic diameter (d_{va}) [*DeCarlo et al.*, 2004] and dual-polarity mass spectra of individual particles from 70-2500 nm in real-time (Chapter 2). The A-ATOFMS features an increased data acquisition rate, increased ion transmission, increased mass resolution, higher mass range, lower power consumption, and more compact packaging as compared to previous ATOFMS instrumentation [*Su et al.*, 2004]. During SOAR, particles were desorbed and ionized using 266 nm radiation from a Q-switched Nd:YAG laser operating at ~0.95 mJ in the summer and ~0.4-0.8 mJ in the fall. Polystyrene latex spheres of known physical diameters from 95-1400 nm were used to complete the single-particle size calibration. This analysis focuses on submicrometer particles (100-1000 nm) due to lower transmission efficiency of the aerodynamic lens system for supermicrometer particles relative to the submicrometer size range. While ATOFMS measurements may be scaled for quantitative particle number and mass concentrations [*Qin et al.*, 2006], scaling was not conducted for the results presented herein, which focus on mass spectral characteristics rather than overall particle concentrations.

An automated valve-controlled thermodenuder (TD) system [*Huffman et al.*, 2008], developed by the University of Colorado and based on the design by Wehner et al. [2002], was utilized in series with the A-ATOFMS. In the fall, a nafion dryer was used to dry the particles prior to the TD and ATOFMS. A drier was not utilized during SOAR I; therefore, in the fall, the particles leaving the TD may be smaller in size due to the evaporation of water in the dryer. With continuous aerosol flow through the TD and bypass line, the particles sampled by the ATOFMS (either heated or unheated) were determined by the TD valve control system, which automatically switched between heated and unheated ambient aerosol. The heated portion of the TD stepped through eight temperature steps with the following TD and valve program: ambient, 150°C, ambient, 200°C, ambient, 175°C, ambient, 150°C, ambient, 125°C, ambient, 100°C, ambient, 75°C, ambient, 50°C. Since each portion of the schedule was maintained for 10 min, one full cycle took 160 min before repeating. Volatilized species were prevented from condensing back onto the particles through use of an activated carbon diffusion denuder. With a flow rate of 0.6 L/min, the residence time of the aerosol in the heating portion of the TD was approximately 9 s.

Dual-ion mass spectra were collected via ATOFMS for 318,431 ambient particles on August 12, 2005 and 1,390,199 ambient particles from November 2-13, 2005. Data collection times were adjusted for delays in transport lines between the TD and ATOFMS, and data collected up to 20 s after the TD valve switch were eliminated to reduce error caused by possible aerosol mixing. Taking this into account, the mass spectra from 162,881 unheated and 144,592 heated particles were analyzed for August 12th; and 789,007 unheated and 563,371 heated particles were analyzed for November 2-13th. Ion peak lists for each mass spectrum were calibrated and extracted using custom software; peaks were detected by a probability accumulation rather than a given intensity threshold. ATOFMS single-particle mass spectra were imported into YAADA, a database written in Matlab (The MathWorks, Inc.), which allows for the analysis of ATOFMS data [*Allen*, 2001].

Following the observation of intense high mass negative oligomeric ions in several single-particle mass spectra, a square-wave filter was created using the mass/charge pattern of these intense oligomeric ions; using this filter, a unique search algorithm was created and run on the unheated and heated particles from August 12th and November 2-13th. For *m*/*z* -200 to -400, peaks within the allowed oligomer envelopes were assigned +1 with peaks falling outside this range -1; these values were multiplied by the normalized peak intensities and summed for each mass spectrum from *m*/*z* -200 to -400. By applying a threshold of 0.2 (95% confidence, 2 standard deviations), particles containing the oligomeric species, including those with low intensity oligomers, were identified. In this way, particles containing "random", or non-oligomeric peaks in the high mass negative ions, were eliminated. An adaptive resonance theory-based clustering method (ART-2a) was then used to classify single-particle mass spectra with a vigilance factor of 0.80, learning rate of 0.05, and 20 iterations [*Song et al.*, 1999]. By comparing the existence and intensity of ion peaks in individual single-particle mass spectra, ART-2a classifies particles into separate clusters based on their mass spectral fingerprints. For SOAR-1 and 2, ART-2a was run separately on each study for three groups of particles:

unheated total, unheated oligomer-containing, and heated oligomer-containing; the percentage of classified particles ranged from 87-94% for each of the six particle sets. All ART-2a clusters were viewed by hand to assign a general particle class based on the general mass spectral fingerprint and to verify a clear oligomeric pattern (for the oligomer-containing ART-2a runs). Particles without a clear oligomeric pattern, including elemental carbon (EC) particles, were excluded from further analysis; this corresponded to 6-30% of the particles from the oligomer-filter results that had been classified by ART-2a. General particle classes are defined by the most dominant chemical species or possible source in an attempt to keep the naming scheme simplified; these classes do not necessarily reflect all of the species present within a particular particle type. Peak identifications within this paper correspond to the most probable ions for a given *m/z* ratio [*Angelino et al.*, 2001; *Silva and Prather*, 2000; *Spencer and Prather*, 2006; *Whiteaker and Prather*, 2003].

3.4 Results and Discussion

3.4.1 Mass Spectral Signatures of Oligomer-Containing Particles

Signatures of oligomeric species were detected in submicrometer single-particle negative ion mass spectra obtained using A-ATOFMS during the SOAR field campaign in Riverside, CA in August 2005. As shown in Figure 3.1, these particles are characterized by high mass negative ions in the 200-400 mass/charge range with repetitive spacings of 12, 14, and 16, characteristic of oligomeric species [*Baltensperger et al.*, 2005]; a corresponding oligomeric pattern was not observed in the positive ion mass spectra. The detection of the oligomers as negative ions suggests that the species

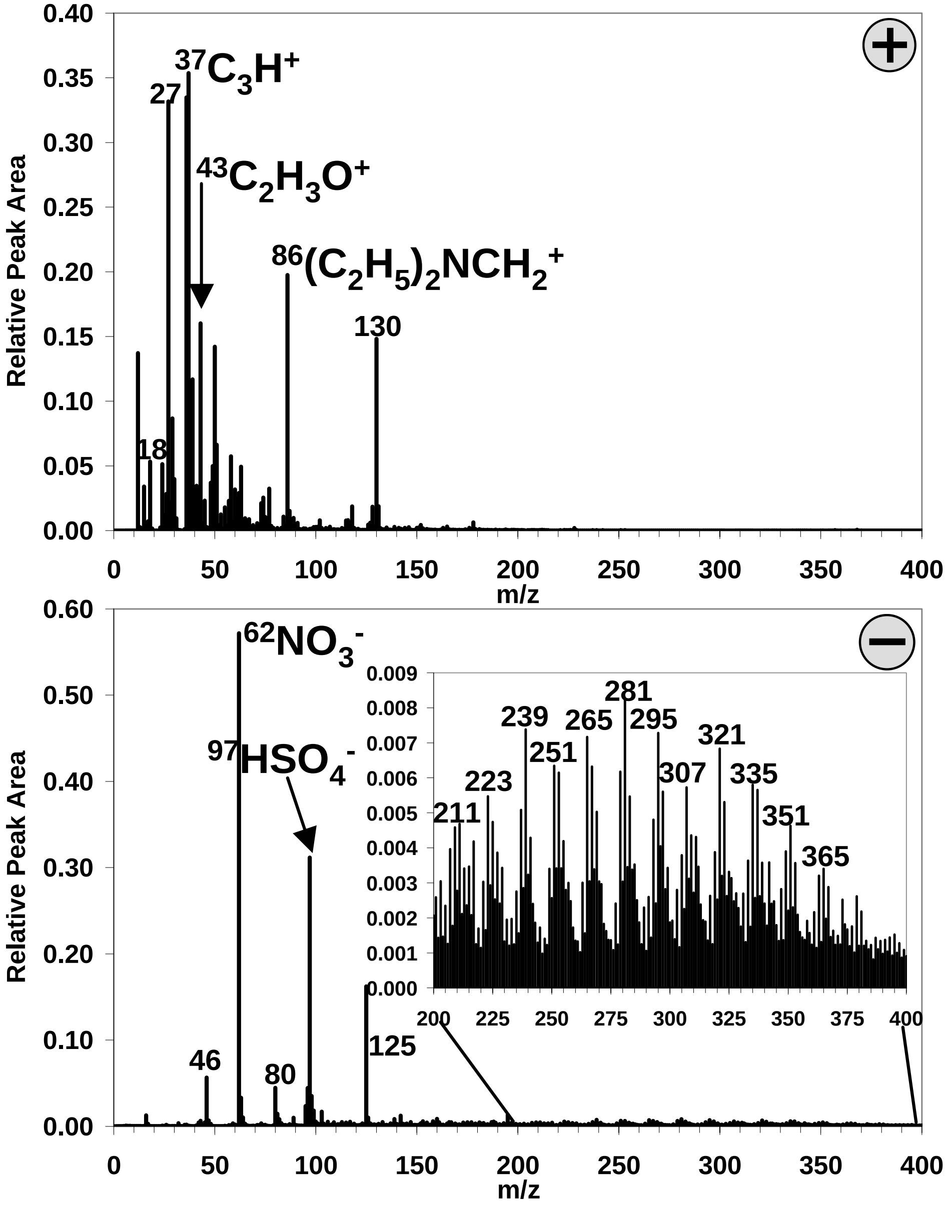

Figure 3.1. Average positive and negative ion mass spectra of the summer unheated OC oligomer-containing particle type.

are deprotonated oxidized organics $(M\text{-}O)^-$; the mass/charge difference pattern can be attributed to the loss of carbon atoms, $-CH_2$ groups, and oxygen atoms [*Samburova et al.*, 2005]. To our knowledge, these are the first reported real-time mass spectrometric measurements of oligomeric species in individual *ambient* aerosols. Using electrospray ionization Fourier transform cyclotron resonance mass spectrometry (FTICR-MS) and triple-quadrupole MS, recent SOAR-1 filter-based results showed an "oligomeric" pattern that corresponded to the stepwise addition of a carbonyl or oxygen in fulvic acid molecules [*Reemtsma et al.*, 2006]. The ATOFMS SOAR oligomeric mass spectral pattern is nearly identical to that observed by triple-quadrupole MS for Riverside water-soluble organosulfate (containing *m/z* -97, HSO_4^-) molecules [*Reemtsma et al.*, 2006]. In general, humic acids are considered refractory organic molecules that can only be thermally vaporized from ~400-575°C [*Andreae and Gelencser*, 2006]; therefore, the use of laser desorption ionization that results in extremely high temperatures, as in this study, or electrospray ionization, as in the previously mentioned study [*Reemtsma et al.*, 2006], are the most effective methods for detecting these high mass refractory organic compounds.

The observed pattern of the oligomeric species in the negative ion mass spectra is similar to that obtained in previous LDI-MS experiments. Oligomeric species were detected from *m/z* 200 to 450 with a mass difference pattern of 14 and 16 Da in water-soluble organic matter extracted from filters sampling in Zurich [*Baltensperger et al.*, 2005; *Kalberer et al.*, 2006; *Samburova et al.*, 2005]. In recent chamber studies, Gross et al. [2006] showed the real-time detection of oligomers with a spacing of 14-16 Da from *m/z* -200 to -750 via ATOFMS as photooxidation products of 1,3,5-trimethylbenzene and α-pinene/1,3,5-trimethylbenzene. In that study, off-line LDI-MS showed good overlap of the oligomeric mass spectra acquired with the ATOFMS data after the adjustment of the spectra to make them more directly comparable [*Gross et al.*, 2006]. However, not surprisingly the negative oligomeric ion peaks observed by Gross et al. [2006], while exhibiting similar mass spacings, do not directly match the *m/z* values observed in this study, suggesting that different, or additional, oligomeric precursors are involved.

Of the total unheated particles (162,881 particles) examined by A-ATOFMS on August 12th, 40% (65,238 particles) contained oligomeric species. By classifying particles based on the dominant chemical species present in the mass spectra, an understanding of the mixing state and source(s) of the particles may be gained. Figure 3.2a shows the relative contributions of different particle types observed on August 12th for all unheated particles. By intersecting these particle types with the oligomer-containing particles, oligomers were found to be associated with four general particle types: organic carbon (OC), amine-rich, vanadium (V)-rich, and EC-OC (Figures 3.2b). The amine-rich particle class was dominated by *m/z* 86($(C_2H_5)_2N{=}CH_2^+$); particle phase amines are formed through photooxidation and gas-particle partitioning [*Angelino et al.*, 2001]. V-rich particles, attributed to ship and automobile emissions, were characterized by high intensity ions at *m/z* 51(V^+) and 67(VO^+) with less intense OC and amine ion peaks [*Qin et al.*, 2009]. EC-OC particles were dominated by *m/z* 12(C^+), 24(C_2^+), and 36(C_3^+) with less intense OC and amine ion peaks. Approximately half (41-55%) of the particles categorized within each of these particle types contained oligomers.

The positive and negative mass spectra of a dominant OC oligomer-containing summer unheated particle type are shown in Figure 3.1. The OC particles containing

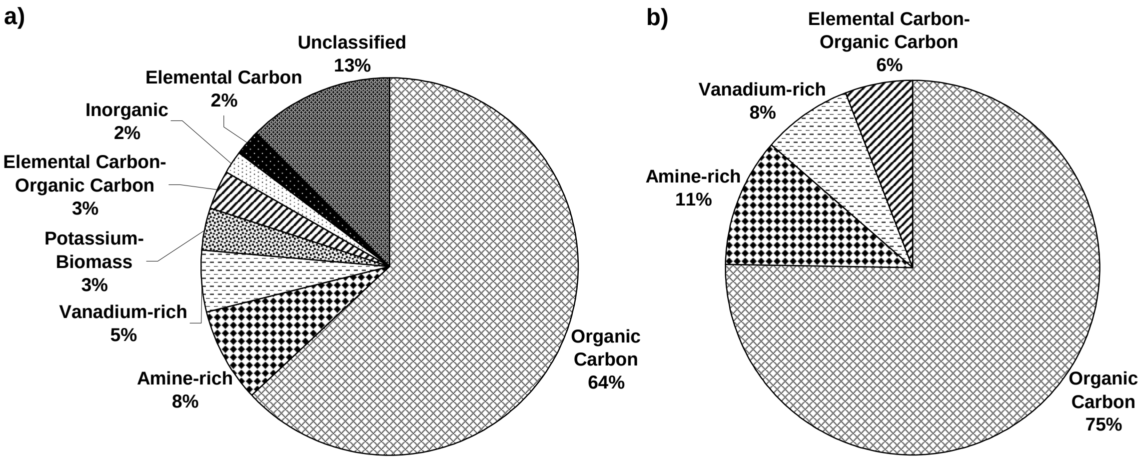

Figure 3.2. Relative contributions of different particle types during the summer for (a) all unheated particles and (b) unheated oligomer-containing particles. Particles not containing the oligomeric pattern are not included in part (b); thus, no "unclassified" particles are shown.

oligomers were dominated by carbonaceous marker ions at *m/z* 27($C_2H_3^+$/CHN^+), 37(C_3H^+), and 43(CH_3CO^+/$CHNO^+$) [*Silva and Prather*, 2000]. The intensity of m/z *43* tracks ozone concentrations and serves as a marker for atmospheric aging and SOA [*Qin et al.*, 2009]. Other prominent positive ions include *m/z* 86, the alkylamine fragment $(C_2H_5)_2N{=}CH_2^+$ [*Angelino et al.*, 2001], and *m/z* 130, an unidentified OC species. OC and amine signatures are present in all of the oligomer-containing particles (Figure 3.3), suggesting the role of SOA formation and gas-particle partitioning, which is also supported by FTICR-MS SOAR high mass results [*Reemtsma et al.*, 2006]. Similar submicrometer OC particles containing amines have been identified by ATOFMS in Riverside previously [*Angelino et al.*, 2001; *Pastor et al.*, 2003b]. Furthermore, for all particle classes, the unheated oligomer-containing particles contain a greater average peak area for *m/z* 43(CH_3CO^+/$CHNO^+$) as compared to the corresponding particles in the same classes that do not contain oligomers, showing that the particles containing oligomers are more heavily oxidized/aged.

The mass spectral features of the negative ions below *m/z* -200 are similar for the four oligomer-containing particles types. These particles contain common peaks at *m/z* -16(O^-), -43(CH_3COH^-), -46(NO_2^-), -62(NO_3^-), -80(SO_3^-), -89($COOHCOO^-$), -97(HSO_4^-), -125($H(NO_3)_2^-$), and -195($H_2SO_4HSO_4^-$). Both laboratory and ambient studies have suggested that oxalic acid (observed as *m/z* -89, $COOHCOO^-$) plays a role in oligomer formation [*Altieri et al.*, 2006; *Gao et al.*, 2004b; *Kalberer et al.*, 2004; *Samburova et al.*, 2005]. All unheated oligomer-containing particles contain secondary nitrate and sulfate acquired during transport across the LA basin [*Appel et al.*, 1978; *Hughes et al.*, 2000; *Khoder*, 2002; *Poschl*, 2005]. During SOAR-1, greater oligomer ion intensities were

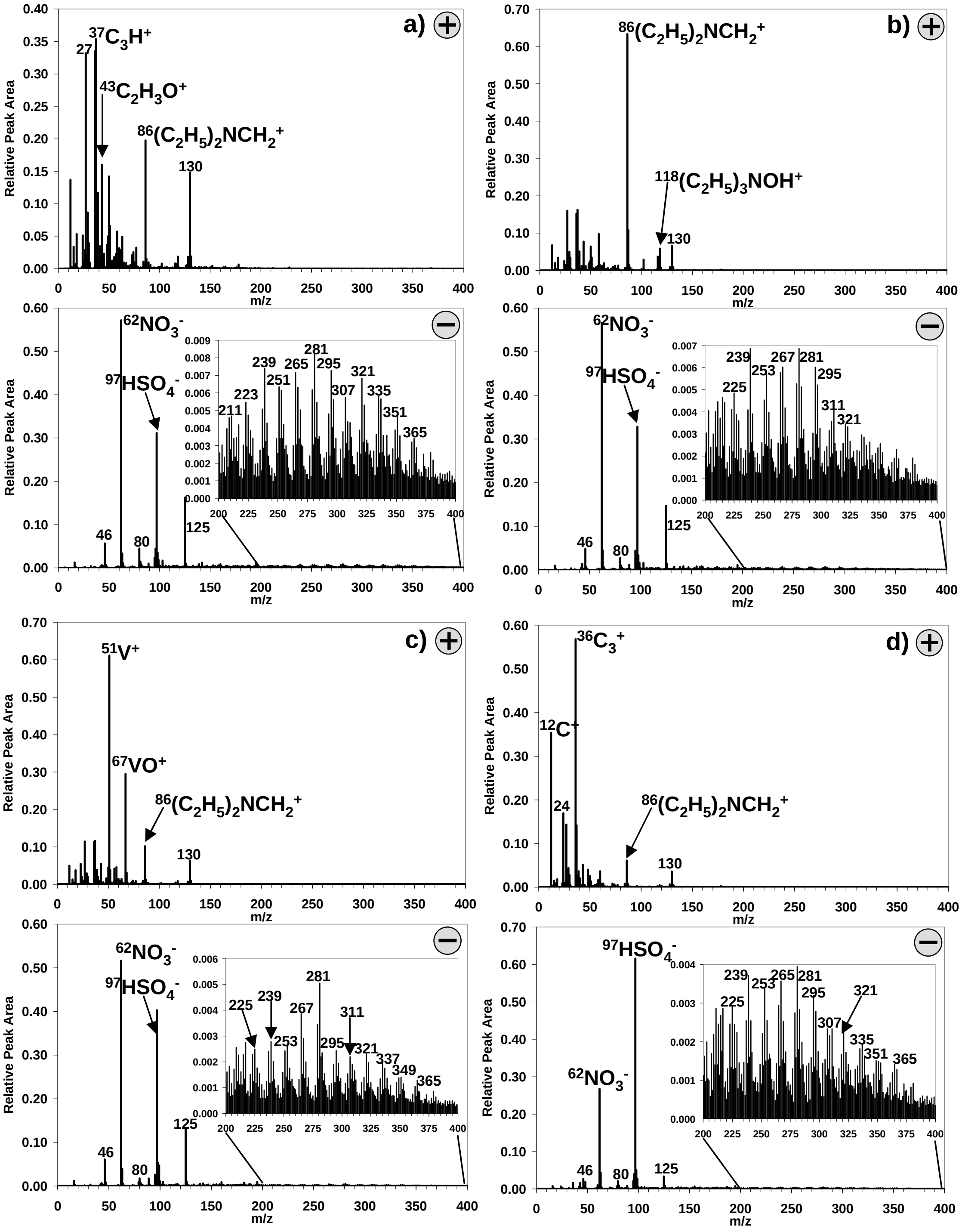

Figure 3.3. Average positive and negative ion mass spectra of the four oligomer-containing summer unheated particle types: (a) OC, (b) amine-rich, (c) V-rich, and (d) EC-OC.

associated with more intense sulfate peaks (*m/z* -97, HSO_4^-) (Figure 3.4). The unheated oligomer-containing particles have a more intense peak at *m/z* -97(HSO_4^-) as compared to the corresponding particles that do not contain oligomers. Furthermore, the oligomer-containing mass spectra have a peak at *m/z* -195, indicating the presence of the sulfuric acid cluster $H_2SO_4HSO_4^-$ [*Murphy and Thomson*, 1995; *Whiteaker and Prather*, 2003], an indicator of particle acidity. In previous laboratory studies, the presence of inorganic acid seed particles, such as sulfuric acid, has been shown to increase SOA production and oligomer formation [*Gao et al.*, 2004b; *Jang et al.*, 2002; *Nozière and Esteve*, 2007]. For the OC and amine-rich particle types, the unheated oligomer-containing spectra also have a larger *m/z* -80(SO_3^-) relative peak area compared to those of the same particle type that do not contain oligomers. The presence of the intense peak at m/z -80 could indicate that organosulfates were present in the oligomeric particles measured in Riverside. Other ambient high mass OC studies have assigned *m/z* -80(SO_3^-) to the fragmentation of organosulfates [*Reemtsma et al.*, 2006; *Romero and Oehme*, 2005]. Furthermore, recent SOA chamber studies suggest that the reaction of carbonyls with acidic aerosol sulfate in the atmosphere can result in organosulfate formation [*Liggio and Li*, 2006; *Surratt et al.*, 2007].

Particle types observed by ATOFMS during SOAR-1 and/or SOAR-2 that did not contain oligomeric species include biomass, V-rich, EC, calcium-EC, ammonium-rich, metals (for example, lead-rich), and inorganic (for example, sodium-rich, calcium-rich, iron-rich), particle types typically associated with primary aerosols [*Poschl*, 2005]. Biomass particles are dominated by m/z 39(K^+) with less intense carbonaceous positive ions, such as *m*/z 27($C_2H_3^+$/CHN^+), 36(C_3^+), and 37(C_3H^+); during SOAR, the negative

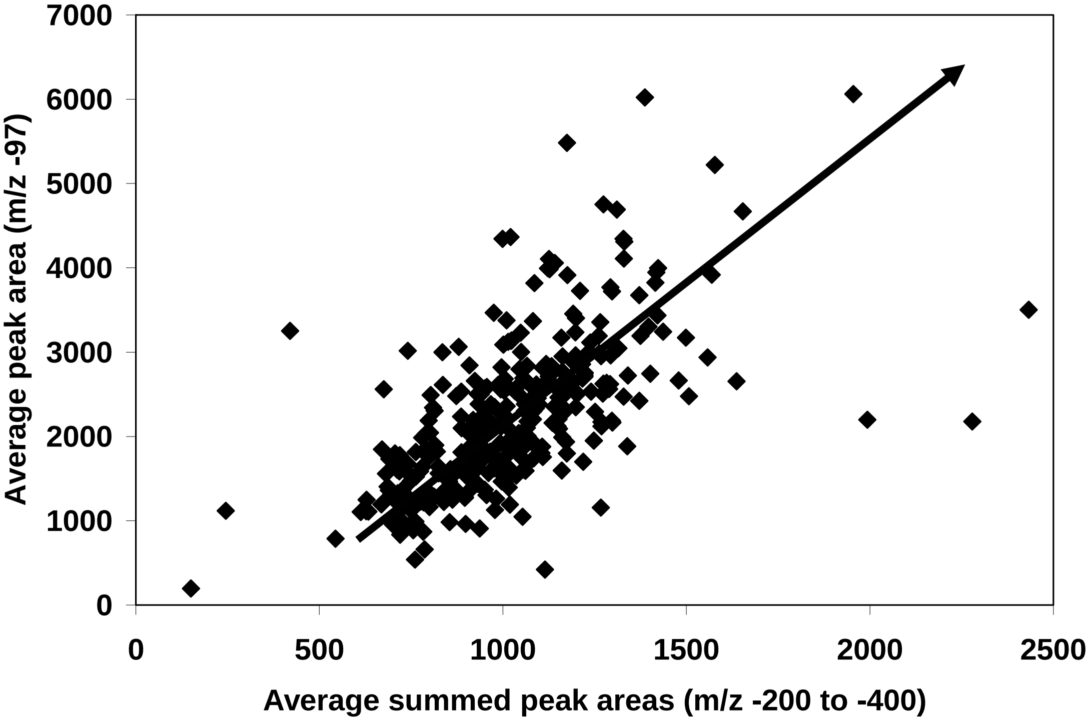

Figure 3.4. Correlation between oligomer intensity (*m/z* -200 to -400) and sulfate intensity (*m/z* -97) for the summer unheated oligomer-containing particles.

ions were dominated by *m*/z -62(NO_3^-), -97(HSO_4^-), and -125($H(NO_3)_2^-$) [*Guazzotti et al.*, 2003; *Silva et al.*, 1999]. In the fall, the V-rich particles have less intense OC and amine ion peaks compared to the summer V-rich particles, indicating less gas-particle partitioning of SOA, which could account for the lack of oligomers in these particles in the fall. The EC particles, typically attributed to vehicle emissions, are characterized by intense carbon cluster positive and negative ions from $C^{+/-}$ to $C_n^{+/-}$ with less intense nitrate (*m*/z -62(NO_3^-)) and sulfate/phosphate (*m*/z -97(HSO_4^-/$H_2PO_4^-$)) markers [*Gross et al.*, 2000; *Guazzotti et al.*, 2001; *Moffet et al.*, 2004; *Pastor et al.*, 2003a]. The mass spectra of the calcium-EC particles are similar to the EC particles with the exception of an intense *m*/z 40(Ca^+) peak than suppresses the positive carbonaceous ions [*Spencer et al.*, 2006]. The ammonium-rich positive mass spectra are dominated by *m*/z 18(NH_4^+) and 30(NO^+) with less intense OC and amine ions; the negative ions are characterized by intense nitrate markers: *m*/z -62(NO_3^-), -125($H(NO_3)_2^-$), and -188(($H_2(NO_3)_3^-$) [*Hughes et al.*, 1999; *Liu et al.*, 2000; *Pastor et al.*, 2003a]. The metals particle type is characterized by particles containing intense ion peaks from metals such as lead (*m*/z 206-208(Pb^+)) or zinc (*m*/z 64, 66, 68(Zn^+)) [*Liu et al.*, 2003]. Finally, the inorganic particle type is characterized by mass spectra with intense peaks due to sodium (*m*/z 23(Na^+)), calcium (*m*/z 40(Ca^+)), and/or iron (*m*/z 54, 56(Fe^+); these spectra are mostly likely from sea-salt and dust particles [*Guazzotti et al.*, 2001; *Silva et al.*, 2000].

3.4.2 Comparison with SOAR-2 (Fall 2005)

Mass spectral signatures of oligomeric species similar to those observed during SOAR-1 (August 12, 2005) were also observed during the subsequent SOAR-2 measurements (November 2-13, 2005) (Figure 3.5). Of the total unheated particles (789,007 particles) examined by ATOFMS during the fall, 33% (256,785 particles) contained oligomeric species. The same major particle types detected during SOAR-1 were also observed during SOAR-2 (Figure 3.6). Although the summer and fall oligomeric species have similar mass spectral patterns and are present in similar particle classes, the mass range of the intense oligomeric ions only extends out to approximately *m/z* -311 in the fall compared to *m/z* -365 in the summer (Figures 3.3 and 3.5), indicating that less particle aging and oligomerization has occurred during the fall. It is also important to note that while the summer and fall oligomers share similar mass spectral signatures, the exact identification of the molecular species of the oligomers is not possible due to mass resolution that is too low.

On the basis of on an in-depth SOAR comparison, particles were found to be less aged in the fall as compared to the summer, most likely due to the reduced ozone concentrations and solar radiation in the fall [*Qin et al.*, 2009]. Importantly, the peak area of m/z 43(CH_3CO^+/$CHNO^+$), a SOA marker, was observed to be lower in the oligomer-containing particles in the fall as compared to the summer. Previous studies show that ambient mass concentrations of ultrafine and fine particles, SOA, and SOA marker compounds are significantly higher in the summer than the winter in the LA basin [*Fine et al.*, 2004; *Pandis et al.*, 1992; *Sardar et al.*, 2005a; *Sardar et al.*, 2005b]. In addition, the contribution of SOA to total organic concentrations is lower during months of lower photochemical activity [*Na et al.*, 2004]. Previously observed high molecular weight acidic organics in Riverside County were suggested to have been formed through photochemical oxidation during the spring and summer [*Hildemann et al.*, 1994]. During

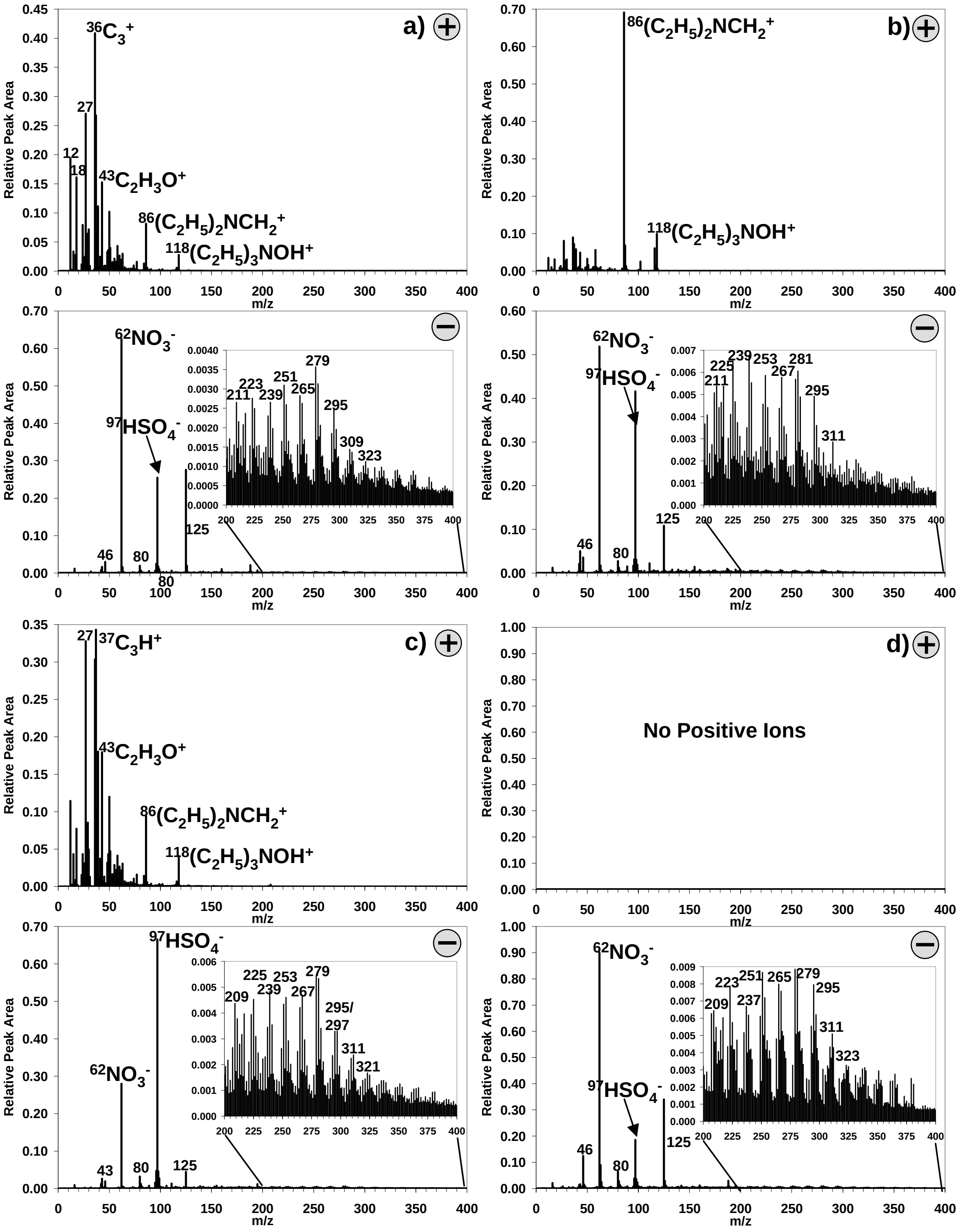

Figure 3.5. Average positive and negative mass spectra of the four oligomer-containing fall unheated particle types: (a) EC-OC, (b) amine-rich, (c) OC, and (d) nitrate-sulfate, which contain only negative ions due to instrumental issues.

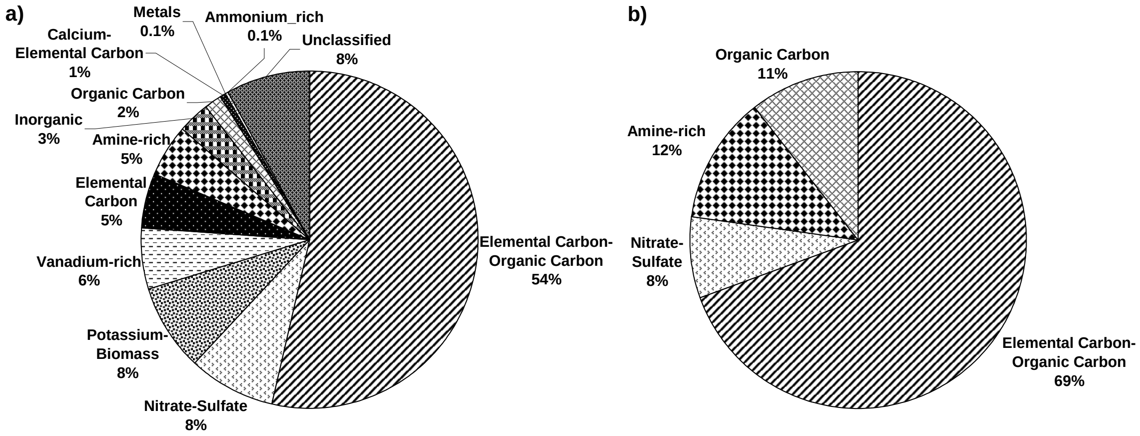

Figure 3.6. Relative contributions of different particle types during the fall for (a) all unheated particles and (b) unheated oligomer-containing particles. Particles not containing the oligomeric pattern are not included in part (b); thus, no "unclassified" particles are shown.

the summer ATOFMS measurements, the ambient temperature ranged from 18 to 31°C with a mean of 23°C compared to 8 to 26°C with a mean of 16°C during the fall measurements. Similarly, ozone concentrations reached as high as 111.2 ppb with a mean of 38.4 ppb for August 12 as compared to an upper limit of 71.8 ppb with a mean of 19.0 ppb for November 2-13. These SOAR-2 results are consistent with a study in Zurich where a more pronounced oligomeric pattern with higher intensities was detected in the summer as compared to the winter; furthermore, in the summer in Zurich, the maximum oligomer molecular weight was correlated with photochemistry and organic acids [*Samburova et al.*, 2005]. Thus, decreased photochemical activity and secondary OC precursor concentrations are also expected to partly account for the decreased degree of oligomerization in the fall.

3.4.3 Aerosol Size Dependence of Oligomer-Containing Mass Spectral Signatures

As shown in Figure 3.7a, for the unheated oligomer-containing particles in the summer, the oligomeric mass spectral pattern increases in intensity, becomes more distinct, and shifts to higher *m/z* values for particles as the particle size decreases from 600 to 140 nm (d_{va}); below 140 nm the oligomeric pattern decreases again, suggesting that lower concentrations of oligomer precursors. From 600 to 1000 nm, the oligomeric pattern is relatively constant (not shown). In contrast, for the oligomer-containing particles in the fall, the oligomeric mass spectral pattern becomes less apparent with decreasing particle size (Figure 3.7b). This can be explained by the ion balance of the major cations and anions, which gives an indication of the acidity of the oligomer-containing particles at different particle sizes for the two seasons. The major cations and

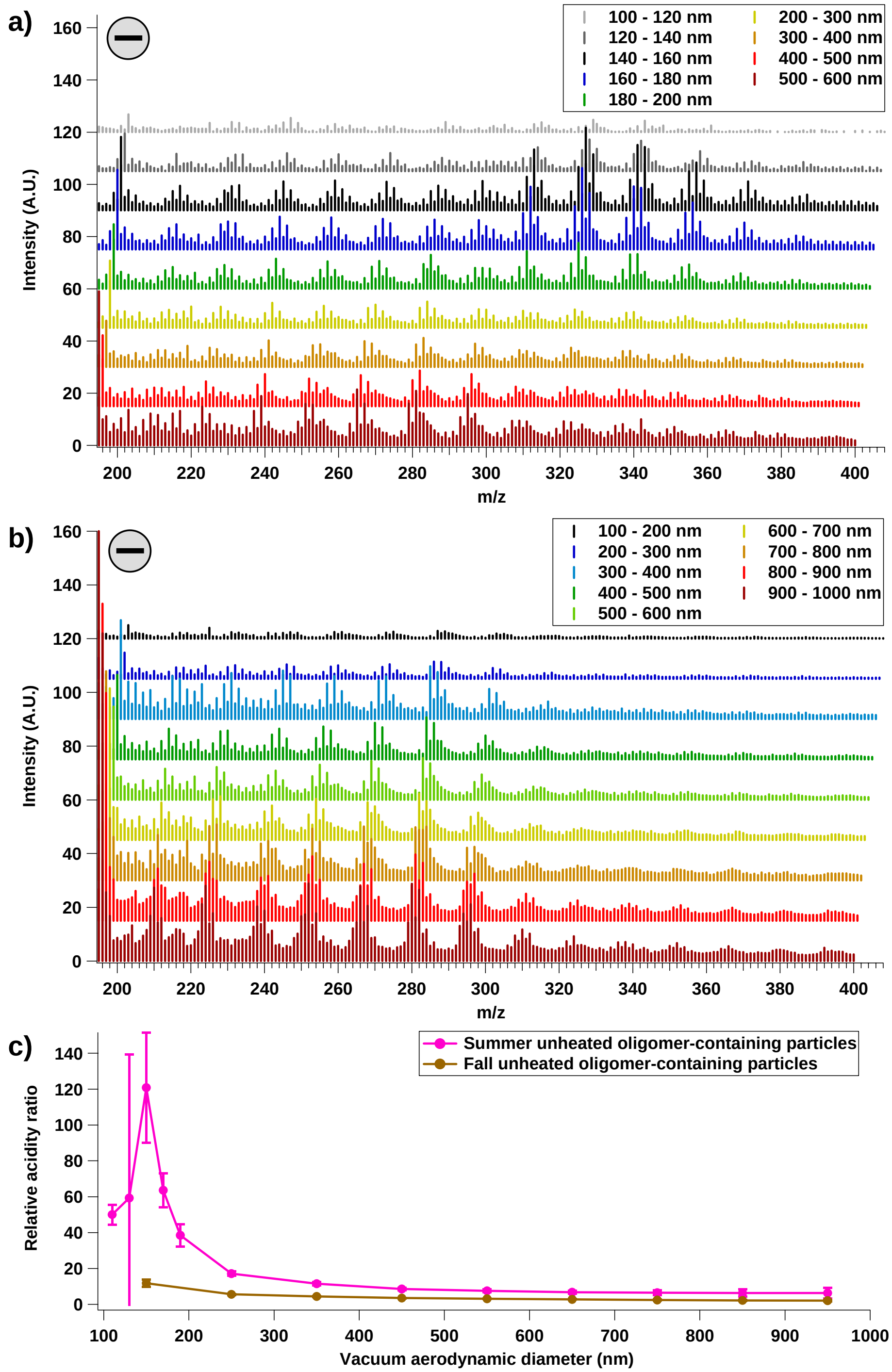

Figure 3.7. Waterfall plots showing the average high mass negative ion mass spectral patterns for the (a) summer and (b) fall unheated oligomer-containing particles within different submicrometer particle size bins. Intensity is reported in arbitrary units (A.U.). (c) Relative acidity ratio, defined as the sum of the absolute average peak areas of nitrate (*m/z* -62(NO_3^-)) and sulfate (m/z -97(HSO_4^-)) divided by ammonium (*m/z* 18(NH_4^+)), as a function of vacuum aerodynamic diameter (nm) for the unheated oligomer-containing particles.

anions detected in Riverside are ammonium, nitrate, and sulfate (Figure 3.1). The relative acidity ratio is defined as the sum of the absolute average peak areas of nitrate (*m/z* -62(NO_3^-)) and sulfate (*m/z* -97(HSO_4^-)) divided by the ammonium ion signal intensity (*m/z* 18(NH_4^+)). The dependence of this ratio on particle size is shown in Figure 3.7c for the unheated oligomer-containing particles. The average peak areas used to calculate these ratios, as well as the OC/EC ion ratios, with respect to particle size are shown in Figure 3.8. As shown in Figure 3.7c, the relative acidity ratio peaks in the summer for the 140-160 nm unheated oligomer-containing particles, the size range that corresponds to the maximum oligomer peak intensities. This indicates that during the summer there is not as much ammonium in the smaller particles to balance the acidity of the sulfate and nitrate species. Furthermore, the relative acidity ratio is similar and becomes constant for both seasons for particles greater than 400 nm in diameter.

As shown in Figures 3.7c and 3.8, the relative acidity ratio, and hence acidity maximum, in the smaller summer particles corresponds to a maximum in the sulfate average peak area, as well as minima in the ammonium and nitrate ion peak areas. Since sulfate peak area increases with decreasing particle size in the summer, this suggests that sulfate formation due to gas-particle partitioning occurs in the smaller submicrometer particles [*Bassett and Seinfeld*, 1984; *Hering and Friedlander*, 1982]. It is expected that the combination of high relative humidity (ranging from 36.9-92.8% with a mean of 68.6%) combined with high levels of sulfate, particularly in the smallest particle sizes, facilitated the formation of more acidic particles in the summer. Previous studies of the eastern LA basin have shown strong acid associated with a 170-250 nm sulfate mode, as well as relatively small amounts of nitrate below 300 nm with submicrometer nitrate

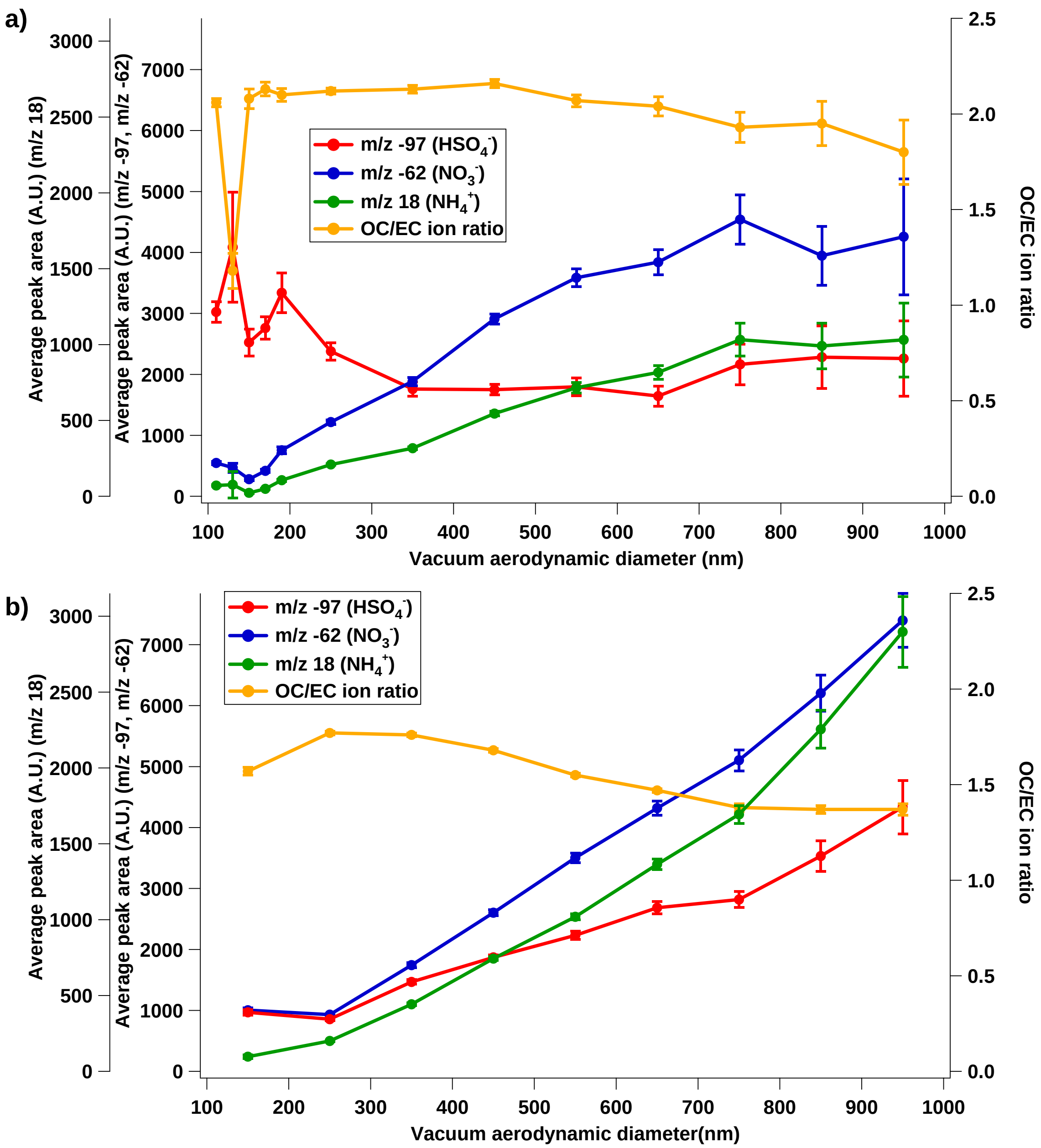

Figure 3.8. OC/EC ion ratios and average peak areas of *m*/*z* 18(NH_4^+), -62(NO_3^-), and -97(HSO_4^-) versus vacuum aerodynamic diameter (nm) for the (a) summer and (b) fall unheated oligomer-containing particles. The OC/EC ion ratio, calculated using the method by Spencer and Prather [2006], is relatively constant versus particle diameter (d_{va}), showing that these oligomer-containing particles possess relatively similar amounts of OC with respect to EC; when all particles, including those not containing oligomers, were considered in considered in the calculation of the OC/EC ion ratio, the OC/EC ion ratio decreased for particles less than 200 nm in diameter, as shown by Spencer and Prather [2006].

correlated with ammonium [*Wall et al.*, 1988]. Similarly, in a recent study in Pittsburgh, PA, Zhang et al. [2007] found that concentrations of ammonium were inadequate to neutralize accumulation mode sulfate, leading to acidic particles, and more acidic time periods were associated with higher SOA mass concentrations.

Furthermore, for the unheated, oligomer-containing particles, the nitrate and ammonium peak areas are correlated and increase with respect to particle size, suggesting the presence of ammonium nitrate, which dilutes the oligomeric precursors and inhibits oligomer formation, particularly at larger submicrometer particle sizes. Bassett and Seinfeld [1983] predicted that if the concentration of ammonia is greater than twice the concentration of sulfate, then ammonia fully neutralizes the sulfate, resulting in particle phase ammonium nitrate and ammonium sulfate. Previous work has shown that ammonium nitrate can contribute more than half of the fine aerosol mass in the LA basin, particularly in the winter due to lower inversion heights and temperatures [*Christoforou et al.*, 2000]. On the basis of chamber studies, Kalberer et al. predicted that oligomerization rates in the atmosphere would be reduced for multicomponent aerosols due to high concentrations of non-oligomerizing components [*Kalberer et al.*, 2004; *Paulsen et al.*, 2006]. Further, the less pronounced oligomeric pattern at larger sizes was predicted for oligomers in the ambient atmosphere as compared to chamber reaction products due to the larger number of potentially oligomerizing reactants in the atmosphere [*Kalberer et al.*, 2006].

2.4.4. Temperature Dependence of Oligomer-Containing Mass Spectral Signatures

In the summer, the oligomeric mass spectral pattern increases in intensity, becomes more distinct, and shifts to higher masses with TD heating of the ambient particles to 200°C (Figure 3.9a). In fact, for the 180-200 nm oligomer-containing particles, the average peak area of *m/z* -321 increases by a factor of 5 with heating to 200°C. These results have potential implications for aerosol techniques that rely on thermal analysis, such as gas chromatography-mass spectrometry (GC/MS), which could be accelerating the formation of oligomeric species during the analysis step.

To examine the loss of semivolatile species with heating, the summer unheated oligomer-containing average mass spectra was compared to the 200°C heated oligomer-containing average mass spectra for the summer measurements. In particular, the intensities of ammonium (*m*/*z* 18(NH_4^+)), amines (*m*/*z* 58($C_2H_5NH{=}CH_2^+$), 86($(C_2H_5)_2N{=}CH_2^+$), 102($(C_2H_5)_3NH^+$), 118($(C_2H_5)_3NOH^+$)), nitrate (*m*/*z* 30($NO^+/CH_2{=}NH_2^+$), -46(NO_2^-), -62(NO_3^-), -125($H(NO_3)_2^-$)), and unidentified OC markers (*m*/*z* 116, 117) were observed to decreased with heating. For the summer oligomer-containing particles, Figure 3.10a shows the decrease in average peak area of nitrate with increasing temperature, as well as the increase in sulfate intensity with increasing temperature. In the fall, nitrate peak area also decreases with heating for the oligomer-containing particles (Figure 3.10b). Due to the loss of nitrate, more electrons are available in the LDI plume to attach to the sulfate and form ions, leading to the increase in sulfate intensity.

In the summer, as shown in Figure 3.9c, the highest TD temperatures corresponds to the highest relative acidity ratio, suggesting an overall increase in the particle acidity

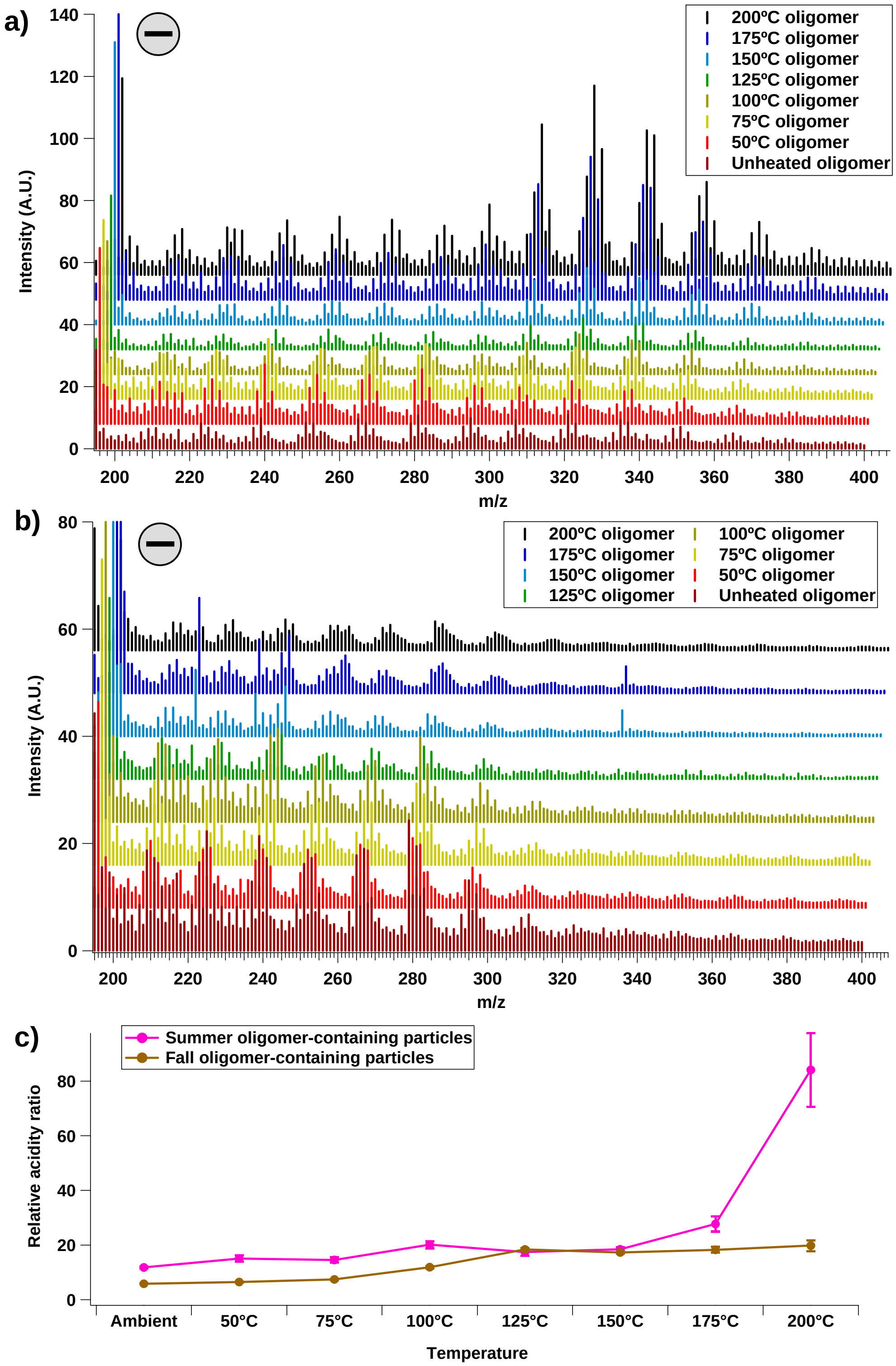

Figure 3.9. Waterfall plots showing the average high mass negative ion mass spectral patterns for the (a) summer and (b) fall oligomer-containing particles heated to varying temperatures. (c) Relative acidity ratio as a function of TD temperature for the oligomer-containing particles.

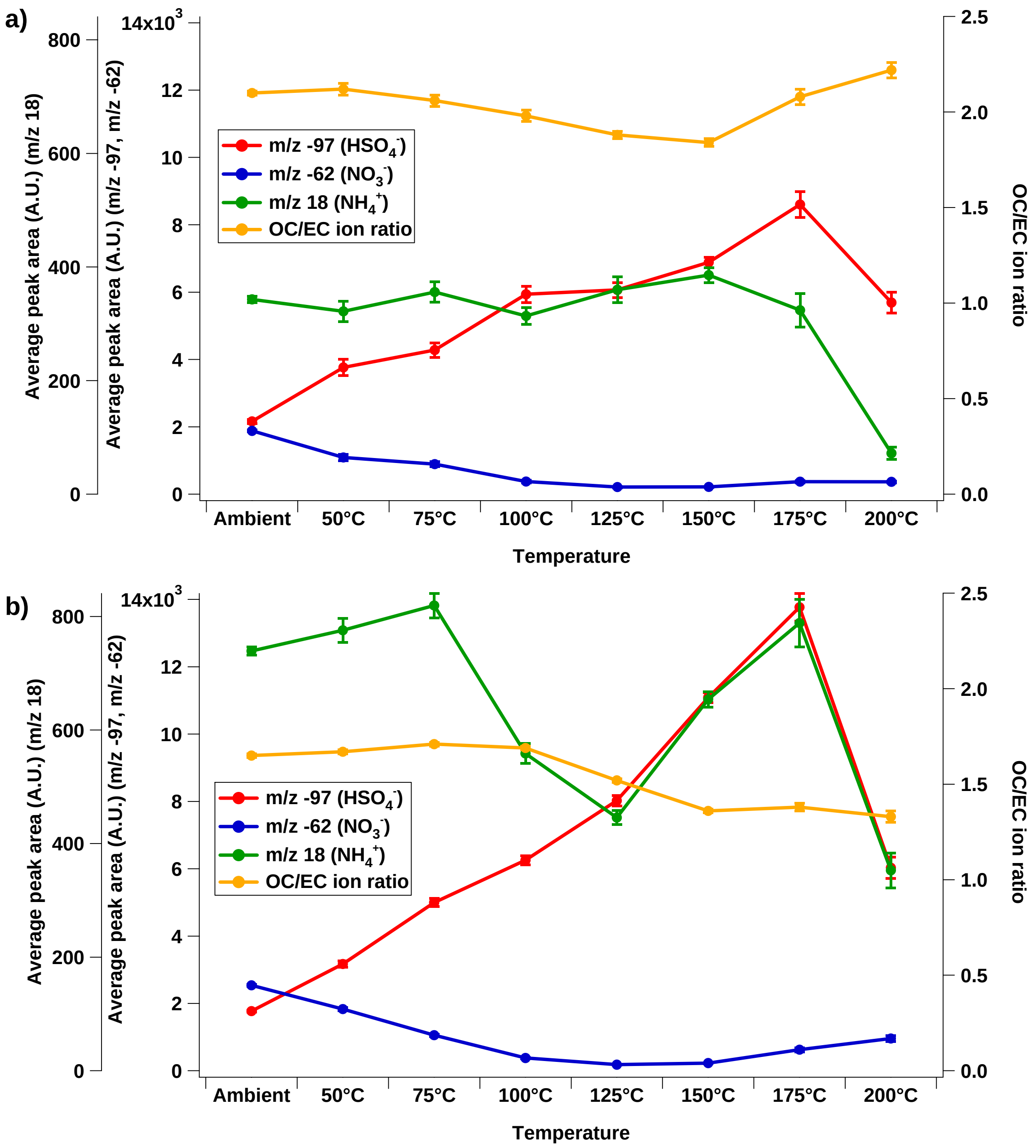

Figure 3.10. OC/EC ion ratios and average peak areas of *m*/*z* 18(NH_4^+), -62(NO_3^-), and -97(HSO_4^-) versus TD temperature for the (a) summer and (b) fall oligomer-containing particles.

due to the volatilization of ammonium nitrate. The higher acidity then serves to catalyze oligomer formation. In contrast, in the fall the oligomeric mass difference pattern decreased with increasing temperature (Figure 3.9b). Correspondingly, no increase in the relative acidity ratio was observed at the highest temperature (Figure 3.9c). The significant loss of ammonium nitrate from 75-125°C (Figure 3.10b), observed during the fall, was not detected during heating of the summer aerosol because most of the ammonium nitrate was partitioned to the gas phase during the higher summer daytime ambient temperatures. The removal of the ammonium nitrate serves to increase the fall relative acidity ratio to its average summer value; however, the increasing TD temperature above 125°C does not increase the fall relative acidity ratio further at higher temperatures, unlike in the summer. In both seasons, a decrease in the sulfate peak area from 175-200°C is correlated with the decrease in ammonium, suggesting the loss of ammonium sulfate (Figures 3.8 and 3.10). Therefore, the increased concentration of ammonium nitrate and decreased particle acidity in the fall accounts for the deviation in behavior of the fall oligomer-containing particles as compared to the patterns observed for the summer oligomer-containing particles.

Therefore, evolution of the oligomeric species with heating in the summer is likely due to two factors: (i) the additional heat from the TD accelerates the kinetics of the formation of the oligomeric species, and (ii) the particle matrix changes as the semivolatile species are removed with heating, leading to a more concentrated, acidic seed that catalyzes oligomer formation. Chamber studies have shown that the molecular size distribution of SOA oligomers shifts to higher masses with increasing time [*Gross et al.*, 2006; *Kalberer et al.*, 2004; *Kalberer et al.*, 2006]. Furthermore, Nozière and Esteve

[2007] recently found that the kinetically limiting step in the formation of the light-absorbing oligomer products of the aldol condensation of acetaldehyde was the addition of each single monomer on an increasingly large molecule; the rate of increase of the absorption index was also found to increase with both acidity and temperature [*Nozière and Esteve*, 2007]. These results suggest that the mass range of the oligomeric species may increase further with additional aging.

Overall, secondary organic precursors, photochemical activity, and particle acidity appear to collectively be playing a role in oligomer formation and the degree of oligomerization. The presence of secondary OC, amines, nitrate, and sulfate in the mass spectra of the oligomer-containing particles is indicative of the aged nature of these particles. A large fraction of the particles detected with the ATOFMS contained oligomers (40%, summer; 33%, fall), suggesting the importance of these species in highly aged environments. Overall, the highest degree of oligomerization was associated with the most acidic particles. The highest degree of oligomerization depended on the following conditions:

- Season: More oligomers were detected in the summer when the aerosol was more photochemically aged and contained a higher amount of sulfate.
- Size/Acidity: The highest degree of oligomerization was detected in smaller accumulation mode particles (140-200 nm) in the summer.
- Temperature: Additional oligomerization occurred at the highest thermodenuder temperatures (175-200°C) in the summer.

In the summer, heat from the thermodenuder, operated between 50°C and 200°C, drove off semivolatile species, increased particle acidity, concentrated oligomeric precursors, and accelerated oligomerization. Differences in oligomer behavior between the summer and fall with respect to particle size and heating are likely due to increased ammonium concentrations, resulting in decreased particle acidity in the fall, and a lower abundance in the fall of secondary organic aerosol, which serve as the precursors of the oligomeric products.

3.5 Acknowledgments

This work was supported by the National Science Foundation (NSF ATM-0321362) and the California Air Resources Board (CARB 04-336). Ryan Moffet and John Holecek helped with SOAR-1 A-ATOFMS data collection, assisted in initial data analysis, and contributed to discussions of the data. Thomas Rebotier developed the square-wave filter to identify the oligomer-containing particles and the automated script to identify the different temperature TD periods. Paul Ziemann (University of California, Riverside), Ken Docherty (University of Colorado, Boulder), and the UC-Riverside Air Pollution Research Center provided support and assistance during the SOAR field campaign, and Alex Huffman and Jose Jimenez (University of Colorado, Boulder) provided and ran the TD system, which was developed under EPA sponsorship (STAR R831080). I also wish to thank the entire Prather Group, particularly Laura Shields, Xueying Qin, and Stephen Toner, support through the SOAR campaigns, as well as Gary Poon for assistance with SOAR-1 A-ATOFMS data collection. Megan McKay and the Goldstein group (University of California, Berkeley) provided ambient temperature and relative humidity data; ozone data was provided by Laura Shields, Xueying Qin, and Stephen Toner. Rainer Volkamer contributed to discussions of the data.

Publication Acknowledgment

Chapter 3 has been reproduced with permission from the American Chemical Society: Denkenberger, K.A., Moffet, R.C., Holecek, J.C., Rebotier, T.P., Prather, K.A. Real-time, single-particle measurements of oligomers in aged ambient aerosol particles. *Environmental Science & Technology*. 2007, 41, 5439-5446.

3.6 References

Allen, J.O. (2001), YAADA: software toolkit to analyze single-particle mass spectral data, *Software reference manual.*

Altieri, K.E., A.G. Carlton, H.J. Lim, B.J. Turpin, and S.P. Seitzinger (2006), Evidence for oligomer formation in clouds: Reactions of isoprene oxidation products, *Environ. Sci. Technol.*, *40*(16), 4956-4960.

Andreae, M.O., and A. Gelencser (2006), Black carbon or brown carbon? The nature of light-absorbing carbonaceous aerosols, *Atmos. Chem. Phys.*, *6*(3131-3148.

Angelino, S., D.T. Suess, and K.A. Prather (2001), Formation of aerosol particles from reactions of secondary and tertiary alkylamines: Characterization by aerosol time-of-flight mass spectrometry, *Environ. Sci. Technol.*, *35*(15), 3130-3138.

Appel, B.R., E.L. Kothny, E.M. Hoffer, G.M. Hidy, and J.J. Wesolowski (1978), Sulfate and nitrate data from California Aerosol Characterization Experiment (ACHEX), *Environ. Sci. Technol.*, *12*(4), 418-425.

Baltensperger, U., M. Kalberer, J. Dommen, D. Paulsen, M.R. Alfarra, H. Coe, R. Fisseha, A. Gascho, M. Gysel, S. Nyeki, M. Sax, M. Steinbacher, A.S.H. Prevot, S. Sjoren, E. Weingartner, and R. Zenobi (2005), Secondary organic aerosols from anthropogenic and biogenic precursors, *Faraday Discuss.*, *130*(265-278.

Bassett, M., and J.H. Seinfeld (1983), Atmospheric Equilibrium-Model Of Sulfate And Nitrate Aerosols, *Atmos. Environ.*, *17*(11), 2237-2252.

Bassett, M.E., and J.H. Seinfeld (1984), Atmospheric Equilibrium-Model Of Sulfate And Nitrate Aerosols.2. Particle-Size Analysis, *Atmos. Environ.*, *18*(6), 1163-1170.

Christoforou, C.S., L.G. Salmon, M.P. Hannigan, P.A. Solomon, and G.R. Cass (2000), Trends in fine particle concentration and chemical composition in Southern California, *J. Air Waste Manage. Assoc.*, *50*(1), 43-53.

DeCarlo, P.F., J.G. Slowik, D.R. Worsnop, P. Davidovits, and J.L. Jimenez (2004), Particle morphology and density characterization by combined mobility and aerodynamic diameter measurements. Part 1: Theory, *Aerosol Sci. Technol.*, *38*(12), 1185-1205.

Fine, P.M., B. Chakrabarti, M. Krudysz, J.J. Schauer, and C. Sioutas (2004), Diurnal variations of individual organic compound constituents of ultrafine and accumulation mode particulate matter in the Los Angeles basin, *Environ. Sci. Technol.*, *38*(5), 1296-1304.

Gao, S., M. Keywood, N.L. Ng, J. Surratt, V. Varutbangkul, R. Bahreini, R.C. Flagan, and J.H. Seinfeld (2004a), Low-molecular-weight and oligomeric components in secondary organic aerosol from the ozonolysis of cycloalkenes and alpha-pinene, *J. Phys. Chem. A*, *108*(46), 10147-10164.

Gao, S., N.L. Ng, M. Keywood, V. Varutbangkul, R. Bahreini, A. Nenes, J.W. He, K.Y. Yoo, J.L. Beauchamp, R.P. Hodyss, R.C. Flagan, and J.H. Seinfeld (2004b), Particle phase acidity and oligomer formation in secondary organic aerosol, *Environ. Sci. Technol.*, *38*(24), 6582-6589.

Gross, D.S., M.E. Gälli, M. Kalberer, A.S.H. Prevot, J. Dommen, M.R. Alfarra, J. Duplissy, K. Gaeggeler, A. Gascho, A. Metzger, and U. Baltensperger (2006), Real time measurement of oligomeric species in secondary organic aerosol with the aerosol time-of-flight mass spectrometer, *Anal. Chem.*, *78*(7), 2130-2137.

Gross, D.S., M.E. Galli, P.J. Silva, S.H. Wood, D.Y. Liu, and K.A. Prather (2000), Single particle characterization of automobile and diesel truck emissions in the Caldecott Tunnel, *Aerosol Sci. Technol.*, *32*(2), 152-163.

Guazzotti, S.A., K.R. Coffee, and K.A. Prather (2001), Continuous measurements of size-resolved particle chemistry during INDOEX-Intensive Field Phase 99, *J. Geophys. Res.*, *106*(D22), 28607-28627.

Guazzotti, S.A., D.T. Suess, K.R. Coffee, P.K. Quinn, T.S. Bates, A. Wisthaler, A. Hansel, W.P. Ball, R.R. Dickerson, C. Neususs, P.J. Crutzen, and K.A. Prather (2003), Characterization of carbonaceous aerosols outflow from India and Arabia: Biomass/biofuel burning and fossil fuel combustion, *J. Geophys. Res.*, *108*(D15).

Haagen-Smit, A.J. (1952), Chemistry and physiology of Los Angeles smog, *Ind. Eng. Chem.*, *44*(6), 1342-1346.

Hering, S.V., and S.K. Friedlander (1982), Origins Of Aerosol Sulfur Size Distributions In The Los-Angeles Basin, *Atmos. Environ.*, *16*(11), 2647-2656.

Hildemann, L.M., M.A. Mazurek, G.R. Cass, and B.R.T. Simoneit (1994), Seasonal trends in Los-Angeles ambient organic aerosol observed by high-resolution gas-chromatography, *Aerosol Sci. Technol.*, *20*(4), 303-317.

Huffman, J.A., P.J. Ziemann, J.T. Jayne, D.R. Worsnop, and J.L. Jimenez (2008), Development and characterization of a fast-stepping/scanning thermodenuder for chemically-resolved aerosol volatility measurements, *Aerosol Sci. Technol.*, *42*(5), 395-407.

Hughes, L.S., J.O. Allen, P. Bhave, M.J. Kleeman, G.R. Cass, D.Y. Liu, D.F. Fergenson, B.D. Morrical, and K.A. Prather (2000), Evolution of atmospheric particles along trajectories crossing the Los Angeles basin, *Environ. Sci. Technol.*, *34*(15), 3058-3068.

Hughes, L.S., J.O. Allen, M.J. Kleeman, R.J. Johnson, G.R. Cass, D.S. Gross, E.E. Gard, M.E. Galli, B.D. Morrical, D.P. Fergenson, T. Dienes, C.A. Noble, P.J. Silva, and K.A. Prather (1999), Size and composition distribution of atmospheric particles in southern California, *Environ. Sci. Technol.*, *33*(20), 3506-3515.

Jang, M., and R.M. Kamens (2001), Atmospheric secondary aerosol formation by heterogeneous reactions of aldehydes in the presence of a sulfuric acid aerosol catalyst, *Environ. Sci. Technol.*, *35*(24), 4758-4766.

Jang, M.S., N.M. Czoschke, S. Lee, and R.M. Kamens (2002), Heterogeneous atmospheric aerosol production by acid-catalyzed particle-phase reactions, *Science*, *298*(5594), 814-817.

Kalberer, M., D. Paulsen, M. Sax, M. Steinbacher, J. Dommen, A.S.H. Prevot, R. Fisseha, E. Weingartner, V. Frankevich, R. Zenobi, and U. Baltensperger (2004), Identification of polymers as major components of atmospheric organic aerosols, *Science*, *303*(5664), 1659-1662.

Kalberer, M., M. Sax, and V. Samburova (2006), Molecular size evolution of oligomers in organic aerosols collected in urban atmospheres and generated in a smog chamber, *Environ. Sci. Technol.*, *40*(19), 5917-5922.

Kanakidou, M., J.H. Seinfeld, S.N. Pandis, I. Barnes, F.J. Dentener, M.C. Facchini, R. Van Dingenen, B. Ervens, A. Nenes, C.J. Nielsen, E. Swietlicki, J.P. Putaud, Y. Balkanski, S. Fuzzi, J. Horth, G.K. Moortgat, R. Winterhalter, C.E.L. Myhre, K. Tsigaridis, E. Vignati, E.G. Stephanou, and J. Wilson (2005), Organic aerosol and global climate modelling: a review, *Atmos. Chem. Phys.*, *5*,(1053-1123.

Khoder, M.I. (2002), Atmospheric conversion of sulfur dioxide to particulate sulfate and nitrogen dioxide to particulate nitrate and gaseous nitric acid in an urban area, *Chemosphere*, *49*(6), 675-684.

Kiss, G., E. Tombacz, B. Varga, T. Alsberg, and L. Persson (2003), Estimation of the average molecular weight of humic-like substances isolated from fine atmospheric aerosol, *Atmos. Environ.*, *37*(27), 3783-3794.

Liggio, J., and S.M. Li (2006), Organosulfate formation during the uptake of pinonaldehyde on acidic sulfate aerosols, *Geophys. Res. Lett.*, *33*(13).

Liu, D.Y., K.A. Prather, and S.V. Hering (2000), Variations in the size and chemical composition of nitrate-containing particles in Riverside, CA, *Aerosol Sci. Technol.*, *33*(1-2), 71-86.

Liu, D.Y., R.J. Wenzel, and K.A. Prather (2003), Aerosol time-of-flight mass spectrometry during the Atlanta Supersite Experiment: 1. Measurements, *J. Geophys. Res.*, *108*(D7).

Moffet, R.C., L.G. Shields, J. Bernsten, R.B. Devlin, and K.A. Prather (2004), Characterization of an ambient coarse particle concentrator used for human exposure studies: Aerosol size distributions, chemical composition, and concentration enrichment, *Aerosol Sci. Technol.*, *38*(11), 1123-1137.

Murphy, D.M., and D.S. Thomson (1995), Laser ionization mass spectroscopy of single aerosol particles, *Aerosol Sci. Technol.*, *22*(3), 237-249.

Na, K.S., A.A. Sawant, C. Song, and D.R. Cocker (2004), Primary and secondary carbonaceous species in the atmosphere of Western Riverside County, California, *Atmos. Environ.*, *38*(9), 1345-1355.

Nozière, B., and W. Esteve (2007), Light-absorbing aldol condensation products in acidic aerosols: Spectra, kinetics, and contribution to the absorption index, *Atmos. Environ.*, *41*(1150-1163.

Pandis, S.N., R.A. Harley, G.R. Cass, and J.H. Seinfeld (1992), Secondary organic aerosol formation and transport, *Atmos. Environ.*, *26*(13), 2269-2282.

Pastor, S.H., J.O. Allen, L.S. Hughes, P. Bhave, G.R. Cass, and K.A. Prather (2003a), Ambient single particle analysis in Riverside, California by aerosol time-of-flight mass spectrometry during the SCOS97-NARSTO, *Atmos. Environ.*, *37*,(S239-S258.

Pastor, S.H., J.O. Allen, L.S. Hughes, P. Bhave, G.R. Cass, and K.A. Prather (2003b), Ambient single particle analysis in Riverside, California by aerosol time-of-flight mass spectrometry during the SCOS97-NARSTO, *Atmos. Environ.*, *37*(S239-S258.

Paulsen, D., E. Weingartner, M.R. Alfarra, and U. Baltensperger (2006), Volatility measurements of photochemically and nebulizer-generated organic aerosol particles, *J. Aerosol Sci.*, *37*(9), 1025-1051.

Poschl, U. (2005), Atmospheric aerosols: Composition, transformation, climate and health effects, *Angewandte Chemie-International Edition*, *44*(46), 7520-7540.

Qin, X., L.G. Shields, S.M. Toner, K.A. Pratt, and K.A. Prather (2009), Seasonal comparisons of the single particle mixing state in Riverside, CA during the SOAR 2005 campaign, *Aerosol Sci. Technol.*, *In preparation.*(

Qin, X.Y., P.V. Bhave, and K.A. Prather (2006), Comparison of two methods for obtaining quantitative mass concentrations from aerosol time-of-flight mass spectrometry measurements, *Anal. Chem.*, *78*(17), 6169-6178.

Reemtsma, T., A. These, P. Venkatachari, X. Xia, P. Hopke, A. Springer, and M. Linscheid (2006), Identification of fulvic acids and sulfated and nitrated analogues in atmospheric aerosol by electrospray ionization Fourier transform ion cyclotron resonance mass spectrometry, *Anal. Chem.*, *78*(24), 8299-8304.

Reinhardt, A., C. Emmenegger, B. Gerrits, C. Panse, J. Dommen, U. Baltensperger, R. Zenobi, and M. Kalberer (2007), Ultrahigh mass resolution and accurate mass measurements as a tool to characterize oligomers in secondary organic aerosols, *Anal. Chem.*, *79*(11), 4074-4082.

Romero, F., and M. Oehme (2005), Organosulfates - A new component of humic-like substances in atmospheric aerosols? *J. Atmos. Chem.*, *52*(3), 283-294.

Samburova, V., S. Szidat, C. Hueglin, R. Fisseha, U. Baltensperger, R. Zenobi, and M. Kalberer (2005), Seasonal variation of high-molecular-weight compounds in the water-soluble fraction of organic urban aerosols, *J. Geophys. Res.*, *110*(D23).

Sardar, S.B., P.M. Fine, P.R. Mayo, and C. Sioutas (2005a), Size-fractionated measurements of ambient ultrafine particle chemical composition in Los Angeles using the NanoMOUDI, *Environ. Sci. Technol.*, *39*(4), 932-944.

Sardar, S.B., P.M. Fine, and C. Sioutas (2005b), Seasonal and spatial variability of the size-resolved chemical composition of particulate matter (PM10) in the Los Angeles Basin, *J. Geophys. Res.*, *110*(D7).

Silva, P.J., R.A. Carlin, and K.A. Prather (2000), Single particle analysis of suspended soil dust from Southern California, *Atmos. Environ.*, *34*(11), 1811-1820.

Silva, P.J., D.Y. Liu, C.A. Noble, and K.A. Prather (1999), Size and chemical characterization of individual particles resulting from biomass burning of local Southern California species, *Environ. Sci. Technol.*, *33*(18), 3068-3076.

Silva, P.J., and K.A. Prather (2000), Interpretation of mass spectra from organic compounds in aerosol time-of-flight mass spectrometry, *Anal. Chem.*, *72*(15), 3553-3562.

Song, X.H., P.K. Hopke, D.P. Fergenson, and K.A. Prather (1999), Classification of single particles analyzed by ATOFMS using an artificial neural network, ART-2A, *Anal. Chem.*, *71*(4), 860-865.

Spencer, M.T., and K.A. Prather (2006), Using ATOFMS to determine OC/EC mass fractions in particles, *Aerosol Sci. Technol.*, *40*(8), 585-594.

Spencer, M.T., L.G. Shields, D.A. Sodeman, S.M. Toner, and K.A. Prather (2006), Comparison of oil and fuel particle chemical signatures with particle emissions from heavy and light duty vehicles, *Atmos. Environ.*, *40*(27), 5224-5235.

Streibel, T., J.C. Weh, and S. Mitschke (2006), Thermal desorption/pyrolysis coupled with photoionization time-of-flight mass spectrometry for the analysis of molecular organic compounds and oligomeric and polymeric fractions in urban particulate matter, *Anal. Chem.*, *78*(15), 5354-5361.

Su, Y.X., M.F. Sipin, H. Furutani, and K.A. Prather (2004), Development and characterization of an aerosol time-of-flight mass spectrometer with increased detection efficiency, *Anal. Chem.*, *76*(3), 712-719.

Surratt, J.D., J.H. Kroll, T.E. Kleindienst, E.O. Edney, M. Claeys, A. Sorooshian, N.L. Ng, J.H. Offenberg, M. Lewandowski, M. Jaoui, R.C. Flagan, and J.H. Seinfeld (2007), Evidence for organosulfates in secondary organic aerosol, *Environ. Sci. Technol.*, *41*(2), 517-527.

Tolocka, M.P., M. Jang, J.M. Ginter, F.J. Cox, R.M. Kamens, and M.V. Johnston (2004), Formation of oligomers in secondary organic aerosol, *Environ. Sci. Technol.*, *38*(5), 1428-1434.

Turpin, B.J., and J.J. Huntzicker (1995), Identification of secondary organic aerosol episodes and quantitation of primary and secondary organic aerosol concentrations during SCAQS, *Atmos. Environ.*, *29*(23), 3527-3544.

Wall, S.M., W. John, and J.L. Ondo (1988), Measurement Of Aerosol Size Distributions For Nitrate And Major Ionic Species, *Atmos. Environ.*, *22*(8), 1649-1656.

Wehner, B., S. Philippin, and A. Wiedensohler (2002), Design and calibration of a thermodenuder with an improved heating unit to measure the size-dependent volatile fraction of aerosol particles, *J. Aerosol Sci.*, *33*(7), 1087-1093.

Whiteaker, J.R., and K.A. Prather (2003), Hydroxymethanesulfonate as a tracer for fog processing of individual aerosol particles, *Atmos. Environ.*, *37*(8), 1033-1043.

Zhang, Q., J.L. Jimenez, D.R. Worsnop, and M. Canagaratna (2007), A case study of urban particle acidity and its influence on secondary organic aerosol, *Environ. Sci. Technol.*, *41*(9), 3213-3219.

Chapter 4

4 Real-Time, Single-Particle Volatility, Size, and Chemical Composition Measurements of Aged Urban Aerosols

4.1 Synopsis

Aerosol particles undergo significant atmospheric processing within the Los Angeles basin. To assess the major sources and extent of aging, ambient particle volatility, size, and chemical composition were measured concurrently in real-time during the Study of Organic Aerosols conducted in Riverside, CA in November 2005. A thermodenuder (TD) was coupled to an aerosol time-of-flight mass spectrometer (ATOFMS) to characterize the chemistry of the individual submicron particle cores remaining after heating. At 230°C, aged organic carbon (OC) particles had smaller particle cores (mode <100 nm) compared to biomass burning particles (~180 nm). Aged OC particles contained >50% by volume secondary species, primarily ammonium nitrate, ammonium sulfate, and amines. At 230°C, the chemistry of the remaining cores at 100-150 nm were elemental carbon (29% by number), OC (27%), and biomass burning (15%). Sea salt (47%) and dust (15%) were the major contributors at the larger sizes (750-800 nm). Many particle cores at 230°C possessed similar signatures to fresh vehicle emissions, biomass burning, sea salt, and dust particles, showing that the TD-ATOFMS method can be used to apportion particles in highly aged environments to their original sources, while providing insight into the relative contributions of primary and secondary species.

4.2 Introduction

Atmospheric aerosol particles impact global climate, regional air pollution, and human health [*Poschl*, 2005]. Originating from a variety of sources, such as biomass burning, fossil fuel combustion, and dust suspension, primary aerosol particles undergo physical and chemical transformations (atmospheric aging) during transport [*Poschl*, 2005]. Heterogeneous reactions of particles with trace gases and gas-particle partitioning of semivolatile species, such as ammonium nitrate and oxidized organics, contribute to changes in particle size, structure, and chemical composition [*Poschl*, 2005]. Thus, atmospheric aging provides challenges in the identification of the major particle sources connected with human health risks, making source-specific regulations difficult [*Schlesinger et al.*, 2006].

To examine the sources and chemical aging pathways of different particle types, a thermodenuder (TD) can be used to heat ambient particles, inducing the vaporization of semivolatile species and leaving behind the non-volatile particle cores [*Burtscher et al.*, 2001; *Engler et al.*, 2007]. Size-resolved volatility data, provided by measuring the size distributions of particles before and after heating, is often used to infer the mixing state of the particle core, which is most commonly assumed to be primarily black carbon [*Engler et al.*, 2007]. Volatilization and humidification tandem differential mobility analyzer (VH-TDMA) provided an increased understanding of ambient particle mixing state through hygroscopic behavior measurement [*Johnson et al.*, 2004a]. However, it is challenging using conventional techniques to interpret the size-resolved volatility data for particles containing multiple chemical components and externally mixed aerosol ensembles that are typically observed in the atmosphere [*Burtscher et al.*, 2001]. Further, few studies have measured the chemistry of heated atmospheric particles to directly determine their mixing state. Frey et al. [*Frey et al.*, 2008] found that black carbon (BC) mass concentrations tracked mass concentrations of less-volatile particles during periods of local traffic influence; increased disagreement between BC mass and less-volatile mass was found during periods of long-range transport. An aerosol mass spectrometer, measuring the chemical composition of non-refractory particulate species, was used to examine bulk ambient particle residuals in real-time in Tokyo, Japan [*Kondo et al.*, 2006] and Mexico City [*Huffman et al.*, 2008]. However, it is important to measure the complete chemistry including refractory species, such as black carbon, mineral dust, and sea salt, as these species could contribute significantly to the low volatility particle core.

Herein, an automated TD was coupled to an aerosol time-of-flight mass spectrometer (ATOFMS) to provide the first real-time, individual-particle size and volatility-resolved chemistry measurements. Using laser desorption-ionization, both the refractory and non-refractory particulate species are measured, providing the first on-line measurements of the chemistry of heated individual particle residuals. Aerosol particles undergo significant atmospheric processing within the Los Angeles (LA) basin, and thus, the vast majority of unheated particles show evidence of organic carbon, ammonium, amines, and nitrate accumulated during transport [*Hughes et al.*, 2002; *Qin et al.*, 2009]. A comparison of the chemistry of the unheated aged particles with the heated particle cores is presented, to help provide an improved understanding of particle volatility and ambient aerosol sources.

4.3 Experimental

ATOFMS measurements of single ambient aerosol particles were conducted during the Study of Organic Aerosols field campaign in Riverside, California from November 2-13, 2005 (SOAR-2) (http://cires.colorado.edu/jimenez-group/Field/Riverside05/). Ambient temperature and atmospheric water content were measured using a shielded Vaisala HMP 45AC temperature and RH probe. The ground-based prototype of the aircraft (A)-ATOFMS, described in Chapter 2, measured the vacuum aerodynamic diameter (d_{va}) and dual-polarity mass spectra of individual particles from ~100-1000 nm in real-time. For simplicity, A-ATOFMS will be referred to throughout this chapter as ATOFMS. During SOAR-2, particles were desorbed and ionized using 266 nm radiation from a Q-switched Nd:YAG laser operating at ~0.4-0.8 mJ. Polystyrene latex spheres of known physical diameter from 95-1400 nm were used to complete the single-particle size calibration.

To examine the volatilities of the ambient particles, an automated valve-controlled TD system [*Huffman et al.*, 2008] was utilized in series with the ATOFMS. A nafion dryer was used to dry the particles before the TD. With continuous aerosol flow through the TD (heated) and bypass line (unheated), the particles sampled by the ATOFMS switched between heated and unheated ambient aerosol every 10 minutes. The heated portion of the TD stepped through 8 temperatures: 171°C, 230°C, 201°C, 171°C, 142°C, 113°C, 83°C, 54°C. Since each portion of the schedule was maintained for 10 minutes, one full cycle took 160 minutes before repeating. An activated carbon diffusion denuder prevented volatilized species from condensing back onto the particles. With a flow rate of 0.6 lpm, the residence time of the aerosol in the heating portion of the TD was approximately 9 seconds. For further details and characterization of the TD, refer to Huffman et al. [2008].

Every 10 minutes, the ATOFMS switched between sampling either unheated and heated (54-230°C) ambient particles. In this work, particle residues remaining at 230°C are referred to as cores, although a specific morphology is not defined herein. A total of 1,390,199 size-resolved dual-polarity mass spectra were collected with the ATOFMS from Nov. 2-13, 2005. Data collection times were adjusted for delays in transport lines between the TD and ATOFMS. Data collected up to 20 seconds after the TD valve switch were eliminated to reduce error caused by possible aerosol mixing. Overall, dual-polarity mass spectra from 717,705 unheated and 462,982 heated particles were utilized in this analysis. Single-particle mass spectra were imported into YAADA (www.yaada.org), a software toolkit for Matlab (The MathWorks, Inc.). An adaptive resonance theory-based clustering method (ART-2a) [*Song et al.*, 1999] was used to classify single-particle mass spectra with a vigilance factor of 0.80, learning rate of 0.05, and 20 iterations. ART-2a classifies particles into separate clusters based on the presence and intensity of ion peaks in individual single-particle mass spectra. Peak identifications correspond to the most probable ions for a given m/z ratio based on previous lab and field studies; the peak area of a specific m/z is related the amount of a specific species on each particle [*Bhave et al.*, 2002]. General particle classes are defined by characteristic chemical species or possible source; these labels do not reflect all of the species present within a particular particle class.

For comparison of SOAR particles to particulate source emissions, particle signatures from heavy duty diesel vehicles (HDDV) and gasoline-powered light duty vehicles (LDV) were acquired during dynamometer source studies [*Toner et al.*, 2008]. Fresh ship emissions were acquired during sampling at the Port of Los Angeles [*Ault et al.*, 2009]. The fresh wildfire plume particle mass spectral signature was acquired during a flight over a prescribed burn in Wyoming. The mass spectral signature of unreacted sea salt was acquired during sampling along the California coast, and the unreacted dust signature was acquired in the lab from suspended soil [*Silva et al.*, 2000].

Size-resolved number concentrations of ATOFMS particle classes were calculated using a method described previously by Reinard et al. [2007]. A scanning mobility particle sizer (SMPS, model 3081, TSI, Inc.) in series with the TD provided size-resolved number concentrations of unheated and heated particles during SOAR-2. Particle mobility diameters (d_m) measured by the SMPS must be converted to d_{va} using the following equation, discussed in detail by DeCarlo et al. [2004]:

$$d_{va} = \frac{\rho_{eff}}{\rho_o} d_m \tag{1}$$

where ρ_{eff} is the effective density and ρ_o is the standard density (1.0 g/cm^3). Average size-resolved number concentrations were calculated for 103-995 nm (d_{va}) particles, using an ρ_{eff} of 1.4 g/cm^3, which was representative of most submicron SOAR-2 particles, which were spherical due to the condensation of water, organics, and ammonium nitrate [*Moffet et al.*, 2008]. Using average fractions of ATOFMS particle classes for different size bins, size-resolved number concentrations were calculated for unheated and heated particle classes.

4.4 Results and discussion

4.4.1 Ambient Aerosol Chemistry

From Nov. 2-13, westerly winds were observed from ~9:00-16:00 each day with diurnal trends in RH and ozone; most trajectories showed transport times of up to 12 hours from LA, Irvine, or San Diego to Riverside [*Qin et al.*, 2009]. An average $PM_{2.5}$ (particulate matter < 2.5 µm) mass concentration of 42 µg/m^3 was observed with build-up and stagnation periods leading to an observed maximum of 106 µg/m^3 [*Qin et al.*, 2009]. Individual ambient submicron (100-1000 nm) unheated and heated particles were classified into thirteen general particle classes: aged organic carbon (OC), aromatic, amine, ammonium-rich, elemental carbon-organic carbon (ECOC), inorganic-ECOC, elemental carbon (EC), vanadium, biomass, aged sea salt, dust, metals, and nitrate-sulfate particles with no positive ions (NoPos). The vast majority (~85%) of unheated particles showed evidence of organic carbon, ammonium, and nitrate accumulated during transport to Riverside [*Hughes et al.*, 2002; *Qin et al.*, 2009]; sulfate was also present in most (~70%) particles. The relative contributions of these particle classes with respect to size are shown in Figure 4.1. Mass spectral signatures and size-resolved number concentrations of the aged OC, EC, vanadium, and biomass burning particles classes at ambient and 230ºC are shown in Figure 4.2.

The particles in the aged OC class, which comprised ~60% by number of all unheated particles from d_{va} ~100-1000 nm, contained oxidized organic carbon species,

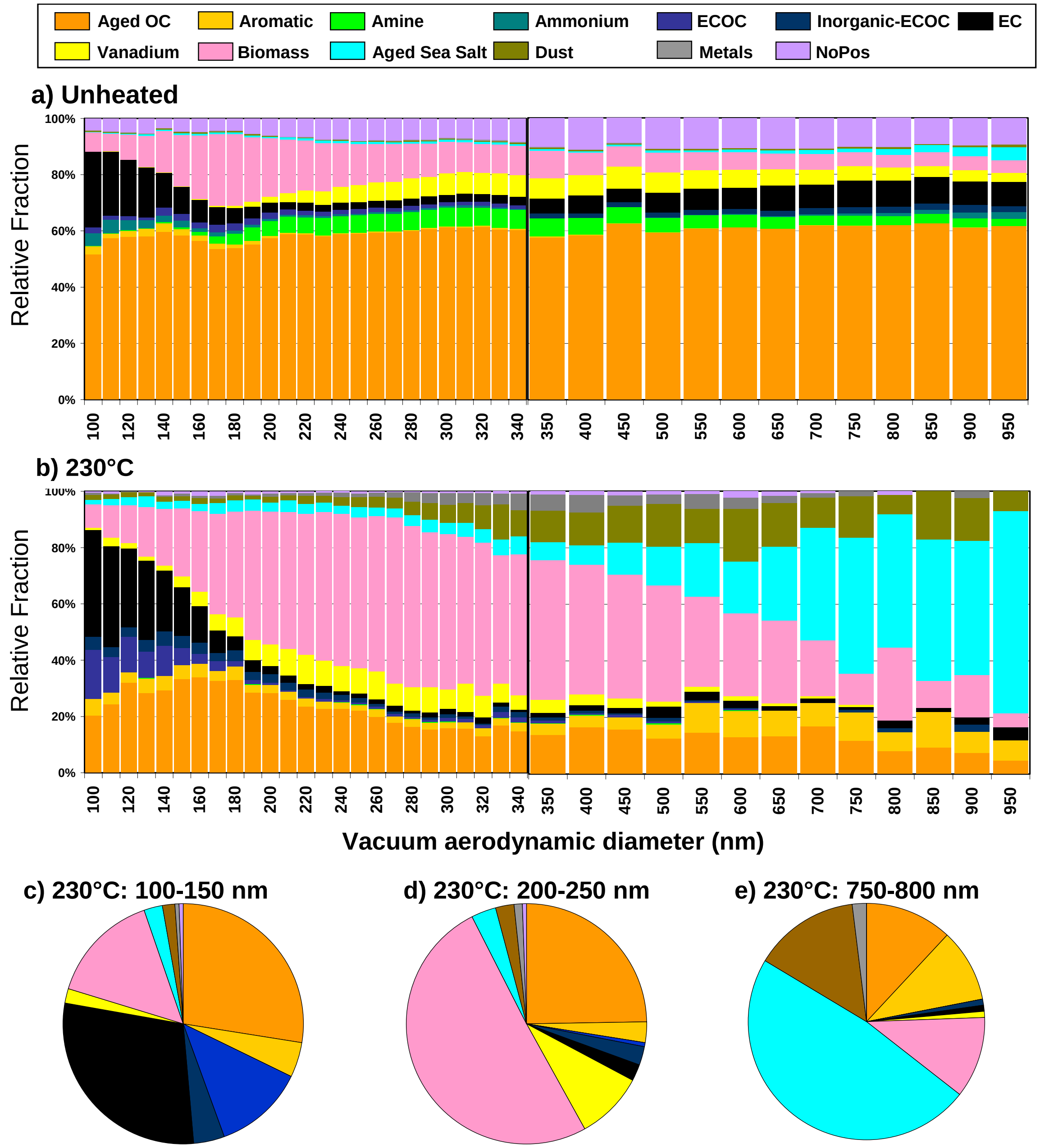

Figure 4.1. Size-resolved chemical composition of a) unheated and b) 230°C heated particles. Size resolution is 10 nm and 50 nm for the ranges of 100-350 nm and 350-1000 nm, respectively. Relative fractions of 230°C particle cores are illustrated for c) 100-150 nm, d) 200-250 nm, and e) 750-800 nm.

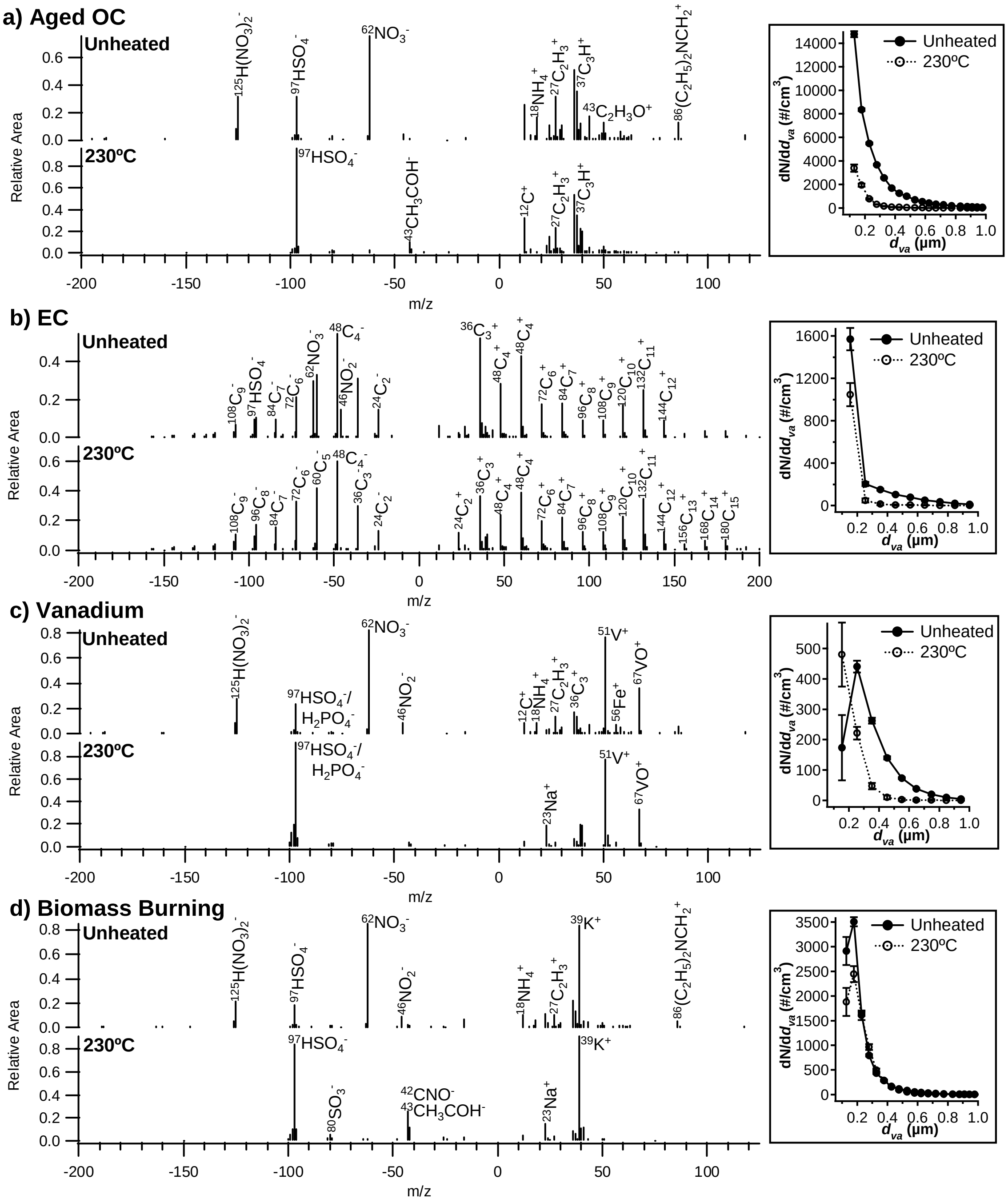

Figure 4.2. Average ATOFMS representative mass spectra and size-resolved number concentrations of unheated and 230°C heated particles for a) aged OC, b) EC, c) vanadium, and d) biomass burning particle classes.

amines, ammonium, nitrate, and sulfate. The mass spectra were dominated by carbonaceous marker ions at *m/z* 12(C^+), 27($C_2H_3^+$/CHN^+), 36(C_3^+), 37(C_3H^+), 43(CH_3CO^+/$CHNO^+$), and 86(($(C_2H_5)_2N{=}CH_2^+$), an alkylamine fragment [*Angelino et al.*, 2001; *Silva and Prather*, 2000]. Other notable ions include ammonium (m/z 18, NH_4^+), nitrate (m/z -62, NO_3^-, and -125, $H(NO_3)_2^-$), and sulfate (m/z -97, HSO_4^-) due to the aged nature of the Riverside particles [*Hughes et al.*, 2000]. Previously, secondary organic carbon has been shown to comprise 50% of the total $PM_{2.5}$ (particulate matter < 2.5µm) organic carbon mass in Riverside County in November [*Na et al.*, 2004].

Mass spectral signatures for the EC particles, attributed to vehicle emissions, were characterized by intense carbon cluster positive and negative ions from $C^{+/-}$ to $C_n^{+/-}$ with less intense nitrate and sulfate markers [*Shields et al.*, 2007; *Sodeman et al.*, 2005]. EC particles comprised 17 ± 1% by number in the unheated 103-153 nm d_{va} size bin, with reduced contribution (3-10%) at greater diameters. With heating, nitrate was vaporized from the particles, concurrent with a decrease in particle size. Vanadium-containing particles, attributed to ship, automobile, and industrial emissions [*Qin et al.*, 2009], were characterized by intense positive ions at *m/z* 51(V^+) and 67(VO^+) with less intense carbonaceous ion peaks [*Qin et al.*, 2009]. The negative ions are characterized by nitrate, sulfate, and phosphate. Ammonium, OC, and nitrate volatilized upon heating. The biomass burning particle class, which comprised ~10-24% by number of all unheated particles from d_{va} 100-400 nm, was characterized by an intense potassium ion with less intense carbonaceous positive ions; the negative ions are dominated by nitrate and sulfate [*Guazzotti et al.*, 2003; *Silva et al.*, 1999]. With heating, ammonium, amines, nitrate, and semi-volatile OC volatilized from the particles.

Other particle types included: aromatic, amine, ammonium, ECOC, inorganic-ECOC, aged sea salt, dust, and metals. The mass spectral signatures and size-resolved number concentrations of these particle classes are shown in Figure 4.3. The aromatic particles were characterized by carbonaceous marker ions, aromatic fragment ions (*m/z* 51($C_4H_3^+$), 63($C_5H_3^+$), 77($C_6H_5^+$), 115($C_9H_7^+$), 165($C_{13}H_9^+$), 189($C_{15}H_9^+$)), a monoaromatic molecular ion (m/z 139(4-nitrophenol)), and polycyclic aromatic hydrocarbon (PAH) molecular ions (m/z 128(naphthalene), 152(acenaphthylene), 202(pyrene/fluoranthene), 276(benzo [*ghi*] perylene)) [*Silva and Prather*, 2000; *Sodeman et al.*, 2005]. Nitrate (m/z -46, NO_2^-, and -62, NO_3^-) and sulfate are present in the negative ion mass spectra. With heating, nitrate is removed from these particles. The presence of *m/z* -26(CN^-), -42(CNO^-), -43(CH_3COH^-), and -80(SO_3^-) become readily apparent in the 230°C spectra. The presence of m/z -26 and -46 is indicative of organonitrate and nitro-PAH compounds in diesel exhaust [*Bezabeh et al.*, 1997]. The amine-rich particle class was dominated by *m/z* 86($(C_2H_5)_2N{=}CH_2^+$) with less intense amine marker ions at *m/z* 58($C_2H_5NHCH_2^+$), 102($(C_2H_5)_3NH^+$), and 118($(C_2H_5)_3NOH^+$) [*Angelino et al.*, 2001].

The ammonium-rich positive mass spectra are dominated by *m/z* 18(NH_4^+) and 30(NO^+) with less intense OC and amine marker ions; the negative ions are characterized by intense nitrate markers: *m/z* -62(NO_3^-), -125($H(NO_3)_2^-$), and -188(($H_2(NO_3)_3^-$) [*Hughes et al.*, 1999]. It is important to note that these nitrate clusters correspond to periods with very high ambient nitrate mass concentrations. Ammonium nitrate is formed when NO_x, emitted from vehicles, is oxidized to nitric acid (HNO_3) and reacts with gas-phase ammonia (NH_3), primarily from livestock emissions [*Russell and Cass*, 1986]. At

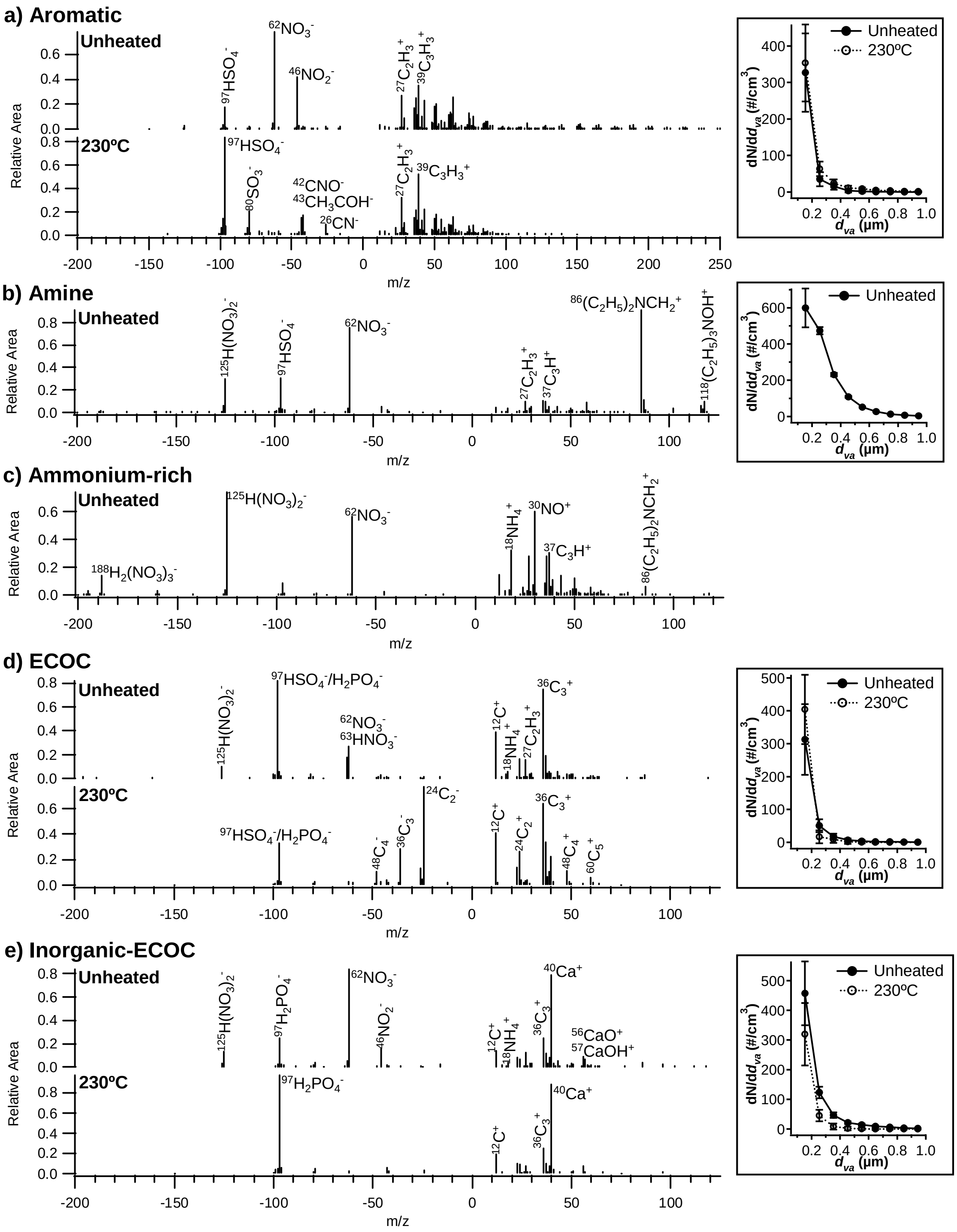

Figure 4.3. Average ATOFMS representative mass spectra and size-resolved number concentrations of unheated and 230°C heated particles for the following particle types: a) aromatic, b) amine, c) ammonium-rich, d) ECOC, e) inorganic-ECOC, f) aged sea salt, g) dust, h) metals (Zn-rich shown). A size distribution is not shown for the ammonium-rich particle class due to low ATOFMS particle counts.

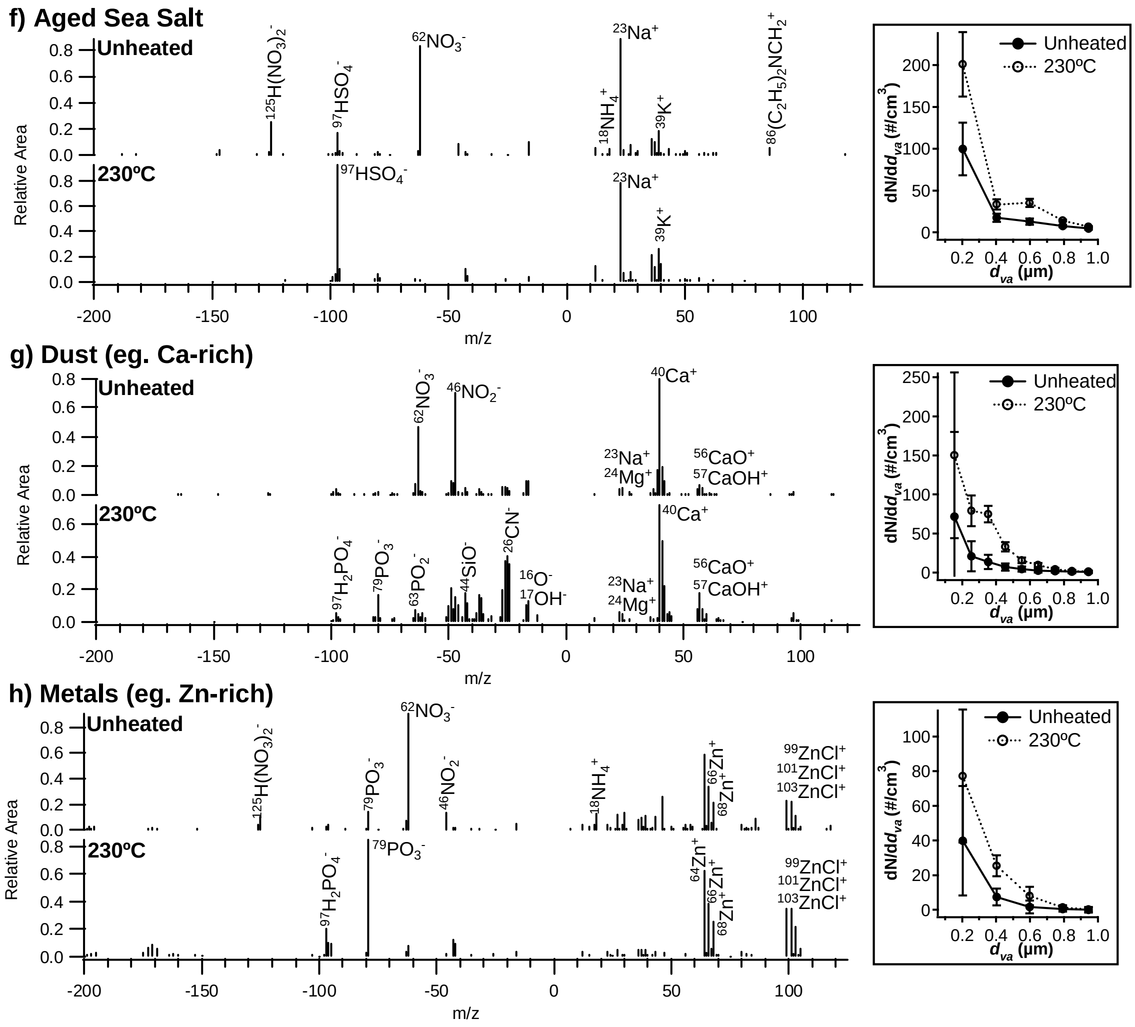

Figure 4.3. Continued.

maximum, the ammonium-rich particle type contributed 2 ± 1% by number to the unheated d_{va} 892-995 nm size bin. The relatively large size of these unheated ammonium nitrate particles is likely due to the Kelvin effect, wherein ammonium nitrate deposits on larger particles where surface curvature effects on vapor pressure are minimal [*Bassett and Seinfeld*, 1984].

ECOC particle mass spectra are dominated by carbon cluster ions at *m/z* 12(C^+), 24(C_2^+), and 36(C_3^+) with less intense OC and amine ion peaks. The negative ion mass spectra are characterized by nitrate (*m/z* -62, NO_3^-, -63, HNO_3^-, and -125, $H(NO_3)_2^-$) and sulfate. Calcium (*m/z* 40, Ca^+) and the carbon cluster ions at *m/z* 48(C_4^+), 60(C_5^+), -24(C_2^-), -36(C_3^-), and -48(C_4^-) became more apparent with heating due to the loss of a semi-volatile ammonium, OC, and nitrate. Further, the appearance of *m/z* -79(PO_3^-) with heating indicates that *m/z* -97 can be attributed to both HSO_4^- and $H_2PO_4^-$; the loss of nitrate with heating causes more electrons to be available in the LDI plume that can attach to neutral phosphate and form ions.

The aged sea salt particles were characterized by intense sodium, potassium, nitrate, and sulfate ion markers with smaller ammonium and carbonaceous ion markers [*Qin et al.*, 2009]. With heating, ammonium, amines, and nitrate are volatilized from these aged sea salt particles. The mass spectra of a representative calcium-rich dust particle type are shown in Figure 4.3g and are characterized by inorganic peaks at *m/z* 23(Na^+), 24(Mg^+), 40(Ca^+), 56(CaO^+), 57($CaOH^+$), -46(NO_2^-), and -62(NO_3^-) [*Pastor et al.*, 2003]. With heating, CN^- (m/z -26), silicates (*m/z* -44, SiO^-, and -60, SiO_2^-), and phosphate (*m/z* -63, PO_2^-, -79, PO_3^-, and -97, $H_2PO_4^-$) become prominent with the loss of nitrate. The mass spectra of a representative zinc-rich particle type are shown in Figure

4.3h and characterized by zinc (*m/z* 64, 66, 68), zinc chloride (*m/z* 99, 101, 103), nitrate, and phosphate with smaller carbonaceous ion peaks. With heating, ammonium, OC, and nitrate are volatilized. Figure 4.4 shows representative average mass spectra of 230°C heated particles for four other metal-rich particle types: a) Ba-rich, b) Pb-rich, c) Mo-rich, and d) Sn-rich.

With aging, secondary species can mask particles' primary source "fingerprints". Thus, heating with the TD can be used to volatilize non-refractory secondary species, making the primary source signature more identifiable, as described below. Since gas-particle partitioning occurs more commonly than nucleation in urban environments, an understanding of the primary particle population is important in understanding urban air pollution as gas/particle partitioning depends not only on surface area and volume, but also on the chemistry and resulting interactions on the surface of the available primary particles [*Poschl*, 2005].

4.4.2 Chemically-Resolved Volatility

Overall, a systematic decrease in particle size was observed with heating from ambient temperature (average 16°C, range 8-26°C) up to 230°C, as shown in Figure 4.5. However, the strength of the TD-ATOFMS system is that it directly measures the size-resolved chemical composition of the individual particle residues following heating, providing an improved understanding of the original sources of the particle cores. For the aged OC particles, the most abundant submicron particle type in Riverside, the particles shifted to smaller diameters with heating from 54-230°C (Figures 4.1 and 4.6).

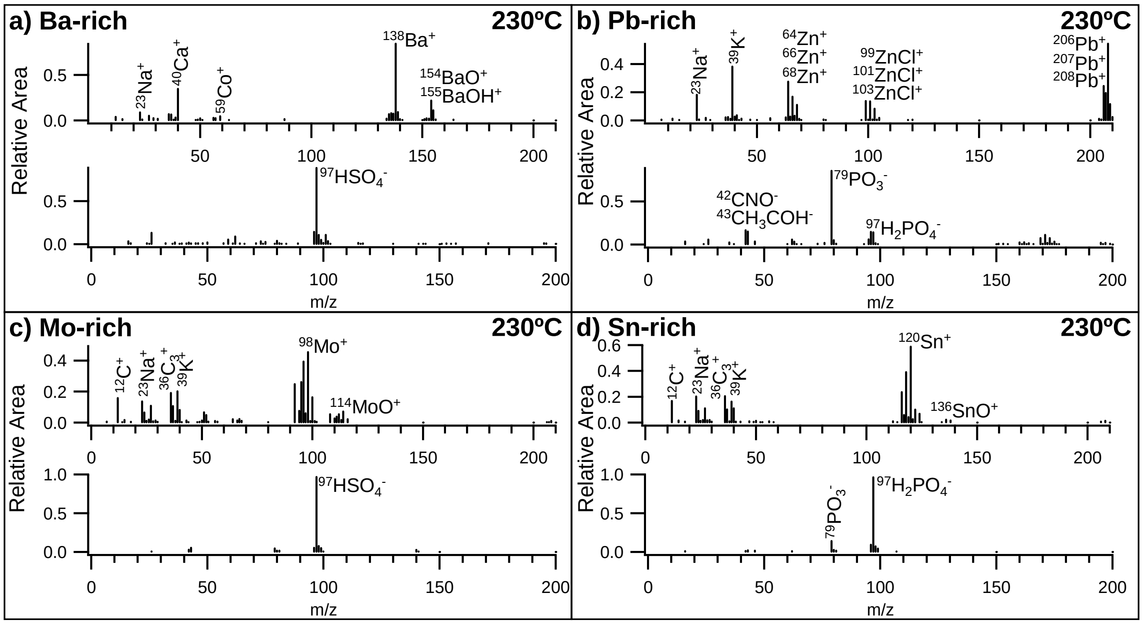

Figure 4.4. Representative average positive and negative mass spectra of 230°C heated particles for four metal-rich particle types: a) Ba-rich, b) Pb-rich, c) Mo-rich, and d) Sn-rich.

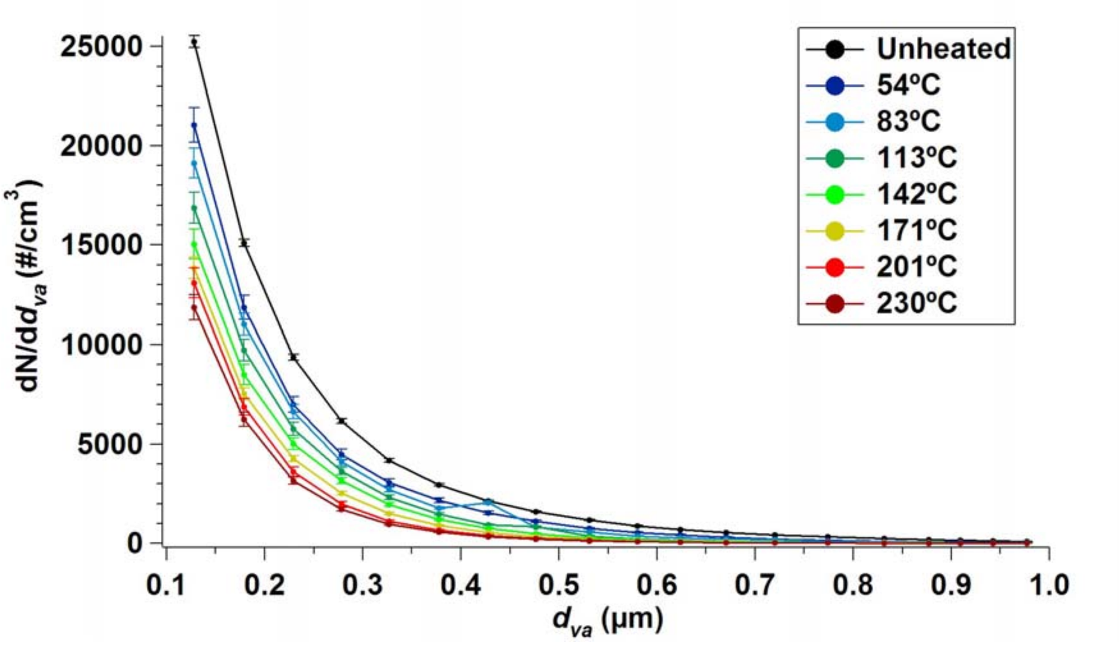

Figure 4.5. Average size-resolved number concentrations with ~50 nm size bins (d_{va} = 103-995 nm) as measured by the SMPS from Nov. 2-13 for ambient temperature to 230ºC. Variation over the course of the study is shown by standard error bars.

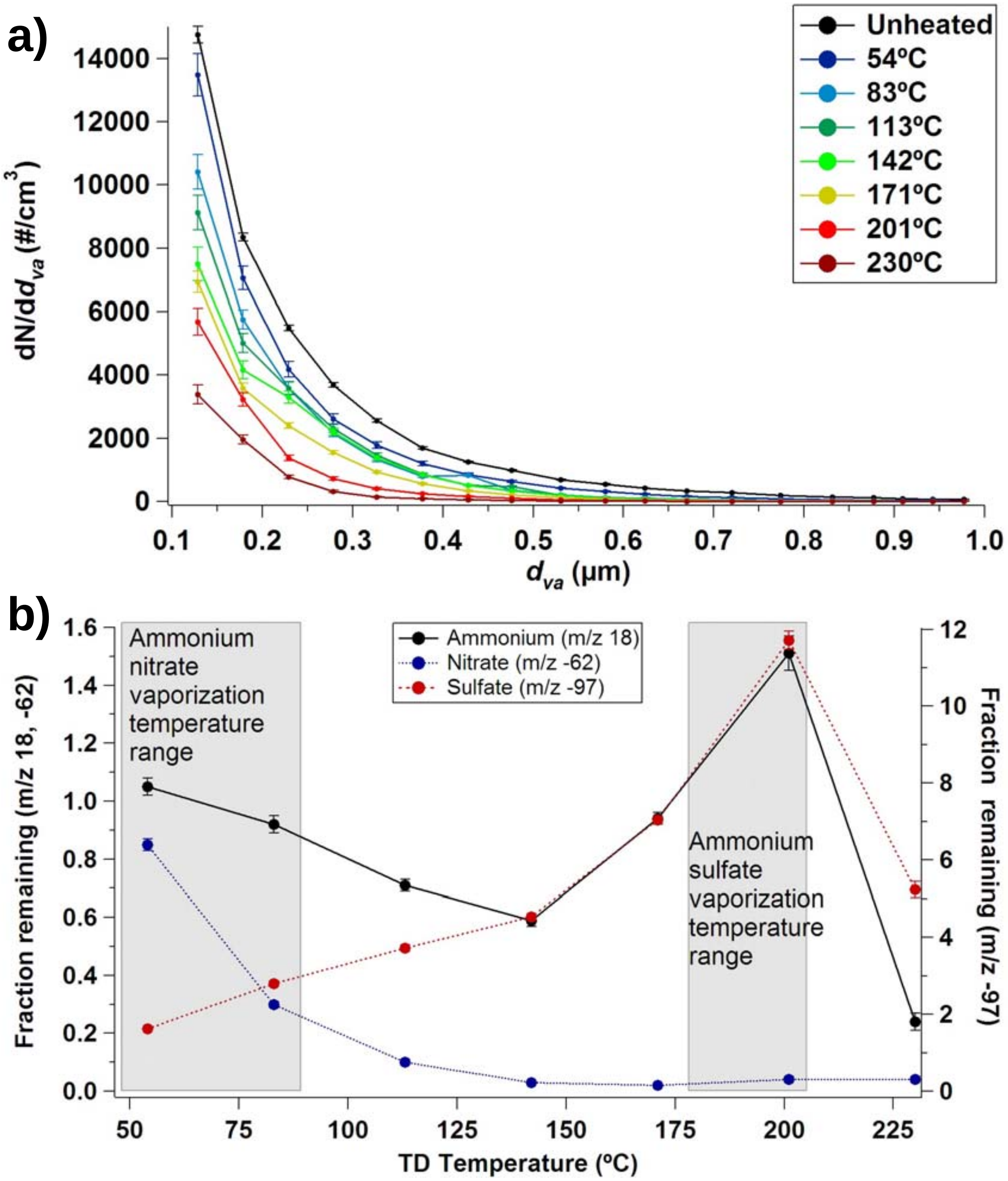

Figure 4.6. a) Size-resolved number concentrations of unheated and heated (54-230°C) aged OC particles. b) Fractions of ammonium, nitrate, and sulfate remaining at different TD temperatures (54-230°C) for aged OC particles with respect to the vaporization temperature ranges of ammonium nitrate [*Johnson et al.*, 2004b] and ammonium sulfate [*Johnson et al.*, 2004a].

Parallel ATOFMS particle optical measurements showed that these aged OC particles were spherical [*Moffet et al.*, 2008], allowing average particle volume to be calculated, from which the approximate volume fraction of the average aged OC particle remaining at each TD temperature (54-230°C) was calculated. The volatilization of ammonium (m/z 18, NH_4^+), nitrate (m/z -62, NO_3^-), and sulfate (m/z -97, HSO_4^-) were then examined with respect to TD temperature (54-230°C) for all of the aged OC particles (Figure 4.6). For comparison, the vaporization temperature ranges of ammonium nitrate and ammonium sulfate are 48-89°C [*Johnson et al.*, 2004b] and 178-205°C [*Johnson et al.*, 2004a], respectively. Through comparison of average volume and ion marker peak area fractions remaining at different TD temperatures, approximate contributions of secondary species to the average unheated particle may be calculated. These are likely conservative estimates as they are biased by the measurement of particles in the 100-1000 nm (d_{va}) size range, and thus, they cannot account for particles entering this range from larger sizes (>1.0 µm) and leaving this size range as they shift to the ultrafine mode (<100 nm). For aged OC particles, ammonium nitrate contributes 22 ± 6% to the average particle volume, assuming that ammonium nitrate is the primary volatile component below 113°C. Further, ~90% of the nitrate was found to be in the form of ammonium nitrate; the remaining ~10% of the nitrate was found to be primarily non-volatile aminium nitrate salts (Chapter 5). The decrease in sulfate peak area from 201-230°C was correlated with the decrease in ammonium due to the loss of ammonium sulfate; considering the volume loss from 201-230°C, ammonium sulfate is estimated to contribute 19 ± 9% by volume to the average unheated aged OC particle. Volume loss from 113-171°C is attributed primarily to the loss of organic carbon species (6 ± 7%); however, while organic carbon was observed to volatilize across the temperature range, some of the organic carbon in the form of oligomers (Chapter 3) remained at 230°C, as shown by the organic carbon markers in Figure 4.2. In addition to organic carbon and aminium nitrate salts, sulfate remaining at 230°C was in the form of sulfuric acid, aminium sulfate (Chapter 5), and likely organosulfates within these aged OC particles.

The increase in sulfate intensity with heating to 201°C (Figures S3-S6) is hypothesized to be caused by the loss of nitrate, whereby more electrons were available in the laser desorption-ionization plume to attach to the sulfate and form ions. Recent SOAR-1 results from Huffman et al. [2009] found increased sulfate mass at 142°C compared to ambient temperature. There is also some evidence of possible recondensation of ammonium sulfate at 230°C prior to the activated carbon diffusion denuder [*Huffman et al.*, 2008].

To further investigate the impacts of single-particle mixing state on volatility, secondary species on vanadium-containing, biomass burning, aged sea salt, and dust particles were examined (Figures 4.2, 4.7, 4.8, and 4.9). Similar to the aged OC class, nitrate was found to be primarily in the form of ammonium nitrate for the vanadium-containing and biomass burning particle types. However, sulfate remaining at 230°C is hypothesized to be in the forms of $VOSO_4$ and K_2SO_4, which volatilize at 600°C and above 1000°C, respectively [*Knudsen et al.*, 2004; *Vlaev et al.*, 2007]. For the aged sea salt and dust particle classes, the heated size distributions of these particle types included supermicron particles that shrank into the submicron size range with heating, resulting in higher number concentrations at 230°C compared to ambient temperature (see Figure 4.9). For the aged sea salt class, a significant fraction of the nitrate and sulfate did not

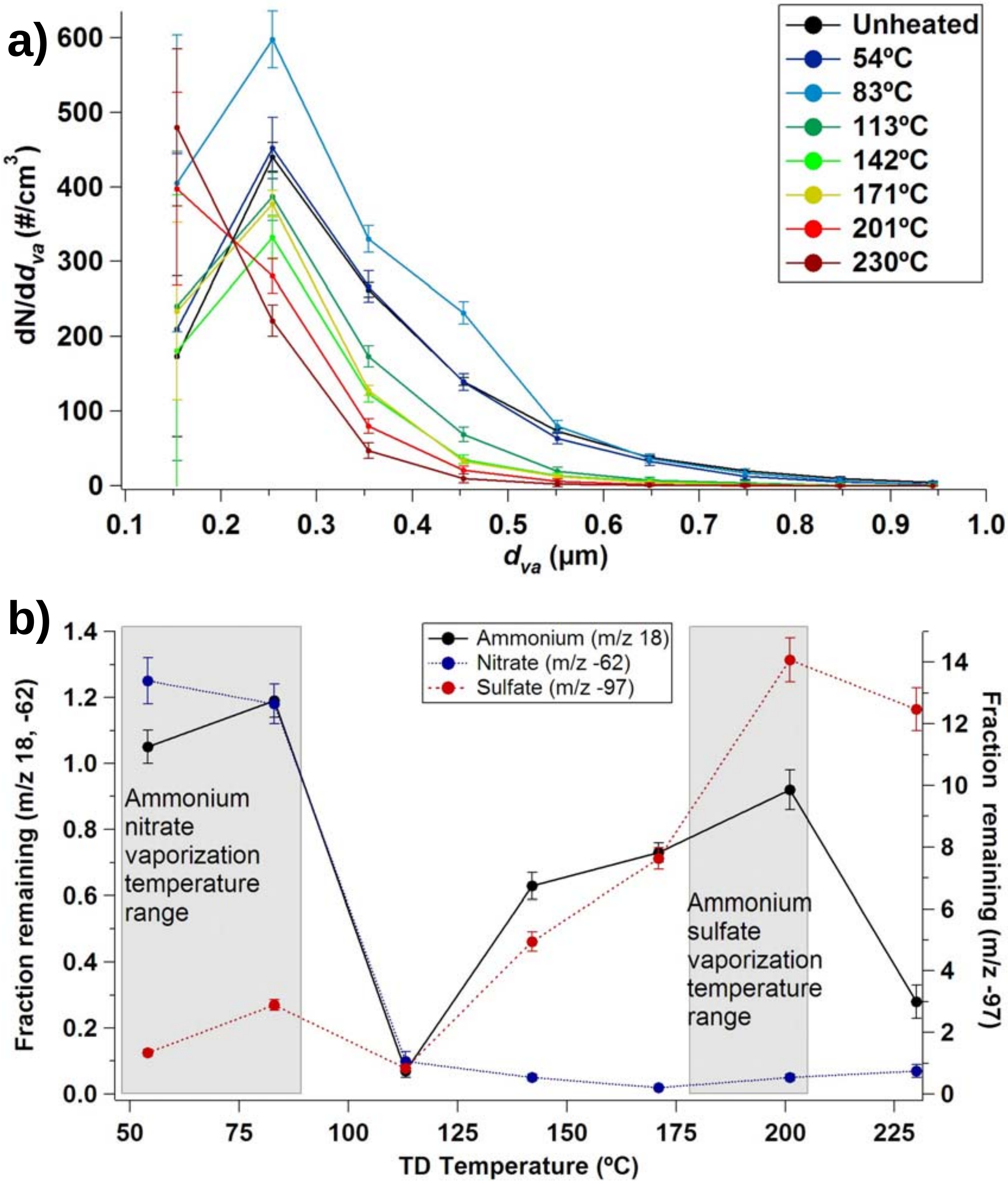

Figure 4.7. a) Size-resolved number concentrations of unheated and heated (54-230°C) vanadium-containing particles. b) Fractions of ammonium, nitrate, and sulfate at different TD temperatures (54-230°C) for vanadium-containing particles with respect to the vaporization temperature ranges of ammonium nitrate [*Johnson et al.*, 2004b] and ammonium sulfate [*Johnson et al.*, 2004a].

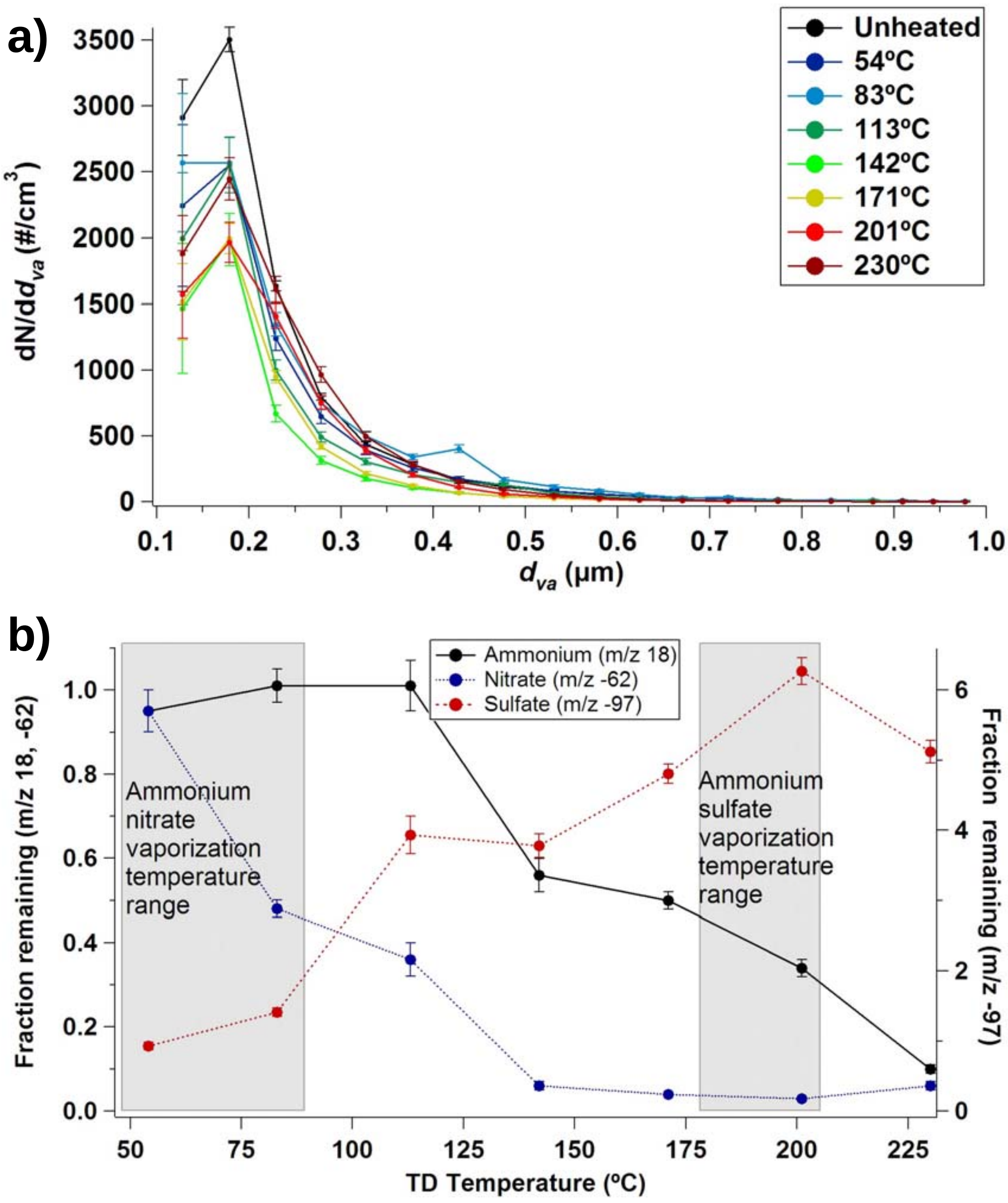

Figure 4.8. a) Size-resolved number concentrations of unheated and heated (54-230°C) biomass burning particles. b) Fractions of ammonium, nitrate, and sulfate at different TD temperatures (54-230°C) for biomass burning particles with respect to the vaporization temperature ranges of ammonium nitrate [*Johnson et al.*, 2004b] and ammonium sulfate [*Johnson et al.*, 2004a].

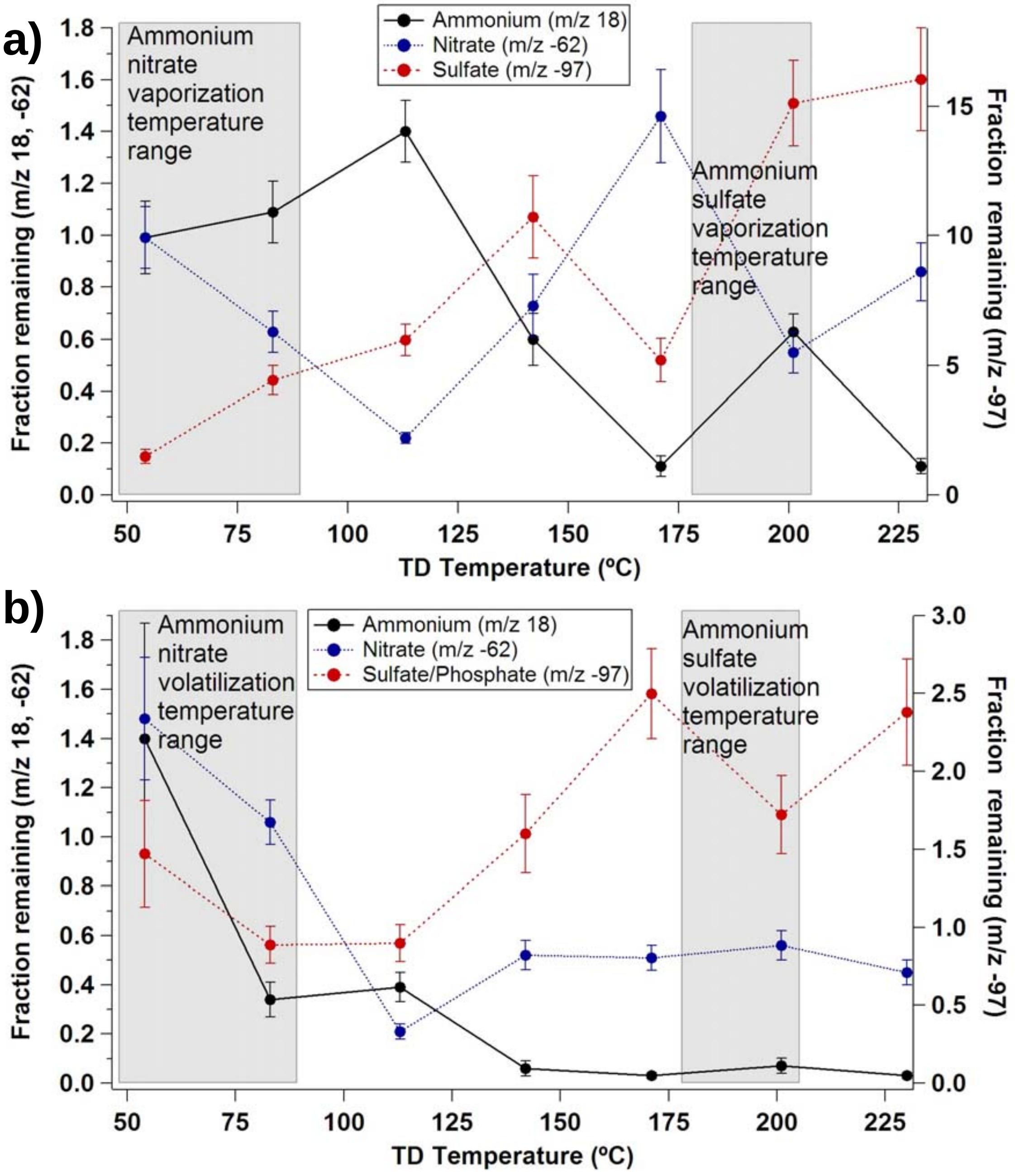

Figure 4.9. Fractions of ammonium, nitrate, and sulfate at different TD temperatures (54-230°C) for a) aged sea salt and b) dust particles with respect to the vaporization temperature ranges of ammonium nitrate [*Johnson et al.*, 2004b] and ammonium sulfate [*Johnson et al.*, 2004a].

volatilize at 230°C, suggesting nitrate and sulfate were in the forms of $NaNO_3$ and Na_2SO_4, which volatilize at >300°C, similar to NaCl [*Engler et al.*, 2007]. During transport across the LA basin, sea salt particles undergo heterogeneous chemical reactions, wherein nitric acid and sulfuric acid react with NaCl [*Hughes et al.*, 2002]. The average dust particle contained a significant fraction of ammonium nitrate; however, nearly half of the nitrate was present in non-volatile forms, such as $Ca(NO_3)_2$. Thus, the volatilities of sulfate and nitrate were found to be dependent on particle mixing state. Therefore, the volatility of a particular species cannot be assumed to be the same for all particles, even in an aged urban environment, such as Riverside. Future publications will investigate the predicted versus measured gas-particle partitioning of various chemical species with respect to season and particle class.

4.4.3 Aerosol Core Chemistry at 230°C

The TD-ATOFMS system allowed the complete chemistry of individual ambient particle cores at 230°C to be measured for the first time. As discussed above, secondary coatings of ammonium nitrate, organic carbon, and ammonium sulfate volatilized with heating. Figure 4.1 shows the relative fractions of particle types observed in Riverside with respect to size for the 230°C heated particles; the evolution of the size-chemistry distribution from ambient temperature to 230°C is shown in Figure 4.10. Two secondary semivolatile particle types, amine and ammonium-rich, volatilized prior to 230°C. The abundance of the amine particles, present from ambient temperatures up to 142°C from ~170-1000 nm, decreased by ~63% with heating above 54°C with only ~8% by number

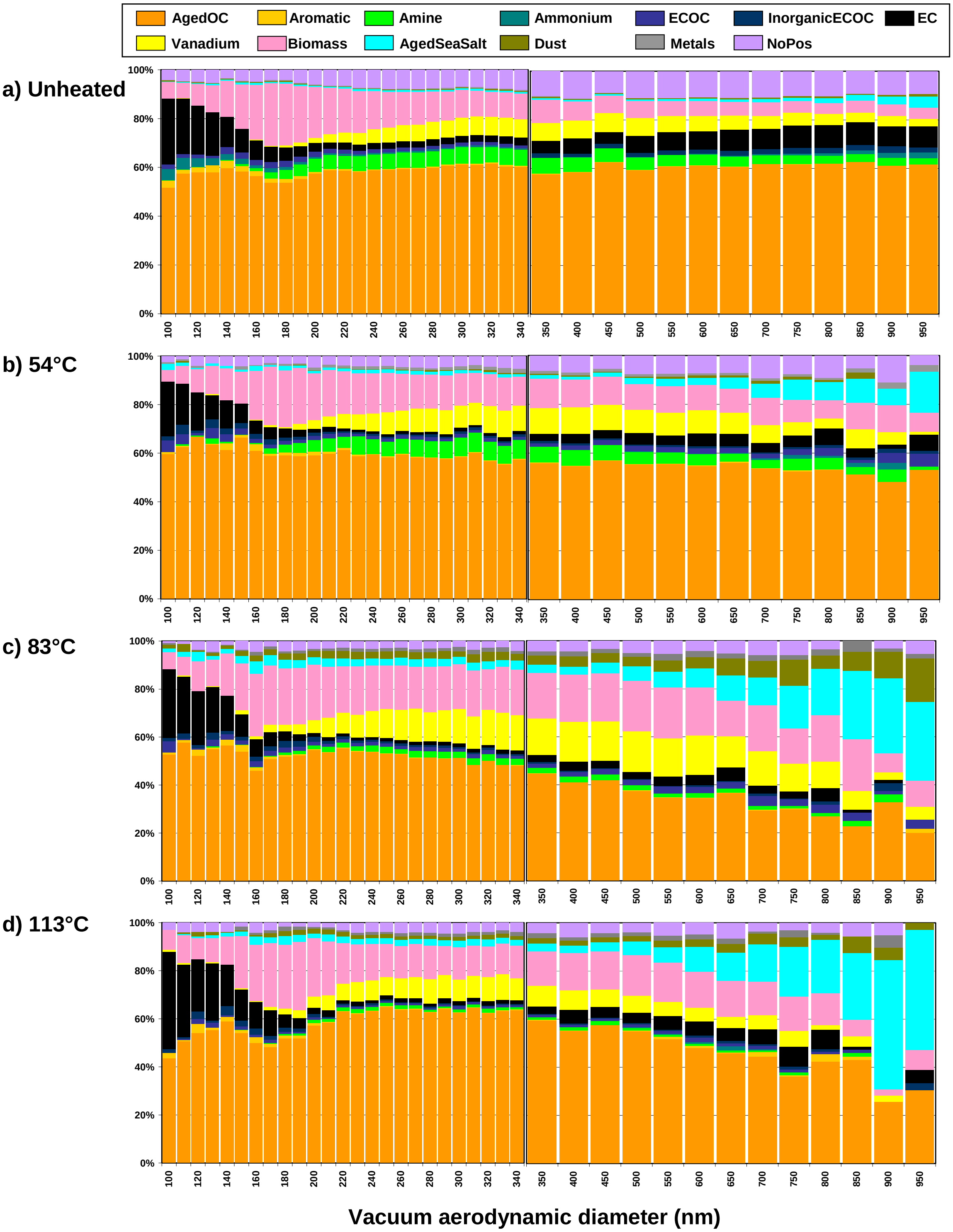

Figure 4.10. Size-resolved chemical composition for the 13 general particle types for: a) unheated, b) 54°C, c) 83°C, d) 113°C, e) 142°C, f) 171°C, g) 201°C, and h) 230°C. Size resolution is 10 nm and 50 nm for the ranges of 100-350 nm and 350-1000 nm, respectively.

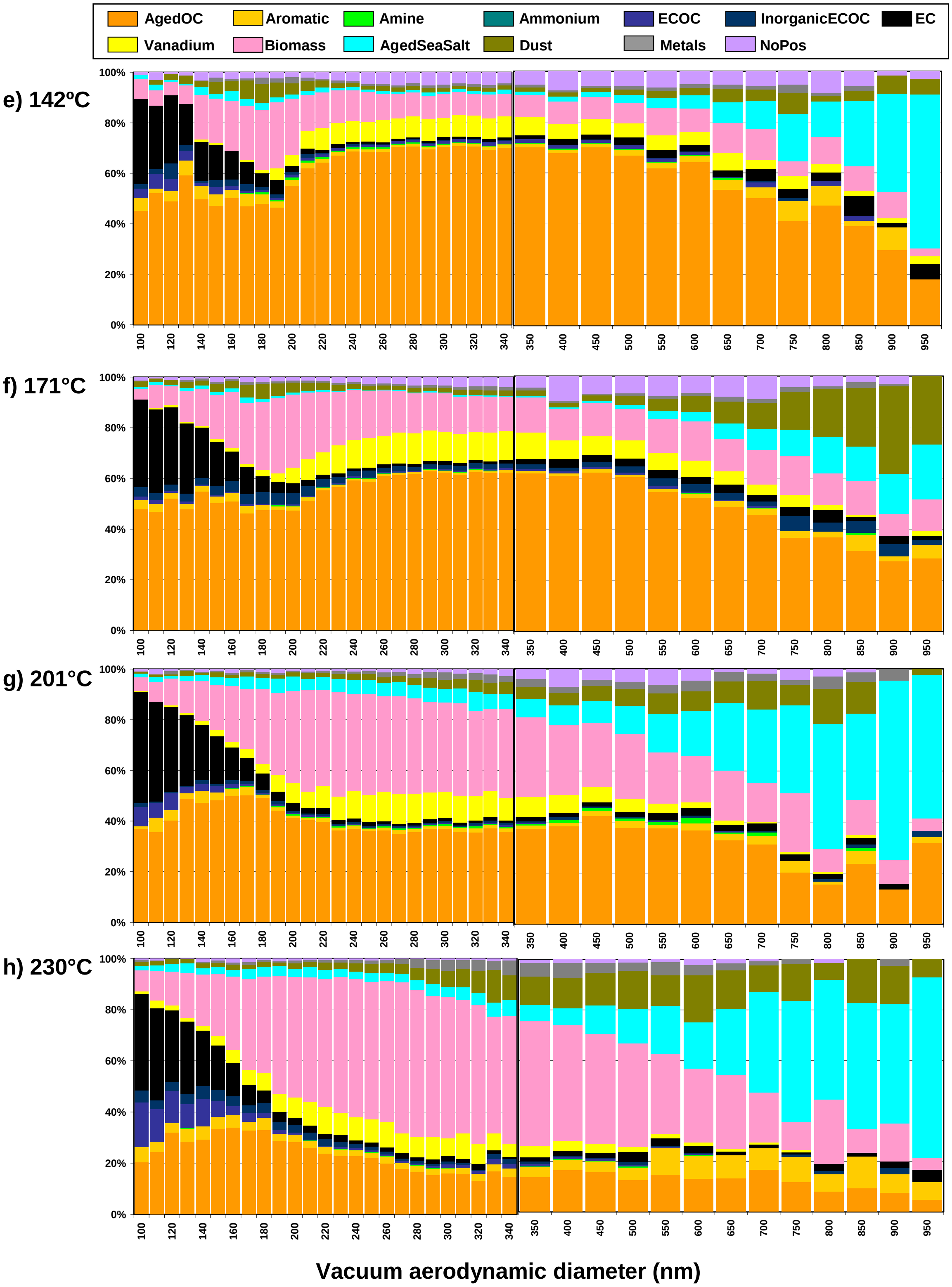

Figure 4.10. Continued.

present above 113°C, suggesting these amine species are quite volatile. The ammonium-rich particle type, consisting of primarily ammonium nitrate, was not present at 54°C, consistent with laboratory studies showing a volatilization temperature range of 48-89°C for ammonium nitrate [*Johnson et al.*, 2004a]. As these two semivolatile particle types are internal mixtures of carbonaceous and inorganic species, it is likely that these heated particles shifted to <100 nm in diameter or became reclassified as aged OC particles following volatilization of the amines or ammonium nitrate, respectively.

The aged OC and vanadium-containing particle types decreased significantly in size with increasing temperature, with the majority of remaining particles estimated to be less than 100 nm in diameter (Figure 4.1). Aged OC particles accounted for ~60% of the unheated submicron (100-1000 nm) particles by number; the relative contribution of these aged OC particles decreased with heating, particularly for the larger (>350 nm) particles, accounting for only ~20% by number of the 230°C particles across all sizes. For particles >100 nm, the average aged OC particle diameter decreased from 242 ± 2 nm to 177 ± 12 nm with heating to 230°C, showing the significant fraction of volatilized species. Considering the average particle volume, less than 53 ± 7% by volume of the average submicron aged OC particle was found to remain at 230°C; this represents an upper limit since most particles shifted to <100 nm with heating. For the vanadium-containing particle type, the average particle diameter decreased from 334 ± 35 nm to 201 ± 37 nm with heating to 230°C; this corresponds to a volatile fraction of at least 64 ± 15%. Previously, volatility measurements have shown a volume loss of ~80% with heating to 350°C for submicron urban particles [*Clarke et al.*, 2004].

The size distributions of several particle classes (aromatic, ECOC, inorganic-ECOC, EC, and biomass burning) did not show significant shifts with heating, as expected for fresh particles containing smaller fractions of secondary species. Previous thermodenuder studies of traffic-related particles showed that, prior to heating at 280°C, nearly 100% of particles with initial diameters of 150 nm were non-volatile [*Wehner et al.*, 2004]. The biomass burning particle results agree with previous findings that biomass burning particles are less volatile with a greater fraction of refractory OC than pollution plume particles [*Clarke et al.*, 2007]. In particular, biomass burning particles have relatively large cores due to the presence of refractory salts, such as KCl and K_2SO_4, which volatilize at temperatures above 700°C, as well as soot [*Clarke et al.*, 2007; *Knudsen et al.*, 2004]. The mode positioned at ~180 nm for 230°C is consistent with that of fresh biomass burning emissions and was the largest of all combustion-type particles observed [*Reid et al.*, 2005].

As expected, the aged sea salt and dust particles had the largest particle diameters at 230°C. As discussed in the above section, the fractional contributions of aged sea salt and dust particle types increased with heating primarily due to the volatilization of semivolatile coatings and water from supermicron particles [*Qin et al.*, 2009]. The increased contributions of sea salt and dust particles to the larger submicron particle cores can be seen in Figure 4.1.

With heating, the percentage of particles with metal signatures increased by a factor of 6 at 54°C, due to the volatilization of semivolatile species, causing these particles to be reclassified as metal-rich. The most abundant metals observed at 230°C included vanadium, zinc, barium, lead, molybdenum, and tin (Figures 4.1, 4.3, and 4.4).

Posing negative human health effects, trace metals present in particulate matter are of considerable importance [*Schlesinger et al.*, 2006]. However, small metal particles produced in combustion fumes quickly become coated in the atmosphere, making detection difficult. A detailed discussion of the mass spectral signatures, sources, and temporal patterns of metal-rich particles detected during SOAR is presented elsewhere [*Shields et al.*, 2008]; however, it is important to note that metals are not typically detected in aged environments by single particle mass spectrometry as they are masked by high levels of secondary coatings. Based on these thermodenuder results, it appears they must be masked by high levels of secondary coatings, suggesting that the overall fraction of metal-containing particles is greater than previously estimated [*Shields et al.*, 2008]. However, there is some evidence of toxicity related to the chemical composition of the particle surface [*Schlesinger et al.*, 2006], and, thus, studies are needed to determine the relative toxicity of coated (aged) versus uncoated metal-containing particles. Future laboratory studies will quantify the amount of secondary coatings necessary to mask these trace metal signals and examine corresponding health impacts.

In summary, at 230°C, the main particle types present from 100-150 nm were elemental carbon (29% by number), OC (27%), and biomass burning (15%). Correspondingly, biomass burning (51%) and OC (25%) were the primary particle types at 200-250 nm, and sea salt (47%) and dust (15%) were found at 750-800 nm. Future studies will size-select particles prior to TD heating to better quantify the fractions of secondary species versus particle core. The TD-ATOFMS method has provided insight into the contributions of different forms of secondary species, such as ammonium nitrate vs. sodium nitrate, with respect to individual particle cores.

4.4.4 Comparison of Particle Cores with Source Emissions

If the semivolatile material volatilized from the particle phase at 230°C is composed of mostly secondary species, then the particle core should resemble non-volatile primary particle-phase source emissions. To test this hypothesis, the mass spectral signatures of the aged unheated and 230°C heated particles were each compared to freshly emitted particles from previous source studies, described in the supporting information, using a method similar to Toner et al. [2008]. Briefly, the mass spectral signatures of the SOAR-2 particle types were compared to the mass spectral signatures resulting from various source studies; dot products were calculated for the ion peaks in the compared spectra (Figure 4.11). Lower dot products (i.e. blue) indicate less similarity between the SOAR-2 and source particles; whereas high dot products (i.e. red) indicate more similarity. To examine the similarity of the unheated and 230°C heated aged OC particles, the mass spectra were compared, giving a dot product of 0.62, illustrating the dramatic change in particle chemical composition with heating. The aged OC particles were likely primary combustion emission particles transformed by the accumulation of the secondary reaction products [*Kleeman et al.*, 1999]. It is likely that ammonium nitrate, ammonium sulfate, amines, and organic carbon were acquired due to condensation and aqueous-phase processing during the night when lower temperatures and higher relative humidity (average 72%, range of 16-96%) were encountered [*Munger et al.*, 1990]. Following removal of semivolatile species with heating to 230°C, concurrent with a decrease in particle size, the heated OC particle mass spectral signature was nearly identical to that of fresh OC particles emitted from light duty vehicles (LDV)

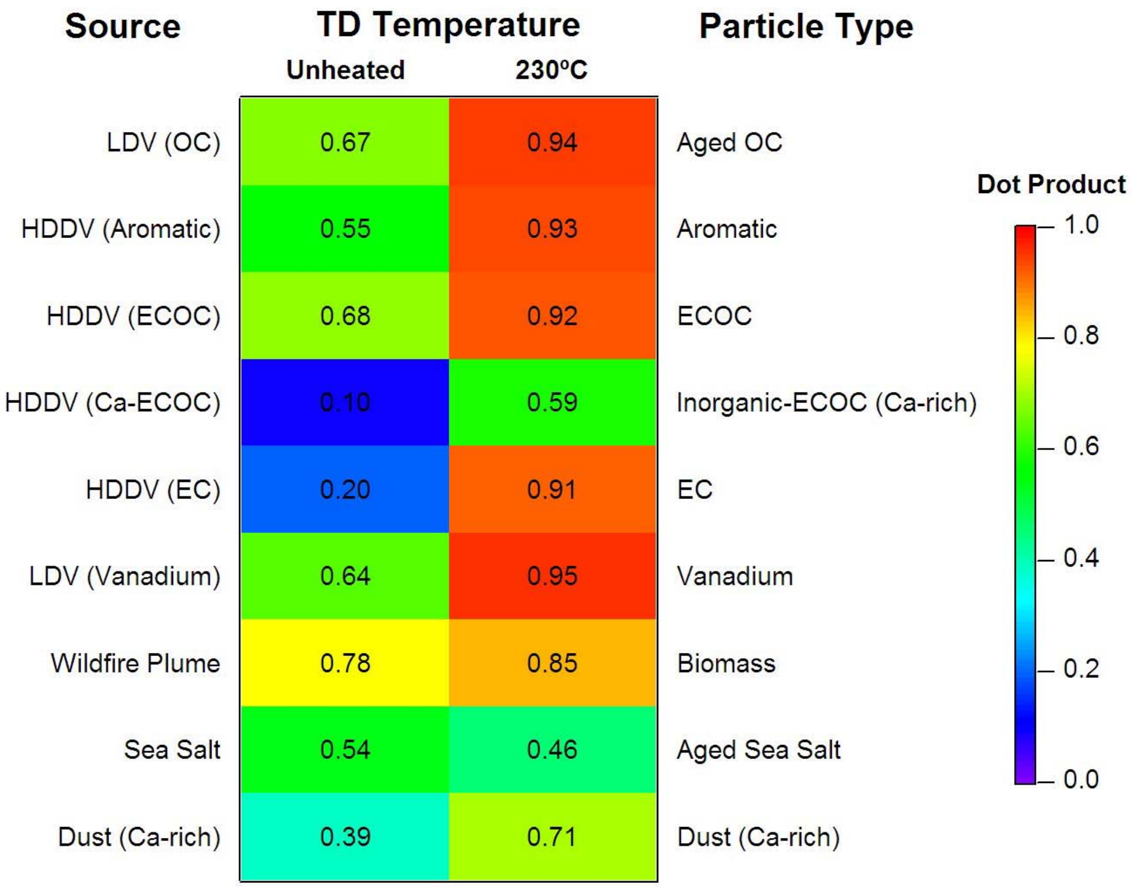

Source	TD Temperature Unheated	TD Temperature 230°C	Particle Type
LDV (OC)	0.67	0.94	Aged OC
HDDV (Aromatic)	0.55	0.93	Aromatic
HDDV (ECOC)	0.68	0.92	ECOC
HDDV (Ca-ECOC)	0.10	0.59	Inorganic-ECOC (Ca-rich)
HDDV (EC)	0.20	0.91	EC
LDV (Vanadium)	0.64	0.95	Vanadium
Wildfire Plume	0.78	0.85	Biomass
Sea Salt	0.54	0.46	Aged Sea Salt
Dust (Ca-rich)	0.39	0.71	Dust (Ca-rich)

Figure 4.11. Dot product comparisons of mass spectral signatures of freshly emitted source particles (light duty vehicles (LDV), heavy duty diesel vehicles (HDDV), wildfire, sea salt, and dust) with unheated and 230°C heated SOAR-2 particles.

[*Sodeman et al.*, 2005]. The dot product between the LDV emissions [*Sodeman et al.*, 2005] and Riverside particles increases with heating from 0.67 for the unheated particles to 0.94 for the 230°C heated aged OC particles.

Other heated particle types also resembled fresh vehicle emissions (Figure 4.11). For the aromatic particle type (Figure 4.3), similar polycyclic aromatic hydrocarbon (PAH)-containing particles have been previously identified in heavy duty diesel vehicles (HDDV) and LDV emissions [*Shields et al.*, 2007; *Sodeman et al.*, 2005]. The dot product comparison between HDDV aromatic particle emissions and these Riverside particles improves with heating from 0.55 to 0.93, showing a nearly identical signature to HDDV emissions at 230°C. Similarly, the mass spectral signature of the ECOC particle type resembles fresh HDDV emissions previously detected by ATOFMS [*Shields et al.*, 2007] with the dot product increasing from 0.68 to 0.92 with heating. The Ca-rich ECOC particles were likely residual oil particles from HDDV exhaust [*Toner et al.*, 2006]; Na/K-dominant ECOC particles were likely unburned fuel particles from LDV exhaust [*Spencer et al.*, 2006]. The 230°C Ca-rich ECOC particles showed an improved match (0.59) to the HDDV Ca-ECOC [*Toner et al.*, 2006] compared to the unheated particles (0.10); however, the relatively low dot product observed for the heated Ca-ECOC particles suggests that another unidentified source could also be contributing to these particles. The EC mass spectral signature resembles fresh HDDV emissions [*Shields et al.*, 2007] with the dot product increasing from 0.20 to 0.91 with heating. The heated vanadium-containing particles were an excellent match to vanadium-containing LDV particles [*Sodeman et al.*, 2005] (0.95) and vanadium-containing ship emissions [*Ault et al.*, 2009] (0.94), increasing from 0.64 and 0.62 for the unheated particles, respectively.

For unheated particles characterized by distinctive source signatures, the results were mixed. Comparison of the aged biomass particles with fresh biomass particles collected within a wildfire plume provides a good match with both the unheated (0.78) and 230°C heated particles (0.85) since potassium dominates the comparison. Unlike other particle types, the dot product between fresh sea salt and the aged sea salt does not increase with heating (0.54 vs. 0.46), due to the irreversibility of chloride replacement by nitrate and sulfate during atmospheric aging. The mass spectral signature of the heated aged dust particles is similar to that of fresh suspended dust particles [*Silva et al.*, 2000] with a dot product of 0.71 compared to 0.39 for the unheated dust; however, similar to the sea salt, the lower observed dot product for the heated dust particles is due to irreversible heterogeneous chemical reactions.

Thus, the TD-ATOFMS method has been shown to apportion particles in highly aged environments to their original sources, while providing insight into the relative contributions of primary and secondary species. Future TD-ATOFMS studies in different environments are expected to further our understanding of primary particle sources and gas/particle partitioning.

4.5 Acknowledgements

This work was supported by the National Science Foundation (NSF ATM-0321362) and the California Air Resources Board (CARB 04-336). We thank Paul Ziemann (UC-Riverside), Ken Docherty (CU-Boulder), and the UC-Riverside Air Pollution Research Center for support during SOAR-2 and Alex Huffman and Jose Jimenez (CU-Boulder) for use of the TD system. Mike Cubison (CU-Boulder) provided

SMPS data. Megan McKay and the Goldstein group (UC Berkeley) provided ambient temperature and relative humidity data. We also thank the Prather group, particularly Laura Shields, Xueying Qin, and Stephen Toner, for support during SOAR-2.

Chapter 4 has submitted for publication in *Environmental Science & Technology*: Pratt, K.A., Prather, K.A. Real-time, single-particle volatility, size, and chemical composition measurements of aged urban aerosols.

4.6 References

Angelino, S., D.T. Suess, and K.A. Prather (2001), Formation of aerosol particles from reactions of secondary and tertiary alkylamines: Characterization by aerosol time-of-flight mass spectrometry, *Environ. Sci. Technol.*, *35*(15), 3130-3138.

Ault, A.P., C.J. Gaston, Y. Wang, G. Dominguez, M.H. Thiemens, and K.A. Prather (2009), Single particle mixing state of individual ship plumes at the Port of Los Angeles, *Environ. Sci. Technol.*, *Submitted*(

Bassett, M.E., and J.H. Seinfeld (1984), Atmospheric Equilibrium-Model Of Sulfate And Nitrate Aerosols.2. Particle-Size Analysis, *Atmos. Environ.*, *18*(6), 1163-1170.

Bezabeh, D.Z., T.M. Allen, E.M. McCauley, P.B. Kelly, and A.D. Jones (1997), Negative ion laser desorption ionization time-of-flight mass spectrometry of nitrated polycyclic aromatic hydrocarbons, *J. Am. Soc. Mass Spectrom.*, *8*(6), 630-636.

Bhave, P.V., J.O. Allen, B.D. Morrical, D.P. Fergenson, G.R. Cass, and K.A. Prather (2002), A field-based approach for determining ATOFMS instrument sensitivities to ammonium and nitrate, *Environ. Sci. Technol.*, *36*(22), 4868-4879.

Burtscher, H., U. Baltensperger, N. Bukowiecki, P. Cohn, C. Hüglin, M. Mohr, U. Matter, S. Nyeki, V. Schmatloch, N. Streit, and E. Weingartner (2001), Separation of volatile and non-volatile aerosol fractions by thermodesorption: instrumental development and applications, *J. Aerosol Sci.*, *32*(427-442.

Clarke, A., C. McNaughton, V. Kapustin, Y. Shinozuka, S. Howell, J. Dibb, J. Zhou, B. Anderson, V. Brekhovskikh, H. Turner, and M. Pinkerton (2007), Biomass burning and pollution aerosol over North America: Organic components and their influence on spectral optical properties and humidification response, *J. Geophys. Res.*, *112*(D12).

Clarke, A.D., Y. Shinozuka, V.N. Kapustin, S. Howell, B. Huebert, S. Doherty, T. Anderson, D. Covert, J. Anderson, X. Hua, K.G. Moore, C. McNaughton, G. Carmichael, and R. Weber (2004), Size distributions and mixtures of dust and black carbon aerosol in Asian outflow: Physiochemistry and optical properties, *J. Geophys. Res.*, *109*(D15).

DeCarlo, P.F., J.G. Slowik, D.R. Worsnop, P. Davidovits, and J.L. Jimenez (2004), Particle morphology and density characterization by combined mobility and aerodynamic diameter measurements. Part 1: Theory, *Aerosol Sci. Technol.*, *38*(12), 1185-1205.

Engler, C., D. Rose, B. Wehner, A. Wiedensohler, E. Brüggemann, T. Gnauk, G. Spindler, T. Tuch, and W. Birmili (2007), Size distributions of non-volatile particle residuals (Dp<800 nm) at a rural site in Germany and relation to air mass origin, *Atmos. Chem. Phys.*, *7*(22), 5785.

Frey, A., D. Rose, B. Wehner, T. Muller, Y. Cheng, A. Wiedensohler, and A. Virkkula (2008), Application of the volatility-TDMA technique to determine the number size distribution and mass concentration of less volatile particles, *Aerosol Sci. Technol.*, *42*(817-828.

Guazzotti, S.A., D.T. Suess, K.R. Coffee, P.K. Quinn, T.S. Bates, A. Wisthaler, A. Hansel, W.P. Ball, R.R. Dickerson, C. Neususs, P.J. Crutzen, and K.A. Prather (2003), Characterization of carbonaceous aerosols outflow from India and Arabia: Biomass/biofuel burning and fossil fuel combustion, *J. Geophys. Res.*, *108*(D15).

Huffman, J.A., K.S. Docherty, A.C. Aiken, M.J. Cubison, I.M. Ulbrich, P.F. DeCarlo, D. Sueper, J.T. Jayne, D.R. Worsnop, P.J. Ziemann, and J.L. Jimenez (2009), Chemically-resolved aerosol volatility measurements from two megacity field results, *Atmos. Chem. Phys. Discuss.*, *9*(2645-2697.

Huffman, J.A., P.J. Ziemann, J.T. Jayne, D.R. Worsnop, and J.L. Jimenez (2008), Development and characterization of a fast-stepping/scanning thermodenuder for chemically-resolved aerosol volatility measurements, *Aerosol Sci. Technol.*, *42*(5), 395-407.

Hughes, L.S., J.O. Allen, P. Bhave, M.J. Kleeman, G.R. Cass, D.Y. Liu, D.F. Fergenson, B.D. Morrical, and K.A. Prather (2000), Evolution of atmospheric particles along trajectories crossing the Los Angeles basin, *Environ. Sci. Technol.*, *34*(15), 3058-3068.

Hughes, L.S., J.O. Allen, M.J. Kleeman, R.J. Johnson, G.R. Cass, D.S. Gross, E.E. Gard, M.E. Galli, B.D. Morrical, D.P. Fergenson, T. Dienes, C.A. Noble, P.J. Silva, and K.A. Prather (1999), Size and composition distribution of atmospheric particles in southern California, *Environ. Sci. Technol.*, *33*(20), 3506-3515.

Hughes, L.S., J.O. Allen, L.G. Salmon, P.R. Mayo, R.J. Johnson, and G.R. Cass (2002), Evolution of nitrogen species air pollutants along trajectories crossing the Los Angeles area, *Environ. Sci. Technol.*, *36*(18), 3928-3935.

Johnson, G., Z. Ristovski, and L. Morawska (2004a), Application of the VH-TDMA technique to coastal ambient aerosols, *Geophys. Res. Lett.*, *31*(16).

Johnson, G.R., Z. Ristovski, and L. Morawska (2004b), Method for measuring the hygroscopic behaviour of lower volatility fractions in an internally mixed aerosol, *J. Aerosol Sci.*, *35*(4), 443-455.

Kleeman, M.J., L.S. Hughes, J.O. Allen, and G.R. Cass (1999), Source contributions to the size and composition distribution of atmospheric particles: Southern California in September 1996, *Environ. Sci. Technol.*, *33*(23), 4331-4341.

Knudsen, J.N., P.A. Jensen, and K. Dam-Johansen (2004), Transformation and release to the gas phase of Cl, K, and S during combustion of annual biomass, *Energy Fuels*, *18*(5), 1385-1399.

Kondo, Y., Y. Komazaki, Y. Miyazaki, N. Moteki, N. Takegawa, D. Kodama, S. Deguchi, M. Nogami, M. Fukuda, T. Miyakawa, Y. Morino, M. Koike, H. Sakurai, and K. Ehara (2006), Temporal variations of elemental carbon in Tokyo, *J. Geophys. Res.*, *111*(D12).

Moffet, R.C., X. Qin, T. Rebotier, H. Furutani, and K.A. Prather (2008), Chemically segregated optical and microphysical properties of ambient aerosols measured in a single-particle mass spectrometer, *J. Geophys. Res.*, *113*(doi:10.1029/2007JD009393.

Munger, J.W., J. Collett, B. Daube, and M.R. Hoffmann (1990), Fogwater chemistry at Riverside, California, *Atmos. Environ.*, *24B*(2), 185-205.

Na, K.S., A.A. Sawant, C. Song, and D.R. Cocker (2004), Primary and secondary carbonaceous species in the atmosphere of Western Riverside County, California, *Atmos. Environ.*, *38*(9), 1345-1355.

Pastor, S.H., J.O. Allen, L.S. Hughes, P. Bhave, G.R. Cass, and K.A. Prather (2003), Ambient single particle analysis in Riverside, California by aerosol time-of-flight mass spectrometry during the SCOS97-NARSTO, *Atmos. Environ.*, *37,*(S239-S258.

Poschl, U. (2005), Atmospheric aerosols: Composition, transformation, climate and health effects, *Angewandte Chemie-International Edition*, *44*(46), 7520-7540.

Qin, X., L.G. Shields, S.M. Toner, K.A. Pratt, and K.A. Prather (2009), Seasonal comparisons of the single particle mixing state in Riverside, CA during the SOAR 2005 campaign, *Aerosol Sci. Technol.*, *In preparation.*(

Reid, J.S., R. Koppmann, T.F. Eck, and D.P. Eleuterio (2005), A review of biomass burning emissions part II: intensive physical properties of biomass burning particles, *Atmos. Chem. Phys.*, *5*(799-825.

Reinard, M.S., K. Adou, J.M. Martini, and M.V. Johnston (2007), Source characterization and identification by real-time single particle mass spectrometry, *Atmos. Environ.*, *41*(9397-9409.

Russell, A.G., and G.R. Cass (1986), Verification Of A Mathematical-Model For Aerosol Nitrate And Nitric-Acid Formation And Its Use For Control Measure Evaluation, *Atmos. Environ.*, *20*(10), 2011-2025.

Schlesinger, R.B., N. Kunzli, G.M. Hidy, T. Gotschi, and M. Jerrett (2006), The health relevance of ambient particulate matter characteristics: Coherence of toxicological and epidemiological inferences, *Inhalation Toxicol.*, *18*(2), 95-125.

Shields, L.G., X. Qin, S.M. Toner, and K.A. Prather (2008), Characterization of trace metals in single urban particles during the SOAR 2005 campaign, *Sci. Total Environ.*, *Submitted*(

Shields, L.G., D.T. Suess, and K.A. Prather (2007), Determination of single particle mass spectral signatures from heavy-duty diesel vehicle emissions for PM2.5 source apportionment, *Atmos. Environ.*, *41*(18), 3841-3852.

Silva, P.J., R.A. Carlin, and K.A. Prather (2000), Single particle analysis of suspended soil dust from Southern California, *Atmos. Environ.*, *34*(11), 1811-1820.

Silva, P.J., D.Y. Liu, C.A. Noble, and K.A. Prather (1999), Size and chemical characterization of individual particles resulting from biomass burning of local Southern California species, *Environ. Sci. Technol.*, *33*(18), 3068-3076.

Silva, P.J., and K.A. Prather (2000), Interpretation of mass spectra from organic compounds in aerosol time-of-flight mass spectrometry, *Anal. Chem.*, *72*(15), 3553-3562.

Sodeman, D.A., S.M. Toner, and K.A. Prather (2005), Determination of single particle mass spectral signatures from light-duty vehicle emissions, *Environ. Sci. Technol.*, *39*(12), 4569-4580.

Song, X.H., P.K. Hopke, D.P. Fergenson, and K.A. Prather (1999), Classification of single particles analyzed by ATOFMS using an artificial neural network, ART-2A, *Anal. Chem.*, *71*(4), 860-865.

Spencer, M.T., L.G. Shields, D.A. Sodeman, S.M. Toner, and K.A. Prather (2006), Comparison of oil and fuel particle chemical signatures with particle emissions from heavy and light duty vehicles, *Atmos. Environ.*, *40*(27), 5224-5235.

Toner, S.M., L.G. Shields, D.A. Sodeman, and K.A. Prather (2008), Using mass spectral source signatures to apportion exhaust particles from gasoline and diesel powered vehicles in a freeway study using UF-ATOFMS, *Atmos. Environ.*, *42*(568-581.

Toner, S.M., D.A. Sodeman, and K.A. Prather (2006), Single particle characterization of ultrafine and accumulation mode particles from heavy duty diesel vehicles using aerosol time-of-flight mass spectrometry, *Environ. Sci. Technol.*, *40*(12), 3912-3921.

Vlaev, L.T., V.G. Georgieva, and S.D. Genieva (2007), Products and kinetics of non-isothermal decomposition of vanadium(IV) oxide compounds, *J. Thermal. Anal. Cal.*, *88*(3), 805-812.

Wehner, B., S. Philippin, A. Wiedensohler, V. Scheer, and R. Vogt (2004), Variability of non-volatile fractions of atmospheric aerosol particles with traffic influence, *Atmos. Environ.*, *38*(36), 6081-6090.

Chapter 5

5 Seasonal Volatility Dependence of Ambient Particle Phase Amines

5.1 Synopsis

During the summer and fall of 2005 in Riverside, California, the seasonal volatility behavior of submicrometer aerosol particles was investigated by coupling an automated thermodenuder system to an online single-particle mass spectrometer. A strong seasonal dependence was observed for the gas/particle partitioning of alkylamines within individual ambient submicrometer aged organic carbon particles internally mixed with ammonium, nitrate, and sulfate. In the summer, the amines were strongly correlated with nitrate and sulfate, suggesting the presence of aminium nitrate and sulfate salts which were nonvolatile and comprised ~6-9% of the average particle mass at 230 °C. In the fall, 86 ± 1% of the amines volatilized below 113 °C with aminium nitrate and sulfate salts representing less than 1% of the particle mass at 230 °C. In the summer, a more acidic particle core led to protonation of the amines and subsequent formation of aminium sulfate and nitrate salts; whereas, in the fall, the particles contained more ammonium and thus were less acidic, causing fewer aminium salts to form. Therefore, the acidity of individual particles can greatly affect gas/particle partitioning of organic species in the atmosphere, and the concentrations of amines, as strong bases, should be included in estimations of aerosol pH.

5.2 Introduction

Atmospheric aerosol particles play a major role in impacting global climate, regional air pollution, and human health [*Kanakidou et al.*, 2005]. Organic carbon (OC) can comprise up to 50% of the total fine aerosol mass at continental midlatitudes [*Kanakidou et al.*, 2005], and in some areas, such as the eastern Los Angeles (LA) basin, secondary organic aerosol (SOA) can also represent a significant fraction of the total organic aerosol mass [*Turpin and Huntzicker*, 1995]. During atmospheric transport, particles undergo heterogeneous reactions with trace gases as well as gas-to-particle partitioning of semivolatile species, causing changes in particle size, structure, and chemical composition [*Kanakidou et al.*, 2005]. Understanding the partitioning of organic carbon species between the gas and particle phases remains one of the major challenges in predicting aerosol chemistry in regional and global atmospheric chemical transport models [*Kanakidou et al.*, 2005]. In particular, semivolatile organic nitrogen species, suggested to be a significant portion of the OC aerosol mass [*Murphy et al.*, 2007], are not well understood with regard to gas-particle partitioning. The atmospheric lifetimes of organic nitrogen species are dependent on the distributions between the gas and particle phases for the different species, which in turn determine their role in the global nitrogen cycle [*Neff et al.*, 2002]. One class of semivolatile organic nitrogen species, alkylamines, is emitted from many of the same sources as ammonia, an abundant atmospheric species which has been extensively studied. In particular, a major source of nitrogen species is animal husbandry, where amine concentrations represent up to 23% of those measured for ammonia [*Schade and Crutzen*, 1995; *Sorooshian et al.*, 2008]. Amines have also been identified in urban and rural atmospheres in both the gas and particle phases, including within fog and rainwater [*Angelino et al.*, 2001; *Gronberg et al.*, 1992; *McGregor and Anastasio*, 2001]. Recent measurements show fine particulate amine concentrations of 0.5-6 $\mu g/m^3$ (up to ~20% of the organic matter mass) during winter inversions in Utah [*Silva et al.*, 2008].

Amines can undergo oxidation by OH, O_3, and/or NO_3 to form amides, nitramines, and imines, which can also partition to the particle phase [*Murphy et al.*, 2007; *Schade and Crutzen*, 1995; *Silva et al.*, 2008]. Once in the particle phase, amines can undergo further reactions to form high-molecular-weight compounds [*Murphy et al.*, 2007; *Silva et al.*, 2008; *Zahardis et al.*, 2008]. In addition, gas-phase aliphatic amines, which are stronger bases than ammonia, compete to form salts through the following reactions with nitric acid (HNO_3) and sulfuric acid (H_2SO_4), leading to secondary aerosol formation [*Angelino et al.*, 2001; *Murphy et al.*, 2007].

$$NR_{3(g)} + HNO_{3(g)} \rightleftarrows HNR_3NO_{3(s)} \xrightarrow{T,RH,pH} HNR_3{}^{+}{}_{(aq)} + NO_3{}^{-}{}_{(aq)} \qquad (1)$$

$$2NR_{3(g)} + H_2SO_{4(g)} \rightleftarrows (HNR_3)_2SO_{4(s)} \xrightarrow{T,RH,pH} 2(HNR_3)^{+}{}_{(aq)} + SO_4{}^{2-}{}_{(aq)} \qquad (2)$$

Particle phase amines associated with sulfate and nitrate have been observed in both chamber [*Angelino et al.*, 2001; *Murphy et al.*, 2007] and field measurements [*Tan et al.*, 2002]. Notably, chamber experiments by Murphy et al. [2007] demonstrated the stability of nitrate salts of trimethylamine and triethylamine in the particle phase, even at very low relative humidity (RH <10%). However, one hypothesis suggests that if relative humidity is high and water is present in the particles, the aminium salts will dissolve into their ionic forms, shifting the equilibrium of the gas-phase amines toward the particle phase [*Angelino et al.*, 2001], potentially yielding greater particle phase amine mass than predicted by Murphy et al. [2007]. As such, the gas/particle partitioning model described by Pankow [2003] assumes that amines, as strong bases, are only volatile when present in their neutral, non-salt forms. In addition, due to low vapor pressures, organic acids may also form salts with amines, as suggested by measurements of atmospheric nanoparticles [*Smith et al.*, 2008] and thermodynamic calculations [*Barsanti et al.*, 2009].

To study the volatility behavior of alkylamine species within aged ambient particles in Riverside, CA, an automated thermodenuder (TD) was coupled to a real-time, single-particle mass spectrometer to characterize the chemical composition of the remaining individual submicrometer ambient organic carbon-containing particles following heating. Using the TD, semivolatile species were vaporized at different temperatures, leaving behind particle cores that were compared to the unheated particle chemistry [*Burtscher et al.*, 2001]. Herein, the partitioning of amines associated with nitrate and sulfate as a function of temperature and particle acidity are examined for individual organic carbon particles internally mixed with nitrate, sulfate, and ammonium.

5.3 Experimental

5.3.1 Ambient Measurements

Measurements of individual submicrometer ambient aerosol particles by aerosol time-of-flight mass spectrometry (ATOFMS) were conducted during the Study of Organic Aerosols in Riverside (SOAR, August and November 2005, http://cires.colorado.edu/jimenez-group/Field/Riverside05/). The sampling site at the University of California, Riverside campus was located about ~60 miles east of Los Angeles, CA. Ambient temperature and atmospheric water content measurements were made using a shielded Vaisala HMP 45AC temperature and RH probe. The ATOFMS results presented here focus on TD-conditioned aerosol chemistry measurements made on August 12, 2005 (SOAR-1) and November 2-13, 2005 (SOAR-2). August 12th was the only summer day during which TD-conditioned aerosol chemistry was measured; however, it was typical of the particle chemistries and sources observed during SOAR-1 [*Qin et al.*, 2009]. From July 30 to August 15, 2005, a strong diurnal pattern was observed for ozone, particle mass concentrations, and ambient meteorological conditions, as shown in Table 5.1 [*Qin et al.*, 2009]. On August 12th, the wind predominantly (~80% frequency) came from the west, crossing the LA basin en route to Riverside; during SOAR-2, westerly winds were observed ~50% of the sampling time, with winds from the southwest contributing ~45% of the time [*Qin et al.*, 2009].

An automated valve-controlled TD system [*Huffman et al.*, 2008] was utilized in series with the ATOFMS. In the fall only, a nafion dryer was used to dry the particles before the TD. In addition to water, the drying process may have removed some of the neutral amines and ammonium nitrate from the particle phase. However, the non-volatile aminium salts would not have been removed. Thus, the drying during the fall is not expected to impact the aminium salt mass present at 230°C. With continuous aerosol flow through the TD (heated) and bypass line (unheated), the particles sampled by the ATOFMS switched between heated and unheated ambient aerosol every 10 min. The heated portion of the TD stepped through 8 temperature steps: 171, 230, 201, 171, 142, 113, 83, and 54 °C; temperatures noted here refer to actual temperatures, rather than set-points [*Huffman et al.*, 2008]. Since each portion of the schedule was maintained for 10 min, one full cycle took 160 min before repeating. An activated carbon diffusion denuder

Table 5.1. Averages and standard deviations of ozone, ambient meteorological conditions, $PM_{2.5}$ mass concentrations (measured at the California Air Resources Board Rubidoux site), and $PM_{1.0}$ agedOC-nitrate-sulfate particle type mass concentrations for July 30 – August 15, 2005 compared to August 12, 2005 [*Qin et al.*, 2009].

	SOAR-1	
	July 30 - Aug. 15, 2005	**Aug. 12, 2005**
Ozone (ppb)	34.9 (33.3)	26.2 (26.0)
Relative humidity (%)	56.8 (19.2)	68.6 (18.5)
Ambient temperature (°C)	25.7 (5.3)	22.9 (4.6)
Wind speed (m/s)	0.9 (0.8)	0.9 (0.8)
Wind direction (deg.)	224 (66)	223 (62)
$PM_{2.5}$ mass concentrations (µm/m^3)	33 (13)	37 (18)
$PM_{1.0}$ agedOC-nitrate-sulfate particle type mass concentrations (µm/m^3)	6.1 (3.3)	7.0 (3.4)

prevented volatilized species from condensing back onto the particles. With a flow rate of 0.6 lpm, the residence time of the aerosol in the heating portion of the TD was approximately 9 s.

The ground-based prototype of the aircraft (A)-ATOFMS, described in detail in Chapter 2, was utilized to measure the vacuum aerodynamic diameter (d_{va}) and dual-polarity mass spectra of individual particles from ~70-1000 nm in real time. Particles were desorbed and ionized using 266 nm radiation from a Q-switched Nd:YAG laser; thus, one or two photon ionization would provide 4.7 or 9.4 eV, readily ionizing the alkylamines with lower ionization potentials (~7.5 eV) compared to most organic species (~8-12 eV) [*NIOSH*, 2007]. The use of lower laser powers can lead to decreased ion fragmentation [*Steele et al.*, 2003]; however, while a slightly lower average laser power was utilized in the fall (~0.6 mJ) compared to the summer (~0.95 mJ), the amine signature was not found to be impacted. Polystyrene latex spheres (PSLs) of known physical diameter from 95-1400 nm were used for the particle size calibration. Dual-polarity mass spectra were collected with the ATOFMS for 318,431 ambient particles on August 12, 2005 and 1,390,199 ambient particles from November 2-13, 2005. Data collection times were adjusted for delays in transport lines between the TD and ATOFMS, and data collected up to 20 seconds after the TD valve switch were eliminated to reduce error caused by possible aerosol mixing. Taking this delay into account, the mass spectra from 141,757 unheated and 119,888 heated particles were analyzed for August 12, and 717,705 unheated and 462,982 heated particles were analyzed for November 2-13.

For detailed analysis, single-particle mass spectra were imported into YAADA (www.yaada.org), a software toolkit for Matlab (The MathWorks, Inc.), for analysis. An adaptive resonance theory-based clustering method (ART-2a) [*Song et al.*, 1999] was then used to group single-particle mass spectra with a vigilance factor of 0.80, learning rate of 0.05, 20 iterations, and regrouping with a vigilance factor of 0.85. ART-2a classifies particles into separate clusters based on the presence and intensity of ion peaks in individual single-particle mass spectra. Peak identifications within this paper correspond to the most probable ions for a given *m/z* ratio. The ART-2a clusters resulting from the analysis of single SOAR unheated and heated particles (100-1000 nm) were classified into thirteen general particle types: aged organic carbon (mixed with ammonium, sulfate, and nitrate, herein referred to as the aged OC particle type), aromatic, amine, ammonium-rich, elemental carbon-organic carbon (ECOC), inorganic-ECOC, elemental carbon (EC), vanadium, biomass, aged sea salt, dust, metals, and nitrate-sulfate particles with no positive ions (NoPos). The size-resolved chemistry of the unheated particles is shown in Figure 5.1 for SOAR-1 (summer) and SOAR-2 (fall). It should be noted that the vast majority of unheated particles show evidence of organic carbon markers, nitrate, and sulfate due to aging during transport across the LA basin to Riverside [*Hughes et al.*, 2000]. Detailed descriptions of mass spectral, size, and temporal patterns of the majority of the unheated SOAR ATOFMS particle types are described elsewhere [*Qin et al.*, 2009]. Herein, we focus on the aged OC (nitrate-sulfate) particle type, described below.

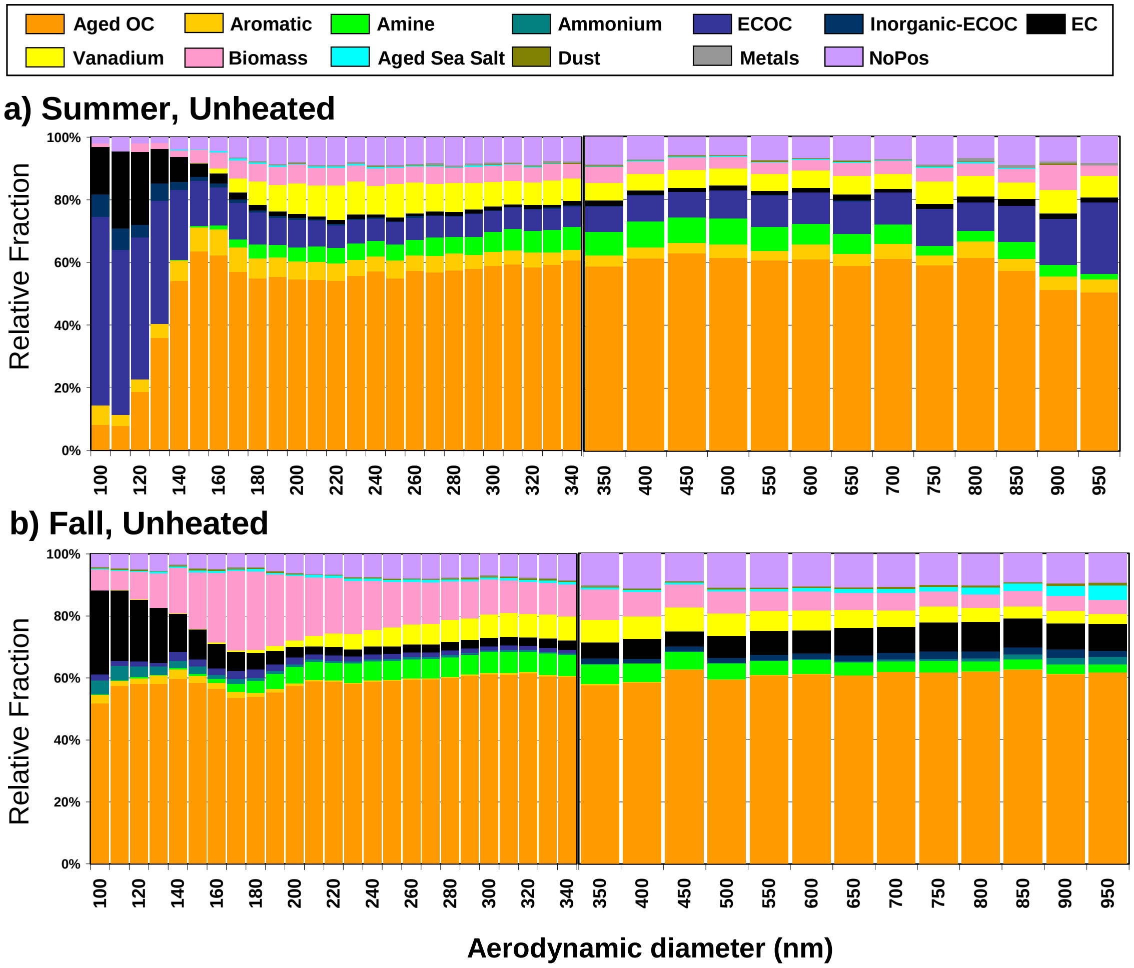

Figure 5.1. Size-resolved chemical composition of unheated particles during (a) SOAR-1 (summer) and (b) SOAR-2 (fall). Size resolution is 10 nm and 50 nm for the ranges of 100-350 nm and 350-1000 nm, respectively. The majority of the particles greater than ~150 nm show evidence of internally mixed organic carbon, ammonium, nitrate, and sulfate.

5.3.2 Amine Mass Calibration

To determine the mass of amines present in the submicrometer aged OC (nitrate-sulfate) particle type during SOAR, triethylamine vapor was coated onto PSLs, which serve as proxies for the SOAR OC particle matrix. A schematic of the experimental setup is shown in Figure 5.2. An aqueous (milli-Q water) solution of 270 nm PSLs (Invitrogen Corp.) was atomized using filtered ambient air at a flow rate of 3.0 L·min^{-1}. The PSLs were dried using two silica gel diffusion dryers and the flow subsequently split between exhaust (1.0 L·min^{-1}) and a differential mobility analyzer (DMA, TSI, Inc., Model 3081, sample flow = 2.0 L·min^{-1}, sheath flow = 5.0 L·min^{-1}) to narrow the particle distribution. The size-selected PSLs were passed through a dilution chamber where supplemental filtered ambient air was added (0.2 L·min^{-1}), followed by introduction into a glass mixing chamber (~ 20 L, residence time ~10 min). To initiate coating, gas phase precursors were introduced by placing liquid reservoirs directly within the reaction chamber; the headspace over these reservoirs acted as the vapor source. In the initial experiment, aiming to condense amine salts onto the PSL seed, two flasks each containing ~2mL of either TEA (Acros Organics, 99+%) or nitric acid (Sigma-Aldrich, 99.999+%) were quickly (<1 min) placed directly into the chamber. During this trial, extensive homogeneous nucleation was observed between TEA and nitric acid, overwhelming the PSL seeds (results not shown). To eliminate new particle formation, and partition TEA exclusively to PSLs, a second experiment was performed in which TEA only was coated onto PSLs. The chamber output flowed through two inline activated carbon denuders spiked with sodium carbonate and boric acid, respectively, to remove any gaseous reactants prior to parallel analysis by a scanning mobility particle

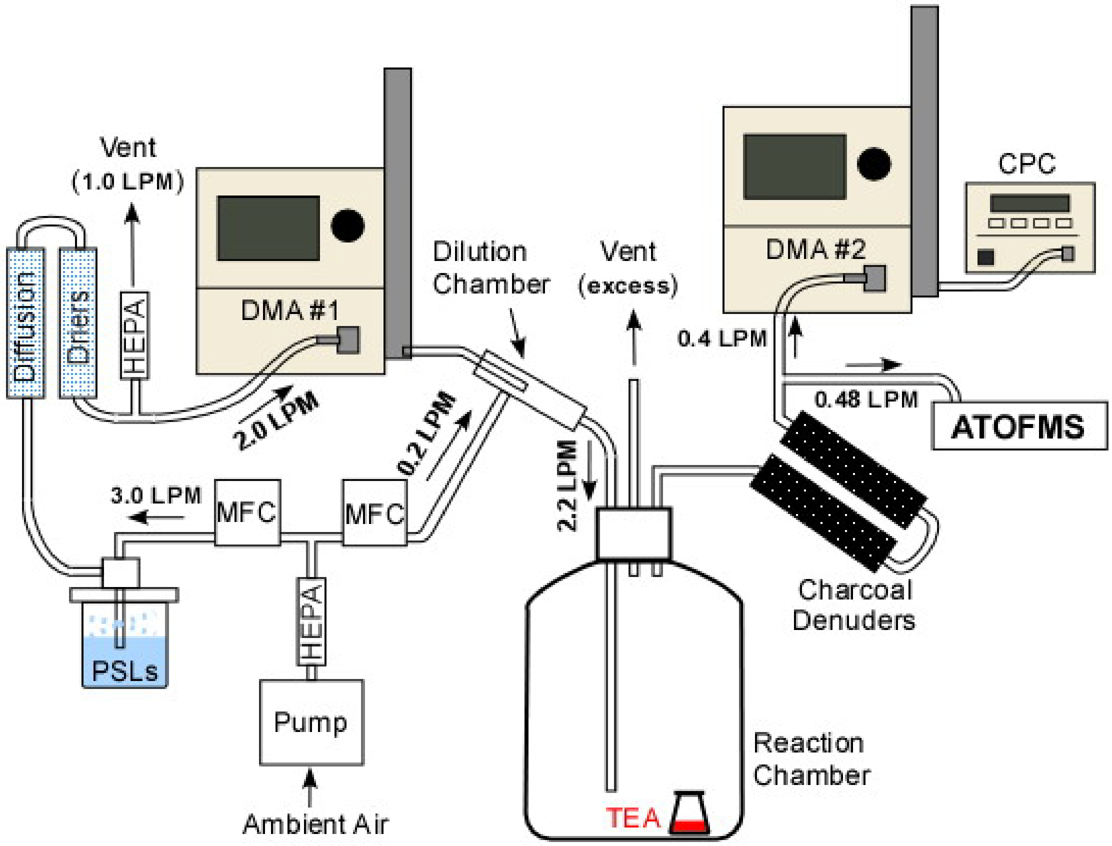

Figure 5.2. Amine mass calibration experimental set-up (MFC = mass flow controller; TEA = triethylamine; DMA = differential mobility analyzer; CPC = condensation particle counter; ATOFMS = aerosol time-of-flight mass spectrometer).

sizer (SMPS, TSI, Inc., DMA model 3081 – 0.4/4.0 LPM; CPC Model 3010) to monitor the particle size distribution and A-ATOFMS to obtain the single particle mass spectra and vacuum aerodynamic diameter (D_{va}). Background SMPS scans were obtained prior to addition of PSLs to confirm that the system was free of particle contamination; SMPS scans of uncoated PSLs were made to ensure a monodisperse seed aerosol distribution. Representative SMPS and ATOFMS size distributions of the uncoated and TEA-coated PSLs are shown in Figure 5.3.

The single particle mass spectra for uncoated and TEA-coated PSLs were imported into MatLab (The MathWorks, Inc.) for analysis following the methods described for treating the SOAR data. The dominant cluster of uncoated PSLs was identified as the PSL mass spectral signature (Figure 5.4b); only the TEA-coated aerosols exhibiting this specific PSL fingerprint (Figure 5.4a) were used in subsequent analysis to ensure a realistic comparison between coated and uncoated particles. In the TEA-coated PSLs, an ion peak representative of TEA is present at *m/z* 86($(C_2H_5)_2NCH_2^+$). It should be noted that the potential exists for differences in the UV absorption and ionization efficiency between protonated (salt bound) and neutral TEA, which would impact the calibration parameters of these two species; however these effects were not characterized in this study.

The polydisperse TEA coated particles were divided into 2 nm D_{va} size bins from 274-302 nm; subsequently bins from 274-280 nm and 292-302 nm were merged due to low ATOFMS particle counts. The average D_{va} and mass spectrum were calculated for each size bin as described below. A trend was observed whereby the *m/z* 86 peak area increased with decreasing D_{va}, as shown in Figure 5.5. However, the SMPS scans of

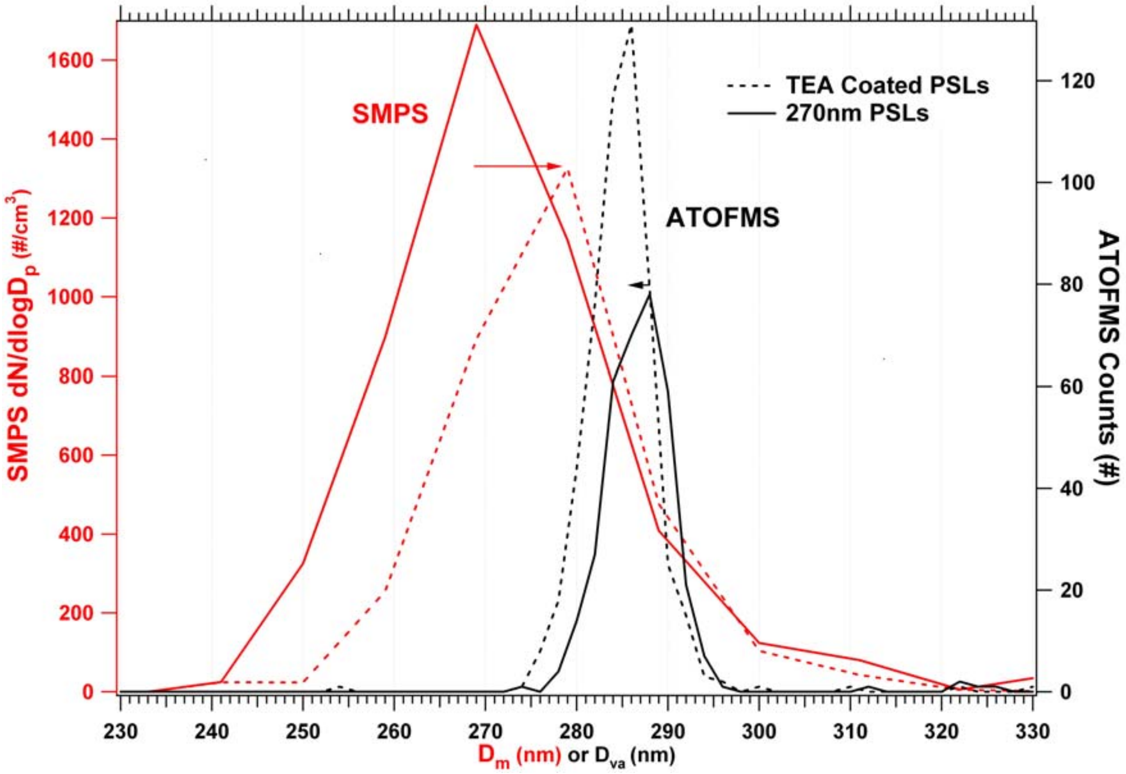

Figure 5.3. Size distributions of uncoated (solid) and TEA-coated (dashed) 270 nm PSLs. SMPS distributions of mobility diameter are shown in red; ATOFMS distributions of vacuum aerodynamic diameter are in black. The arrows indicate the shifts of the respective distributions.

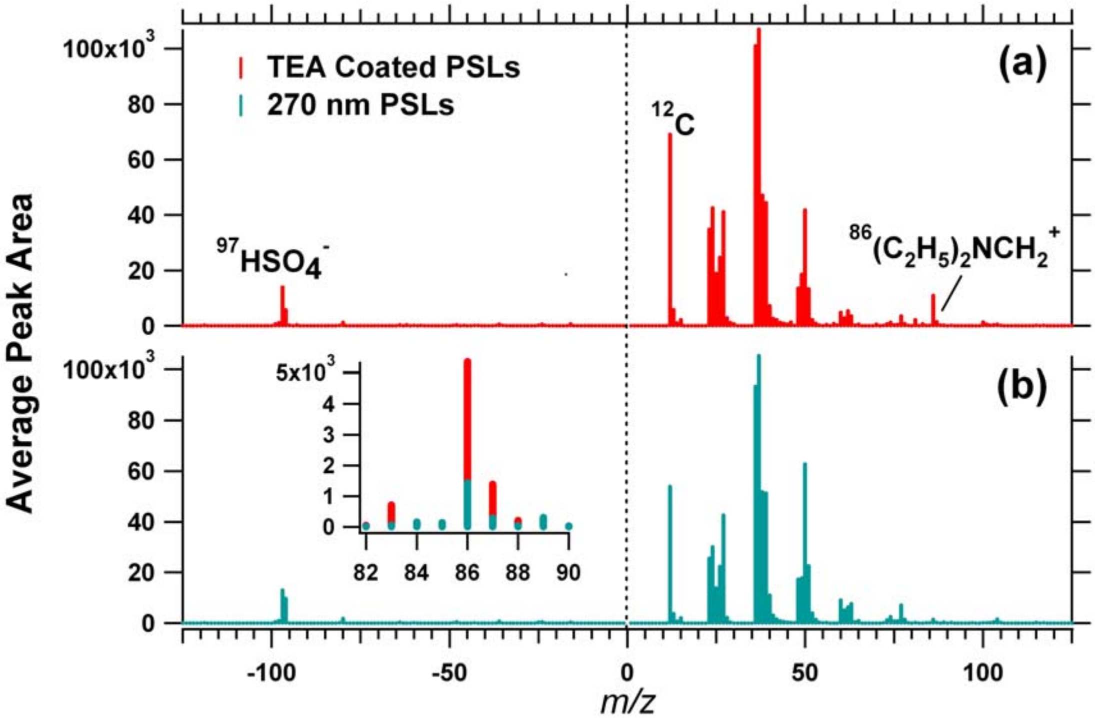

Figure 5.4. Average mass spectra of (a) PSLs coated with TEA and (b) uncoated 270 nm PSLs. The inset shows a comparison of the *m/z* 86 peak intensities.

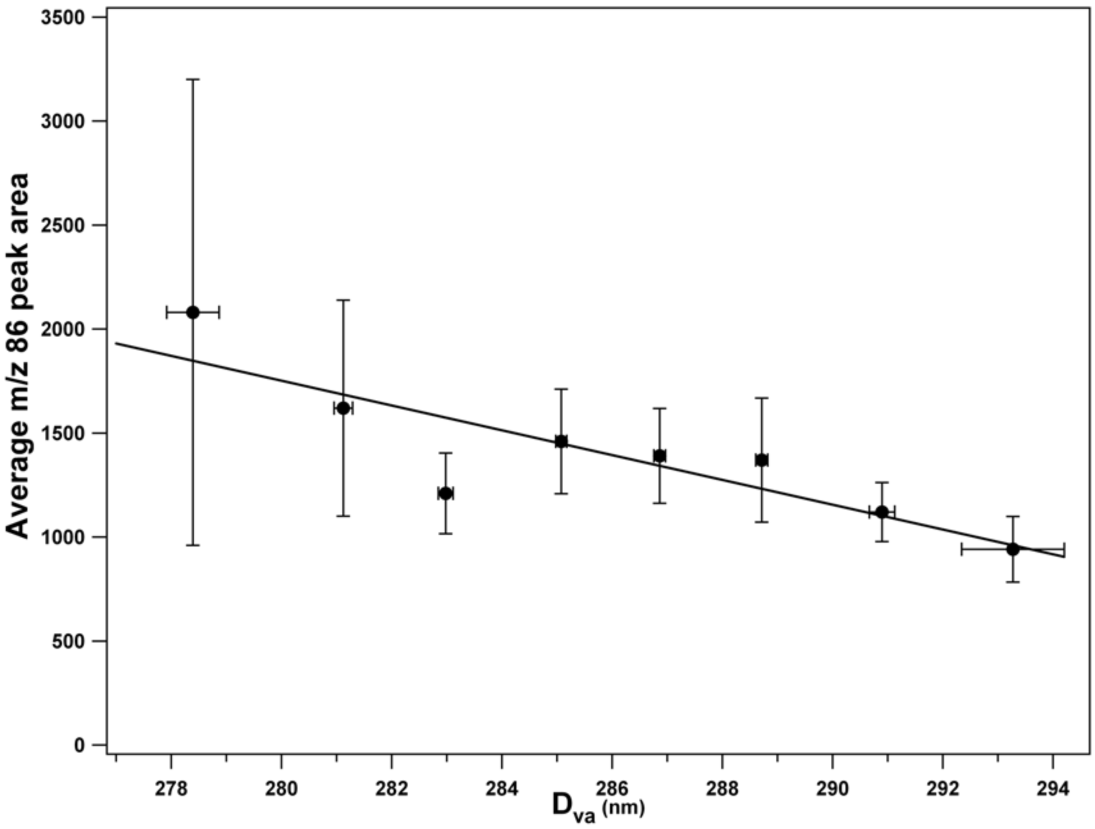

Figure 5.5. Absolute area of *m/z* 86 vs vacuum aerodynamic diameter for the TEA-coated PSLs.

TEA coated PSLs displayed a shift to larger mobility diameter D_m, consistent with an increase in particle volume upon coating. These observations and the following relationship between D_{va} and D_m [*DeCarlo et al.*, 2004]:

$$\rho_p = \frac{D_{va}}{D_m}\rho_0 \tag{3}$$

where ρ_p is the particle density and ρ_0 is the standard density (1 g/cm^3), indicate a decrease in particle density upon addition of TEA, consistent with the relative material densities of PSLs (1.05 g/cm^3) and TEA (0.75 g/cm^3). The particle density of TEA coated aerosols is therefore given by:

$$\rho_p = \frac{\rho_{PSL}V_{PSL} + \rho_{TEA}V_{TEA}}{V_p} \tag{4}$$

where V_p is the coated particle volume, which can be obtained from D_m, as this measurement is not influenced by particle density and the partitioning of TEA is not expected to alter the particle morphology of the spherical seed PSLs. Rearranging Equation 4 and substituting for ρ_p ultimately yields:

$$m_{TEA} = \rho_{TEA}V_{TEA} = {\pi}/{6}\,(D_m^2 \cdot D_{va} \cdot \rho_0 - D_{PSL}^3 \cdot \rho_{PSL}) \tag{5}$$

where m_{TEA} is the mass of TEA. The D_m values corresponding to each D_{va} bin were estimated by:

$$D_{m,equiv} = D_{va} - (\overline{D_{va}} - \overline{D_m}) - 2(D_{va} - \overline{D_{va}}) \tag{6}$$

where D_{va} represents the average vacuum aerodynamic diameter of a given size bin and $\overline{D_{va}}$ and $\overline{D_m}$ represent the mode diameters of the full ATOFMS and SMPS size distributions, respectively. The wide size bins (~10 nm) used in the SMPS scans precluded direct correlation to the 2nm D_{va} used in the ATOFMS data. Substituting these estimated D_m values into Equation 5 yields the average mass of TEA on individual particles within each size bin.

The corresponding peak area of the *m/z* 86 amine marker was then related to the calculated amine mass to generate a calibration curve (Figure 5.6). To account for detector sensitivity and voltage setting changes between 2005 and 2009, the total summed peak areas of the average mass spectra of uncoated 270 nm PSLs run on the A-ATOFMS during SOAR and this amine calibration experiment were compared, and the peak areas in this experiment were scaled to accommodate for any changes in overall mass spectral intensities. Finally, the calibration experiment data was fit using a linear regression forced through the origin and weighted by the standard deviation in *m/z* 86 peak area. The amine mass present in the aged OC particles in SOAR-1 and SOAR-2 was determined by inserting the average peak areas at each temperature into the calibration curve. All reported uncertainties represent the 95% confidence intervals. The errors associated with the derived ambient amine masses are primarily due to uncertainties in the amine calibration experiment; in general, the 95% confidence intervals associated with the average ambient *m/z* 86 peak area was less than ~6% of the value, with the exception of the low SOAR-2 areas at 201-230 ºC, where errors of 13-17% were observed.

The mass fraction of TEA was also calculated by ratioing the calculated TEA mass to the total particle mass, estimated from mean particle volume at each temperature (calculated from the mean particle vacuum aerodynamic diameter) and the aged OC particle effective density determined during SOAR-2 (1.38 ± 0.06 g/cm^3)

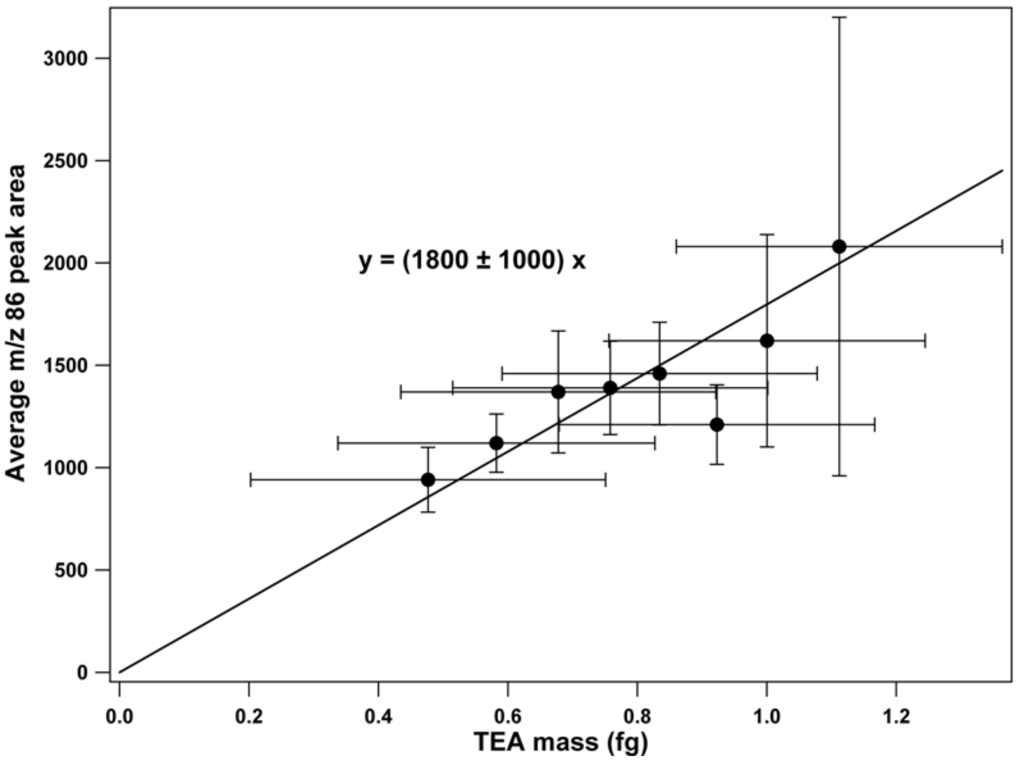

Figure 5.6. Absolute area of *m/z* 86 vs derived TEA mass for the TEA-coated PSLs.

[*Moffet et al.*, 2008]. The mass fraction of amines present as aminium salts within the SOAR aged OC (nitrate-sulfate) particles was calculated based on the mass of TEA present at 230°C. While a combination of nitrate and sulfate salts were present in the aged OC particles, the masses of aminium salts were calculated for three extremes: 100% H-TEA-NO_3, 100% H-TEA-HSO_4, and 100% $(H\text{-}TEA)_2SO_4$. Given the number of moles of TEA calculated to be present in the 230ºC and the molecular weights of the various aminium salts, the masses of aminium salts were estimated and compared to the calculated total particle masses of the unheated and 230°C heated particles. In this way, the mass fractions were estimated for a range of possible aminium salt species. To reduce error, average fractions of amines remaining at each temperature are based on *m/z* 86 absolute peak areas, a reasonable assumption considering the observed proportionality of *m/z* 86 peak area to mass.

5.4 Results and Discussion

Particles containing internally mixed organic carbon, ammonium, nitrate, and sulfate, herein referred to as the aged OC particle type, comprised ~60% by number of all particles across the entire size range from d_{va} ~150-1000 nm during SOAR-1 (summer) and SOAR-2 (fall) (see Figure 5.1). As shown in Figure 5.7, the unheated aged OC particle type was characterized by carbonaceous marker ions at *m/z* 12(C^+), 27($C_2H_3^+$/CHN^+), 36(C_3^+), 37(C_3H^+), and 43(CH_3CO^+/$CHNO^+$) [*Silva and Prather*, 2000], as well as ammonium (*m/z* 18, NH_4^+), nitrate (*m/z* -62, NO_3^-, and -125, $H(NO_3)_2^-$), and sulfate (*m/z* -97, HSO_4^-), all indicators of the aged nature of the Riverside aerosol [*Hughes et al.*, 2000]. These particles were also characterized by marker ions for

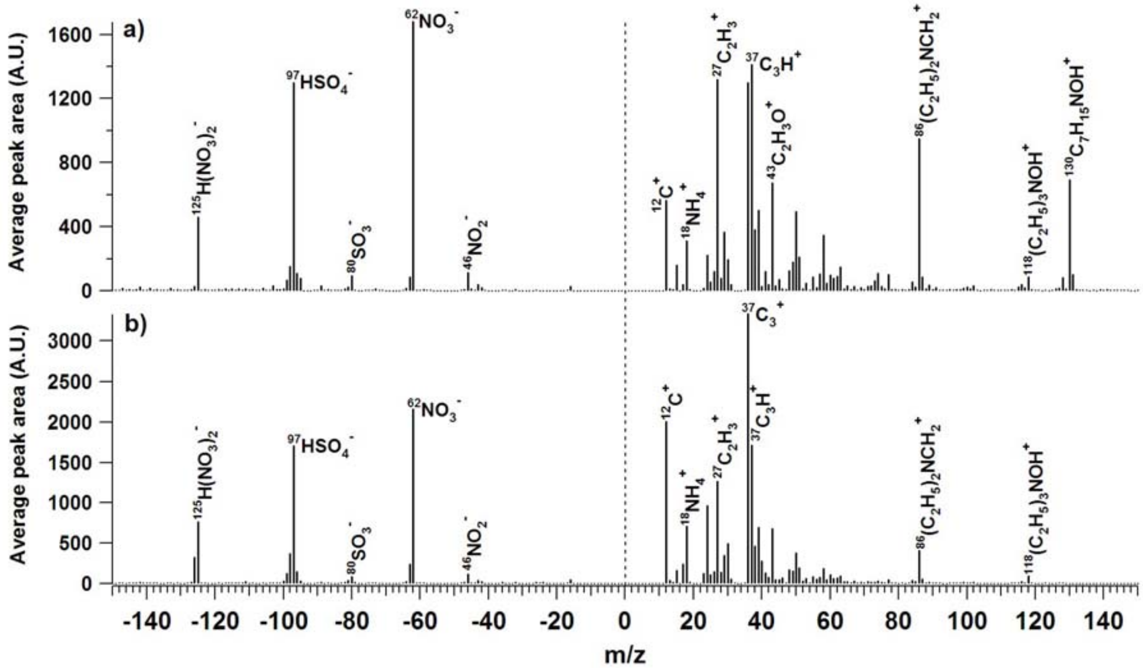

Figure 5.7. Average positive and negative mass spectra of the unheated aged OC (nitrate-sulfate) particles during (a) summer and (b) fall. Peak areas are reported in arbitrary units (A.U.).

alkylamines, *m/z* 86($(C_2H_5)_2NCH_2^+$) and 102($(C_2H_5)_3NH^+$), as well as oxidized amines, represented by *m/z* 118($(C_2H_5)_3NOH^+$) [*Angelino et al.*, 2001]. Previously, Angelino et al. [2001] found contributions of triethylamine and diethylamine to these marker ions; herein, *m/z* 86 is used as a general marker ion for the presence of amines. During SOAR-1, SOA was found to comprise ~45-90% of the total submicrometer organic mass depending on time of day (peak morning traffic vs. afternoon photochemical episodes) [*Docherty et al.*, 2008]; previous studies have shown lower SOA contributions in the fall due to lower photochemical activity [*Na et al.*, 2004]. In addition, oligomers (at *m/z* -200 to -400) were observed in approximately half of the unheated aged OC particles in both the summer and fall, although higher mass nonvolatile oligomers were detected in the summer [*Denkenberger et al.*, 2007].

In the summer, the presence of an intense peak at *m/z* 130, not observed in the fall, is proposed to be either an oxidized form of triethylamine or the $[MH]^+$ peak of N,N-diethylpropionamide ($C_7H_{15}NO$), which may be formed through the following dehydration reaction between propionic acid and diethylamine, observed as a small peak at *m/z* 58 $[MH]^+$ [*Angelino et al.*, 2001].

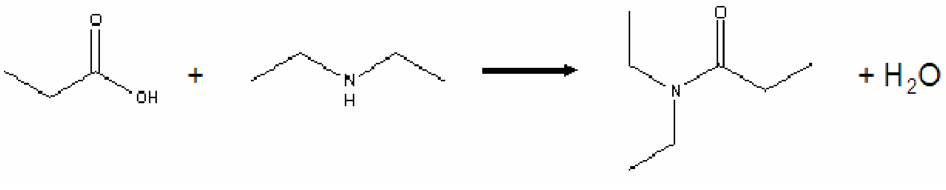

(7)

Propionic acid, the third most abundant gas phase organic acid in the LA basin, is formed primarily through secondary photochemical reactions and reaches its highest concentrations during summer smog episodes in the eastern LA basin [*Kawamura et al.*, 2000; *Nolte et al.*, 1999]. Particle phase amide formation has been suggested to be significant in the polluted, ozone-rich troposphere [*Zahardis et al.*, 2008]. With a calculated vapor pressure of 0.444 Torr at 25°C, N,N-diethylpropionamide is significantly less volatile than it's parent compound diethylamine with a calculated vapor pressure of 218 Torr (25°C) [*Advanced Chemistry Development*, 2006]; likewise, *m/z* 130 does not vaporize from the particle phase with heating to 230°C. The peak at *m/z* 130 has been also been observed in chamber experiments conducted during July 2006, probing the gas-to-particle partitioning of TEA via homogeneous reaction with nitric acid (Figure 5.8), similar to the experiment completed by Angelino et al. [2001]. The experimental setup was similar to that described above for the amine coating experiments with the following key differences: (1) the atomizer and diffusion dryers were not used as a seed aerosol was not provided; (2) the flow rate of filtered ambient air into the chamber was 4.0 $L \cdot min^{-1}$, providing shorter residence time; (3) the chamber contained two flasks containing nitric acid and TEA. In previous chamber experiments by Angelino et al. [*Angelino et al.*, 2001], amine oxidation products were also observed due to gas-phase oxidants present in the filtered air utilized.

To probe the specific associations between amines, ammonium, nitrate, and sulfate within the SOAR aged OC particles, ternary plots of the relative distributions of the peak areas of ammonium (*m/z* 18), amines represented by *m/z* 86, nitrate (*m/z* -62), and sulfate (*m/z* -97) at different temperatures for individual aged OC particles are shown in Figure 5.9. The relative amounts and associations of either nitrate (a,c) or sulfate (b,d) with amines and ammonium are displayed for both seasons. A particle containing primarily amines relative to ammonium, nitrate, and sulfate would appear at the top vertex, primarily ammonium at the right vertex, and nitrate or sulfate would appear at the

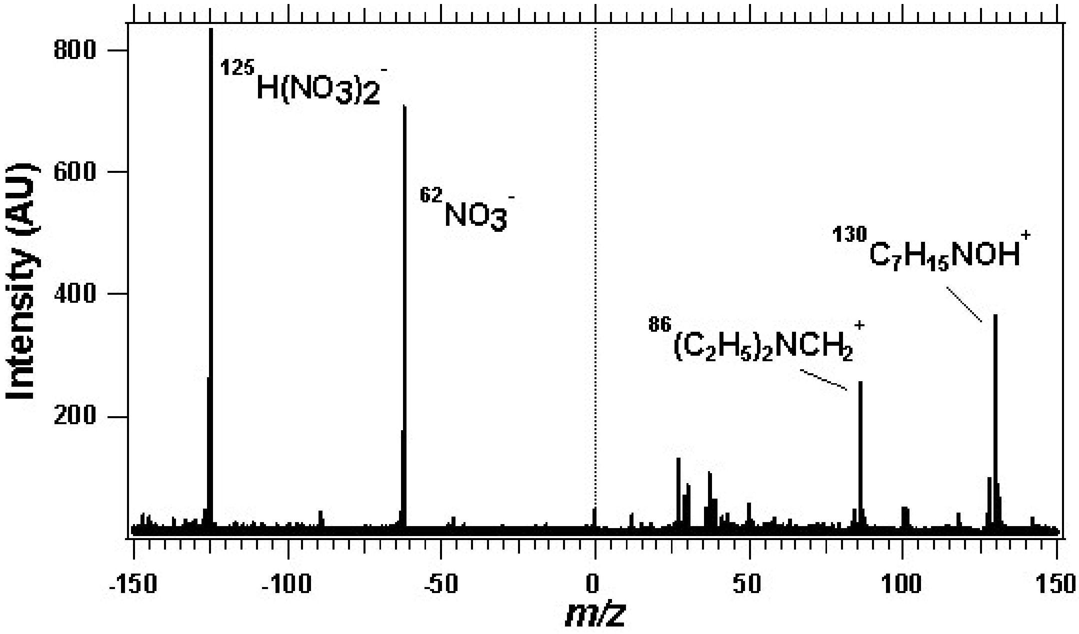

Figure 5.8. Positive and negative mass spectra of a single particle exhibiting *m/z* 130 measured during TEA-nitric acid chamber experiments.

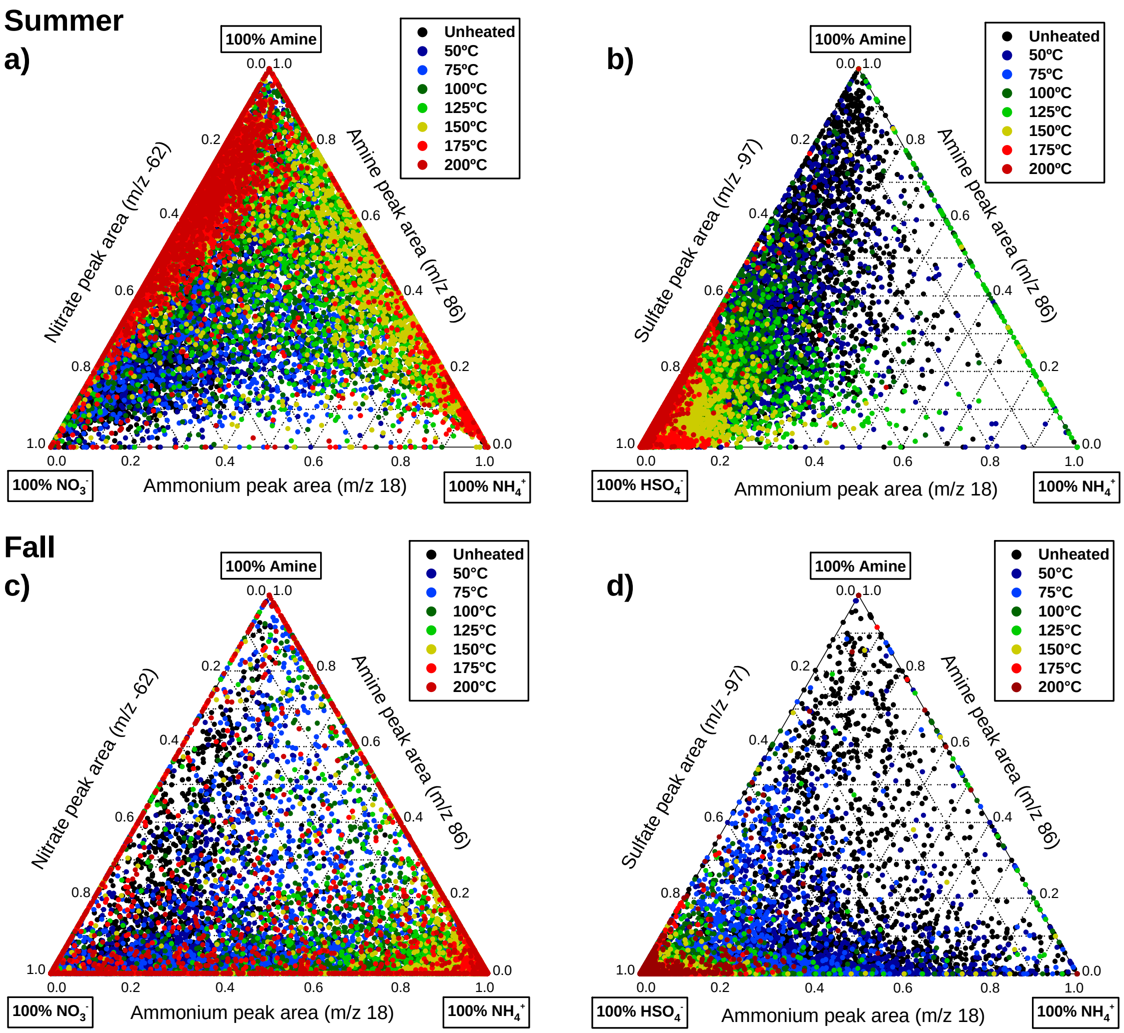

Figure 5.9. Summer (a,b) and fall (c,d) ternary plots show the relative distributions of peak areas of ammonium (*m/z* 18 (NH_4^+)), amines (*m/z* 86 ($(C_2H_5)_2NCH_2^+$)), nitrate (*m/z* -62 (NO_3^-)), and sulfate (*m/z* -97 (HSO_4^-)) for the unheated and heated (54-230°C) aged OC (nitrate-sulfate) particles. Random samples of ~2,000 single particles are plotted for each temperature.

left vertex. In the summer, the particles are distributed along the amine-nitrate and amine-sulfate axes, suggesting nitrate and sulfate are more strongly associated with amines compared to ammonium. This strong correlation between amines and nitrate and sulfate at 230 °C in the summer supports the presence of aminium nitrate and sulfate salts which are non-volatile, as predicted by Pankow [2003]. However, in the fall, the unheated particles are distributed primarily along the ammonium-nitrate and ammonium-sulfate axes, suggesting nitrate and sulfate are more strongly associated with ammonium compared to amines. The lack of aminium salts in the fall is because the particles were neutralized and hence the unbound amines were readily volatilized at temperatures below 113 °C, as discussed below. Ammonium and nitrate volatilized at temperatures less than 113 °C, consistent with previously reported volatilization temperature (~48-89 °C) [*Johnson et al.*, 2004]. Thus, in the summer, aminium nitrate and aminium sulfate remained in the particles at 230 °C, compared to primarily ammonium sulfate in the fall.

To calculate the relative fraction of amines remaining at each TD temperature, the average absolute peak area of *m/z* 86($(C_2H_5)_2NCH_2^+$) at each temperature was divided by that observed for the unheated aged OC particles (Figure 5.10a). Next, to quantitatively assess the contribution of amines to particle mass, the average amine mass in the aged OC particle type (Figure 5.10b) was determined using a triethylamine mass/peak area calibration curve derived from the amine mass calibration experiment. Using the average vacuum aerodynamic diameter measured for the aged OC particle type at each TD temperature, the average mass fraction of amines per particle was calculated (Figure 5.10c). For the SOAR unheated aged OC particles, approximately twice as much amine mass was present in the summer (0.5 ± 0.3 fg/particle; 1.7 ± 0.9%) compared to the fall

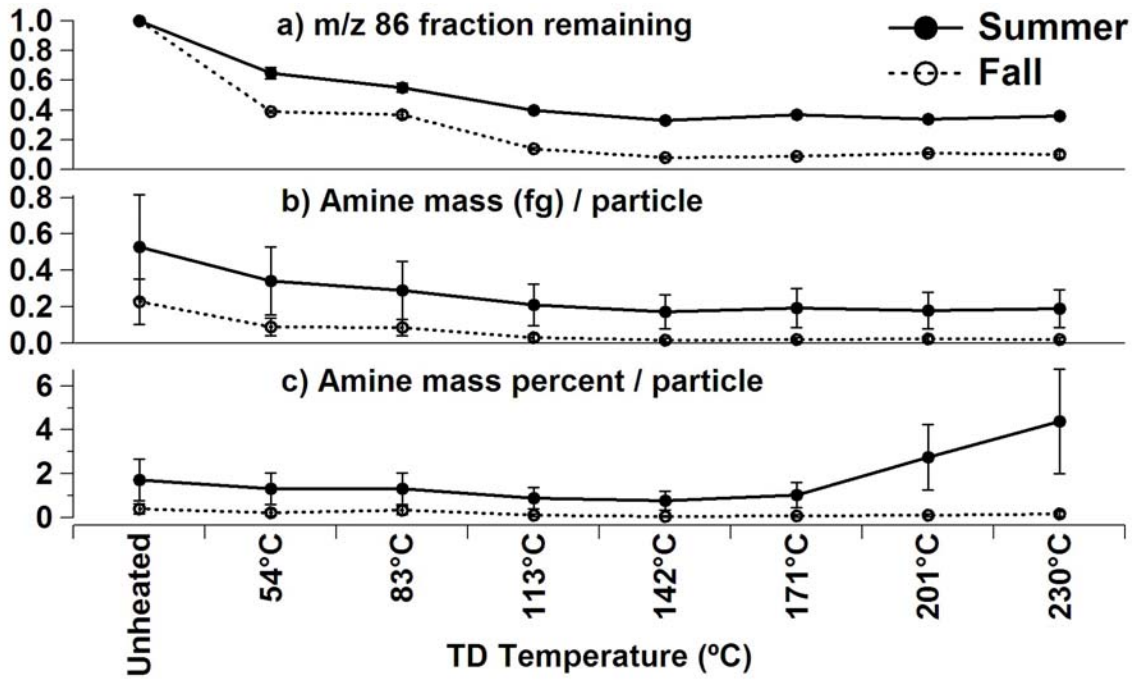

Figure 5.10. For aged OC (nitrate-sulfate) particles, the (a) fraction of *m/z* 86 peak area remaining over the range of thermodenuder temperatures from 54-230 °C is shown relative to the unheated particles (ambient temperature averages of 22.9 °C and 15.6 °C in the summer and fall, respectively). In addition, the (b) amine mass/particle and (c) amine mass percent/particle are shown for each temperature.

(0.2 ± 0.1 fg/particle; 0.4 ± 0.2%). During both the summer and fall, the amine mass/particle decreased with increasing temperature to 113 °C and then stabilized at ~0.2 ± 0.1 fg/particle and less than 0.1 fg/particle, respectively. These results are consistent with the vaporization of neutral diethylamine and triethylamine up to ~113 °C (boiling points of 57.3 ± 8.0 °C and 90.5 ± 8.0 °C, respectively [*Advanced Chemistry Development,* 2009]). The amines remaining above 113 °C must be in the form of aminium salts. Consistent with the association of amines with nitrate and sulfate in the summer, 36 ± 1% of the amines present at ambient temperature remained in the aged OC particle type at 230 °C in the summer. However, in the fall, only 10 ± 2% of the amines remained at 230 °C, consistent with the decreased abundance of aminium salts due to high levels of ammonium in the particles, as discussed below. Similarly, in the summer, a greater fraction (13 ± 1%) of nitrate remained at 230 °C compared to the fall (4 ± 1%) (Figure 5.11), consistent with more aminium nitrate salts present in the summer compared to the fall. However, as shown in Figure 5.9, a higher fraction of aminium salts was in the form of aminium sulfate, compared to aminium nitrate; this is likely due to the fact that sulfuric acid is a stronger acid than nitric acid (pKa -3.19 ± 0.15 vs. -1.4, respectively) [*Advanced Chemistry Development,* 2009]. At 230 °C, amines represented 4 ± 2% by mass/particle in the summer, compared to only 0.2 ± 0.1% by mass/particle in the fall. The increasing amine mass fraction above 171 °C in the summer was due to the volatilization of other species leaving behind primarily aminium salts and ammonium sulfate; whereas, in the fall, the amine mass fraction did not increase with temperature due to the minor contribution of aminium salts. Considering the potential nitrate, bisulfate, and sulfate salts of triethylamine, the aminium salt mass fraction at 230 °C in

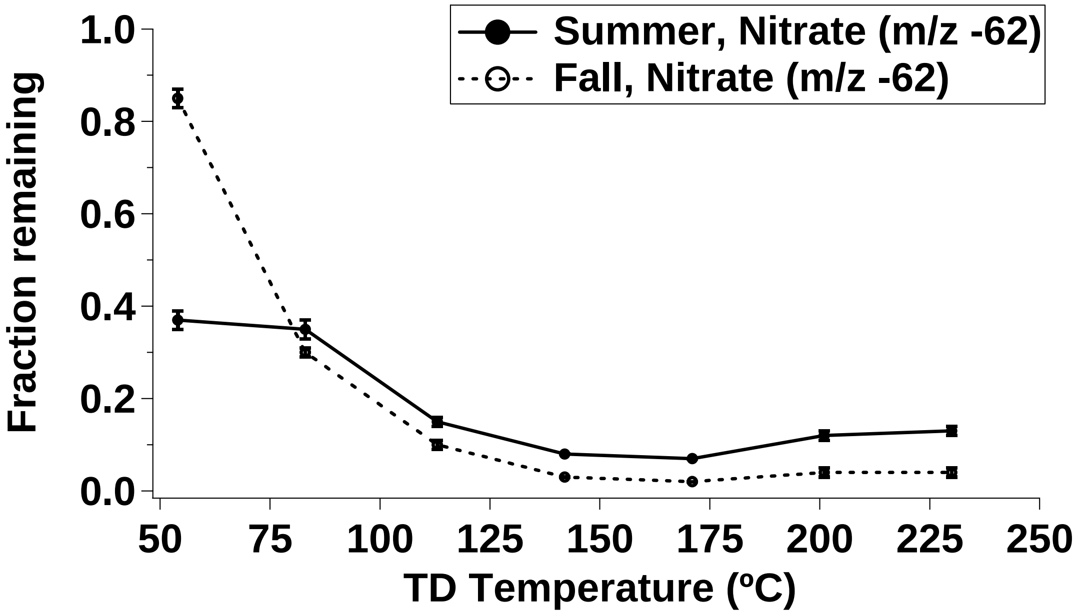

Figure 5.11. Relative fractions of nitrate (*m/z* -62 (NO_3^-)) remaining on the aged OC (nitrate-sulfate) particles at each TD temperature during SOAR-1 and SOAR-2.

the aged OC (nitrate-sulfate) particles was estimated at ~6-9% in the summer compared to less than 1% in the fall. In the unheated particles, aminium nitrate and sulfate salts were found to contribute ~1% and ~0.6% to the total particle mass in the summer.

Although not the focus of this Chapter, an amine-dominant particle type, comprised ~5-8% by number of the particles ~200-700 nm in diameter during both SOAR-1 and SOAR-2. The mass spectra were dominated by *m/z* 86($(C_2H_5)_2NCH_2^+$) with less intense amine marker ions at *m/z* 58($C_2H_5NHCH_2^+$), 102($(C_2H_5)_3NH^+$), and 118($(C_2H_5)_3NOH^+$) [*Angelino et al.*, 2001]; nitrate and sulfate were observed in the negative ions. Using the calibration curve derived herein, these unheated particles were found to be 18 ± 10% and 12 ± 6% amine by mass fraction during the summer and fall, respectively. However, as discussed in Chapter 4, the amine-dominant particle type nearly disappears at ~113 °C, consistent with the volatilization of neutral amines and the reclassification of the particles within the aged OC type. This is shown by the amine mass/particle decreasing from 7 ± 4 fg/particle at ambient temperature to 4 ± 3 fg/particle at 113 °C in these amine-dominant particles in the summer; likewise, in the fall, the amine-dominant particles contain 6 ± 3 fg amines/particle at ambient temperature and 2 ± 1 fg amines/particle at 113 °C.

Several possible explanations exist for higher amine mass concentrations in the unheated aged OC particle type in the summer compared to the fall. Ammonia has a higher vapor pressure (5990 Torr at 25 °C) than triethylamine and diethylamine (56.1 and 218 Torr at 25 °C, respectively) [*Advanced Chemistry Development,* 2009]. During the summer, higher ambient temperatures were observed (17.6-30.9 °C with a mean of 22.9 °C) compared to the fall (8.4-26.1 °C with a mean of 15.6 °C). While ammonia and amines are emitted from the same sources [*Schade and Crutzen*, 1995; *Sorooshian et al.*, 2008], primarily the Chino dairy area to the west of Riverside, their differing vapor pressures impact initial volatilization at the source during the different seasons, likely causing more ammonia and amines to be present in the vapor phase in the summer [*Stelson and Seinfeld*, 1982]; however, gas-phase concentrations of these species during SOAR were not measured. The lower vapor pressure of the amines compared to ammonia allowed them to more readily partition to the particle phase in the summer at the higher ambient temperatures observed; however, the particle-phase chemistry impacted the protonation and gas/particle partitioning of the amines once in the particle phase. At the lower fall ambient temperatures, ammonia competes with amines to form ammonium nitrate and ammonium sulfate/bisulfate [*Barsanti et al.*, 2009] which is supported by the greater particle phase ammonium concentrations (2.30 ± 0.04 times) observed in the aged OC particle type in the fall compared to the summer. This observation is consistent with previous studies showing higher concentrations of ammonium nitrate in the eastern LA basin in the fall (up to ~50% of the fine aerosol mass) [*Hughes et al.*, 2002; *Kim et al.*, 2000]. Thermodynamic calculations have shown that increasing ammonia/amine gas-phase ratios from 100 ppt/10 ppt to 1000 ppt/1 ppt led to lower predicted fractions of protonated amines in aqueous nanometer-sized particles (60.5% vs. 1.5%) [*Barsanti et al.*, 2009]. In addition to gas-phase concentrations, Henry's Law constants (K_H) and acid dissociation constants (pK_a) must be considered in the prediction of the partitioning of amines relative to ammonia [*Barsanti et al.*, 2009]. Triethylamine is a stronger base than ammonia (pK_a 10.62 ± 0.25 vs. 9.24 ± 0.10) [*Advanced Chemistry Development*, 2009] and has a Henry's Law constant of similar magnitude (K_H 29 M atm^{-1} vs 62 M atm^{-1}) [*Barsanti et al.*, 2009], allowing the amines to compete for protons even when at lower concentrations.

In acidic particles, amines will become protonated and remain in the particle phase, forming aminium salts [*Barsanti et al.*, 2009; *Pankow*, 2003]; thus one expects to see seasonal differences in the partitioning of amines due to changes in particle acidity. In the summer, the aged OC particles were more acidic, as shown by a more intense (1.39 ± 0.04 times) sulfuric acid cluster ion peak at *m/z* -195 ($H_2SO_4HSO_4^-$), a proxy of non-neutralized sulfate and particle acidity. In addition, higher oxalate (*m/z* -89($COOHCOO^-$)) ion peak areas (1.62 ± 0.03 times) were observed in the summer compared to the fall, suggesting that, in addition to nitric and sulfuric acid, organic acids could also form aminium salts, as suggested by Smith et al. [2008] and Barsanti et al. [2009]. While oxalic acid, for example, has a higher pK_a than nitric acid (1.38 ± 0.54 vs -1.4) [*Advanced Chemistry Development*, 2009], it has a substantially lower vapor pressure (2.51 x 10^{-6} Torr vs 49.8 Torr) [*Advanced Chemistry Development,* 2009], allowing it to partition more readily to the particle phase to form aminium organic salts. Due to the increased particle acidity in the summer, a higher amine fraction is believed to be protonated, leading to increased concentrations of aminium salts in the summer compared to the fall, as observed. Further, we hypothesize that the higher atmospheric water content in the summer (15.9-20.5 mMol/Mol with a mean of 18.9 mMol/Mol) compared to the fall (5.5-16.5 mMol/Mol with a mean of 12.6 mMol/Mol) caused more aminium salts to dissolve within the particle phase, causing an equilibrium shift of the amines from the gas to the particle phase [*Angelino et al.*, 2001]. This equilibrium shift would further explain the higher amine mass concentrations in the unheated aged OC particles in the summer compared to the fall. In this way, aminium salts may contribute to aerosol growth, as suggested by Barsanti et al. [2009].

Generally, pH is estimated using an ion balance of ammonium with nitrate and sulfate. However, previous studies have shown differences in calculated and measured pH for submicrometer aerosols [*Yao et al.*, 2007]. Based on the relatively significant contribution of amines shown during this study, it is recommended that particle acidity calculations take into account the presence of amines which act as even stronger bases than ammonia in atmospheric aerosols. Thus, for the aged OC (nitrate-sulfate) particles in this study, the particles would be predicted to be more acidic than in actuality based on only ammonium, sulfate, and nitrate concentrations. To illustrate this point, relative acidity ratios are calculated for the SOAR-1 and SOAR-2 aged OC particles; defined as the sum of the absolute average peak areas of nitrate (*m/z* -62 (NO_3^-)) and sulfate (*m/z* -97(HSO_4^-)) divided by ammonium (*m/z* 18(NH_4^+)) (i.e., the typical ion balance method used for calculating pH) or the sum of ammonium and amines (*m/z* 86($(C_2H_5)_2N{=}CH_2^+$)). These resulting ratios are shown in Figure 5.12. In the summer, the relative acidity ratio is overpredicted by a factor of 4 when amines are not taken into consideration, showing the significant role of amines as bases in the summer. In the fall, the addition of amines to the relative acidity ratio does not change the value dramatically (factor of 1.6) when ammonium is the dominant base.

These measurements represent the first quantification of the volatility behavior and mass contribution of amines to individual aged atmospheric particles. During SOAR, the partitioning of amines between the gas and particle phases depended strongly on particle acidity. The more acidic particles in the summer resulted in protonation of the

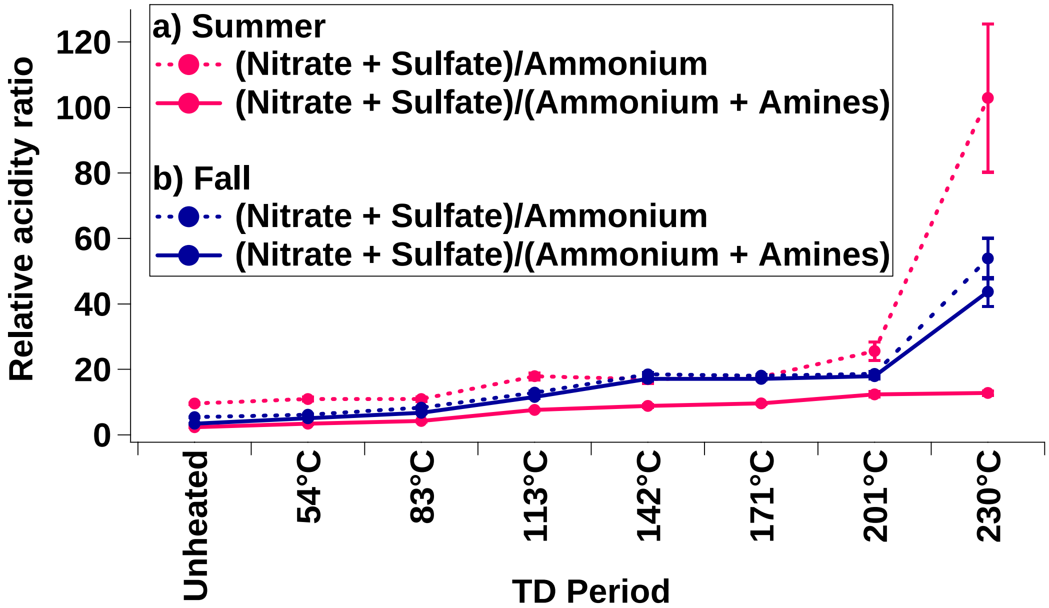

Figure 5.12. Relative acidity ratios for summer and fall for each thermodenuder period (unheated, 54°C, 83°C, 113°C, 142°C, 171°C, 201°C, 230°C) for the aged OC (nitrate-sulfate) particles. The ratios are defined as the sum of the absolute average peak areas of nitrate (*m/z* -62 (NO_3^-)) and sulfate (*m/z* -97 (HSO_4^-)) divided by ammonium (*m/z* 18 (NH_4^+)) or the sum of ammonium and amines (*m/z* 86 ($(C_2H_5)_2NCH_2^+$)).

amines, causing the formation of aminium sulfate and nitrate salts, which did not volatilize at temperatures up to 230 °C. These amine salts represent low-volatility organic carbon species that could potentially be missed by thermal analysis methods. In the fall, higher particulate ammonium concentrations and more basic particle cores produced fewer aminium salts, causing 86 ± 1% of the amines to volatilize below 113 °C. The abundance of organic carbon mixed with amine salts, as observed in this study, may form a barrier that prevents the salts from remaining at equilibrium with the gas phase [*Murphy et al.*, 2007]. Previous chamber studies have found aminium nitrate salts repartition back to the gas phase under low RH conditions (<10%) [*Murphy et al.*, 2007]; however, under the conditions of this study, this revolatilization process did not occur because the presence of water caused the aminium salts to dissolve, shifting the equilibrium of the gas-phase amines toward the particle phase. Further, previous chamber studies have not examined the partitioning of the amine salts with respect to pH, shown in this SOAR data to be a critical parameter affecting gas/particle partitioning. Laboratory studies of the competition between ammonia and different amine species for sulfuric, nitric, and organic acids, as a function of temperature, RH, and particle size, and the relative abundance of amines and ammonia are planned to further understand the partitioning of amines in the atmosphere. Further, it is important to note that the average bulk pH of a collection of ambient particles may in fact not be representative of the pH of any individual particle; thus, the single-particle mixing state of atmospheric aerosols must be used as a measure of pH to fully understand the partitioning of semivolatile species such as amines in gas/particle partitioning processes.

5.5 Acknowledgements

This work was supported by the National Science Foundation (NSF ATM-0321362) and the California Air Resources Board (CARB 04-336). Together Lindsay Hatch, supported by an NSF graduate research fellowship, and I completed the amine mass calibration; Lindsay wrote the amine mass calibration method portion of this Chapter and contributed to discussions of the data. Prof. Paul Ziemann (UC-Riverside), Ken Docherty (CU-Boulder), the UC Riverside Air Pollution Research Center, and the Prather Group, particularly Gary Poon, Xueying Qin, Laura Shields, and Stephen Toner, provided support during SOAR. Alex Huffman (CU Boulder) and Prof. Jose Jimenez provided and ran the TD system, developed under EPA sponsorship (STAR R831080). Megan McKay and the Goldstein group (UC-Berkeley) provided the atmospheric water content and ambient temperature data. The California Air Resources Board provided $PM_{2.5}$ mass concentrations for the Rubidoux site.

Publication Acknowledgment

Chapter 5 has been reproduced with permission from the American Chemical Society: Pratt, K.A., Hatch, L.E., Prather, K.A. Seasonal volatility dependence of ambient particle phase amines. *Environmental Science & Technol*ogy, 2009, In Press.

5.6 References

Calculated using Advanced Chemistry Development (ACD/Labs) Software V8.14 for Solaris, SciFinder Scholar, American Chemical Society, 2006.

NIOSH Pocket Guide to Chemical Hazards, Department of Health and Human Services, Centers for Disease Control and Prevention, National Institute for Occupational Safety and Heath, 2007.

Calculated using Advanced Chemistry Development (ACD/Labs) Software V8.14 for Solaris, SciFinder Scholar, American Chemical Society, 2009.

Angelino, S., D.T. Suess, and K.A. Prather (2001), Formation of aerosol particles from reactions of secondary and tertiary alkylamines: Characterization by aerosol time-of-flight mass spectrometry, *Environ. Sci. Technol.*, *35*(15), 3130-3138.

Barsanti, K.C., P.H. McMurry, and J.N. Smith (2009), The potential contribution of organic salts to new particle growth, *Atmos. Chem. Phys.*, *9*(2949-2957.

Burtscher, H., U. Baltensperger, N. Bukowiecki, P. Cohn, C. Hüglin, M. Mohr, U. Matter, S. Nyeki, V. Schmatloch, N. Streit, and E. Weingartner (2001), Separation of volatile and non-volatile aerosol fractions by thermodesorption: instrumental development and applications, *J. Aerosol Sci.*, *32*(427-442.

DeCarlo, P.F., J.G. Slowik, D.R. Worsnop, P. Davidovits, and J.L. Jimenez (2004), Particle morphology and density characterization by combined mobility and aerodynamic diameter measurements. Part 1: Theory, *Aerosol Sci. Technol.*, *38*(12), 1185-1205.

Denkenberger, K.A., R.C. Moffet, J.C. Holecek, T.P. Rebotier, and K.A. Prather (2007), Real-time, single-particle measurements of oligomers in aged ambient aerosol particles, *Environ. Sci. Technol.*, *41*(5439-5446.

Docherty, K.S., E.A. Stone, I.M. Ulbrich, P.F. DeCarlo, D.C. Snyder, J.J. Schauer, R.E. Peltier, R.J. Weber, S.M. Murphy, J.H. Seinfeld, B.D. Grover, D.J. Eatough, and J.L. Jimenez (2008), Apportionment of primary and secondary organic aerosols in southern California during the 2005 Study of Organic Aerosols in Riverside (SOAR-1), *Environ. Sci. Technol.*, *42*(7655-7662.

Gronberg, L., P. Lovkvist, and J.A. Jonsson (1992), Measurement of aliphatic-amines in ambient air and rainwater, *Chemosphere*, *24*(10), 1533-1540.

Huffman, J.A., P.J. Ziemann, J.T. Jayne, D.R. Worsnop, and J.L. Jimenez (2008), Development and characterization of a fast-stepping/scanning thermodenuder for chemically-resolved aerosol volatility measurements, *Aerosol Sci. Technol.*, *42*(5), 395-407.

Hughes, L.S., J.O. Allen, P. Bhave, M.J. Kleeman, G.R. Cass, D.Y. Liu, D.F. Fergenson, B.D. Morrical, and K.A. Prather (2000), Evolution of atmospheric particles along trajectories crossing the Los Angeles basin, *Environ. Sci. Technol.*, *34*(15), 3058-3068.

Hughes, L.S., J.O. Allen, L.G. Salmon, P.R. Mayo, R.J. Johnson, and G.R. Cass (2002), Evolution of nitrogen species air pollutants along trajectories crossing the Los Angeles area, *Environ. Sci. Technol.*, *36*(18), 3928-3935.

Johnson, G., Z. Ristovski, and L. Morawska (2004), Application of the VH-TDMA technique to coastal ambient aerosols, *Geophys. Res. Lett.*, *31*(16).

Kanakidou, M., J.H. Seinfeld, S.N. Pandis, I. Barnes, F.J. Dentener, M.C. Facchini, R. Van Dingenen, B. Ervens, A. Nenes, C.J. Nielsen, E. Swietlicki, J.P. Putaud, Y. Balkanski, S. Fuzzi, J. Horth, G.K. Moortgat, R. Winterhalter, C.E.L. Myhre, K. Tsigaridis, E. Vignati, E.G. Stephanou, and J. Wilson (2005), Organic aerosol and global climate modelling: a review, *Atmos. Chem. Phys.*, *5,*(1053-1123.

Kawamura, K., S. Steinberg, and I.R. Kaplan (2000), Homologous series of C-1-C-10 monocarboxylic acids and C-1-C-6 carbonyls in Los Angeles air and motor vehicle exhausts, *Atmos. Environ.*, *34*(24), 4175-4191.

Kim, B.M., S. Teffera, and M.D. Zeldin (2000), Characterization of PM2.5 and PM10 in the South Coast Air Basin of southern California: Part 2 - Temporal variations, *J. Air Waste Manage. Assoc.*, *50*(12), 2045-2059.

McGregor, K.G., and C. Anastasio (2001), Chemistry of fog waters in California's Central Valley: 2. Photochemical transformations of amino acids and alkyl amines, *Atmos. Environ.*, *35*(6), 1091-1104.

Moffet, R.C., X. Qin, T. Rebotier, H. Furutani, and K.A. Prather (2008), Chemically segregated optical and microphysical properties of ambient aerosols measured in a single-particle mass spectrometer, *J. Geophys. Res.*, *113*(doi:10.1029/2007JD009393.

Murphy, S.M., A. Sorooshian, J.H. Kroll, N.L. Ng, P. Chhabra, C. Tong, J.D. Surratt, E. Knipping, R.C. Flagan, and J.H. Seinfeld (2007), Secondary aerosol formation from atmospheric reactions of aliphatic amines, *Atmos. Chem. Phys.*, *7*(9), 2313-2337.

Na, K.S., A.A. Sawant, C. Song, and D.R. Cocker (2004), Primary and secondary carbonaceous species in the atmosphere of Western Riverside County, California, *Atmos. Environ.*, *38*(9), 1345-1355.

Neff, J.C., E.A. Holland, F.J. Dentener, W.H. McDowell, and K.M. Russell (2002), The origin, composition and rates of organic nitrogen deposition: A missing piece of the nitrogen cycle? *Biogeochemistry*, *57*(1), 99-136.

Nolte, C.G., M.P. Fraser, and G.R. Cass (1999), Gas phase C-2-C-10 organic acids concentrations in the Los Angeles atmosphere, *Environ. Sci. Technol.*, *33*(4), 540-545.

Pankow, J.F. (2003), Gas/particle partitioning of neutral and ionizing compounds to single and multi-phase aerosol particles. 1. Unified modeling framework, *Atmos. Environ.*, *37*(24), 3323-3333.

Qin, X., L.G. Shields, S.M. Toner, K.A. Pratt, and K.A. Prather (2009), Seasonal comparisons of the single particle mixing state in Riverside, CA during the SOAR 2005 campaign, *Aerosol Sci. Technol.*, *In preparation.*(

Schade, G.W., and P.J. Crutzen (1995), Emission of aliphatic-amines from animal husbandry and their reactions - potential source of N2O and HCN, *J. Atmos. Chem.*, *22*(3), 319-346.

Silva, P.J., M.E. Erupe, D. Price, J. Elias, Q.G.J. Malloy, Q. Li, B. Warren, and D.R. Cocker (2008), Trimethylamine as precursor to secondary organic aerosol formation via nitrate radical reaction in the atmosphere, *Environ. Sci. Technol.*, *42*(13), 4689-4696.

Silva, P.J., and K.A. Prather (2000), Interpretation of mass spectra from organic compounds in aerosol time-of-flight mass spectrometry, *Anal. Chem.*, *72*(15), 3553-3562.

Smith, J.N., M.J. Dunn, T.M. VanReken, K. Iida, M.R. Stolzenburg, P.H. McMurry, and L.G. Huey (2008), Chemical composition of atmospheric nanoparticles formed from nucleation in Tecamac, Mexico: Evidence for an important role for organic species in nanoparticle growth, *Geophys. Res. Lett.*, *35*(L04808), doi:10.1029/2007GL032523.

Song, X.H., P.K. Hopke, D.P. Fergenson, and K.A. Prather (1999), Classification of single particles analyzed by ATOFMS using an artificial neural network, ART-2A, *Anal. Chem.*, *71*(4), 860-865.

Sorooshian, A., S.M. Murphy, S. Hersey, H. Gates, L.T. Padro, A. Nenes, F.J. Brechtel, H. Jonsson, R.C. Flagan, and J.H. Seinfeld (2008), Comprehensive airborne characterization of aerosol from a major bovine source, *Atmos. Chem. Phys.*, *8*(5489-5520.

Steele, P.T., H.J. Tobias, D.P. Fergenson, M.E. Pitesky, J.M. Horn, G.A. Czerwieniec, S.C. Russell, C.B. Lebrilla, E.E. Gard, and M. Frank (2003), Laser power dependence of mass spectral signatures from individual bacterial spres in bioaerosol mass spectrometry, *Anal. Chem.*, *75*(5480-5487.

Stelson, A.W., and J.H. Seinfeld (1982), Relative humidity and temperature dependence of the ammonium nitrate dissociation constant, *Atmos. Environ.*, *16*(5), 983-992.

Tan, P.V., G.J. Evans, J. Tsai, S. Owega, M.S. Fila, and O. Malpica (2002), On-line analysis of urban particulate matter focusing on elevated wintertime aerosol concentrations, *Environ. Sci. Technol.*, *36*(16), 3512-3518.

Turpin, B.J., and J.J. Huntzicker (1995), Identification of secondary organic aerosol episodes and quantitation of primary and secondary organic aerosol concentrations during SCAQS, *Atmos. Environ.*, *29*(23), 3527-3544.

Yao, X., T.Y. Ling, M. Fang, and C.K. Chan (2007), Size dependence of in situ pH in submicron atmospheric particles in Hong Kong, *Atmos. Environ.*, *41*(382-393.

Zahardis, J., S. Geddes, and G.A. Petrucci (2008), The ozonolysis of primary aliphatic amines in fine particles, *Atmos. Chem. Phys.*, *8*(1181-1194.

Chapter 6

6 Real-time, flight-based Measurements of Vertical Profiles of Single-Particle Mixing States

6.1 Synopsis

The overall impact of aerosols on climate strongly depends strongly on their vertical distribution in the atmosphere. To fully develop global climate models, direct measurements of the size-resolved mixing states of atmospheric particles are needed as a function of altitude. The Ice in Clouds Experiment – Layer Clouds used an aircraft aerosol time-of-flight mass spectrometer to directly measure the vertical profiles of size-resolved aerosol mixing states in cloud-free air over Wyoming and northern Colorado. Biomass burning represented the largest source of submicron particles: ~33-39% by number from 1-7 km. These biomass burning particles became more strongly associated with sulfate and sulfuric acid at higher altitudes as the concentrations of ammonium and nitrate decreased. At all altitudes, organic carbon particles were the second most abundant type (maximum of ~33% from 1.2-2.0 km) with soot-dominated particles comprising 14-22% from 1-7 km. The fraction of sulfuric acid particles, both externally and internally mixed, increased with altitude (up to ~9 and 37%, respectively), likely due to aircraft emissions and cloud processing of SO_2. At all altitudes, fresh soot was less abundant than aged soot, a finding which has important climate implications due to the stronger absorption and hygroscopic properties of these more aged particles.

6.2 Introduction

Atmospheric aerosols strongly influence the energy balance of the Earth and the hydrological cycle by scattering and absorbing solar and terrestrial radiation and acting as cloud condensation and ice nuclei [*Poschl*, 2005]. The physical, optical, and hygroscopic properties of particles strongly depend on whether different chemical species are mixed within a single particle (internal mixing) or in different particles (external mixing) [*Fuzzi et al.*, 2006]. During transport in the atmosphere, aerosol particles undergo physical and chemical transformations through cloud processing and reactions with atmospheric gases [*Poschl*, 2005]. Due to the evolving physical and chemical properties of the distribution of aerosols, quantifying aerosol impacts on radiative forcing and clouds represents a challenging task [*Solomon et al.*, 2007]. For example, as externally mixed soot particles age, they convert to internally mixed particles with a soot core surrounded by sulfate, ammonium, organics, nitrate, and water [*Moffet and Prather*, 2009]. This results in a positive radiative forcing second only to CO_2 [*Ramanathan and Carmichael*, 2008]. The majority of in-situ aerosol measurements have been made at ground level; however, the direct and indirect radiative forcings depend on aerosol vertical and horizontal profiles [*Solomon et al.*, 2007]. Thus, in-situ, size-dependent aerosol chemical composition and mixing state (internal/external) measurements are needed as a function of altitude for the further development and evaluation of global climate models [*Fuzzi et al.*, 2006].

Aircraft-based measurements of individual particles have traditionally been made using off-line microscopy techniques. For example, using electron microscopy, Pósfai *et al*. [1999] found an increasing fraction of sulfate particles containing soot with increasing altitude, likely due to aircraft emissions; thus, these more hygroscopic soot particles are more effective cloud condensation nuclei (CCN) at altitudes where cloud formation is more probable. Real-time aerosol analysis methods reduce sampling artifacts and allow direct measurements of changing aerosol populations with high temporal resolution [*Sullivan and Prather*, 2005]. Previous airborne, real-time, single-particle chemistry measurements have been made using particle analysis by laser mass spectrometry [*Murphy et al.*, 1998]. Herein, we report results from the first set of flights using the recently-developed aircraft aerosol time-of-flight mass spectrometry (A-ATOFMS) [*Pratt et al.*, 2009]. Size-resolved single-particle mixing state measurements of both refractory and non-refractory species, acquired in real-time as a function of altitude, provide insight into the range of mixing states of atmospheric aerosols. The sources and mixing state of individual particles, including the relative mixing of biomass burning, organic carbon, and soot particles with secondary species, including ammonium, nitrate, sulfate, and sulfuric acid, are described for the first aircraft-based dual-polarity single-particle measurements.

6.3 Experimental

Measurements of individual ambient aerosol particles by A-ATOFMS were conducted during the Ice in Clouds Experiments – Layer Clouds (ICE-L) from November – December 2007 aboard the National Center for Atmospheric Research/National Science Foundation (NCAR/NSF) C-130 aircraft based in Broomfield, Colorado. Data are presented from 14 flights (November 1, 5, 7, 13, 16, 18, 20, 29, 30; December 10, 11, 12, 13, 16) from ~1.2 – 7.0 km above mean sea level (AMSL) over northern Colorado, western Nebraska, southwestern South Dakota, and Wyoming (approximately 39.8-

44.5°N, 102.8-109.7°W) (Figure 6.1). Latitude, longitude, and altitude were sampled at 10 Hz by a Garmin GPS and averaged to 1 Hz. Ambient condensation nuclei (CN) concentrations were measured using a condensation particle counter (CPC, TSI Model 3760), detecting particles greater than ~13 nm in size.

The A-ATOFMS, described in Chapter 2, measured the vacuum aerodynamic diameter (d_{va}) and dual-polarity mass spectra of individual particles from ~70-1200 nm in real-time. Briefly, following a ^{210}Po neutralizer and pressure-controlled inlet, particles are focused in an aerodynamic lens system. Particles are optically detected by two continuous wave 532 nm lasers spaced 6.0 cm apart, providing particle velocity and, thus, d_{va}; polystyrene latex spheres of known physical diameter from 95-1500 nm were used to complete the single-particle size calibration. During ICE-L, particles were desorbed and ionized using 266 nm radiation from a Q-switched Nd:YAG laser operating at ~0.4-0.6 mJ. Positive and negative ions resulting from individual particles are detected within the time-of-flight mass spectrometer.

While the field campaign focused on cloud studies, A-ATOFMS size-resolved dual-polarity mass spectra were collected in clear (cloud-free) air for 13,180 individual particles; this does not include data from within two smoke plumes. Single-particle mass spectra were imported into YAADA (www.yaada.org), a software toolkit for MATLAB (The MathWorks, Inc.). Single-particle mass spectra were tagged with the altitude, latitude, longitude, and CN concentration present at the time that each particle was sampled. An adaptive resonance theory-based clustering method (ART-2a) [*Song et al.*, 1999] was used to classify single-particle mass spectra with a vigilance factor of 0.80, learning rate of 0.05, and 20 iterations. ART-2a classifies particles into separate clusters

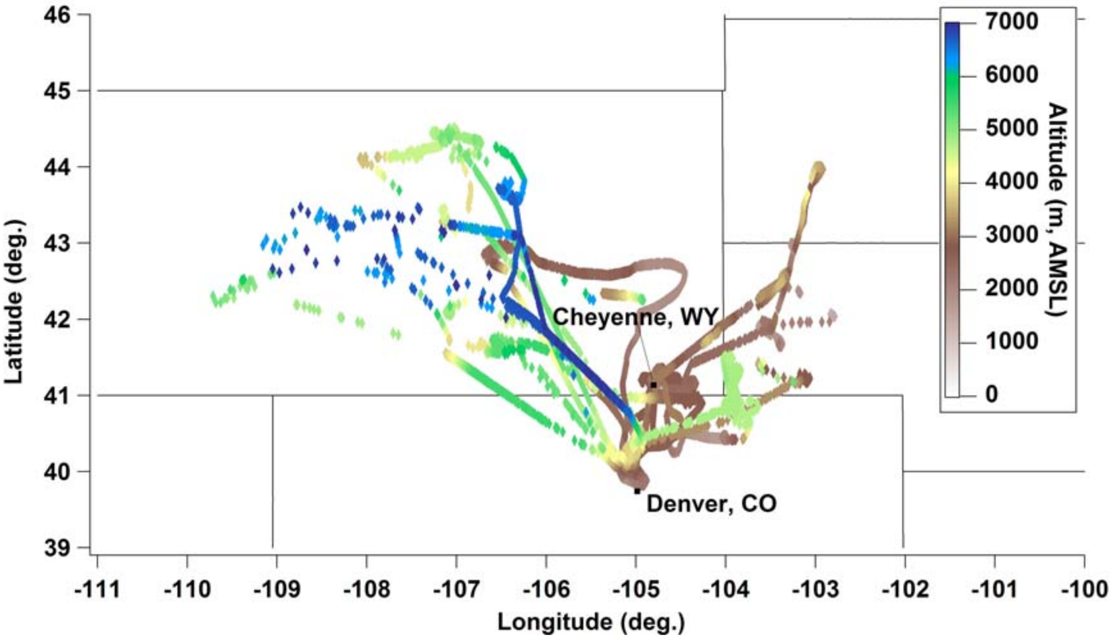

Figure 6.1. Latitude (deg. N), longitude (deg. W), and altitude (m, AMSL) of ATOFMS clear air sampling. Each point represents one chemically analyzed particle.

based on the presence and intensity of ion peaks in individual single-particle mass spectra. Resulting ART-2a clusters were classified into general particle classes, which are defined by the characteristic chemical species or possible source; these labels do not necessarily reflect all of the species present within a particular particle type. Peak identifications correspond to the most probable ions for a given m/z ratio based on previous lab and field studies.

To investigate single-particle mixing state, the presence of ammonium (*m/z* 18(NH_4^+)), nitrate (*m/z* -62(NO_3^-)), sulfate (*m/z* -97(HSO_4^-)), and sulfuric acid (*m/z* -195($H_2SO_4HSO_4^-$)) [*Froyd et al.*, 2009; *Miller et al.*, 2005] was examined with respect to altitude for the major particle classes. First, individual particles containing each of these *m/z* markers were identified using a peak area threshold of 100 (arbitrary units). The average peak area of each specific *m/z* is related the amount of each particular species on a particle [*Bhave et al.*, 2002]; therefore, for those particles containing each *m/z* marker, average peak areas were calculated to examine the relative amount of that species on a particular class of particles.

6.4 Results and Discussion

Average CN number concentrations decreased with increasing altitude (Figure 6.2) from ~5000/cm^3 at 1-2 km MSL to ~200/cm^3 at 6-7 km with the boundary layer top at approximately 3.1 km. Consistent with measurements near an urban center (Denver, CO), the highest CN concentrations (~60,000/cm^3) were observed at low altitudes following take-off at 1729 m from Broomfield, CO. Average CN concentrations from 5-7 km (~227/cm^3) are similar to previous CN concentration measurements for November-

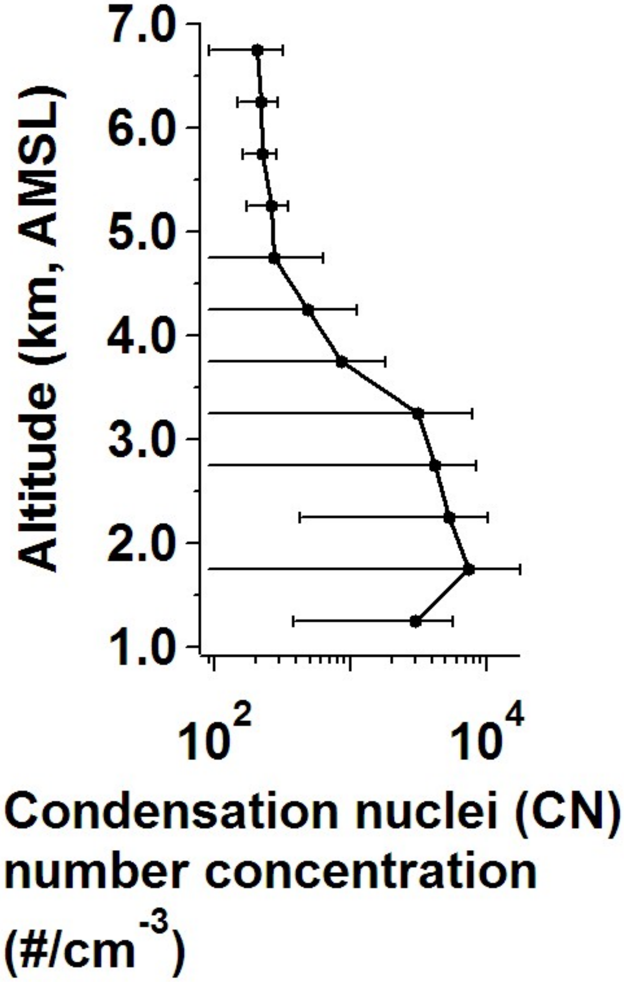

Figure 6.2. Average CN concentrations with standard deviations for periods of ATOFMS clear air sampling during ICE-L. Altitude is binned by 0.5 km.

December at 5-10 km over Wyoming (~300/cm^3) [*Hofmann*, 1993]. Thus, the single-particle chemical composition discussed below is generally representative of a remote continental location.

6.4.1 Altitude-resolved individual particle chemical mixing state

To examine individual particle chemical mixing states with respect to altitude, submicron particles were classified within 13 general particle classes: biomass burning, organic carbon (OC), aromatic, amine, elemental carbon/organic carbon (ECOC), elemental carbon (EC), biological, salt (Na-K-Cl), mineral dust, metal, sulfate-nitrate (particles with no positive ions), and sulfuric acid. The relative contributions of each particle type with respect to altitude are shown in Figure 6.3; for a more detailed examination, Figure 6.4 illustrates the relative fractions of these particle types with respect to particle diameter, as well as altitude.

Contributions from wildfires, prescribed burns, and residential wood burning resulted in the biomass burning class representing the largest source of submicron particles: ~33-39% by number from 1-7 km (Figure 6.3). This agrees with previous flight-based PALMS measurements which found that ~33% of particles sampled in the North American background troposphere were characterized by a biomass burning signature [*Hudson et al.*, 2004]. Further, long-term surface measurements have shown that biomass burning contributes ~30% on average annually to the total fine particle mass in the western U.S. [*Park et al.*, 2007]. The mass spectra of biomass burning particles (Figure 6.5a) were characterized by an intense potassium ion peak with less intense carbonaceous marker ions (eg. *m/z* 12(C^+), 27($C_2H_3^+$), 36(C_3^+), 37(C_3H^+), -26(CN^-))

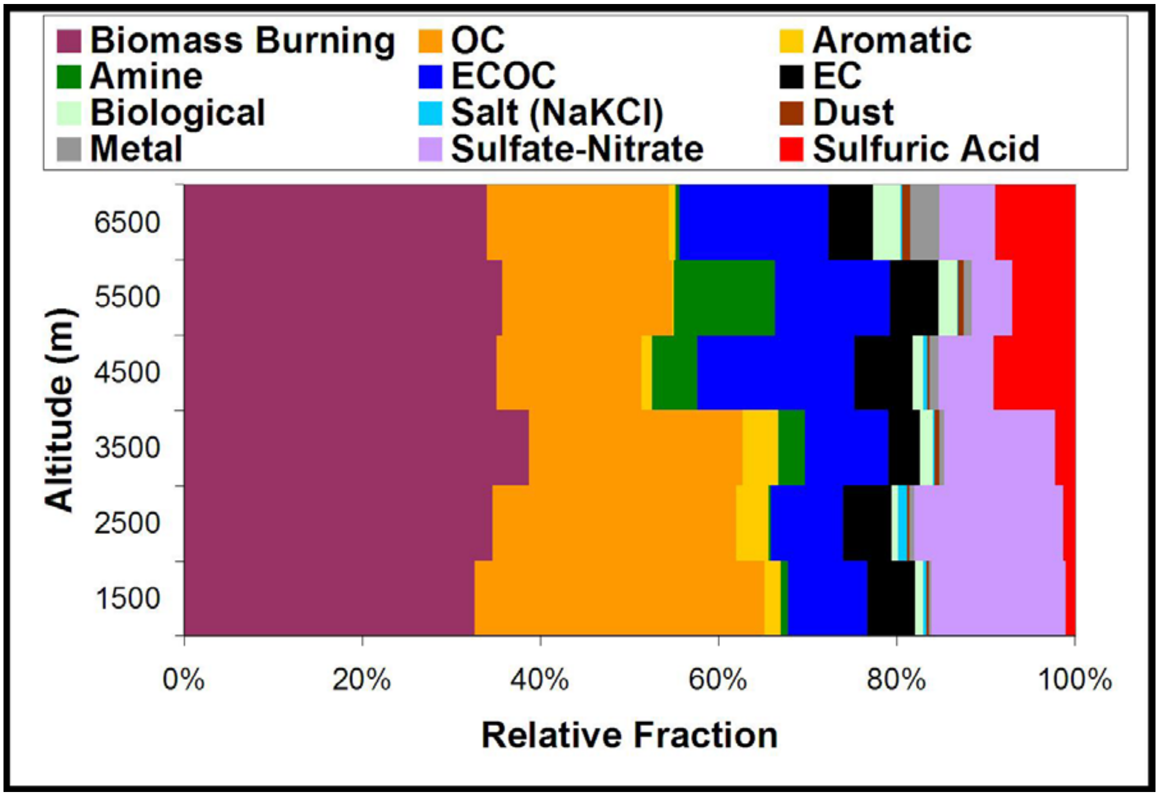

Figure 6.3. Relative number fractions of particle classes with respect to altitude, binned by 1 km.

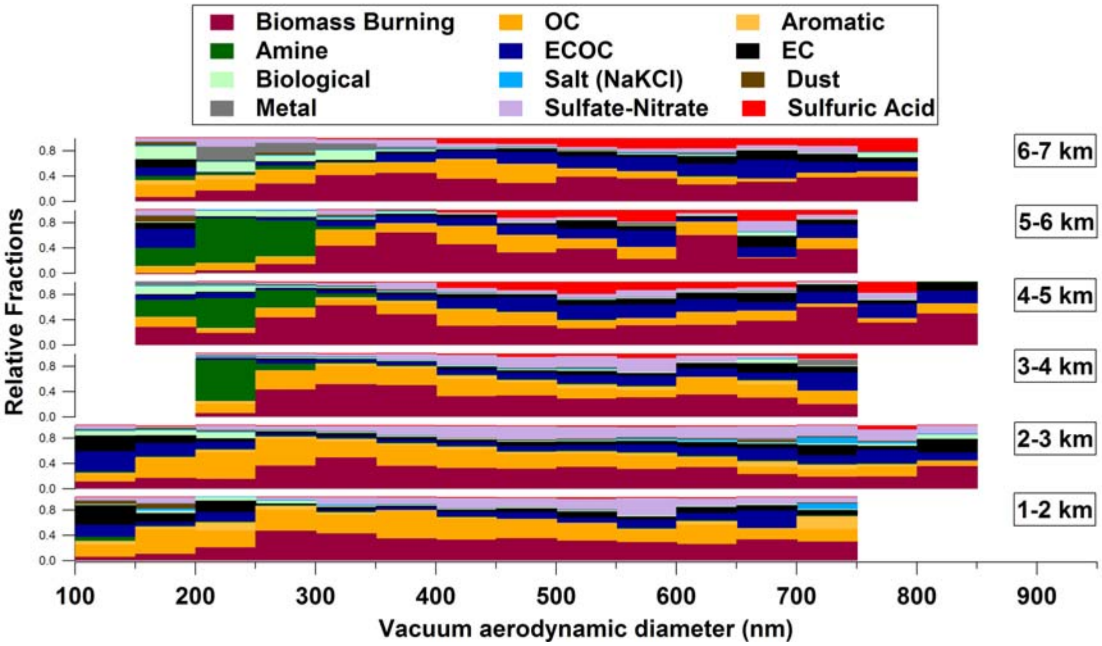

Figure 6.4. Relative fractions of particle classes with respect to particle diameter (d_{va}, nm) and altitude (km, AMSL).

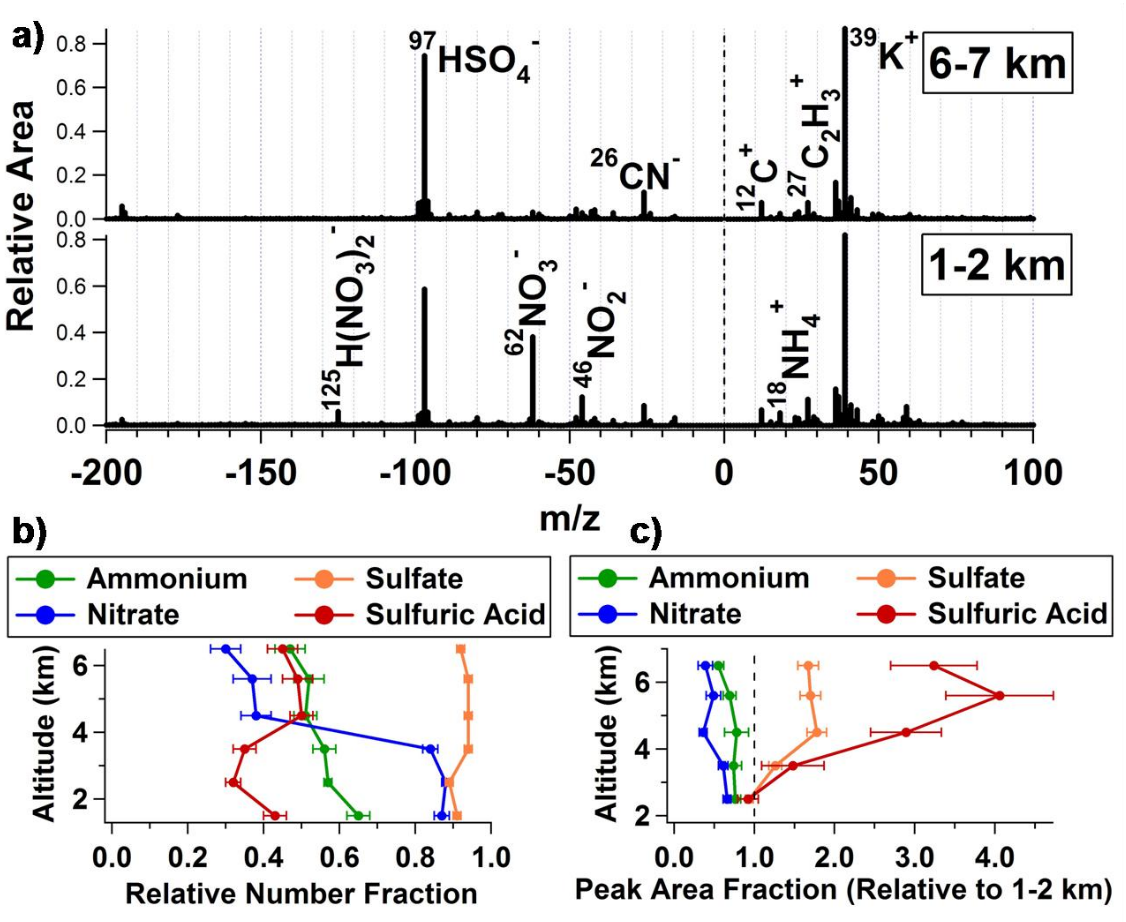

Figure 6.5. (a) Average mass spectra of biomass burning particles at 1-2 and 6-7 km AMSL. (b) Relative number fractions of biomass burning particles containing ammonium (*m/z* 18(NH_4^+)), nitrate (*m/z* -62(NO_3^-), sulfate (*m/z* -97(HSO_4^-)), and sulfuric acid (*m/z* -195($H_2SO_4HSO_4^-$) with respect to altitude from 1-7 km, binned by 1 km. (c) Average peak areas of ammonium, nitrate, sulfate, and sulfuric acid for biomass burning particles at different altitudes with respect to the 1-2 km AMSL average.

[*Silva et al.*, 1999]. With increasing altitude from 1-7 km, the fraction of biomass burning particles mixed with ammonium decreased from 65 ± 3% to 47 ± 4% (Figure 6.5b). Similarly, the fraction of biomass burning particles containing nitrate decreased significantly from 87 ± 1% from 1-3 km to 35 ± 4% from 4-7 km. In addition, the average amounts of ammonium and nitrate on these individual particles decreased 45 ± 7% and 61 ± 9%, respectively, from 1-7 km (Figure 6.5c). In contrast, the fraction of biomass burning particles containing sulfate stayed relatively constant with altitude while the average amount of sulfate on these individual particles increased by 67 ± 13% from 1-7 km. The increasing accumulation of sulfate on biomass burning particles with increasing altitude is consistent with aging [*Posfai et al.*, 2003] and cloud processing. Lastly, the fraction of biomass burning particles containing sulfuric acid was relatively constant (~32-50%) at all altitudes; however, the relative amount of sulfuric acid on these particles increased by a factor of 4.0 ± 0.7 from 1-6 km, consistent with decreasing ammonium concentrations and increased aqueous phase processing with altitude.

The relative fraction of OC particles was greatest (~33%) near the surface (1.2-2.0 km) with decreased abundance (~16-21%) above 4 km, suggesting decreased transport to the free troposphere compared to biomass burning particles. As shown in Figure 6.6a, the OC particle class mass spectral signature was dominated OC marker ions, including *m/z* 27($C_2H_3^+$/CHN^+), 37(C_3H^+), 43(CH_3CO^+/$CHNO^+$), 50($C_4H_2^+$/C_3N^+), 59($C_3H_9N^+$), and 142($C_{11}H_{10}^+$/$C_8H_{16}NO^+$) [*Angelino et al.*, 2001; *Erupe et al.*, 2008; *Silva and Prather*, 2000]. Oxidized OC is shown at all altitudes through the presence of the intense *m/z* 43 peak, likely related to gas-phase oxidation within the boundary layer and cloud processing at higher altitudes. Sulfate is present in ~87-97% of OC particles at all

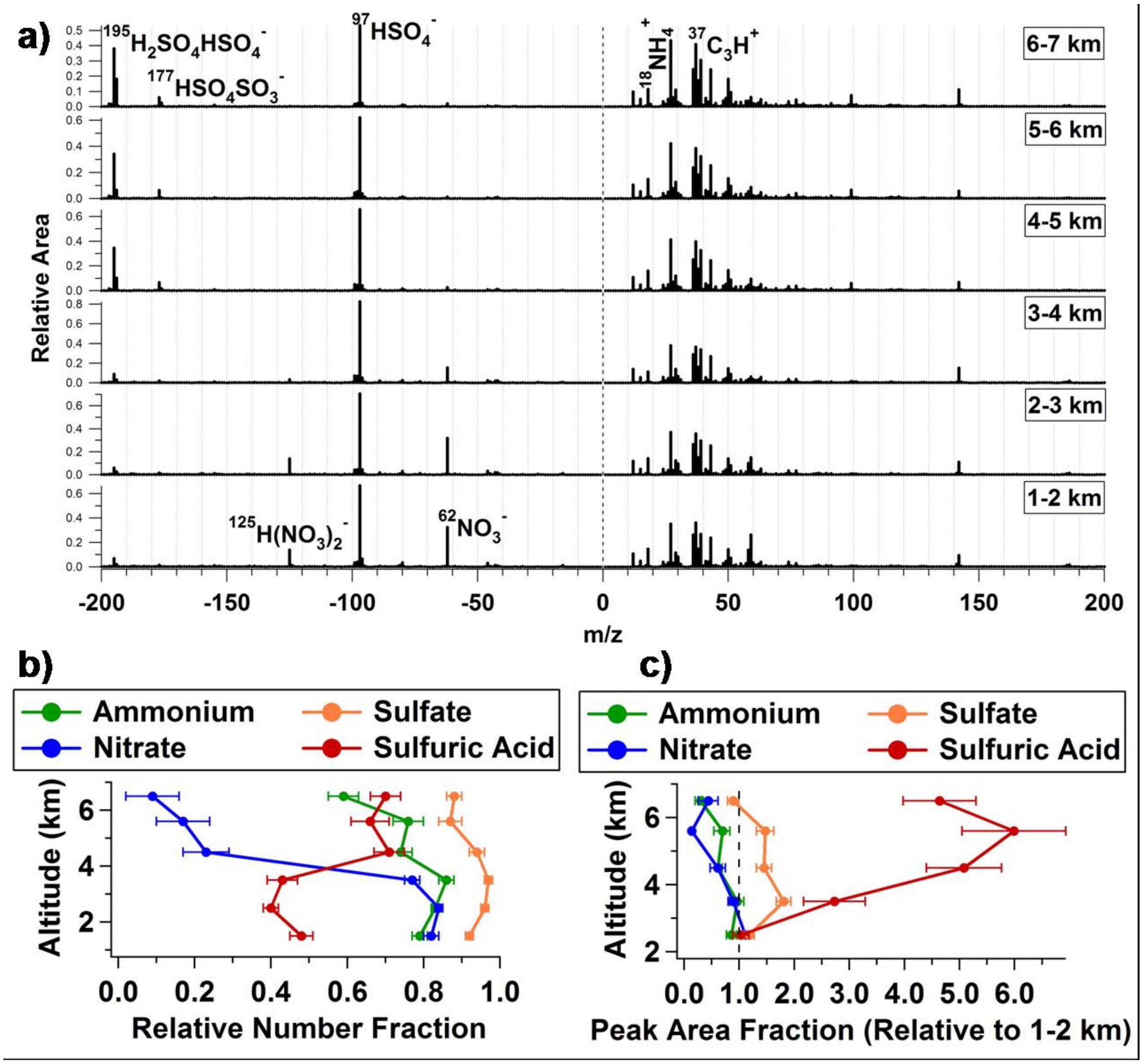

Figure 6.6. (a) Average mass spectra of OC particles at 1-2 and 6-7 km AMSL. (b) Relative number fractions of OC particles containing ammonium (*m/z* 18(NH_4^+)), nitrate (*m/z* -62(NO_3^-), sulfate (*m/z* -97(HSO_4^-)), and sulfuric acid (*m/z* -195($H_2SO_4HSO_4^-$) with respect to altitude from 1-7 km, binned by 1 km. (c) Average peak areas of ammonium, nitrate, sulfate, and sulfuric acid for OC particles at different altitudes with respect to the 1-2 km AMSL average.

altitudes (Figure 6.6b). The fraction of OC particles mixed with ammonium decreased slightly (20 ± 5%) from 1-7 km, but the amount of ammonium on these particles decreased 70 ± 5%. Similarly, the average amount of nitrate on the OC particles decreased with increasing altitude (Figure 6.6c), and while 82 ± 2% of OC particles were mixed with nitrate at 1-2 km, few (9 ± 7%) contained nitrate at 6-7 km. In contrast, the fraction of OC particles containing sulfuric acid increased from 40 ± 2% at 2-3 km to 70 ± 4% at 6-7 km with the relative amount of sulfuric acid increasing by 6.0 ± 0.9 from 1-6 km.

Two minor sub-classes of OC particles were observed: aromatic and amine. The aromatic particles had a minor contribution (~2-4% by number) below 4 km with contributions of $\leq$1% from 4-7 km; generally, aromatics are associated with "brown" light-absorbing carbon [*Andreae and Gelencser*, 2006]. The mass spectral signatures of these particles (Figure 6.7) were characterized by OC marker ions, aromatic fragment ions (*m/z* 51($C_4H_3^+$), 63($C_5H_3^+$), 77($C_6H_5^+$), 91($C_7H_7^+$), 115($C_9H_7^+$), 165($C_{13}H_9^+$), 189($C_{15}H_9^+$), 219($C_{17}H_{15}^+$)), polycyclic aromatic hydrocarbon (PAH) molecular ions (*m/z* 178 (phenanthrene/anthracene), 202 (pyrene/fluoranthene)), and organic nitrogen [*Silva and Prather*, 2000]. Overall, the aromatic particles were mixed with ammonium, nitrate, and sulfate; however, sulfuric acid was not observed on these particles. Given the presence of a coniferous wood burning tracer (1-methyl-7-isopropylphenanthrene, *m/z* 234 and its major fragments, *m/z* 219, 205, and 189) [*Bente et al.*, 2006] during this early winter (Nov.-Dec.) study, the leading source of these aromatic particles, primarily found within the boundary layer, is hypothesized to be residential wood burning. The second OC particle sub-type were particles with dominant amine signatures, which contributed

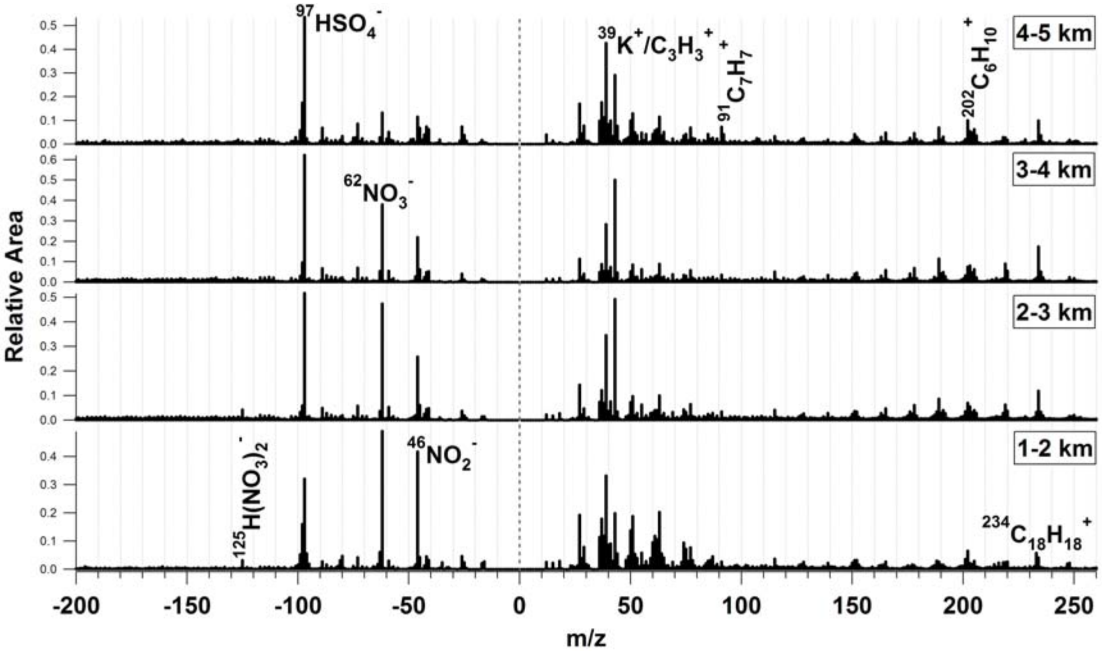

Figure 6.7. Average mass spectra of the aromatic particle class with respect to altitude, binned by 1 km AMSL.

$\leq$1% by number at 1-3 km and 6-7 km. However, from 3-6 km, the contribution of amine particles increased from ~3-11% with these particles occupying the smallest (i.e. 150-300 nm) size range (Figure 6.4), potentially suggesting nucleation as an important formation mechanism [*Barsanti et al.*, 2009]. As such, the mass spectra of amine-containing particles varied as a function of altitude. From 1-3 km, the mass spectral signature (Figure 6.8) is typified by OC, ammonium, nitrate, sulfate, and amine markers: *m/z* 58($C_2H_5NHCH_2^+$), 59(trimethylamine), and 142($C_8H_{16}NO^+$) [*Angelino et al.*, 2001; *Erupe et al.*, 2008]. In contrast, from 3-7 km, the amines are not mixed with ammonium or sulfate but instead they are mixed with other OC species, chloride, nitrate, phosphate, and an amine marker at *m/z* 118($(C_2H_5)_3NOH^+$). Previous single-particle mass spectrometry measurements have shown ~30-80% of the aerosol mass in the free troposphere to be carbonaceous [*Murphy et al.*, 2006]. While a small soot core may be present in some of the observed OC particles, OC was found to be the major carbonaceous species (compared to soot) present in these free tropospheric aerosols, considering all OC-containing particle types.

The overall radiative forcing of aerosols depends strongly on the vertical distribution of soot; recent estimates suggest that soot absorption could offset the direct cooling effect of aerosols [*Myhre*, 2009]. Fresh and aged soot particles [*Moffet and Prather*, 2009] are classified here within the EC and ECOC particle types, respectively. The relative contribution of soot increased from ~14-22% with increasing altitude (1-7 km); aircraft emissions and biomass burning have been suggested as the major sources of soot in the remote free troposphere [*Posfai et al.*, 1999]. The mass spectra of these particles (Figure 6.9a) were distinguished by both positive and negative ion carbon

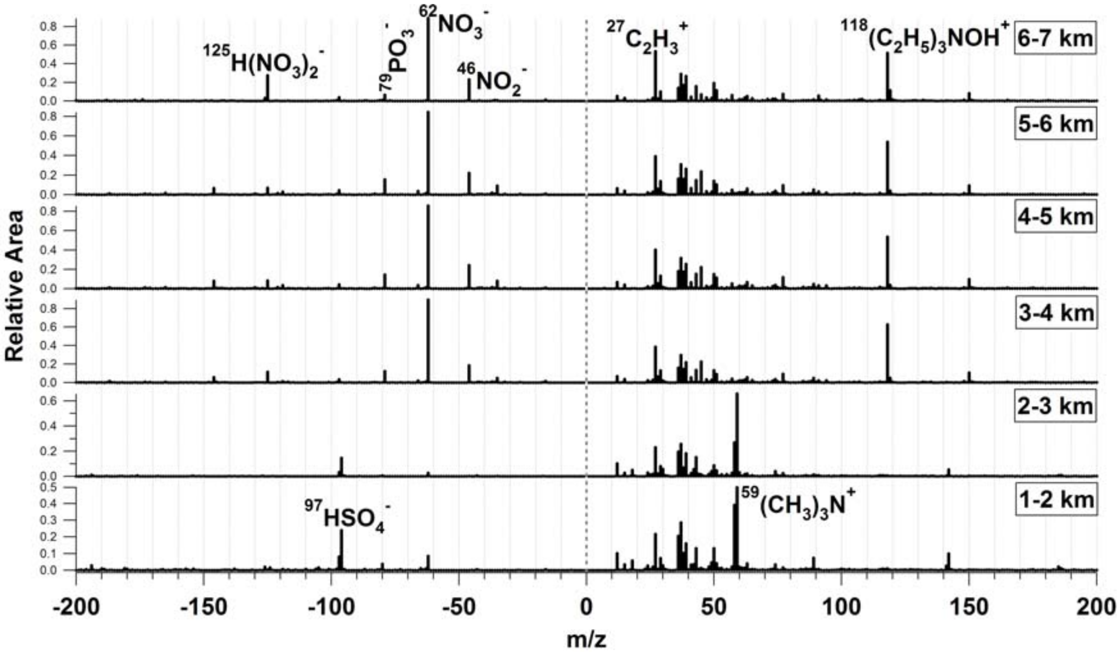

Figure 6.8. Average mass spectra of the amine particle class with respect to altitude, binned by 1 km AMSL.

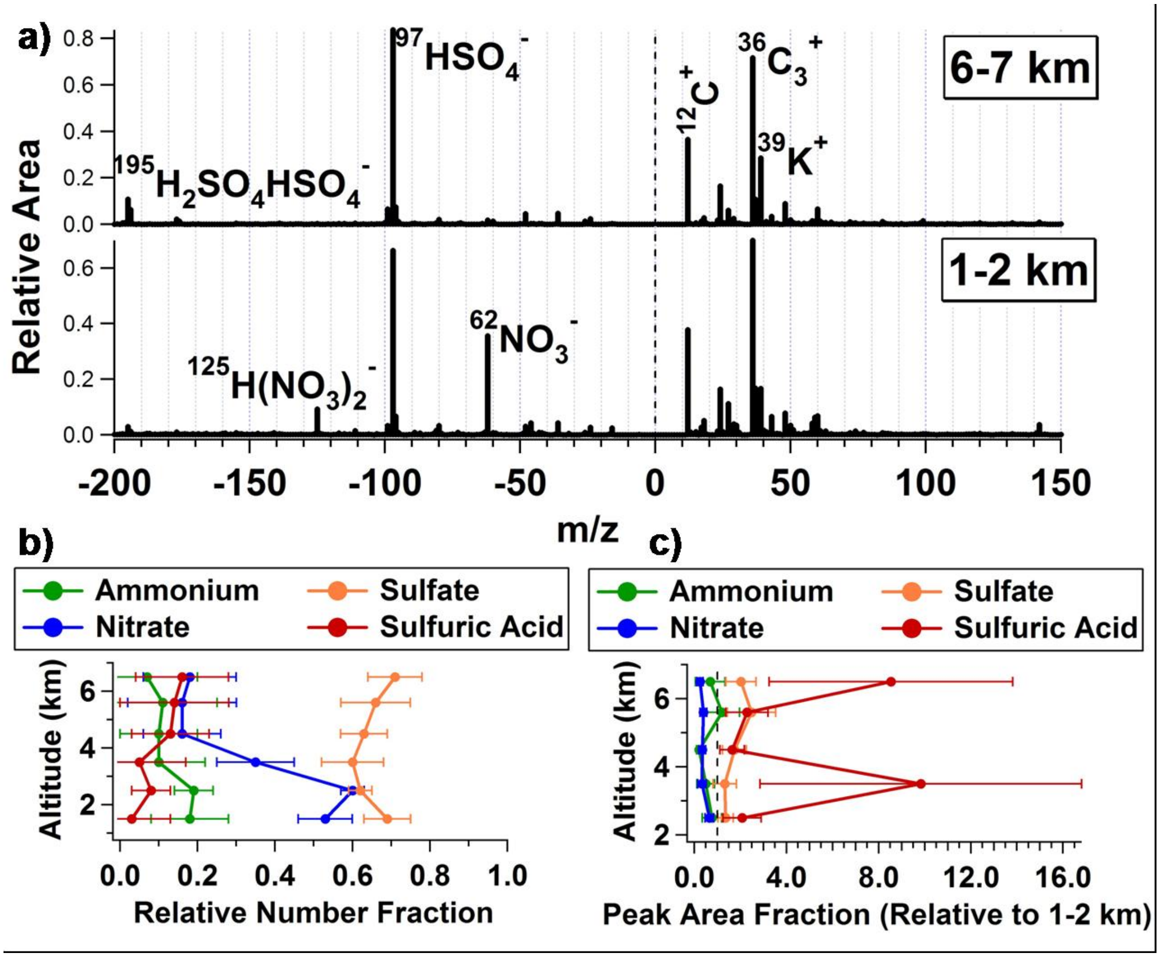

Figure 6.9. (a) Average mass spectra of fresh soot (EC) particles at 1-2 and 6-7 km AMSL. (b) Relative number fractions of fresh soot (EC) particles containing ammonium (*m/z* 18(NH_4^+)), nitrate (*m/z* -62(NO_3^-), sulfate (*m/z* -97(HSO_4^-)), and sulfuric acid (*m/z* -195($H_2SO_4HSO_4^-$) with respect to altitude from 1-7 km, binned by 1 km. (c) Average peak areas of ammonium, nitrate, sulfate, and sulfuric acid for fresh soot (EC) particles at different altitudes with respect to the 1-2 km AMSL average.

clusters ions (C_n^+, C_n^-), as well as potassium in biomass burning derived soot (~40-65% by number); the mass spectra of the aged soot (ECOC) particles (Figure 6.10a) were characterized by carbon cluster positive ions (C_n^+), OC, and potassium. Considering only soot particles, aged soot (ECOC) particles were more prevalent than fresh soot (EC) at all altitudes with the contribution fresh soot decreasing with altitude from ~38% to 23% from 1-7 km (Figure 6.3), as expected due to aging during transport away from ground-based sources.

Here we present the first in-situ measurements of the mixing state of soot as a function of altitude (Figures 6.9 and 6.10). The mixing state of soot with ammonium, nitrate, sulfate, and sulfuric acid was found to vary with respect to organic carbon content (EC vs. ECOC particles). From 1-7 km, up to 19 ± 5% of EC particles were mixed with ammonium (Figure 6.9b); whereas, with the exception of 1-2 km, approximately 2-3 times as many ECOC particles contained ammonium with the number fraction decreasing from 63 ± 3% at 2-3 km to 44 ± 6% at 6-7 km (Figure 6.10b). In addition, larger amounts of ammonium were observed on ECOC particles compared to EC particles. With regard to nitrate, EC and ECOC particles displayed similar trends with altitude with the relative fractions of particles containing nitrate decreasing significantly from 1-7 km: 53 ± 7% to 18 ± 12% and 89 ± 3% to 16 ± 7%, respectively. For the nitrate-containing soot particles, the relative amounts of nitrate on these particles decreased by 75 ± 13% and 87 ± 3% from 1-7 km for the EC and ECOC particles, respectively (Figures 6.9c and 6.10c). The majority of both EC (~60-71%) and ECOC (~94-98%) particles contained sulfate at all altitudes; however, the relative amount of sulfate on these particles increased by factors of 2.5 ± 1 and 2.4 ± 0.4, respectively, with increasing altitude from 1-6 km. In

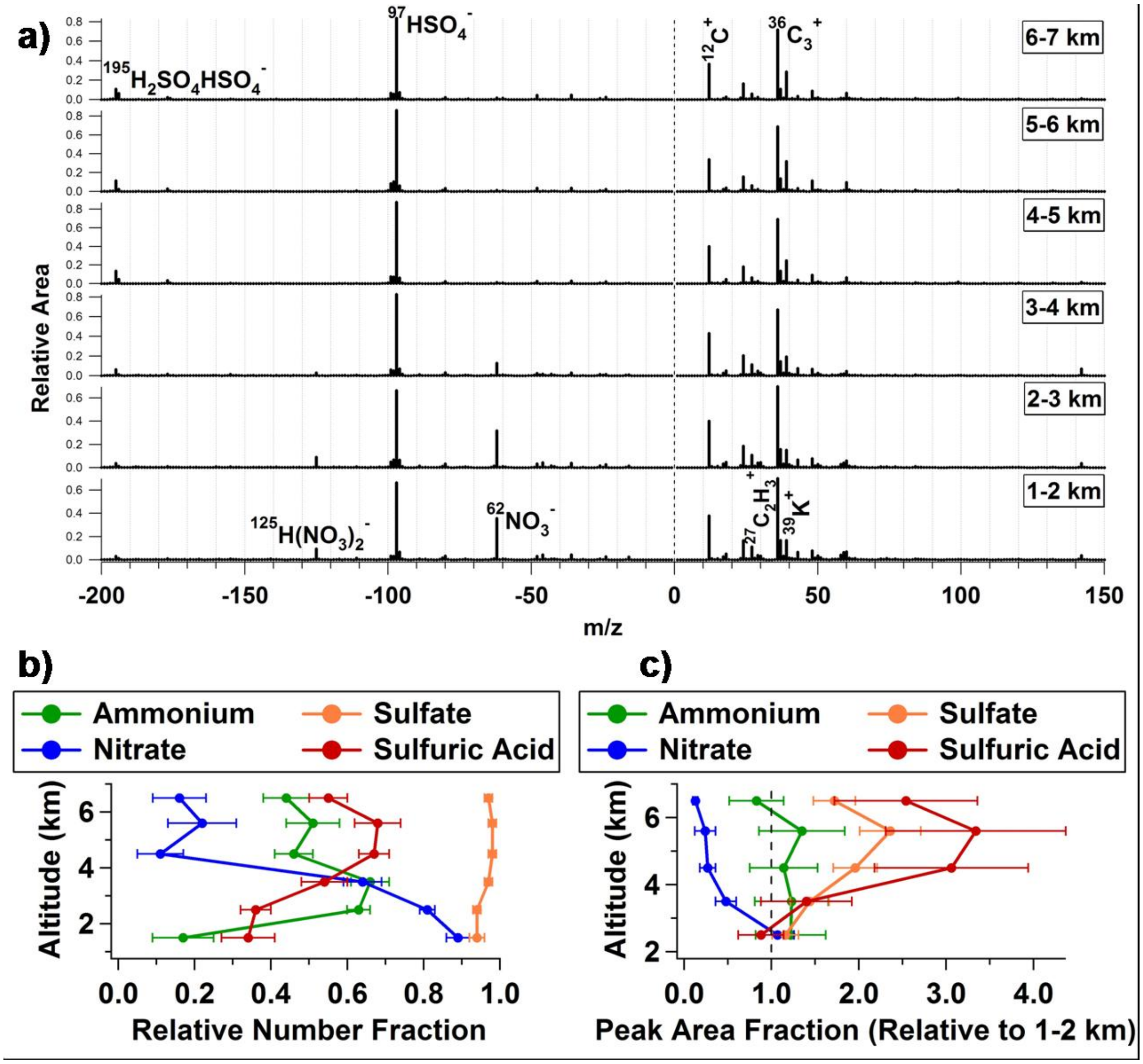

Figure 6.10. (a) Average mass spectra of aged soot (ECOC) particles at 1-2 and 6-7 km AMSL. (b) Relative number fractions of aged soot (ECOC) particles containing ammonium (*m/z* 18(NH_4^+)), nitrate (*m/z* -62(NO_3^-)), sulfate (*m/z* -97(HSO_4^-)), and sulfuric acid (*m/z* -195($H_2SO_4HSO_4^-$)) with respect to altitude from 1-7 km, binned by 1 km. (c) Average peak areas of ammonium, nitrate, sulfate, and sulfuric acid for aged soot (ECOC) particles at different altitudes with respect to the 1-2 km AMSL average.

addition to SO_2 lofted with biomass burning plumes and from coal-fired power plants, it is likely that sulfur emissions from aircraft [*Kjellstrom et al.*, 1999] contributed to the increased sulfate content on the ECOC and EC particles at higher altitudes. The fraction of EC particles mixed with sulfuric acid increased from 0.03 ± 0.10% at 1-2 km to 16 ± 12% at 6-7 km. However, a greater fraction of ECOC particles contained sulfuric acid with 34 ± 7% by number at 1-2 km compared to 55 ±5% at 4-7 km; similar to the biomass burning and OC particles, the relative amount of sulfuric acid on the ECOC particles increased by 2.5 ± 0.8 with increasing altitude. We hypothesize that water adsorption in the atmosphere onto more hygroscopic oxidized OC particles, as compared to fresh hydrophobic soot particles, increases production of sulfuric acid through aqueous-phase processing, leading to the observed higher concentrations of sulfuric acid on OC-containing particles relative to EC particles. This observation suggests that the OC-containing particles have been cloud processed, in contrast to the fresh soot particles. This preferential enhancement of the sulfuric acid on OC-containing particles contrasts previous laboratory studies which concluded that sulfuric acid condenses on particles at a similar rate regardless of chemical composition; however, these experiments were performed at low relative humidity (<0.5%) [*Zhang et al.*, 2008].

Several minor particle classes were observed: biological, salt (Na-K-Cl), mineral dust, metal-containing, and sulfate-nitrate. Characterized by OC, sodium, potassium, calcium, organic nitrogen, nitrate, and phosphate (Figure 6.11) [*Fergenson et al.*, 2004], the contribution of biological particles increased steadily with altitude from ~1-3%. The positive ion mass spectra of the salt particle type (Figure 6.12) were dominated by sodium, potassium, calcium, magnesium, and sodium chloride clusters (*m/z*

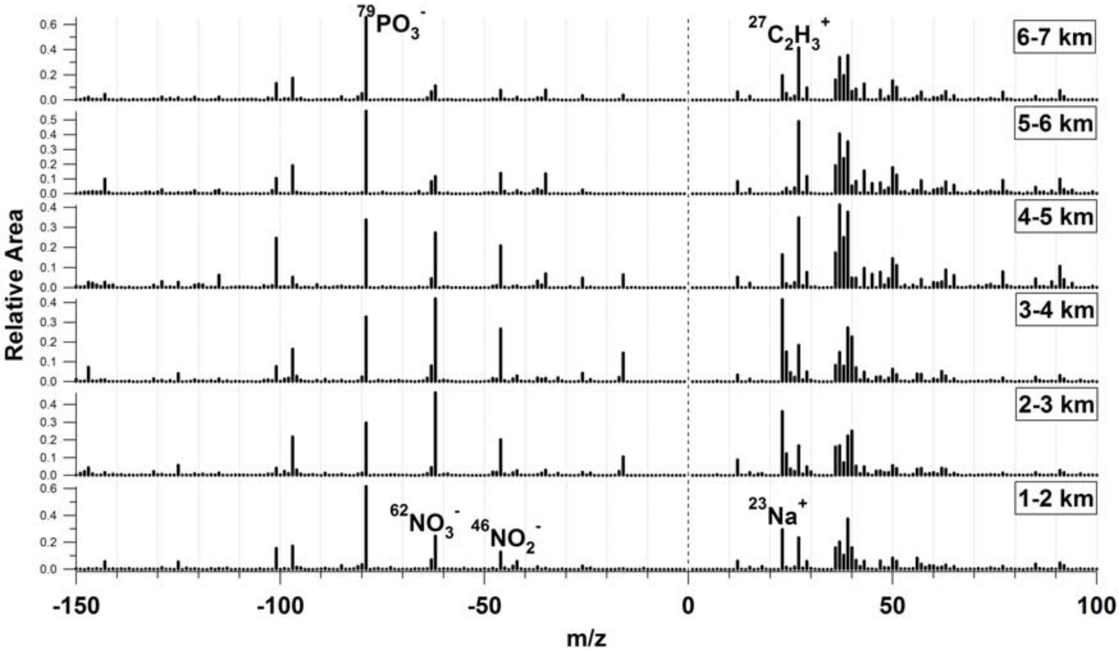

Figure 6.11. Average mass spectra of biological particles with respect to altitude, binned by 1 km AMSL.

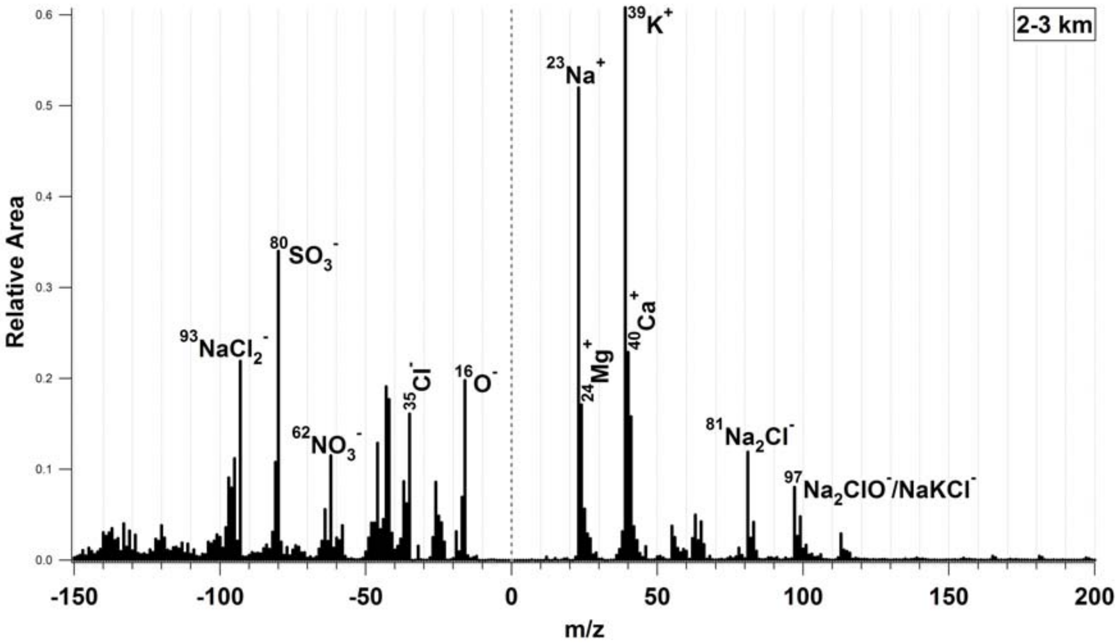

Figure 6.12. Average mass spectra of salt (NaKCl) particles with respect to altitude, binned by 1 km AMSL.

81,83(Na_2Cl^+), 97,99(Na_2ClO^+)); the corresponding negative ions were characterized by chloride, nitrate, and sulfate, in addition to *m/z* -16(O^-), -26(CN^-), -42(CNO^-), -43(CH_3COH^-/$HCHO^-$), and -93,-95,-97($NaCl_2^-$). Salts contributed ~0.1-1.0% by number with the highest contribution at 2-3 km, suggesting most contribution from local sources, such as road de-icing salts. This is consistent with previous measurements by Murphy et al. [2006] who observed <1% of 0.2-2.0 μm particles in the free troposphere to be salts (NaCl). Submicron mineral dust also represented less than <1% by number at all altitudes; however, the chemical composition of the dust changed with altitude (Figure 6.13). From 1-3 km, the mass spectral signature was distinguished by potassium and calcium ions with lower intensity sodium, aluminum, OC, nitrate, phosphate, sulfate, and silicates (*m/z* -60(SiO_2^-), -76(SiO_3^-)). At 3-4 km, a transition to aluminum-rich dust occurred with the mass spectral signatures from 4-7 km dominated by aluminum, including *m/z* 70(Al_2O^+), and nitrate. Particles with intense metal (e.g., Fe, Li, Ba) ion signatures increased in abundance from 0.3-3.3% with increasing altitude. From 1-3 km, particles containing an intense iron marker (*m/z* 56(Fe^+)) were mixed with calcium, OC, nitrate, phosphate, and sulfate (Figure 6.14). With a transition at 3-4 km, the mass spectral signature became dominated by lithium and barium (*m/z* 138(Ba^+), 154(BaO^+), 155($BaOH^+$)), in addition to OC, iron, nitrate, phosphate, and sulfate. Lastly, particles containing both sulfate and nitrate for which no positive ion mass spectra were collected (Figure 6.15) followed the altitude profile of OC particles with contributions of ~12-17% below 4 km and ~5-6% from 4-7 km.

In summary, at lower altitudes, ammonium was significantly mixed with all particle types except the EC, salt, dust, sulfate-nitrate, and sulfuric acid particle classes.

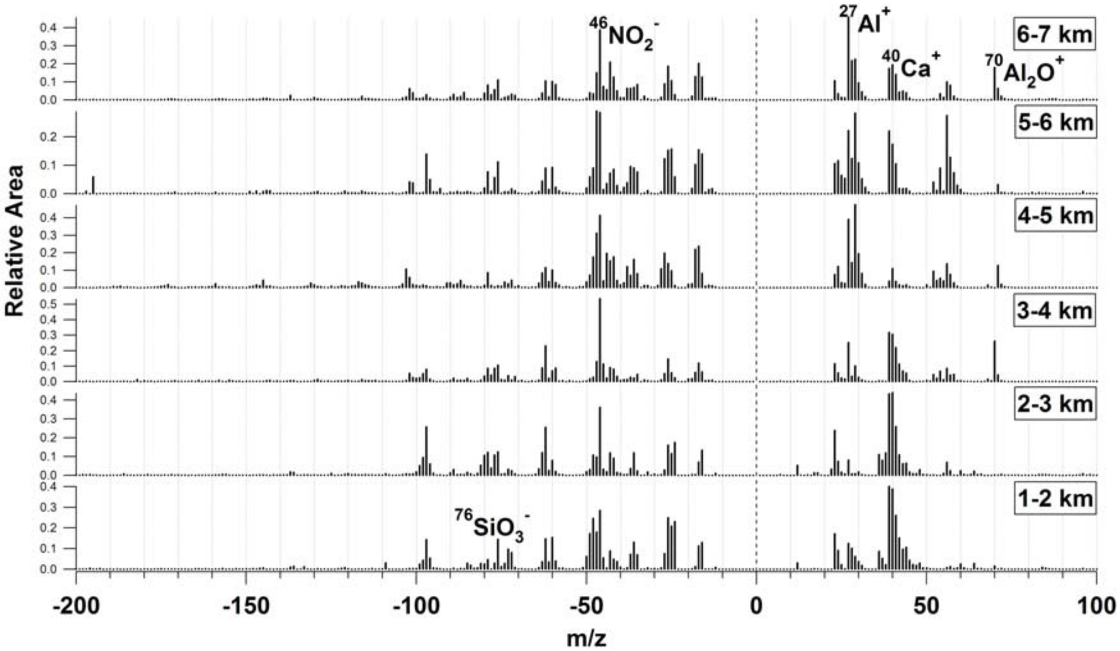

Figure 6.13. Average mass spectra of mineral dust particles with respect to altitude, binned by 1 km AMSL.

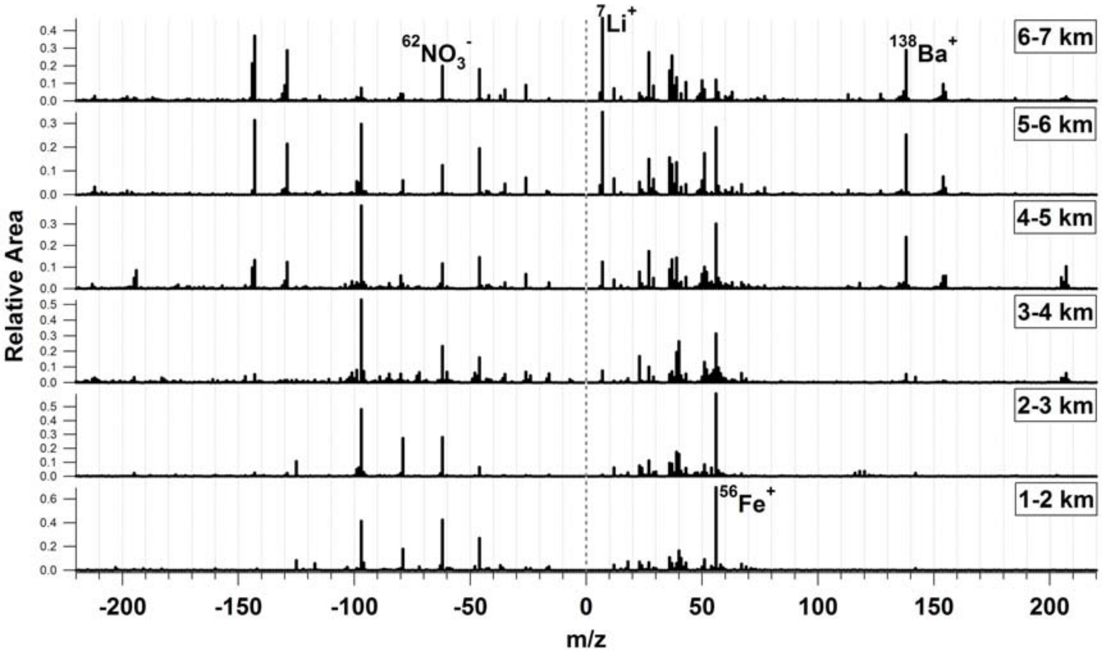

Figure 6.14. Average mass spectra of the metal-containing particle class with respect to altitude, binned by 1 km AMSL.

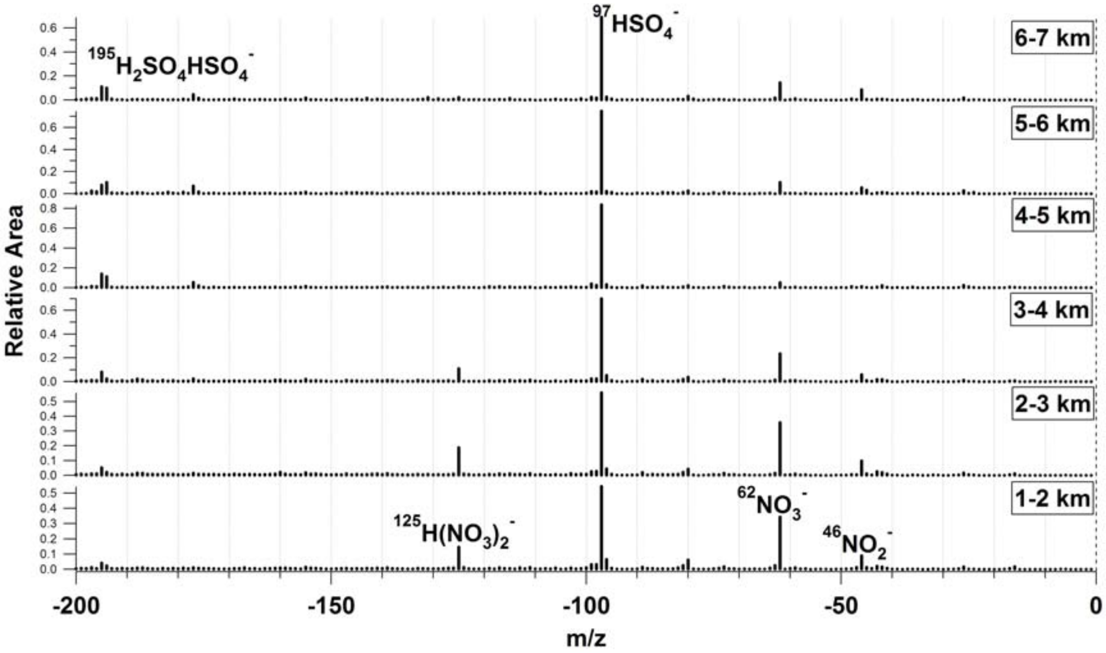

Figure 6.15. Average mass spectra of the sulfate-nitrate particle class with respect to altitude, binned by 1 km AMSL.

More common, nitrate was mixed with all particle types except the sulfuric acid particle class, which was mainly present at higher altitudes. In addition to decreasing ammonium and nitrate concentrations, the relative fractions of ammonium- and nitrate-containing particles decreased with increasing altitude: 50 ± 2% to 33 ± 2% and 73 ± 1% to 23 ± 3%, respectively (Figure 6.16). In contrast to the representation in the 2007 Intergovernmental Panel on Climate Change (IPCC) report [*Solomon et al.*, 2007], this study did not observed externally mixed nitrate particles at any altitude. Previous studies have attributed decreases in ammonium and nitrate masses with increasing altitude to the majority of NH_3 and NO_x sources being at the Earth's surface [*Lee et al.*, 2003]. Sulfate was found to be mixed with all particle types except biological particles. The fraction of all particles mixed with sulfate (~81-87%) was relatively constant with altitude (Figure 6.16); in general, the amount of sulfate on these particles increased with altitude due to sources of SO_x in the upper troposphere. In agreement with these results, previous studies found ~50-90% of particles in the upper troposphere to be carbonaceous-sulfate mixtures [*Murphy et al.*, 2006]; in another study, ~60% of particles were found to contain sulfate at ~5 km within the northern mid-latitudes (31-46°N) [*Murphy et al.*, 1998].

Due to decreasing ammonium concentrations with altitude and cloud processing of SO_2, the fraction of particles internally mixed with sulfuric acid increased with altitude from 24 ± 2% at 2-3 km to 37 ± 4% at 6-7 km. At the lower altitudes, a greater fraction of the sulfate is neutralized and occurs in the form of ammonium sulfate; whereas, the higher altitude particles were more acidic, as shown through the presence of sulfuric acid, similar to that observed by Froyd *et al.* [2009] in the tropical troposphere. Sulfuric acid

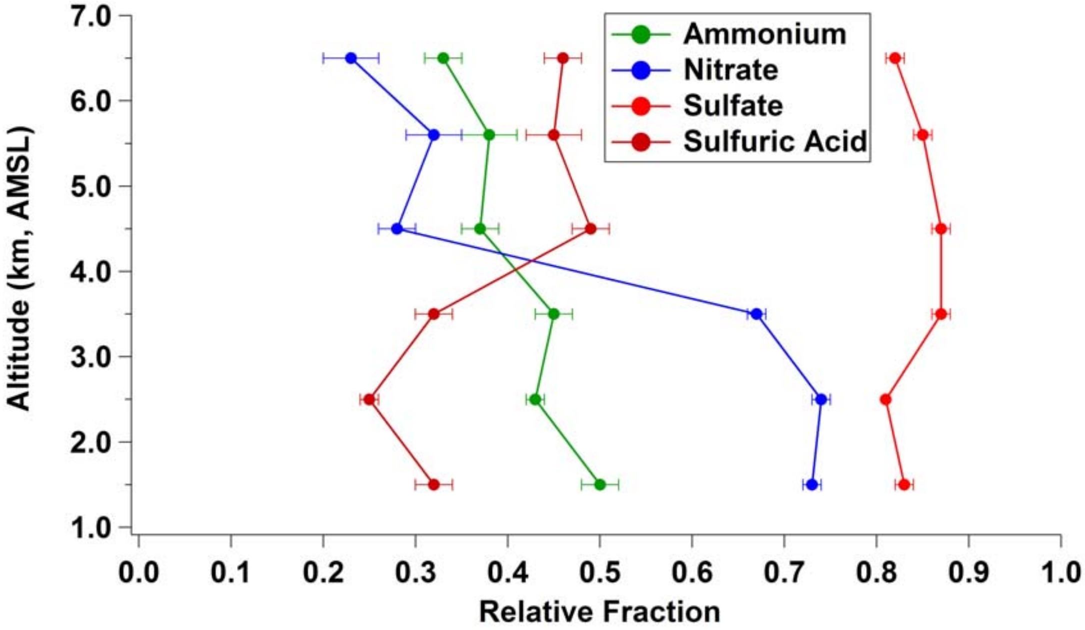

Figure 6.16. Number fraction with altitude for all particles containing each secondary species.

was internally mixed within the biomass burning, OC, amine, ECOC, dust, metal, and sulfate-nitrate particles. In addition, externally mixed sulfuric acid particles were observed to comprise 1-2% by number of all particles below 4 km and 7-9% above 4 km. In addition to SO_2 cloud processing, pure sulfuric acid particles primarily form in the remote free troposphere from the oxidation of SO_x in aircraft exhaust [*Miller et al.*, 2005] in the absence of volcanic emissions. Previously, Brock *et al.* [2004] observed the formation of sulfuric acid particles through cloud processing at altitudes up to 8 km from long-range transported SO_2. During ICE-L, these externally mixed sulfuric acid particles were characterized by only negative ion mass spectra consisting of *m/z* -97(HSO_4^-), -177($HSO_4SO_3^-$), -195($H_2SO_4HSO_4^-$), and -293((H_2SO_4)2SO_3^-) (Figure 6.17); these particles were primarily greater than 400 nm in diameter (Figure 6.4), further suggesting they had undergone cloud processing [*Finlayson-Pitts and Pitts*, 2000].

6.5 Conclusions

To reduce the assumptions and uncertainties associated with modeling the impacts of aerosols on direct and indirect radiative forcing, direct measurements of the vertical profiles of the chemistry of atmospheric particles are required. In 2007, the IPCC report [*Solomon et al.*, 2007] considered the major particle types to be sulfate, fossil fuel organic carbon, fossil fuel black carbon, biomass burning, nitrate, and mineral dust; however, the single-particle measurements discussed herein show a different representation. We have shown how single-particle mixing state changes as a function of altitude due to secondary processing as well changes in sources. Biomass burning was the largest single source of particles: ~33-39% by number from 1-7 km. The mixing

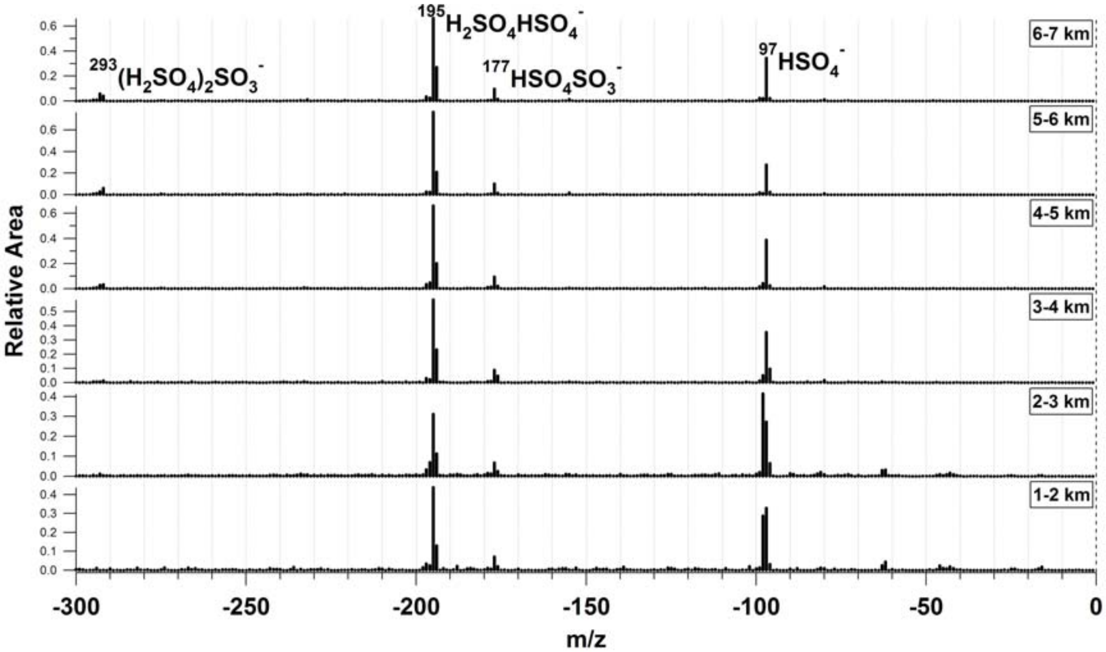

Figure 6.17. Average mass spectra of sulfuric acid particles with respect to altitude, binned by 1 km AMSL.

of these particles varied with altitude; as the concentrations of ammonium and nitrate decreased with altitude, the biomass burning particles became more strongly associated with sulfate and sulfuric acid at higher altitudes due to aging and cloud processing. Thus, the optical and hygroscopic properties of these biomass burning particles must be examined as a function of mixing state to integrate this particle type properly in climate models. In the future, the relative contribution of biomass burning particles is expected to rise due to increasing wildfire activity, particularly in the western U.S., associated with higher large-wildfire frequency, longer wildfire durations, and longer wildfire seasons [*Westerling et al.*, 2006].

At all altitudes, OC particles were more abundant than soot particles with the greatest relative contributions near the surface (~33% from 1.2-2.0 km) compared to soot (14-22% from 1-7 km). Internal mixing of ammonium and nitrate with OC particles decreased with altitude in contrast to sulfate, which stayed relatively constant, and sulfuric acid, which increased with altitude. At 6-7 km, ~70% of OC particles contained sulfuric acid compared to ~40-50% below the boundary layer where ammonium was more prevalent. In fact, the fraction of both externally- and internally-mixed sulfuric acid particles increased with altitude, likely due to aircraft emissions and cloud processing of lofted SO_2. Sulfuric acid was found to preferentially partition to OC-containing particles with few EC particles mixed with sulfuric acid, suggesting that fresh EC particles did not participate in cloud processing. Future aircraft emissions and laboratory studies should assess aging and plume evolution as a function of particle mixing state to investigate this observed partitioning preference. Further, aged soot was more prevalent than fresh soot, supporting the mixing state assumptions of Jacobson [2001] in calculating the direct radiative forcing of soot. Due to mixing with sulfate at altitudes where clouds are relatively abundant, these aged soot particles are expected to impact cloud reflectivity, cloud lifetime, and precipitation. Further, at higher altitudes, these soot particles have a greater probability of being above clouds with the ability to absorb reflected radiation, leading to even more warming [*Ramanathan and Carmichael*, 2008]. Overall, internally mixed soot is more absorbing than externally mixed soot and is second only to CO_2 for positive radiative forcing [*Ramanathan and Carmichael*, 2008]. The vertically-resolved mixing state results shown herein further illustrate the importance of the incorporation of internally mixed soot, as well as other particle types, into global climate models.

6.6 Acknowledgements

We thank the ICE-L C-130 crew and investigators for their support. NSF and NCAR are acknowledged for financial support. Location and CN data were provided by the NCAR Earth Observing Laboratory (EOL) (http://data.eol.ucar.edu).

Chapter 6 is in preparation for submission to the *Journal of Geophysical Research*: Pratt, K.A., Prather, K.A. Real-time, flight-based measurements of vertical profiles of single-particle mixing states.

6.7 References

Angelino, S., D.T. Suess, and K.A. Prather (2001), Formation of aerosol particles from reactions of secondary and tertiary alkylamines: Characterization by aerosol time-of-flight mass spectrometry, *Environ. Sci. Technol.*, *35*(15), 3130-3138.

Barsanti, K.C., P.H. McMurry, and J.N. Smith (2009), The potential contribution of organic salts to new particle growth, *Atmos. Chem. Phys.*, *9*(2949-2957.

Bente, M., T. Adam, T. Ferge, S. Gallavardin, M. Sklorz, T. Streibel, and R. Zimmermann (2006), An on-line aerosol laser mass spectrometer with three, easily interchangeable laser based ionisation methods for characterisation of inorganic and aromatic compounds on particles, *Int. J. Mass Spectrom.*, *258*(86-94.

Bhave, P.V., J.O. Allen, B.D. Morrical, D.P. Fergenson, G.R. Cass, and K.A. Prather (2002), A field-based approach for determining ATOFMS instrument sensitivities to ammonium and nitrate, *Environ. Sci. Technol.*, *36*(22), 4868-4879.

Erupe, M.E., D.J. Price, P.J. Silva, Q.G.J. Malloy, L. Qi, B. Warren, and D.R. Cocker (2008), Secondary organic aerosol formation from reaction of tertiary amines with nitrate radical, *Atmos. Chem. Phys. Discuss.*, *8*(16585-16608.

Fergenson, D.P., M.E. Pitesky, H.J. Tobias, P.T. Steele, G.A. Czerwieniec, S.C. Russell, C.B. Lebrilla, J.M. Horn, K.R. Coffee, A. Srivastava, S.P. Pillai, M.T.P. Shih, H.L. Hall, A.J. Ramponi, J.T. Chang, R.G. Langlois, P.L. Estacio, R.T. Hadley, M. Frank, and E.E. Gard (2004), Reagentless detection and classification of individual bioaerosol particles in seconds, *Anal. Chem.*, *76*(2), 373-378.

Forster, P., V. Ramaswamy, P. Artaxo, T. Berntsen, R. Betts, D.W. Fahey, J. Haywood, J. Lean, D.C. Lowe, G. Myhre, J. Nganga, R. Prinn, G. Raga, M. Schulz, and R. Van Dorland, *Climate Change 2007: The Physical Science Basis. Contribution of Working Group I to the Fourth Assessment Report of the Intergovernmental Panel on Climate Change*, Cambridge University Press, Cambridge, UK, 2007.

Fuzzi, S., M.O. Andreae, B.J. Huebert, M. Kulmala, T.C. Bond, M. Boy, S.J. Doherty, A. Guenther, M. Kanakidou, K. Kawamura, V.M. Kerminen, U. Lohmann, L.M. Russell, and U. Poschl (2006), Critical assessment of the current state of scientific knowledge, terminology, and research needs concerning the role of organic aerosols in the atmosphere, climate, and global change, *Atmos. Chem. Phys.*, *6*(2017-2038.

Hofmann, D.J. (1993), Twenty years of balloon-borne tropospheric aerosol measurements at Laramie, Wyoming, *J. Geophys. Res.*, *98*(D7), 12753-12766.

Hudson, P.K., D.M. Murphy, D.J. Cziczo, D.S. Thomson, J.A. de Gouw, C. Warneke, J. Holloway, J.R. Jost, and G. Hubler (2004), Biomass-burning particle measurements: Characteristic composition and chemical processing, *J. Geophys. Res.*, *109*(D23).

Jacobson, M.C. (2001), Strong radiative heating due to the mixing state of black carbon in atmospheric aerosols, *Nature, 409*(695-697.

Kjellstrom, E., J. Feichter, R. Sausen, and R. Hein (1999), The contribution of aircraft emissions to the atmospheric sulfur budget, *Atmos. Environ., 33*(3455-3465.

Lee, Y.-N., R. Weber, Y. Ma, D. Orsini, K. Maxwell-Meier, D. Blake, S. Meinardi, G. Sachse, C. Harward, T.-Y. Chen, D. Thornton, F.-H. Tu, and A. Bandy (2003), Airborne measurement of inorganic ionic components of fine aerosol particles using the particle-into-liquid sampler coupled to ion chromatography technique during ACE-Asia and TRACE-P, *J. Geophys. Res.*, *108*(D23), doi:10.1029/2002JD003265.

Middlebrook, A.M., D.S. Thomson, and D.M. Murphy (1997), On the purity of laboratory-generated sulfuric acid droplets and ambient particles studied by laser mass spectrometry, *Aerosol Sci. Technol., 27*(3), 293-307.

Miller, T.M., J.O. Ballenthin, A.A. Viggiano, B.E. Anderson, and C.C. Wey (2005), Mass distribution and concentrations of negative chemiions in the exhaust of a jet engine: Sulfuric acid concentrations and observation of particle growth, *Atmos. Environ.*, *39*(3069-3079.

Moffet, R.C., and K.A. Prather (2009), In-situ measurements of the mixing state and optical properties of soot: Implications for radiative forcing estimates, *Proc. Natl. Acad. Sci. U. S. A.*, *Accepted*(

Murphy, D.M., D.J. Cziczo, K.D. Froyd, P.K. Hudson, B.M. Matthew, A.M. Middlebrook, R.E. Peltier, A. Sullivan, D.S. Thomson, and R.J. Weber (2006), Single-particle mass spectrometry of tropospheric aerosol particles, *J. Geophys. Res.*, *111*(D23S32), doi:10.1029/2006JD007340.

Murphy, D.M., D.S. Thomson, and T.M.J. Mahoney (1998), In situ measurements of organics, meteoritic material, mercury, and other elements in aerosols at 5 to 19 kilometers, *Science*, *282*(5394), 1664-1669.

Park, R.J., D.J. Jacob, and J.A. Logan (2007), Fire and biofuel contributions to annual mean aerosol mass concentrations in the United States, *Atmos. Environ.*, *41*(7389-7400.

Poschl, U. (2005), Atmospheric aerosols: Composition, transformation, climate and health effects, *Angewandte Chemie-International Edition*, *44*(46), 7520-7540.

Posfai, M., J.R. Anderson, P.R. Buseck, and H. Sievering (1999), Soot and sulfate aerosol particles in the remote marine troposphere, *J. Geophys. Res.*, *104*(D17), 21685-21693.

Posfai, M., R. Simonics, J. Li, P.V. Hobbs, and P.R. Buseck (2003), Individual aerosol particles from biomass burning in southern Africa: 1. Compositions and size distributions of carbonaceous particles, *J. Geophys. Res.*, *108*(D13), doi:10.1029/2002JD002291.

Ramanathan, V., and G. Carmichael (2008), Global and regional climate changes due to black carbon, *Nature Geoscience*, *1*(221-227.

Silva, P.J., D.Y. Liu, C.A. Noble, and K.A. Prather (1999), Size and chemical characterization of individual particles resulting from biomass burning of local Southern California species, *Environ. Sci. Technol.*, *33*(18), 3068-3076.

Silva, P.J., and K.A. Prather (2000), Interpretation of mass spectra from organic compounds in aerosol time-of-flight mass spectrometry, *Anal. Chem.*, *72*(15), 3553-3562.

Song, X.H., P.K. Hopke, D.P. Fergenson, and K.A. Prather (1999), Classification of single particles analyzed by ATOFMS using an artificial neural network, ART-2A, *Anal. Chem.*, *71*(4), 860-865.

Sullivan, R.C., and K.A. Prather (2005), Recent advances in our understanding of atmospheric chemistry and climate made possible by on-line aerosol analysis instrumentation, *Anal. Chem.*, *77*(12), 3861-3885.

Westerling, A.L., H.G. Hidalgo, D.R. Cayan, and T.W. Swetnam (2006), Warming and earlier spring increase western U.S. forest wildfire activity, *Science*, *313*(940-943.

Zhang, R., A.F. Khalizov, J. Pagels, D. Zhang, H. Xue, and P.H. McMurry (2008), Variability in morphology, hygroscopicity, and optical properties of soot aerosols during atmospheric processing, *Proc. Natl. Acad. Sci. U. S. A.*, *105*(30), 10291-10296.

Chapter 7

7 *In situ* Detection of Biological Particles in Cloud Ice Crystals

7.1 Synopsis

The impact of aerosol particles on the formation and properties of clouds is one of the largest remaining sources of uncertainty in climate change projections. Certain aerosol particles, known as ice nuclei, initiate ice crystal formation in clouds, thereby affecting precipitation and the global hydrological cycle. Laboratory studies suggest that some mineral dusts and primary biological particles – such as bacteria, pollen and fungi – can act as ice nuclei. Here we use aircraft – aerosol time-of-flight mass spectrometry to directly measure the chemistry of individual cloud ice crystal residues (obtained after evaporation of the ice), which were sampled at high altitude over Wyoming. We show that biological particles and mineral dust comprised most of the ice crystal residues: mineral dust account for ~50% of the residues and biological particles for ~33%. Along with concurrent measurements of cloud ice crystal and ice nuclei concentrations, these observations suggest that certain biological and dust particles initiated ice formation in the sampled clouds. Finally, we use a global aerosol model to show long-range transport of desert dust, suggesting that biological particles can enhance the impact of desert dust storms on the formation of cloud ice.

7.2 Introduction

The effects of aerosol particles on the formation and properties of clouds represent the largest remaining sources of uncertainty in the prediction of climate change [*Solomon et al.*, 2007]. Certain aerosol particles can nucleate cloud ice crystals, thereby acting as ice nuclei and impacting the global hydrological cycle through precipitation initiation [*Lohmann and Feichter*, 2005]. However, due to low atmospheric concentrations and related sampling challenges, ice nuclei are relatively poorly understood in comparison to cloud condensation nuclei [*Lohmann and Feichter*, 2005]. Laboratory studies suggest the ability of certain mineral dusts and primary biological particles, such as bacteria, pollen, and fungi, to act as ice nuclei [*Möhler et al.*, 2007]. However, while measurements of precipitation and low altitude liquid cloud water have shown the presence of microorganisms [*Christner et al.*, 2008a; *Christner et al.*, 2008b; *Saxena*, 1983], there have been no direct measurements of biological particles participating in ice phase processes [*Möhler et al.*, 2007]. Although ice-nucleation active bacteria have been detected in the clear atmosphere up to 7 km [*Jayaweera and Flanagan*, 1982], previous measurements of biological particles in cloud have focused on offline measurement methods following collection of low-altitude liquid-phase bulk cloud water [*Deguillaume et al.*, 2008; *Saxena*, 1983].

Here we present in-situ, real-time aerosol chemical composition, ice nuclei, and microphysical measurements of individual cloud ice crystals at high altitudes over Wyoming. Biological and mineral dust particles were found to comprise the majority of the ice crystal residues. Since large-scale dust storms increase the concentration of microorganisms in the atmosphere [*Kellogg and Griffin*, 2006], the concurrent long-range transport and participation in cloud formation of biological particles and dust shown herein suggest that biological material adds to the impact of Asian and Saharan dust storms on ice cloud processes globally [*Sassen*, 2005].

7.3 Experimental

Measurements of an orographic wave cloud were made aboard the National Science Foundation/National Center for Atmospheric Research C-130 aircraft over Wyoming (43°N, 107°-108°W) at 7.9-8.3 km above mean sea level (m.s.l.) on 7 November 2007 during the Ice in Clouds Experiment – Layer Clouds (ICE-L). In this study, real-time measurements of ice-nucleating particle concentrations were made in parallel with size-resolved chemical composition measurements of individual ice particle residues, both concurrent with cloud phase measurements. Cloud ice crystals with diameters greater than 7 µm were selected using a counterflow virtual impactor (CVI); water was evaporated from the crystals at 50°C, providing residual particles for real-time, *in situ* analysis [*Ogren et al.*, 1985]. Number concentrations of residual particles from 0.5-1.2 µm in diameter were measured using an optical particle counter.

To measure the number concentrations of ice-nucleating aerosol particles, a continuous flow diffusion chamber (CFDC) [*Rogers et al.*, 2001] re-processed ice residues <1.2 µm in diameter (see supplementary information) at the cloud observation temperature and at a relative humidity (with respect to water) exceeding 100% (to 103%) to simulate ice formation conditions at expected wave cloud parcel entry conditions. The CFDC ice nuclei data followed Poisson statistics; thus, the standard deviation is noted as the uncertainty. Simultaneous *in situ* measurements of the size-resolved chemical composition of individual submicrometer residual particles were made using aircraft aerosol time-of-flight mass spectrometry (A-ATOFMS), described in Chapter 2. Positive- and negative-ion mass spectra were detected for the time period discussed for 46 cloud ice residues with vacuum aerodynamic diameters from 140 to 700 nm. Standard errors of particle type number percentages were calculated on the basis of Poisson statistics. Residual particles were classified into distinct types (such as dust versus biological) on the basis of the ion patterns in single-particle mass spectra; peak identifications correspond to the most probable ions for each *m/z* ratio.

A two-dimensional optical array cloud probe (2D-C, Particle Measuring Systems) was used as the primary measurement system for number concentrations of cloud ice crystals greater than 50 μm in diameter. An additional two-dimensional cloud probe (2D-S, Stratton Park Engineering Company) measured stereoscopic images for better resolution, compared with the 2D-C, at sizes even below 50 μm. The lack of supercooled droplets during the ice cloud transects was verified using the Rosemount icing detector (RICE, model 871). A forward scattering spectrometer probe (FSSP-100, Particle Measuring Systems) measured liquid and ice particle concentrations in the size range of ~2-90 μm on this flight, but is known to suffer shattering artifacts in clouds containing larger ice crystals [*Heymsfield*, 2007]. The target cloud was all ice in this case, so FSSP data are not utilized here. The Wyoming cloud radar and lidar are airborne remote sensors that provided vertical cross-sections from the aircraft to infer properties of cloud particle phase, size, and concentration [*Leon et al.*, 2006; *Wang et al.*, 2008]. The method of Wang and Sassen [2002] using combined aircraft-based lidar and radar measurements was utilized to derive effective ice crystal sizes and ice water content as a function of altitude.

The National Oceanic and Atmospheric Administration (NOAA) Air Resources Laboratory Hybrid Single-Particle Lagrangian Integrated Trajectory (HYSPLIT) model was used for air mass back trajectory analysis [*Draxler and Rolph*, 2003]. Surface dust simulations were examined using the Navy Aerosol Analysis and Prediction System (NAAPS) global aerosol model (www.nrlmry.navy.mil/aerosol/). The Navy Operational Global Atmospheric Prediction System (NOGAPS) provided weather modeling and observations. Satellite imagery was provided by the National Aeronautics and Space Administration Sea-viewing Wide Field-of-view Sensor (SeaWiFS) (http://oceancolor.gsfc.nasa.gov/SeaWiFS/).

For additional validation of the biological mass spectral signature, *Pseudomonas syringae*, a known bacterial ice nucleus [*Vali et al.*, 1976], was run into the A-ATOFMS for comparison with the biological particles detected in the cloud ice crystals. The *Pseudomonas syringae* pv. Tomato DC3000 culture was grown on media consisting per L of 10 g Bacto Proteose Peptone, 15 g Bacto Agar, 15 mL glycerol, 0.986 g $MgSO_4 \cdot 7H_20$, and 1.5 g K_2HPO_4 with a pH of ~7. The culture was grown aerobically at 28°C to a lawn of bacteria. The liquid culture was centrifuged and washed in milli-Q water three times before being resuspended in milli-Q water to ensure only bacteria were sampled by the A-ATOFMS.

7.4 Results and Discussion

To characterize the physical properties of the target orographic wave cloud, time series profiles were examined for the following aircraft-based measurements: ambient temperature, vertical velocity, ice crystal number concentrations (20-30 μm and >30 μm), and maximum ice diameter (μm) (Figure 7.1). The vertical wind velocity pattern is indicative of the wave cloud structure; however, the motions are relatively weak, particularly at the higher altitude (after ~21:17 UTC). The 2D-S data, which should be less impacted by shattering, show that some small crystals below the 2D-C threshold were present in lower concentrations over most of the flight path. Figure 7.2 shows radar reflectivity, ice crystal effective diameter and ice crystal (>50 μm) number concentrations, as well as aerosol residue (0.5 – 1.2 μm in diameter) and CFDC ice nuclei number concentrations derived from the CVI residual particles. At ~21:09 UTC, an ice cloud at -31°C was entered in a downstream to upstream pass along the wind vector at ~7.9 km m.s.l. Ice crystals were observed in concentrations of 13.8 ± 3.7 L^{-1}, with average ice nuclei concentrations of 1.6 ± 1.3 L^{-1} measured at -31°C from the CVI residual particles. At ~21:15, the same cloud was entered at a higher elevation (~8.3 km) and lower temperature (-34°C) in the opposite direction (downwind-upwind). The CFDC temperature was lowered from -31 to -34°C to match the cloud temperature at this level. Both ice crystal and ice nuclei concentrations (averages of 56.6 ± 7.5 L^{-1} and 4.7 ± 2.2 L^{-1}, respectively) were higher for this flight leg.

Figure 7.3 provides vertical structure of clouds based on radar and lidar measurements. The radar is more sensitive to large ice particles than small water droplets; thus, radar reflectivity factor (Z_e) provides a cross-sectional vertical distribution of ice

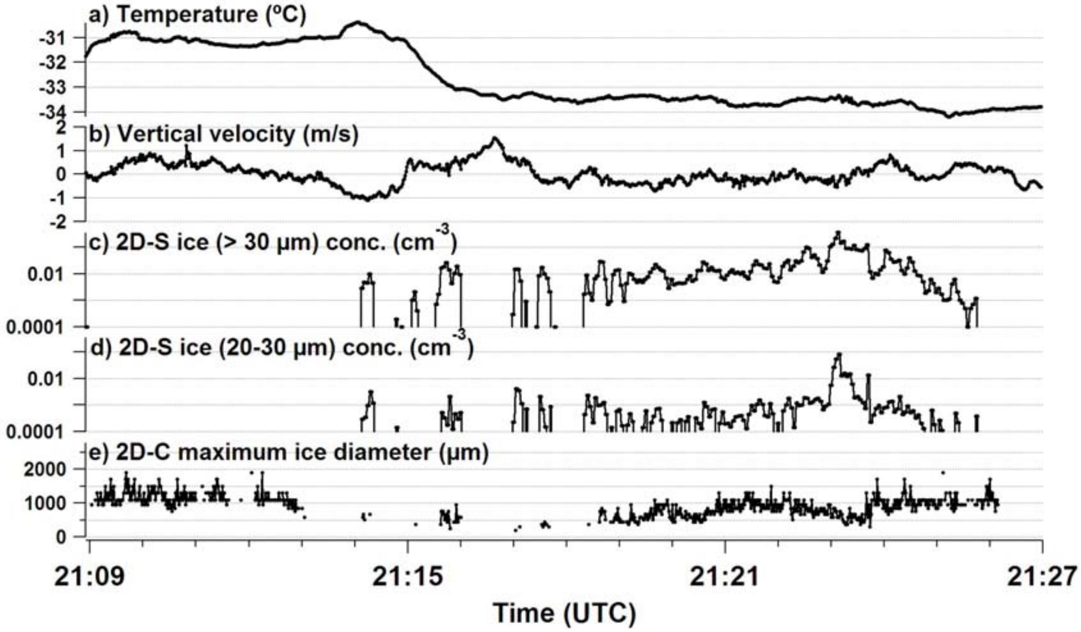

Figure 7.1. Cloud microphysical properties: a) ambient temperature (°C), b) vertical velocity (m/s), c) 2D-S ice crystal (>30 μm) number concentrations (cm^{-3}), d) 2D-S ice crystal (2-30 μm) number concentrations (cm^{-3}), and e) 2D-C maximum ice diameters (μm). Note that 2D-S data was not available for the first cloud pass.

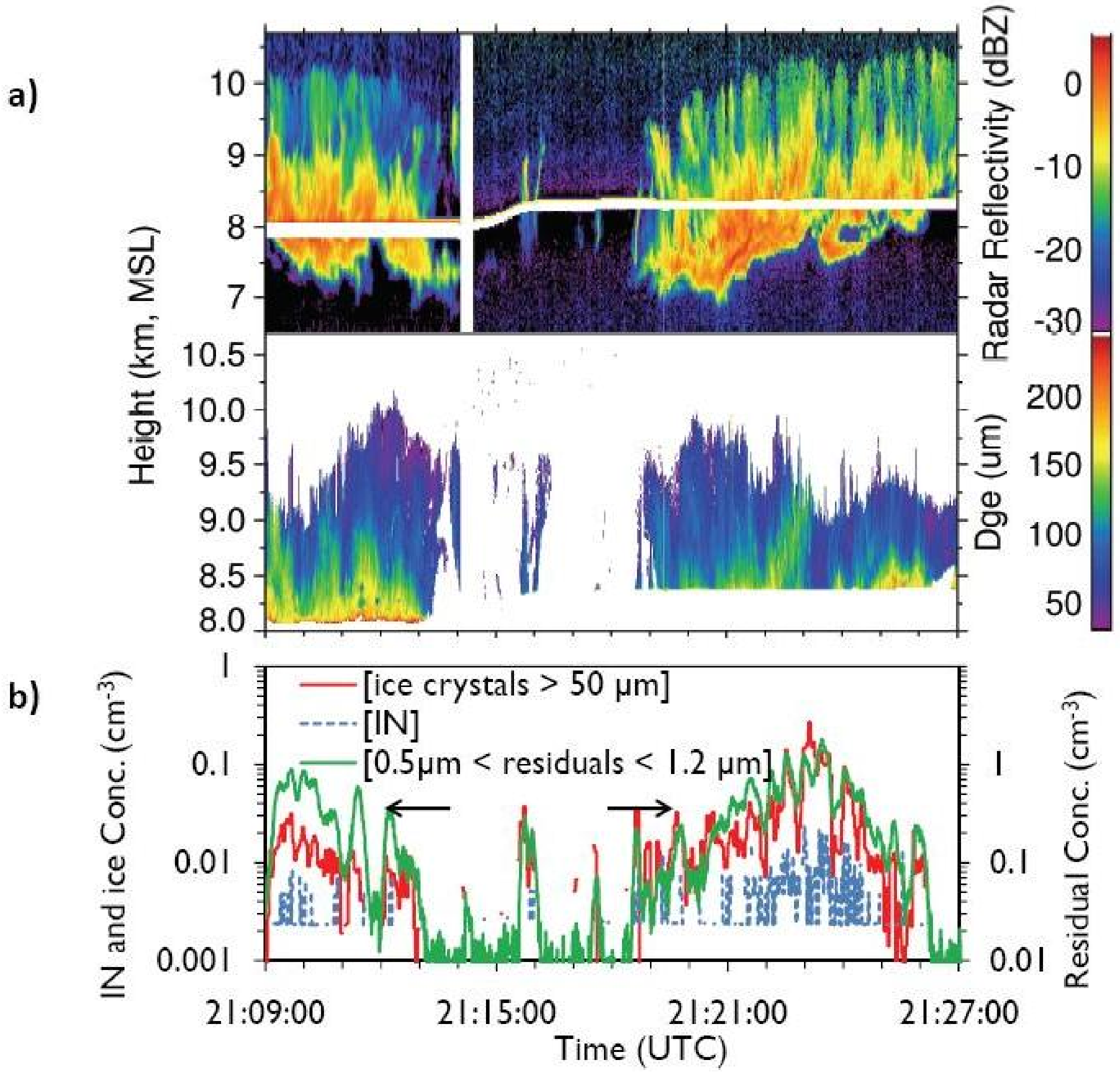

Figure 7.2. Ice cloud microphysical properties: a) Upward- and downward-pointing radar reflectivity with respect to flight time and derived general effective size (D_{ge}) of ice crystals from combined lidar and radar measurements. b) Aerosol (0.5-1.2 µm) and ice nuclei (IN) number concentrations measured in series with the CVI with respect to flight time. Ice crystal (>50 µm) number concentrations (2D-C) were measured in parallel to the CVI measurements. All concentrations are 1 Hz data except the aerosol (30 s running mean). Arrows indicate wind direction through cloud.

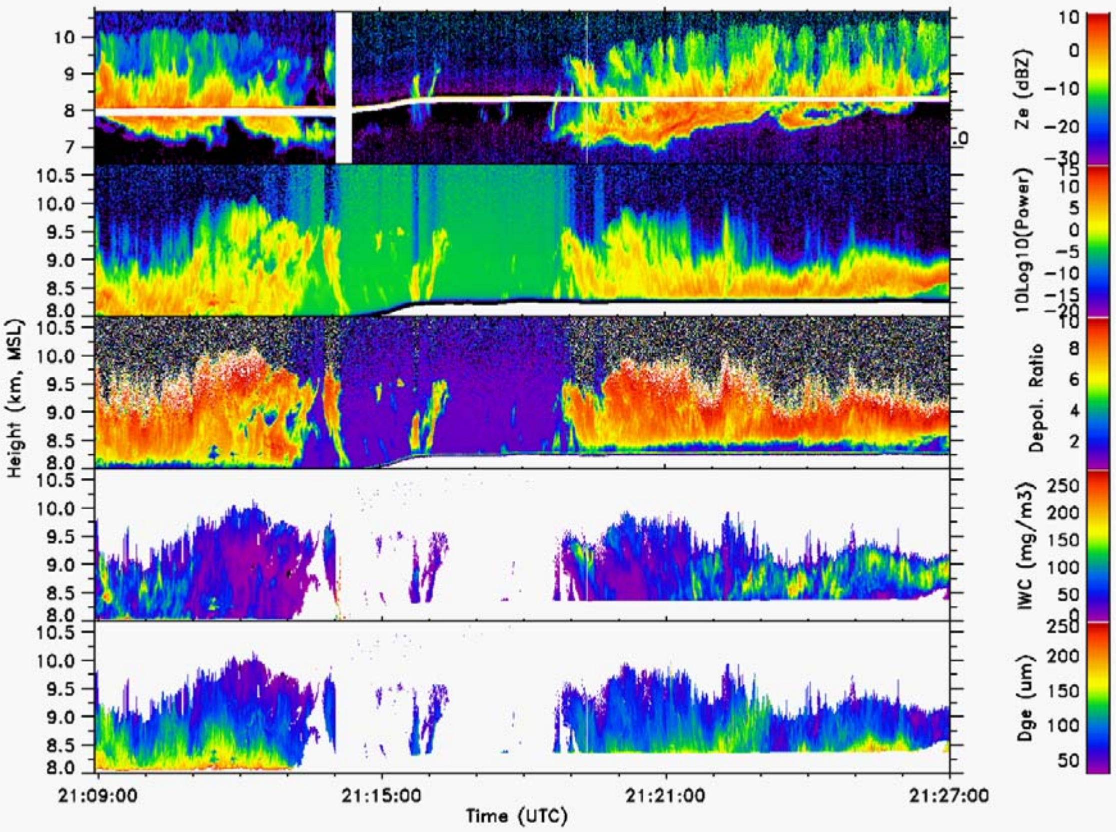

Figure 7.3. a) Upward- and downward-pointing radar reflectivity (dBZ). b) Lidar (upward pointing) attenuated backscattering power (uncalibrated). c) Lidar linear depolarization ratio (uncalibrated). d) Radar and lidar-derived ice water content (IWC) (mg/m^3). e) Lidar- and radar-derived effective ice crystal size (D_{ge}) (μm). Note that low depolarization ratios within 200 m for this case are caused by the saturation of the lidar perpendicular detection channel.

crystals. The lidar is more sensitive to high concentrations of small water droplets than low concentrations of large ice crystals. Therefore, the occurrence of supercooled water droplets can be identified based on strong lidar backscattering power and low lidar linear depolarization ratio in the absence of horizontal oriented ice crystals. For the first cloud pass, the lidar depolarization ratio measurements indicate a few small zones of supercooled liquid water aloft; however, no supercooled liquid is present above 8.65 km in the first cloud pass or at any altitude for the second pass. The regions of higher radar reflectivity at altitudes below ~8.7 km in both passes suggest the presence of large ice particles through a deep layer, which is supported by effective ice crystal sizes up to 200 μm. Radar and lidar data indicate that the cloud extended to ~10.3 km in altitude; however, 8.3 km was the maximum aircraft altitude. By taking advantage of different particle size sensitivities of the radar and lidar, vertical distributions of ice water content (IWC) and ice general effective size (D_{ge}) can be retrieved from the lidar and radar measurements. High IWC and small D_{ge} regions indicate main ice generation regions. Ice crystal dimensions up to 1,500 μm and 1,000 μm were measured in the two respective cloud passes (Figure 7.1), suggesting that some ice crystals settled from higher altitudes; this is supported by the distribution of radar-derived Doppler crystal fallspeeds having a modal value of 0.7 m s^{-1} during both cloud passes. Large ice crystals falling quickly out of the generation regions are responsible for the D_{ge} increase with height decrease. In addition, at the highest cloud altitudes, the effective crystal sizes support the presence of smaller crystals, likely in higher number concentrations.

The measured concentrations of cloud residual particles 0.5 – 1.2 μm in diameter exceed 2D-C ice crystal concentrations by up to a factor of 30; this is likely due to multiple causes. As discussed above, some ice crystals were present that were smaller than the 2D-C minimum threshold of 50 μm diameter. Also, while the CVI efficiently samples particles (density = 1.0 g cm^{-3}) between about 8 and 50 μm diameter [*Twohy et al.*, 2003], larger particles strike CVI internal surfaces and are likely to break up upon impact. The high residual number concentrations may reflect effective impaction scavenging by ice crystals through the deep cloud layer; the scavenged particles could then be released (along with the original ice nuclei) upon crystal breakup and evaporation in the CVI. A 1:1 correspondence between ice crystal concentration and CVI residuals is not expected due to problems in sampling a representative distribution of large cloud hydrometeors at high speed around an aircraft fuselage [*Twohy and Rogers*, 1993]. For the C-130 aircraft, the CVI inlet could not be mounted far enough from the fuselage relative to the aircraft's large fuselage diameter, so some ice sizes were "shadowed" while others were enhanced at the inlet location.

In the presence of non-nucleation scavenging, ice nuclei are expected to represent only a small fraction of the number of residual particles even for the low temperatures of this cloud [*Richardson et al.*, 2007]. Other factors that could limit the ice nuclei number concentrations assessed are the limitation of the size range of ice nuclei sampled in this dusty cloud and limitations on ice nucleation mechanisms assessed by the CFDC compared to those that may be present in the observed cloud. In the first case, we note that the CFDC measured ice nuclei in this study only for particles below about 1.2 μm, the 50% cut-point of an impactor couplet operated upstream of the CFDC. This impactor is presently required to distinguish ice crystals nucleated in the CFDC from non-activated aerosol particles using optical methods. The CFDC was operated to emphasize condensation/immersion freezing as expected for the cloud entry region of the orographic wave cloud on the basis of previous studies [*Cooper and Vali*, 1981]. Processing at 101 to 103% relative humidity should have reproduced the range of supersaturations expected for the cloud updrafts (0.5 to 1.5 m s^{-1}) and CCN concentrations (<100 cm^{-3}) in this case. The CFDC technique cannot effectively assess contact freezing nucleation by the classical definition of interstitial aerosol colliding with drops, although consideration of cloud parcel times and (Brownian and phoretic) scavenging rates [*Young*, 1974] for the limited liquid cloud regions present in this case suggest an extremely limited possibility for standard contact freezing nucleation. Furthermore, most particles are probably fully activated to the liquid phase at cloud edge or in other liquid regions for the aerosol and updraft conditions present. In this case, the possibility of contact freezing "inside-out" [*Durant and Shaw*, 2005] cannot be ruled out, especially since strong ice formation leads to evaporation of the remaining liquid particles. Based on the laboratory studies of Durant and Shaw [2005], this process could be effective at about at 4 to 5°C warmer temperature than the immersion freezing process for the same ice nuclei. In this sense, our data collected at -34°C support a possible contact freezing "inside-out" contribution nearly strong enough to explain cloud ice concentrations at -31°C. This does not provide clear evidence for this non-standard contact freezing process, but we simply note the possible role of such a mechanism in this particular case.

Overall, these results suggest that ice formation was dominated by heterogeneous ice nucleation processes in the cloud regions sampled, but with significant contributions of particles nucleated at higher altitude and lower temperatures settling into the flight level. Heterogeneous processes are the only viable source for ice formation based on the cloud pass temperatures (-31 to -34ºC) alone [*Baker*, 1997]. Nevertheless, as indicated, the cloud extended more than 1.5 km above the highest flight level, with consequent temperatures as low as -40°C that also permit homogeneous freezing nucleation if saturation conditions rise to water saturation in cloud parcels. However, the influence of homogeneous freezing is inferred only for a short period along the cloud pass at ~21:23 UTC when the concentrations of ice crystals below 30 µm increased sharply (Figure 7.1). Although ice crystal concentrations exceed CFDC ice nuclei number concentrations by an order of magnitude on average, we believe that lower ice nuclei concentrations primarily reflect CFDC processing at a temperature warmer than the heterogeneous ice nucleation temperature of the settled ice crystals. We also note that ice nuclei and ice crystal concentrations agree best at cloud inflow regions and show poorer agreement deep in the cloud where crystal sedimentation was occurring. While consideration of ice nucleation mechanisms alone suggests that ice crystal residual compositions are representative of heterogeneous ice nuclei and some contribution from particles freezing homogeneously, the concentrations of cloud residual particles were greater than the measured ice crystal concentrations, indicating extra non-nucleation-related scavenging of particles.

During ICE-L, A-ATOFMS provided *in situ* detection of biological particles [*Fergenson et al.*, 2004; *Russell*, 2009] in real time from the residues of individual cloud droplets and ice crystals. As shown in Figure 7.4, biological and mineral dust particles represented most (83 ± 6%) of ice crystal residues within the high-altitude ice cloud. 50 ± 12% of the ice residues were found to be mineral dust and 33 ± 10% biological residues. Minor ice crystal residue particle types included salts (sodium/potassium

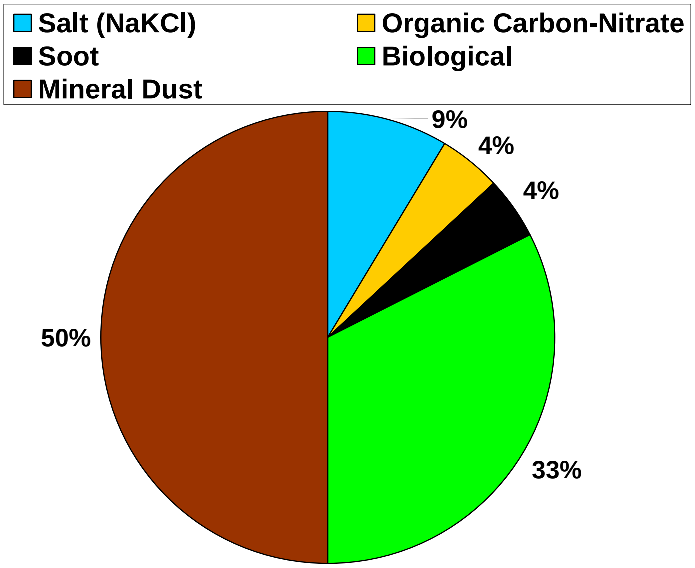

Figure 7.4. Chemical composition of ice crystal residues: Relative contributions of different particle types as measured by the A-ATOFMS for 46 submicrometer (140-700 nm) ice residual particles sampled from 21:09-21:27 UTC. 60 ± 13% of the mineral dust was internally mixed with humic and/or biological material.

chloride), organic carbon mixed with nitrate, and soot. The positive- and negative-ion mass spectra of a representative biological ice residual particle are shown in Figure 7.5a. This 260 nm biological residue is characterized by calcium, sodium, organic carbon, organic nitrogen, and phosphate. Previously, Fergenson *et al*. [2004] used ATOFMS to distinguish two Bacillus spore species from one another and from other biological and non-biological background material. More intense ion signals from the inorganic components compared with carbonaceous species do not reflect mass fractions. Due to the lower ionization potentials of alkali and alkaline earth metals, ATOFMS is more sensitive to calcium and sodium compared to carbonaceous species (eg. see Gross *et al*. [2000]), causing the ion peak areas of calcium in the biological mass spectra to be greater than those of the organic carbon markers. Relative sensitivity factors would need to be used to obtain actual mass fractions [*Gross et al.*, 2000]. Unlike mineral dust [eg., *Silva et al.*, 2000], biological particles show significant contributions from organic carbon species while lacking common marker ions observed in dust, such as aluminosilicates (i.e. SiO_2^-, SiO_3^-, AlO^-, Al^+). For additional validation of the biological mass spectral signature, *Pseudomonas syringae*, a known bacterial ice nucleus [*Vali et al.*, 1976], was run into the A-ATOFMS for comparison with the biological particles detected in the cloud ice crystals. Representative mass spectra are shown in Figure 7.6. Previously, electron microscopy analysis has shown calcium to a major component of whole *P. syringae* cells, particularly during the early phase of bacterial multiplication [*El-Masry and Sigee*, 1989]. Using a method similar to Toner *et al.* [2008], the *P. syringae* mass spectral signature was compared to the average “biological” ice crystal residue mass spectra using calculated dot products for the ion peaks in the spectra. Lower dot products

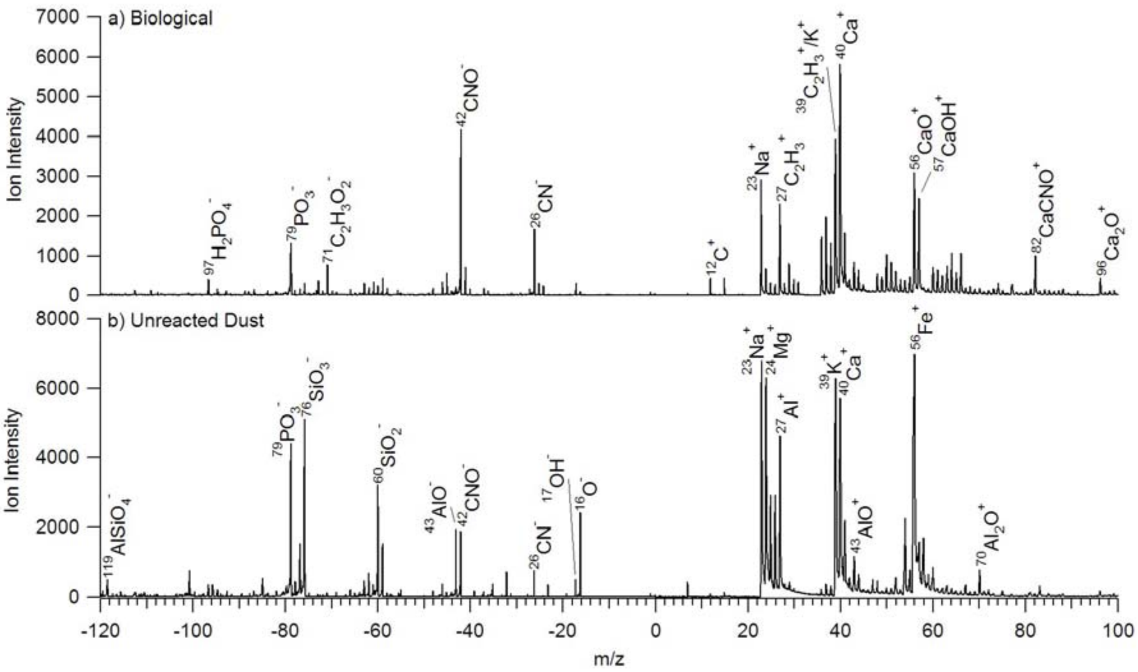

Figure 7.5. Representative chemical composition of biological and dust particles: Positive- and negative-ion mass spectra of representative individual biological (a) and mineral dust (b) CVI ice residual particles.

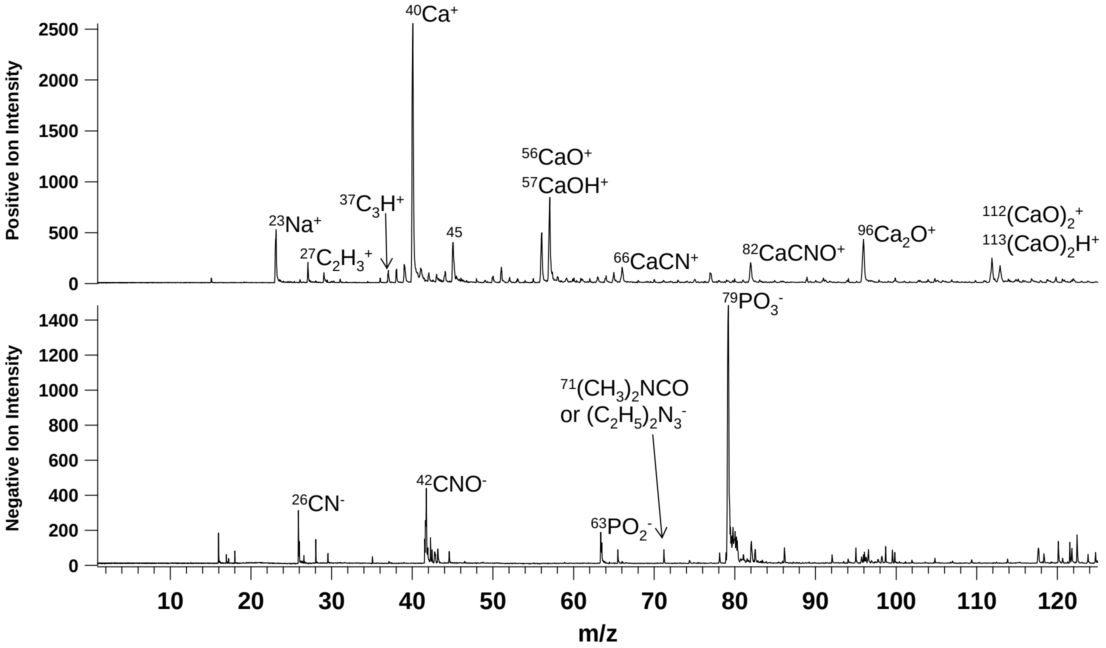

Figure 7.6. Representative single-particle positive- and negative-ion mass spectra of *Pseudomonas syringae.*

indicate less similarity between the two sets of particles; whereas high dot products indicate more similarity. In this case, the mass spectral comparison showed a strong similarity (dot product = 0.7) between the *P. syringae* and ice crystal residue biological particles, supporting the ICE-L signature as biological in origin. It is important to note, however, that the good agreement here does not necessarily imply that the biological particles detected in the ice residues were *P. syringae*. All ICE-L biological particles contained nearly identical negative ion mass spectral markers with positive ion organic markers. The ion signals of the inorganic components, namely sodium, magnesium, potassium, and calcium, differed in intensity within the individual particles, suggesting a diversity of biological particle types, including bacteria, fungal spores, and/or plant material.

Importantly, the use of dual-polarity mass spectrometry enabled the A-ATOFMS to unambiguously distinguish biological particles from non-biological carbonaceous and inorganic particles, a previous limitation in the detection of biological particles in cloud ice [*Möhler et al.*, 2007]. Previous real-time measurements of ice nuclei and ice crystal residues have shown dominant contributions by mineral dust [*Cziczo et al.*, 2004; *Richardson et al.*, 2007]. The positive- and negative-ion mass spectra of a representative mineral dust ice residual particle are shown in Figure 7.5b. This 340 nm dust particle, representative of a phyllosilicate clay particle [*Gallavardin et al.*, 2008a], is characterized by intense inorganic markers, including sodium, magnesium, potassium, calcium, iron, and aluminosilicates, as well as less intense ion markers of organic nitrogen and phosphate. Most (87 ± 8% by number) of the mineral dust particles detected in the cloud ice residues were characterized as phyllosilicate clays, such as illite, montmorrillonite, and kaolinite [*Gallavardin et al.*, 2008a], which are known ice nuclei [*Salam et al.*, 2006]. 60 ± 13% of the dust particles contained both organic nitrogen and phosphate, suggesting internal mixing of biological material with the mineral dust, which may have increased the ice nucleation efficiency of the dust. Less than half (30 ± 17%) of the sampled dust particles contained nitrate and/or sulfate, and no ammonium was detected on any dust particles, similar to previously measured mineral dust ice residues [*Cziczo et al.*, 2004]. This suggests lofting to high altitudes near the source of the dust storm, followed by transport in the mid and upper troposphere, with very low interactions of the dust with pollutants during transport. As recent laboratory studies have shown decreased ice nucleation efficiencies for mineral dust coated by nitrate, sulfate, and organics [*Gallavardin et al.*, 2008b], it is possible that the coated mineral dust, as well as the minor salt and organic carbon particle types observed, froze homogeneously or were scavenged by falling ice crystals within the deep cloud.

Cloud ice residues were sampled at 7.9 – 8.3 km m.s.l., which corresponded to equivalent potential temperatures (θ_e) of 323.6 – 324.6 K. Unfortunately, due to aircraft and mission constraints, the cloud inflow was not well characterized. However, Figure 7.7 shows the relative fractions of different chemical composition particle types sampled in clear air at 7.5 – 7.8 km MSL, which corresponded to θ_e of 322.1-324.1. This provides a comparison between the general air mass and sampled cloud ice residues. Compared to the cloud ice residues (Figure 2), the biological and mineral dust particles were enhanced by a factor of ~3 in the cloud ice compared to the clear air; whereas, the organic carbon-nitrate particles were enhanced in the clear air compared to the cloud ice by a factor of ~14. This suggests preferential nucleation and/or scavenging of the biological particles

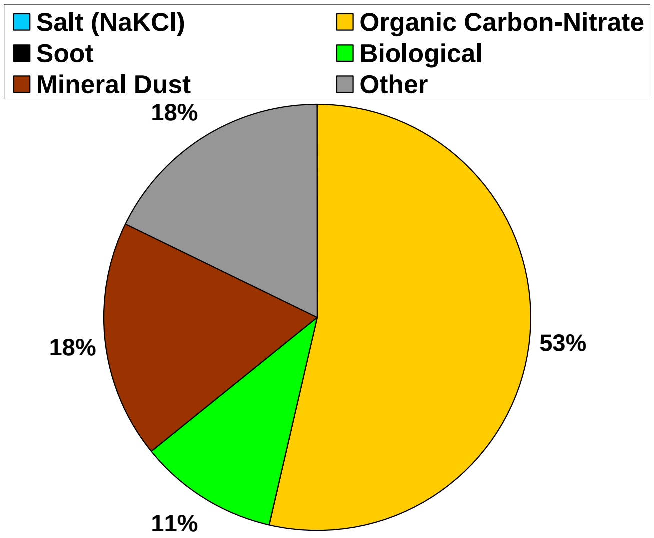

Figure 7.7. Relative contributions of different particle types as measured by the A-ATOFMS for 28 submicron (145-715 nm) ambient particles collected in clear air at 7.5 – 7.8 km m.s.l.

and mineral dust. In summary, the significant fractions of mineral dust and biological particles in the ice residues suggest their possible favored role in ice formation.

To further identify the source region of the biological and mineral dust particles affecting the ice clouds over Wyoming, a global aerosol model, a meteorological model, surface observations, satellite imagery, and air mass back trajectory analysis were used. The sampling altitude precludes the possibility of a local source of the dust and biological particles. The absence of surface observations of dust, high winds, and low visibility near or upwind of Wyoming also make a local source unlikely. Instead, the observational evidence points to East Asia as the likely source of the dust. This long-range transport phenomena has been documented previously for spring [*Husar et al.*, 2001; *McKendry et al.*, 2007] and fall [*Wells et al.*, 2007]. Surface observations of high winds, dust storms, and reduced visibility were reported in Mongolia and China on October 29 and 30 and November 1. The Navy Operational Global Atmospheric Prediction System (NOGAPS) analyses reveal that the East Asian deserts were impacted by a deepening trough east of the Sayan Mountains (50N, 110E) that moved east across the source region on October 29 and 30. Possible approximate source regions include 43N, 107E; 43N, 113E; 47N, 112E. SeaWiFS satellite imagery shows obscuration of surface features in central China and Mongolia on these days, most likely due to dust. Simulations from the Navy Aerosol Analysis and Prediction System global aerosol model show that the surface winds associated with the trough were sufficient to generate a mild dust event that was then advected as an elevated plume northeast across Japan on November 1. A second East Asian dust mobilization event was observed on November 1 by high winds over eastern Mongolia but this event headed southeast towards Korea. Both the NAAPS simulations and HYSPLIT back trajectories (Figure 7.8) [*Draxler and Rolph*, 2003] indicate that the late-October dust event could have reached the upper tropopause over Wyoming by November 7. However, NAAPS transports the dust too far north, reaching the Canadian plains instead of Wyoming, and HYSPLIT back trajectories end up south of the dust source regions of East Asia. These two results are consistent and expected since both approaches use operational numerical weather prediction models for the calculations. Evidently the flow was more zonal than predicted by either of the dynamical models. It should also be noted that uncertainty increases with trajectory length; thus, it was important in this study to use multiple methods and observations to locate the most likely source region of the dust.

Another possible source of the dust may have been the deserts of Northern Africa. Observations of high winds, dust storms, and reduced visibility were reported along the coast from October 26 through November 1 as a low passed eastward across the Mediterranean. The plumes are easily seen over the ocean in SeaWiFS imagery. NAAPS simulations show the dust was transported north into central Europe and then eastward across central Asia before the concentrations became too small to track. This pathway of Saharan dust to East Asia, including continued transport across the Pacific Ocean has been documented in the past.

In addition, the average mineral dust cloud ice residue mass spectral signature was compared to ATOFMS mass spectral signatures of previously measured dust and soil samples [*Coffee*, 2002] using calculated dot products for the ion peaks in the spectra. The dust cloud ice residues showed greater similarity to several Asian dusts and soils (mass spectral comparison dot products >0.7) compared to most North American dusts

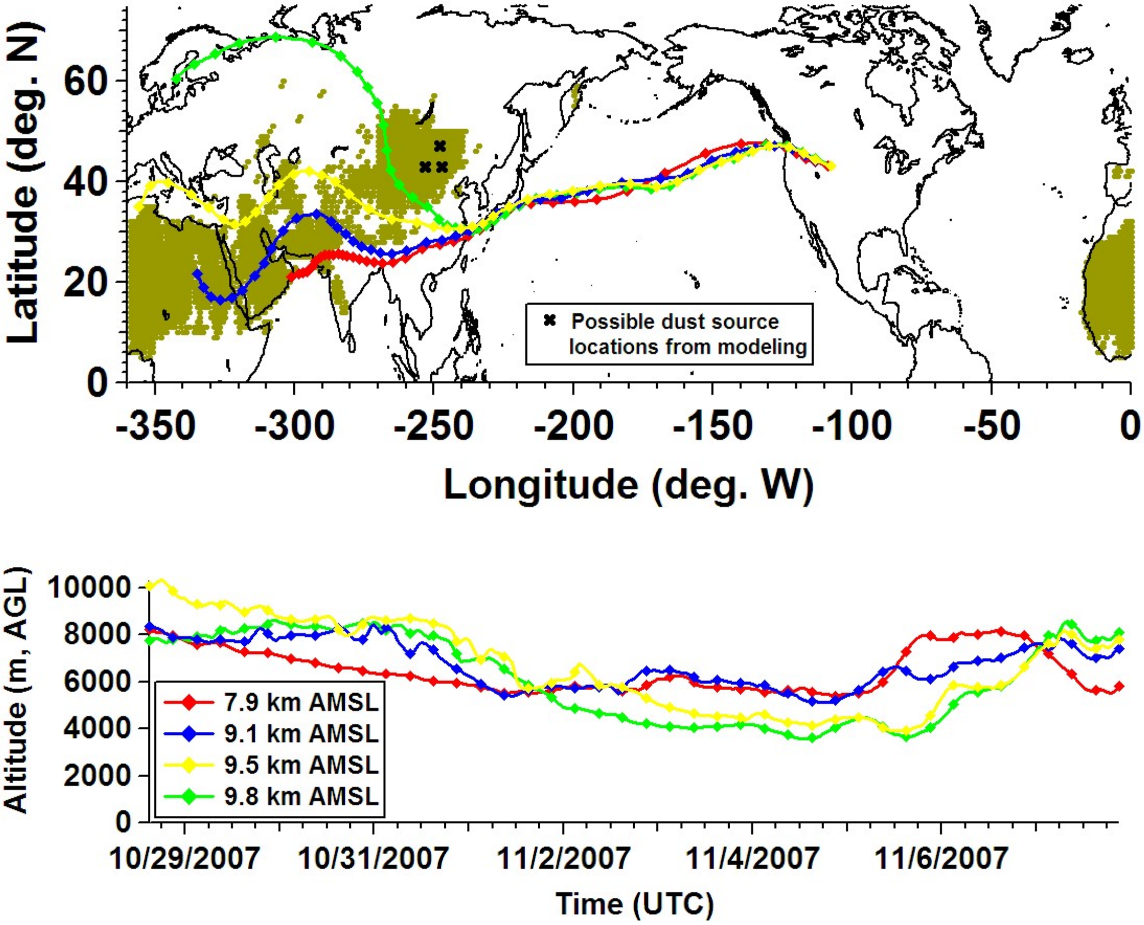

Figure 7.8. NOAA HYSPLIT air mass back trajectories originating over Wyoming, showing transport from over Asia and Africa. Dust source regions in Asia and Africa are noted in brown; the NAAPS dust source region is derived from the USGS 1-km Global Land Cover Characteristics Data Base Version 1.2 and the Total Ozone Mapping Spectrometer (TOMS) Aerosol Index (AI) [*Walker et al.*, 2009]. Erodible land was first defined as the fractional coverage of the eight USGS land use types known to produce dust. In the Sahara, Southwest Asia, and the Taklamakan regions, the distribution was further refined based on the annual mean values of the TOMS AI.

and soils (dot products <0.6). In particular, Zhehbeitai sand from Shanxi, China [*Coffee*, 2002], sand from Ya Dan Gansu, China [*Coffee*, 2002], and fresh dust detected during the ACE-Asia (*R/V* Ronald Brown) [*Sullivan et al.*, 2007] and PACDEX (Gosan, Korea) field campaigns showed good similarity (dot products = 0.70, 0.72, 0.75, and 0.73, respectively) to the dust cloud ice residues. Poor similarity was found for Montana soil (NIST 2710) [*Coffee*, 2002] (dot product = 0.55), for example. The similarity of the mineral dust ice residues to the Asian dust is likely due to the high phyllosilicate content of Asian dust, which ranges from 32-58% with illite and montmorrillonite as the most abundant clay minerals [*Jeong*, 2008].

In summary, these results indicate that the dust and biological particles were probably lofted from central China and eastern Mongolia on 29-30 October or 1 November 2007 and transported at an altitude of ~7.5 km across the Pacific Ocean and western United States. These models also show lofting of dust from Sudan or the Sahara [*McKendry et al.*, 2007] occurring 29-31 October 2007, followed by trans-Asia transport. Supporting the assignment of Asian dust transport, the chemistry of the dust ice residues showed the highest similarity to several Asian dusts and soils in comparison with most North American dusts and soils, discussed further in the supplementary information. These dust mixing state results demonstrate that it cannot always be assumed that long-range transported dust is always aged, or reacted; this has implications for the treatment of the anthropogenic indirect aerosol effect within mixed-phase cloud models [*Hoose et al.*, 2008], as well as the direct radiative forcing of mineral dust aerosol within global climate models. Although the long-range co-transport of dust and biological particles at high altitudes has been observed previously [*Kellogg and Griffin*, 2006], long-range transported biological particles have not been directly identified in clouds. Furthermore, the on-line simultaneous detection of biological and mineral dust particles suggests a terrestrial source of these biological particles.

Ice nucleation active biological particles have been detected previously in precipitation [*Christner et al.*, 2008a]; however, demonstration of a direct connection between biological particles and ice crystals in clouds has remained elusive [*Möhler et al.*, 2007]. In this study, dual-polarity single-particle mass spectrometry measurements enalbed the *in situ* and unambiguous detection of biological particles in cloud ice. This provides the first evidence for the involvement of biological particles, likely bacteria, fungal spores, and/or plant material, in ice processes. This was the only ICE-L wave cloud flight (1 of 9) affected by long-range transported dust, and notably ice nuclei number concentrations reported herein were among the top 2% of those measured from cloud residues during all ICE-L wave cloud sampling, supporting the important role that dust and biological particles may play in cloud ice processes. Thus, it is suggested that future studies target ice clouds over the western United States during the spring season when Asian dust storms reach their maximum frequency. The identification of a significant fraction of biological particles within cloud ice crystals affected by heterogeneous freezing represents a significant step forward in establishing an understanding of the interaction of biological particles with cloud processes. Herein, long-range transported biological and dust particles involved in cloud ice formation highlight the importance of the interplay between land surface and free troposphere processes and their effects on cloud processes. With increasing frequency and intensity of dust storms predicted as a consequence of climate change and land use changes in desert regions [*Solomon et al.*, 2007], the presence and transport of biological particles and mineral dust at high altitudes from large-scale dust storms will probably increase and may affect ice cloud processes, creating previously unidentified climate-system feedbacks and impacts on precipitation, human health, and ecosystems.

7.5 Acknowledgements

Prof. Kimberly Prather and I acknowledge financial support from NSF (ATM-0650659, ATM-0321362); I performed the A-ATOFMS measurements, data analysis, and wrote the manuscript. Dr. Paul J. DeMott (Colorado State Univ.) provided the CFDC measurements and contributed to writing; financial support was provided by NSF (ATM-0611936). Dr. Jeffrey R. French and Prof. Zhien Wang (Univ. of Wyoming) provided lidar and radar data; financial support was provided by NSF (ATM-0645644). NSF and NCAR are acknowledged for financial support of ICE-L, as well Dr. Andrew J. Heymsfield (NCAR), who processed the cloud probe data. The Office of Naval Research (PE-0602435N) is acknowledged for financial support for D.L. Westphal, who performed surface and long-range transport modeling. Prof. Cynthia H. Twohy (Oregon State University) coordinated and ran the CVI during flight; financial support was provided by NSF (ATM-0612605). Cloud probe data were provided by NCAR/EOL under sponsorship of NSF (http://data.eol.ucar.edu). Dr. Samuel Haimov (Univ. of Wyoming) processed the radar data. Dr. Anthony J. Prenni (Colorado State Univ.) and Dr. Trude Eidhammer (NCAR) assisted with CFDC measurements and data analysis. Cassandra Gaston assisted with the *P. syringae* A-ATOFMS data collection; Prof. Jack Dixon and Robert Dowen III provided the *P. syringae* cultures. Prof. Sonia Kreidenweis (Colorado

State Univ.) is thanked for discussions. The authors acknowledge the NOAA ARL for the provision of HYSPLIT (http://www.arl.noaa.gov/ready.html).

Publication Acknowledgment

Chapter 7 has been reproduced with permission from the Nature Publishing Group: Pratt, K.A., DeMott, P.J., French, J.R., Wang, Z., Westphal, D.L., Heymsfield, A.J., Twohy, C.H., Prenni, A.J., Prather, K.A. In-situ detection of biological particles in cloud ice crystals. *Nature Geoscience*, 2009, 2, 398-401.

7.6 References

Baker, M.B. (1997), Cloud microphysics and climate, *Science*, *276*(1072-1078.

Christner, B.C., R. Cal, C.E. Morris, K.S. McCarter, C.M. Foreman, M.L. Skidmore, S.N. Montross, and D.C. Sands (2008a), Geographic, seasonal, and precipitation chemistry influence on the abundance and activity of biological ice nucleators in rain and snow, *Proc. Natl. Acad. Sci. U. S. A.*, *105*(48), 18854-18859.

Christner, B.C., C.E. Morris, C.M. Foreman, R. Cai, and D.C. Sands (2008b), Ubiquity of biological ice nucleators in snowfall, *Science*, *319*(1214.

Coffee, K.R., Single particle characterization of soil and dust particulate matter in the urban and marine environments, University of California, Riverside, Riverside, CA, 2002.

Cooper, W.A., and G. Vali (1981), The origin of ice in mountain cap clouds, *J. Atmos. Sci.*, *38*(1244-1259.

Cziczo, D.J., D.M. Murphy, P.K. Hudson, and D.S. Thomson (2004), Single particle measurements of the chemical composition of cirrus ice residue during CRYSTAL-FACE, *J. Geophys. Res.*, *109*(D04201), doi:10.1029/2003JD004032.

Deguillaume, L., M. Leriche, P. Amato, P.A. Ariya, A.-M. Delort, U. Poschl, N. Chaumerliac, H. Bauer, A.I. Flossmann, and C.E. Morris (2008), Microbiology and atmospheric processes: chemical interaction of primary biological aerosols, *Biogeosciences*, *5*(1073-1084.

Draxler, R.R., and G.D. Rolph (2003), HYSPLIT (HYbrid Single-Particle Lagrangian Integrated Trajectory) Model access via NOAA ARL READY Website (http://www.arl.noaa.gov/ready/hysplit4.html), *NOAA Air Resources Laboratory*, Silver Spring, MD.

Durant, A.J., and R.A. Shaw (2005), Evaporation freezing by contact nucleation inside-out, *Geophys. Res. Lett.*, *32*(L20814), doi:10.1029/2005GL024175.

El-Masry, M.H., and D.C. Sigee (1989), Electron probe X-ray microanalysis of *Pseudomonas syringae* pv. *tabaci* isolated from inoculated tobacco leaves, *Physiol. Mol. Plant Path.*, *34*(557-573.

Fergenson, D.P., M.E. Pitesky, H.J. Tobias, P.T. Steele, G.A. Czerwieniec, S.C. Russell, C.B. Lebrilla, J.M. Horn, K.R. Coffee, A. Srivastava, S.P. Pillai, M.T.P. Shih, H.L. Hall, A.J. Ramponi, J.T. Chang, R.G. Langlois, P.L. Estacio, R.T. Hadley, M. Frank, and E.E. Gard (2004), Reagentless detection and classification of individual bioaerosol particles in seconds, *Anal. Chem.*, *76*(2), 373-378.

Gallavardin, S., U. Lohmann, and D. Cziczo (2008a), Analysis and differentiation of mineral dust by single particle laser mass spectrometry, *Int. J. Mass Spectrom.*, *274*(56-63.

Gallavardin, S.J., K.D. Froyd, U. Lohmann, O. Moehler, D.M. Murphy, and D.J. Cziczo (2008b), Single particle laser mass spectrometry applied to differential ice nucleation experiments at the AIDA chamber, *Aerosol Sci. Technol.*, *42*(773-791.

Gross, D.S., M.E. Galli, P.J. Silva, and K.A. Prather (2000), Relative sensitivity factors for alkali metal and ammonium cations in single particle aerosol time-of-flight mass spectra, *Anal. Chem.*, *72*(2), 416-422.

Heymsfield, A.J. (2007), On measurements of small ice particles in clouds, *Geophys. Res. Lett.*, *34*(L23812), doi:10.1029/2007GL030951.

Hoose, C., U. Lohmann, R. Erdin, and I. Tegen (2008), The global influence of dust mineralogical composition on heterogeneous ice nuclation in mixed-phase clouds, *Environ. Res. Lett.*, *3*(doi:10.1088/1748-9326/3/2/025003.

Husar, R.B., D. Tratt, B.A. Schichtel, S.R. Falke, F. Li, D. Jaffe, S. Gassó, T. Gill, N.S. Laulainen, F. Lu., M. Reheis, Y. Chun, D. Westphal, B.N. Holben, C. Geymard, I. McKendry, N. Kuring, G.C. Feldman, C. McClain, R.J. Frouin, J. Merrill, D. DuBois, F. Vignola, T. Murayama, S. Nickovic, W.E. Wilson, K. Sassen, and N. Sugimoto (2001), The Asian dust events of April 1998, *Journal of Geophysical Research*, *106*(18,317-18,330.

Jayaweera, K., and P. Flanagan (1982), Investigations on biogenic ice nuclei in the Arctic atmosphere, *Geophys. Res. Lett.*, *9*(1), 94-97.

Jeong, G.Y. (2008), Bulk and single-particle mineralogy of Asian dust and a comparison with its source soils, *Journal of Geophysical Research*, *113*(doi:10.1029/2007JD008606.

Kellogg, C.A., and D.W. Griffin (2006), Aerobiology and the global transport of desert dust, *Trends in Ecology and Evolution*, *21*(11), 638-644.

Leon, D., G. Vali, and M. Lothon (2006), Dual-doppler analysis in a single plane from an airborne platform, *J. Atmos. Oceanic Technol.*, *23*(3-22.

Lohmann, U., and J. Feichter (2005), Global indirect aerosol effects: a review, *Atmos. Chem. Phys.*, *5,*(715-737.

McKendry, I.G., K.B. Strawbridge, N.T. O'Neill, A.M. Macdonald, P.S.K. Liu, W.R. Leaitch, K.G. Anlauf, L. Jaegle, T.D. Fairlie, and D.L. Westphal (2007), Trans-Pacific transport of Saharan dust to western North America: A case study, *J. Geophys. Res.*, *112*(D01103), doi:10.1029/2006JD007129.

Möhler, O., P.J. DeMott, G. Vali, and Z. Levin (2007), Microbiology and atmospheric processes: the role of biological particles in cloud physics, *Biogeosciences*, *4*(6), 1059-1071.

Ogren, J.A., J. Heintzenberg, and R.J. Charlson (1985), In-situ sampling of clouds with a droplet to aerosol converter, *Geophys. Res. Lett.*, *12*(3), 121-124.

Richardson, M.S., P.J. DeMott, S.M. Kreidenweis, D.J. Cziczo, E.J. Dunlea, J.L. Jimenez, D.S. Thomson, L.L. Ashbaugh, R.D. Borys, D.L. Westphal, G.S. Casuccio, and T.L. Lersch (2007), Measurements of heterogeneous ice nuclei in the western United States in springtime and their relation to aerosol characteristics, *J. Geophys. Res.*, *112*(D02209), doi:10.1029/2006JD007500.

Rogers, D.C., P.J. DeMott, S.M. Kreidenweis, and Y. Chen (2001), A continuous-flow diffusion chamber for airborne measurements of ice nuclei, *J. Atmos. Oceanic Technol.*, *18*(725-741.

Russell, S.C. (2009), Microorganism characterization by single particle mass spectrometry, *Mass Spectrom. Rev.*, *28*(376-387.

Salam, A., U. Lohmann, B. Crenna, G. Lesins, P. Klages, D. Rogers, R. Irani, A. MacGillivray, and M. Coffin (2006), Ice nucleation studies of mineral dust particles with a new continuous flow diffusion chamber, *Aerosol Sci. Technol.*, *40*(2), 134-143.

Sassen, K. (2005), Dusty ice clouds over Alaska, *Nature*, *434*(456.

Saxena, V.K. (1983), Evidence of the biogenic nuclei involvement in Antarctic coastal clouds, *J. Phys. Chem.*, *87*(21), 4130-4134.

Silva, P.J., R.A. Carlin, and K.A. Prather (2000), Single particle analysis of suspended soil dust from Southern California, *Atmos. Environ.*, *34*(11), 1811-1820.

Solomon, S., D. Qin, M. Manning, Z. Chen, M. Marquis, K.B. Averyt, M. Tignor, and H.L. Miller, Climate Change 2007: The Physical Science Basis. Contribution of Working Group I to the Fourth Assessment Report of the Intergovernmental Panel on Climate Change, pp. 996, Cambridge University Press, New York, NY, 2007.

Sullivan, R.C., S.A. Guazzotti, D.A. Sodeman, and K.A. Prather (2007), Direct observations of the atmospheric processing of Asian mineral dust, *Atmos. Chem. Phys.*, *7*(1213-1236.

Toner, S.M., L.G. Shields, D.A. Sodeman, and K.A. Prather (2008), Using mass spectral source signatures to apportion exhaust particles from gasoline and diesel powered vehicles in a freeway study using UF-ATOFMS, *Atmos. Environ.*, *42*(568-581.

Twohy, C.H., and D. Rogers (1993), Airflow and water drop trajectories at instrument sampling points around the Beechcraft King Air and Lockheed Electra, *J. Atmos. Oceanic Technol.*, *10*(566-578.

Twohy, C.H., J.W. Strapp, and M. Wendisch (2003), Performance of a counterflow virtual impactor in the NASA Icing Research Tunnel, *J. Atmos. Oceanic Technol.*, *20*(781-790.

Vali, G., M. Christensen, R.W. Fresh, E.L. Galyan, L.R. Maki, and R.C. Schnell (1976), Biogenic Ice Nuclei 2. Bacterial Sources, *J. Atmos. Sci.*, *33*(8), 1565-1570.

Walker, A.L., D.L. Westphal, M. Liu, S.D. Miller, and K.A. Richardson (2009), The Naval Research Laboratory's high resolution (1 km) dust source database for the Middle East and Southwest Asia, *J. Geophys. Res.*, *Submitted.*(

Wang, Z., and K. Sassen (2002), Cirrus cloud microphysical property retrieval using lidar and radar measurements. Part I. Algorithm description and comparison with in situ data, *J. Appl. Meteor.*, *41*(218-229.

Wang, Z., P. Wechsler, J. French, A. Rodi, S. Haimov, G. Vali, D. Leon, and A.L. Pazmany, The new integrated cloud observation capabilities of Wyoming King Air by combining radar, lidar, microwave radiometer and in situ measurements, in *International Conference on Cloud Physics and Precipitation*, Cancun, MX, 2008.

Wells, K.C., M. Witek, P. Flatau, S.M. Kreidenwei, and D.L. Westphal (2007), An analysis of seasonal surface dust aerosol concentrations in the western US (2001-2004): Observations and model predictions, *Atmos. Environ.*, *41*(31), 6585-6597.

Young, K.C. (1974), The role of contact nucleation in ice phase initiation in clouds, *J. Atmos. Sci.*, *31*(768-776.

Chapter 8

8 Playa Salts Serve as Natural Cloud Nuclei

8.1 Synopsis

During the Ice in Clouds Experiment – Layer Clouds (ICE-L), dry lakebed, or playa, salts from the Great Basin region of the United States were identified as a major source of cloud nuclei during several orographic wave cloud flights. Aboard the NSF/NCAR C-130, residues of individual cloud particles were directly characterized in real-time using a counterflow virtual impactor (CVI) in series with the aircraft aerosol time-of-flight mass spectrometer (A-ATOFMS) and Aerodyne compact time-of-flight aerosol mass spectrometer (C-ToF-AMS). In addition, transmission electron microscopy with energy dispersive X-ray analysis (TEM-EDX) and scanning transmission X-ray microscopy with near edge X-ray absorption fine structure spectroscopy (STXM/NEXAFS) analyses of the cloud residues provided additional chemical characterization. For residues of cloud droplets, sodium-potassium-magnesium-calcium-chloride particles characterized by the A-ATOFMS were found to have a similar mass spectral signature to playa salts showing elevated cloud condensation nuclei (CCN) efficiencies. In particular, these salt particles were preferentially observed as residues of large droplets (>19 μm) compared to smaller droplets (>7 μm). While the high CCN activity of sea salt is often considered for marine environments, the presence of playa salts as cloud nuclei in continental North America has not been shown previously. This study suggests that the impact of playa dust on cloud formation is significant due to the apparent cloud-forming ability of playa dust, global abundance of playas, and increasing potential for playa dust storms due to land use changes.

8.2 Introduction

The effects of aerosol particles on cloud formation and properties represent the largest source of uncertainty in climate prediction [*Solomon et al.*, 2007]. Certain aerosol particles can serve as cloud condensation nuclei (CCN) or ice nuclei (IN), indirectly affecting climate by changing cloud reflectivity, cloud lifetime, and precipitation patterns [*Andreae and Rosenfeld*, 2008]. To model current and future climate change, the aerosol population and corresponding cloud nucleating ability must be understood, particularly with regard to spatial and temporal variability. The critical supersaturation (S_c) at which a particle activates to become a cloud droplet is proportional to the third power of its diameter and to the first power of its soluble fraction [*Junge and McLaren*, 1971]. While chemical composition is less important than size, it is predicted to have a significant role in the activation of aerosols containing less than approximately 10-15% soluble material [*Junge and McLaren*, 1971; *Roberts et al.*, 2002]. Thus, Dusek et al. [2006] suggested that regional and global climate models can assume a "typical" size distribution to estimate CCN abundance and the effects of aerosols on cloud physics. However, Hudson [2007] examined the relationship between particle size and S_c for a greater range of ambient conditions, showing greater variability than observed by Dusek et al. [2006], particularly for "clean" air masses. Due to variability between different air masses, Hudson [2007] concluded that particle chemistry must be considered to avoid inaccurate estimates of CCN. Recently, Twohy and Anderson [2008] observed salts (chloride and sulfate salts of Na, K, Ca, and Mg) as preferred cloud droplet nuclei for particles < 0.2 μm in diameter. However, most cloud studies have focused on marine locations with few studies investigating the chemical composition of clouds in remote continental locations.

Uncoated mineral dust particles are generally assumed to be insoluble, not acting as CCN until becoming coated with sulfate, nitrate, or chloride, for example [*Andreae and Rosenfeld*, 2008]. However, Twohy et al [2009] found submicron African dust near the source acted as CCN, and recent work has highlighted the role of dust mineralogy on cloud activation properties [*Kelly et al.*, 2007]. In particular, dust from dry lakebeds, or playas, is generally composed of ~10-44% soluble salts [*Abuduwaili et al.*, 2008; *Blank et al.*, 1999; *Reheis*, 1997; *Singer et al.*, 2003]. Salt crusts form on playas following rapid evaporation of a flood surface, which concentrates soluble salts at the top surface layer, producing a fluffy, wind-erodible crystalline surface [*Blackwelder*, 1931; *Lowenstein and Hardie*, 1985; *Russell*, 1883]. Common playa evaporite minerals include halite, gypsum, mirabilite, thenardite, epsomite, trona, sylvite, carnallite, calcite/aragonite, dolomite, hanksite, northupite, and aphthitalite [*Bryant et al.*, 1994; *Droste*, 1961; *Güven and Kerr*, 1966; *Lowenstein and Hardie*, 1985]. Chemical analysis of playa dust have shown increased mass fractions of potassium, chloride, sulfate, and sodium with respect to the bulk (deeper) playa soil [*Blank et al.*, 1999].

Playas are present globally [*Jones and Deocampo*, 2004; *Prospero et al.*, 2002] and contribute to the high global dust burden [*Andreae and Rosenfeld*, 2008]. Formenti et al. [2003] identified the presence of playa salts within Saharan dust plumes over the Atlantic Ocean. Recent laboratory CCN measurements demonstrated that a more hygroscopic fraction of playa dust showed CCN activities similar to sodium chloride;

whereas, a less hygroscopic fraction heterogeneously nucleated ice at lower relative humidities than required for homogeneous ice nucleation at temperatures below -40 °C [*Koehler et al.*, 2007]. Studies in the western U.S. hypothesized that playa dust may be incorporated into clouds and rained out when air masses encounter mountain ranges [*Reheis*, 2006; *Reheis and Kihl*, 1995]. Recent satellite-based studies of Aral Sea dust storms suggest that playa dust particles act as giant CCN and promote precipitation [*Rudich et al.*, 2002].

Results, described herein, from the Ice in Clouds Experiment – Layer Clouds (ICE-L) provide the first *in-situ* chemical composition measurements of playa salts within cloud droplets and ice crystals. A detailed chemical characterization of the cloud residues is presented using a variety of mass spectrometry and electron microscopy techniques. CCN measurements are shown for a playa crust sample with similar chemistry to that of the cloud residues sampled during ICE-L. Further, the impacts of cloud microphysics on the incorporation of the playa salts within the orographic wave cloud are discussed.

8.3 Experimental

8.3.1 Overview and Cloud Sampling

Measurements of orographic wave clouds were made aboard the National Science Foundation/National Center for Atmospheric Research (NSF/NCAR) C-130 aircraft during the Ice in Clouds Experiment – Layer Clouds (ICE-L). For this work, we primarily focus on measurements made on November 16, 2007 during research flight #3 (RF03) over Wyoming (41.6-42.8°N, 105.8-108.5°W) at 5.9-7.0 km above mean sea level (MSL). The National Oceanic and Atmospheric Administration (NOAA) Air Resources Laboratory HYSPLIT (Hybrid Single-Particle Lagrangian Integrated Trajectory) model was utilized for air mass back trajectory analysis [*Draxler and Rolph*, 2003]. In clear air, an Ultra High Sensitivity Aerosol Spectrometer (UHSAS, Particle Metrics Inc., Boulder, CO) provided size-resolved aerosol number concentrations (0.1-1.0 μm in diameter). Clear air total condensation nuclei (CN) concentrations were measured using a condensation particle counter (CPC, TSI Model 3760), detecting particles >~13 nm in diameter.

Cloud particle size distributions, habits and phase were measured with a suite of instruments. Cloud droplet size distributions from 2-50 μm were measured with a cloud droplet probe (CDP, Droplet Measurement Technologies, Boulder, CO). A two dimensional optical array cloud probe (2D-C, Particle Measuring Systems Inc., Boulder, CO) was used as the primary measurement of number concentrations of cloud ice crystals >50 μm in diameter; this probe was updated with fast electronics. The presence of supercooled droplets was detected using a Rosemount icing detector (Model 871, Rosemount Engineering Co., Minneapolis, MN). A cloud particle imager (CPI, Stratton Park Engineering Company Inc., Boulder, CO) was used to identify the presence of small droplets, as well as particle habits for particles above ~40-50 μm.

Cloud residual particles were isolated using a counterflow virtual impactor (CVI) [*Noone et al.*, 1988; *Twohy et al.*, 1997]. The CVI separates individual cloud droplets and ice crystals from interstitial aerosol and gases, collecting and concentrating them within a small flow of high-purity dry nitrogen gas heated to 50 ºC. Cloud particles (droplets and ice crystals) with aerodynamic diameters >7 μm or >19 μm were selected using the CVI. Condensed water was evaporated providing individual residual particles for in-situ analysis, described below. While cloud particles larger than ~50 μm are collected, they may shatter due to inertial forces or upon contact with internal inlet surfaces [*Twohy et al.*, 1997]. The break-up of a large ice crystal may result in more than one residual particle if the initial ice crystal had previously collected liquid droplets or scavenged aerosol particles during its lifetime. Size distributions of the CVI residual nuclei were measured with a Particle Measuring Systems LAS-Air 1001 optical particle counter, which groups particles in eight size ranges between 0.1 and 4.0 μm diameter. The time resolution of the LAS-Air is six seconds. Droplet concentrations are enhanced within the CVI, so a 10:1 dilution system was employed ahead of the LAS-Air to avoid coincidence (multiple particles in the sensing volume); data have been corrected for both enhancement and subsequent dilution. Ambient particle impactor samples, described below, were also collected through the CVI inlet by turning off the counterflow, allowing it to function as a simple subisokinetic aerosol inlet. All internal surfaces of the C-130 aircraft CVI inlet were composed of stainless steel.

Aerosol and cloud residue chemical composition were measured using real-time mass spectrometry and electron microscopy, described below. For CVI data analysis, time periods were divided into three categories: liquid, ice, and mixed phase (both liquid droplets and ice crystals present simultaneously); CVI sampling of >19 μm cloud particles occurred during a cloud period consisting of primarily liquid droplets. CVI sampling occurred during periods with equivalent potential temperatures (θ_e) of 318.3-323.8 K. Thus, for the mass spectrometry analysis, clear air analysis time periods with θ_e values within this range were chosen for comparison with the in-cloud periods.

8.3.2 Aircraft aerosol time-of-flight mass spectrometer (A-ATOFMS)

In-situ measurements of the size-resolved chemical composition of individual submicron residual particles were made using the recently developed aircraft aerosol time-of-flight mass spectrometer (A-ATOFMS) (Chapter 2). The A-ATOFMS measures in real-time the vacuum aerodynamic diameter (d_{va}) and dual-polarity mass spectra of individual particles from ~70-1200 nm (d_{va}). Following a ^{210}Po neutralizer and pressure-controlled inlet, particles are focused in an aerodynamic lens system. Particles are optically detected by two continuous wave 532 nm lasers spaced 6.0 cm apart, providing particle velocity and, thus, d_{va}. Polystyrene latex spheres of known physical diameter from 95-1500 nm were used for the particle size calibration. During ICE-L, particles were desorbed and ionized using 266 nm radiation from a Q-switched Nd:YAG laser operating at ~0.4-0.6 mJ. Positive and negative ions resulting from individual particles are detected within the time-of-flight mass spectrometer. For the analysis discussed herein, 283 individual particles were chemically analyzed: 35 particles during clear air sampling, 23 during liquid CVI sampling, 124 during mixed phase CVI sampling, 80 during ice CVI sampling, and 21 during the 18 μm cut-point CVI sampling. Standard errors of particle type number percentages were calculated based on Poisson statistics.

Mass spectral peak identifications correspond to the most probable ions for a given m/z ratio based on previous lab and field studies. Based on dual-polarity mass spectra, individual particles were divided into 6 categories: salt (Na-K-Mg-Ca-Cl, described in Section 8.3.1), biomass, organic carbon (OC), soot, sulfate, and other. The mass spectra of the biomass particles, from wildfires and wood combustion, are dominated by potassium (*m/z* 39(K^+)) with less intense carbonaceous positive ions [*Silva* *et al.*, 1999]; most of the biomass particles contained sulfate (*m/z* -97(HSO_4^-)), and to a lesser extent, nitrate (*m/z* -62(NO_3^-)). The OC particles were characterized by carbonaceous marker ions at *m/z* 12(C^+), 27($C_2H_3^+$/CHN^+), 36(C_3^+), and 37(C_3H^+); ammonium (*m/z* 18(NH_4^+)), amines, and sulfate were typically observed in these particles. The soot particles, dominated by carbon cluster ions (C_n^-), were often mixed with potassium and sulfate; a fraction of these particles contain organic carbon markers as well. The sulfate particles were characterized by having only negative ion mass spectra with intense peaks at *m/z* -97(HSO_4^-) and -195($H_2SO_4HSO_4^-$). The "other" particle category contains less abundant particles, such as biological particles and particles providing only negative ion mass spectra containing both nitrate and sulfate.

8.3.3 Transmission electron microscopy – Energy dispersive X-ray analysis (TEM-EDX)

Downstream of the CVI inlet, a two-stage round-jet impactor [*Rader and Marple*, 1985] allowed separation of particles by size. At typical sampling pressures of 500 mb, the small particle impactor plate collected 0.11 to 0.59 μm diameter unit-density particles, or 0.08 to 0.42 μm diameter 1.7 g cm^{-3} density particles. The large particle plate collected larger particles up to several microns in size. Particles were impacted onto transmission electron microscope (TEM) grids (nickel base coated with formvar and carbon) and were analyzed individually via TEM with energy dispersive X-ray analysis (EDX). Initial analysis was performed with an older Philips CM-12 scanning transmission electron microscope with limited ability to detect light elements from atomic number 8 (oxygen) and below, while later analyses were performed on a new

Hitachi S-5500 instrument which was able to detect elements down to 6 (carbon) with excellent spectral resolution. Samples from this flight that were analyzed on both microscopes gave similar results in terms of particle categorization, although better detection of non-volatile carbon and superior imaging were obtained with the newer microscope. Note that some organics and nitrates volatilize under the vacuum environment of the microscope. The 5 min clear air sample discussed herein was taken at θ_e values of 315.9-317.2 K, which is lower than the θ_e values during cloud sampling. The mixed-phase CVI sample was collected for 1 min 10 sec at θ_e of 321.7-322.3 K. Approximately 50-100 particles were randomly selected and analyzed per stage per sample. Standard errors of particle type number percentages were calculated based on Poisson statistics.

For TEM-EDX analysis, particles were classified into nine primary types as given in Table 8.1. “Mixed” types were particles described by multiple categories; for example, crustal dust with sulfate or salts as these may be important for their role as both IN and CCN. Particles were classified as “unknown” if they did not fit into any of the specific categories or did not produce detectable X-ray signatures above background (for example, volatile organics or nitrates). This is the same classification scheme as used by Twohy and Anderson [2008], with the addition of the biomass category which would have been included in the “salts” category in previous work. Particles containing stainless steel markers are not included in the particle types shown.

Table 8.1. TEM-EDX particle classification scheme.

Category	*TEM-EDX Compositional Signature*
Crustal dust	Silicates (rich in Si, variable Na, Mg, Al, K, Ca, and Fe), carbonates (Mg and/or Ca with large C peak), phosphates (rare).
Soot	Carbon only. Characteristic morphology (chain aggregates).
Organic	Amorphous or irregular and may contain minor S and K, as well as C.
Sulfates	Ammonium sulfate/bisulfate and sulfuric acid. S, O only.
Industrial Metals	Metals such as Al, Fe, Cr, Ti, Mn, Co, Zn, Cu.
Salts	Combinations of Na, K, Ca and Mg with S or Cl.
Biomass Salts	Sulfates with potassium, may contain C as well.
Mixed	Combinations of two or more of above categories

8.3.4 Compact time-of-flight aerosol mass spectrometer (C-ToF-AMS)

The Aerodyne compact time-of-flight aerosol mass spectrometer (C-ToF-AMS) [*Drewnick et al.*, 2005] measured the mass concentrations of non-refractory species (organics, sulfate, nitrate, ammonium, and a fraction of chloride) in real-time. Particles of d_{va} ~50-800 nm are focused by an aerodynamic lens system, sent through a 3.5% chopper, and then impacted onto a tungsten vaporizer operated at 550-560^{o}C. The chopper can be operated in three modes to gather either background mass spectra, ensemble average mass spectra over all particle sizes, or size-resolved mass spectra. Measurements of refractory chloride and other semi-refractory species are reported herein, but concentrations of these species are significantly underestimated by the C-ToF-AMS because they only undergo surface ionization [*Allan et al.*, 2004] at the vaporizer temperature (550-560^{o}C) used. Once vaporized, molecules undergo electron impact ionization and are extracted at a rate of ~53 kHz into a time-of-flight mass analyzer. For this airborne deployment, the C-ToF-AMS was fitted with a pressure-controlled inlet [*Bahreini et al.*, 2008] to prevent fluctuations in particle sizing and focusing with ambient pressure.

Detection limits for out of cloud aerosol were calculated as the standard deviation of the noise when measuring filtered air: organics (0.06 μg/m^3), sulfate (0.02 μg/m^3), nitrate (0.01 μg/m^3), ammonium (0.07 μg/m^3), and chloride (0.01 μg/m^3). Detection limits for measurements made in cloud were calculated as the standard deviation of measurements made on the CVI inlet during cloud-free periods: organics (0.003 μg/m^3), sulfate (0.0006 μg/m^3), nitrate (0.0007 μg/m^3), ammonium (0.0007 μg/m^3), and chloride (0.0005 μg/m^3). In practice, detection is often limited by counting statistics at low aerosol loadings. Lower detection limits during CVI sampling were due to the enrichment of particles by the CVI and entrainment in N_2 (rather than air); corrections for CVI enhancements (typically a factor of ~20-30) were completed for reported detection limits and mass concentrations. One important issue concerning C-ToF-AMS data is the collection efficiency of particles within the instrument [*Huffman et al.*, 2005]; in this study, C-ToF-AMS mass loadings were not corrected for collection efficiency (CE) due to possible changes in particle phase [*Matthew et al.*, 2008] between clear air and CVI dry residue sampling. By not adjusting the mass loadings for CE, we are effectively assuming a collection efficiency of 1, although we note that the CE likely varied during the flight. Standard deviations are noted as uncertainties for average species mass fractions. Oxygen/carbon (O/C) ratio were calculated following the method of Aiken et al. [2008]:

$$O/C = (0.0382 \pm 0.0005)(x) + (0.0794 \pm 0.0070) \qquad (1)$$

where x is the percentage of organic aerosol mass from *m/z* 44 (CO_2^+).

8.3.5 Scanning transmission X-ray microscopy/Near edge X-ray absorption fine structure spectroscopy (STXM/NEXAFS)

Three large stage impactor samples, collected as described in Section 2.3, were analyzed with scanning transmission X-ray microscopy (STXM) with near edge X-ray absorption fine structure spectroscopy (NEXAFS) at Lawrence Berkeley National Laboratory's Advanced Light Source (ALS) [*Kilcoyne et al.*, 2003]. The STXM microscope used in this experiment was located at beam line 11.0.2 at the ALS. The 3 min 50 sec clear air sample discussed herein was taken at θ_e values of 320.2-322.1 K, which is within the θ_e values of cloud sampling. The ice phase CVI sample was collected for 4 min 35 sec at θ_e of 319.0-323.1 K; similarly, the 18 μm cut-point CVI sample was collected for 7 min 30 sec in primarily liquid phase at θ_e of 319.3-322.8 K. The sample grids were affixed over holes drilled in aluminum holder plates specially designed for the microscope. Once the samples were placed in the microscope chamber, the chamber was pumped down to 80 mTorr and filled with ~0.5 atm of He prior to operating the microscope. For each sample region of interest, ~100 images were acquired over the carbon K edge from 278 to 320 eV. Peaks arising from the potassium L_2 and L_3 edges occur at ~299 and 297 eV respectively. For some of the carbonate samples, the presence of calcium was confirmed at the L_2 and L_3 edges occurring at 353 and 349 eV respectively [*Henke et al.*, 1993].

Maps of elemental carbon (EC), organic carbon (OC), potassium (K), and regions rich in non-carbon elements (inorganic, In) were used to classify the different particle types seen in the different samples [*Moffet et al.*, 2009]. EC regions were identified as those regions containing greater than 35% carbon-carbon sp^2 hybridized double bonds [*Hopkins et al.*, 2007]. The pre-edge region occurring around 278 eV is proportional to the number of non-carbon atoms and the difference between the post-edge and pre-edge regions is proportional to the number of carbon atoms. Inorganic (In) regions were identified by the ratio of the pre-edge height to post edge height (h_{pre}/h_{post}); if h_{pre}/h_{post} was greater than 0.4, the area is defined as being dominated by inorganic material on a thickness basis. Finally, if an area contained absorbance due to COOH groups at 288 eV (near the carbon edge), the region was identified as containing OC. Particle class labels

(OC, OCEC, OCECIn, and OCIn) are used to identify particles that contain one or more of these three components (In, OC and/or EC).

8.3.6 Continuous flow diffusion chamber (CFDC)

To measure the number concentrations of ice-nucleating aerosol particles in real-time, a continuous flow diffusion chamber (CFDC) [*Rogers et al.*, 2001] re-processed cloud residues near the cloud observation temperature and at a relative humidity (with respect to water) exceeding 100% to simulate ice formation conditions at expected wave cloud parcel entry conditions. This means of operating the CFDC emphasized condensation/immersion freezing nucleation as is expected for the cloud entry regions of orographic wave clouds on the basis of previous studies [*Cooper and Vali*, 1981]. Use of an impactor limited sampling to primarily submicron particles (<~1.2 μm in diameter) prior to CFDC processing in order to distinguish ice crystals nucleated in the CFDC from non-activated aerosol particles using optical methods.

8.3.7 Laboratory measurements

For comparison to ICE-L results, dry lakebed crust particles from Owens Lake, CA were aerosolized by dry generation using N_2, as detailed previously by Sullivan et al. [2009]. The A-ATOFMS, described above, was used to measure particle chemistry in tandem with measurements of CCN activity. For CCN analysis, aerosolized particles were passed through a ^{210}Po neutralizer and then size-selected (80, 90, and 100 nm) using a differential mobility analyzer (DMA, Model 3081, TSI inc.) to obtain a monodisperse aerosol distribution. Total particle concentrations were measured by a condensation particle counter (CPC, model 3010, TSI Inc.) and compared to the number concentrations of particles activated within a miniature cloud condensation nuclei counter (CCNc) at supersaturations of ~0.1-1.1% [*Roberts and Nenes*, 2005]. The supersaturation of the CCNc is a function of the column temperature gradient (dT), which was calibrated using $(NH_4)_2SO_4$ (Aldrich, 99.999% purity). Activation curves of CCN/CN ratios, providing the fraction of activated particles, were generated by scanning through supersaturations (column dT) at a fixed dry diameter; the critical supersaturation (S_c) is defined as CCN/CN = 0.5. The contribution of multiply charged particles was corrected using the method of Rose et al. [2008]. Herein, CCN activity is presented as the single hygroscopicity parameter kappa (κ) [*Petters and Kreidenweis*, 2007], which was determined by plotting S_c for each dry diameter (D_d) on a log-log plot with the different S_c-D_d pairs for each sample falling on κ isolines. Uncertainty in κ is from errors associated with the CCNc supersaturation calibration and from selecting a monodisperse aerosol using a DMA.

8.4 Results and Discussion

8.4.1 Single-Particle Mixing State and Origin of Playa Salts

While flying through mixed-phase orographic wave clouds over Wyoming during ICE-L, the A-ATOFMS identified playa salts among the residues of cloud droplets and ice crystals. Figure 8.1 shows an example A-ATOFMS mass spectrum of an individual salt residue from an evaporated cloud droplet. These salt particles are characterized by intense sodium (*m/z* 23, Na^+), magnesium (*m/z* 24, Mg^+), potassium (*m/z* 39, K^+), and calcium (*m/z* 40, Ca^+) ion peaks with less intense positive ions at *m/z* 55(KO+),

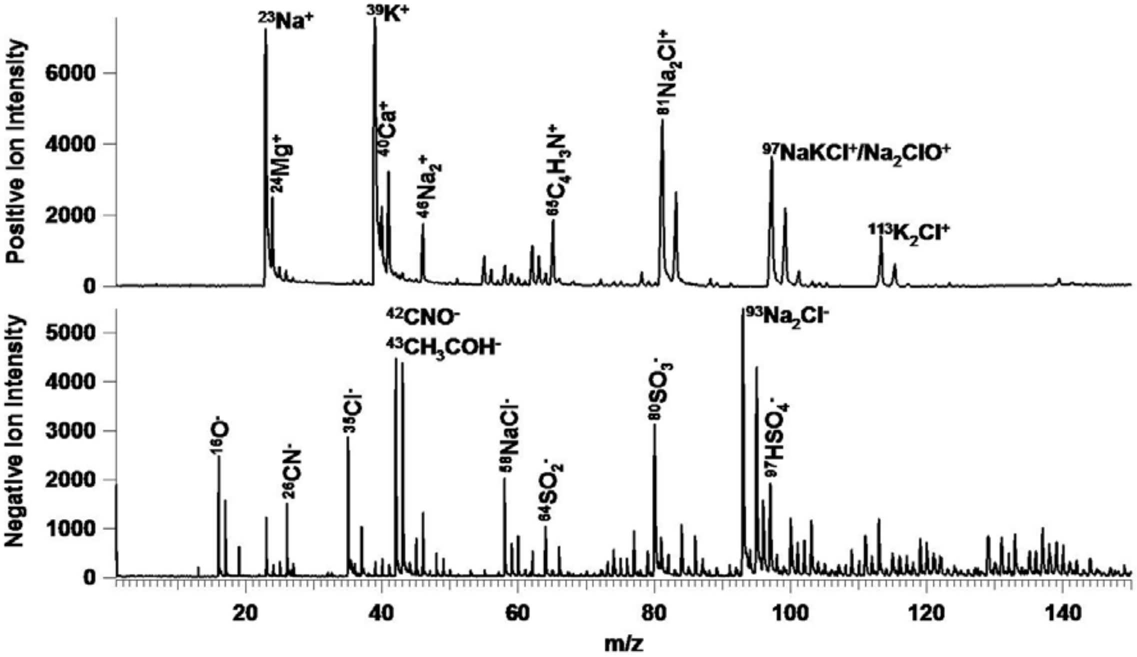

Figure 8.1. Representative A-ATOFMS positive and negative ion mass spectra of a single cloud droplet residue salt.

56(KOH^+/CaO^+), 81(Na_2Cl^+), and 97(Na_2ClO^+), for example. The negative ion mass spectra feature distinguishing peaks at *m/z* -16(O^-), -17(OH^-), -26(CN^-), -35(Cl^-), -42(CNO^-), -58($NaCl^-$), and -93($NaCl_2^-$). The high relative intensities of the magnesium, calcium, and negative ion organic nitrogen markers, in particular, distinguish these playa salts from sea salt [*Gard et al.*, 1998]. A fraction of the negative ion mass spectra also contain carbon cluster ions (C_n^-), silicates, phosphate, nitrate, and/or sulfate. The mass spectral signatures of these salts are expected for the typical evaporite minerals associated with playas, including halite (NaCl), gypsum ($CaSO_4 \cdot 2H_2O$), mirabilite ($Na_2SO_4 \cdot 10H_2O$), thenardite (Na_2SO_4), epsomite ($MgSO_4 \cdot 7H_2O$), trona ($NaHCO_3 \cdot Na_2CO_3 \cdot 2H_2O$), sylvite (KCl), carnallite ($KCl \cdot MgCl_2 \cdot 6H2O$), calcite/aragonite ($CaCO_3$), dolomite ($CaMg(CO_3)_2$), hanksite ($Na_{22}K(SO_4)_9(CO_3)_2Cl$, borax ($Na_2B_4O_7 \cdot 10H_20$), northupite ($Na_3Mg(CO_3)_2Cl$), and aphthitalite ($K_2SO_4$) [*Bryant et al.*, 1994; *Droste*, 1961; *Güven and Kerr*, 1966; *Lowenstein and Hardie*, 1985]. To further confirm the most probable source of these salts, dry lakebed crust particles from Owens Lake, CA were compared using the A-ATOFMS using the analysis method of Toner et al. [2008]. The mass spectral signature of the Owens Lake crust was compared to the average mass spectrum of the cloud residue salts using calculated dot products for the ion peaks in the spectra. Lower dot products indicate less similarity between the two sets of particles; whereas high dot products indicate greater similarity. In this case, the mass spectral comparison showed a strong similarity (dot product = 0.7) between the Owens Lake crust and cloud residue salt particles, supporting the ICE-L signature as playa dust, as opposed to sea salt (dot product = 0.58).

TEM-EDX analysis of cloud residues also showed the presence of salts, defined as containing Na, K, Ca, and Mg with S or Cl (Table 8.1). An example TEM image and corresponding EDX spectrum are shown in Figure 8.2 for a single cloud residue salt, likely from a liquid droplet. In addition to the salt-defining elements, this particle contains C, O, F, Zn, and P above background levels. This signature is in excellent agreement with that determined by A-ATOFMS, as discussed above, as well as previous proton-induced X-ray emission (PIXE) analysis of playa sediments, where samples contained Na, Ca, Si, and trace metals [*Gill et al.*, 2002]. For Owens Lake (CA) playa sediments, silicon and aluminum contents ranged from ~16-22% and ~3-5% by mass, respectively; Zn content was found to be ~46-100 ppm [*Gill et al.*, 2002]. It should also be noted that a "halo" surrounds the solid residue salt shown in Figure 8.2. During previous aircraft-based aerosol sampling over Montana, NaCl particles from the Great Salt Lake area were detected simultaneously with soil particles [*Hobbs et al.*, 1985]. Using scanning electron microscopy (SEM)-EDX, volatile "haloes" containing Si and Cl with trace S were found surrounding soil particles containing Si and Al with trace Fe and K [*Hobbs et al.*, 1985].

To further characterize the cloud residue salts with particular focus on the organic component, STXM/NEXAFS was utilized to examine the elemental carbon (EC), organic carbon (OC), potassium (K), and regions rich in non-carbon (inorganic, In) elements within individual particles. Figure 8.3 shows chemical component maps for a single mixed inorganic/organic (OCIn) cloud residue collected during the 18 μm CVI cut-point sampling period, primarily liquid droplets, as discussed below. For this particular particle, Ca, K, COOH groups, and CO_3 are all internally mixed. As discussed above,

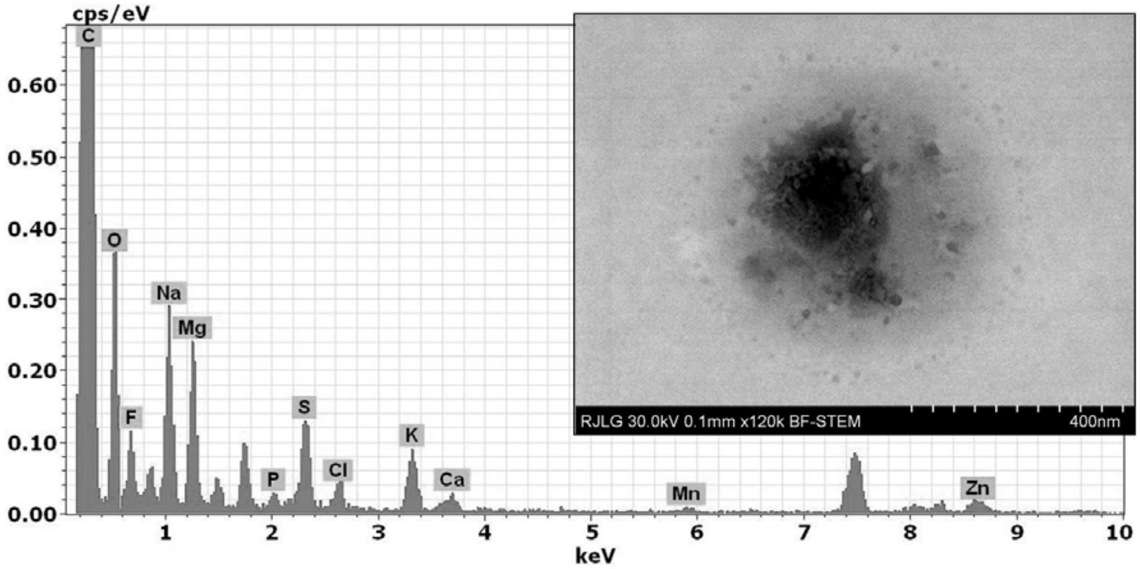

Figure 8.2. TEM image of cloud residue salt with corresponding EDX spectrum.

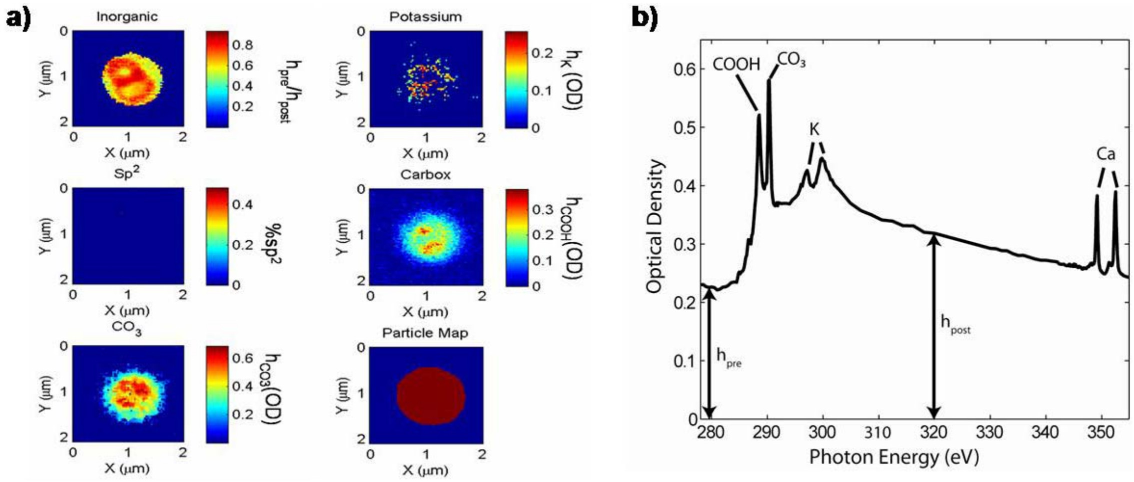

Figure 8.3. (a) STXM/NEXAFS maps of inorganic, potassium, sp^2 bonds, COOH and CO$_3$ for a single residue of a cloud droplet (> 19μm). (b) STXM/NEXAFS spectrum over the area of the individual cloud droplet residue shown in part (a).

Ca, K, and carbonate are common components of playa evaporite minerals. Based upon STXM/NEXAFS analysis, the "haloes" observed by TEM-EDX were likely from an oxidized organic coating, presumably from cloud processing [*Chen et al.*, 2007]. This is further confirmed by an elevated C-ToF-AMS O/C ratio (0.86 ± 0.36), indicative of oxygenated organic species [*Aiken et al.*, 2008] present during cloud droplet residue sampling. Indeed, the A-ATOFMS observed ion peaks of possible organic acids, including *m/z* -43(CH_3COH^-/$HCNO^-$), -73($C_2HO_3^-$, glyoxylic acid), -159($C_7H_{11}O_4^-$, pimelic acid), and -173($C_8H_{13}O_4^-$, suberic acid), within the mass spectral signatures of the playa salt cloud droplet residues.

While our focus is on research flight #3, sodium chloride salts enriched in Mg, Ca, and K were observed during ICE-L orographic wave cloud flights (RF02, RF03, RF04) when the air masses passed over the Great Basin region. As shown in Figure 8.4, examination of HYSPLIT [*Draxler and Rolph*, 2003] air mass back trajectories for the Mg-Ca-K-enriched salt flights (RF02, RF03, RF04) show transport over the northern edge of the Great Basin region of Nevada and Utah, the largest dust source region in the U.S. [*Prospero et al.*, 2002; *Washington et al.*, 2003]. The Great Basin region, once the sites of Lake Lahontan and Lake Bonneville during the Quaternary period, contains many playas [*Güven and Kerr*, 1966], as shown in Figure 8.4 [*Soller and Reheis*, 2004]. During flights in which these enriched salts were not observed, the air masses followed more northerly trajectories, over land where playas are not present in abundance. For the "salt" flights, air mass back trajectories show transport times of less than 18 hours from northern Utah and Nevada. While the vertical profiles of these HYPSLIT trajectories do not show transport within the boundary layer, previous measurements of playa dust

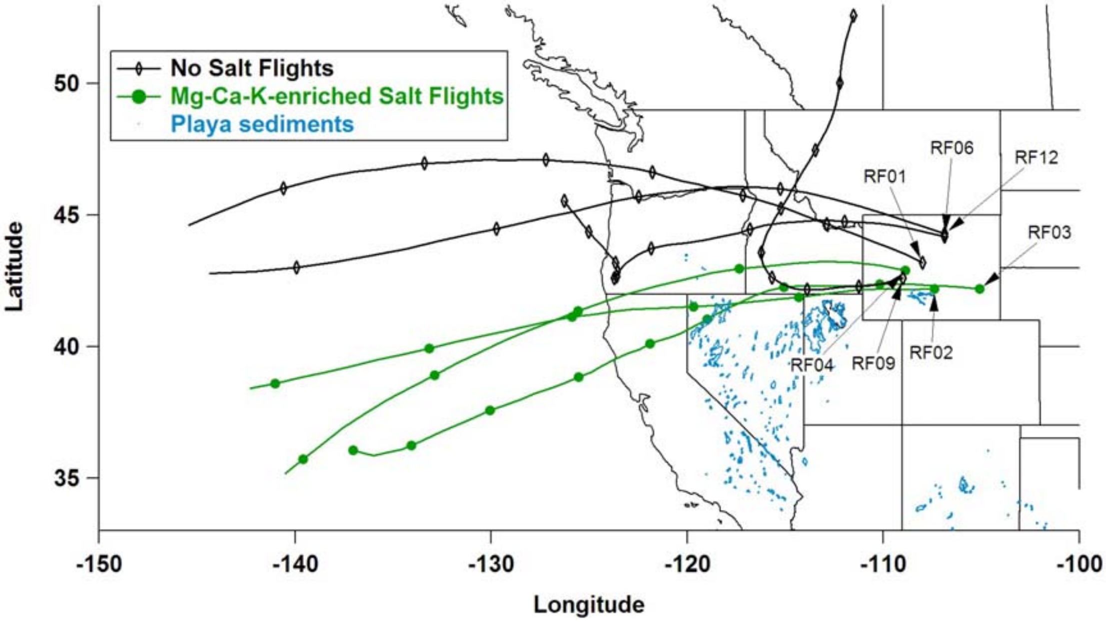

Figure 8.4. HYSPLIT air mass back trajectories (up to 48 hrs, with dots shown every 6 hrs) for ICE-L orographic wave cloud flights, classified as either having Na-Mg-Ca-K-Cl salts present (green) or not (black). For reference, a map of playa sediments [*Soller and Reheis*, 2004] is shown.

storms have shown high wind speeds [*Pelletier*, 2006], rapid lofting to high altitudes (> 2 km above ground level) [*Cahill et al.*, 1996; *Reid et al.*, 1994], as well as associated long-range transport [*Formenti et al.*, 2003]. For RF03, elevated mass concentrations of particulate matter less than 10 μm or 2.5 μm (PM_{10} and $PM_{2.5}$) were observed in Salt Lake City and Logan City, UT on November 16, 2007. For example, at the Utah State Division of Air Quality North Salt Lake monitoring site in Salt Lake City, the 24 h PM_{10} mass concentration was 86 $\mu g/m^3$ on Nov. 16, compared to the monthly average of 44 $\mu g/m^3$ (standard deviation (σ) 25 $\mu g/m^3$). Likewise, at the Rose Park monitoring site in Salt Lake City, the 24 h $PM_{2.5}$ mass concentration was 30.3 $\mu g/m^3$ on Nov. 16, compared to the monthly average of 13.5 $\mu g/m^3$ (σ 7.3 $\mu g/m^3$). Together these trajectories and PM observations further support the detection of playa salts from the Great Basin region.

8.4.2 Supercooled Liquid Droplets

To evaluate the ability of playa salts to act as CCN, the chemistry and CCN ability of Owens (dry) Lake crust was evaluated. Having a similar A-ATOFMS mass spectral signature to the cloud residue salts, the Owens (dry) Lake crust had an elevated CCN activity (high hygroscopicity) ($\kappa = 0.84 \pm 0.10$) compared to that measured previously by Koehler et al. [2009] for most mineral dust ($\kappa \leq 0.08$). Previous CCN measurements of dry-generated Owens Lake dust found 35% of the particles to have a κ of 0.69 with 65% having a κ of 0.05 [*Koehler et al.*, 2007]; the higher κ value obtained herein is due to the analysis of the top, more soluble, crystalline crust only. For comparison, highly-CCN-active particles are considered to be those with κ values between 0.5 and 1.4 with NaCl having a κ of 1.12-1.28 [*Petters and Kreidenweis*, 2007], showing that playa salts can have CCN activities similar to those of sea salt.

To further understand the activation of the supercooled liquid droplets observed within the orographic wave clouds observed during RF03, the maximum cloud supersaturation was modeled using the 1-D parcel model described by Heymsfield et al. [1991]. Using the average temperature (-21.8 °C), pressure (333 Torr), and altitude (6573 m) with a peak updraft velocity of 2.6 m/s of the first (and lowest altitude) liquid phase cloud pass, the maximum supersaturation was estimated to be ~8%, similar to previous observations of supercooled liquid wave clouds [*Heymsfield and Miloshevich*, 1993]. Of course, 8% supersaturation is unimaginably high for cumulus but the supersaturations reach very high levels because the droplet growth rates, which deplete the buildup of supersaturation, are relatively low at temperature of -20 °C [*Heymsfield and Miloshevich*, 1993]. No evidence of collision-coalescence was observed in the model; similarly, CPI, radar, and lidar data showed no evidence of drizzle formation. Thus, in contrast to the warms clouds observed by Rudich et al. [2002], the playa salts were not observed to initiate precipitation during RF03. To examine the particles activated as cloud droplets during RF03, measured clear air particle and cloud droplet number concentrations were compared. During the clear air measurement periods (θ_e = 318.3-323.8 K), number concentrations of particles 0.1-1.0 μm in diameter averaged 25 cm^{-3} (maximum 164 cm^{-3}) with average CN concentrations of 217 cm^{-3} (maximum 704 cm^{-3}). During liquid-only sampling, average cloud droplet number concentrations, as measured by the CDP, were 66 cm^{-3} (maximum 125 cm^{-3}). This comparison suggests that all particles greater than 100 nm, as well as a fraction of 13-100 nm particles, likely served as nuclei for cloud droplet formation, which is important as A-ATOFMS and TEM-EDX measurements focused on particles >100 nm.

To examine the variation of aerosol chemistry with cloud droplet diameter, CVI sampling was completed at two different CVI cut-points (7 μm and 19 μm). Sampling of cloud droplets >7 μm was completed at altitudes of 6.6 – 7.7 km and ambient temperatures of -21 to -32 °C; sampling of cloud droplets >19 μm was completed at 7.2 km and -26 to -27 °C. Average cloud droplet size distributions during these two periods are shown in Figure 8.5; residue chemistry, as measured by the A-ATOFMS and AMS are also shown. During the >19 μm period, the average cloud droplet number concentration, measured by the CDP, was 59 cm^{-3} (maximum 125 cm^{-3}) with a small contribution of cloud ice particles (> 50 μm) of 2 L^{-1} on average (maximum of 18 L^{-1}) measured by the 2DC probe. As shown in Figure 8.5b and 8.5e, the playa salts were preferentially found in larger cloud droplets with the number fraction increasing from 57 ± 14% to 90 ± 8% with the increase in CVI cut-point. For residues of the larger cloud droplets, STXM/NEXAFS analysis classified all measured particles as internally mixed organic carbon and inorganic components, with ~71% mixed with carbonate and ~29% mixed with potassium as well (Table 8.2). Concurrent with the increase in the relative fraction of playa salts, the C-ToF-AMS non-refractory mass fractions showed an increase in organics (38 ± 17% to 75%) and decrease in sulfate and ammonium (Figure 8.5); as shown by the A-ATOFMS mass spectra and confirmed with STXM/NEXAFS, the majority of the organics measured by the C-ToF-AMS were internally mixed with the playa salts. Although within uncertainties (shown as σ), the C-ToF-AMS observed a higher O/C ratio [*Aiken et al.*, 2008] for the organic species observed during >7 μm and

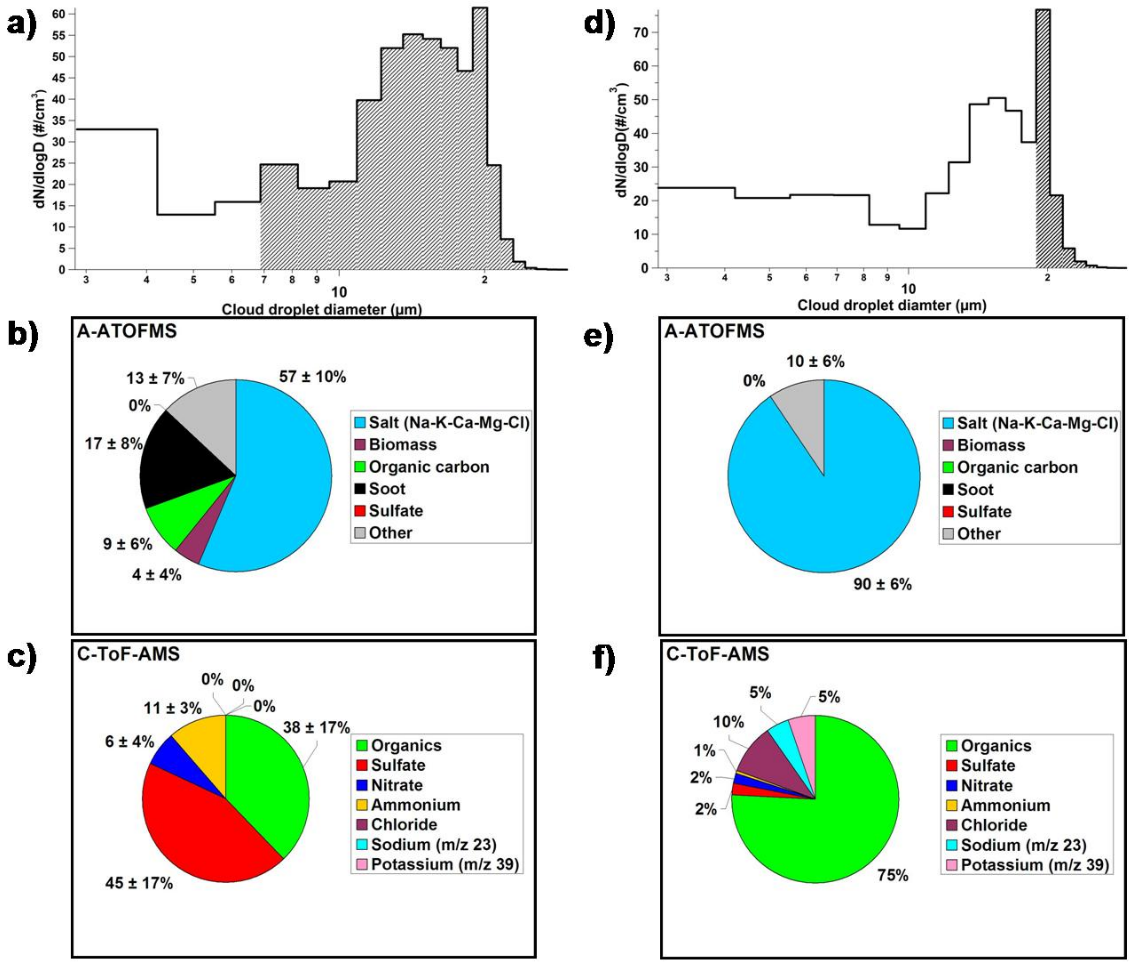

Figure 8.5. Average cloud droplet size distributions, measured by the CDP, are shown for the CVI sampling periods corresponding to cloud droplet cut-points of (a) > 7 µm and (d) > 19 µm. Shaded areas represent the cloud droplet diameters sampled by the A-ATOFMS and C-ToF-AMS during each sampling condition. Relative number fractions of particle types measured by the A-ATOFMS for residues of cloud droplets > 7 µm and > 19 µm are shown in (b) and (e), respectively. Relative non-refractory mass fractions measured by the C-ToF-AMS for residues of cloud droplets > 7 µm and > 19 µm are shown in (c) and (f), respectively. While C-ToF-AMS ion peaks at *m/z* 23 and 39 are not quantitative measures of Na and K, they indicate the presence of these species; all other species mass fractions are quantitative.

Table 8.2. STXM/NEXAFS individual particle classifications. Plain black numbers in the table represent the number of particles in each sample that contained specified particle type: organic carbon (OC), organic carbon-elemental carbon (OCEC), organic carbon-elemental carbon-inorganic (OCECIn), and organic carbon-inorganic (OCIn). The numbers of particles found to have CO_3 and/or K are shown in parentheses.

Type	**>19 µm liquid**	**Ice**	**Clear air**
OC	0	2	1
OCEC	0	1	0
OCECIn	0	0	1
OCIn	17, (12 CO_3), (5 K)	6, (6 CO_3), (3 K)	7, (2 CO_3), (1 K)

>19 μm cloud droplet residue sampling (0.84 ± 0.36 vs. 1.19 ± 0.15, respectively), suggesting that the larger cloud droplets may have undergone additional cloud processing during transport. In addition to the probable organic acids observed by the A-ATOFMS to be internally mixed with the >7 μm cloud droplet playa salt residues, additional ion peaks of potential organic acids were observed for the >19 μm cloud droplet playa salt residues: *m/z* -45 ($HCOO^-$, formic acid), -87 ($C_3H_3O_3^-$, pyruvic acid), and -103 ($C_3H_3O_4^-$, malonic acid) [*Sullivan and Prather*, 2007]. The O/C ratio observed by the C-ToF-AMS during >19 μm sampling is among the highest reported, significantly above reported values for laboratory secondary organic aerosol [eg., *Aiken et al.*, 2008; *Hildebrandt et al.*, 2009], highlighting the need to further understand cloud processing of organics. Previously, Sun et al. [2009] observed an O/C ratio of 1.08 for organic aerosol, hypothesized to have undergone aqueous phase processing during transport over the Pacific Ocean to Whistler Mountain (Canada).

While organics are generally considered to be less efficient CCN than most inorganics, small amounts of salt (<5% of dry mass for NaCl) have been found to greatly decrease the S_c of even slightly soluble organic compounds [*Bilde and Svenningsson*, 2004]. At the vaporization temperature utilized by the C-ToF-AMS during ICE-L (550-560^{o}C), the C-ToF-AMS is unable to efficiently detect refractory species present in sea salt (eg., NaCl); however, due to the low ionization potentials of Na and K, a small fraction of the salts may undergo surface ionization [*Allan et al.*, 2004]. Through comparison of the C-ToF-AMS non-refractory mass concentrations with residue volume concentrations, measured by the CVI OPC, it is estimated that ~39-62% and ~39-68% of the aerosol mass was refractory during the >7 and >19 μm periods, respectively; this refractory mass was not detected by the C-ToF-AMS. However, qualitatively, the C-ToF-AMS observed higher Na, K, and Cl signals in the larger cloud droplets, in agreement with the enrichment of playa salts in the larger cloud droplets, as measured by the A-ATOFMS.

The observed enrichment of playa salts in the larger cloud droplets is consistent with the relationship between cloud droplet size and S_c with the largest drops forming on the largest, most hygroscopic CCN [*Hudson and Rogers*, 1986]. Twohy et al. [1989] used a parcel model to predict size-dependent droplet chemistry for an ammonium sulfate small aerosol mode and a sea salt large aerosol mode; similar to that observed herein, sea salt was calculated to be within the largest droplets, showing that bulk droplet composition does not represent the composition of individual cloud droplets. For coastal stratus clouds heavily influenced by sea salt, Munger et al. [1989] observed higher Na^+, Ca^{2+}, and Mg^{2+} concentrations in larger droplets with higher concentrations of SO_4^{2-}, NO_3^-, NH_4^+, and H^+ in smaller droplets, similar to that observed for the RF03 residues. It is predicted that cloud drops will retain the size-resolved chemistry of the original CCN until coalescence produces drizzle-sized drops [*Ogren and Charlson*, 1992]. Previous satellite measurements observed that playa dust from the Aral Sea region increased cloud drop size and promoted precipitation [*Rudich et al.*, 2002]. For particle sizes similar to large mineral dust [*Patterson and Gillette*, 1977; *Reid et al.*, 1994], playa salts can serve as giant CCN [*Andreae and Rosenfeld*, 2008], increasing cloud droplet size similar to large hygroscopic salts used in cloud seeding studies [*Drofa*, 2006; *Ghate et al.*, 2007].

8.4.3 Cloud Ice Residues

During sampling in cloud ice regions, the 2DC probe concentrations averaged 57 L^{-1} (σ 113 L^{-1}) with sampling at 6.5 – 7.7 km (-21 to -31 °C). Similar to the >19 μm droplet residues, the ice residues were dominated by playa salts internally mixed with organics, as shown in Figure 8.6. This was further confirmed by STXM/NEXAFS analysis, which showed that 6 out of the 9 analyzed ice residues were internally mixed organics and inorganics (Table 8.2). Approximately half as many ice salt residues were internally mixed with sulfate and/or nitrate (28 ± 5%) compared to the cloud droplet salt residues (69 ± 13%) (Figure 8.7). This is consistent with lower mass fractions of sulfate and nitrate measured by the C-ToF-AMS for the ice residues compared to the cloud droplet residues (Figures 8.5 and 8.6). Similarly, Cziczo et al. [2004] observed large, unreacted sea salt particles as residues of cirrus ice produced by homogeneous freezing. It was hypothesized that the preferential freezing of sea salt was likely due to the extensive water uptake of NaCl, resulting in larger, more dilute, sea salt particles which were most likely to freeze compared to the smaller, more numerous sulfate/K/organic/nitrate particles observed in the clear air [*Cziczo et al.*, 2004]. Similarly, organic carbon/sulfate particles were not observed by the A-ATOFMS for the RF03 ice residues. Similar to the >19 μm cloud droplet residues, the O/C ratio observed by the C-ToF-AMS during ice residue sampling was elevated (1.15 ± 0.25), indicative of highly oxygenated organic aerosol [*Aiken et al.*, 2008]. In addition to the probable organic acid ion peaks observed during cloud droplet residue sampling, oxalic acid (*m/z* -89($C_2HO_4^-$) and *m/z* -179(($(C_2O_4H)_2H^-$)) [*Sullivan and Prather*, 2007] was observed to be preferentially mixed with the playa salt ice residues.

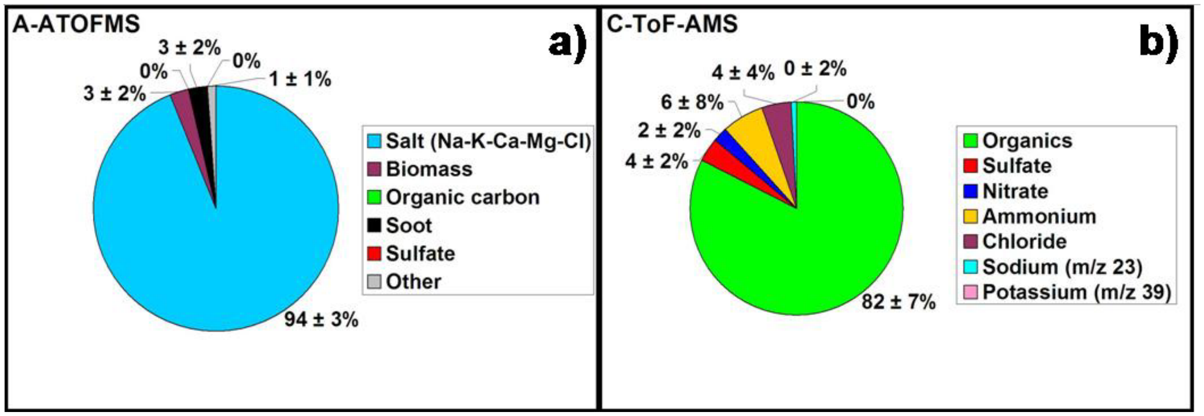

Figure 8.6. (a) Relative number fractions of particle types measured by the A-ATOFMS for residues of cloud ice > 7 µm. 78% of the salts were observed to be internally mixed with organics. (b) Relative non-refractory mass fractions measured by the C-ToF-AMS for residues of cloud ice > 7 µm.

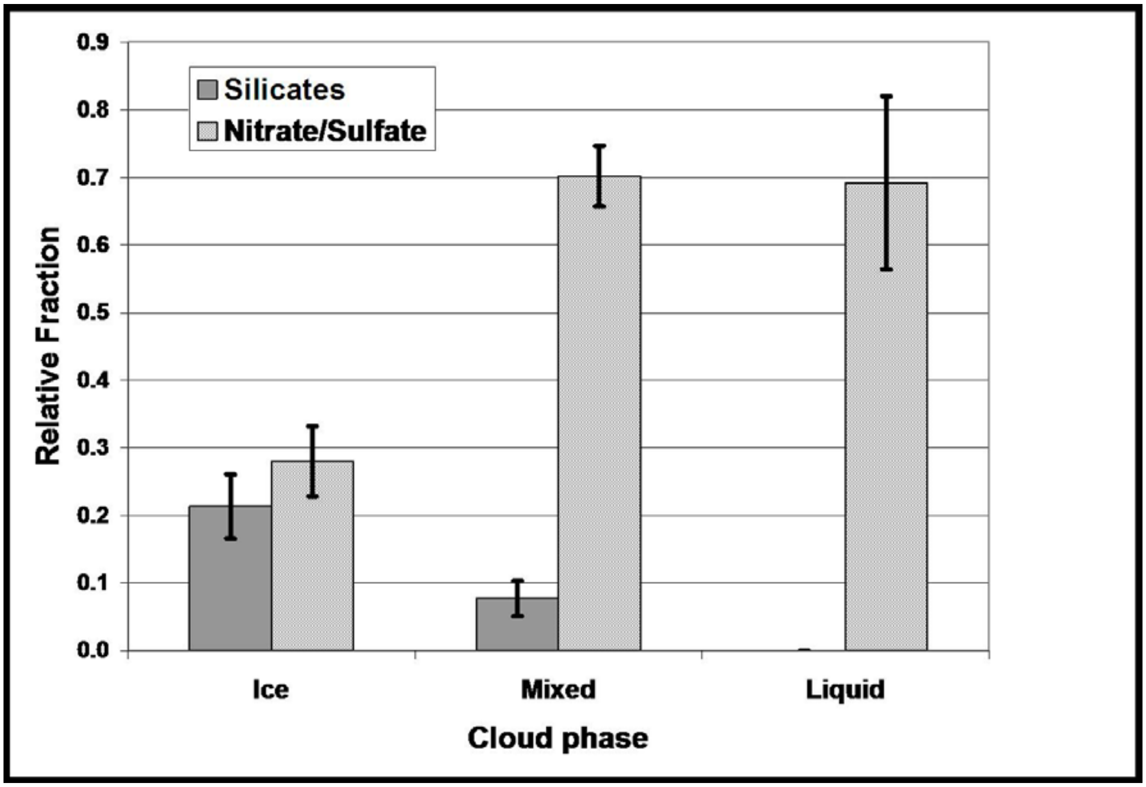

Figure 8.7. Relative number fractions of cloud residues identified as salts, measured by the A-ATOFMS, found to be internally mixed with silicates or nitrate and/or sulfate.

Despite sampling at temperatures above -31 °C, the wave cloud tops reached below -38 °C, allowing homogeneous freezing to occur in dilute solution droplets and activated cloud droplets [*DeMott and Rogers*, 1990], as comfirmed by the radar signature and a kinematic 1-D model [*Field et al.*, 2009]. During RF03, wave-following and falling homogeneously-nucleated ice from above the sampling altitude greatly influenced the sampled ice residues [*Field et al.*, 2009], suggesting that the majority of the ice playa salt residues were homogeneously frozen at higher altitudes, similar to the ice sea salt residues observed by Cziczo et al. [2004]. Riming, as indicated in CPI images (not shown), would have contributed additional soluble salts to the ice. However, in addition to homogeneous freezing, the Field et al. [2009] model also indicated a small contribution (~6 L^{-1} to the total ice particle concentration of ~50 L^{-1}) of heterogeneous condensation/immersion freezing. This is consistent with a maximum ice nuclei concentration of 3 L^{-1} measured by the CFDC operating at -31 °C and a supersaturation (with respect to water) of up to 1%, for the ice residues. For previous marine anvil cirrus ice measurements by the CFDC, a small fraction of the salts were found to act as ice nuclei, freezing below water saturation [*Prenni et al.*, 2007]. Previous laboratory measurements have shown playa dust (less hygroscopic, inefficent CCN) to nucleate ice heterogeneously at lower relative humidities than required for homogeneous freezing of aqueous particles at temperatures less than -40 °C; smaller contributions to heterogeneous ice formation from about -37 to -40 °C were also observed [*Koehler et al.*, 2007]. However, the study by Koehler et al. [2007] did not report ice formation for activated fractions of <1% or examine playa dust greater than 400 nm in size, which may have shown heterogeneous ice formation at temperatures above -37 °C. For the RF03 ice salt residues, 21 ± 5% (20 ± 4% of the total ice residues) were found to contain silicates, while none of the cloud droplet salt residues contained silicates. We can assume that ~2-3% of these "dust-like" playa salts may activate as ice nuclei [*Field et al.*, 2006; *Prenni et al.*, 2009]. Considering the concentration of residues measured by the CVI OPC, we estimate that an average of 2.9 – 4.4 L^{-1} (range of 1.1 – 8.0 L^{-1} given uncertainties) playa dust may have been IN active. This estimate is in excellent agreement with the modeled (~6 L^{-1}) and measured IN concentrations (3 L^{-1}, average of 1.0 L^{-1}, σ 0.7 L^{-1}), suggesting that the silicate-containing playa salts may have served as heterogeneous ice nuclei. Further, during sampling regions containing only cloud droplets, IN concentrations were below the detection limit (0.1 L^{-1}) of the CFDC, consistent with the relatively low abundance of silicate-containing particles present.

It should be noted that during cloud ice sampling, a significant fraction 35 ± 5% of the total ice residue mass spectra also contained markers of inlet metals, such as chromium (*m/z* 52, Cr^+), manganese (*m/z* 55, Mn^+), iron (*m/z* 56, Fe^+), and molybdenum (*m/z* 98, Mo^+), indicating that a fraction of the salts impacted the stainless steel CVI aircraft inlet during sampling, as previously observed in even higher concentrations by Murphy et al. [2004]. Indeed, a greater concentration (~50 times) of ice residues >110 nm, as measured by the CVI OPC, than ice crystals, as measured by the 2DC, further indicating the occurrence of ice crystal shattering within the CVI inlet, as well as possible residue multiplication due to dissolved salts within homogeneously frozen ice crystals. However, while the positive ion mass spectra were influenced by these metals, the distinguishing positive ion mass spectral signature of the playa salt (i.e., Na, K, Mg, Ca) was still present, allowing the residues to be classified as salts. Further, the negative ion mass spectra of these particles were identical to salt particles that had not collided with the inlet (i.e., did not contain Cr, Mn, Fe, Mo), showing how the dual-polarity mass spectrometer of the A-ATOFMS can help distinguish the source signature of the residue despite interferences from the inlet metals. Although inlet metals were only observed during ice-containing sampling periods, no correlation was observed between ice particle size (or riming) and the presence of inlet metals in the A-ATOFMS mass spectra. Murphy et al. [2004] suggested that these metal enhancements could influence IN measurements in clouds; however, ice nuclei concentrations measured within clouds behind the CVI during ICE-L did not generally seem enhanced relative to IN concentrations measured in ambient air at similar processing conditions [*Field et al.*, 2009].

8.4.4 Mixed Phase Cloud Residues

Concurrent CVI sampling by the A-ATOFMS, C-ToF-AMS, and impactor for TEM-EDX analysis was conducted for mixed phase (coexisting supercooled liquid droplets and ice particles) cloud residues, allowing a comparison of the three aerosol chemical analysis techniques (Figure 8.8). During mixed phase sampling (-20 to -32°C, 6.4-7.9 km), supercooled droplets, measured by the CDP, were present at an average of 44 cm^{-3} (maximum 144 cm^{-3});; cloud ice particles, measured by the 2DC probe, were present at an average of 10 L^{-1} (σ 14 L^{-1}) with maximum concentrations reaching near 1 cm^{-3}. The relative contribution of the ice particles to the mixed phase residues is expected to be enhanced since residue multiplication can occur from ice particles larger than ~75 μm (aerodynamic diameter) that may break up within the CVI inlet

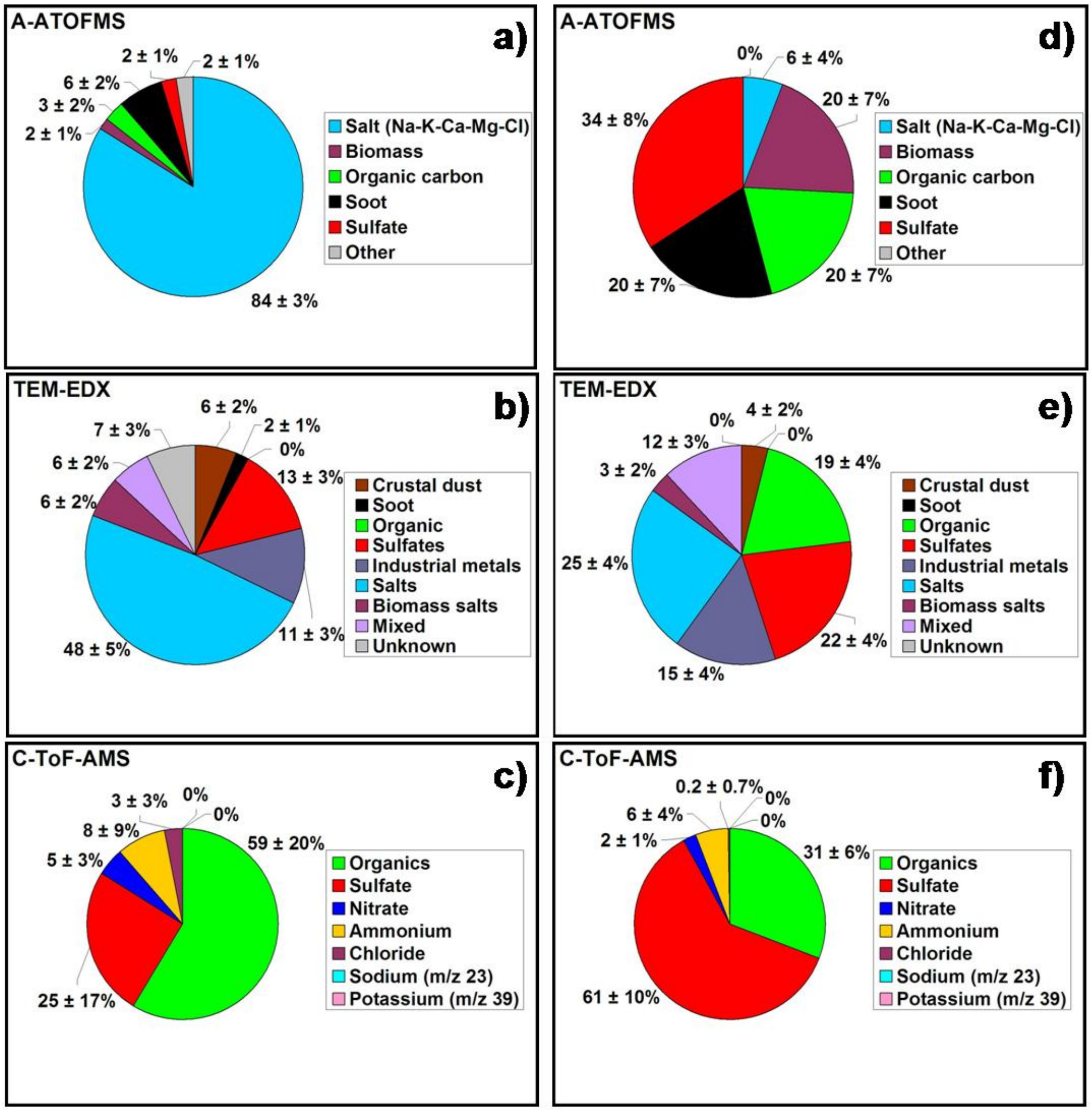

Figure 8.8. Relative number fractions of particle types measured by the (a, d) A-ATOFMS and (b, e) TEM-EDX for mixed phase cloud residues and clear air particles, respectively. Relative non-refractory mass fractions measured by the C-ToF-AMS for (c) mixed phase cloud residues and (f) clear air particles.

[*Twohy et al.*, 2003]. The fraction of mixed-phase residues containing inlet metals, as measured by the A-ATOFMS, was minor (4 ± 2%). For the mixed-phase TEM-EDX sample, 3% of the small impactor stage residues and 7% of the large impactor stage residues contained stainless steel markers (not shown), in agreement with that observed by the A-ATOFMS. As expected for these mixed phase residues, the relative fraction of playa salts (84 ± 3%), as measured by the A-ATOFMS, was between that of the droplet residues (57 ± 10%) and ice residues (94 ± 3%) (Figures 8.5, 8.6, and 8.8). Similarly, the organic mass fraction, as measured by the C-ToF-AMS, increased from droplets (38 ± 17%) to mixed phase (59 ± 20%) to ice (82 ± 7%), with a corresponding increase in the O/C ratio (0.84 ± 0.36 to 1.00 ± 0.31 to 1.15 ± 0.25, respectively). While the number fraction of salts containing sulfate and/or nitrate was similar for the mixed phase (70 ± 4%) and droplets (69 ± 13%) (Figure 8.7), the mass fraction of sulfate in all residues decreased from droplets (45 ± 17%) to mixed phase (25 ± 17%) to ice (4 ± 2%). Comparison of the TEM-EDX small and large particle impactor stages showed the salts were enhanced in the large stage (74 ± 5%, not shown) compared to the small stage (48 ± 5%), in agreement with the presence of large playa salts with a size distribution similar to that of mineral dust [*Patterson and Gillette*, 1977]. In contrast, TEM-EDX showed a greater fraction of sulfate particles for the small stage (13 ± 3%) compared to the large stage (5 ± 2%, not shown).

For comparison between TEM-EDX, A-ATOFMS, and C-ToF-AMS, one must first consider the relationship between particle geometric diameter (d_g), measured by TEM, and vacuum aerodynamic diameter (d_{va}), measured by the A-ATOFMS and C-

ToF-AMS. For spherical particles with no voids, d_g and d_{va} are related by the following equation:

$$d_{va} = d_g \frac{\rho_p}{\rho_0} \qquad (1)$$

where ρ_0 is the standard density (1 g cm^{-3}) and ρ_p is the average particle density for a multiple component particle [*DeCarlo et al.*, 2004]. Thus, the size ranges of the A-ATOFMS and C-ToF-AMS are most similar to the small impactor stage, which collected approximately 0.08 to 0.42 μm (d_g) or 0.136 to 0.714 μm (d_{va}) particles, compared to the large impactor stage (> 0.42 μm d_g or > 0.714 μm d_{va}), given an assumed effective density of ~1.7 g m^{-3} for the salt particles, as observed previously for ambient sea-salt particles at low relative humidity [*Moffet et al.*, 2008b]. It also should be noted that the TEM-EDX sample was collected for a shorter time period than the A-ATOFMS and C-ToF-AMS mixed phase residue samples, which may yield minor differences in the samples. Comparison of the relative fractions of different particle types measured by the A-ATOFMS and TEM-EDX (Figure 8.8a and 8.8b) shows a smaller fraction of salts detected by TEM-EDX compared to the A-ATOFMS, although some of the salts are included in the TEM-EDX "mixed" particle category. In a previous comparison ATOFMS and scanning electron microscopy (SEM)-EDX of K- and Na-containing particles in Mexico City, the ATOFMS observed twice as many particles containing Cl compared to SEM-EDX due to the increased sensitivity of the ATOFMS, as well as possible Cl loss reactions following filter collection [*Moffet et al.*, 2008a]. In agreement, the A-ATOFMS observed 6 ± 2% of the mixed phase residues to be silicate-containing salts, whereas TEM-EDX categorized 6 ± 2% of the residues as crustal dust. The large fraction of industrial metals observed by TEM-EDX may have been above the vacuum aerodynamic diameter range of the A-ATOFMS due to high densities, accounting for this discrepancy between the two results. Lastly, TEM-EDX identified a greater fraction of sulfate particles compared to the A-ATOFMS (13 ± 3% vs. 2 ± 1%, respectively); however, it is likely that a fraction of these particles were internally mixed with organics and/or soot and, thus, were classified by the A-ATOFMS as such. Overall, the A-ATOFMS and TEM-EDX were found to be in good agreement.

8.4.5 Comparison to Clear Air

In the ambient air surrounding the orographic wave clouds, the A-ATOFMS observed the majority of submicron particles to be either externally mixed sulfate or an internal carbonaceous/sulfate mixture (biomass, organic carbon, and soot particle types), which is consistent with the majority of the non-refractory submicron mass being composed of organics and sulfate, as measured by the C-ToF-AMS (Figure 8.8f). Given the uncertainties associated with the observed low mass loadings, the C-ToF-AMS did not observe a significant difference in the mass fractions of organics, sulfate, nitrate, and ammonium between the ambient air and cloud droplet residues; similar O/C ratios (0.77 ± 0.28 vs. 0.84 ± 0.36) were observed for the organic aerosol as well. As the primary measurements of the playa salts were for particle diameters greater than 100 nm, it is important to examine the role of these particles in cloud droplet activation. As discussed in Section 8.3.2, all particles >100 nm in diameter are expected to activate as cloud droplets, given average clear air number concentrations (0.1-1.0 μm particles) of 25 cm^{-3} (maximum 164 cm^{-3}) and cloud droplet number concentrations of 66 cm^{-3} (maximum 125 cm^{-3}). However, observations discussed herein show that this did not hold for the measured chemistry of droplets >7 μm. During CVI sampling of liquid droplets >7 μm, an average of 88% (σ 40%) of droplets, as measured by the CDP, were larger than this diameter; in comparison, during >19 μm sampling, 35% (σ 18%) of droplets were larger than this larger diameter. In fact, the total submicron non-refractory mass measured by the C-ToF-AMS for liquid droplet (>7 μm) sampling (0.019 ± 0.006 μg m^{-3}) was only 6 ± 2% of that observed for the ambient air (0.34 ± 0.09 μg m^{-3}), although this particularly low fraction is likely also due to preferential activation of larger, more refractory salts compared to smaller organic-sulfate particles. Further, CVI residues >110 nm in diameter had average number concentrations of only 1.7 ± 1.5 cm^{-3}; however, concentrations were much greater for residues <110 nm (16 cm^{-3} (σ 14 cm^{-3})) for which chemistry was not measured by A-ATOFMS and TEM-EDX, although non-refractory mass for >50 nm particles was measured by the C-ToF-AMS. Thus, while all particles >100 nm did not result in cloud droplets >7 μm, it is unclear whether all clear air particles >100 nm activated as predicted.

A-ATOFMS and TEM-EDX results both show an enrichment of the playa salts in the cloud residues compared to the clear air. Similar enrichments were observed by Cziczo et al. [2004], wherein 26% of homogeneously frozen ice residues were sea salt compared to <1% outside of the cirrus; however, these anvil cirrus clouds were associated with convective systems which were hypothesized to transport sea salt from the surface. Twohy and Anderson [2008] observed similar enrichments of salts in <0.2 μm cloud droplet residues collected within eastern Pacific stratocumulus, Caribbean Sea small cumulus, and Indian Ocean small cumulus compared to ambient particles.

However, for wintertime layer clouds over the midwestern US and Canada, this enrichment was not observed due to a lack of marine NaCl salts present [*Twohy and Anderson*, 2008]. During ICE-L, the enrichment of playa salts may be the result of examining only >7 μm cloud particles which selectively represented only the largest, most hygroscopic residues, as discussed in Section 8.4.2. Numerous studies have observed Na, Ca, and Mg to be enriched in larger droplets [*Bator and Collett*, 1997; *Gieray et al.*, 1997; *Menon et al.*, 2000; *Munger et al.*, 1989; *Vong et al.*, 1997]. However, while an increased fraction of salts were in the large impactor stage for the TEM-EDX mixed-phase cloud residues, the clear air TEM-EDX results show an increased fraction of salts within the small impactor stage (21 ± 4%, Figure 8e) compared to the larger stage (9 ± 4%, not shown). The TEM-EDX "mixed" and crustal dust categories were within uncertainties for the small and large impactor stages. Thus, while an enrichment of playa salts was observed in the cloud residues, it is uncertain whether this observation would hold if the entire cloud droplet population, including cloud droplets <7 μm, had been measured. Further, in comparison to the liquid, mixed, and ice phase sampling, externally mixed sulfate particles, measured by A-ATOFMS and TEM-EDX, were significantly enhanced in the clear air. In addition, for the ice residues, organics were found to preferentially freeze compared to sulfate (C-ToF-AMS), possibly due to the internal mixing of a fraction of the organics with playa salts, as confirmed by STXM/NEXAFS analysis.

Due to the significant hygroscopicity of the playa salts, as described in Section 8.4.2, it is likely that submicron playa salts, observed as dry cloud residues, retained water under the clear air sampling conditions of RF03 (average relative humidity of 42%

(σ 29%)). In fact, Cziczo et al. [1997] observed artificial sea salt, containing Na^+, Mg^{2+}, Ca^{2+}, K^+, Cl^-, SO_4^{2-}, HCO_3^-, and Br^-, to contain liquid water even at low relative humidity (12%). Magnesium chloride and calcium chloride, enriched in playa salts compared to sea salt, have significantly lower deliquescence relative humidities (DRHs) ($MgCl_2{\cdot}6H_2O$, 33%; $CaCl_2{\cdot}6H_2O$, 28.3%) compared to sodium chloride (NaCl, 75.3%) [*Tang et al.*, 1997]. Further, mixtures of these salts have even lower mutual DRHs: ~24% for $CaCl_2{\cdot}6H_2O$+NaCl+KCl and 32% for $MgCl_2{\cdot}6H_2O$+NaCl [*Kelly and Wexler*, 2006]. For previous measurements, a DRH of ~70% was observed for the more hygroscopic mode of the Owens Lake dust [*Koehler et al.*, 2007]; however, this dust was less CCN active compared to the Owens Lake crust examined herein, as discussed in Section 8.4.2, suggesting a lower DRH of the RF03 playa salts. Further, the cloud residue playa salts were found to be internally mixed with organics; Carrico et al. [2008] found a reduction or elimination of clear deliquescent phase transitions for organic-inorganic mixtures compared to that expected for inorganic species. In fact, hygroscopicity measurements associated with ambient organic aerosol (O/C = 0.92 ± 0.33) suggested that oxidized organics internally mixed with inorganic salts enhance water uptake at low relative humidities [*Hersey et al.*, 2009]. Previously, Matsuki et al. [2009] observed a large fraction of carbonate particles to be already deliquesced under clear-sky conditions. The A-ATOFMS and C-ToF-AMS utilize aerodynamic lens inlets with low transmission above 1 μm (d_{va}) [*Liu et al.*, 2007; *Pratt et al.*, 2009], similar to the aircraft inlets used during ICE-L for A-ATOFMS and C-ToF-AMS clear air sampling (in contrast to the CVI inlet used for clear air impactor sampling). Thus, if the playa salts were already deliquesced in the clear air, causing them to be >1 μm (i.e. above the 1 μm inlet cut-point), they would not have been observed by the A-ATOFMS and C-ToF-AMS.

8.5 Conclusions

Playa salts, comprised of Na-K-Mg-Ca-Cl salts, internally mixed with oxidized organic species presumably produced by cloud processing, have been shown to act as cloud nuclei in orographic wave clouds over Wyoming. The unique ability of the A-ATOFMS to distinguish between sea salt and playa salts was essential to the conclusion of this study. Excellent agreement was achieved between the aerosol chemical analysis techniques used in this study (A-ATOFMS, C-ToF-AMS, TEM-EDX, STXM/NEXAFS). The techniques are complementary, combining together to enable an unprecedented characterization of single-particle mixing state with quantification of non-refractory particle components. Similar to previous observations of sea salt in marine environments, these playa salts were enhanced in larger droplets (>19 μm) compared to smaller droplets (>7 μm). Enhancement of the playa salts in ice, compared to the clear air and droplets, was also observed, due to influences of homogeneous freezing and riming. A small fraction of silicate-containing playa salts were hypothesized to contribute to be important in the heterogeneous ice nucleation observed in the wave clouds on this day.

Although the generation of wind-blown dust from playas is relatively well-known, the importance of playa dust globally in cloud formation is uncertain. Previous studies of the CCN and IN abilities of playa dust have suggested their importance in cloud formation [*Koehler et al.*, 2007]. Further, satellite-based studies of the dust storms from the Aral Sea have suggested that playa salts promote precipitation and act as giant CCN [*Rudich et al.*, 2002]; however, cloud residue analysis was not completed to confirm the chemistry and associated CCN activity of the observed dust. Thus, these ICE-L results represent the first direct detection of playa salts serving as cloud nuclei within clouds. Due to the global abundance of playas [*Jones and Deocampo*, 2004; *Prospero et al.*, 2002] and increasing potential for playa dust storms due to land use changes [*Gill*, 1996], it is particularly important to understand the impact of playa dust on clouds. Based on the results shown herein, we suggest that playa salts impact cloud droplet and ice formation and cloud properties, particularly in remote continental locations. In-depth studies of the salt-producing potentials of playas globally are needed to further evaluate the transport, mixing, and cloud interactions of these salts in the global atmosphere. The implications of this study impact land use decisions and climate predictions, particularly of the indirect effect and precipitation patterns.

8.6 Acknowledgments

Prof. Kimberly Prather, Cassandra Gaston, and I acknowledge financial support from NSF (ATM-0650659, ATM-0321362). Cassandra Gaston performed the laboratory A-ATOFMS and CCN measurements. In addition to auxiliary data analysis of CFDC and cloud probe data, I performed the ICE-L A-ATOFMS measurements, all A-ATOFMS data analysis, and wrote the manuscript. Prof. Cynthia Twohy ran the CVI and completed TEM-EDX data analysis; financial support was provided by NSF (ATM-0612605). Dr. Paul DeMott ran the CFDC and was supported by NSF (ATM-0611936). Prof. John Seinfeld and Dr. Shane Murphy acknowledge NSF for support of ICE-L

(ATM-0340832) and NASA for an Earth and Space Sciences Fellowship; Dr. Murphy conducted the C-ToF-AMS measurements and analysis. For STXM/NEXAFS measurements and analysis, Dr. Ryan Moffet, Tobias Henn, and Dr. Mary Gilles acknowledge support from the Department of Energy's Office of Biological and Environmental Research, Atmospheric Science Program, and Office of Basic Energy Sciences (DE-AC02-05CH11231), as well as the Lawrence Berkeley National Laboratory Glenn T. Seaborg Fellowship for Dr. Moffet. The authors thank the ICE-L C-130 crew and investigators for their support. NSF and NCAR are acknowledged for financial support of the ICE-L field campaign, as well as the work of A.J. Heymsfield and D.C. Rogers. TEM-EDX was completed by Julia Sobolik at Oregon State University and by Traci Lersch at the RJ LeeGroup, Inc. Cloud probe data were provided by NCAR/EOL under sponsorship of NSF (http://data.eol.ucar.edu). Total PM_{10} and $PM_{2.5}$ mass concentrations in Utah were provided by the Utah State Division of Air Quality. Gregory Roberts (UCSD) is thanked for use of the CCNc. David Soller and Marith Reheis (USGS) are acknowledged for provision of the playa sediments map. ICE-L lidar and radar data were provided by Zhien Wang, Jeffrey French, and Samuel Haimov (University of Wyoming). Sonia Kreidenweis (Colorado State University) and Trude Eidhammer (NCAR) are thanked for discussions. The authors acknowledge the NOAA ARL for the provision of the HYSPLIT READY website (http://www.arl.noaa.gov/ready.html) used in this publication.

Chapter 8 is in preparation for submission to the *Journal of Geophysical Research*: Pratt, K.A., Twohy, C.H., Murphy, S.M., Moffet, R.M., Heymsfield, A.J.,

Gaston, C.J., DeMott, P.J., Field, P.R., Rogers, D.C., Henn, T.R., Gilles, M.K., Seinfeld, J.H., Prather, K.A. Playa salts serve as natural cloud nuclei.

8.7 References

Abuduwaili, J., M.V. Gabchenko, and X. Junrong (2008), Eolian transport of salts - A case study in the area of Lake Ebinur (Xinjiang, Northwest China), *J. Arid Environ.*, *72*(1843-1852.

Aiken, A.C., P.F. DeCarlo, J.H. Kroll, D.R. Worsnop, J.A. Huffman, K.S. Docherty, I.M. Ulbrich, C. Mohr, J.R. Kimmel, D. Sueper, Y. Sun, Q. Zhang, A. Trimborn, M. Northway, P.J. Ziemann, M.R. Canagaratna, T.B. Onasch, M.R. Alfarra, A.S.H. Prevot, J. Dommen, J. Duplissy, A. Metzger, U. Baltensperger, and J.L. Jimenez (2008), O/C and OM/OC ratios of primary, secondary, and ambient organic aerosols with high-resolution time-of-flight aerosol mass spectrometry, *Environ. Sci. Technol.*, *42*(4478-4485.

Allan, J.D., K.N. Bower, H. Coe, H. Boudries, J.T. Jayne, M.R. Canagaratna, D.B. Millet, A.H. Goldstein, P.K. Quinn, R.J. Weber, and D.R. Worsnop (2004), Submicron aerosol composition at Trinidad Head, California, during ITCT 2K2: Its relationship with gas phase volatile organic carbon and assessment of instrument performance, *J. Geophys. Res.*, *109*(D23S24), doi:10.1029/2003JD004208.

Andreae, M.O., and D. Rosenfeld (2008), Aerosol-cloud-precipitation interactions. Part 1. The nature and sources of cloud-active aerosols, *Earth-Science Rev.*, *89*(13-41.

Bahreini, R., E.J. Dunlea, B.M. Matthew, C. Simons, K.S. Docherty, P.F. DeCarlo, J.L. Jimenez, C.A. Brock, and A.M. Middlebrook (2008), Design and operation of a pressure-controlled inlet for airborne sampling with an aerodynamic aerosol lens, *Aerosol Sci. Technol.*, *42*(6), 465-471.

Bator, A., and J.L. Collett (1997), Cloud chemistry varies with drop size, *J. Geophys. Res.*, *102*(D23), 28071-28078.

Bilde, M., and B. Svenningsson (2004), CCN activation of slightly soluble organics: the importance of small amounts of inorganic salt and particle phase, *Tellus*, *56B*(2), 128-134.

Blackwelder, E. (1931), The lowering of playas by deflation, *Am. J. Sci.*, *21*(140-144.

Blank, R.R., J.A. Young, and F.L. Allen (1999), Aeolian dust in a saline playa environment, Nevada, USA, *J. Arid Environ.*, *41*(4), 365-381.

Bryant, R.G., B.W. Sellwood, A.C. Millington, and N.A. Drake (1994), Marine-like potash evaporite formation on a continental playa - Case-study from Chott-El-Djerid, Southern Tunisia, *Sedimentary Geology*, *90*(3-4), 269-291.

Cahill, T.A., T.E. Gill, J.S. Reid, E.A. Gearhart, and D.A. Gillette (1996), Saltating particles, playa crusts and dust aerosols at Owens (dry) Lake, California, *Earth Surface Processes And Landforms*, *21*(621-639.

Carrico, C.M., M.D. Petters, S.M. Kreidenweis, J.L. Collett, G. Engling, and W.C. Malm (2008), Aerosol hygroscopicity and cloud droplet activation of extracts of filters from biomass burning experiments, *J. Geophys. Res.*, *113*(D08206), doi:10.1029/2007JD009274.

Chen, J., R.J. Griffin, A. Grini, and P. Tulet (2007), Modeling secondary organic aerosol formation through cloud processing of organic compounds, *Atmos. Chem. Phys.*, *7*(20), 5343-5355.

Cooper, W.A., and G. Vali (1981), The origin of ice in mountain cap clouds, *J. Atmos. Sci.*, *38*(1244-1259.

Cziczo, D.J., D.M. Murphy, P.K. Hudson, and D.S. Thomson (2004), Single particle measurements of the chemical composition of cirrus ice residue during CRYSTAL-FACE, *J. Geophys. Res.*, *109*(D04201), doi:10.1029/2003JD004032.

Cziczo, D.J., J.B. Nowak, J.H. Hu, and J.P.D. Abbatt (1997), Infrared spectroscopy of model tropospheric aerosols as a function of relative humidity: Observation of deliquescence and crystallization, *Journal of Geophysical Research*, *102*(D15), 18843-18850.

DeCarlo, P.F., J.G. Slowik, D.R. Worsnop, P. Davidovits, and J.L. Jimenez (2004), Particle morphology and density characterization by combined mobility and aerodynamic diameter measurements. Part 1: Theory, *Aerosol Sci. Technol.*, *38*(12), 1185-1205.

DeMott, P.J., and D.C. Rogers (1990), Freezing nucleation rates of dilute-solution droplets measured between -30-degrees-C and -40-degrees-C in laboratory simulations of natural clouds, *Journal Of The Atmospheric Sciences*, *47*(9), 1056-1064.

Draxler, R.R., and G.D. Rolph (2003), HYSPLIT (HYbrid Single-Particle Lagrangian Integrated Trajectory) Model access via NOAA ARL READY Website (http://www.arl.noaa.gov/ready/hysplit4.html), *NOAA Air Resources Laboratory*, Silver Spring, MD.

Drewnick, F., S.S. Hings, P. DeCarlo, J.T. Jayne, M. Gonin, K. Fuhrer, S. Weimer, J.L. Jimenez, K.L. Demerjian, S. Borrmann, and D.R. Worsnop (2005), A new time-of-flight aerosol mass spectrometer (TOF-AMS) - Instrument description and first field deployment, *Aerosol Sci. Technol.*, *39*(637-658.

Drofa, A.S. (2006), Formation of cloud microstructure during hygroscopic seeding, *Izvestiya Atmospheric And Oceanic Physics*, *42*(3), 326-336.

Droste, J.B. (1961), Clay minerals in sediments of Owens, China, Searles, Panamint, Bristol, Cadiz, and Danby Lake Basins, California, *Geol. Soc. America Bull.*, *72*(1713-1722.

Dusek, U., G.P. Frank, L. Hildebrandt, J. Curtius, J. Schneider, S. Walter, D. Chand, F. Drewnick, S. Hings, D. Jung, S. Borrmann, and M.O. Andreae (2006), Size matters more than chemistry for cloud-nucleating ability of aerosol particles, *Science*, *312*(5778), 1375-1378.

Field, P.R., A.J. Heymsfield, D.C. Rogers, J. Stith, P.J. DeMott, S. Haimov, S.M. Murphy, K.A. Pratt, C. Twohy, K.A. Prather, J.H. Seinfeld, B.J. Shipway, T. Eidhammer, and A.J. Prenni (2009), Contrasting ice nucleation in two lee wave clouds observed during the ICE-L campaign, *Journal of Atmospheric Sciences*, *In Preparation.*(

Field, P.R., O. Mohler, P. Connolly, M. Kramer, R. Cotton, A.J. Heymsfield, H. Saathoff, and M. Schnaiter (2006), Some ice nucleation characteristics of Asian and Saharan desert dust, *Atmos. Chem. Phys.*, *6*(2991-3006.

Formenti, P., W. Elbert, W. Maenhaut, J. Haywood, and M.O. Andreae (2003), Chemical composition of mineral dust aerosol during the Saharan Dust Experiment (SHADE) airborne campaign in the Cape Verde region, September 2000, *J. Geophys. Res.*, *108*(D18), doi:1029/2002JD002648.

Gard, E.E., M.J. Kleeman, D.S. Gross, L.S. Hughes, J.O. Allen, B.D. Morrical, D.P. Fergenson, T. Dienes, M.E. Galli, R.J. Johnson, G.R. Cass, and K.A. Prather (1998), Direct observation of heterogeneous chemistry in the atmosphere, *Science*, *279*(5354), 1184-1187.

Ghate, V.P., B.A. Albrecht, P. Kollias, H.H. Jonsson, and D.W. Breed (2007), Cloud seeding as a technique for studying aerosol-cloud interactions in marine stratocumulus, *Geophys. Res. Lett.*, *34*(L14807), doi:10.1029/2007GL029748.

Gieray, R., P. Wieser, T. Engelhart, E. Swietlicki, H.-C. Hansson, B. Mentes, D. Orsini, B. Martinsson, B. Svenningsson, K.J. Noone, and J. Heintzenberg (1997), Phase partitioning of aerosol constituents in cloud based on single-particle and bulk analysis, *Atmos. Environ.*, *31*(16), 2491-2502.

Gill, T.E. (1996), Eolian sediments generated by anthropogenic disturbance of playas: Human impacts on the geomorphic system and geomorphic impacts on the human system, *Geomorphology*, *17*(1-3), 207-228.

Gill, T.E., D.A. Gillette, T. Niemeyer, and R.T. Winn (2002), Elemental geochemistry of wind-erodible playa sediments, Owens Lake, California, *Nuclear Instruments & Methods In Physics Research Section B-Beam Interactions With Materials And Atoms*, *189*(209-213.

Güven, N., and P.F. Kerr (1966), Selected Great Basin playa clays, *Am. Mineral.*, *51*(1056-1067.

Henke, B.L., E.M. Gullikson, and J.C. Davis (1993), *Atomic Data and Nuclear Data Tables*, *54*(181).

Hersey, S.P., A. Sorooshian, S.M. Murphy, R.C. Flagan, and J.H. Seinfeld (2009), Aerosol hygroscopicity in the marine atmosphere: a closure study using high-time-resolution, multiple-RH DASH-SP and size-resolved C-ToF-AMS data, *Atmos. Chem. Phys.*, *9*(2543-2554.

Heymsfield, A.J., and L.M. Miloshevich (1993), Homogeneous ice nucleation and supercooled liquid water in orographic wave clouds, *Journal of Atmospheric Sciences*, *50*(15), 2335-2353.

Heymsfield, A.J., L.M. Miloshevich, A. Slingo, K. Sassen, and D.O.C. Starr (1991), An observational and theoretical study of highly supercooled altocumulus, *Journal of Atmospheric Sciences*, *48*(7), 923-945.

Hildebrandt, L., N.M. Donahue, and S.N. Pandis (2009), High formation of secondary organic aerosol from the photo-oxidation of toluene, *Atmos. Chem. Phys.*, *9*(9), 2973-2986.

Hobbs, P.V., D.A. Bowdle, and L.F. Radke (1985), Particles in the lower troposphere over the high plains of the United States. Part I: Size distributions, elemental compositions and morphologies, *Journal Of Climate And Applied Meteorology*, *24*(1344-1356.

Hopkins, R.J., A.V. Tivanski, B.D. Marten, and M.K. Gilles (2007), Chemical bonding and structure of black carbon reference materials and individual carbonaceous atmospheric aerosols, *J. Aerosol Sci.*, *38*(573-591.

Hudson, J.G. (2007), Variability of the relationship between particle size and cloud-nucleating ability, *Geophys. Res. Lett.*, *34*(8), doi:10.1029/2006GL028850.

Hudson, J.G., and C.F. Rogers (1986), Relationship between critical supersaturation and cloud droplet size: Implications for cloud mixing processes, *Journal Of The Atmospheric Sciences*, *43*(21), 2341-2359.

Huffman, J.A., J.T. Jayne, F. Drewnick, A.C. Aiken, T. Onasch, D.R. Worsnop, and J.L. Jimenez (2005), Design, modeling, optimization, and experimental tests of a particle beam width probe for the Aerodyne aerosol mass spectrometer, *Aerosol Sci. Technol.*, *39*(1143-1163.

Jones, B.F., and D.M. Deocampo (2004), Geochemistry of saline lakes, *Treatise on Geochemistry*, *5*(393-424.

Junge, C., and E. McLaren (1971), Relationship of cloud nuclei spectra to aerosol size distribution and composition, *J. Atmos. Sci.*, *28*(3), 382-390.

Kelly, J.T., C.C. Chuang, and A.S. Wexler (2007), Influence of dust composition on cloud droplet formation, *Atmos. Environ.*, *41*(14), 2904-2916.

Kelly, J.T., and A.S. Wexler (2006), Water uptake by aerosol: Water activity in supersaturated potassium solutions and deliquescence as a function of temperature, *Atmos. Environ.*, *40*(24), 4450-4468.

Kilcoyne, A.L.D., T. Tyliszczak, W.F. Steele, S. Fakra, P. Hitchcock, K. Franck, E. Anderson, B. Harteneck, E.G. Rightor, G.E. Mitchell, A.P. Hitchcock, L. Yang, T. Warwick, and H. Ade (2003), Interferometer-controlled scanning transmission X-ray microscopes at the Advanced Light Source, *J. Synchrotron Rad.*, *10*(2), 125-136.

Koehler, K.A., S.M. Kreidenweis, P.J. DeMott, M.D. Petters, A.J. Prenni, and C.M. Carrico (2009), Hygroscopicity and cloud droplet activation of mineral dust aerosol, *Geophys. Res. Lett.*, *36*(L08805), doi:10.1029/2009GL037348.

Koehler, K.A., S.M. Kreidenweis, P.J. DeMott, A.J. Prenni, and M.D. Petters (2007), Potential impact of Owens (dry) Lake dust on warm and cold cloud formation, *J. Geophys. Res.*, *112*(doi:10.1029/2007JD008413.

Liu, P.S.K., R. Deng, K.A. Smith, L.R. Williams, J.T. Jayne, M.R. Canagaratna, K. Moore, T.B. Onasch, D.R. Worsnop, and T. Deshler (2007), Transmission efficiency of an aerodynamic focusing lens system: Comparison of model calculations and laboratory measurements for the Aerodyne aerosol mass spectrometer, *Aerosol Sci. Technol.*, *41*(8), 721-733.

Lowenstein, T.K., and L.A. Hardie (1985), Criteria for the recognition of salt-pan evaporites, *Sedimentology*, *32*(627-644.

Matsuki, A., A. Schwarzenboeck, H. Venzac, P. Laj, S. Crumeyrolle, and L. Gomes (2009), Effect of surface reaction on the cloud nucleating properties of mineral dust: AMMA aircraft campaign in summer 2006, *Atmos. Chem. Phys. Discuss.*, *9*(1797-1830.

Matthew, B.M., A.M. Middlebrook, and T.B. Onasch (2008), Collection efficiencies in an Aerodyne aerosol mass spectrometer as a function of particle phase for laboratory generated aerosols, *Aerosol Sci. Technol.*, *42*(884-898.

Menon, S., V.K. Saxena, and B.D. Logie (2000), Chemical heterogeneity across cloud droplet size spectra in continental and marine air masses, *Journal of Applied Meteorology*, *39*(887-903.

Moffet, R.C., Y. Desyaterik, R.J. Hopkins, A.V. Tivanski, M.K. Gilles, Y. Wang, V. Shutthanandan, L.T. Molina, R. Gonzalez Abraham, K.S. Johnson, V. Mugica, M.J. Molina, A. Laskin, and K.A. Prather (2008a), Characterization of aerosols containing Zn, Pb, and Cl from an industrial region of Mexico City, *Environ. Sci. Technol.*, *42*(19), 7091-7097.

Moffet, R.C., T.R. Henn, A. Laskin, and M.K. Gilles (2009), Automated assay of internally mixed individual particles using X-ray spectromicroscopy maps, *Anal. Chem.*, *Submitted*(

Moffet, R.C., X. Qin, T. Rebotier, H. Furutani, and K.A. Prather (2008b), Chemically segregated optical and microphysical properties of ambient aerosols measured in a single-particle mass spectrometer, *J. Geophys. Res.*, *113*(doi:10.1029/2007JD009393.

Munger, J.W., J. Collett, B. Daube, and M.R. Hoffmann (1989), Chemical composition of coastal stratus clouds: Dependence on droplet size and distance from the coast, *Atmos. Environ.*, *23*(10), 2305-2320.

Murphy, D.M., D.J. Cziczo, P.K. Hudson, D.S. Thomson, J.C. Wilson, T. Kojima, and P.R. Buseck (2004), Particle generation and resuspension in aircraft inlets when flying in clouds, *Aerosol Sci. Technol.*, *38*(4), 400-408.

Noone, K.J., J.A. Ogren, J. Heintzenberg, R.J. Charlson, and D.S. Covert (1988), Design and calibration of a counterflow virtual impactor for sampling of atmospheric fog and cloud droplets, *Aerosol Sci. Technol.*, *8*(3), 235-244.

Ogren, J.A., and R.J. Charlson (1992), Implications for models and measurements of chemical inhomogeneities among cloud droplets, *Tellus*, *44*(3), 208-225.

Patterson, E.M., and D.A. Gillette (1977), Commonalities in measured size distributions for aerosols having a soil-derived component, *J. Geophys. Res.*, *82*(15), 2074-2082.

Pelletier, J.D. (2006), Sensitivity of playa windblown-dust emissions to climatic and anthropogenic change, *Journal Of Arid Environments*, *66*(1), 62-75.

Petters, M.D., and S.M. Kreidenweis (2007), A single parameter representation of hygroscopic growth and cloud condensation nucleus activity, *Atmos. Chem. Phys.*, *7*(8), 1961-1971.

Pratt, K.A., J.E. Mayer, J.C. Holecek, R.C. Moffet, R.O. Sanchez, T.P. Rebotier, H. Furutani, M. Gonin, K. Fuhrer, Y. Su, S. Guazzotti, and K.A. Prather (2009), Development and characterization of an aircraft aerosol time-of-flight mass spectrometer, *Anal. Chem.*, *81*(5), 1792-1800.

Prenni, A.J., P.J. DeMott, C. Twohy, M.R. Poellot, S.M. Kreidenweis, D.C. Rogers, S.D. Brooks, M.S. Richardson, and A.J. Heymsfield (2007), Examinations of ice formation processes in Florida cumuli using ice nuclei measurements of anvil ice crystal particle residues, *J. Geophys. Res.*, *112*(D10221), doi:10.1029/2006JD007549.

Prenni, A.J., M.D. Petters, S.M. Kreidenweis, C.L. Heald, S.T. Martin, P. Artaxo, R.M. Garland, A.G. Wollny, and U. Pöschl (2009), Relative roles of biogenic emissions and Saharan dust as ice nuclei in the Amazon basin, *Nature Geoscience*, *2*(402-405.

Prospero, J.M., P. Ginoux, O. Torres, S.E. Nicholson, and T.E. Gill (2002), Environmental characterization of global sources of atmospheric soil dust identified with the Nimbus 7 Total Ozone Mapping Spectrometer (TOMS) absorbing aerosol product, *Rev. Geophys.*, *40*(1), doi:10.1029/2000RG0000095.

Rader, D.J., and V.A. Marple (1985), Effect of ultra-Stokesian drag and particle interception on impaction characteristics, *Aerosol Sci. Technol.*, *4*(141-156.

Reheis, M.C. (1997), Dust deposition downwind of Owens (dry) Lake, 1991-1994: Preliminary findings, *J. Geophys. Res.*, *102*(D22), 25999-26008.

Reheis, M.C. (2006), A 16-year record of eolian dust in Southern Nevada and California, USA: Controls on dust generation and accumulation, *J. Arid Environ.*, *67*(3), 487-520.

Reheis, M.C., and R. Kihl (1995), Dust deposition in southern Nevada and California, 1984-1989 - Relations to climate, source area, And source lithology, *J. Geophys. Res.*, *100*(D5), 8893-8918.

Reid, J.S., R.G. Flocchini, T.A. Cahill, and R.S. Ruth (1994), Local meteorological, transport, and source aerosol characteristics of late autumn Owens Lake (dry) dust storms, *Atmos. Environ.*, *28*(9), 1699-1706.

Roberts, G.C., P. Artaxo, J. Zhou, E. Swietlicki, and M.O. Andreae (2002), Sensitivity of CCN spectra on chemical and physical properties of aerosol: A case study from the Amazon Basin, *J. Geophys. Res.*, *107*(D20), doi:10.1029/2001JD000583.

Roberts, G.C., and A. Nenes (2005), A continuous-flow streamwise thermal-gradient CCN chamber for atmospheric measurements, *Aerosol Sci. Technol.*, *39*(3), 206-221.

Rogers, D.C., P.J. DeMott, S.M. Kreidenweis, and Y. Chen (2001), A continuous-flow diffusion chamber for airborne measurements of ice nuclei, *J. Atmos. Oceanic Technol.*, *18*(725-741.

Rose, D., S.S. Gunthe, E. Mikhailov, G.P. Frank, U. Dusek, M.O. Andreae, and U. Poschl (2008), Calibration and measurement uncertainties of a continuous-flow cloud condensation nuclei counter (DMT-CCNC): CCN activation of ammonium sulfate and sodium chloride aerosol particles in theory and experiment, *Atmos. Chem. Phys.*, *8*(5), 1153-1179.

Rudich, Y., O. Khersonsky, and D. Rosenfeld (2002), Treating clouds with a grain of salt, *Geophys. Res. Lett.*, *29*(22), 2060, doi:10.1029/2002GL016055.

Russell, I.C. (1883), Playas and playa-lakes, *Pop. Sci.*, *22*(380-383.

Silva, P.J., D.Y. Liu, C.A. Noble, and K.A. Prather (1999), Size and chemical characterization of individual particles resulting from biomass burning of local Southern California species, *Environ. Sci. Technol.*, *33*(18), 3068-3076.

Singer, A., T. Zobeck, L. Poberezsky, and E. Argaman (2003), The PM_{10} and $PM_{2.5}$ dust generation potential of soils/sediments in the Southern Aral Sea Basin, Uzbekistan, *J. Arid Environ.*, *54*(4), 705-728.

Soller, D.R., and M.C. Reheis, *Surficial materials in the conterminous United States*, U.S. Geological Survey Open-file Report 03-275, scale 1:5,000,000., 2004.

Solomon, S., D. Qin, M. Manning, Z. Chen, M. Marquis, K.B. Averyt, M. Tignor, and H.L. Miller, Climate Change 2007: The Physical Science Basis. Contribution of Working Group I to the Fourth Assessment Report of the Intergovernmental Panel on Climate Change, pp. 996, Cambridge University Press, New York, NY, 2007.

Sullivan, R.C., M.J.K. Moore, M.D. Petters, S.M. Kreidenweis, G.C. Roberts, and K.A. Prather (2009), Effect of chemical mixing state on the hygroscopicity and cloud nucleation properties of calcium mineral dust particles, *Atmos. Chem. Phys.*, *9*(3303-3316.

Sullivan, R.C., and K.A. Prather (2007), Investigations of the diurnal cycle and mixing state of oxalic acid in individual particles in Asian aerosol outflow, *Environ. Sci. Technol.*, *41*(8062-8069.

Sun, Y., Q. Zhang, A.M. Macdonald, K. Hayden, S.M. Li, J. Liggio, P.S.K. Liu, K.G. Anlauf, W.R. Leaitch, A. Steffen, M. Cubison, D.R. Worsnop, A. van Donkelaar, and R.V. Martin (2009), Size-resolved aerosol chemistry on Whistler Mountain, Canada with a high-resolution aerosol mass spectrometer during INTEX-B, *Atmos. Chem. Phys.*, *9*(9), 3095-3111.

Tang, I.N., A.C. Tridico, and K.H. Fung (1997), Thermodynamic and optical properties of sea salt aerosols, *J. Geophys. Res.*, *102*(D19), 23269-23275.

Toner, S.M., L.G. Shields, D.A. Sodeman, and K.A. Prather (2008), Using mass spectral source signatures to apportion exhaust particles from gasoline and diesel powered vehicles in a freeway study using UF-ATOFMS, *Atmos. Environ.*, *42*(568-581.

Twohy, C.H., and J.R. Anderson (2008), Droplet nuclei in non-precipitating clouds: composition and size matter, *Environ. Res. Lett.*, *3*(045002.

Twohy, C.H., P.H. Austin, and R.J. Charlson (1989), Chemical consequences of the initial diffusional growth of cloud droplets: a clean marine case, *Tellus*, *41B*(1), 51-60.

Twohy, C.H., S.M. Kreidenweis, T. Eidhammer, E.V. Browell, A.J. Heymsfield, A.R. Bansemer, B.E. Anderson, G. Chen, S. Ismail, P.J. DeMott, and S.C. Van Den Heever (2009), Saharan dust particles nucleate droplets in eastern Atlantic clouds, *Geophys. Res. Lett.*, *36*(L01807), doi:10.1029/2008GL035846.

Twohy, C.H., A.J. Schanot, and W.A. Cooper (1997), Measurement of condensed water content in liquid and ice clouds using an airborne counterflow virtual impactor, *J. Atmos. Oceanic Technol.*, *14*(1), 197-202.

Twohy, C.H., J.W. Strapp, and M. Wendisch (2003), Performance of a counterflow virtual impactor in the NASA Icing Research Tunnel, *J. Atmos. Oceanic Technol.*, *20*(781-790.

Vong, R.J., B.M. Baker, F.J. Brechtel, R.T. Collier, J.M. Harris, A.S. Kowalski, N.C. McDonald, and L.M. McInnes (1997), Ionic and trace element composition of cloud water collected on the Olympic Peninsula of Washington state, *Atmos. Environ.*, *31*(13), 1991-2001.

Washington, R., M. Todd, N.J. Middleton, and A.S. Goudie (2003), Dust-storm source areas determined by the total ozone monitoring spectrometer and surface observations, *Annals Of The Association Of American Geographers*, *93*(2), 297-313.

Chapter 9

9 Conclusions and Future Directions

9.1 Synopsis

Herein, this dissertation described important advances in our understanding of single-particle mixing state, particularly with regard to particle chemical composition, volatility, and impacts on clouds, gained through application of the aircraft aerosol time-of-flight mass spectrometer (A-ATOFMS) during the 2005 Study of Organic Aerosols in Riverside (SOAR) and 2007 Ice in Clouds Experiment – Layer Clouds (ICE-L). Section 9.2 provides a summary and discussion of these results. In addition, a brief ground-based inter-comparison of the nozzle-inlet ATOFMS, ultrafine (UF)-ATOFMS, and A-ATOFMS completed during SOAR-1 and is described in Section 9.3. Lastly, Section 9.4 describes several ongoing and suggested future projects resulting from the work described in this thesis.

9.2 Conclusions

During transport in the atmosphere, particles undergo a number of physical and chemical transformation processes including coagulation, heterogeneous reactions with trace gases, gas-particle partitioning of semivolatile species, and cloud/fog aqueous processing, leading to changes in particle size, morphology, and chemistry. Particle physical, optical, hygroscopic, and toxicological properties are highly dependent on the chemical mixing state. Due to the ever-changing physical and chemical properties and the spatial and temporal variability of the distribution of aerosols, the measurement of atmospheric aerosols represents a challenging task. To gain further insight into the size-resolved chemistry of individual atmospheric particles, a smaller aerosol time-of-flight mass spectrometer (ATOFMS) with increased data acquisition capabilities and lower power consumption was developed for aircraft-based studies. This aircraft (A)-ATOFMS is the first reported dual-polarity laser mass spectrometer for aircraft-based studies, allowing the complete mixing state, including both refractory and non-refractory species, of single particles to be investigated with respect to altitude. The A-ATOFMS has been field-tested on the ground during the Study of Organic Aerosols in Riverside, CA (SOAR) and aboard an aircraft during the Ice in Clouds Experiment – Layer Clouds (ICE-L). Herein, this dissertation described important advances in our understanding of single-particle mixing state, particularly with regard to particle chemical composition, volatility, and impacts on clouds, gained through application of the A-ATOFMS during SOAR and ICE-L.

As described in Chapter 2, ground-based field testing of the A-ATOFMS during SOAR shows increased data acquisition rates (>3x), mass resolution, and ion transmission compared to previous ATOFMS instruments. A-ATOFMS results from ICE-L represent the first aircraft-based collection of dual-polarity single-particle mass spectra and the first detection of high mass positive ions out to ~*m/z* 2000 in individual particles. In addition, high time resolution of single-particle mixing state was shown to be important for airborne studies as well as ground-based studies near particle sources where concentrations and chemistry vary rapidly.

Due to the increased mass range and mass resolution of the A-ATOFMS, the presence of oligomeric species (*m/z* range of -200 to -400) in individual ambient submicrometer particles was detected for the first time during SOAR (Chapter 3). Secondary organic precursors, photochemical activity, and particle acidity were suggested to collectively be playing a role in oligomer formation and the degree of oligomerization in the summer and fall in Riverside, CA. Further, increased oligomer intensities in the summer were observed when the particles were first heated with a thermodenuder; we hypothesized that heat removed semivolatile species, thereby increasing particle acidity, while concentrating the oligomeric precursors and accelerating oligomer formation.

To provide an improved assessment of highly aged particles in the eastern Los Angeles Basin, an automated thermodenuder (TD) was coupled to the A-ATOFMS to characterize the chemistry of the remaining individual submicron ambient particles cores following heating with 10 minute resolution (Chapter 4). Aged organic carbon particles had smaller particle cores compared to biomass burning particles and contained high fractions by volume of secondary species, primarily ammonium nitrate, amines, and ammonium sulfate, which volatilized with heating up to 230°C. In contrast, only small shifts in size with heating were observed for fresher combustion particles. Many of the particle residues at 230°C possessed similar mass spectral signatures to fresh vehicle emissions, biomass burning, sea salt, and dust particles. This suggests the TD-ATOFMS method could be a useful tool for source apportionment of ambient aerosols in aged atmospheres, while providing further insight into the relative contributions of primary and secondary species in ambient aerosols.

As shown in Chapter 5, the TD-ATOFMS method utilized during SOAR showed a strong seasonal dependence in the gas/particle partitioning of alkylamines within individual ambient submicron aged organic carbon particles internally mixed with ammonium, nitrate, and sulfate. Lower volatility in the summer was due to the presence of aminium nitrate and sulfate salts which comprised ~6-9% of the average particle mass at 230°C. Whereas, in the fall, 86 ± 1% of the amines volatilized below 113°C with aminium nitrate and sulfate salts representing less than 1% of the particle mass at 230°C. Particle acidity was found to impact protonation of the amines and subsequent formation of aminium sulfate and nitrate salts; further, it was determined that the concentrations of amines, as strong bases, should be included estimates of aerosol pH.

Chapter 6 describes the first measurements of vertical profiles of individual particle mixing states, which were the first aircraft-based, single-particle, dual-polarity mass spectrometry measurements made using the A-ATOFMS during ICE-L. Biomass burning was the largest single source of submicron particles (~33-39% by number) observed in this study from ~1.2 – 7.0 km. In contrast to ammonium and nitrate, the relative fractions of particles mixed with sulfate and sulfuric acid, as well as the relative amounts of these species within individual particles, generally increased with altitude, likely due to contributions from biomass burning and aircraft emissions. Sulfuric acid was found to preferentially partition to OC-containing particles with few elemental carbon particles mixed with sulfuric acid, impacting both direct and indirect radiative forcing.

For cloud sampling during ICE-L, a counterflow virtual impactor (CVI) was utilized to isolate cloud droplets and ice crystals, the residues of which were then analyzed in real-time using the A-ATOFMS. As discussed in Chapter 7, the A-ATOFMS allowed the in-situ, unambiguous detection of biological particles in cloud ice for the first time. Biological and mineral dust particles transported from Asia or Africa represented the majority (83 ± 6%) of ice crystal residues within the high altitude ice cloud. Parallel measurements of ice nuclei particle concentrations indicate that the cloud ice crystals were impacted by heterogeneous freezing, showing the potentially significant role of biological particles in cloud ice formation. Further, global aerosol dust modeling, air mass trajectory analysis, and mineral dust chemical composition show that the dust was transported from Asia or Africa, suggesting that biological particles may enhance the impact of desert dust storms on the formation of cloud ice.

Lastly, Chapter 8 discusses the dominant role of playa salts as cloud condensation and ice nuclei measured on several orographic wave cloud flights during ICE-L. Sodium-potassium-magnesium-calcium-chloride particles characterized by the A-ATOFMS were found to have a similar mass spectral signature to playa salts that showed elevated cloud condensation nuclei (CCN) efficiencies. Similar to previous observations of sea salt in marine environments, these playa salts were enhanced in larger droplets (>19 μm) compared to smaller droplets (>7 μm). Enhancement of the playa salts in ice, compared to the clear air and droplets, was also observed due to influences of homogeneous freezing and riming. A small fraction of silicate-containing playa salts were hypothesized to contribute to the minor influence of heterogeneous ice nucleation in the wave clouds. These results represent the first direct detection of playa salts as cloud nuclei.

9.3 ATOFMS Inter-Comparison

Chapter 2 included a brief ground-based inter-comparison of the nozzle-inlet ATOFMS, ultrafine (UF)-ATOFMS, and A-ATOFMS completed during SOAR-1. Here, additional work completed that was not included in the A-ATOFMS development manuscript is presented. It should be noted that Xueying Qin and Laura Shields provided the SOAR-1 nozzle-inlet and UF-ATOFMS data, respectively.

In general, excellent agreement was observed for the mass spectra of the different ambient particle types between the A-ATOFMS, UF-ATOFMS, and ATOFMS. For illustration purposes, example single-particle mass spectra collected by the A-ATOFMS, ATOFMS, and UF-ATOFMS are shown in Figure 9.1 for three example particle types: a) elemental carbon, b) vanadium, and c) biomass. The mass spectral fingerprints of the same particle type are very similar for each of the three instruments. As discussed in Chapter 2, the A-ATOFMS has been shown through analysis of polystyrene latex spheres (PSLs) of known size to feature a higher mass resolution and mass range in comparison to the ATOFMS and UF-ATOFMS due to greater sensitivity and ion transmission. This is also evident in the ambient mass spectra collected during SOAR. For the ATOFMS and UF-ATOFMS, ringing is evident in intense individual ion peaks (Figure 9.1, inset examples). In contrast to the A-ATOFMS and nozzle-inlet ATOFMS mass spectra, the UF-ATOFMS negative ion mass spectra often include signal cross-talk, or noise, from the positive ion detector (Figure 9.1). While the nozzle-inlet ATOFMS used in this study has the same mass spectrometer as the UF-ATOFMS, it features electronics to isolate the positive and negative ion detectors from one another, preventing cross-talk. In addition to physically separating the A-ATOFMS ion detectors (in contrast to the nozzle-inlet

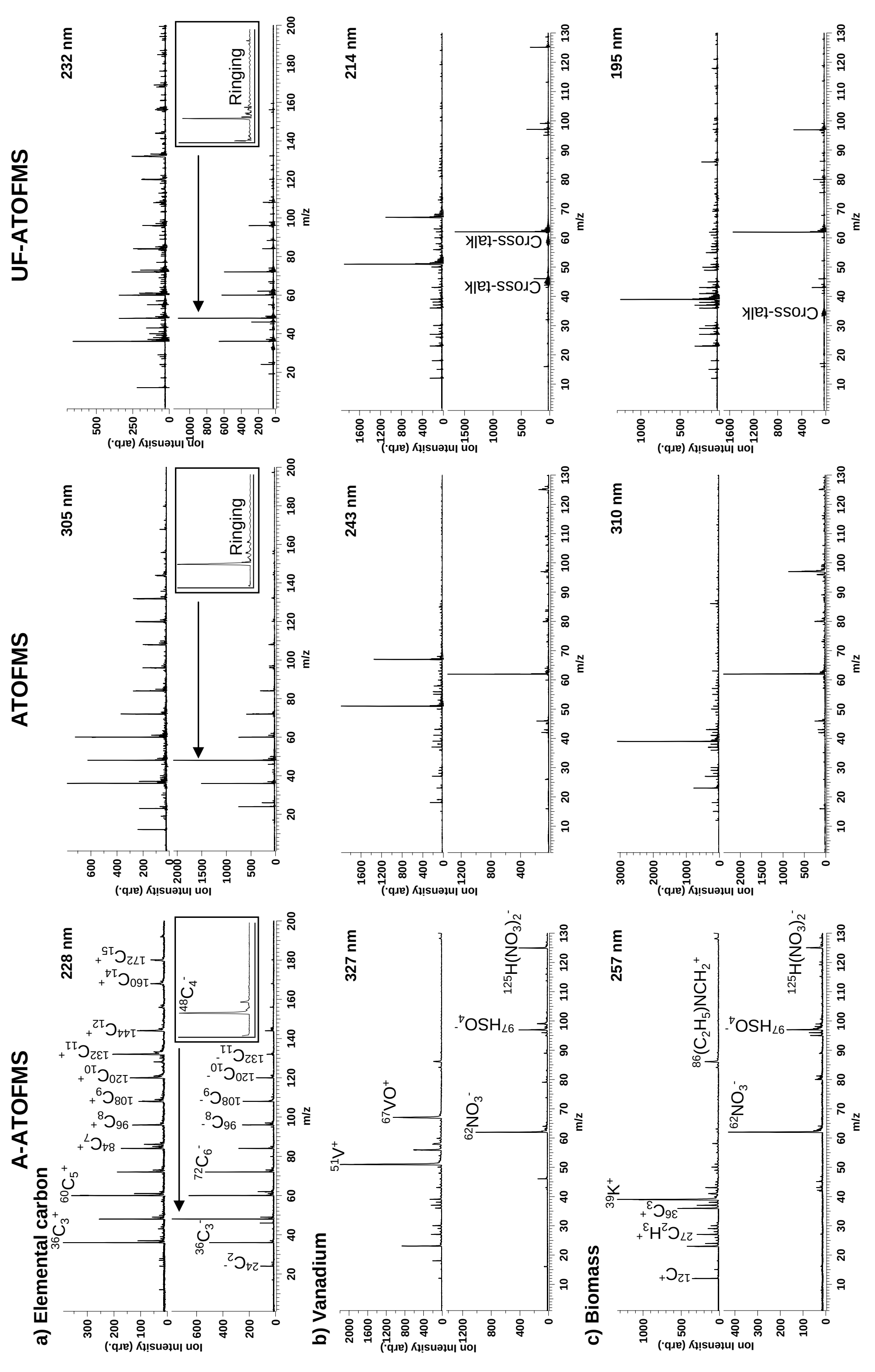

Figure 9.1. Comparison of single-particle mass spectra collected by the A-ATOFMS, ATOFMS, and UF-ATOFMS for three example particle types: a) elemental carbon, b) vanadium, and c) biomass. Evidence of ringing in spectra of the ATOFMS and UF-ATOFMS and signal cross-talk in the UF-ATOFMS spectra are highlighted.

ATOFMS and UF-ATOFMS), the ion detectors of the A-ATOFMS (25 mm bipolar time-of-flight detectors, Burle Electro-Optics Inc., Sturbridge, MA), in contrast, consist of scintillators and photomultiplier tubes in addition to the microchannel plates used by the ATOFMS and UF-ATOFMS; this isolates the positive and negative ion detectors and prevents any cross-talk.

Furthermore, few particles with positive ion only mass spectra were observed from single particles by the A-ATOFMS in contrast to the nozzle-inlet ATOFMS and the UF-ATOFMS. For example, between 1:00 and 7:00 on August 10th, only 327 out of 104,284 hit particles (0.3%) produced only positive ion mass spectra using the A-ATOFMS. In comparison, 24% (8,225 out of 33,797) and 28% (6,765 out of 23,898) of the hit particles produced only positive ion mass spectra using the UF-ATOFMS and nozzle-inlet ATOFMS, respectively. This is due in part to the increased sensitivity and ion transmission of the A-ATOFMS compared to the UF-ATOFMS and nozzle-inlet ATOFMS. In addition, the particles sampled through the nozzle inlet are expected to have a higher water content compared to those sampled through the aerodynamic lens system, which has been shown to evaporate water from particles [*Zelenyuk et al.*, 2006]. While the water content of particles sampled through the nozzle inlet is representative of the ambient atmospheric and therefore advantageous for particle optical measurements [*Moffet et al.*, 2008b], water on particles has been shown to suppress the formation of negative ions during the laser desorption/ionization process [*Neubauer et al.*, 1998]. During this particular time period (August 10, 2005 1:00-7:00), high relative humidity conditions were present (average, 79%). As expected, the nozzle-inlet ATOFMS obtained a greater percentage of positive ion only single particle mass spectra in comparison to the UF-ATOFMS and A-ATOFMS; however, since the percentages of positive ion only mass spectra are similar between the ATOFMS and UF-ATOFMS, it is expected that the main difference between these instruments and the A-ATOFMS is the sensitivity of the mass spectrometer. Interestingly, for the A-ATOFMS during this same time period, 12,057 out of 104,284 (12%) hit particles produced only negative ion mass spectra. The lack of positive ions was likely due to too high of a software threshold setting, which is used to avoid saving gas-phase mass spectra.

Further, as discussed in Chapter 3, unique high mass negative ions in the -200 to -400 mass/charge range with repetitive spacings of 12, 14, and 16 units were observed in ~40% of the particles sampled by A-ATOFMS during SOAR-1. However, while the same particles were also observed by nozzle-inlet ATOFMS and UF-ATOFMS, these oligomers were not clearly observed by the ATOFMS and UF-ATOFMS due to lower ion transmission at higher mass/charge values. It should be noted that low intensity oligomers have been observed previously by the nozzle-inlet ATOFMS during smog chamber experiments when the oligomeric species were present at higher concentrations [*Gross et al.*, 2006].

For each ATOFMS instrument, the ART-2a clusters resulting from the analysis of the SOAR-1 single particles were classified into eight general particle types: aged organic carbon (AgedOC), elemental carbon-organic carbon (ECOC), calcium (Ca)-ECOC, elemental carbon (EC), amine, vanadium, biomass, and dust. Detailed descriptions of mass spectral, size, and temporal patterns of these SOAR ATOFMS particle types have been described previously [*Qin et al.*, 2009]. It should be noted that the vast majority of particles show evidence of organic carbon, nitrate (m/z -62, NO_3^-), and sulfate (m/z -97,

HSO_4^-) due to the aged nature of the Riverside particles. One additional particle type is included in this analysis that was not discussed by Qin et al. [2009]: Ca-ECOC, which was observed only in particles <200 nm; these particles are characterized by a large Ca^+ (m/z 40) peak with smaller carbonaceous ion markers, as well as nitrate (m/z -62, NO_3^-) and sulfate (m/z -97, HSO_4^-) ion peaks. These Ca-ECOC particles are likely residual oil particles from heavy-duty diesel vehicle exhaust [*Spencer et al.*, 2006].

Size-resolved chemical composition of particles sampled using the A-ATOFMS, UF-ATOFMS, and ATOFMS is shown in Figure 9.2 for August 10, 2005 05:00 – 11:00. With the exception of the ultrafine particles, which had fewer than 50 ART-2a clusters, the top 50 ART-2a clusters are shown for each instrument size range: A-ATOFMS (70-1000 nm, 88622 particles), UF-ATOFMS (60-350 nm, 30561 particles), and ATOFMS (350-1000 nm, 5761 particles). In addition, the A-ATOFMS and UF-ATOFMS show good agreement for the relative fractions of different particle types below 350 nm with the main difference being the relative fractions of ECOC versus AgedOC particles (Figure 9.2). The greater fraction of AgedOC particles below 150 nm, as observed by the A-ATOFMS, is speculated to be due to reduced deflection of these small particles within the source region due to the use of a neutralizer by the A-ATOFMS, but not employed by the UF-ATOFMS. Above 350 nm, the A-ATOFMS and ATOFMS show relatively good agreement between the relative fractions of different particle types. Differences in the relative fractions of the AgedOC, ECOC, EC, and amine particles are attributed to the decreased sensitivity of the positive ion detector in the nozzle-inlet ATOFMS during SOAR-1, wherein OC and amine peaks were observed with lower intensities compared to the A-ATOFMS and UF-ATOFMS. Following the field campaign, the positive ion

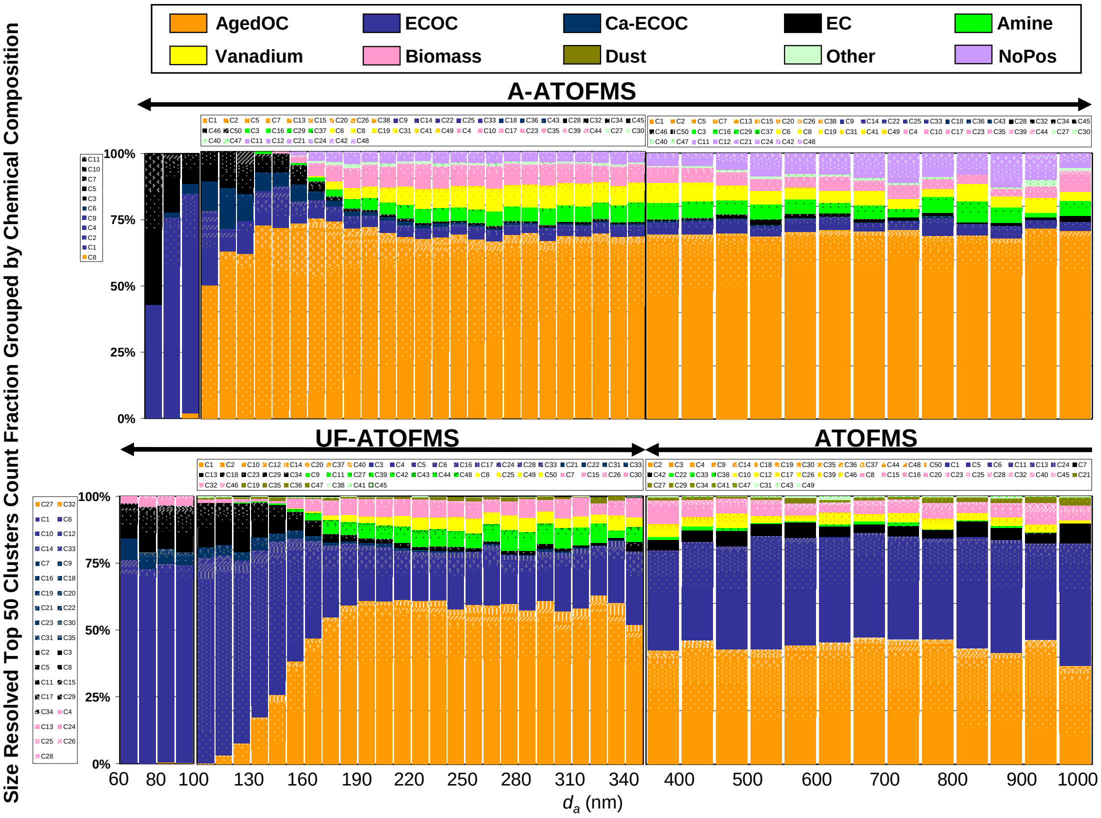

Figure 9.2. Size-resolved chemical composition of the A-ATOFMS (70-1000 nm), UF-ATOFMS (60-350 nm), and ATOFMS (350-1000 nm) for the top 50 ART-2a clusters for each instrument and size range (with the exception of the ultrafine particles, which had fewer resulting clusters). Different ART-2a clusters within one general particle type are represented by various patterns within a particular color. Size resolution is 10 nm and 50 nm for the ranges of 60-350 nm and 350-1000 nm, respectively.

detector was replaced in the ATOFMS. Overall, the relative fractions of major particle types observed during other time periods also showed consistency between the three instruments. The detection of ambient particles by a nozzle inlet (ATOFMS) versus an aerodynamic lens inlet (UF-ATOFMS and A-ATOFMS) does not seem to depend greatly on chemical composition.

9.4 Current Work and Future Directions

Much of the research started during this thesis is still currently in progress or has resulted in spin-off projects. Here, examples of this current and future work are discussed.

During SOAR-1, ATOFMS results showed the presence of methanesulfonate ($CH_3SO_3^-$, MSA) within single ambient particles during a major phytoplankton bloom off the California coast [*Gaston et al.*, 2009]. Concurrent thermodenuder sampling using the A-ATOFMS has resulted in the first volatility measurement of MSA in these ambient particles. For both SOAR-1 (August 12, 2005) and SOAR-2 (November 2-13, 2005), MSA was found to volatilize between 83°C and 113°C regardless of particle type. Previous laboratory volatility studies of pure 100 nm MSA particles showed a volatilization temperature of 171 ± 5°C; however, for particles consisting of 90% MSA and 10% ammonium sulfate, a reduced volatilization temperatures were observed for both the MSA (142°C) and ammonium sulfate (188°C compared to 205°C for pure particles) [*Johnson et al.*, 2004]. Similarly, for particles consisting of 10% MSA and 90% ammonium sulfate, the observed MSA volatilization temperature range was ~90-120°C [*Johnson et al.*, 2005]; this temperature range is in agreement with that observed during SOAR, further showing the importance of molecular interactions in multi-component particles. It also emphasizes differences in the volatility of various sulfate-containing species (e.g., organosulfate, ammonium sulfate, sulfuric acid, sodium sulfate, potassium sulfate) which impact Los Angeles basin aerosols. Gaston et al [2009] hypothesized the catalytic role of vanadium in the MSA formation based on the increased levels of MSA on vanadium-containing particles; the heated MSA-containing particles show potential importance of other metals, including iron, chromium, and zinc.

Although not discussed in this thesis, additional TD/A-ATOFMS measurements in Riverside, CA in August 2006 were conducted to follow-up on the detection of oligomeric species detected in August 2005, as discussed in Chapter 3. For this campaign, the A-ATOFMS mass sampling range was set to reach ~*m/z* 2000 rather than ~*m/z* 440 as was completed during SOAR-1 and SOAR-2. Preliminary results show the presence of potential oligomeric species from ~*m/z* 500 to 2000 in the positive ion mass spectra, as shown in Figure 9.3. Future work with this dataset should examine mixing states of these species, as well as their response to heating with the TD.

Cassandra Gaston has also been working to compare the presence of MSA-containing particles in Riverside, CA during SOAR-1, SOAR-2, summer 2006, and summer 2007. Similarly, Jessie Creamean is using unheated A-ATOFMS data from the summer of 2006 for an inter-annual (2005-2007) comparison of the size-resolved aerosol chemistry in Riverside, CA [*Creamean et al.*, 2009]. Preliminary work has shown excellent agreement between the mass spectra of Mexico City fresh biomass burning particles [*Moffet et al.*, 2008a] and SOAR-2 aged biomass burning particles heated to 230°C; Elizabeth Fitzgerald and Lindsay Hatch are planning to use the Mexico City and

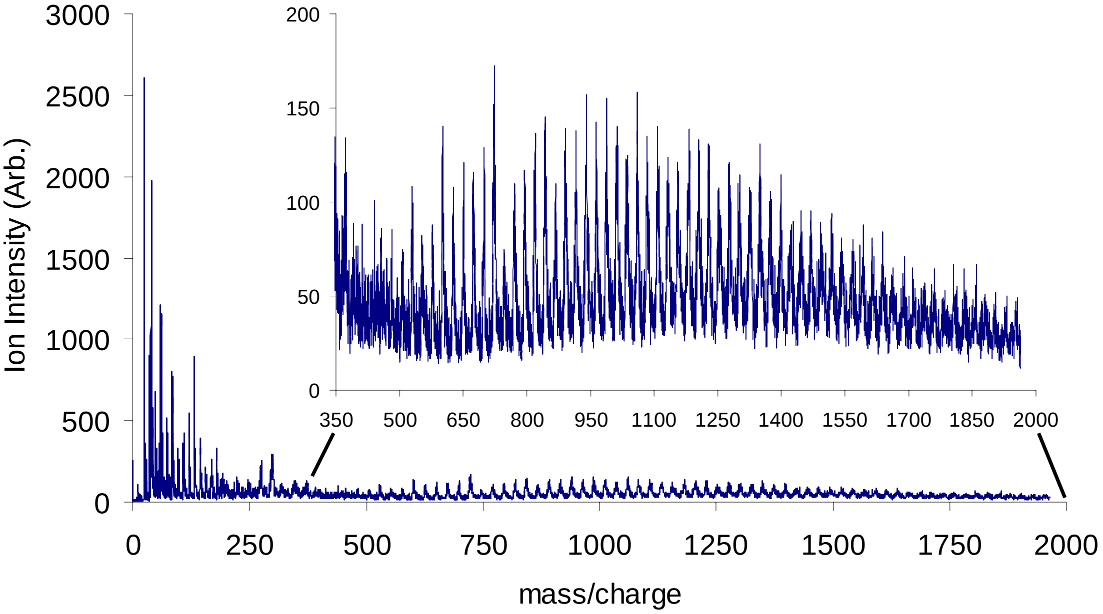

Figure 9.3. Single-particle positive ion mass spectrum from a 270 nm ambient particle detected in Riverside, CA in August 2006.

Riverside data to further examine the aging of biomass burning particles.

Due to the high time resolution of the A-ATOFMS, it was utilized in several experiments during ambient sampling in Riverside, CA. In collaboration with Dr. Susanne Hering and Dr. Gregory Lewis of Aerosol Dynamics Inc., John Holecek and I examined whether chemical changes occur in ambient particles with water condensation within a growth tube [*Hering and Stolzenburg*, 2005]. Preliminary analysis did not show major chemical changes; Melanie Zauscher is now using the growth tube to grow <50 nm particles for ATOFMS analysis. Cassandra Gaston has examined changes in ambient aerosol chemistry following concentration within the miniature versatile aerosol concentration enrichment system (mVACES) [*Ning et al.*, 2006] for SOAR-2 measurements taken in collaboration with Prof. Sioutas and Dr. Katherine Moore of the University of Southern California. Lindsay Hatch has examined TD-ATOFMS data from a smog chamber study of organonitrates in collaboration with Prof. Paul Ziemann at the University of California, San Diego. In addition, the A-ATOFMS was utilized to study SOA formation from the photooxidation of C_2H_2 by OH radicals in the presence of Suwannee River fulvic acid seed aerosol in collaboration with Dr. Rainer Volkamer, now at the University of Colorado, and Dr. Paul Ziemann at the University of California, San Diego [*Volkamer et al.*, 2009]. However, the inorganic signal, namely Na^+ and K^+, was found to overwhelm the positive ion organic carbon signal for the fulvic acid aerosols, as observed in previous LDI-MS studies [*Samburova et al.*, 2005]; the presence of sodium was likely due to the use of aqueous NaOH in the extraction of humic and fulvic acids from natural waters (http://ihss.gatech.edu/). Sulfate was the major species identified in the negative ion mass spectra, possibly due to the presence of organosulfates in the fulvic acid, as previously observed [*Romero and Oehme*, 2005]. Upon addition of the C_2H_2 to the seed aerosol, high mass (> *m/z* 200) species were not observed; only a small enhancement in the number of particles containing *m/z* -43(CH_3COH^-) was observed upon addition of C_2H_2.

As shown in this thesis, the TD-ATOFMS system can provide single-particle, mixing state-resolved volatility for various species. Chapters 4 and 5 examined the volatility of particle phase species, including amines, ammonium nitrate, and ammonium sulfate, for example. To use the SOAR TD-ATOFMS data to further understand the impacts of single-particle mixing state on volatility, I established collaboration with Dr. Kelly Barsanti at the National Center for Atmospheric Research. Through thermodynamic modeling, Dr. Barsanti has examined the gas/particle partitioning of various organic species [*Barsanti and Pankow*, 2004; *Barsanti and Pankow*, 2005; *Barsanti and Pankow*, 2006], including aminium salts [*Barsanti et al.*, 2009]. We developed a research plan to compare the volatility of different SOAR aerosol species using TD curves, such as those shown in Chapter 2, to that predicted from gas/particle partitioning modeling. Our overarching goal was to examined the impact of mixing state (chemical interactions) on gas/partitioning. In addition, we wanted to examine whether we could use thermodynamic parameters, such as vapor pressures and enthalpies of vaporization, to predict the partitioning of different chemical species from a given particle type considering the relative fractions of different species within the multi-component SOAR particles. Preliminary work has shown differences in the volatility of various sulfate-containing species, as discussed above, as well as nitrate-containing species. To identify compounds likely contributing to the A-ATOFMS organic carbon signal, data (speciated organics) from the thermal desorption aerosol gas chromatograph/mass spectrometer – flame ionization detector (TAG) instrument operated during SOAR will be considered [*Williams et al.*, 2009]. Further, using TD curves scaled for size bias (see Chapter 4), the rate of mass loss (per °C) may be examined. In addition, volatility differences due to annual, seasonal, diurnal, and air mass patterns may be examined using the TD/A-ATOFMS datasets from Riverside, CA; for example, using the methods described in Chapter 5, Figure 9.4 shows that more non-volatile aminium salts were present in the afternoon compared to the morning during SOAR-2. This collaboration with Dr. Barsanti has been taken over by Lindsay Hatch who also plans to complete laboratory TD studies to further understand the gas/particle partitioning observed during ambient studies.

A-ATOFMS measurements during ICE-L have led to important advances in our understanding of aerosol mixing state with altitude (Chapter 6), as well as aerosol interactions with ice (Chapter 7) and mixed phase clouds (Chapter 8). A summary of ATOFMS data from the ICE-L flights is given in Table 9.1. Several other ICE-L collaborative manuscripts are in preparation and are discussed briefly here. Paul Field at the UK Met Office modeled the ice nucleation occurring in two ICE-L wave clouds (during RF03 and RF04) with substantially different ice concentrations and has used aerosol chemistry data, including that from the A-ATOFMS, to help explain his observations. This manuscript has been submitted to the *Journal of Atmospheric Sciences*: Field, P.R., Heymsfield, A.J., Rogers, D.C., Stith, J., DeMott, P.J., Haimov, S., Murphy, S.M., Pratt, K.A., Twohy, C., Prather, K.A., Seinfeld, J.H., Shipway, B.J., Eidhammer, T., Prenni, A.J. Contrasting the ice nucleation in two lee wave clouds

Table 9.1. Summary of A-ATOFMS data during ICE-L flights.

Flight	Date	Cloud Type	Primary Particle Types	Notes
TF02	11/1/2007	N/A	OC, Biomass	No CVI sampling, some interstitial aerosol
TF03	11/5/2007	N/A	OC, Biomass	Short CVI test, low altitude cloud
TF04	12/12/2007	N/A	Biomass, Sulfate	Calibration flight
RF01	11/7/2007	Wave	Dust & Bio in cloud	Pratt et al. 2009 (Nature Geoscience)
RF02	11/13/2007	Wave	Salts (Cloud), Biomass (Clear)	Poor clear air characterization
RF03	11/16/2007	Wave	Salts (Cloud), Sulfate (Clear)	Pratt et al. 2009 (JGR)
RF04	11/18/2007	Wave	Salts (Cloud), Sulfate (Clear)	Field et al. 2009 (JAS)
RF05	11/20/2007	Upslope	Biomass, OC, ECOC	Aged particles; Iced inlet during flight
RF06	11/29/2007	Wave	Biomass	
RF07	11/30/2007	Upslope	OC, Aromatic	
RF08	12/4/2007	Wave	N/A	Poor statistics
RF09	12/10/2007	Wave	Biomass, Aromatic	
RF10	12/11/2007	Upslope	Biomass, Aromatic	
RF11	12/13/2007	Wave	Salts, Biomass	
RF12	12/16/2007	Wave	Biomass	Pratt et al. 2009 (JAS)

Morning (Aug. 12, 3:50 – 6:20 PST)

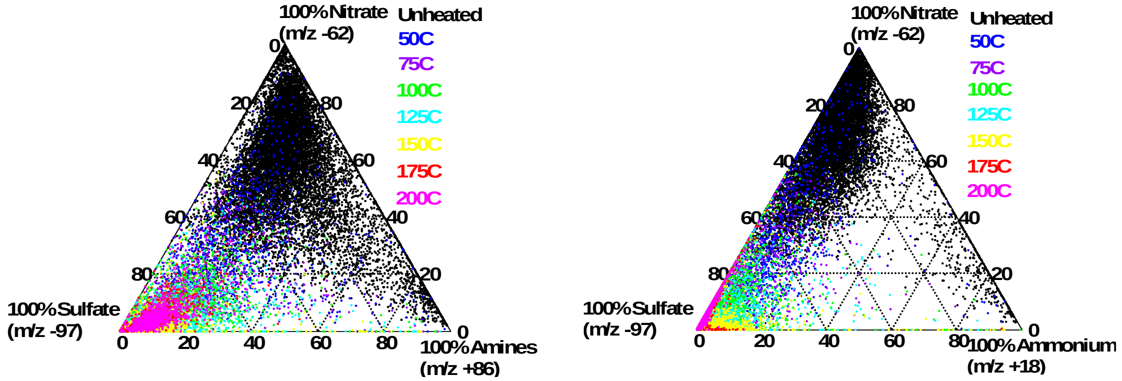

Afternoon (Aug. 12, 17:10 – 19:40 PST)

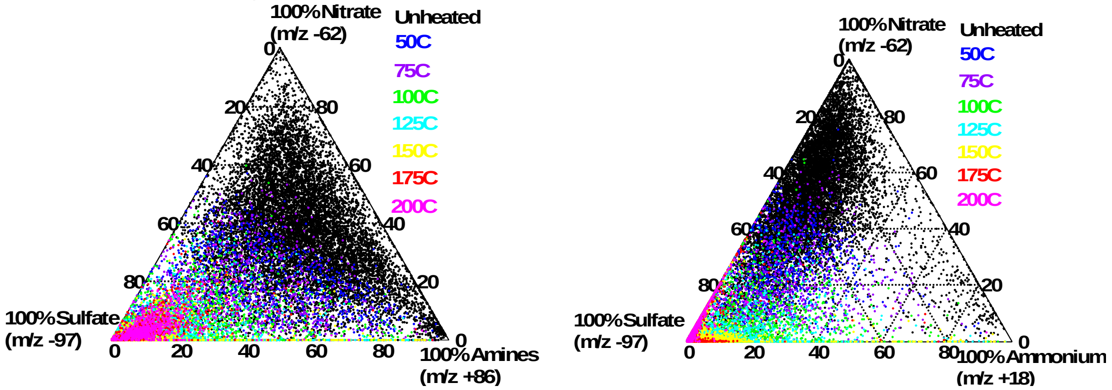

Figure 9.4. Ternary plots comparing nitrate and sulfate associations with amines and ammonium in the morning and afternoon during SOAR-1 for aged organic carbon particles.

observed during the ICE-L campaign. Similarly, Trude Eidhammer at the National Center for Atmospheric Research used aerosol chemistry data, included that from the A-ATOFMS, to define the aerosols in a heterogeneous ice nucleation parameterization which was used to predict ice concentrations observed in an orographic wave cloud during ICE-L (RF04); this manuscript, titled “Ice initiation by aerosol particles: Measured and predicted ice nuclei concentrations versus measured ice crystal concentrations in an orographic wave cloud”, has been submitted to the *Journal of Atmospheric Sciences*.

During research flight #12 (RF12) during ICE-L, aged biomass burning particles were identified within an orographic wave cloud influenced by homogeneous freezing over Wyoming using a counterflow virtual impactor (CVI) in series with the A-ATOFMS. These biomass burning particles were characterized by elemental carbon, organic carbon, potassium, potassium-sulfate clusters, levoglucosan, oxalic acid, ammonium, sulfate, and sulfuric acid in particular. To further characterize these particles and compare the aerosol chemistry instrumentation aboard the C-130 aircraft during ICE-L, I am currently comparing results from electron microscopy, a single-particle soot photometer, a compact time-of-flight aerosol mass spectrometer (C-ToF-AMS), and the A-ATOFMS in collaboration with Prof. Cynthia Twohy (Oregon State University), Dr. R. Subramanian (Droplet Measurement Technologies), and Dr. Shane Murphy and Prof. John Seinfeld (California Institute of Technology). In this manuscript, I will present a comparison between the cloud ice residues and surrounding clear air particles with detailed chemical characterization provided through size-resolved single-particle chemical composition, non-refractory aerosol mass concentration, and single-particle black carbon number and mass concentration data. In the clear air, preliminary electron microscopy and A-ATOFMS results show excellent agreement with the relative fractions of the observed particle types within errors with the biomass and sulfate particle types contributing ~1/3 each. The relative fraction of different particles types, as observed by the A-ATOFMS, are shown in Figure 9.5 for the clear air particles and ice residues. This work is also in collaboration with Dr. Andrew Heymsfield at the National Center for Atmospheric Research who has helped with interpretation of the cloud probe data. In addition, Dr. James Hudson at the Desert Research Institute has provided clear air cloud condensation nuclei (CCN) concentrations at different supersaturations for a comparison of measured vs. predicted CCN based on the measured aerosol chemistry. This manuscript, titled "In-situ chemical characterization of aged biomass burning aerosols impacting cold wave clouds", is in preparation for submission.

During ICE-L, the smoke plumes of two Wyoming Bureau of Land Management (BLM) prescribed burns were intercepted aboard C-130 aircraft. Prescribed fires provide the opportunity for a detailed characterization of both burn conditions and consequent emissions in a real-world setting, combining the advantages of studying wildfires and laboratory fires. The young smoke plumes were investigated in detail utilizing a unique suite of real-time aerosol instrumentation, measuring size-resolved single-particle chemical composition, size-resolved non-refractory mass concentrations, and size-resolved single-particle soot number and mass concentrations in collaboration with Dr. R. Subramanian (Droplet Measurement Technologies) and Dr. Shane Murphy and Prof. John Seinfeld (California Institute of Technology). Concurrent measurements of CCN

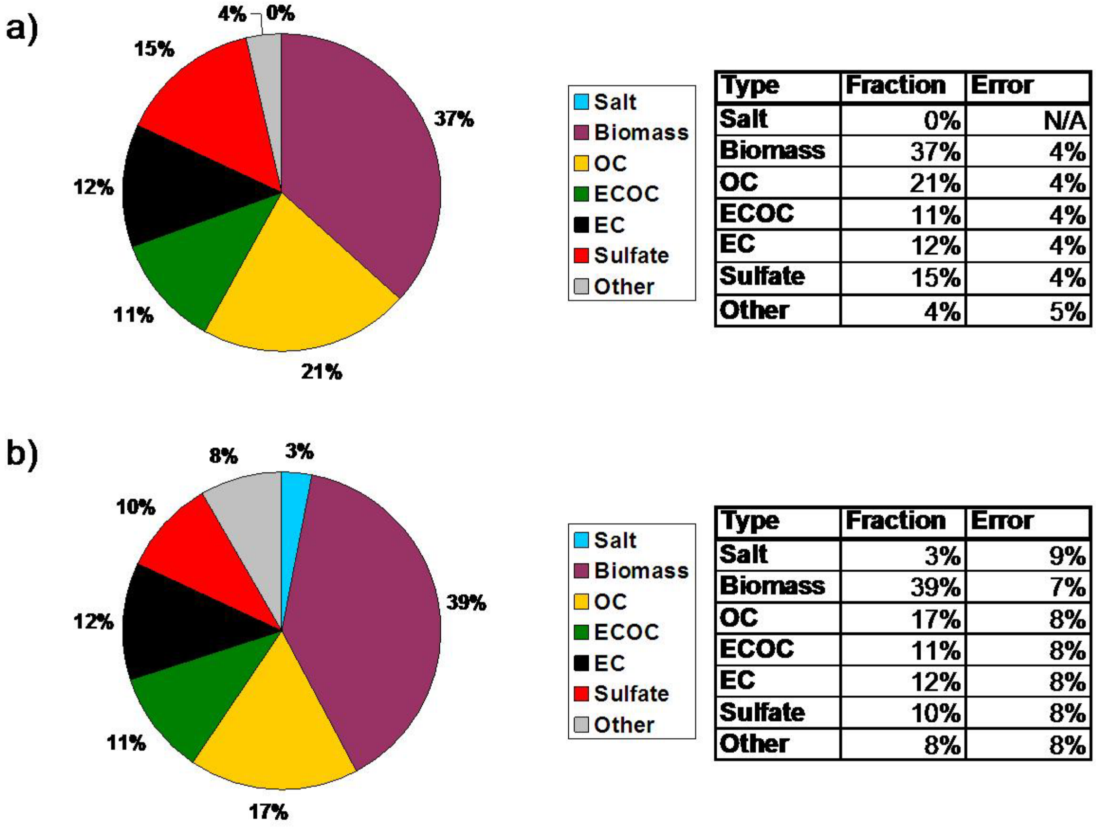

a)

Type	Fraction	Error
Salt	0%	N/A
Biomass	37%	4%
OC	21%	4%
ECOC	11%	4%
EC	12%	4%
Sulfate	15%	4%
Other	4%	5%

b)

Type	Fraction	Error
Salt	3%	9%
Biomass	39%	7%
OC	17%	8%
ECOC	11%	8%
EC	12%	8%
Sulfate	10%	8%
Other	8%	8%

Figure 9.5. Relative fraction of A-ATOFMS particle types observed during RF12 for a) clear air particles within the same equivalent potential temperature range of the orographic ice cloud and b) ice particle residues influenced by homogeneous freezing.

and ice nuclei (IN) by Dr. Gregory Kok (Droplet Measurement Technologies) and Dr. Paul DeMott (Colorado State University) have allowed an investigation of possible cloud impacts with knowledge of size-resolved chemical composition. Due in part to high particle concentrations, IN concentrations observed within these smoke plumes were among the highest measured during ICE-L. In particular, this study benefits from knowledge, which I obtained through the Wyoming BLM, regarding burn conditions and fuel on the ground at the times of the smoke plume sampling. Preliminary results show that the RF01 smoke plume had aged for ~17-30 minutes prior to sampling compared to an aging time of ~3 min to 1.3 hours for the RF03 smoke plume sampling. Figure 9.6 shows the size-resolved particle number concentrations during sampling of these two smoke plumes. This manuscript, in preparation for submission to the *Journal of Geophysical Research*, profiles these two smoke plumes and provides a detailed discussion of the chemical composition of these biomass burning aerosols.

As stated in Chapter 7, the IN number concentrations observed during RF01 were among the top 2% of those measured from cloud residues during all ICE-L wave cloud sampling. During periods of other ICE-L concurrent cloud sampling of the continuous flow diffusion chamber (CFDC) and A-ATOFMS, IN concentrations were generally less than 1 per L (personal communication, Dr. Paul DeMott, Colorado State University) likely due to significant contributions from homogeneous freezing. Thus, Dr. DeMott and I are working to establish correlations between IN number concentrations and aerosol chemistry, as measured by the A-ATOFMS and C-ToF-AMS (Dr. Shane Murphy, California Institute of Technology), during all periods of sampling from take-off to in-cloud CVI sampling. These comparisons encompass data from RF01, RF03, RF04,

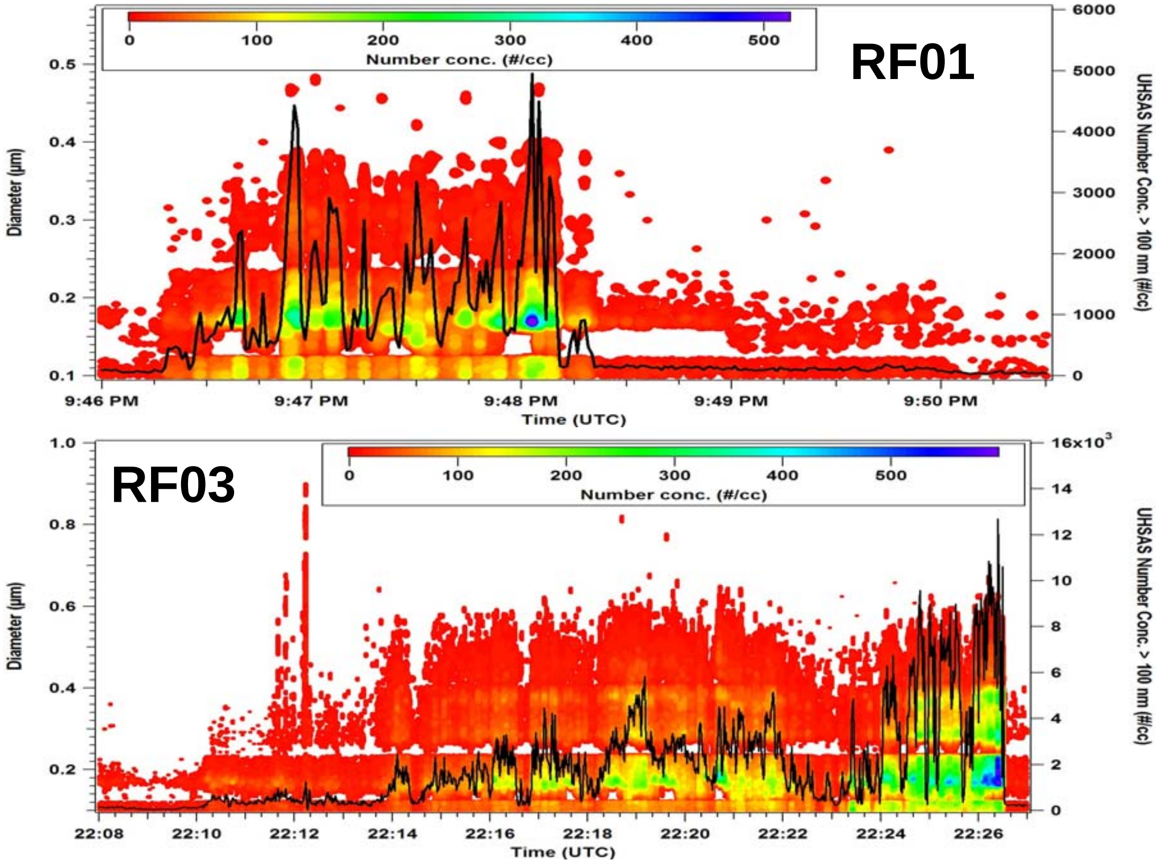

Figure 9.6. Temporal profiles of the size-resolved (colorscale) and total (black line) particle number concentrations of the two prescribed burn smoke plumes intercepted during RF01 and RF03. This data from the ultra high sensitivity aerosol spectrometer (UHSAS) was provided by the NCAR Earth Observing Laboratory (http://data.eol.ucar.edu).

RF06, RF11, and RF12. RF08 was not utilized due to low A-ATOFMS statistics, and other flights were eliminated due to CFDC operating issues. At the annual American Geophysical Union (AGU) meeting in December 2008, I discussed the preliminary results of CFDC-ATOFMS comparisons (Figure 9.7), which showed salts (Na-K-Cl) and particles containing more chloride, to be correlated with low IN concentrations, as expected [*Andreae and Rosenfeld*, 2008]. In addition, elevated IN concentrations were observed when organic carbon particles with oxalic acid were observed by the A-ATOFMS (Figure 9.7c) and predicted in laboratory studies by Zobrist et al. [2006]. Current work involves binning the CFDC processing temperature, incorporating C-ToF-AMS non-refractory mass concentrations, and using peak area thresholds in addition to peak areas to identify particles containing any amount of a certain species.

Dr. Roy Rasmussen and Dr. Jeff Stith at the National Center for Atmospheric Research have indicated interest in modeling the upslope clouds encountered during ICE-L (RF05, RF07, and RF10) and incorporating real-time aerosol chemistry results measured by the A-ATOFMS and C-ToF-AMS. However, Cynthia Twohy (Oregon State University) has expressed caution in interpreting the cloud residue results from these flights as the CVI is not well characterized for these types of clouds, particularly under icing conditions, such as those observed during RF05. Further, an in-depth comparison of CVI residues concentrations and cloud droplet/ice crystal concentrations must be completed. Nonetheless, I present here a preliminary comparison of the primarily supercooled liquid cloud residues from the upslope clouds encountered during RF05 as measured by the C-ToF-AMS (Dr. Shane Murphy and Prof. John Seinfeld, California Institute of Technology) and A-ATOFMS. The parallel measured allowed the

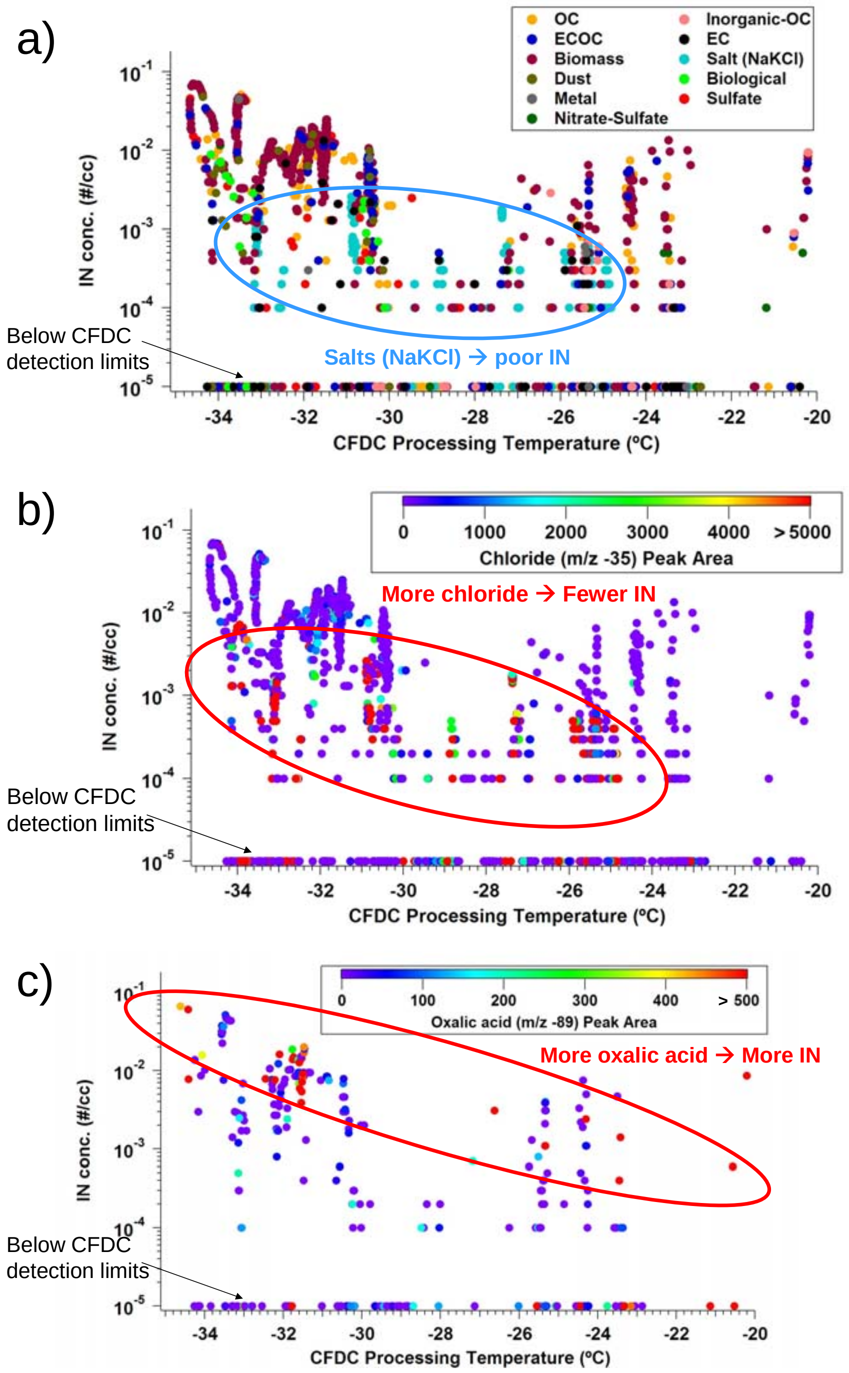

Figure 9.7. Correlations between ice nuclei (IN) concentrations and aerosol chemistry from CFDC and A-ATOFMS measurements. For individual particles, IN concentration as a function of CFDC processing temperature is plotted as a function of aerosol chemistry for a particular sampling time. IN concentrations below CFDC detection limits are shown at $10^{-5}/cm^3$ for visualization purposes. Aerosol chemistry is plotted as a function of a) particle type, b) chloride peak area for all particles, and c) oxalic acid peak area for organic carbon particles.

mass concentrations of non-refractory species and mixing state of individual cloud residues (both refractory and non-refractory species) to be examined in real-time. Within these boundary layer clouds, residues were found to be highly aged with sulfate and nitrate internally mixed with nearly all particles, including mineral dust, as shown in Figure 9.8. Biomass burning, vehicles, and agriculture were found to be the dominant sources of the cloud residues.

Preliminary ICE-L data analyses of other flights show potentially interesting findings. The orographic wave clouds studied during RF06 are suggested to be similar to those observed in RF12 in that IN concentrations were low (personal communication, Dr. Paul DeMott, Colorado State University), and the mixed phase clouds were impacted by biomass burning. Interestingly, both clear air and cloud residue particles during RF07 (upslope cloud) and RF09 (wave cloud) are impacted by aromatic-containing particles, potentially originating from pesticides [*Whiteaker and Prather*, 2003], wood burning [*Bente et al.*, 2006], or aircraft emissions [*Agrawal et al.*, 2008], for example. In addition, ground-based A-ATOFMS measurements on the tarmac at the Rocky Mountain Metropolitan Airport (RMMA) were made to investigate the impact of small aircraft on air pollution. During sampling, short, rapid increases in particle concentrations, likely due to aircraft or helicopter emissions, were observed, as shown in Figure 2.9. Aviation gasoline is the largest single source of airborne Pb emissions in the US [*Murphy et al.*, 2007]. In particular, one hundred octane low-lead (100LL) fuel, containing 2.12 grams of Pb per gallon is used by small piston engine aircraft [*US EPA* 2008]. Further, studies of the weekly cycle of particulate Pb show increased levels on weekends, likely due to recreational aircraft emissions [*Murphy et al.*, 2008]. Jet engine emissions have been

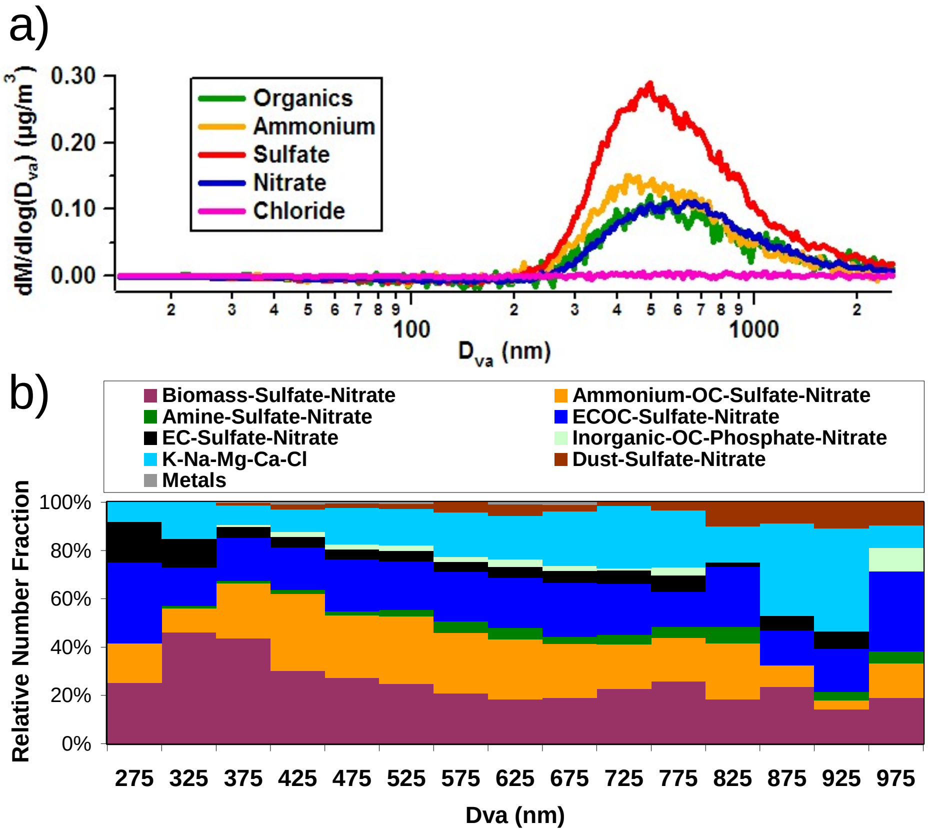

Figure 9.8. a) C-ToF-AMS size-resolved mass concentrations of non-refractory organics, ammonium, sulfate, nitrate, and chloride for RF05 cloud residues. b) A-ATOFMS size-resolved mixing state of individual RF05 cloud residues. Note: C-ToF-AMS figure provided by Dr. Shane Murphy and Prof. John Seinfeld, California Institute of Technology.

studied significantly more than small aircraft emissions; however, the leaded fuel used by these small aircraft poses health risks [*Florea and Büsselberg*, 2006], particularly due to the fact that they are primarily operated at small airports near residential areas. The mass spectral signature of an example Pb-containing particle observed during sampling at the RMMA is shown in Figure 9.9. Using air traffic control audio files, the type of aircraft and time of take-off/landing can be determined for a specific time; comparison with the observed aerosol spikes may provide additional confirmation of aircraft emissions. In addition, I acquired samples of 100LL and JetA fuel to characterize the aircraft fuels used at the RMMA and compare the mass spectral signatures to the aerosol chemistry observed at the airport, similar to that completed for vehicle emissions by Spencer et al. [2006].

Several laboratory studies have been developed as a result of the ICE-L results described in this thesis. As discussed in Chapter 7, Cassandra Gaston and I ran *Pseudomonas syringae*, known bacterial ice nuclei [*Vali et al.*, 1976], into the A-ATOFMS to characterize its mass spectral signature, which was found to be similar to those of the biological particles encountered during ICE-L. While several single-particle mass spectrometry studies have investigated biological particles [*Russell*, 2009], it is yet to be known whether the ATOFMS can distinguish between plant material, fungal spores, pollen, algae, and bacteria, for example, based on mass spectral signatures. For example, using laser microprobe mass spectrometry, Seydel et al [1992] used Na^+/K^+ ratios to examine bacterial viability. The ability to distinguish in real-time the type of bioaerosol present and whether it is dead or alive would be helpful in increasing our understanding of the atmospheric cycling of primary biological particles [*Deguillaume et al.*, 2008].

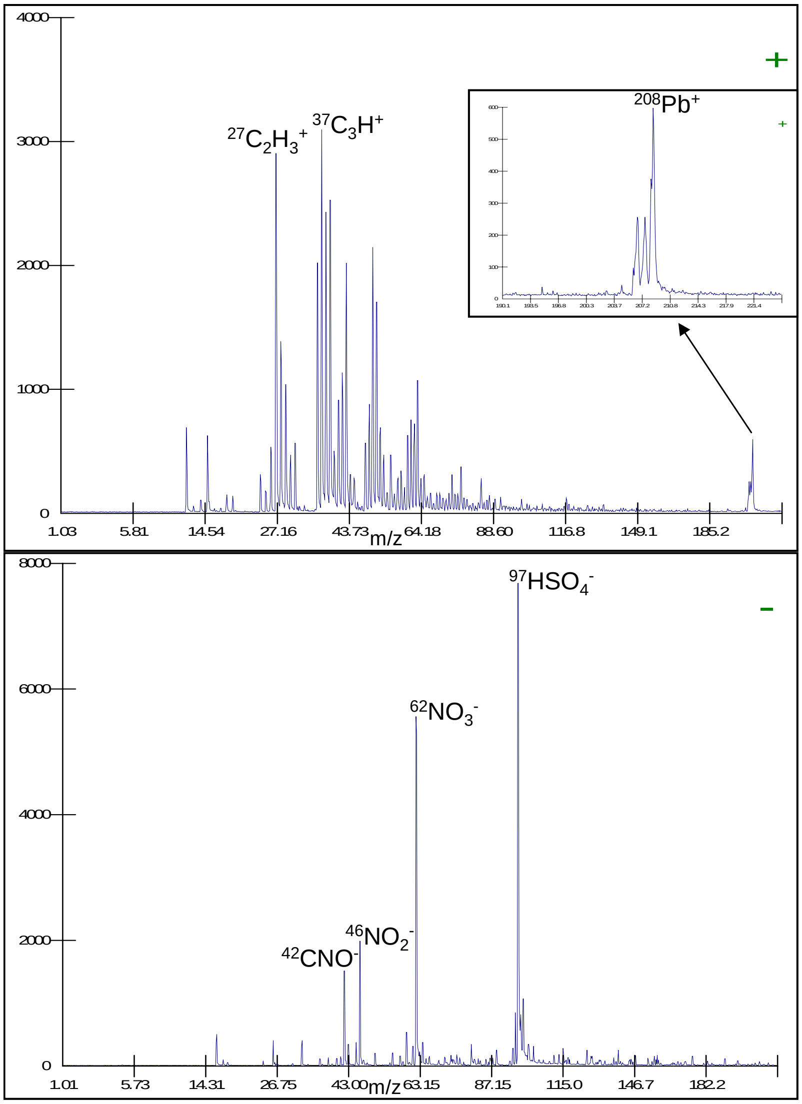

Figure 9.9. Mass spectral signature of a single Pb-containing particle sampled at the Rocky Mountain Metropolitan Airport.

While presenting the results of the impact of dry lakebed salts on clouds (Chapter 8) at the 10th International Conference on Salt Lake Research in 2008, I was approached by Joel Gilbert and Prof. Tom Gill from the University of Texas at El Paso regarding some interesting "Milky Rain" samples acquired in southwestern New Mexico in January 2008. Based on ICP-MS analysis and other data, they suggested that the rain may have been influenced by dust from nearby playas. Cassandra Gaston and I used the A-ATOFMS to examine the rainwater samples, as well as soil samples from the Willcox and Lordsburg Playas. With the exception of one rainwater sample (AZ99), all milky rainwater samples contained residues with similar mass spectral signatures to those of the Willcox and Lordsburg Playa dust; control rainwater samples did not match these playa samples. In particular, the milky rain residues and playa dust were characterized by Na, K, Ca, Mg, aluminosilicates, and Cl, as well as some organic nitrogen and phosphate. In addition, Kaitlyn Suski completed ion chromatography analysis on the rainwater samples and found the presence of sulfate, which was dissolved in the rainwater and thus not present on the residues analyzed by the A-ATOFMS. I am working with Joel Gilbert to include this analysis in an overview manuscript about the "Milky Rain" event.

Similarly, Cassandra Gaston, Kaitlyn Suski, and I have been working together to investigate the aerosol chemistry and correlated CCN properties of playa dust. Previous studies of the CCN ability of playa dust have assumed particle chemistry [*Koehler et al.*, 2007]; however, we have observed a range of CCN abilities (κ = ~0.002 to 0.84 using the methodology of Petters and Kreidenweis [2007]) for different playa samples obtained from Prof. Tom Gill (University of Texas at El Paso), Wes Thompson (BIO-WEST, Inc.), Dr. Ryan Sullivan (now at Colorado State University), and Prof. Kim Prather. These different CCN abilities appear to be correlated with aerosol chemistry, measured using the A-ATOFMS and IC, which show differences in soluble volume fractions and silicate content, for example.

To conclude, the research described in this dissertation has provided significant insight into our understanding of the impacts and mixing states of atmospheric particles. Beyond the work shown above, additional development of the A-ATOFMS should include redesign of the laser alignment system for increased sensitivity in tuning the laser beam, a faster desorption/ionization laser and software/computer upgrade for faster data acquisition (providing even higher time resolution, which is important for cloud sampling), and further miniaturization to allow easy integration into small aircraft, such as the CIRPAS Twin Otter aircraft, where space is limited. In addition, to further our understanding of the impact of aerosols on the hydrologic cycle, the chemistry of cloud residues, as done during ICE-L, should be coupled with precipitation measurements, such as those just completed by Andrew Ault and Jessie Creamean during the 2009 CalSeed study.

9.5 References

United State Environmental Protection Agency. Lead emissions from the use of leaded aviation gasoline in the United States: Technical support document, EPA420-R-08-020, 2008.

Agrawal, H., A.A. Sawant, K. Jansen, J.W. Miller, and D.R. Cocker (2008), Characterization of chemical and particulate emissions from aircraft engines, *Atmos. Environ.*, *42*(4380-4392.

Andreae, M.O., and D. Rosenfeld (2008), Aerosol-cloud-precipitation interactions. Part 1. The nature and sources of cloud-active aerosols, *Earth-Science Rev.*, *89*(13-41.

Barsanti, K.C., P.H. McMurry, and J.N. Smith (2009), The potential contribution of organic salts to new particle growth, *Atmos. Chem. Phys.*, *9*(2949-2957.

Barsanti, K.C., and J.F. Pankow (2004), Thermodynamics of the formation of atmospheric organic particulate matter by accretion reactions - Part 1: aldehydes and ketones, *Atmos. Environ.*, *38*(4371-4382.

Barsanti, K.C., and J.F. Pankow (2005), Thermodynamics of the formation of atmospheric organic particulate matter by accretion reactions - Part 2: dialdehydes, methylglyoxal, and diketones, *Atmos. Environ.*, *39*(35), 6597-6607.

Barsanti, K.C., and J.F. Pankow (2006), Thermodynamics of the formation of atmospheric organic particulate matter by accretion reactions - Part 3: carboxylic and dicarboxylic acids, *Atmos. Environ.*, *40*(34), 6676-6686.

Bente, M., T. Adam, T. Ferge, S. Gallavardin, M. Sklorz, T. Streibel, and R. Zimmermann (2006), An on-line aerosol laser mass spectrometer with three, easily interchangeable laser based ionisation methods for characterisation of inorganic and aromatic compounds on particles, *Int. J. Mass Spectrom.*, *258*(86-94.

Creamean, J.M., K.A. Pratt, A.P. Ault, X. Qin, C.J. Gaston, and K.A. Prather (2009), Inter-annual comparison of real-time, single-particle ambient aerosol measurements using ATOFMS in Riverside, CA, *Aerosol Sci. Technol.*, *In Preparation.*(

Deguillaume, L., M. Leriche, P. Amato, P.A. Ariya, A.-M. Delort, U. Poschl, N. Chaumerliac, H. Bauer, A.I. Flossmann, and C.E. Morris (2008), Microbiology and atmospheric processes: chemical interaction of primary biological aerosols, *Biogeosciences*, *5*(1073-1084.

Florea, A.-M., and D. Büsselberg (2006), Occurrence, use and potential toxic effects of metals and metal compounds, *BioMetals*, *19*(419-427.

Gaston, C.J., K.A. Pratt, X. Qin, and K.A. Prather (2009), Real-time detection and mixing-state of methansulfonate in single aerosol particles at an inland urban location during a phytoplankton bloom, *Environ. Sci. Technol.*, *In Preparation*(

Gross, D.S., M.E. Gälli, M. Kalberer, A.S.H. Prevot, J. Dommen, M.R. Alfarra, J. Duplissy, K. Gaeggeler, A. Gascho, A. Metzger, and U. Baltensperger (2006), Real time measurement of oligomeric species in secondary organic aerosol with the aerosol time-of-flight mass spectrometer, *Anal. Chem.*, *78*(7), 2130-2137.

Hering, S.V., and M.R. Stolzenburg (2005), A method for particle size amplification by water condensation in a laminar, thermally diffusive flow, *Aerosol Sci. Technol.*, *39*(5), 428-436.

Johnson, G.R., Z. Ristovski, and L. Morawska (2004), Method for measuring the hygroscopic behaviour of lower volatility fractions in an internally mixed aerosol, *J. Aerosol Sci.*, *35*(4), 443-455.

Johnson, G.R., Z.D. Ristovski, B. D'Anna, and L. Morawska (2005), Hygroscopic behavior of partially volatilized coastal marine aerosols using the volatilization and humidification tandem differential mobility analyzer technique, *J. Geophys. Res.*, *110*(D20).

Koehler, K.A., S.M. Kreidenweis, P.J. DeMott, A.J. Prenni, and M.D. Petters (2007), Potential impact of Owens (dry) Lake dust on warm and cold cloud formation, *J. Geophys. Res.*, *112*(doi:10.1029/2007JD008413.

Moffet, R.C., B. de Foy, L.T. Molina, M.J. Molina, and K.A. Prather (2008a), Measurement of ambient aerosols in northern Mexico City by single particle mass spectrometry, *Atmos. Chem. Phys.*, *8*(4499-4516.

Moffet, R.C., X. Qin, T. Rebotier, H. Furutani, and K.A. Prather (2008b), Chemically segregated optical and microphysical properties of ambient aerosols measured in a single-particle mass spectrometer, *J. Geophys. Res.*, *113*(doi:10.1029/2007JD009393.

Murphy, D.M., S.L. Capps, J.S. Daniel, G.J. Frost, and W.H. White (2008), Weekly patterns of aerosol in the United States, *Atmos. Chem. Phys.*, *8*(2729-2739.

Murphy, D.M., P.K. Hudson, D.J. Cziczo, S. Gallavardin, K.D. Froyd, M.V. Johnston, A.M. Middlebrook, M.S. Reinard, D.S. Thomson, T. Thornberry, and A.S. Wexler (2007), Distribution of lead in single atmospheric particles, *Atmos. Chem. Phys.*, *7*(3195-3210.

Neubauer, K.R., M.V. Johnston, and A.S. Wexler (1998), Humidity effects on the mass spectra of single aerosol particles, *Atmos. Environ.*, *32*(14/15), 2521-2529.

Ning, Z., K.F. Moore, A. Polidori, and C. Sioutas (2006), Field validation of the new miniature versatile aerosol concentration enrichment system (mVACES), *Aerosol Sci. Technol.*, *40*(1098-1110.

Petters, M.D., and S.M. Kreidenweis (2007), A single parameter representation of hygroscopic growth and cloud condensation nucleus activity, *Atmos. Chem. Phys.*, *7*(8), 1961-1971.

Qin, X., L.G. Shields, S.M. Toner, K.A. Pratt, and K.A. Prather (2009), Seasonal comparisons of the single particle mixing state in Riverside, CA during the SOAR 2005 campaign, *Aerosol Sci. Technol.*, *In preparation.*(

Romero, F., and M. Oehme (2005), Organosulfates - A new component of humic-like substances in atmospheric aerosols? *J. Atmos. Chem.*, *52*(3), 283-294.

Russell, S.C. (2009), Microorganism characterization by single particle mass spectrometry, *Mass Spectrom. Rev.*, *28*(376-387.

Samburova, V., R. Zenobi, and M. Kalberer (2005), Characterization of high molecular weight compounds in urban atmospheric particles, *Atmos. Chem. Phys.*, *5*(2163-2170.

Seydel, U., M. Haas, E.T. Rietschel, and B. Lindner (1992), Laser microprobe mass spectrometry of individual bacterial organisms and of isolated bacterial compounds: a tool in microbiology, *J. Microbio. Methods*, *15*(167-183.

Spencer, M.T., L.G. Shields, D.A. Sodeman, S.M. Toner, and K.A. Prather (2006), Comparison of oil and fuel particle chemical signatures with particle emissions from heavy and light duty vehicles, *Atmos. Environ.*, *40*(27), 5224-5235.

Vali, G., M. Christensen, R.W. Fresh, E.L. Galyan, L.R. Maki, and R.C. Schnell (1976), Biogenic Ice Nuclei 2. Bacterial Sources, *J. Atmos. Sci.*, *33*(8), 1565-1570.

Volkamer, R., P.J. Ziemann, and M.J. Molina (2009), Secondary organic aerosol formation from acetylene (C_2H_2): seed effect on SOA yields due to organic photochemistry in the aerosol aqueous phase, *Atmos. Chem. Phys.*, *9*(1907-1928.

Whiteaker, J.R., and K.A. Prather (2003), Detection of pesticide residues on individual particles, *Anal. Chem.*, *75*(1), 49-56.

Williams, B.J., A.H. Goldstein, N.M. Kreisberg, S.V. Hering, K.A. Prather, L. Shields, X. Qin, J.J. Schauer, D.C. Snyder, D. Worsnop, J.L. Jimenez, and K.S. Docherty (2009), Hourly speciated organic aerosol composition in southern California, *In Preparation*(

Zelenyuk, A., D. Imre, and L.A. Cuadra-Rodriguez (2006), Evaporation of water from particles in the aerodynamic lens inlet: An experimental study, *Anal. Chem.*, *78*(19), 6942-6947.

Zobrist, B., C. Marcolli, T. Koop, B.P. Luo, D.M. Murphy, U. Lohmann, A.A. Zardini, U.K. Krieger, T. Corti, D.J. Cziczo, S. Fueglistaler, P.K. Hudson, D.S. Thomson, and T. Peter (2006), Oxalic acid as a heterogeneous ice nucleus in the upper troposphere and its indirect aerosol effect, *Atmos. Chem. Phys.*, *6*(3115-3129.